



Efficient FRET-assisted  
computational structural modelling

Inaugural-Dissertation

zur Erlangung des Doktorgrades  
der Mathematisch-Naturwissenschaftlichen Fakultät  
der Heinrich-Heine-Universität Düsseldorf

vorlegt von

**Mykola Dimura**  
aus Kiew

Düsseldorf, Juli 2019

Institute of Molecular Physical Chemistry,  
Heinrich-Heine-University Düsseldorf

Institute for Pharmaceutical and Medicinal Chemistry,  
Heinrich-Heine-University Düsseldorf

Printed with the permission of  
Department of Mathematics and Natural Sciences  
Heinrich-Heine-University Düsseldorf

1. Referee: Prof. Dr. C. A. M. Seidel
2. Referee: Prof. Dr. H. Gohlke

Date of oral examination: 26.05.2020



*To my father and Roma*

## Abstract

Structures of biomacromolecules and their complexes are often key to understanding the molecules' functions and underlying mechanisms. For large multidomain proteins, biomacromolecular complexes, partially unstructured proteins, and systems with lowly populated conformational states, experimental structure determination remains challenging. Computational structural modelling techniques aim at elucidation of molecular mechanisms in biological systems, but trade-offs between the required computational power and accuracy of obtained models still remain prohibitive. Förster resonance energy transfer (FRET) experiments yield state-specific structural information on complex constructs, including very dynamic systems with short-lived states and for time scales down to microseconds. However, FRET experiments need to be combined with computer simulations to solve the issue that FRET data is usually too sparse to cover all structural details. This hybrid approach opens up a possibility for a rational and formalized experiment design aimed at highest accuracy and detail with minimal possible effort and expense.

To realize the potential of FRET-assisted hybrid modelling approach, in this work, efforts were focused on two areas: avoiding unnecessary experimental work by prioritizing the most informative measurements and using the obtained experimental data as efficiently as possible. Construction of a detailed structural model requires data from multiple FRET experiments. Automated selection of most informative FRET pairs based on the computational structural modelling was implemented in order to minimize the number of measurements. Methods to enhance computational modelling using FRET data were implemented for simulations at different levels of coarse-graining, from FRET-restrained all-atom Molecular Dynamics simulations to FRET-guided normal mode-based coarse-grained geometric simulations and FRET-restrained rigid body sampling. In order to assess the accuracy of produced models, quantitative quality estimate based on careful cross-validation analysis was implemented for FRET-assisted structures. Thorough propagation of experimental errors onto structural modelling results enabled reliable precision estimation and opened up a possibility to verify error estimation procedures by benchmarking against yardstick molecules like double-stranded RNA. These methods were proven in benchmarks with simulated fluorescence data and in experiments with T4 lysozyme protein, where resolution of  $\sim 3$  Å was achieved for FRET-selected conformers, and the structural mechanism behind the enzyme's catalytic function was demonstrated. Study of human guanylate binding protein 1 (hGBP1) allowed to connect its conformational dynamics to immune response mechanism. Investigation of chromatin fibre complex helped understanding the mechanisms behind the gene access regulation. These studies establish a streamlined FRET-assisted computational structural modelling procedure and reliable quality assessment of the results. Synergetic combination of FRET experiments and computational structural modelling techniques reveal mechanisms of biomolecular interactions at an otherwise inaccessible detail and scope.

## Acknowledgments

I'm deeply grateful to my supervisor Prof. Dr. Claus A.M. Seidel for the opportunity to contribute to the development of world class projects in the field of fluorescence, together with the domain-leading scientists and with an access to cutting edge equipment. I'm also most grateful to my second supervisor Prof. Dr. Holger Gohlke for the possibility to learn the most advanced computational modelling and supercomputing techniques and for the introduction to the practices of effective work and collaboration management. I would like to thank both of my supervisors for the advice during my first steps as a researcher and invaluable scientific contributions to our research projects.

I am grateful to Dr. Thomas Peulen for his kind willingness to discuss all kind of scientific topics that I've been puzzling with over the years and for being an excellent work partner and co-author in all of our projects. My deepest appreciation goes to Dr. Suren Felekyan for our work on T4L, Chromatin, Nucleosome, TGR5 and projects. I thank Dr. Christian Hanke for work on Quantitative FRET and other projects, proofreading of this thesis, his efforts to maintain the functioning of supercomputing cluster and for being a very friendly office mate. I am grateful to Dr. Oleg Opanasyuk for his help and discussions on all kind of scientific and mathematic topics. I thank Aishwaria Prakash for our joint work on Quantitative FRET project. I thank Prof. Dr. Hugo Sanabria, Dr. Dmytro Rodnin, Dr. Katharina Hemmen and Dr. Ralf Kühnemuth for the work on T4L paper and providing experimental data for the "Automated FRET" manuscript. I am grateful to Dr. Annemarie Greife, Dr. Qijun Ma and Dr. Christoph Gertzen for the collaboration on the TGR5 article. I thank Dr. Sinan Kilic, Prof. Dr. Gaurav Arya, Prof. Dr. Beat Fierz and Dr. Hayk Vardanyan for the work on Chromatin project. I am grateful to Peter Sippel and Stephan Schott for maintaining flawless functioning of the computer cluster. I am grateful to Milana Popara for proof-reading this dissertation.

Finally, I offer my deepest appreciation to Olga Doroshenko for the work on Chromatin project, and, especially, for her support and encouragement in all this time.

**This thesis is based on the following articles and manuscripts:****Published articles**

- **M. Dimura**, T.-O. Peulen, C. A. Hanke, A. Prakash, H. Gohlke, C.A.M. Seidel, 2016. “Quantitative FRET studies and integrative modelling unravel the structure and dynamics of biomolecular systems”. *Current Opinion in Structural Biology*, 40, pp.163-185. **(Supplement A)**
- H. Sanabria, D. Rodnin, K. Hemmen, T.-O. Peulen, S. Felekyan, M.R. Fleissner, **M. Dimura**, F. Koberling, R. Kühnemuth, W. Hubbell, H. Gohlke, C.A.M. Seidel, 2020 „Resolving dynamics and function of transient states in single enzyme molecules“. *Nature Communications* 11(1), pp.1-15. **(Supplement B)**
- S. Kilic, S. Felekyan, O. Doroshenko, I. Boichenko, **M. Dimura**, H. Vardanyan, L.C. Bryan, G. Arya, C.A.M. Seidel, B. Fierz, 2018. „Single-molecule FRET reveals multiscale chromatin dynamics modulated by HP1 $\alpha$ “. *Nature Communications*, 9(1), p.235. **(Supplement D)**
- A. Greife, S. Felekyan, Q. Ma, C.G. Gertzen, L. Spomer, **M. Dimura**, T.-O. Peulen, C. Wöhler, D. Häussinger, H. Gohlke, V. Keitel, C.A.M. Seidel, 2016. „Structural assemblies of the di-and oligomeric G-protein coupled receptor TGR5 in live cells: an MFIS-FRET and integrative modelling study“. *Scientific reports*, 6, p.36792. **(Supplement E)**

**Manuscripts in revision**

- T.-O. Peulen, C.S. Hengstenberg, R. Biehl, **M. Dimura**, C. Lorenz, A. Valeri, S. Ince, T. Vöpel, B. Faragó, H. Gohlke, J.P. Klare, A. Stadler, C.A.M. Seidel, C. Herrmann „Integrative dynamic structural biology unveils conformers essential for the oligomerization of a large GTPase“. **(Supplement C)**
- **M. Dimura**, T.-O. Peulen, H. Sanabria, D. Rodnin, K. Hemmen, C.A.M. Seidel, H. Gohlke „Automated and optimally FRET-assisted structural modelling“ **(Chapter 2)**

## Contributions

### Chapter 2:

#### **Quantitative FRET studies and integrative modelling unravel the structure and dynamics of biomolecular systems**

M. Dimura, T.-O. Peulen, H. Sanabria, D. Rodnin, K. Hemmen, C. A. M. Seidel, H. Gohlke

M.D. developed methods and performed programming and computations. H.S., D.R., K.H. and T.P. designed T4L FRET network, prepared, labelled and analysed experimental data for T4 Lysozyme. M.D. C.S. and H.G. analysed data, discussed the results, and wrote the paper. C.S. and H.G. performed study design and supervised the project.

### Supplement A:

#### **Quantitative FRET studies and integrative modelling unravel the structure and dynamics of biomolecular systems**

M. Dimura, T.-O. Peulen, C. A. Hanke, A. Prakash, H. Gohlke, C.A.M. Seidel

All authors wrote the manuscript. T.P., C.H. and A.P. simulated and analysed fluorescence data. M.D. performed and implemented FRET guided structural modelling. M.D. and T.P. analysed modelling results. H.G. and C.S. planned and supervised the research project.

### Supplement B:

#### **Resolving dynamics and function of transient states in single enzyme molecules**

H. Sanabria, D. Rodnin, K. Hemmen, T.-O. Peulen, S. Felekyan, M.R. Fleissner, M. Dimura, F. Koberling, R. Kühnemuth, W. Hubbell, H. Gohlke, C.A.M. Seidel

H.S. and K.H. purified and labelled the protein. H.S., T.P., K.H., and D.R. measured and analysed the FRET experiments. T.P., M.D. and H.G. performed structural screening. M.R.F. performed and analysed EPR experiments. W.H. performed study design and EPR analysis. S.F. developed fluorescence analysis tools. F.K. and R.K. developed fluorescence instrumentation and gave technical support. All authors discussed the results and commented on the manuscript. H.S., K.H., W.H. and C.A.M.S. wrote the paper. H.G. contributed to the writing of the paper. C.A.M.S. supervised the project.

**Supplement C:****Integrative dynamic structural biology unveils conformers essential for the oligomerization of a large GTPase**

T.-O. Peulen, C.S. Hengstenberg, R. Biehl, M. Dimura, C. Lorenz, A. Valeri, S. Ince, T. Vöpel, B. Faragó, H. Gohlke, J.P. Klare, A. Stadler, C.A.M. Seidel, C. Herrmann

TOP, CSH, RB, MD, CL, HG, JPK, AS, CAM, and CH wrote the manuscript. MD performed the molecular and coarse-grained simulations under the supervision of HG. CSH prepared samples for smFRET and performed protein activity assays. SI and CL prepared samples for SAXS measurements. TV prepared sampled for EPR measurements. CL and AS performed and analysed SAXS measurements. RB, AS and BF performed NSE measurements and analysis. TOP, CSH, and AV performed the smFRET measurements under the supervision of CAM. TOP analysed the smFRET measurements. JPK performed and analysed the EPR measurements. TOP combined the FRET, EPR, and SAXS measurements in a meta-analysis for integrative modelling. CH, CAM, JPK and AS planned and supervised the research project.

**Supplement D:****Single-molecule FRET reveals multiscale chromatin dynamics modulated by HP1 $\alpha$** 

S. Kilic, S. Felekyan, O. Doroshenko, I. Boichenko, M. Dimura, H. Vardanyan, L.C. Bryan, G. Arya, C.A.M. Seidel, B. Fierz

B.F. coordinated the project. B.F., S.K. and C.A.M.S. conceived and designed the studies. B.F. supervised chromatin synthesis and reconstitution, and smTIRF studies. C.A.M.S. supervised the confocal smFRET studies and quantitative FRET analysis. S.K. synthesized labelled chromatin fibres, modified histones, and performed smTIRF experiments. I.B. produced phosphorylated HP1 $\alpha$  and performed TIRF experiments. L.C.B. produced synthetic histones. S.F., O.D., S.K. and H.V. performed and analysed confocal FRET experiments. Kinetic modelling was performed by S.F., C.A.M.S. and B.F. PDA was performed by S.F. G.A. performed coarse-grained simulations. G.A. and B.F. generated chromatin models. O.D. and M.D. performed FPS analysis with chromatin models. All authors were involved in data analysis and interpretation. All co-authors wrote the manuscript.

**Supplement E:****Structural assemblies of the di- and oligomeric G-protein coupled receptor TGR5 in live cells: an MFIS-FRET and integrative modelling study**

A. Greife, S. Felekyan, Q. Ma, C.G. Gertzen, L. Spomer, M. Dimura, T.-O. Peulen, C. Wöhler, D. Häussinger, H. Gohlke, V. Keitel, C.A.M. Seidel

V.K., H.G. and C.A.M.S. conceived the study and supervised the project. A.G. and Q.M. performed the MFISFRET measurements. S.F. and A.G. analysed the MFIS-FRET data. L.S. and C.W. performed molecular biology experiments and provided biological material. T.O.P. performed oligomer and tetramer simulations. C.G. and M.D. performed structural modelling of TGR5 dimers and tetramers and explicit and implicit linker simulations. H.G. analysed molecular modelling and simulation data. A.G., C.G., V.K., H.G. and C.A.M.S. wrote the paper. All authors reviewed the manuscript. D.H. approved the manuscript.

## Table of Contents

Chapter 1. Overview .....	1
1.1. Introduction .....	1
1.2. Current approaches to FRET-assisted structural modelling .....	4
1.3. Aims .....	6
1.4. Principles of FRET-assisted structural modelling .....	8
1.4.1. FRET-assisted structural modelling workflow .....	8
1.4.2. Collection of prior knowledge on the system .....	9
1.4.3. Conformational expansion of the prior .....	10
1.4.4. Efficient selection of FRET pairs .....	10
1.4.5. Sample preparation, measurements and data analysis .....	11
1.4.6. Models of the fluorescent dyes .....	12
1.4.7. Scoring of the structural models by FRET .....	14
1.4.8. Estimation of conformational precision .....	24
1.4.9. Quality checks .....	28
1.4.10. FRET-guided computational structural modelling .....	29
1.4.11. Estimation of $N_{fit,param.}$ for FRET-assisted structural models .....	34
1.5. Short summaries of the supplementary articles and manuscripts .....	36
1.5.1. Discovering a new conformational state of T4 Lysozyme by FRET .....	36
1.5.2. Determination of structural dynamics of human guanylate binding protein 1 using the data from four experimental techniques. ....	39
1.5.3. Benchmarking accuracy of the workflow using <i>in silico</i> FRET data .....	44
1.5.4. Resolving the chromatin dynamics by FRET and coarse-grained structural modelling .....	47
1.5.5. Determination of the oligomerisation interface of the G-protein coupled receptor TGR5 using fluorescent protein labels .....	53
1.6. Conclusions .....	58
1.7. References .....	61
Chapter 2. Automated and optimally FRET-assisted structural modelling .....	66
2.1. Abstract .....	66
2.2. Introduction .....	66
2.3. Results .....	67
2.4. Conclusions .....	73



2.5. Methods.....	73
2.5.1. Proteins used in the benchmark. ....	73
2.5.2. Quality metric for evaluation of FRET pair sets: $\langle\langle\text{RMSD}\rangle\rangle$ . ....	74
2.5.3. FRET screening. ....	75
2.5.4. Selection of a set of optimal FRET pairs. ....	76
2.5.5. Estimation of the complexity of the structural model.....	78
2.5.6. Unbiased conformation sampling by NMSim. ....	79
2.5.7. FRET-guided NMSim.....	79
2.5.8. FRET-restrained MD. ....	80
2.5.9. T4 Lysozyme site specific mutation, purification and labelling.....	82
2.5.10. FRET Experiments and Analysis.....	82
2.6. Acknowledgments.....	84
2.7. References.....	85
2.8. Supplementary information .....	89

## Supplementary articles

Supplement A. Quantitative FRET studies and integrative modelling unravel the structure and dynamics of biomolecular system

Supplement B. Resolving dynamics and function of transient states in single enzyme molecules

Supplement C. Integrative dynamic structural biology unveils conformers essential for the oligomerization of a large GTPase

Supplement D. Single-molecule FRET reveals multiscale chromatin dynamics modulated by HP1 $\alpha$

Supplement E. Structural assemblies of the di-and oligomeric G-protein coupled receptor TGR5 in live cells: an MFIS-FRET and integrative modelling study

# Chapter 1. Overview

---

## 1.1. Introduction

Life sciences and their application in medicine, biotechnology and agriculture can be seen as engineering of biological systems. Unfortunately, sufficiently detailed blueprints for many biological machines are still missing, especially for the dynamic aspects of the molecular mechanisms<sup>1,2</sup>. Most significant functional elements in the machinery of life are biomacromolecules: proteins and nucleic acids. Understanding the function, structure, and dynamics of these elements is therefore immensely valuable for the advance of life sciences. The level of detail needed for comprehensive description of biomacromolecules is determined by size of the smallest functional block i.e. atom. Van der Waals radius of an atom ( $\sim 1.7 \text{ \AA}$  for carbon) defines the target for the spatial resolution of the practically useful model of a biomacromolecule. At the same time the dimensions of a virus particle can reach hundreds of nanometres, so the size of the system can be thousands of times bigger than the size of individual elements.

The second requirement for a structural and dynamic model of biological molecular machine is imposed by the timescales of the fastest and longest relevant processes that occur in biomacromolecules. For example, lifetime of a hydrogen bond is approximately 10 picoseconds<sup>3</sup>, the rotation of a protein sidechain occur on a nanosecond timescale<sup>4</sup>, register shift of DNA histone octamer in a chromatin fibre takes about 100 milliseconds (Supplement D), and synthesis of a protein by ribosome can take seconds to minutes<sup>5</sup>. Thus, comprehensive description of a biological system should cover a timespan of up to minutes with the time resolution of nanoseconds or even higher. Another challenge is that certain biochemical processes can only be reproduced to full extent in specific and intricate environment of a live cell, which precludes *in vitro* measurements.

Historically most of the knowledge about the structure of biomacromolecules came from two experimental techniques: X-ray crystallography and nuclear magnetic resonance spectroscopy (NMR). Importance of these two techniques for the field is hard to overestimate. However, both methods have critical restrictions<sup>1</sup>. X-ray crystallography requires biomacromolecular system of interest to be crystallized, which is not always possible and excludes physiologically important environments and whole clusters of relevant systems, like, e.g. intrinsically disordered proteins; it

also does not allow observing molecular motions. NMR spectroscopy provides an insight into the structural dynamics, but only for processes in restricted range of time scales and, primarily, for systems of limited size (up to 50-70 kDa for homomeric systems)<sup>6</sup>. This stimulated the advance of alternative macromolecule structure determination techniques, which accelerated in recent years.

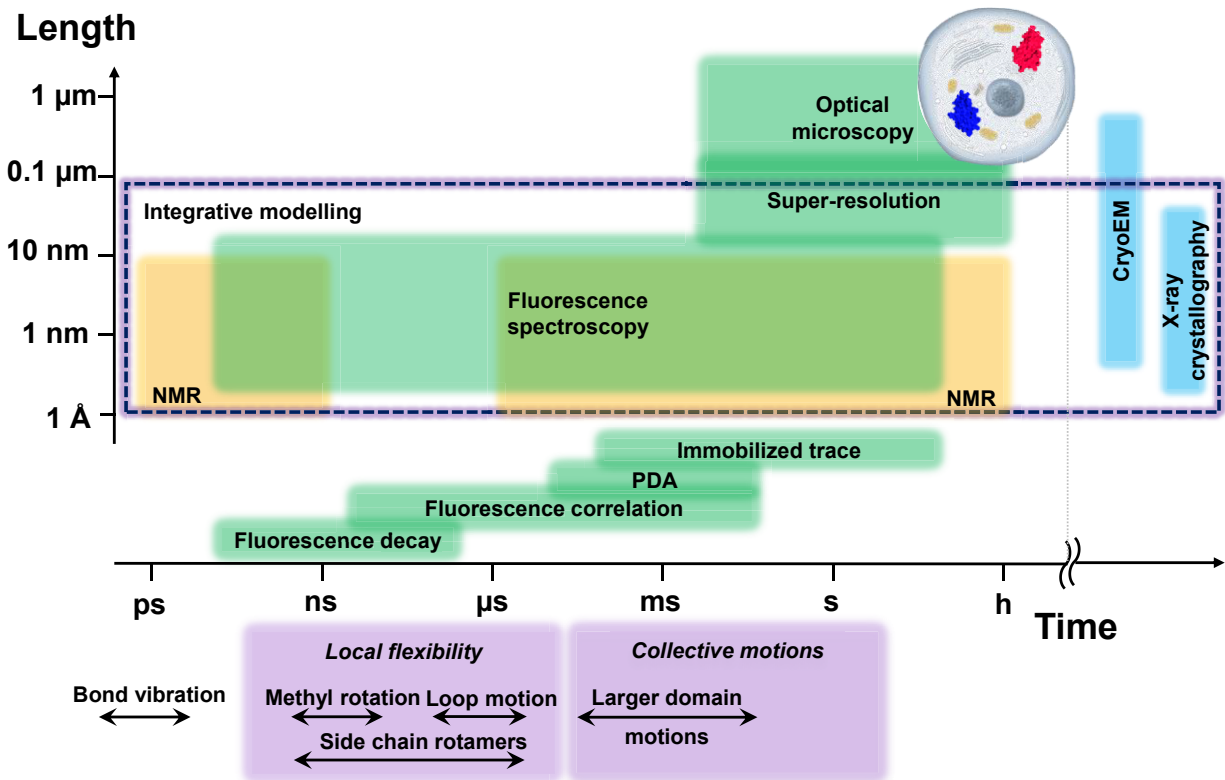


**Figure 1 | Spatial and temporal resolution of experimental techniques used in structural biology.** Spatiotemporal resolution of each technique is indicated by a coloured box. Different types of fluorescence-based methods are shown in the lower part of the plot in green. Based on Dror et al<sup>1</sup>.

One of the rapidly developing methods for structure determination is fluorescence spectroscopy and, in particular, measurements of Förster resonance energy transfer (FRET). Among the advantages of fluorescence spectroscopy is high selectivity up to single-molecule level, direct observation of kinetics with unrivalled time resolution of up to picoseconds<sup>7</sup>, availability of measurements in living cells, and possibility to measure distances within the biomolecular complexes with Ångström accuracy via FRET<sup>8</sup>.

Fluorescence spectroscopy involves measurements of light absorption and emission of the fluorescent moieties within the biomolecules. Fluorescent moieties can be either natural like tryptophan and tyrosine or artificially introduced like, rhodamines or cyanines. This way distance

between a donor (D) and acceptor (A) fluorophores, can be monitored. In confocal multi-parameter FRET detection (MFD) single-molecule FRET (smFRET) experiments, freely diffusing molecules are repeatedly excited by a pulsed light source, and the emitted fluorescence photon is detected with picosecond time-resolution by Time-Correlated Single Photon Counting (TCSPC) for several milliseconds per molecule in the observation volume referred to as diffusion time ( $t_{diff}$ , **Figure 2A**)<sup>9</sup>. smFRET experiments allow one to study kinetics and do not require any special measures to synchronize the molecules prior to the analysis. Consequently, it is possible to reliably probe protein kinetics over seven decades in time (sub ns to ms). The MFD histograms are generated by analysing two complementary FRET-indicators, the average FRET-efficiency,  $E$ , and the fluorescence-averaged donor lifetime in the presence of acceptor, for individual single-molecule events<sup>9-11</sup>. An MFD-histogram (**Figure 2B**) is particularly valuable to reveal the number of states, identify dynamics, and to inform on state connectivities. Additional information on the structural dynamics of biomolecules can be obtained using other fluorescent spectroscopy techniques: fluorescence correlation spectroscopy quantifies exchange dynamics among the states by determining relaxation times<sup>12,13</sup>, analysis of fluorescence decays reveals populations of states and equilibrium distance distributions<sup>14</sup>, time-resolved anisotropy analysis allows one to observe local flexibility of the molecule at the labelling position and control the dye behaviour, which improves the accuracy of the dye model and inter-dye distances<sup>15</sup>.

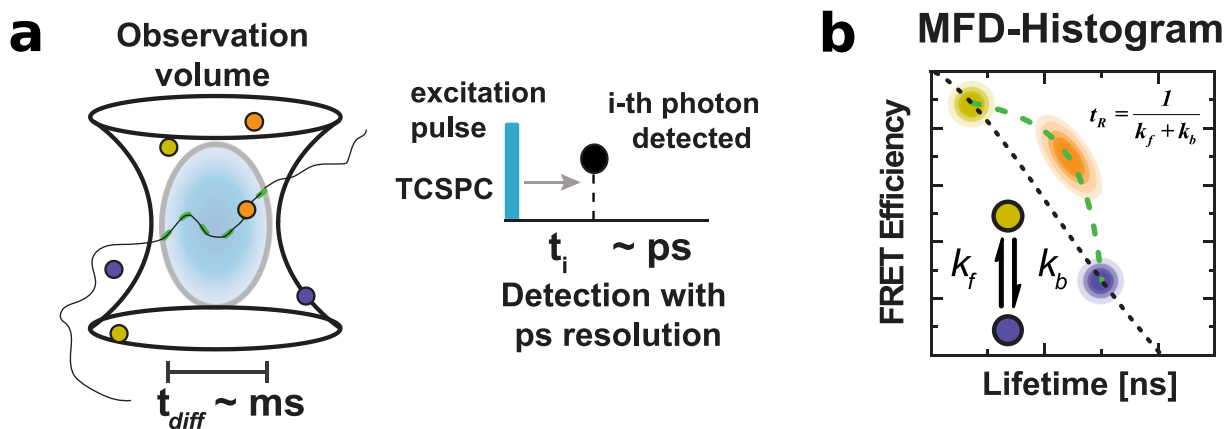


**Figure 2 | Single-molecule Multiparameter Fluorescence Detection (MFD) experiments.** (A) In MFD-experiments of freely diffusing single molecules, the emitted fluorescent photons (“bursts”) are detected with ps resolution (with respect to the exciting laser pulse) during the diffusion (on the ms time scale) of the molecule through the observation volume (diffusion time,  $t_{diff}$ ). (B) In single-molecule MFD experiments, the fluorescence bursts - averaged over ms – are analysed e.g. with respect to their fluorescence lifetime or FRET-efficiency  $E$  and displayed in multidimensional frequency histograms (2D MFD-histogram). Molecules that adopt a stable conformation during

burst duration are located along the static FRET-line (black, see also Supplement B SI section 1.2). Assuming that the two limiting states (yellow and blue) exchange on timescales faster than ms with exchange rate constants  $k_f$  and  $k_b$ , we find only a single population (orange) shifted towards a longer fluorescence lifetime that is located on the dynamic FRET-line (green) connecting these two limiting states. Thus, FRET-lines serve as a visual guide to interpret 2D MFD-histograms, with deviations from the static FRET-line being indicative for the dynamic averaging and dynamics at the sub-ms and ms timescales. An example of an MFD-histogram based upon experimental data can be seen in **Figure 19a**. Adapted from Supplement B.

One of the challenges, associated with FRET measurements, is the sparsity of obtained data, since one measurement only provides information about a single distance within the biomolecule or molecular complex, whereas the whole system can consist of millions of atoms<sup>16</sup>.

## 1.2. Current approaches to FRET-assisted structural modelling

Currently every experimental method has some specific limitations in ability to resolve structural and dynamic details of biomacromolecules and their assemblies, so that no single experimental method can be used as a universal and comprehensive tool for investigation of structural dynamics<sup>1</sup>. These challenges triggered the advance of hybrid structural modelling approach in the last years<sup>17</sup>. In integrative/hybrid structural modelling methods several experimental and computational techniques are combined in order to reconstruct the biochemical picture from pieces coming from different techniques. The measurements of FRET from a donor to an acceptor fluorophore provides unique insights, based upon the high time resolution, which allows one to detect intermediates of exchanging systems in solution, their kinetics, and the complementary distance information, probed by multiple independent FRET pairs<sup>18,19</sup>.

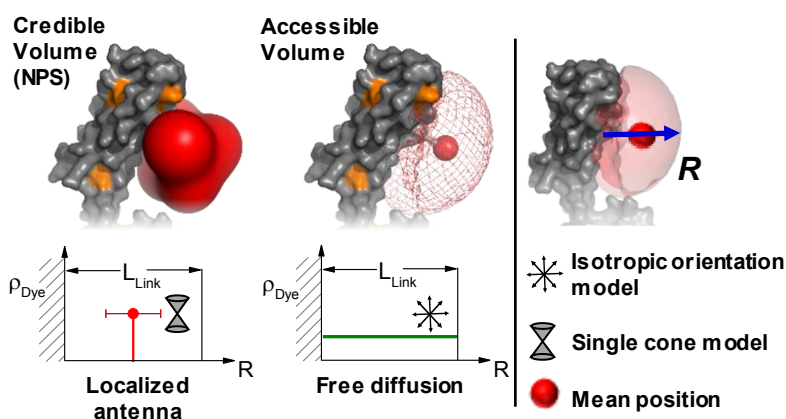


**Figure 3 | Models of dye density distributions.** Nano Positioning System approach (localized antenna) is shown on the left<sup>20</sup>, red surface represents the uncertainty of a fixed dye position. FRET

*Positioning and Screening approach (free diffusion) is shown in the center<sup>21</sup>. Red mesh represents the sterically allowed space of the fluorophore, tethered to the protein. See also Supplement A.*

However, FRET measurements report inter-dye distances and the number of FRET pairs is limited. Integrated methods can leverage experimental data that by itself would be insufficient to determine structures with satisfactory accuracy. Due to the long-range FRET information (typically 20-100 Å), the hybrid-FRET modelling approach is especially suitable to characterize the tertiary, super-tertiary, and quaternary structures of biomolecular systems<sup>22</sup>.

Several approaches were developed recently to describe the spatial and orientational dye density in hybrid-FRET models in order to improve their precision and accuracy.

The Nano Positioning System (NPS) approach assumes a label adopting a single position with a defined conformation of the fluorophore linker and the fluorophore wobbling in a cone<sup>20</sup> (**Figure 3**). It relies upon an assumption, that fluorophores are located at the same position with respect to the macromolecule. Since the position of the dye is initially unknown multiple measurements are used to localize it within a credible volume for a given confidence level. NPS approach was recently extended to include other dye models as well<sup>23</sup>.

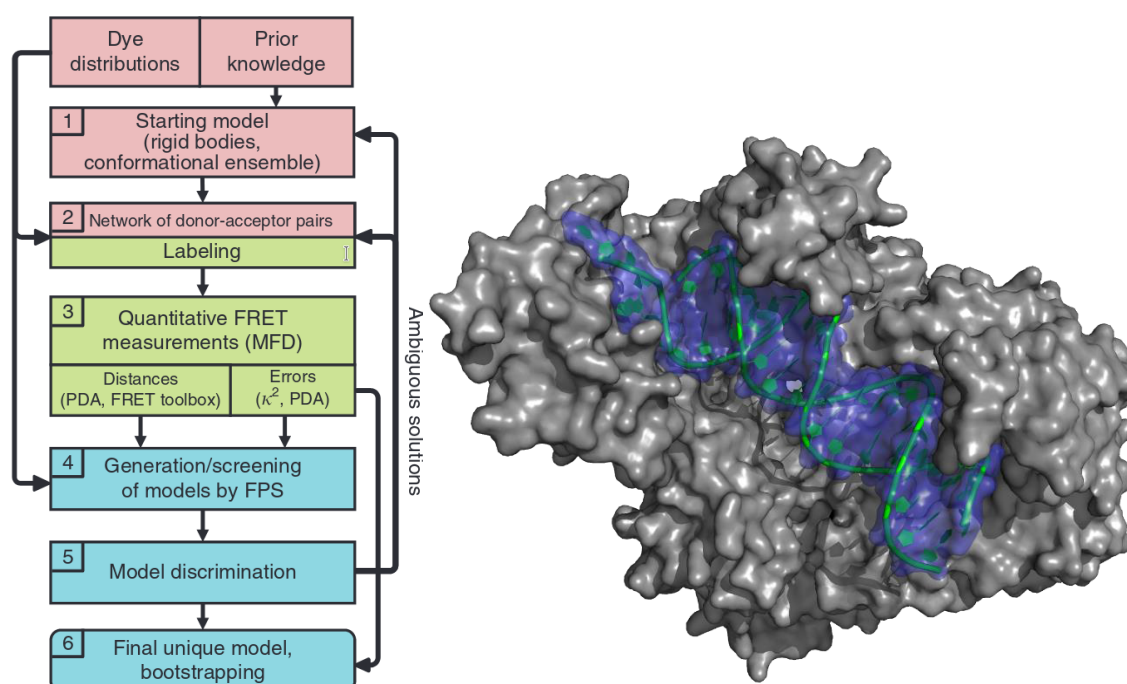


**Figure 4 | Workflow for FRET positioning and screening (left) and complex of HIV-1 reverse transcriptase and primer/template DNA (right). Adapted from Kalinin et al<sup>21</sup>.**

The FRET Positioning and Screening (FPS) approach introduced by Kalinin et al<sup>21</sup> uses another approximation in the dye model, where a freely diffusing fast rotating dye samples all orientations and all positions within the reach of the flexible dye linker (**Figure 3**). The authors successfully reconstruct the binding poses of the DNA primer/template (dp/dt) in complex with the HIV-1 reverse transcriptase protein (RT:dp/dt). Authors use 20 FRET pairs in order to resolve the position of the DNA in the “tunnel” of RT. When both RT and the DNA are modelled as rigid bodies with shape taken from the crystal structure, accuracy of the FRET-assisted reconstruction compared to crystal structure of the complex is 0.5 Å as measured by the root mean square deviation of the phosphorous atoms<sup>21</sup>. The article also demonstrates the reconstruction of the conformation of the flexible single-stranded DNA template overhang. Accuracy of the overhang model is not tested, since there are no crystal structures available for comparison. The paper also outlines the workflow for FRET-assisted rigid body docking (RBD) (**Figure 4**).

In FRET-assisted rigid body docking approach, a molecular system is decomposed into a small set of 2-10 fully rigid sections called “bodies”. Bodies typically represent macromolecule’s domains, subdomains, secondary structure elements or other structural elements. These bodies are then moved with respect to each other in order to find an orientation, which minimises the deviation of FRET-distances, from those determined in experiment. Sterically ds-DNA is similar to a bolt, where groves represent the threading, and the RT has ridges, analogous to a nut. Rigid body modelling of RT:dp/dt is similar to a screw in a nut, which is a 1-dimensional problem, since rotation of the DNA dp/dt is coupled to its translation. As shown by Kalinin et al. For this 1-dimensional system, FRET-assisted structural modelling can certainly be used for accurate structure determination, given that prior knowledge on the biomacromolecule and the fluorescent label is incorporated in the process. The question of how much further such approach could be extended became the motivation of my thesis.

### 1.3. Aims

The overall goal of this thesis is to establish the means to acquire accurate and detailed integrative/hybrid structural models of the biomacromolecular systems, that are inaccessible by one technique alone, using a combination of fluorescence spectroscopy and computational structural modelling. To achieve that, I address two directions: (I) improvement of the accuracy of

the final structural models and (II) reduction of time and effort necessary to obtain these models. In more detail, I answer several questions in my thesis:

- Which FRET measurements are most useful, how to select those and how many FRET measurements are required to achieve a given precision and accuracy? (Section 1.4.4)
- How could the dye models be improved in order to increase the information content of the measurements? (Section 1.4.6)
- How can one assess the accuracy and quality of a FRET-assisted computational structural model? (Sections 1.4.9,1.4.11)
- How could the data from FRET experiments inform the computational techniques to generate new structural models? (Section 1.4.10)
- How should one use the experimental data acquired in cells using fluorescent proteins as labels? (Section 1.5.5)
- Can we use FRET-assisted structural modelling to resolve systems of higher dimensionality than HIV-1 RT:dp/dt complex? (Chapter 2)
- What is complexity of a computational structural model in the context of a FRET experiment? (Section 2.5.5)

The answers to these questions were developed and tested while investigating diverse biomacromolecular systems. Here, I first mention the *in silico* benchmark. Afterwards, I report several experimental applications ordered by the molecular weight of the molecular assembly. Proof of concept and the benchmark was performed for a set of five structurally diverse proteins using *in silico* FRET data (Chapter 2). The same benchmark was applied to an existing set of experimental data collected for the small T4 Lysozyme protein, consisting of 164 amino acids with a total molecular weight of 18.6 kDa (Supplement B). The human guanylate binding protein 1 (hGBP1), which is a large protein of 592 residues (molecular weight of 65.3 kDa), served as an example of underdetermined system, where conformational transition was studied by a combination of three experimental methods: small-angle X-ray scattering (SAXS), pulsed electron paramagnetic resonance (EPR) and FRET spectroscopy (Supplement C). The investigation of conformational dynamics of the 12-mer nucleosome array (2.3 megadaltons, 13680 residues) highlights the capabilities of FRET-assisted structural modelling of very large complexes (thousands of kilodaltons, Supplement D). One special case involved the modelling of fluorescent



protein labels for the in vivo study of the oligomerization of G-protein coupled receptor TGR5, using a custom, specifically developed linker model (Supplement E).

The software, which was developed for the workflow is now publicly available.

## 1.4. Principles of FRET-assisted structural modelling

### 1.4.1. FRET-assisted structural modelling workflow

In order to achieve the aforementioned aims, I implemented three main additions to the original 7-step workflow for FRET-assisted structural modelling shown in Kalinin et al<sup>21</sup> (**Figure 5**).

- Automated selection of informative FRET pairs in step 3 of the workflow (section 1.4.4).
- Evaluation of the complexity of the structural model and cross-validation for more reliable quality control and precision estimation, indicated here by  $\chi_n^2$  (step 5, section 1.4.7).
- Two additional FRET-guided structure generation methods: one based upon NMSim<sup>24</sup> coarse-grained modelling software and one for molecular dynamics (MD) simulations (step 6, section 1.4.10).

In the modified workflow, computation of a structural model of a biomacromolecular system is achieved in seven steps (Chapter 2, **Figure 5b**): (1) Collection of *prior* knowledge about the system; (2) Processing of *prior* knowledge and formulation of the initial hypothesis in the form of a conformational ensemble using NMSim<sup>24</sup>; (3) Design of the experiment, selection of the labelling pairs with the highest informational content; (4) Preparation of the sample, measurements and analysis of experimental data; (5) scoring of the *prior* structural models against the experimental data; (6) adjustment of the initial models using the newly obtained experimental data; (7) quality assessment for the constructed model.

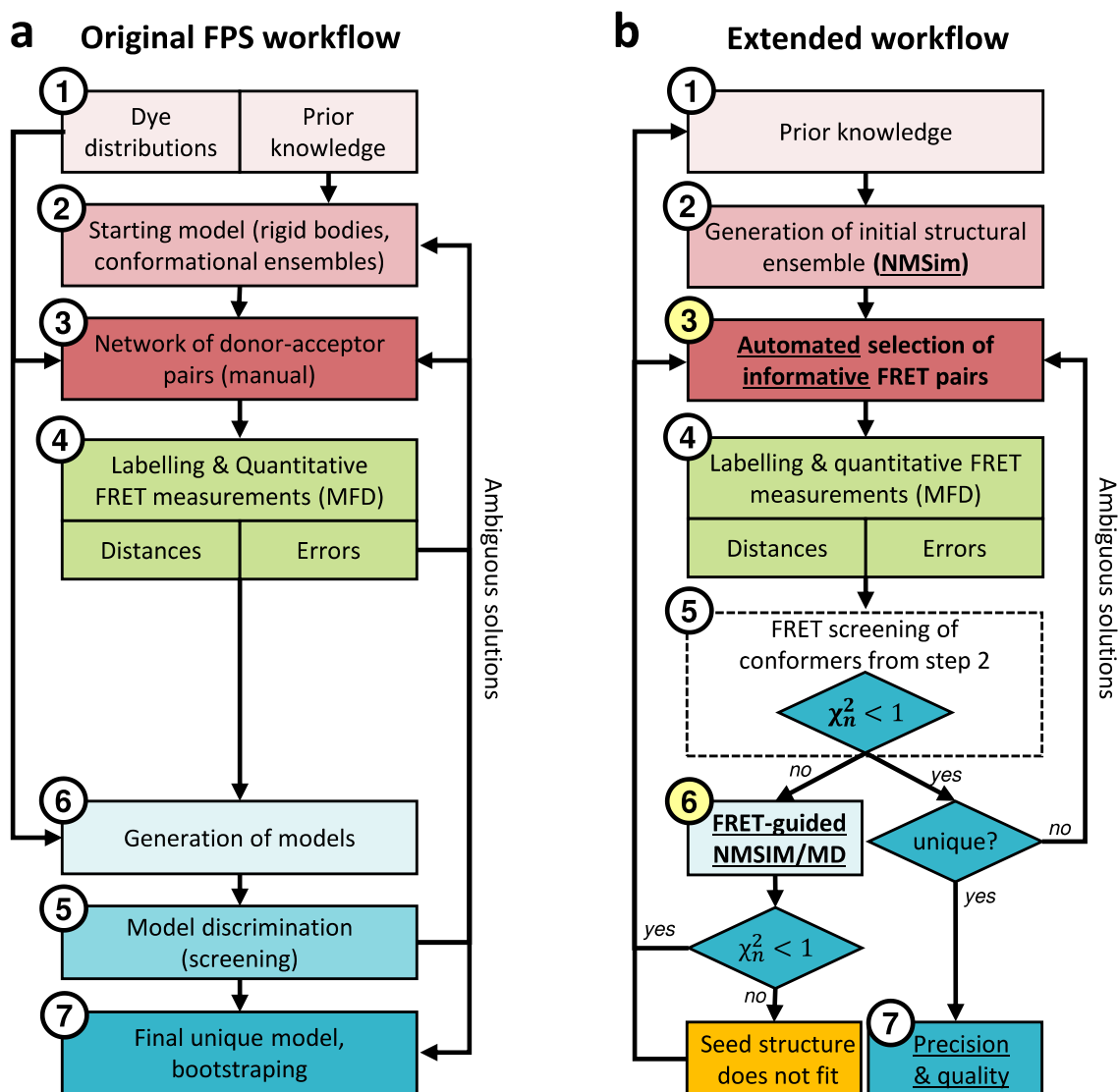


**Figure 5 | Step-by-step workflow for automated and optimally FRET-assisted structural modelling.** (a) Original workflow for FRET-restrained positioning and screening from Kalinin *et al.* article<sup>21</sup>. (b) Extended workflow. Bold underlined font and yellow background of the step numbers highlights the newly developed steps. See also Chapter 2.

### 1.4.2. Collection of prior knowledge on the system

In step 1, *prior* information can be obtained from several sources: if a multistate system is investigated, some of its states could be available from X-ray crystallography, NMR or other experimental techniques via the Protein Data Bank (PDB)<sup>25</sup>; *prior* models can also be constructed using physics-based<sup>26-28</sup> or statistics-based<sup>29</sup> computational methods, using similar systems as a reference (template-based modelling)<sup>30,31</sup>, using the co-evolutionary information<sup>32-34</sup> or any combination of these methods. These sources typically provide multiple conformations, which are combined into an initial ensemble and used later as a starting point for further modelling.

### 1.4.3. Conformational expansion of the prior

In step 2, the initial structural ensemble is expanded by an appropriate conformational sampling technique. This conformational sampling can be performed by rigid-body docking, NMSim<sup>24</sup> normal-mode based structural modelling approach or other coarse-grained structural modelling technique. At this stage broadness of sampling is more important than accuracy or physical correctness of the conformations. Level of coarse-graining is problem specific; it is defined by the diversity and reliability of the initial ensemble. For example, in the case of chromatin fibre (Supplement D), rigid-body docking was employed with rigid units as large as a whole nucleosome, while linker DNA was represented by a flexible chain under geometric restrictions (length, exclusion effects). Large proteins like human guanylate binding protein 1 (Supplement C) may require multi-scale modelling with rigid-body docking, normal-mode based geometric coarse-grained modelling (NMSim<sup>24</sup>) and all-atom molecular dynamics simulations (MD). For a small enzyme with a good *prior* ensemble, all-atom molecular dynamics simulations can provide sufficiently broad sampling (Chapter 2).

### 1.4.4. Efficient selection of FRET pairs

In step 3, the selection of FRET pairs for measurement was so far done manually by a researcher, based on the expectations about the possible directions of conformational change and labelling restrictions. Within this work this approach was quantified, automated and implemented in a novel algorithm for experiment planning (section 2.5.4). This algorithm automatically finds a set of most informative FRET pairs optimized for highest model precision using the least measurements, based on a given *prior* structural ensemble. In essence the algorithm iteratively calculates which inter-dye distance can lead to the most significant reduction in the uncertainty of the prior, if measured. It considers expected uncertainties of the measurements and how they propagate to the actual distances, as well as redundancy and complementarity between FRET pairs. Since sensitivity of experiment is distance-dependent, pair selection algorithm also accounts for that. For example, assuming that the FRET-averaged efficiency can be measured with constant level of uncertainty  $E = E \pm \Delta E$ ,  $\Delta E = const$ , and using the efficiency-distance relationship  $E = 1/(1 + R_E^6/R_0^6)$ , the uncertainty of FRET-averaged inter-dye distance  $R_E$  will be distance-dependent:

$$\Delta R_E = \Delta E \cdot \frac{(R_0^6 + R_E^6)^2}{6R_0^6 R_E^5}$$

In this experiment design approach, additional restrictions for label and pair selection can be set, such as: labelling site accessibility, effect on function and structural stability as determined from mutation analysis or sequence coevolution data. The minimum required number of measured FRET pairs is defined by the accuracy of the prior and desired precision and confidence level. However, high accuracy of the prior is not mandatory, since potential overfitting is prevented by cross validation in steps 5 and 7.

#### **1.4.5. Sample preparation, measurements and data analysis**

Step 4 consists of sample preparation, FRET data acquisition and analysis, and estimation and propagation of uncertainties, latter being especially relevant for hybrid structural modelling (Supplement A). Both underestimation and overestimation of uncertainties lead to deterioration of the model quality, which has to be alleviated by more measurements. If the errors are overestimated, different structural models falsely appear to be indistinguishable within the error bounds, so statistical significance has to be unnecessarily increased by additional observations. If errors are underestimated, correct model appears insufficiently accurate, suggesting a more detailed and complex model, which, after more measurements, will again appear inaccurate. One of the key advantages of fluorescence experiments for hybrid structural modelling is the possibility to access most important sources of uncertainties exactly and statistically correctly from photon statistics. However, for some sources of uncertainties like orientation factor  $\kappa^2$  and refractive index, precise estimation is harder and has to be determined empirically by calibration against reference samples. To assure accurate error estimation, state of the art data analysis techniques were complemented by careful calibration and benchmarking<sup>14</sup>. Critical contribution to reliable error estimation was done by a recent community-wide accuracy benchmark study, conducted by the collaboration of 20 labs<sup>8</sup>. It provided the calibration data, like standard deviations of measured FRET efficiencies in single-molecule FRET experiments, collected specifically with the “aim of achieving reliable structural models of biomolecular systems by smFRET-based hybrid methods”. Additionally, global fitting of multiple fluorescence datasets was used for single molecule and bulk fluorescence measurements (Supplement C, Supplement D). In global fitting approach parameters are shared between different experimental datasets to prevent overfitting, reduce uncertainties of derived models, and, ultimately, reduce the number of required experimental measurements.

### 1.4.6. Models of the fluorescent dyes

Quantitative hybrid structural modelling with fluorescence data is impossible without accurate dye models (Supplement A). A dye model defines the positioning and motions of the fluorescent label with respect to the biomacromolecule of interest. Uncertainties in the inter-dye distances, caused by dye model inaccuracies are an integral part of overall error estimation procedure. Two types of fluorophore labels are described here: organic dyes and fluorescent proteins.

Organic dyes are typically tethered to a biomolecule by a flexible linker about 20 Ångström in length. Previously, explicit models of the fluorophores in all-atom molecular dynamics (MD) simulations were demonstrated successfully<sup>35-37</sup>. However, such simulations are costly and require intricate parametrisations of the fluorophore moieties, which can be challenging. Since linkers are flexible, it is possible to make strong assumptions about the mobility of the fluorophore moiety<sup>38</sup>. Mobile fluorophore on a tether can be modelled as a spatial distribution of dye positions limited by the linker length and environment exclusion effects – dye accessible volume (AV).

These assumptions result in accurate predictions of mean inter-dye distances between the donor and acceptor, so for many applications uniform distribution can be used, given proper control by fluorescence anisotropy analysis<sup>21,39</sup>. In order to account for the less mobile dye behaviour due to interactions between the fluorophore and the surface of the biomolecule, contact volume (ACV) correction was introduced to accessible volume approach, further reducing the overall uncertainty of the experimentally determined inter-dye distance. Using fluorescence anisotropy analysis, fraction of the fluorophore, trapped on the surface of the protein  $x_{trapped}$  is estimated from residual anisotropy  $r_\infty$  and the fundamental anisotropy  $r_0$ :  $x_{trapped} = r_\infty/r_0$ .

Another dye model was developed for fluorescence experiments that use fluorescent proteins (FPs) as labels: green fluorescent protein (GFP), red fluorescent protein (RFP), their variants, and similar dyes (Supplement E). Fluorescent protein labels are typically attached to proteins of interest using a peptide linker from several to dozens of amino acids in length. Behaviour of linker-FP complex is usually too complex to be represented by a uniform AV, length of such a complex at full extension can be high (up to 100 Ångström), peptide linker can form folded or semi-folded states, and polymer chain dynamics can dominate over dye diffusion. To account for this complexity, linker-chain weighting was introduced as an additional correction to AV.

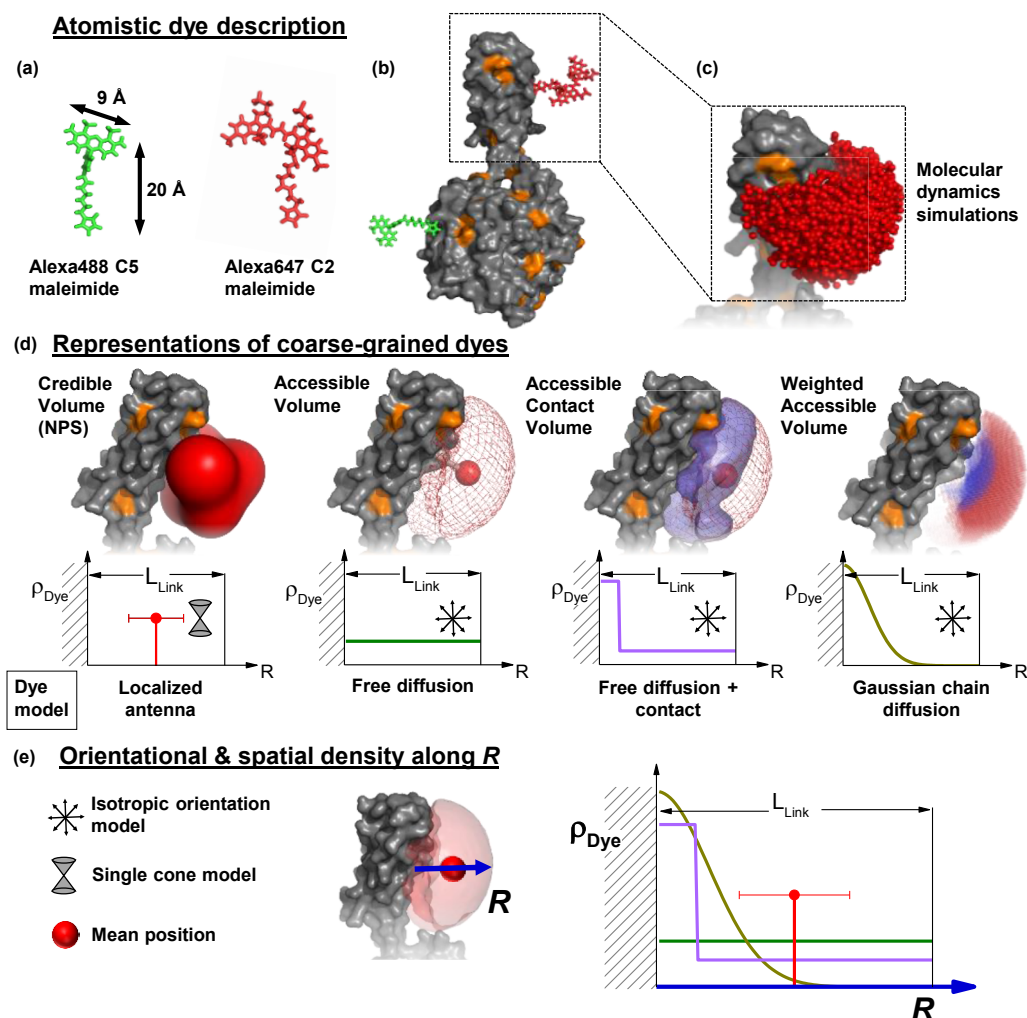


**Figure 6 | Treatment of dye labels in FRET-assisted modelling.** (a) The donor and acceptor dyes, for example, Alexa488 C5 maleimide (green) and Alexa647 C2 maleimide (red), respectively, are typically attached to the biomolecule via long ( $\sim 20$  Å) flexible linkers. (b) Dye labels attached to Atlastin-1 (grey surface) to give an impression of the sizes compared to a protein. (c) Molecular dynamics simulations provide the spatial distribution of dye molecules. (d) Representation of coarse-grained dye labels. On the top different dye representations are shown. On the bottom the spatial density  $\rho_{\text{Dye}}$  along a vector  $R$  starting at the attachment point in the direction of the dye mean position is shown for the corresponding dye models. The original Nano Positioning System (NPS)<sup>20</sup> assumes the accessible volume as prior information (uncertainty), which is reduced by a set of FRET measurements with fixed satellites resulting in an uncertainty distribution (red) of a fixed localized dye (antenna). The orientation of the dyes follows a diffusion in a cone model highlighted by a pictogram. Following  $R$ , the dye is located at a specific position (vertical red line) with an uncertainty. Accessible volume (AV, mesh) models provide the sterically allowed space of the dye molecule attached to the protein as calculated by the FPS program<sup>21</sup>. Here, the linkers of Alexa488 and Alexa647 are approximated as flexible tubes. The large sphere indicates the mean dye position. For a dye freely diffusing inside of its AV a uniform spatial distribution is assumed. The accessible contact volume (ACV<sup>40</sup>) provides a similar description as the AV, but defines an area close to the surface as contact volume (violet). Here, the density  $\rho_{\text{Dye}}$  in the contact volume is weighted six times stronger and are defined as part of the AV which is closer than 3 Å from the

macromolecular surface. For the corresponding model, where a dye freely diffuses within the AV and its diffusion is hindered close to the surface, the spatial density  $\rho_{\text{Dye}}$  along R is approximated by a step function:  $\rho_{\text{Dye}}(R < 3 \text{ \AA}) = 6 \cdot \rho_{\text{Dye}}(R \geq 3 \text{ \AA})$ . The weighted accessible volume is a modification of AV where  $\rho_{\text{Dye}}$  along R is approximated by an empirical weighting function inspired by Gaussian chain<sup>41</sup>. To illustrate the effect of the proposed weighting of  $\rho_{\text{Dye}}$  the weighted AV is coloured from blue (high density) to red (low density). **(e)** Comparison of the normalized spatial population densities  $\rho_{\text{Dye}}$  of the above dye models. Adapted from Dimura et al (Supplement A).

This correction is expressed as a user-defined function, which relates linker extension to probability, so many conventional polymer models can be applied, e.g. random coil, wormlike chain, etc. It is also demonstrated, how a linker model can be parametrized specifically for a given peptide sequence using coarse-grained modelling or free energy estimation based on all-atom molecular dynamics simulations (Supplement E).

#### 1.4.7. Scoring of the structural models by FRET

##### The $\chi^2$ distribution

Once the experimental data are analysed, the number of states, the corresponding fluorescent variables and their errors were estimated, they can be compared with the structural models obtained at step 2. In step 5, the fluorescence experiment is effectively conducted *in silico* for each conformation from the prior. Relevant observables estimated *in silico* (i.e. inter-dye distance of the FRET pair (i),  $R_{\text{mod}}^{(i)}$ ) are compared to the experimentally measured values ( $R_{\text{exp}}^{(i)}$ ) and corresponding errors ( $\Delta R_{\text{exp}}^{(i)}$ ). Here I describe the application of hypothesis testing using  $\chi^2$  statistic for the specific case of FRET-assisted computational structural modelling. More details about the background and the theory behind can be found in the section 7.2.1 of the book “Bayesian Logical Data Analysis for the Physical Sciences” by Phil Gregory<sup>42</sup>. For each structural model I, statistically test the **null hypothesis** that the “FRET data matches this structural model (conformer)”. To refute the null hypothesis, I need to show, that deviations of individual FRET measurements (inter-dye distances) from those predicted from the given conformation are larger than those, that would be expected from the estimated error. For this purpose, the  $\chi^2$  value is calculated for each conformer: differences between the *in silico* values ( $R_{\text{mod}}^{(i)}$ ) and measured values ( $R_{\text{exp}}^{(i)}$ ) are divided by the corresponding estimated errors ( $\Delta R_{\text{exp}}^{(i)}$ ), squared and added.

$$\chi^2 = \sum_{i=1}^{N_{measurements}} \left( \frac{R_{mod}^{(i)} - R_{exp}^{(i)}}{\Delta R_{exp}^{(i)}} \right)^2 \quad (1.1)$$

The value of this sum quantifies, how strongly the structural model deviates from experiment, as expressed in the units of estimated errors. Assuming that  $R_{exp}^{(i)}$  are independent random variables sampled from Gaussian distributions  $N(R_{mod}^{(i)}, \Delta_{exp}^{(i)})$ , the distribution of the  $\chi^2$  sum is:

$$f_{N_{dof}}(\chi^2) = \frac{1}{2^{N_{dof}/2} \Gamma(N_{dof}/2)} (\chi^2)^{N_{dof}/2-1} e^{-\chi^2/2} \quad (1.2)$$

$f(\chi^2 | N_{dof})$  is the probability density function of  $\chi^2$  distribution (**Figure 8**), where  $N_{dof}$  corresponds to the *number of degrees of freedom* or sometimes *degree of freedom (dof, eq. 1.5)*. Where gamma function  $\Gamma(z) = \int_0^\infty x^{z-1} e^{-x} dx$ , as derived by Daniel Bernoulli for a complex argument  $z$  with a positive real part.

Expected value of  $\chi^2$  distribution,  $\langle \chi^2 \rangle$  and its standard deviation  $\sigma_{\chi^2}$  are defined by its only parameter  $N_{dof}$ :

$$\langle \chi^2 \rangle = N_{dof} \quad (1.3)$$

$$\sigma_{\chi^2} = \sqrt{2N_{dof}} \quad (1.4)$$

### The complexity of the model ( $N_{fit.param.}$ )

The shape of the  $\chi^2$  distribution is defined by the number of degrees of freedom  $N_{dof}$ .

$$N_{dof} = N_{measurements} - N_{fit.param.} \quad (1.5)$$

The value of  $N_{fit.param.}$  quantifies the **complexity of the model**, expressed as the number of relevant parameters that fully define a conformation. It is similar in meaning to the number of fit parameters in a regression. Depending on how a computational structural model is constructed, quantitative estimation of its complexity can be challenging. Unfortunately, even for linear models estimating number of degrees of freedom is highly nontrivial and for nonlinear models no general and reliable methods to estimate  $N_{dof}$  are known<sup>43,44</sup>. However,  $N_{dof}$  can be derived heuristically,



as described in the section 2.5.5. Relative uncertainty of  $N_{dof}$  is lower, when the number of measurements is higher, so that  $N_{measurements}$  is much larger than  $N_{fit.param.}$ .

For a special case of a rigid-body model  $N_{fit.param.}$  can be estimated exactly:

$$N_{fit.param.} = (N_{bodies} - 1) * 6 - N_{bonds} \quad (1.6)$$

where  $N_{bodies}$  is the number of bodies in the model and  $N_{bonds}$  is the number of hard distance restraints between bodies. Each rigid body can be translated in three orthogonal directions and rotated around three orthogonal axes. Since only the position of bodies with respect to each other is of interest, frame of reference is fixed to one of the bodies.

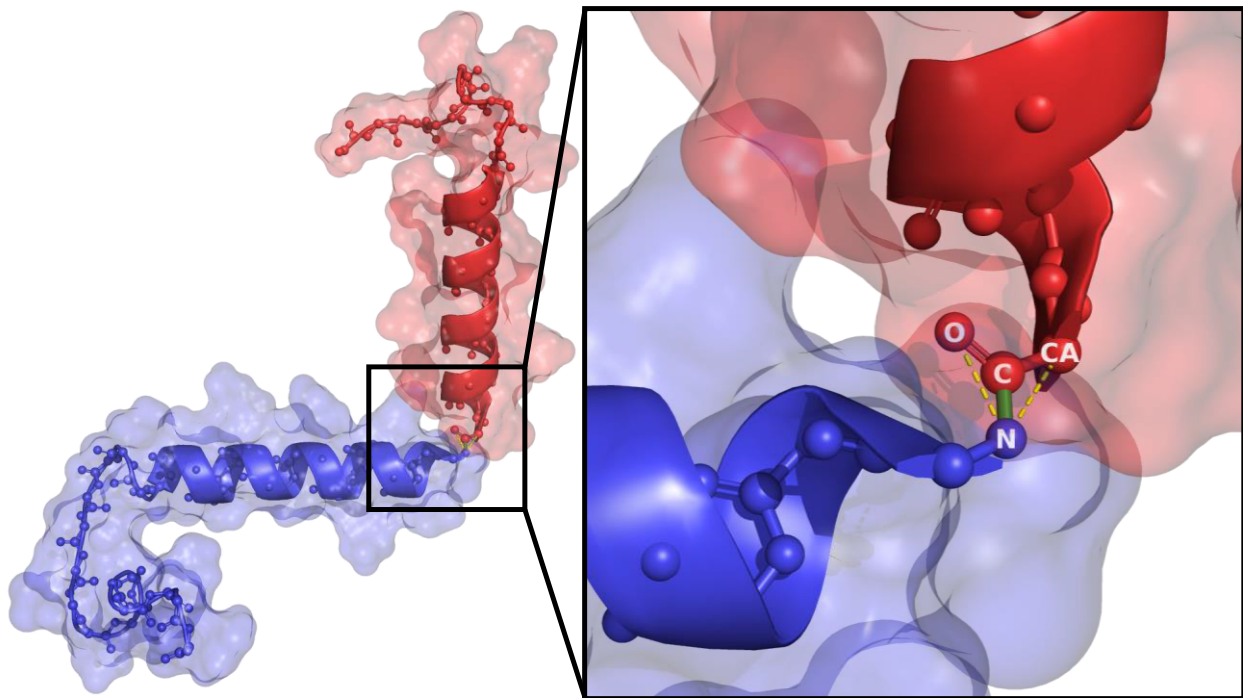


**Figure 7** | *An exemplary rigid body model of two-helix peptide AGL55. Overview and a close-up view of the AGAMOUS-like 55 (AGL55) protein (PDB ID: 6bzj). In this example the protein is described by two rigid bodies (red and blue), each containing one alpha-helix (conformations of the C- and N-terminal loops are neglected). The bodies are connected by the peptide bond (green). Since the length of the peptide bond is small (1.32 Å) and due to the steric clashes, possible motions of the nitrogen atom (labelled with “N”) in the blue body with respect to the red body are negligible. Only the rotation of the blue body around the nitrogen atom is possible.*

For example, for a protein with two rigid domains, connected by a peptide bond, one can assume that the distance between the carbonyl carbon (C) and nitrogen (N) of the peptide bond is fixed, since it is a covalent bond (**Figure 7**). Then, using the equation 1.6, one could conservatively

calculate  $N_{fit,param.} = (2 - 1) * 6 - 1 = 5$ . The last “-1” term corresponds to the peptide bond. I designate the two rigid bodies here as “blue” and “red”. The blue body includes the nitrogen atom, which forms the peptide bond between the bodies (“blue nitrogen”), and the carbonyl carbon is a part of the red body (“red carbon”). Since the peptide bond length is short (1.32 Å), motion of the blue nitrogen with respect to the red body is strongly restricted by steric clashes and can be completely neglected here. One could add two additional bonds (yellow) between the blue nitrogen and red oxygen, and between the blue nitrogen and red  $\alpha$ -carbon. These two additional bonds will not restrict the motions of the blue body with respect to the red any further. Effectively, these two additional bonds were already included in the model implicitly due to the steric clashes. Now, using equation 1.6, I calculate:

$$N_{fit,param.} = (2 - 1) * 6 - 3 = 3 \quad (1.7)$$

This corresponds to three directions of rotation possible for the blue body with respect to the red.  $N_{fit,param.}$  can also be called the *number of degrees of freedom in the model*, which should not be confused with the  $N_{dof}$  of the  $\chi^2$  distribution.

If the FRET-guiding is used in a combination with a complex conformational model like a FRET-restrained MD simulation or FRET-guided NMSim,  $N_{fit,param.} = N_{FRET\ restraints}$  is a good estimate for the model complexity. In this case  $\chi^2$  test is transformed into a cross-validation approach, and the quality of the resulting structural model is determined from the measurements, that were not used for FRET-guiding.

### ***p*-values**

Using the chi-squared probability density function (Eq. 1.2), it is possible to determine a degree of certainty that the experiment does not match the model (conformer) also called ***p*-value** or significance. *p*-value quantifies, how unlikely is a value of  $\chi^2$  larger than the one observed, assuming the model is correct (null hypothesis is true), typically interpreted as the area under the right tail of the function (**Figure 8**). The ***p*-value** is the probability that the true model would give  $\chi^2$  that is as large as observed one or larger.

$$p = \int_{\chi^2}^{+\infty} f_{N_{dof}}(\chi^2) d\chi^2 \quad (1.8)$$

$p$ -value can take values from 0 to 1. Small  $p$ -value (e.g.  $p < 0.003$ ) either means that the measured data is different from what is expected for the model, so the model can be discarded or that the errors are underestimated. If the  $p$ -value is small, one can say, that “the null-hypothesis is rejected”, i.e. the experimental data does not fit to the model. In other words, low  $p$ -value means, that assuming the given model is correct, it is unlikely to collect an experimental dataset which is, purely by chance, so far away from the model. This indicates, that the initial assumption, that the model is correct, should be discarded. The meaning of  $p$ -value might feel counterintuitive, and the difficulties of its interpretation are broadly discussed in the literature<sup>45-49</sup>.

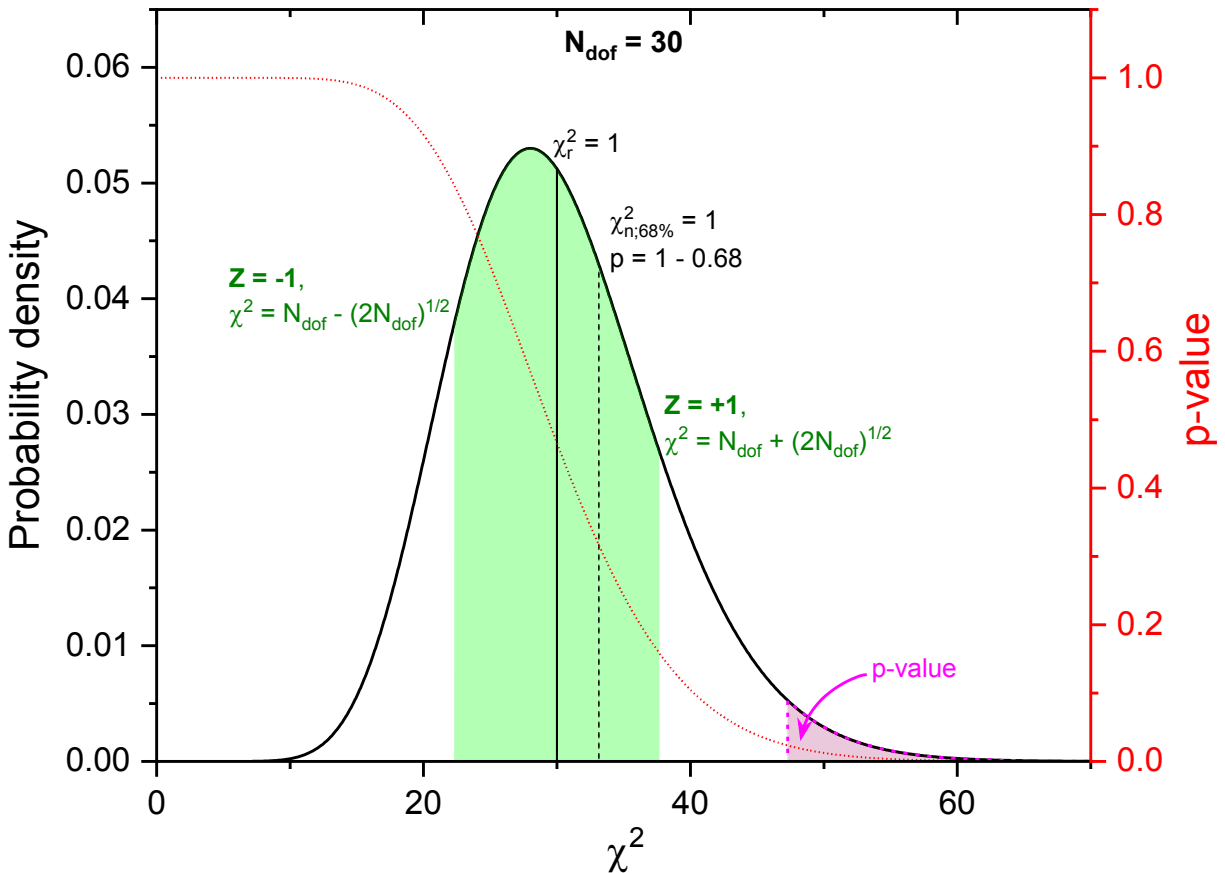


**Figure 8 | The chi-squared distribution with 30 degrees of freedom.** The probability density function is shown as a solid black curve. Integral of this function (eq. 1.2) over an interval defines the probability to observe a  $\chi^2$ -value in that interval for a set of experiments with  $N_{\text{dof}}$  degrees of freedom. The  $p$ -value is indicated by a red dotted line on the secondary Y-axis. The green area covers the standard score range  $-1 < Z < +1$ . The solid vertical black line indicates the expected (mean) value of  $\chi^2$  or, which is equivalent,  $\chi_r^2 = 1$ . The dashed vertical black line is for  $1 - p = 0.68$  or equivalently,  $\chi_n^2 = 1$ . The magenta-filled area indicates the  $p$ -value of a model, indicated by the vertical dashed magenta line.

Precise threshold for  $p$ -values, which justifies rejection of the null hypothesis can vary depending on the context and the field. For a normal distribution, values taken within one standard deviation of the mean cover  $\sim 68.3\%$  probability.  $p$ -values lower than  $1 - 0.683 = 0.317$  correspond to the confidence level of “one sigma”. In particle physics there is a convention, that discovery can only be qualified, when a five-sigma effect is shown, which corresponds to  $p$ -values lower than  $5.7 \times 10^{-5}\%$ . In other fields and contexts, however, two (5%) and three (0.3%) sigma confidence levels are used ubiquitously.  $p$ -values can also be indicated by asterisks: one asterisk (\*) stands for  $p \leq 0.05$ , \*\* stands for  $p \leq 0.01$ , \*\*\* - for  $p \leq 0.001$ , \*\*\*\* - for  $p \leq 0.0001$ .

Too large  $p$ -value (e.g.  $p > 0.997$ ) can indicate overfitting, meaning that  $N_{fit,param.}$  is underestimated or it can be due to overestimated errors. Comparison of different models that are not discarded (i.e.  $0.003 < p < 0.997$ ) with each other has limited value, since for them difference in  $\chi^2$  is comparable to the uncertainty of  $\chi^2$ , so there is not enough statistical evidence to strongly prefer one such model over another<sup>43</sup>.

If there is a reason to suspect, that extremely low or extremely high  $p$ -value is caused by an inaccurate error estimate, approximate magnitude of such inaccuracy can be calculated. Let's assume for simplicity, that the error estimates  $\Delta R_{est,exp}^{(i)}$  deviate from the true errors  $\Delta R_{exp}^{(i)}$  by a constant scaling factor  $\theta$ :  $\Delta R_{est,exp}^{(i)} = \theta \cdot \Delta R_{exp}^{(i)}$ . Then from the equation 1.1 we obtain:

$$\chi_{est}^2 = \sum_{i=1}^{N_{measurements}} \left( \frac{R_{mod}^{(i)} - R_{exp}^{(i)}}{\theta \cdot \Delta R_{exp}^{(i)}} \right)^2 = \frac{\chi^2}{\theta^2} \quad (1.9)$$

Assuming, the model is correct and using equations 1.3 and 1.4 the estimate of the scaling factor can be expressed as:

$$\theta = \sqrt{\frac{\langle \chi^2 \rangle}{\chi_{est}^2}} \pm \frac{\partial \theta}{\partial \chi^2} \sigma_{\chi^2} = \sqrt{\frac{N_{dof}}{\chi_{est}^2}} \pm \frac{1}{\sqrt{2\chi_{est}^2}} \quad (1.10)$$

## Z-scores

Another way to statistically access observed  $\chi_{obs}^2$  value is to measure how far out it falls in the tails, using the units of standard deviation of  $\chi^2$  distribution (not to be confused with measurement errors). Since the expected value of  $\chi^2$  distribution,  $\langle \chi^2 \rangle$  and its standard deviation  $\sigma_{\chi^2}$  are defined

by its only parameter  $N_{dof}$  (Eq. 1.3, 1.4), the inconsistency of the data and the model can be quantified by a standard score  $Z$ :

$$Z = \frac{\chi_{obs}^2 - \langle \chi^2 \rangle}{\sigma_{\chi^2}} = \frac{\chi_{obs}^2 - N_{dof}}{\sqrt{2N_{dof}}} \quad (1.11)$$

For  $\chi^2$  distribution  $Z$ -scores can take real values in the range  $-\sqrt{N_{dof}/2} < Z < +\infty$ . Large positive  $Z$ -scores (e.g.  $Z > 5$ ) have the same meaning as small  $p$ -values. When the  $N_{fit.param.}$  parameter is underestimated and  $N_{dof}$  is large ( $N_{dof} > 20$ ),  $Z$ -scores converge to large negative values, e.g.  $Z < -3$ , thus being indicative of the overfitting or underestimated experimental errors.

### Reduced and normalized $\chi^2$ values

Since the expected value of  $\chi^2$  equals the number of degrees of freedom (Eq. 1.3), the reduced value of  $\chi^2$  per degree of freedom, referred to as  $\chi_r^2$  can be a useful indicator for the inconsistency between the model and the experimental data:

$$\chi_r^2 = \chi^2 / N_{dof} \quad (1.12)$$

For large  $N_{dof} > 30$ , value of  $\chi_r^2 = 1$  indicates, that the mismatch between the model and the observation is as large as expected from the measurement errors,  $\chi_r^2 < 1$  indicates overfitting and  $\chi_r^2 \gg 1$  indicates a poor model.

$$\lim_{N_{dof} \rightarrow \infty} (p | \chi_r^2 = 1) = 0.5 \quad (1.13)$$

However, for smaller  $N_{dof}$ , different models with  $\chi_r^2 = 1$  correspond to different  $p$ -values, depending on  $N_{dof}$  (**Figure 9**). When several models with different  $N_{dof}$  are compared and  $N_{dof} < 30$ , usage of  $\chi_r^2$  can be inconvenient. To overcome this problem, I use the  $\chi^2$  value normalized by the  $\chi^2$  at a fixed  $p$ -value, e.g.  $1 - p = 68\%$ :

$$\chi_n^2 = \chi^2 / \chi_{68\%}^2 \quad (1.14)$$

Where  $\chi_{68\%}^2$  can be found from equation 1.8:

$$1 - 0.68 = \int_{\chi_{68\%}^2}^{+\infty} f_{N_{dof}}(\chi^2) d\chi^2 \quad (1.15)$$

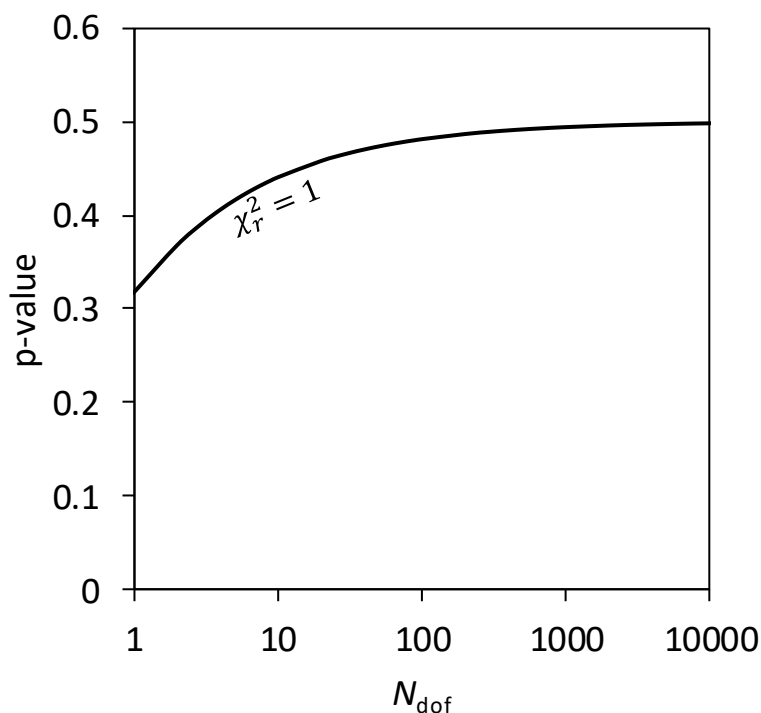


**Figure 9** | Dependency of the p-value on the number of degrees of freedom for a constant value of  $\chi_r^2 = 1$ . Constant value of reduced chi-squared value  $\chi_r^2 = 1$  corresponds to different p-values, depending on the number of degrees of freedom in the test.

Solution to this equation is given in equations 2.8 and 2.9. Interpretation of  $\chi_n^2$  is similar to  $\chi_r^2$ , but it is more robust for  $N_{dof} < 30$  and can be applied, when models of different complexity ( $N_{fit.param.}$ ) are compared to the same set of experimental data. A model with  $\chi_n^2 = 1$  has p-value  $p = 1 - 0.68$  exactly, i.e. a mismatch between such a model and the observation is in accord with the measurement errors.

### Using $\chi^2$ statistics for FRET-assisted modelling: an example of T4 lysozyme

In this example, I calculate the statistical quantities for the conformational state  $C_1$  of T4 Lysozyme. As summarized in the section 1.5.1, 33 FRET pairs were studied for the T4 lysozyme protein. Three short-lived conformational states ( $C_1$ ,  $C_2$ , and  $C_3$ ) were characterised by combining single-molecule and ensemble multiparameter FRET detection, EPR spectroscopy, mutagenesis, and FRET-positioning and screening (**Figure 18**). As a result, three sets of 33 inter-dye distance were formed, corresponding to the three states. In Supplement B, the known crystal structures of the T4 Lysozyme (T4L) are compared to these three FRET datasets. Two datasets ( $C_1$ ,  $C_2$ ) were identified to match the crystal structures of the T4L available in the Protein Data Bank (PDB). The conformation of the third state  $C_3$  does not match any of the conformers, available in the PDB.

In this example I focus on dataset for  $C_1$ . FRET based inter-dye distances and estimates of corresponding experimental errors are provided in the supplementary table S2D of the Supplement B. First, I estimate the  $N_{dof}$  for the ensemble of T4L crystal structures (**Figure 18a**). Close inspection of the ensemble reveals that the structure of  $N$ - and  $C$ -terminal subdomains does not change, only their mutual orientation. Using this observation, I approximate ensemble of the T4L crystal structures by two rigid bodies corresponding to the  $N$ - and  $C$ -terminal subdomains, connected by the peptide bond. This rigid body model consists of 2 bodies connected by the peptide bond. Since the peptide bond is short (1.32 Å) and taking steric clashes into account, effectively there are 3 bonds in the model, just like in the example above (eq. 1.7), I have 33 measurements, 2 bodies and 3 bonds:

$$N_{dof} = 33 - ((2 - 1) * 6 - 3) = 30$$

For the crystal structure with the PDB ID 148L, I obtain  $\chi^2 = 50.82$  (Eq. 1.1, vertical solid magenta line on **Figure 10**). Using equation 1.8, I find a  $p$ -value = 0.01 for the dataset  $C_1$  and conformer 148L. This means, that the probability that 148L is the correct model and measurements are so much off by chance is 1%. Thus, this conformation does not seem to match to the inter-dye distances measured for state  $C_1$ . In the same way, I find  $\chi^2 = 26.15$  and  $p$ -value = 0.67 for conformation 172L, which means, that the structure and inter-dye distances match within the errors. The same conclusion could be drawn from  $Z$ -scores alone: for conformers 172L and 148L  $Z$ -scores are -0.5 and 1.53 respectively (eq. 1.11).

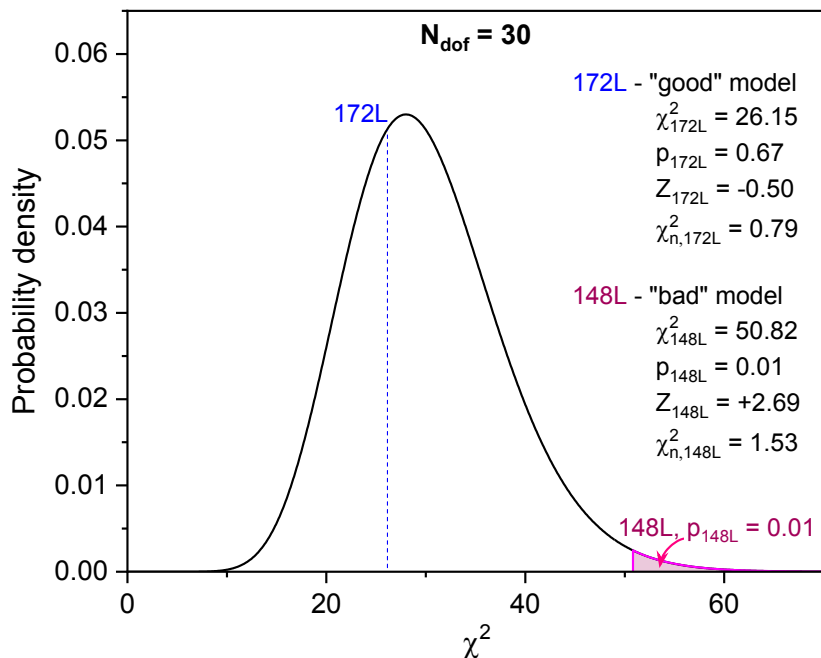


**Figure 10** | *The chi-squared distribution on the example of T4L crystal structures. The probability density function is shown as the solid black curve. The vertical dashed blue line indicates the “open” crystal structure of T4 lysozyme (PDBID 172L) compared to the FRET experimental dataset for  $C_1$  state (good model); the vertical solid magenta line indicates the crystal structure of the “closed” crystal structure (PDBID: 148L) compared to the FRET experimental dataset for the same  $C_1$  state (bad model). The area under the curve, highlighted in light magenta is the  $p$ -value for the 148L model, calculated for the dataset  $C_1$ . One can see from the plot, that the conformer 148L does not match the dataset  $C_1$ , while conformer 172L agrees with the  $C_1$  data.*

In the same manner, any ensemble of structures can be compared to experimental data. It is convenient to display the  $\chi_n^2$  of the conformers against some structural feature, like distance between relevant structural elements in the molecule, some convenient angle, or a similarity score against a reference structure, e.g. fraction of native contacts (Q)<sup>50,51</sup>, global distance test (GDT-TS)<sup>52</sup>, template modelling score (TM-score)<sup>53</sup>, local distance difference test (IDDT)<sup>54</sup>, or root-mean-square deviation of atomic positions (RMSD, Eq. 2.1). For the case of T4L dataset  $C_1$ , I plot  $\chi_n^2$  of available crystal structures against the RMSD of  $C_\alpha$  atoms, using conformation 172L as the reference, since it has the lowest  $\chi_n^2$  (FRET-best structure, **Figure 11**). This representation highlights structural variability of the conformations below the  $p$ -value threshold of one sigma ( $\chi_n^2 = 1$ ).



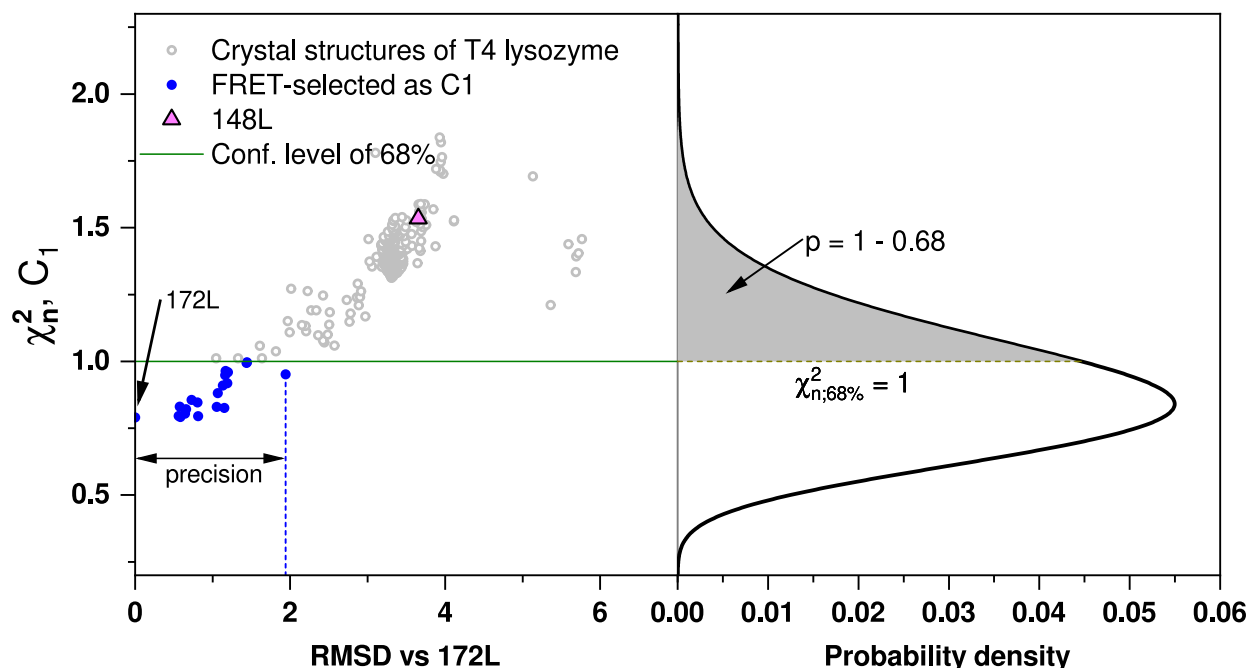


**Figure 11 | Selection of conformers by FRET.** Y-axis shows the  $\chi_n^2$  value, calculated for the FRET dataset  $C_1$ . Circles represent a set of distinct potential conformers (prior ensemble), formed from the 571 X-ray and NMR structures of T4 lysozyme from the PDB. On the left, x-axis shows the RMSD against the reference conformer (172L, lowest  $\chi_n^2$ ). The horizontal line at  $\chi_n^2 = 1$  indicates the confidence level of 68%. The RMSDs of the structures below the threshold  $\chi_n^2 = 1$  define the precision of the model. Conformers above the threshold (grey circles) are discarded, since they don't match to the FRET experimental dataset  $C_1$ , given the confidence level of 68%. On the right, chi-squared probability density function is shown (transposed view of **Figure 8**).

#### 1.4.8. Estimation of conformational precision

Different definitions of the terms “accuracy” and “precision” are used in the context of model assessment in physical sciences. In this thesis I use the convention defined in the ISO standard 5725-1:1994<sup>55</sup> and illustrated in the **Figure 12**.

##### ISO 5725. Section 0.1:

ISO 5725 uses two terms "trueness" and "precision" to describe the accuracy of a measurement method. "**Trueness**" refers to the closeness of agreement between the arithmetic mean of a large number of test results and the true or accepted reference value. "**Precision**" refers to the closeness of agreement between test results.

##### ISO 5725. Section 0.6:

The general term **accuracy** is used in ISO 5725 to refer to both trueness and precision.

The term accuracy was at one time used to cover only the one component now named trueness, but it became clear that to many persons it should imply the total displacement of a result from a reference value, due to random as well as systematic effects.

The term bias has been in use for statistical matters for a very long time, but because it caused certain philosophical objections among members of some professions (such as medical and legal practitioners), the positive aspect has been emphasized by the invention of the term trueness.

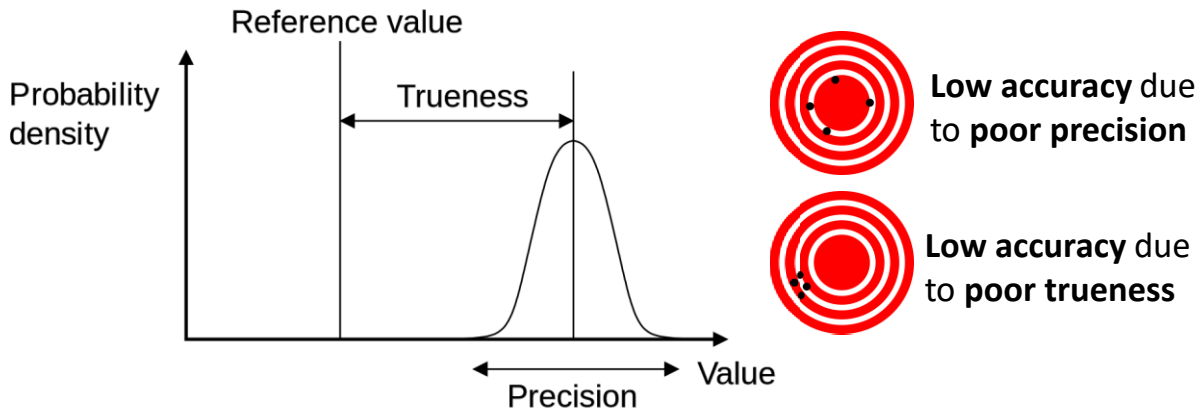


**Figure 12 | Precision, trueness, and accuracy according to ISO 5725-1:1994.**

In the step 7 of the workflow (**Figure 5b**), the precision of the obtained conformers is estimated by propagating the errors of experimentally determined parameters. However, since the error estimates are partially derived from the calibration studies with known DNA rulers<sup>8</sup>, they also account for the trueness component of accuracy, at least in part. As summarized in Hellenkamp et al.<sup>8</sup> and Peulen et al.<sup>14</sup>, the total relative error  $\delta R_E = \Delta R_E / R_E$  of FRET-averaged inter-dye distance  $R_E$  can be expressed as:

$$\begin{aligned} \delta R_E^2 = & \delta R_E^2(\text{noise}) + \underbrace{\delta R_E^2(\gamma) + \delta R_E^2(\alpha) + \delta R_E^2(B_G) + \delta R_E^2(B_R)}_{\delta R_E^2(\text{calibration})} \\ & + \underbrace{\delta R_E^2(J) + \delta R_E^2(n) + \delta R_E^2(\kappa^2)}_{\delta R_E^2(R_0)} + \delta R_E^2(\text{dye model}) \end{aligned} \quad (1.16)$$

The total error is composed of four major components: the error caused by the photon shot noise  $\delta R_E^2(\text{noise})$ , the error directly related to the instrument  $\delta R_E^2(\text{calibration})$ , the error of the Förster radius  $\delta R_E^2(R_0)$  and the error of the dye model  $\delta R_E^2(\text{dye model})$ . Instrument-related error  $\delta R_E^2(\text{calibration})$  includes contributions from uncertainties in: the ratio of donor and acceptor

detectability  $\gamma$  ( $\delta R_E^2(\gamma)$ ), donor emission crosstalk  $\alpha$  ( $\delta R_E^2(\alpha)$ ), green background  $B_G$  ( $\delta R_E^2(B_G)$ ) and red background  $B_R$  ( $\delta R_E^2(B_R)$ ). The Förster radius error  $\delta R_E^2(R_0)$  includes contributions from uncertainties in: the overlap integral  $J$  ( $\delta R_E^2(J)$ ), the refractive index  $n$  ( $\delta R_E^2(n)$ ) and dye orientation factor  $\kappa^2$  ( $\delta R_E^2(\kappa^2)$ ).

For lifetime-based analysis, the total relative error  $\delta R_{DA} = \Delta R_{DA}/R_{DA}$  of inter-dye distance  $R_{DA}$  can be expressed as:

$$\begin{aligned} \delta R_{DA}^2 = & \delta R_{DA}^2(\text{noise}) + \underbrace{\delta R_{DA}^2(D_{\text{only reference}})}_{\delta R_{DA}^2(\text{calibration})} \\ & + \underbrace{\delta R_{DA}^2(J) + \delta R_{DA}^2(n) + \delta R_{DA}^2(\kappa^2)}_{\delta R_{DA}^2(R_0)} + \delta R_{DA}^2(\text{dye model}) \end{aligned} \quad (1.17)$$

Here,  $\delta R_{DA}^2(D_{\text{only reference}})$  is the error associated with the donor-only reference, which may originate from fluorescent impurities, unreacted dye or unspecific labeling of the biomolecule. Other contributions to the total relative error  $\delta R_{DA}$  of inter-dye distance  $R_{DA}$  have the same causes, as in the case of the total relative error  $\delta R_E$  of FRET-averaged inter-dye distance  $R_E$ .

The error caused by the photon shot noise  $\delta R_E^2(\text{noise})$  can be estimated directly from the experimental data for a given FRET pair. However, for  $\delta R_E^2(\text{calibration})$ ,  $\delta R_E^2(R_0)$  and  $\delta R_E^2(\text{dye model})$ , accurate estimation from the experimental data itself is not possible. In order to improve the accuracy of error estimates, calibration experiments are performed. Recently, in a blind study, six differently labelled DNA-ruler molecules were measured by 20 participating labs<sup>8</sup>. The study showed, that the standard deviation of FRET efficiencies measured this way is between 0.02 and 0.05. Our models for estimating the  $\delta R_E^2(\text{calibration})$ ,  $\delta R_E^2(R_0)$  and  $\delta R_E^2(\text{dye model})$  are adjusted in order to reproduce these standard deviations and additional experimental data is being collected for more accurate calibration of error estimates (Eq. 1.10, **Figure 13**).

In order to compare the measured FRET efficiency to a conformational model, one has to account for the dye linker behaviour. The model of this behaviour or “dye model” can deviate from the “true” dye behaviour. The error of the dye model  $\delta R_E^2(\text{dye model})$  characterizes the uncertainty of the conversion from inter-dye distance to the distance between the atoms in the backbone of the macromolecule, typically  $C_\alpha$  atoms for proteins or P atoms for nucleic acids. The magnitude and distribution of this deviation is assessed by calibration measurements and, for convenience, incorporated into the overall inter-dye distance error<sup>8</sup>.

Inter-dye distance error is propagated to the error in the positioning of atoms in the molecule, also called resolution. First, the conformation with the highest  $p$ -value is selected from the *prior* (best structure). This structure is progressively modified away from the best until the  $p$ -value reaches the desired confidence level, e.g. 68% or one sigma. Since modification of the best structure can go in different directions, it is repeated many times to explore, how far from the best structure can it be changed, remaining within the experimental error boundaries. Deviation between the best conformation and the structures on the edge of the error boundary  $RMSD_{max}$  can be reported as precision at a given confidence level (Eq. 1.18). This precision estimate agrees with the factual accuracy benchmarked against the X-ray crystal structure for the T4 Lysozyme, a protein with two subdomains (Chapter 2, Supplement B). Ensemble of structures, which fall below the threshold  $\chi_n^2 = 1$  is also referred as FRET-selected ensemble (**Figure 11**). Using these conformations, two additional precision quantifiers can be reported: unweighted average RMSD against the FRET-best structure  $\langle RMSD \rangle$  (Eq. 1.19), and average RMSD weighted by the  $p$ -values of each structure  $\langle RMSD \rangle_p$  (Eq. 1.20).

$$RMSD_{max} = \max_{\chi_n^2 < 1} RMSD_i \quad (1.18)$$

$$\langle RMSD \rangle = \frac{1}{N_{sel}} \sum_{i=1}^{N_{sel}} RMSD_i \quad (1.19)$$

$$\langle RMSD \rangle_p = \frac{1}{\sum p_i} \sum_{i=1}^{N_{sel}} p_i \cdot RMSD_i \quad (1.20)$$

$RMSD_i$  is the RMSD of the conformer ( $i$ ) in the FRET-selected ensemble against the conformer with the lowest  $\chi_n^2$  (best structure),  $p_i$  is the  $p$ -value of a FRET-selected conformer ( $i$ ), and  $N_{sel}$  is the number of conformers in the FRET-selected ensemble.

To highlight the residue-specific uncertainty of the FRET-assisted model, root mean square fluctuations (RMSF) within the FRET-selected ensemble can be calculated.

$$RMSF_{atom} = \sqrt{\frac{1}{N_{conf}} \sum_{conf=1}^{N_{conf}} \|\overrightarrow{r_{conf,atom}} - \langle \overrightarrow{r_{conf,atom}} \rangle\|^2} \quad (1.21)$$

RMSF, however, should be analysed cautiously as it depends on the superposition of structures, which is performed prior to the calculation. This can be avoided, if a superposition-free score for structural dissimilarity is used instead, for example the distance difference test (IDDT)<sup>54</sup>.

### 1.4.9. Quality checks

The accuracy of a structural model can be assessed from the distribution of deviations between the model-derived distances and experimentally measured values (**Figure 13**). Systematic errors can be identified by plotting the experimentally-derived inter-dye distance  $R_{DA,exp}$  against the model-derived distance  $R_{DA,model}$  (**Figure 13a**). In such representation points should ideally be scattered around the 1:1 line. If the slope of the linear fit in this representation deviates significantly from 1.0, one should check for systematic errors, e.g. incorrect estimation of the Förster radius.

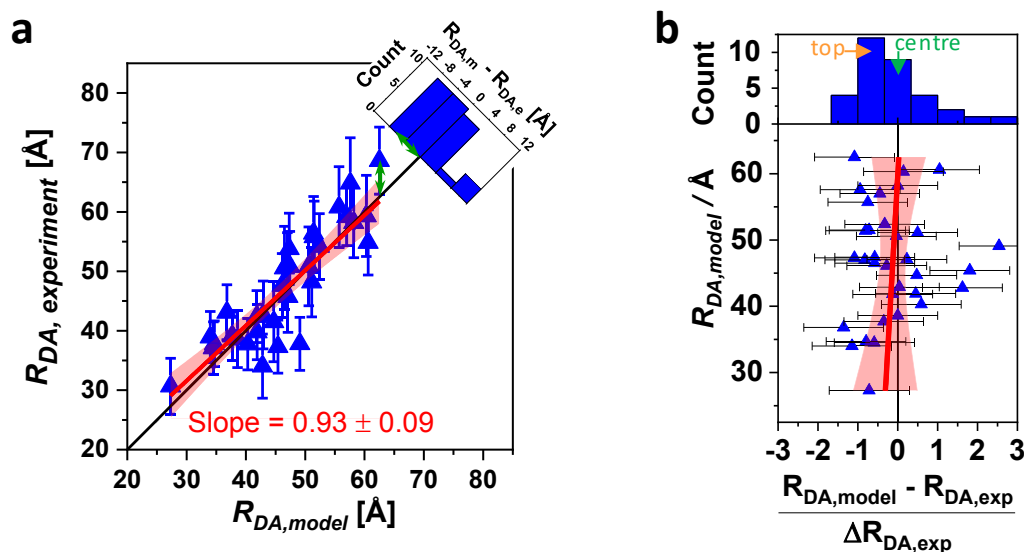


**Figure 13 | Comparison of distances derived from structural model vs distances determined from experiment.** (a) The experimental distances  $R_{DA,experimental}$  are plotted against the model distances  $R_{DA,Model}$  from the best structure and fitted linearly (red lines), 95% confidence band is shown in light red. The black lines show a 1:1-relationship. Histogram of the non-weighted residuals is shown in the inset. Small green arrow indicates the deviation, that is projected to the histogram in the inset, it goes parallel to the Y axis, not perpendicular to the 1:1 line. Adapted from Supplement B. (b) Histogram of weighted residuals. Deviations between measured distances and distances predicted from the “best” structural model are normalized by the errors (weighted). Linear fit and 95% confidence band is shown in red. The highest bar is indicated by the orange arrow. Adapted from **Figure 5C** in Supplement B.

The same data can be analysed more conveniently, if the deviations between the model and experimental distances are normalized by the errors, representing so called weighted or normalized residuals (**Figure 13b**). In this representation one can immediately perform four checks<sup>43,56</sup>:

- 1) Points should fall on both sides of the Y axis approximately symmetrically.
- 2) Histogram of weighted residuals should have the maximum close to 0.
- 3) Standard deviation of weighted residuals should be approximately equal to  $\sqrt{1 - N_{fit.param.}/N_{measurements}}$
- 4) Residuals should not form patterns like waves or trends, i.e. the magnitude of the residual should not depend on the value parameter itself.

The example, shown in the **Figure 13**, passes all four checks. The top of the histogram is slightly shifted left (**Figure 13b**, orange arrow), but not by far: the number of pairs, that land in the highest bar (orange arrow) is only 3 more than for the central bar (green arrow). Strong violations of these four criteria would indicate problems in either analysis of experimental data or structural modelling. Quantitative statistical testing of weighted residuals histograms is possible, for example using Kolmogorov-Smirnov test<sup>57</sup>, however, detailed review of quantitative methods of residual analysis falls beyond the scope of this thesis.

Besides the statistical test, stereochemical scores are often used as part of the quality assessment routine for protein structures determined by X-ray crystallography or NMR spectroscopy<sup>58</sup>. They are a part of the wwPDB X-ray Validation Task Force recommendations<sup>59</sup>, which include scores calculated by MolProbity<sup>60</sup>, PROCHECK<sup>61</sup>, WHAT\_CHECK<sup>62</sup> and other software. For such structures, clashes between atoms, outliers from Ramachandran torsions, and other stereochemical parameters can be of relevance, since the experimental data is typically highly redundant, construction of a model, that violates stereochemical constraints is possible. In the case of FRET-guided structural modelling, experimental data is typically sparse, so the information on the short-range structural features, including stereochemical restraints, is coming mostly from the computational modelling algorithm or the force field. Due to this, FRET-assisted structural models can usually be constructed such, that the stereochemical scores are nearly perfect and assess the underlying computational modelling method, rather than the FRET-assisted structural model as a whole.

#### 1.4.10. FRET-guided computational structural modelling

However, a correct structure can also be absent from the *prior* conformational ensemble, formed at step 2. In this case, in step 5 all models will be correctly identified as experiment-incompatible. To overcome this problem, a new *prior* must be generated in step 6. Since additional experimental

data is collected in step 4, the generation of the new prior can make use of this information. The fluorescence data can be used during the generation of the new prior in order to significantly improve the chances for it to contain accurate conformers.

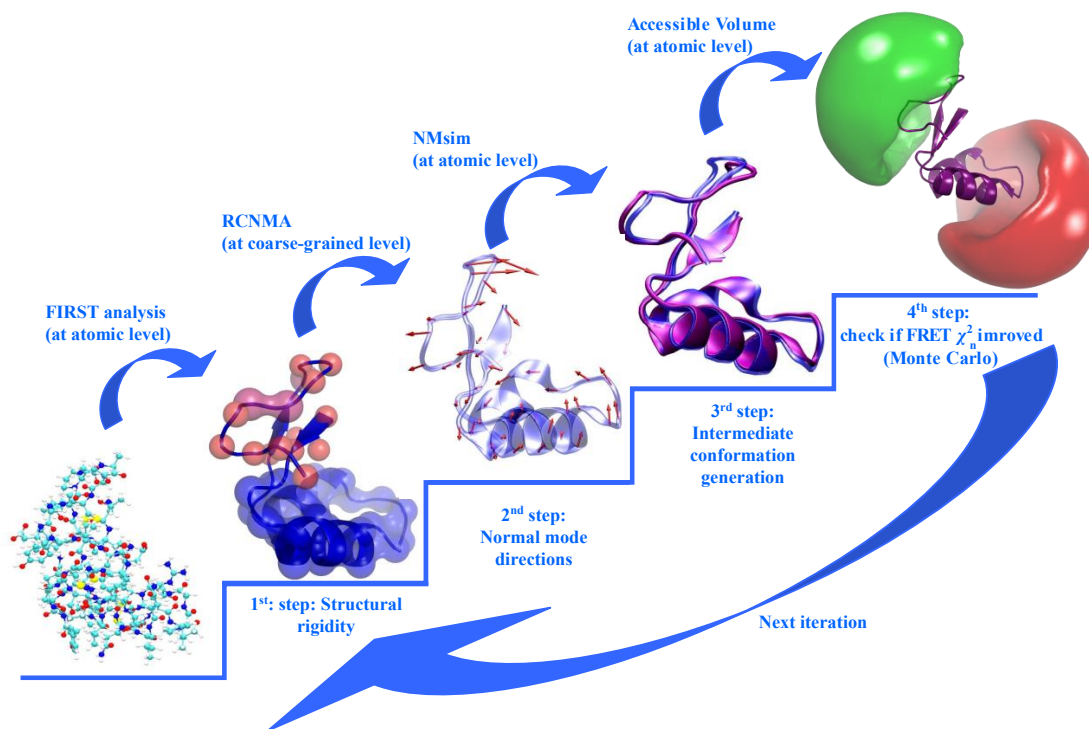


**Figure 14 | FRET-guided NMSim simulations.** NMSim is a normal mode-based geometric simulation approach for multiscale modelling of protein conformational changes using three-step iterations: In the first step, the protein structure is coarse-grained by the software FIRST into rigid parts (coloured blobs) connected by flexible links (single spheres). In the second step, low-frequency normal modes are computed by rigid cluster normal mode analysis (RCNMA). In the third step, a linear combination of the first normal modes is used to bias backbone motions along the low-frequency normal modes, while the side chain motions were biased towards favoured rotamer states. The algorithm is here extended by a fourth step – a Markov Chain Monte Carlo step to prioritize conformations lying in most relevant regions according to the FRET  $\chi_n^2$  value. Depiction of steps 1 to 3 was adapted from Ahmed *et al.*<sup>24</sup>

Kalinin *et al.* have previously showed the application of FRET-restrained rigid body docking (RBD) for FRET-assisted structural modelling<sup>21</sup>. Here, two additional methods for fluorescence-guided structure generation are demonstrated: Markov chain Monte Carlo guiding (MCMC, section 2.5.7, **Figure 14**) for coarse-grained methods and the approach based upon a FRET-restraining potential (restraining, section 2.5.8, **Figure 15**) for molecular dynamics simulations.

The first approach to FRET-assisted conformer generation is an adaptation of Metropolis–Hastings algorithm where  $\chi^2$  is used as the rejection potential (**Figure 14**). In MCMC sampling no explicit

FRET-restraints (forces) are applied, instead conformations are generated iteratively and are accepted if  $\chi^2$  of the new structure is lower than that at previous step. If a newly generated conformation has higher  $\chi^2$  value, it is stochastically rejected and the rejection rate is higher if the increase in  $\chi^2$  is higher. This way MCMC simulation evolves over time towards structures with lower  $\chi^2$  values. However, for a conformation generated in this manner, lower  $\chi^2$  value does not necessarily mean better structure, since it may be caused by a disproportional increase in the overall complexity of the model (overfitting). To distinguish between the overfitting and genuine improvement in the quality of the model, cross validation is used at step 7.

In FRET-restraining approach, inter-dye distances determined by FRET are converted into additional harmonic-like restraints between non-physical pseudo atoms (**Figure 15**). Pseudo atoms are introduced into the system to represent statistical average dye position. They are strongly restrained with respect to the dye attachment residue and two nearby residues, so that the position of a pseudo atom with respect to its attachment residue is kept constant. Pseudo atoms do not interact with other atoms in any manner. FRET-derived inter-dye distances are converted into distances between the average dye positions. Harmonic restraints are then applied between the pseudo atom pairs with an optimum distance at the measured value. Forces exerted by the FRET restraints are capped in order to prevent the rupture of a biomolecule in the simulation. Since conformational changes of the restrained structure can change optimal positioning of pseudo atoms, their placement is updated at intervals of one nanosecond and FRET restraints are recalculated.



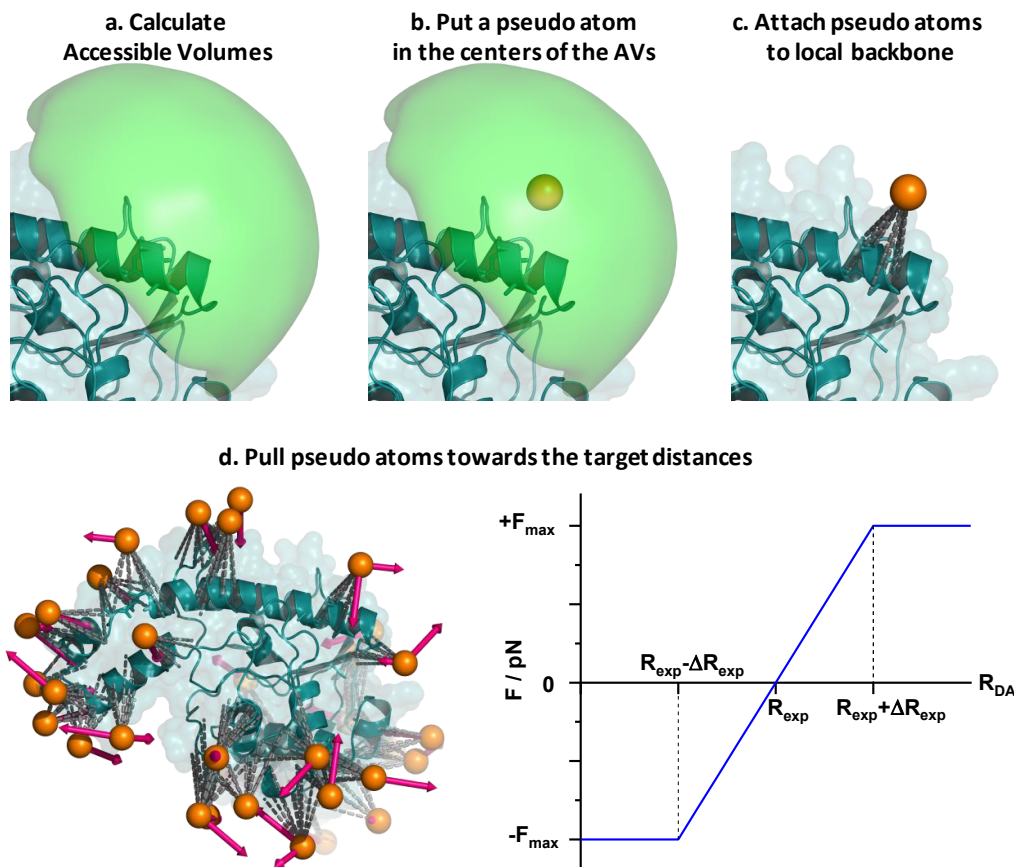


**Figure 15** | FRET-guided MD simulations. **(a)** Accessible Volume (AV) calculations are performed for each labelling position (green semi-transparent surface). **(b)** Pseudo atoms are positioned at the mean position of every accessible volume (orange sphere). **(c)** Pseudo bonds (grey dashed lines) are created between the pseudo atom and nearby  $C_\alpha$  and  $C_\beta$  atoms to keep pseudo atoms in their initial positions relative to the corresponding part of the protein backbone. **(d)** Restraints between pseudo atom pairs are applied to mimic measured inter-dye distances (magenta arrows).

Due to the high computational costs of the all-atom molecular dynamics simulations, all three FRET-guiding approaches are used complementarily: FRET-restrained rigid body docking (RBD) approach is used as the most coarse-grained method, which allows to reorient (sub)domains in the system according to the available FRET data; FRET-guided NMSim recovers stereochemically sound conformers and allows for additional bending of bodies to further accommodate FRET data; and FRET-restrained molecular dynamics simulations allow further minor readjustments of secondary-structure elements and also introduce solvation effects into the structural model, e.g. closing the voids, that were introduced in the RBD or NMSim.

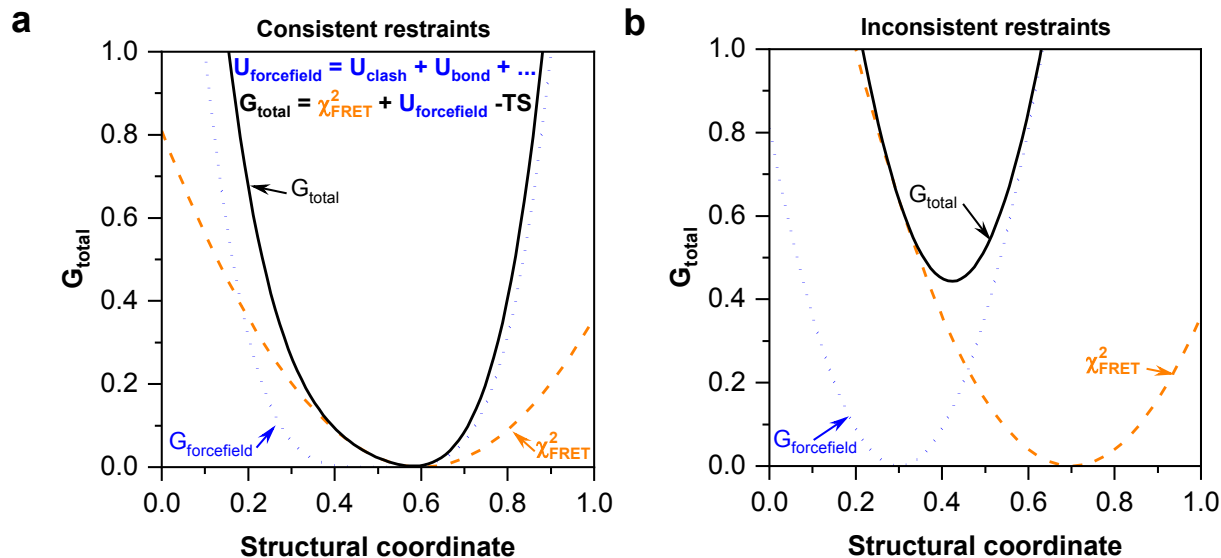


**Figure 16 | Consistency between computational modelling and FRET restraints.** Energy of FRET restraints is shown by the orange dashed line ( $\chi_{\text{FRET}}^2$ ). Dotted blue line indicated the forcefield free energy ( $G_{\text{forcefield}}$ ). Forcefield potential energy includes any non-FRET contributions, for example clash energy, electrostatic interactions, etc. The solid black line represents total free energy ( $G_{\text{total}} = \chi_{\text{FRET}}^2 + G_{\text{forcefield}}$ ). **(a)** Energy minima for FRET restraints and forcefield are overlapping, so the model is consistent. **(b)** Energy minima of FRET and forcefield restraints are separated, so that the model is inconsistent.

A compromise between the physical or knowledge-based constraints and the FRET-data has to be achieved for any FRET-assisted modelling approach. This compromise involves explicit or implicit weighting parameters, which set the balance between the *prior* or forcefield on one side and FRET data – on the other<sup>63</sup>. Ideally, FRET data and the *prior* computational model agree and favour the same conformation, corresponding to a minimum in the free energy landscape. However, even if that is the case, finding this minimum in the *prior* alone can be challenging if the energy landscape has many dimensions and its surface is rough – so called sampling problem. In this case, FRET data can guide the search of this hidden free energy minimum, alleviating the sampling problem. Alternatively, only an uninformative *prior* is available, so a large spectrum of conformations is flagged as acceptable, even though only certain specific conformational states are expected to be of relevance. In this case FRET data can introduce additional constraints and limit the space of possible conformations, ideally to a single structure (**Figure 16a**). If the prior or forcefield disagree with FRET data, resulting structure is much less reliable (**Figure 16b**), and may require further investigation into the cause of the mismatch, which could be due to the

problems with sample preparation, collection or analysis of FRET data, or a false conformational *prior*.

#### 1.4.11. Estimation of $N_{fit,param.}$ for FRET-assisted structural models

Determination of the conformational precision and confidence levels of a FRET-assisted structural model relies upon the accurate estimate of  $N_{dof}$  and more specifically,  $N_{fit,param.}$  (Eq. 1.2, 1.5). For a complex computational structural model like FRET-restrained MD simulation or FRET-guided NMSim, accurate determination of  $N_{fit,param.}$  is challenging. For such models I suggest the heuristic  $N_{fit,param.} = N_{FRET\ restraints}$ . With this approximation, additional FRET pairs are required for the derivation of the confidence levels (cross-validation). These additional FRET pairs are not used for FRET-guiding and serve for overfitting control.

In this example I show, how  $\chi_n^2$  depends on the number of FRET measurements for 3 different conformers of YaaA protein obtained by a FRET-guided NMSim simulations, each started from a different seed structure (**Figure 17a** red, blue and cyan). The fourth conformer, which is represented by cyan-magenta circles, in addition to FRET-guided NMSim, was refined by FRET-restrained MD simulations. All seed conformers were taken from the ensemble of predictions submitted by the participants of CASP 11 challenge for the YaaA protein<sup>64</sup> (Chapter 2). Seed conformers, corresponding to the red and blue curves have folds and secondary structures, that do not match to the crystal structure (**Figure 17b**). Since NMSim does not significantly change the fold of the proteins during the simulation, folds of FRET-guided conformers also do not match to the crystal structure. Seed structure, which corresponds to the cyan curve is the most similar to the crystal structure.

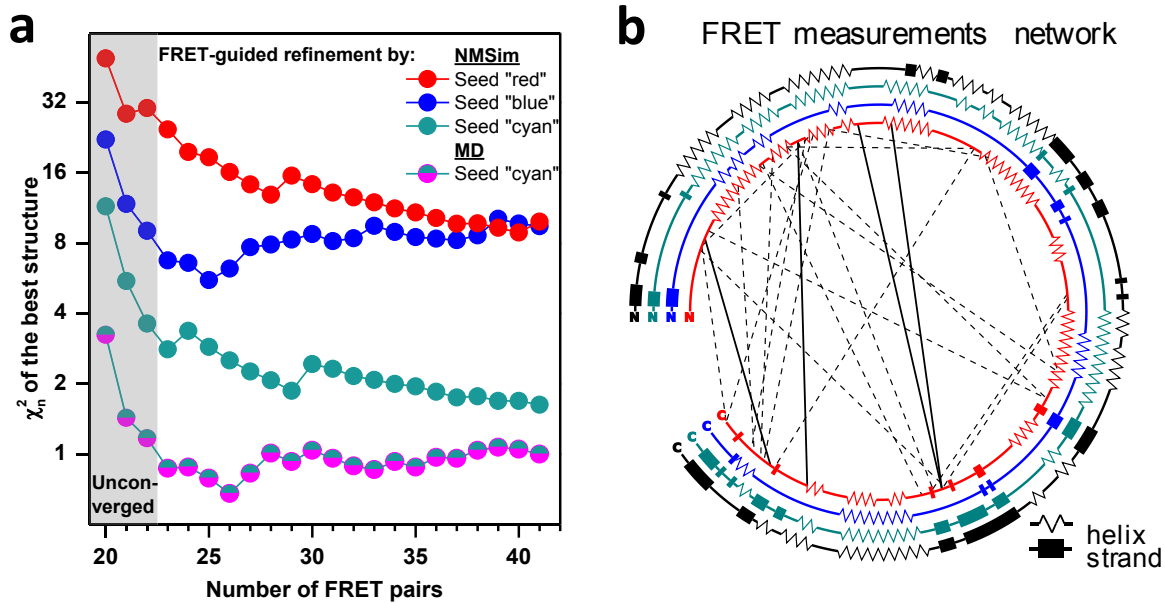


**Figure 17** |  $\chi_n^2$  of the best conformers generated by FRET-guided NMSim<sup>24</sup> and FRET-restrained MD simulation using different seed structures of YaaA protein. (a) Each colour stands for a model with a different fold, obtained from different seed structures.  $\chi_n^2$  starts to converge with  $\sim 23$  selected FRET pairs. 19 FRET restraints were used to generate the FRET-assisted models. (b) Network of FRET pairs used for guided NMSim simulations (dashed) and FRET screening (dashed and solid). Secondary structure elements (zigzag –  $\alpha$ -helix,  $3_{10}$ -helix or  $\pi$ -helix; rectangle –  $\beta$ -bridge or  $\beta$ -ladder, line – loop) for three shown seed structures (red, cyan, blue) and the crystal structure (black). Secondary structure of the cyan seed conformer is the most similar to the crystal structure. Adapted from the **Figure 1** of the Chapter 2.

As one can see in the **Figure 17a**,  $\chi_n^2$  levels-off approximately after 4 additional measurements, which indicates the convergence. I conclude, that for FRET-guided simulations, similar to those shown, even 4-5 additional measurements can be enough for the estimation of confidence levels. One can also see, that over-fitted FRET-guided conformers with incorrect folds (red, blue) can be reliably distinguished from a better model (cyan) with this approach.

This convergence is expected, since for higher number of measurements, the error of  $N_{fit,param}$  causes smaller deviation of  $N_{dof}$ , as compared to the width of the  $\chi^2$  distribution  $\sigma_{\chi^2} = \sqrt{2N_{dof}}$  (Eq. 1.4). Let's assume  $N_{dof}^\varepsilon$  is the incorrectly estimated  $N_{dof}$ :

$$N_{dof}^\varepsilon = N_{dof} - \varepsilon$$

$\varepsilon$  is a constant, which corresponds to the error of this estimate. Then the ratio

$$\frac{\|N_{dof}^{\varepsilon} - N_{dof}\|}{\sigma_{\chi^2}} = \frac{\|\varepsilon\|}{\sqrt{2}\sqrt{N_{measurements} - N_{fit.param.}}}$$

decreases for higher number of measurements.

## 1.5. Short summaries of the supplementary articles and manuscripts

This section summarizes the supplementary articles and manuscripts, focusing primarily on the structural modelling part and my contribution to the project.

### 1.5.1. Discovering a new conformational state of T4 Lysozyme by FRET

This section is based on the manuscript by Sanabria et al (Supplement B).

#### Summary

In this manuscript we seek to unravel the kinetic and dynamic interplay of the conformational states of T4 Lysozyme enzyme (T4L). We characterized three short-lived conformational states by combining single-molecule and ensemble multiparameter FRET detection, EPR spectroscopy, mutagenesis, and FRET-positioning and screening. Two of these states can be attributed to the known conformations, as previously determined by X-ray crystallography and NMR spectroscopy, the newly identified third state, *minor* by population, sampled at 230  $\mu$ s, may be actively involved in the product release step in catalysis.

Structurally, T4L<sup>65</sup> consists of two interrelated subdomains, the N-terminal subdomain (NTsD) and the C-terminal subdomain (CTsD), differing in their folding behaviour and stability<sup>66</sup>. To date, more than 500 structural models of T4L are available within the Protein Data Bank (PDB). In this ensemble, T4L adopts several opening angles corresponding to a classic hinge-bending motion of the NTsD with respect to the CTsD, ranging between the *open* and *closed* conformations (**Figure 18**).

A network of 33 distinct T4L fluorescent experiments was designed, measured and analysed by Hugo Sanabria, Dmitro Rodnin, Katherina Hemmen, and Thomas-Otavio Peulen. Three distinct FRET states were identified experimentally, named  $C_1$ ,  $C_2$ , and  $C_3$ . Correspondingly, three sets of 33 FRET-derived inter-dye distances and uncertainties were determined. I compared these distance sets with the structural models found in the PDB. All of the 578 structures of T4L available in the

PDB were aligned and clustered by a complete hierarchical clustering algorithm, using the RMSD of  $C_\alpha$  atoms as similarity metric and a clustering threshold value of 2 Å.

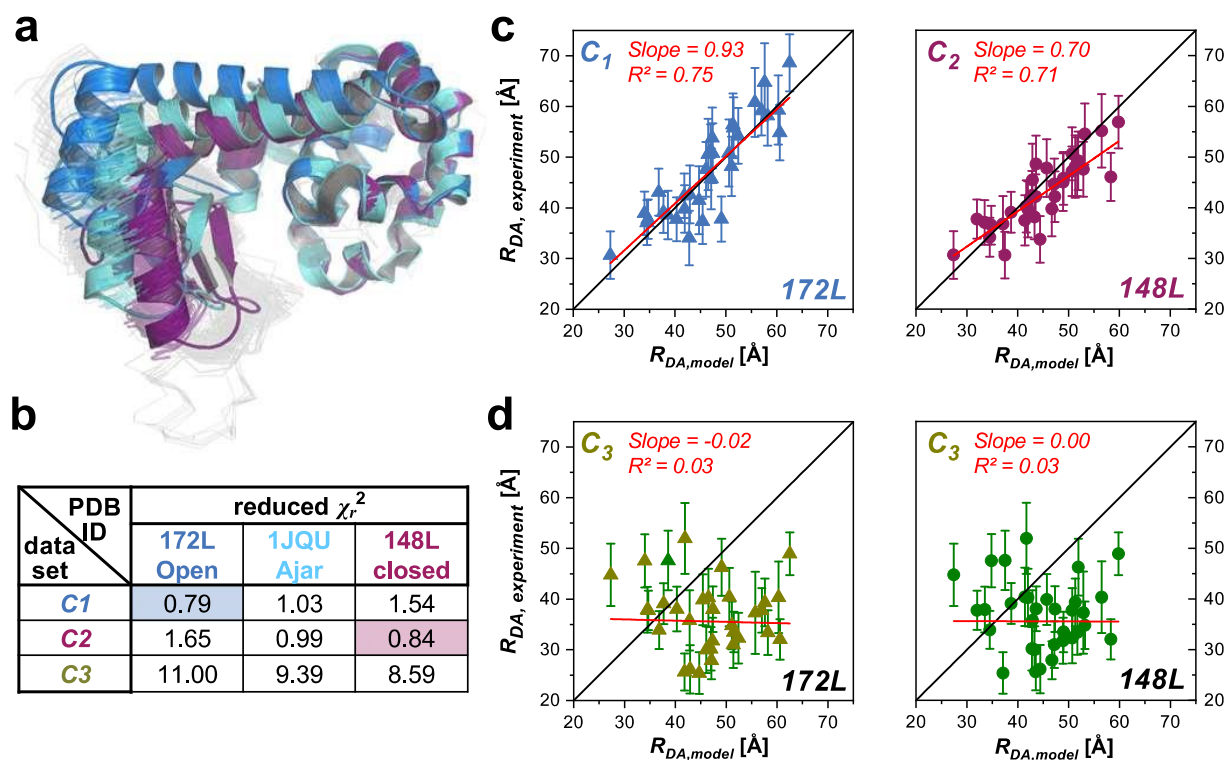


**Figure 18 | Comparison of experimental FRET data to the T4L structures retrieved from the PDB.** (a) Overlay of the PDB structures used for screening. Blue, light blue and violet cartoons show the cluster representative of the open (172L), ajar (1JQU), and closed (148L) conformation of T4L. (b) Reduced  $\chi_r^2$  for each distance set compared to the expected distances from the selected cluster representative. (c) The experimental distances  $R_{DA,experimental}$  of the C1 and C2 dataset are plotted against the model distances  $R_{DA,model}$  from the best PDB structure representative and fitted linearly (red lines). The black lines show a 1:1-relationship. (d) The experimental distances  $R_{DA,experimental}$  of the C3 dataset are plotted against the model distances  $R_{DA,model}$  from the crystal structures 172L and 148L and fitted linearly (red lines). The black lines show a 1:1-relationship. The crystal structures do not fit to the C3 experimental dataset, which is indicated by the slopes close to 0. Adapted from Sanabria et al (Supplement B).

Based on this criterium, structural models of T4L group into three clusters: *open*, *ajar*, and *closed*. The representative structures of these clusters are given by PDB IDs 172L, 1JQU, and 148L for the *open*, *ajar*, and *closed* conformations, respectively (Figure 18a).

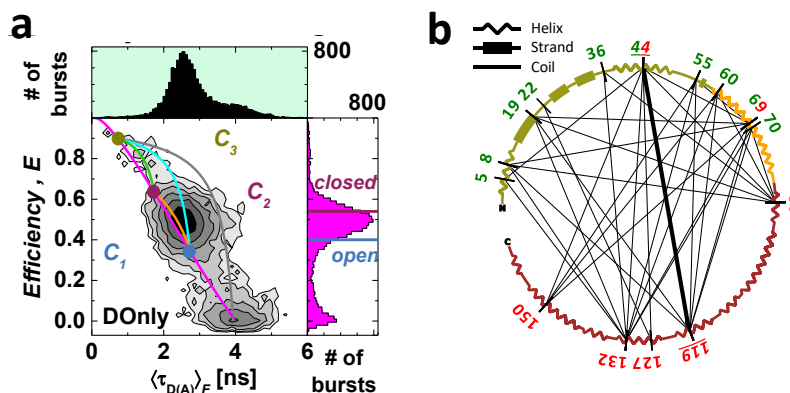


**Figure 19 | FRET studies probe T4L structure and dynamics.** (a) The FRET efficiency,  $E$ , and fluorescence lifetime of Donor ( $D$ ) in the presence of Acceptor ( $A$ ),  $\langle \tau_{D(A)} \rangle_F$ , of the DA-labelled T4 Lysozyme (T4L) variant S44pAcF/R119C shown in two-dimensional MFD-histogram with one-dimensional projections of  $E$  (right) and  $\langle \tau_{D(A)} \rangle_F$  (top). The magenta line (static FRET-line) describe those molecules with a single conformational state. Three limiting states (circles) ( $C_1$ , blue;  $C_2$ , purple;  $C_3$ , yellow) were identified by eTCSPC. The dynamic FRET-lines are shown in orange ( $C_1$ - $C_2$ ), cyan ( $C_1$ - $C_3$ ), and green ( $C_2$ - $C_3$ ). The grey line traces molecules of high FRET-efficiency with a bleaching  $A$ . For comparison, the FRET-efficiencies of the X-ray structures for an open (blue, PDB ID: 172L) and closed (violet, 148L) state (determined by FPS<sup>21</sup>) are shown as horizontal lines in the FRET-efficiency histogram. (b) Secondary structure elements (helix, strand or coil) of T4L and network representing 33 measured distinct FRET-variants of T4L. The labelling position 44 and 119 for donor and acceptor respectively are underlined.

Next, experimental distance sets were compared to the crystal structures. For example, in **Figure 19a**, MFD-histogram shows a FRET indicator for one of the spatial directions of motion in the T4 Lysozyme. Three peaks are identified in the MFD-histogram. The peak located at a low FRET-efficiency  $E$  corresponds to molecules without, or with an inactive, acceptor fluorophore (Donor-only). For an *open* (PDB ID: 172L, blue) and a *closed* (PDB ID: 148L, magenta) conformation, FRET efficiencies  $E$  are shown as horizontal lines in the marginal distributions. They are similar but not identical to known structural models. Due to the dynamic exchange between the states, observed peaks are shifted with respect to the limiting states. The peak around the yellow dot corresponds to the newly identified state  $C_3$ .

The overall agreement (minimum  $\chi_r^2$ , section 1.4.7, Eq. 1.12) between the distance sets  $C_1$  and  $C_2$  is best for conformers 172L and 148L, respectively (**Figure 18b**). In **Figure 18c**, the modelled inter-dye distances  $\langle R_{DA,model} \rangle$  for 172L and 148L are compared to experimental inter-dye distances  $\langle R_{DA,exp} \rangle$  of  $C_1$  and  $C_2$ , respectively. A linear regression (red line) with a slope close to one demonstrates the absence of significant systematic deviations. The cluster of *ajar* conformations



is structurally an intermediate that is halfway between the *open* and *close* conformers. Consequently,  $C_1$  can be assigned as *open* state and  $C_2$  as *closed* state. However, none of the cluster representatives can be assigned to the  $C_3$  state as judged by the disagreement with the data (**Figure 18d**). We conclude that  $C_3$  is an *excited* conformational state of currently unknown structure.

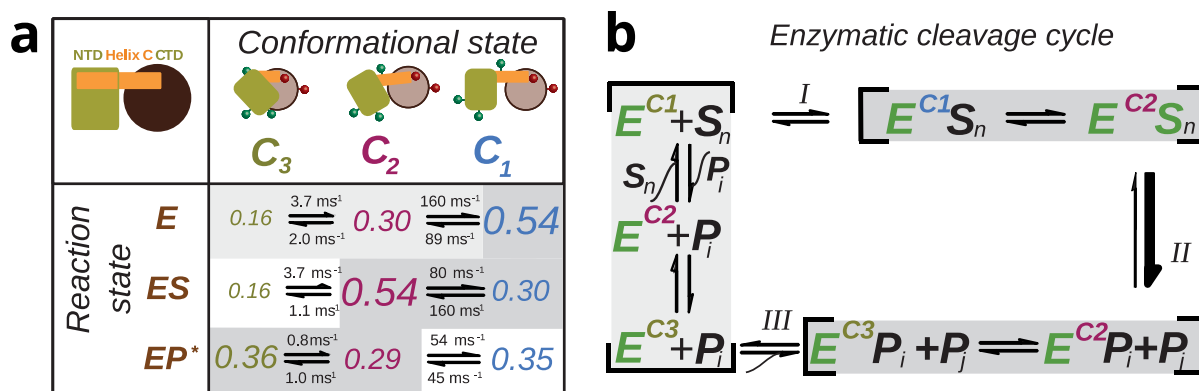


**Figure 20 | Enzymatic cleavage cycle of the T4 lysozyme.** (a) T4L interconverts between three conformational states:  $C_1$ ,  $C_2$ , and  $C_3$ . The different font sizes represent the species fractions  $x_i$  for each conformer. The three enzyme states were monitored via the following three enzyme variants: (i) the free enzyme state  $E$  via S44AcF/I150C; (ii) the enzyme-substrate state  $ES$  via the inactive E11A/S44C/I150C with bound substrate; and (iii) the enzyme product state  $EP$  via the product adduct with T26E/S44AcF/I150C after substrate cleavage. (b) The peptidoglycan chain with  $n$  subunits ( $S_n$ ) is cleaved into two products ( $P_i$  and  $P_j$  with  $n = i + j$ ) by T4L, both of which can be further processed by T4L until only the dimer of N-acetylglucosamine and N-acetylmuramic acid remains. The grey shaded steps indicate the conformational/reaction states observed. Adapted from Sanabria et al (**Figure 7** in Supplement B).

In this study, conformational transitions of an enzyme involved in a cleavage cycle were directly observed by FRET. Based on the previous studies<sup>67</sup> and additional experimental observations (Supplement B), we propose the following relationship between the conformation and the function of T4L (**Figure 20**). The open conformation  $C_1$  is mostly populated to enable substrate binding, the closed conformation  $C_2$  becomes most abundant for the enzyme-substrate complex, and product release occurs in the compact conformation  $C_3$ .

### 1.5.2. Determination of structural dynamics of human guanylate binding protein 1 using the data from four experimental techniques.

This section is based on the manuscript by Peulen et al (Supplement C).

#### Summary

Human guanylate binding protein 1 (hGBP1) is a large 582 residue enzyme from the guanylate binding protein (GBP) family. Proteins in this family are known to undergo conformational



transitions relevant for oligomerization and their biological function – destruction of intra-cellular parasite membranes. The structural mechanism of this process is unknown. In Supplement C a combination of FRET, pulsed electron paramagnetic resonance (EPR), small-angle X-ray scattering (SAXS) and neutron spin echo techniques is used to determine dynamics of sub-domain motions in hGBP1 at the timescales from nanoseconds to milliseconds. Functioning of hGBP1 was found to rely upon the GTP-triggered association of the GTPase-domains followed by dimerization of C-termini relying on a GTP independent flexibility of the C-terminal effector domain in the  $\mu$ s-regime. Flexibility and GTP-hydrolysis seem to control the reversible GBP assembly.

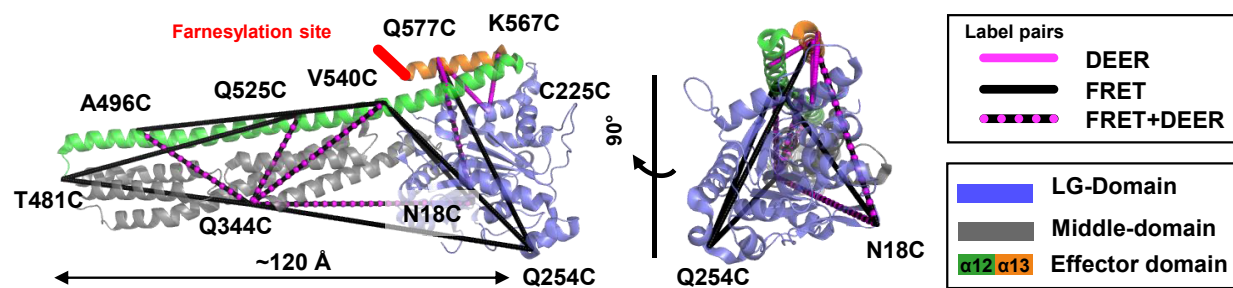


**Figure 21 | Network of pair-wise mutations for DEER and FRET measurements to probe the structural arrangement of the human guanylate binding protein 1 (hGBP1).** The network is shown on top of the crystal structure (hGBP1, PDB-ID: 1DG3). hGBP1 consists of three domains: the large GTPase (LG) domain (blue), a middle domain (grey) and the helices  $\alpha 12/13$  (green/orange). The amino acids highlighted by the labels were used to attach spin-labels and fluorophores for DEER-EPR and FRET experiments, respectively. Magenta and black lines connect the DEER pairs and FRET-pairs, respectively. In hGBP1 the C-terminus is post-translationally modified and farnesylated for insertion into parasite membranes (red).

Previously, X-ray crystallography on the full-length hGBP1 revealed a folded and fully structured protein with the typical architecture of a dynamin superfamily member (**Figure 21**). Earlier biochemical experiments identified the large GTPase (LG) domain as interfaces for GTP-analogue induced homo-dimerization<sup>68</sup>. Live-cell experiments highlighted the relevance of helix  $\alpha 13$  for the immune response<sup>69-71</sup>. However, an association of two  $\alpha 13$  helices requires large-scale structural rearrangements that are inconsistent with the X-ray crystal structures<sup>68</sup>.

For larger proteins determination of structural dynamics is extremely challenging, as there is no single experimental technique that can simultaneously observe motion in biomolecules and determine structure with near atomistic detail. Therefore, a combination of experimental and computational methods is used here to study the molecular prerequisites for hGBP1 dimerization. Analysis of the experimental datasets was performed by: Charlotte Lorenz and Andreas Stadler

(SAXS), Thomas-Otavio Peulen (smFRET<sup>8</sup>), and Johann P. Klare (EPR<sup>72</sup>). Conformational dynamics of hGBP1 was interrogated by a network of 12 FRET pairs and 8 EPR pairs, 5 of these pairs were present in both EPR and FRET networks. These provided us with the insight on specific rearrangements of different protein domains. Analysis of fluorescence data resolved bimodal distance distributions from some FRET pairs with a major and minor subpopulation, referred to as  $M_1$ , and  $M_2$ , respectively.

Given the experimentally derived constraints, in close collaboration with Thomas Peulen we constructed near atomistic computational structural model of the enzyme for subpopulations  $M_1$ , and  $M_2$  (Figure 1). Construction of this model required integration of unrestrained molecular dynamics simulations, rigid body docking guided by the FRET and EPR restraints, normal-mode based coarse grained simulations (NMSim<sup>24,73</sup>) with and without experimental guiding, and screening against the FRET, EPR and SAXS data.

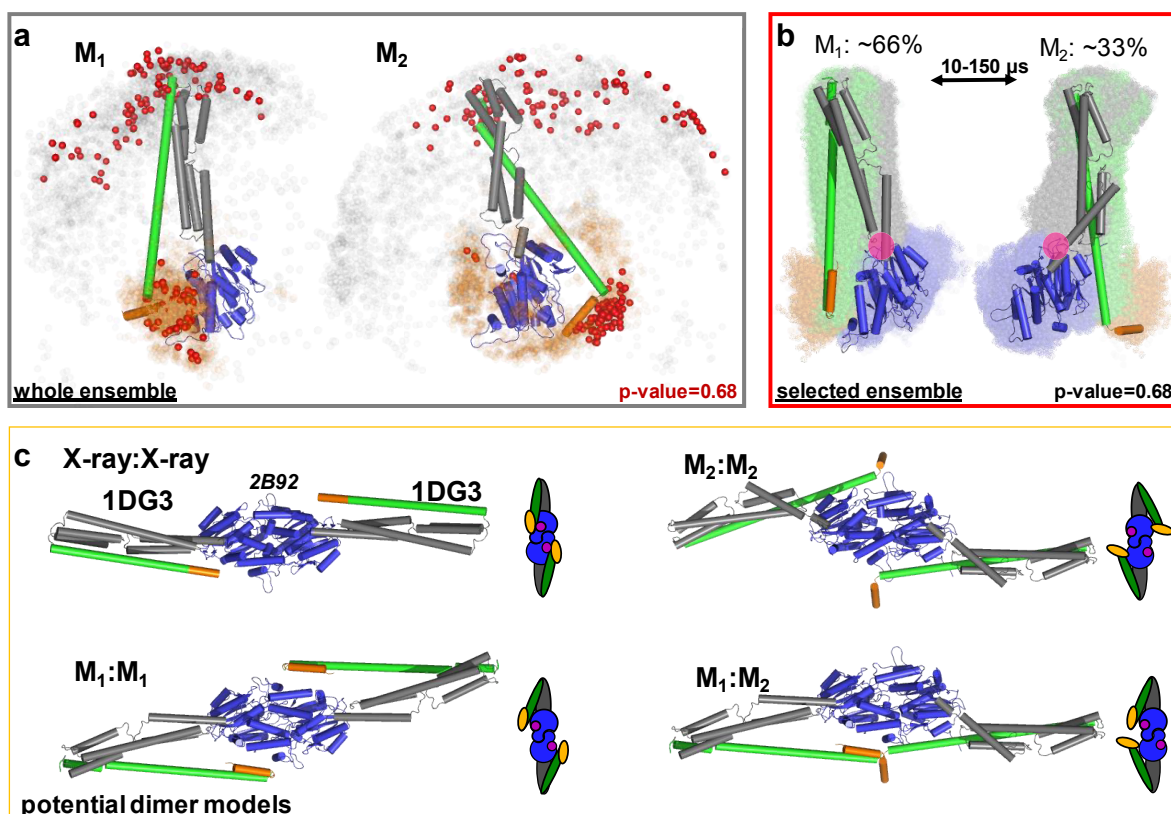


**Figure 22 | Selected conformers and potential dimer models of hGBP1 based on structures generated by integrative modelling of DEER, FRET, and SAXS data. (a)** All structural models for  $M_1$  and  $M_2$  were aligned to the LG domain and are represented by orange and grey dots, indicating the Ca atoms of the amino acids F565 and T481, respectively. The structural model best agreeing with all experiments is shown as cartoon representation. Non-rejected

conformations ( $p$ -value = 0.68) are shown as red spheres. **(b)** Global alignment of all selected structural models ( $p$ -value = 0.68). In the centre, the structure best representing the average of the selected ensembles is shown. The conformational transition from  $M_1$  to  $M_2$  can be described by a rotation around the connecting region of the LG and the middle domain (pivot point PP, shown as a magenta circle). **(c)** Potential hGBP1:hGBP1 dimer structures constructed by superposing the head-to-head interface of the LG domain (PDB-ID: 2B92) to the full-length crystal structure (1DG3), and both models of the states  $M_1$  and  $M_2$ . The LG and middle domain are coloured in blue and grey, respectively. Helices  $\alpha 12$  and  $\alpha 13$  are coloured in green and orange, respectively. As structural models for  $M_1$  and  $M_2$ , the structures best representing the ensemble of possible conformers are shown. Adapted from Peulen et al (Supplement C).

Overall, in the FRET measurements,  $M_1$  agreed better with the X-ray structure than  $M_2$  - the sum of uncertainty weighted squared deviations,  $\chi_{FRET}^2$ , for  $M_1$  is significantly smaller than for  $M_2$  ( $\chi_{FRET}^2(M_1, 1DG3) \sim 17$  vs.  $\chi_{FRET}^2(M_2, 1DG3) \sim 1500$ ).

Molecular dynamics (MD) simulations of up to 2  $\mu$ s in length without experimental restraints were performed to assess the structural dynamics of the full-length crystal structure at the atomistic level and to capture potential motions of hGBP1. Principle component analysis (PCA) revealed kinking motions of the middle domain helix  $\alpha 12/13$  around a pivot point as most dominant motions in the MD simulations (**Figure 23a**).

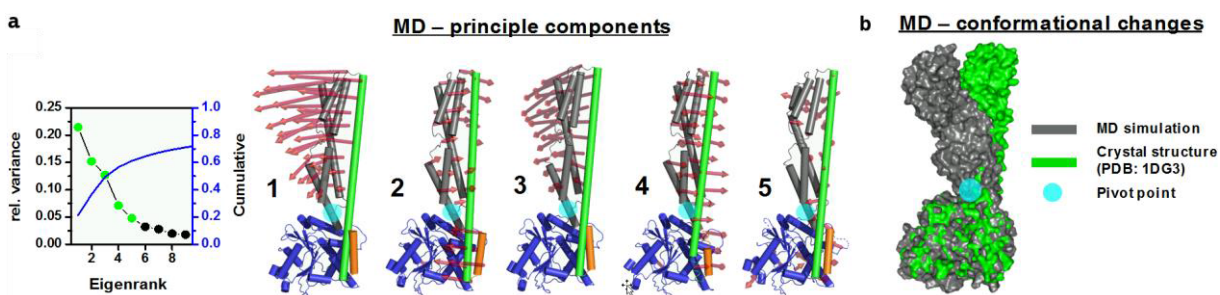


**Figure 23 | Conformational dynamics of hGBP1 studied by molecular dynamics (MD) simulations** **(a)** First five principle components of molecular dynamics (MD) and accelerated molecular dynamics (aMD) simulations starting from the crystal structure (PDB-ID: 1DG3). The LG domain, the middle domain, and the helix  $\alpha 12$ , and  $\alpha 13$  are coloured in blue, grey, green, and orange, respectively. Red arrows indicate the direction of the motion. The components were scaled by a factor of 1.5 for better visibility. The semi-transparent cyan circle corresponds to a pivot point located at the LG domain. The first five principal components (PCs) sorted by the magnitude of the eigenvalues, contribute 60% of the total variance of all simulations. **(b)** Superposition of MD trajectory frame (grey) deviating the most in RMSD ( $\sim 8$  Å) from the crystal structure (green). Both structural models were aligned to the LG domain. Adapted from Peulen et al (Supplement C).

A visual inspection of structures deviating most from the mean reveals a kink at the connector of the LG and the middle domain (**Figure 23b**) consistent with rearrangements required for average

shape as recovered by SAXS. However, the timescale of MD simulations did not allow us to see the larger sub-domain motions needed to explain the M<sub>2</sub> subpopulation of the protein. The time scales of these rearrangements were analysed experimentally by filtered fluorescence correlation spectroscopy<sup>12</sup>, showing that fast dynamics is mainly associated with the helices  $\alpha$ 12/13 and the middle domain, while the slow dynamics is predominantly linked to the LG domain (**Figure 3e** in Supplement C).

The crystal structure of hGBP1 was used as a starting point in the generation of new structural models. First, we identified a set of rigid bodies (RBs) using the MD simulations, knowledge on the individual domains, and rigidity analysis. To this RB assembly, we applied DEER and FRET constraints for guided rigid body docking (RBD). Next, all generated RBD structures were corrected for their stereochemistry using NMSim<sup>24</sup>. NMSim-corrected RBD models were then clustered by a hierarchical agglomerative clustering algorithm<sup>74</sup> using the RMSD as conformation similarity metric and a threshold of 3 Å. Each of all 757 cluster representatives were then used as seeds for short (1 ns) MD-simulations. Conformations from MD simulations were then discriminated by the DEER, FRET, and SAXS data. Structural models were ranked by their agreement with the individual techniques, using the quality measures  $\chi^2_{SAXS}$  and  $\chi^2_{DEER,FRET}$ , which capture deviations between the model and the data for SAXS and for the combined DEER and FRET datasets, respectively. We describe the experimental data by a model, consisting of two-conformers corresponding to sub-populations M<sub>1</sub> and M<sub>2</sub>. To find the best fitting pair of two conformers, theoretical SAXS curves for all possible combinations of structural models of M<sub>1</sub> and M<sub>2</sub> were ranked by their agreement with the SAXS data. For the pair of structural models best agreeing with SAXS the middle domain is kinked towards the LG domain. For DEER and FRET measurements, M<sub>1</sub> and M<sub>2</sub> representatives were ranked by comparing simulated, and experimental average inter-label distances. Generated structural models were ranked using Fisher's method to fuse the experimental data and discriminate the models in a statistically meaningful manner. However, in this step, estimates for the degrees of freedom (dof) of the model and the data can have significant uncertainty. A stability test demonstrates that a change in the number of dofs has only a minor influence on the results. In the final analysis, a p-value of 0.68 discriminated more than 95% of all structural models, leaving models with average RMSDs of 11.2 Å and 14.5 Å for M<sub>1</sub> and M<sub>2</sub>, respectively (**Figure 22b**). For these structures, uncertainties are largest for  $\alpha$ 12/13, which agrees with global motions identified by PCA of the MD simulations.

We suggest, that conformational diversity between  $M_1$  and  $M_2$  is responsible for the formation of the ( $M_1:M_2$ ) dimer, where helices  $\alpha 13$  are located on the same side of their LG domains in line with previous studies<sup>75</sup> (**Figure 22c**). In line with previous studies, which identified preferred pathways to increase the association yield of protein-protein complexes<sup>76</sup>, we suggest that, owing to the conformational flexibility, precursors necessary for formation of higher order oligomers are formed spontaneously before binding of the oligomerization-inducing substrate GTP. The Sau group has previously established the relationship between oligomer formation and defensive activity against hepatitis C virus showing that impairing catalytic activity and oligomer formation by mutations leads also to a decreased antiviral activity<sup>77</sup>.

### 1.5.3. Benchmarking accuracy of the workflow using *in silico* FRET data

This section is based on the article by Dimura et al (Supplement A).

#### Summary

The article reviews recent methodological developments in integrative structural modelling using networks of FRET restrains (hybrid-FRET) and demonstrates a proof of concept for an automated integrative structural modelling and experiment planning workflow to put hybrid-FRET on rails.

The test case is a protein (Atlastin-1) with three conformers exchanging at timescales of 30  $\mu$ s and 10 ms. Data traces of single-molecule FRET experiments with multi-parameter fluorescence detection for typical conditions were simulated<sup>9,12</sup>, and the exchange timescales (30  $\mu$ s and 10 ms) were chosen to illustrate some of the typical regimes for FRET applications. The conformers were previously well-characterized by X-ray crystallography. In this way, the known X-ray structures can serve as unquestioned references for the assessment of the structural models obtained by hybrid-FRET modelling using our FPS toolkit.

## Simulated system: Dynamic protein

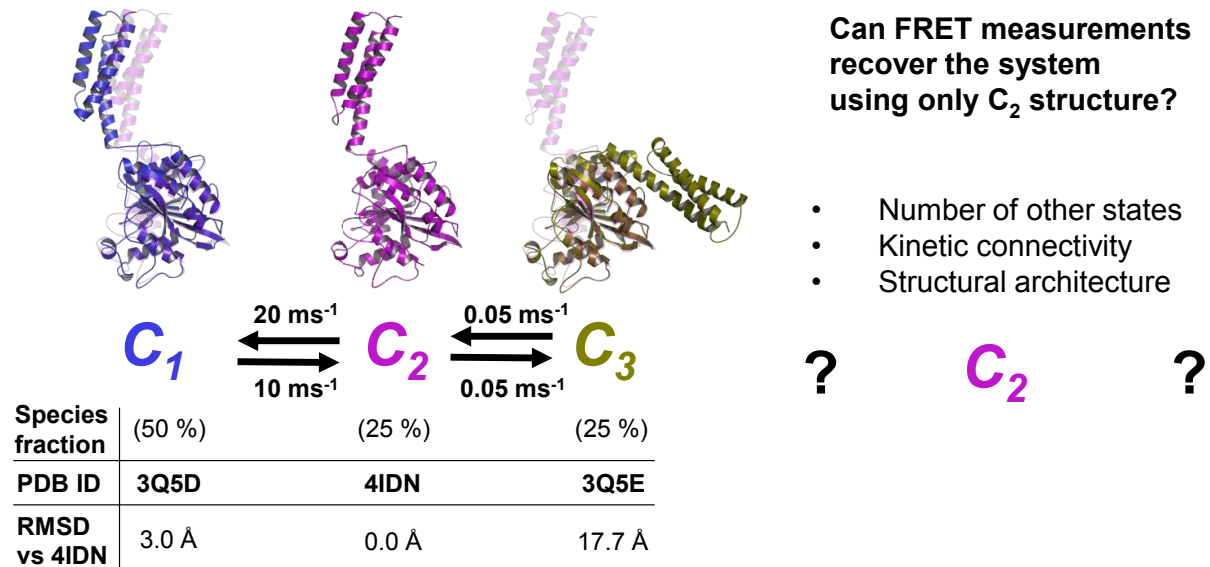


**Figure 24 | Presentation of the test case Atlastin-1.** Three crystal structures of Atlastin-1 were used, termed  $C_1$ ,  $C_2$ , and  $C_3$ . Kinetic exchange between  $C_1$  and  $C_2$  is simulated to be fast, and the exchange between  $C_2$  and  $C_3$  is simulated to be slow. The task is to recover the number of states, their kinetic connectivity, and their structures, given only the structure  $C_2$  and information from smFRET spectroscopy. Adapted from Dimura et al (Supplement A).

In real experiments, fluorescence decays are complex due to DA distance distributions, brightness distributions due to the confocal excitation profile and experimental nuisances such as instrumental response function and detector dark counts. All these aspects are reproduced by the simulations of freely diffusing molecules, to generate realistic photon traces<sup>12</sup>. This way we test the possibility to recover the state specific distance distributions for dynamically exchanging conformations at two different time scales and using different experimental techniques: a time window-based analysis by dynamic photon distribution analysis and sub-ensemble TCSPC analysis. Additionally, we test the effect of using spurious dye models for structural modelling and analysis.



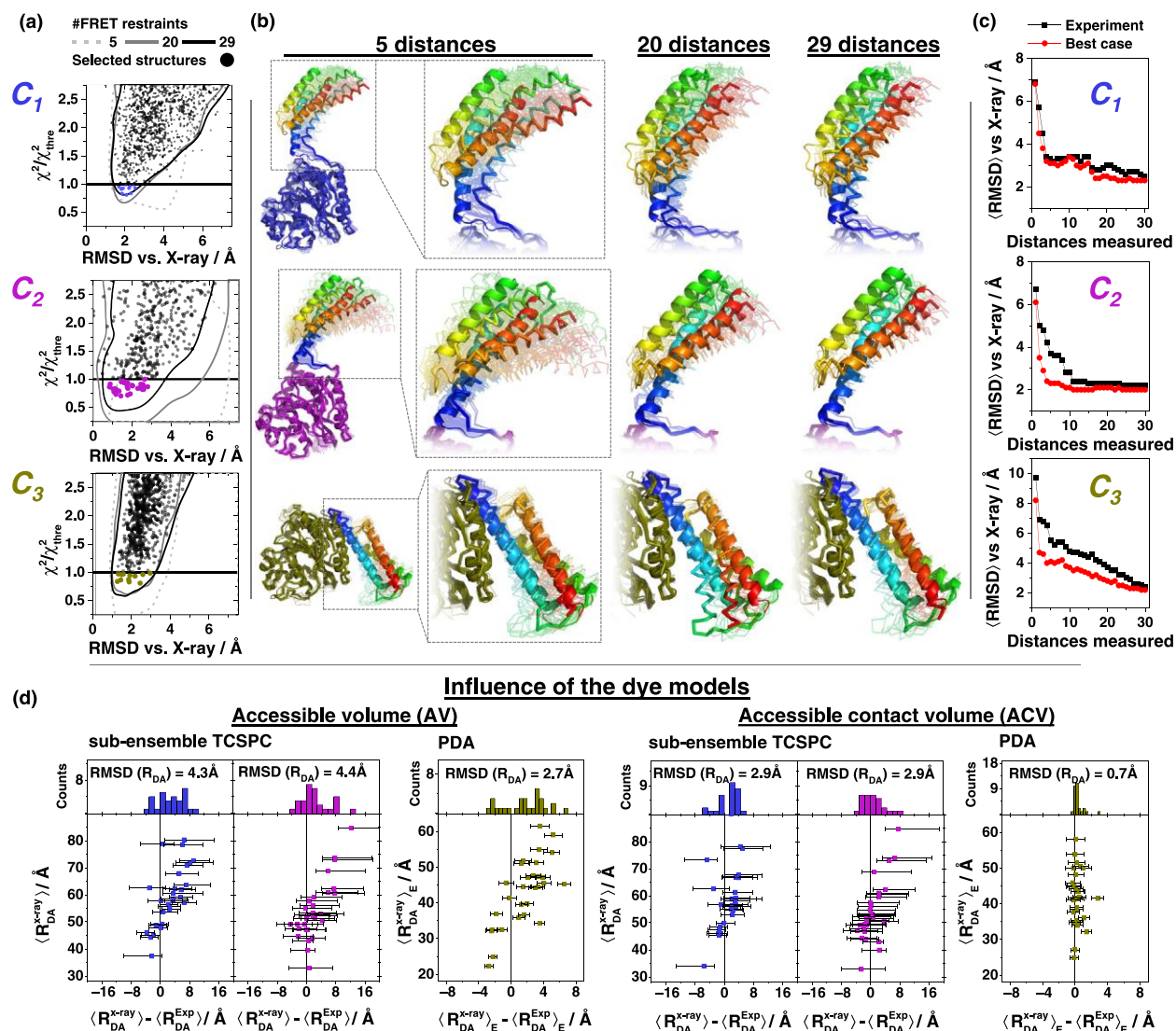


**Figure 25 | Outcome of hybrid-FRET structural modelling of the three Atlastin-1 conformers.** (a) The sum of squared deviations weighted by the estimated experimental error  $\chi^2$  relative to a threshold value estimated for the confidence level of 68% with respect to the best structure is plotted against  $C_\alpha$  root-mean-square deviations (RMSD) from the corresponding crystal structure for 5 (dashed contour), 20 (grey contour), and 29 (black contour) measured distances. Black dots represent conformers corresponding to the set of 29 distances. Contours are drawn using a kernel density estimate. Coloured dots represent selected conformations for the set of 29 distances. RMSD versus X-ray is calculated excluding flexible loops using the residues 35–99, 122–147, 157–189, 209–237, 257–277, 292–332, and 349–437. (b) Overlay of the crystal structures (cartoon representation), selected ensembles (transparent ribbon, 68% confidence), and best structures (solid ribbon) for the sets of 5, 20, and 29 distances. (c) Improvement of the corresponding accuracy with respect to the number of distances measured. Accuracy is calculated as  $\chi^2$ -weighted average  $C_\alpha$  RMSD from the corresponding crystal structure. Black line represents the improvement using experimentally measured distances, the red line represents the best-case scenario where all the distances measured agree perfectly with the ones predicted for the crystal

structure. (d) Comparison for the deviations between measured distances and distances predicted from the crystal structure by AV and ACV dye models. Adapted from Dimura et al (Supplement A).

The accuracy of the method is illustrated by plotting the conformer specific  $\chi^2/\chi_{threshold}^2$  ratio versus the  $C_\alpha$  RMSD of the modelled structures from the corresponding target crystal structure (**Figure 25a**). Cluster representatives below a confidence level of 68 % for 29 distances are shown as coloured dots. An overlay of the selected cluster representatives and the best model structure (highlighted by solid ribbons) visualizes the precision, which is given by the structural diversity within the selection (**Figure 25b**). For all states, the accuracy of the selected structures at a confidence level of 68 % using 29 distances ranges between 2 and 3 Å. Adding extra FRET pairs beyond approximately 20 measurements, does not improve accuracy significantly (**Figure 25c**), even though it could improve the resilience of the method against the systematic errors. We also show, that dye model parameters can be refined in calibration measurements. For example, accessible and contact volume dye model outperforms an incorrectly used (uniform) accessible volume dye model with difference in  $RMSD(R_{DA})$  of  $\sim 2$  Å (**Figure 25d**).

#### 1.5.4. Resolving the chromatin dynamics by FRET and coarse-grained structural modelling

This section is based on the article by Kilic et al (Supplement D).

##### Summary

The dynamic architecture of chromatin fibres, a key determinant of genome regulation, is poorly understood. We reveal structural states and their interconversion kinetics in chromatin fibres using the single-molecule Förster resonance energy transfer studies.

High-resolution structural studies on reconstituted chromatin provided models of chromatin as a two-start helix with two intertwined stacks of nucleosomes and compact tetranucleosomes as basic units<sup>78,79</sup> (**Figure 26**). Other experiments have supported solenoid chromatin structural models<sup>80</sup> or mixed, heterogeneous populations<sup>81</sup>, depending on linker DNA length and the presence of linker histones. In the cryo-EM structure of a chromatin fibre tetranucleosomes arrange in a defined interaction register<sup>79</sup>. Irrespective of the local architecture, chromatin structure is highly dynamic. Mononucleosomes exhibit partial unwrapping of nucleosome-wound DNA<sup>35,82-84</sup>. Dynamic rearrangements beyond the nucleosome were observed using fluorescence approaches in trinucleosomes<sup>85</sup> and using force-spectroscopy on chromatin fibres under tension<sup>86-89</sup>. However,



structural rearrangements in unperturbed chromatin fibres, and the timescales thereof, remain unresolved.

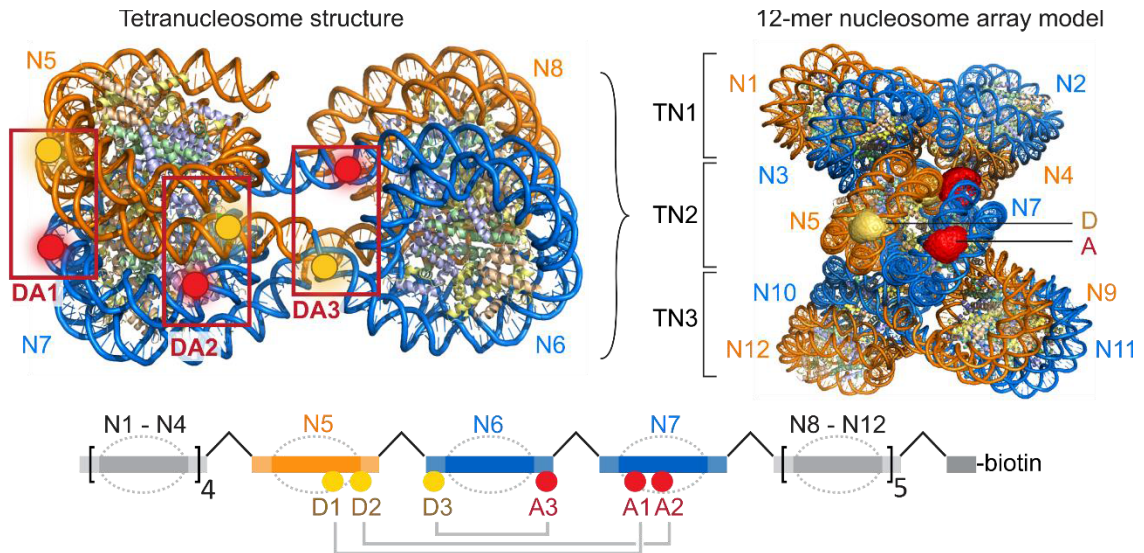


**Figure 26 | X-ray and Cryo-EM structures of Chromatin.** Left: X-ray structure of Tetranucleosome based on Schalch *et al*<sup>78</sup>, showing the three dye pairs DA1, DA2, and DA3. Right: 12-mer chromatin fibre as a stack of three tetranucleosome (TN) units, modelled using the cryo-EM structure of a chromatin fibre<sup>79</sup>. The middle tetranucleosome carries the fluorescent labels, whose accessible volume is displayed. D donor, A acceptor labels, N nucleosomes. Schematic view of the preparative DNA ligation used to introduce fluorescent labels is shown at the bottom.

A 12-mer nucleosome array (N1-N12, **Figure 26**) was fluorescently labelled at three distinct sets of internal positions yielding structural information from several vantage points: (Donor – Acceptor position 1, DA1), DA2 and DA3. The choice of dye configurations was guided by structural modelling<sup>78,79,85</sup> (**Figure 27a**). DA1 senses stacking between nucleosomes N5 and N7, DA2 measures inter-nucleosome interactions closer to the dyad (N5 to N7), DA3 reports on dynamic modes within the linker DNA flanking the central nucleosome (N6). Usage of two fluorescent dye pairs with different distance sensitivities (i.e., Förster Radii,  $R_0 = 82 \text{ \AA}$  and  $R_0 = 52 \text{ \AA}$ ) allowed us to reliably measure inter-dye distances ( $R_{DA}$ ) from  $35 \text{ \AA}$  up to  $150 \text{ \AA}$ .

For all vantage points DA1–3 our analysis revealed compact chromatin fibres ( $E_{\text{FRET}} > 0.8$ ) in rapid exchange with extended structures. Using confocal multi-parameter fluorescence detection<sup>9</sup> (MFD), four limiting FRET species were identified, corresponding to four structural states named (*A*, *B*, *C*, *D*) (**Figure 27a**). In a one-start fibre configuration nucleosomes N5 and N6 make contact. However, additional measurements with chromatin fibres labelled on positions N5 and N6 did not demonstrate FRET, so solenoid or one-start fibre structures did not manifest in our experiments.

Using the recovered inter-dye distance sets as constraints, we assigned molecular structures to species (*A–D*), based on available high-resolution structural data<sup>78,79</sup> and coarse-grained simulations<sup>90</sup> (**Figure 27**, **Figure 28**).

Structural models were built using the cryo-EM structure of a 12-mer nucleosomal array with 177 bp nucleosome repeat length<sup>79</sup>. The accessible contact volume (ACV) was modelled for dyes in the DA1, DA2 or DA3 configuration and the respective distance distributions were employed to calculate an average conformation-weighted inter-dye distance<sup>73</sup>. Two possible fibre structures were considered. First is a stack of three tetranucleosome (TN) units (TN1(N1-N4); TN2(N5-N8); TN3(N9-N12), 4-4-4, register 1) as observed in the cryo-EM structure. Alternatively, tetranucleosomes could stack in a different register (TN1(N3-N6); TN2(N7-N10), with four unstacked nucleosomes at both ends, 2-4-4-2, register 2). This would put the DA1-3 dye pairs into neighbouring tetranucleosomes. Finally, if the nucleosome-nucleosome interactions are local and fibre compaction is non-cooperative, both registers are expected to be populated. Models for both registers were produced and the expected inter-dye distances were calculated for DA1-3 in register 1 and 2.

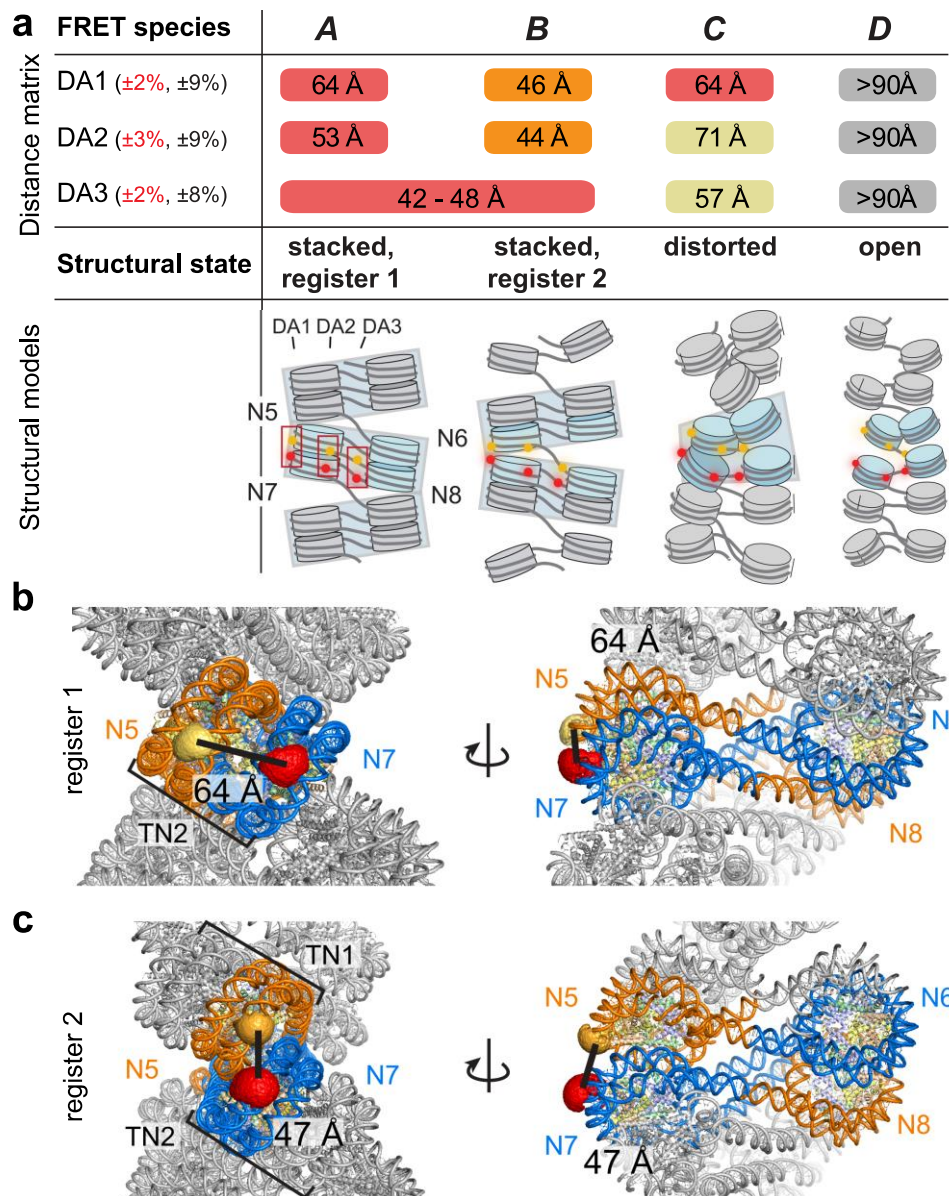


**Figure 27 | Chromatin fibres exist in two rapidly interchanging tetranucleosome stacking registers.** (a) Matrix of the inter-dye distances  $R_{DA}$  for DA1, DA2 and DA3 obtained from dynPDA. Species that cannot be discriminated with a given FRET pair are labelled with the same colour and/or a continuous box. Percentages given in brackets: uncertainties in the observed distances. Red: Precision ( $\Delta R_{DA}(R_{DA})$ ), relevant for relative  $R_{DA}$ . Calculated as s.d. between three PDA analyses of datasets comprising a fraction (70%) of all measured data (subsampling). Black: Absolute uncertainty, mainly determined by the uncertainty in  $R_0$ . The combined average inter-dye distances  $R_{DA}$  over DA1-3 allow us to map each FRET species to a class of corresponding structural states of chromatin. The registers of tetranucleosome units are indicated by light grey boxes. (b) Molecular structure model of a chromatin array, consisting of a stack of 3 tetranucleosomes (register 1) with DA1-positioned dyes in the central tetranucleosome, based on Song et al<sup>79</sup>. The inter-dye distance was evaluated using simulated dye accessible contact volumes (ACV). (c) Molecular structure of a chromatin array, consisting of a stack of 2 tetranucleosomes,

*flanked by two unstacked nucleosomes at each side (register 2) with DA1-positioned dyes on the two central tetranucleosomes and interdye distance from ACV-calculations.*

Distance constraints from DA1 and DA2 showed that FRET species *A* and *B* correspond to conformational states with defined tetranucleosome units in two different interaction registers relative to the FRET labels. Register 1 (*A*) positions the label pairs in the same tetranucleosome unit (**Figure 27b**). Donor-acceptor distances in chromatin fibre conformation are consistent with the reported cryo-EM structure of a 12-mer chromatin fibre<sup>79</sup> as determined by the accessible contact volume simulations<sup>73</sup>. Register 2 (*B*) positions the FRET labels across two neighbouring tetranucleosome units, indicating a fibre structure that exhibits altered nucleosome interactions (**Figure 27c**). Species (*C*) corresponds to a distorted (twisted) tetranucleosome state within register 1. Species (*D*) corresponds to an ensemble of open chromatin fibre conformations.

The effect of nucleosome structural motions is illustrated by the dependency of FRET-average interdye distances DA1 and DA2 on the motion coordinate (**Figure 28e,f**). First, a change of interdye distances was tested with respect to the clamshell-like opening angle between the two nucleosome units (N5, N7, **Figure 28e**). Second, a change of distances DA1 and DA2 with respect to the in-plane nucleosome rotation was tested. One can see, that the DA2 distance senses nucleosome clamshell motion while DA1 does not (**Figure 28e**). Distances observed for state (*C*) could be modelled by a 30° change in the tetranucleosome interaction angle (**Figure 28e**) or by a 30° rotation of one nucleosome relative to its neighbour **Figure 28f**). These conformations still allow interactions at the H2B and H2A four-helix bundle<sup>79</sup> to persist. A clamshell motion by ~10° would be sufficient to explain the experimental data for DA2.

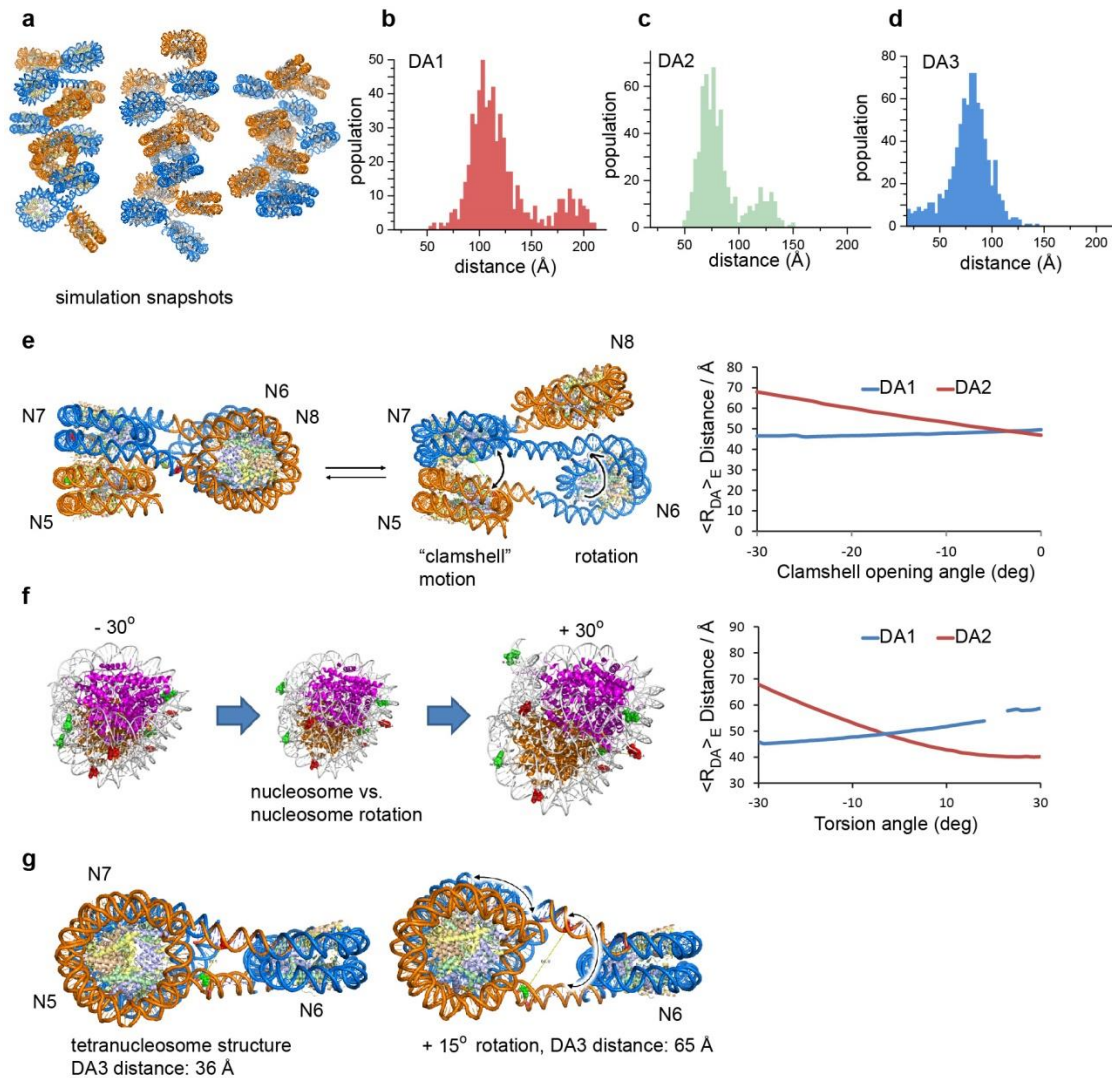


**Figure 28 | Structural models open and dynamic chromatin states.** Structural models of open and dynamic states). (a) Representative snapshots from coarse grained simulations of chromatin fibres following Arya et al<sup>90</sup>. (b) Calculated distance distributions between DA1 dye pairs (between phosphate groups of the modified bases, P-P distances) in the open chromatin ensembles for 100 structures with 12 nucleosomes each. (c) Calculated P-P distance distributions between DA2 dye pairs in open chromatin ensembles from the same structure set as in b. (d) Calculated P-P distance distributions between DA3 dye pairs in open chromatin ensembles for the same structure set as in b. (b-d) Distances are calculated between P atoms of the labelled nucleotide. (e) Dependence of DA1 and DA2 FRET averaged interdye distance on “clamshell”-type opening of the tetranucleosome interface. DA1 is not sensitive to this mode of motion, in contrast to DA2. (f) Dependence of DA1 and DA2 interdye distance on rotational motions between two nucleosomes. DA2 shows stronger angular dependency compared to DA1. (g) Effect of rotational motion on DA3 FRET averaged interdye distance showing that this dye pair is sensitive to the distorted tetranucleosome state (State C in **Figure 27a**).

Unfolded and open chromatin state were modelled by Monte Carlo simulations using an established coarse-grained model of the chromatin fibre<sup>90,91</sup>. An ensemble of open chromatin



conformations was generated using the same temperature and salt conditions as the experiments, but in the absence of inter-nucleosome stacking interactions between the H4 histone tail and the acidic patch. From this ensemble of conformations, a hundred relatively uncorrelated structures were picked (**Figure 28a**). Interdye distances were calculated for all nucleosomes in these structures for DA1-3 (**Figure 28b-d**). Histograms of interdye distances in the ensemble show a peak at 110 Å (and a smaller fraction of structures with 190 Å) for DA1, 80 Å and 120 Å for DA2 and 90 Å for DA3. These distances match the distances expected for subpopulation *D* in experiments (**Figure 27a**).

In summary, we characterized chromatin fibres structurally and kinetically and identified new conformational states (**Figure 6** in Supplement D). We showed that in the compact states nucleosomes are stacked with one of their neighbours. Our observations are compatible with a two-start chromatin fibre model. This results in discrete tetranucleosome units with distinct interaction registers that interconvert dynamically within hundreds of milliseconds as a part of the machinery for gene regulation and compact chromatin access. We also find that the major fraction of chromatin fibres adopts open conformations, that are not identified by X-ray crystallography and cryo-electron microscopy. Additionally, detailed description of labelling procedures, fluorescence measurements, kinetic essays, effect of the change in magnesium concentration, and the role of heterochromatin protein 1 $\alpha$  can be found in Supplement D.

#### **1.5.5. Determination of the oligomerisation interface of the G-protein coupled receptor TGR5 using fluorescent protein labels**

This section is based on the article by Greife et al (Supplement E).

##### **Summary**

TGR5 is the first identified bile acid-sensing G-protein coupled receptor, which has emerged as a potential therapeutic target for metabolic disorders. So far, structural and multimerization properties of TGR5 are largely unknown. We used a combined strategy applying cellular biology, Multiparameter Fluorescence Image Spectroscopy (MFIS) for quantitative FRET analysis, and integrative modelling to obtain structural information about dimerization and higher-order oligomerization assemblies of TGR5.

To date, no high-resolution crystal structure of TGR5 is available. Homology models of TGR5 have been presented based on template structures of other seven transmembrane (7TM) domain

receptors<sup>92-95</sup> (**Figure 29a**). Bioinformatics studies predicted a role for transmembrane helices TM1 and TM4 to TM6 in dimerization; mutation of residues in this region disrupted dimerization<sup>96,97</sup>. AFM, crystallography and FRET studies of GPCRs suggested that oligomerization interfaces are most probably formed by TM1-TM2-helix(H)8 and TM4-TM5 or TM5-TM6 with tetramers arranged in rhomboid, linear and squared formations, depending on the protein<sup>98-102</sup>. Here FRET data collected for TGR5 are discussed with respect to these findings and oligomerization models are suggested (**Figure 30**).

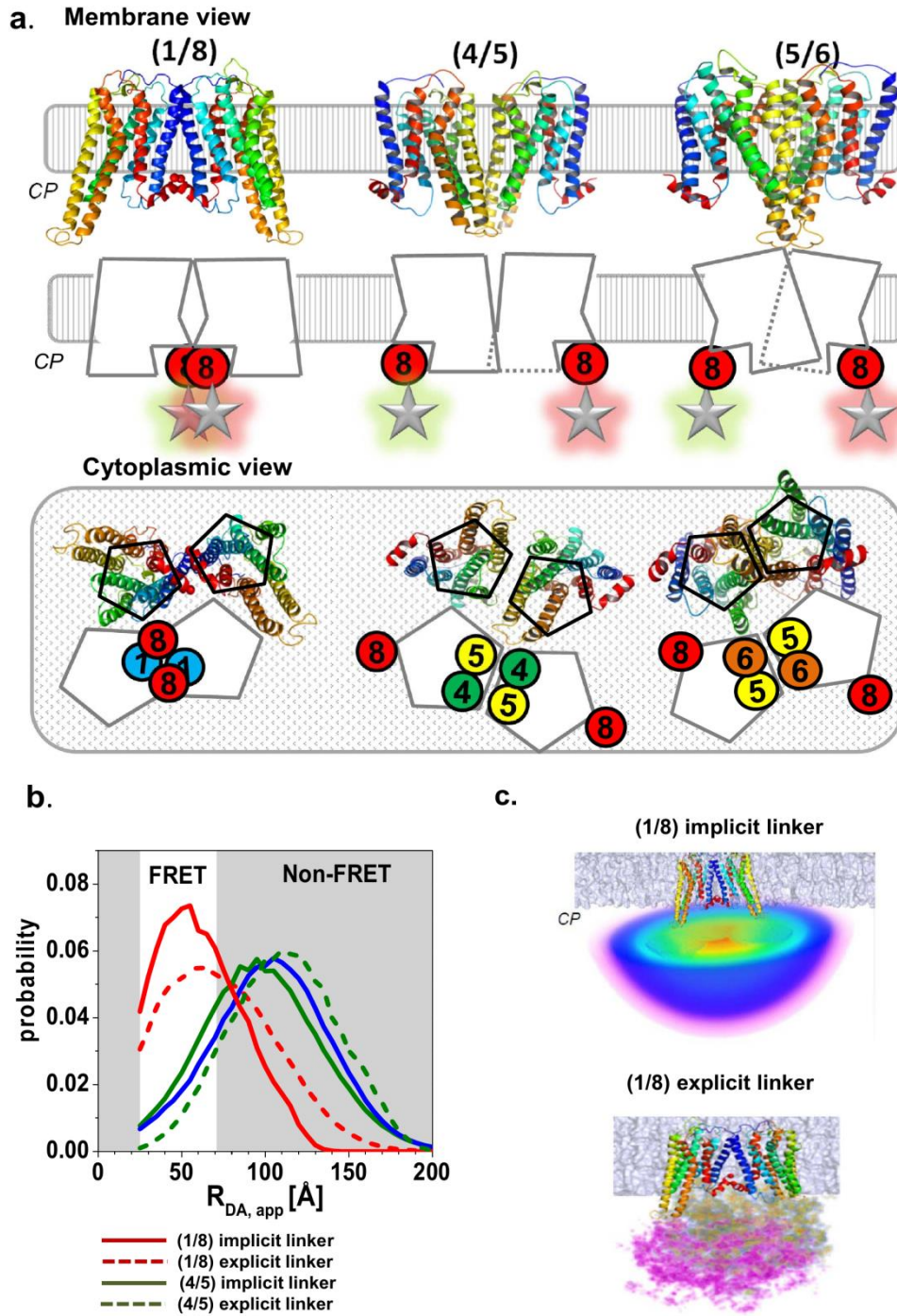


**Figure 29 | Homo-dimerization models and their distance distributions.** (a) Homo-dimerization models with the following interfaces from left to right: (1/8), (4/5) and (5/6). TGR5 monomer helices are rainbow-coloured starting with TM1 in blue to H8 in red. Top row: membrane view of the interface models in cartoon and schematic representation (circles representing TMs). Bottom row: cytoplasmic view of the interface models. The fluorescent proteins, which are attached to the cytoplasmic H8, are presented as stars glowing in green for donor (eGFP) and red for acceptor (mCherry). Abbreviation: CP = cytoplasm. (b) Distance probability distributions calculated with an explicit (dotted line) and implicit linker (solid line) for the homo-dimerization models (1/8)



(red), (4/5) (green), and (5/6) (blue). The non-FRET area is shaded in grey. (c) Positional distributions of the fluorescent probes for the TGR5 (1/8) interface. The implicit linker simulations yield weighted AVs for both fluorophores which overlap and create one huge sphere (top panel). The probability density of the allowed fluorophore positions decreases from red, yellow over green, blue to pink. The explicit linker simulations yield a thermodynamic ensemble (bottom panel) depicted as an orange-blue and purple volume map, respectively. The ensembles also overlap to a high degree. Higher saturation represents higher fluorophore position occupancy. Both methods gave very similar results. Adapted from Greife et al (Supplement E).

As shown in **Figure 29a**, three possible homo-dimerization models were generated with interfaces involving TM1-TM2-H8 (for convenience abbreviated as 1/8 dimer), TM4-TM5 (4/5 dimer), or TM5-TM6 (5/6 dimer). It was previously shown, that for biomolecules labelled by organic fluorophores, FRET can be accurately modelled by accessible volume (AV) simulations.

However, in our case fluorescent protein labels were used. Fluorescent proteins are typically attached to the labelled protein by long peptide linker of up to 200 Å in length at maximum extension, compared to ~20 Å linkers for organic fluorophores. Moreover, peptide linkers and fluorescent proteins can exhibit complex behaviour, which would severely violate the uniform weighting approximation used in the normal AV model. To overcome this challenge, two different modifications of the AV model were developed, compared and applied: (i) Explicit linker simulations based on explicit peptide linker/GFP-MD-simulations followed by calculations of conformational free energies to weight each linker-GFP configuration in the presence of a TGR5 dimer and an implicit membrane bilayer (see also Supplement E SI page 30). (ii) Implicit linker simulations by AV-calculations weighted by a Gaussian chain distribution, so that entropic effects and geometric factors in terms of steric exclusion effects by the TGR5 oligomer and the membrane are taken into account (see also Supplement E SI page 32).

Explicit linker simulations result in a hemispherical arrangement of GFP on the cytoplasmic side, which is centred on the attachment point at helix 8 of TGR5 and each linker/GFP configuration is Boltzmann weighted according to the conformational free energy (**Figure 29c**). Configurations of lower probability are found when GFP approaches TGR5 due to energetically unfavourable contacts.

The implicit linker model (**Figure 29c**) was tested as an alternative to account for dye-linker diffusion. The accessible volume (AV) approach was used to estimate all possible dye positions within the linker length from the attachment point without steric clashes with the macromolecular surfaces. The fluorophores are approximated by a sphere with a defined radius, which is estimated

from the physical dimensions of the molecules. The connecting linker is modelled as a flexible cylinder. To take entropic effects into account, the linker was assumed to obey Gaussian chain behaviour. Thus, the fluorophore distribution density gradually drops as the distance from the attachment point increases.

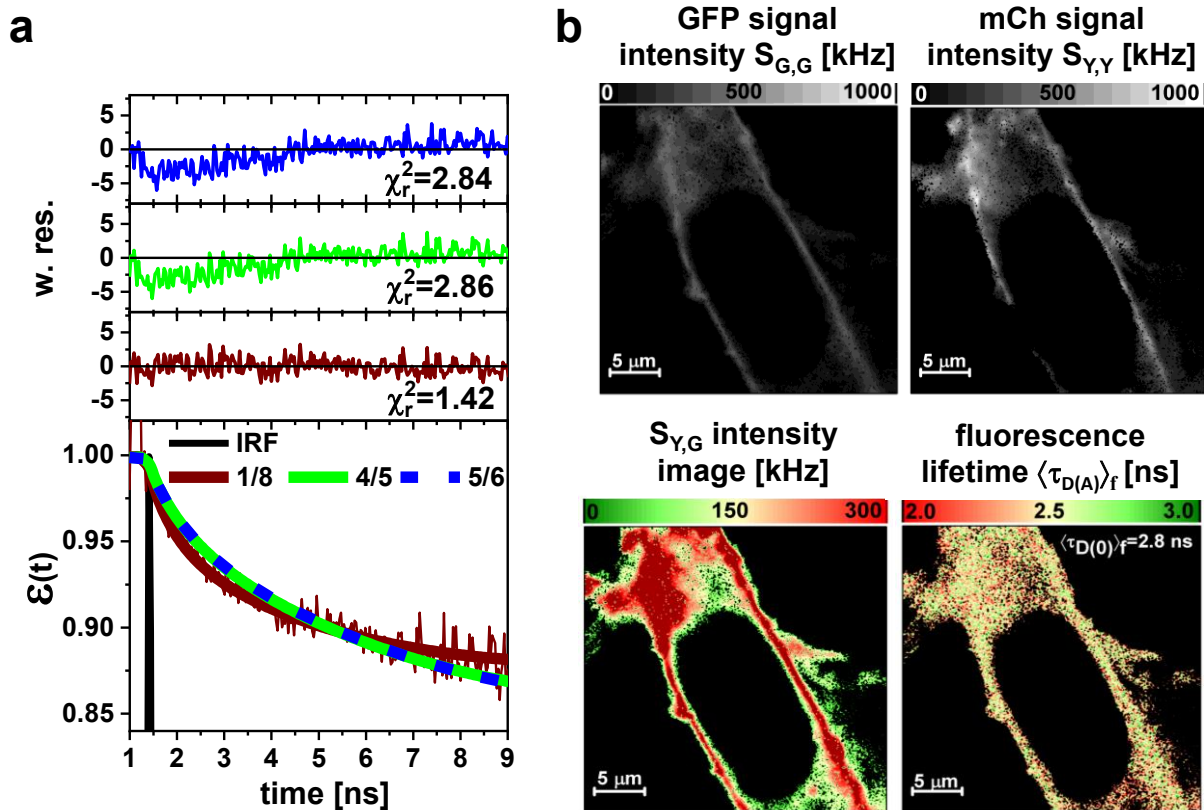


**Figure 30 | Exemplary fluorescence decay and images of HEK293 cells, transiently transfected with TGR5-GFP and TGR5-mCherry.** (a) Fit of the FRET-induced donor quenching curve  $\varepsilon(t)$  on TGR5 Y111A variant with two species normalized to unity: (i) Dimer (fraction  $x_{Dimer}$ ) with the complete distance distribution (FRET and Non-FRET) of the corresponding dimer models (**Figure 29b**) and (ii) donor only/ FRET inactive molecules. Only the distance distribution of the 1/8 dimer model gives a satisfactory fit as judged by the weighted residuals and the reduced chi squared  $\chi_r^2$ . Fit results of TGR5 Y111A for  $x_{Dimer}$ : 1/8 dimer: 0.27; 4/5 dimer: 0.59; 5/6 dimer: 0.73. (b) MFIS analysis of TGR5 Y111A transfected HEK293 cells. Images were obtained by sequential scanning at resolution of 1024 x 1024 pixels. Each picture is shown in a false colour saturation mode and then overlaid by using green and yellow intensity colours. TGR5-GFP and TGR5-mCherry are clearly co-localized at the cell membrane. Images show the comparison by the signal intensity of the donor GFP ( $S_{G,G}$ ), signal intensity of the acceptor mCherry ( $S_{Y,Y}$ ), the detection of yellow mCherry photons after excitation of GFP ( $S_{Y,G}$ , S: signal, Y: yellow emission, G: green excitation) as a result of FRET, and changes in the donor fluorescence lifetime  $\langle\tau_{D(0)}\rangle_f$ . The MFIS measurements show FRET ( $S_{Y,G}$  and changes in  $\langle\tau_{D(A)}\rangle_f$ ) in TGR5 Y111A variant, which indicates at least homo-dimerization.

Both methods for linker simulations gave very similar results. For both dimerization models, interdyer distance at maximum probability in explicit model is within 5 Å from implicit linker model (**Figure 29b**). Both linker simulation techniques predicted that FRET should be able to distinguish a 1/8 dimer from 4/5 dimer and 5/6 dimer, because the interdyer distance distributions have a characteristic peak at short distances (**Figure 29b**). However, the FRET probe distance distributions of the two dimers involving TM5 are expected to be not distinguishable in our FRET experiments.

Residue tyrosine 111 of TGR5 is located in transmembrane helix 3 within the highly conserved motif. The TGR5 Y111A variant, where residue 111 is mutated, shows preferential presence of homo-dimers. Therefore, it is a perfect variant to test which of our distance probe distributions describes the FRET-induced donor quenching curve best (**Figure 30a**).

Only the distance distribution of the 1/8 dimer model gives a statistically satisfactory fit as judged by the weighted residuals (*w.res.*) and the smallest  $\chi_r^2$ . Hence, TM1 and helix 8 most likely form the primary oligomerization interface.

## 1.6. Conclusions

Biomolecules perform their function by undergoing complex structural changes at a broad range of timescales from nanoseconds to hours. The structure and dynamics of biomacromolecular systems can only be fully unravelled by integration of multiple experimental techniques. Computational structural modelling is a convenient common platform for the integration of experimental techniques. Fluorescence spectroscopy opens up a possibility to gain an insight into the structure and dynamics of biomacromolecules at room temperature, in liquid state, and in vivo. FRET experiments are uniquely suitable to provide kinetic information, and to lay out the multi-state systems into the time-ordered structural models, full of intermediates, where previously only end states were observed.

However, fluorescence-based integrative/hybrid structural modelling presents challenges: sparsity of obtained data and complexity of phenomena fluorescent labels are involved in. In order to construct a computational and fluorescence spectroscopy microscope and use it to recover quantitative and precise information about the biomolecular machinery, new methodological developments were necessary.

I developed and implemented necessary components for accurate and efficient fluorescence based biomolecule structure determination, based on computational structural modelling and computer simulations (Chapter 2, Supplement A). These components are:

- Toolkit for automated and efficient FRET experiment design.
- Advanced dye models for organic fluorophores and fluorescent proteins.
- Cross-validation based quality control of fluorescence-based models.
- FRET-enhanced sampling techniques for all-atom molecular dynamics simulations and coarse-grained simulations (specifically, FRET-guided NMSim).

The software implementation of the toolkit is publicly available.

I also demonstrate the application of these developments for a range of different biomacromolecular systems.

- The accuracy of the method was tested on the enzyme T4 lysozyme, a small globular protein with two distinct known crystal structures, accuracy of 2 Ångström was demonstrated (Supplement B, Chapter 2). A third, previously unknown functional state was experimentally discovered. Conformational dynamics of the enzyme was directly linked to its catalytic function.
- For the larger human guanylate binding protein 1, data from three different experimental methods were used to determine a new conformational state and a detailed kinetic model (Supplement C). These conformational rearrangements were linked to oligomer formation, the mechanism behind the immune response function of the protein in cells.
- Extents of applicability for the developed methods were studied by systematic benchmarks using simulated experimental data for 5 additional proteins, consistently demonstrating accuracy of 2.5 Ångström or better and resilience against the false predictions in the cases when the prior is inaccurate (Chapter 2).
- This approach was used to build a large scale 8-state coarse-grained kinetic model of structural dynamics of chromatin fibres, a key component involved in gene access mechanism (Supplement D).
- Advanced and specific dye model was applied to determine the dimerization interface of G-protein coupled receptor TGR5 (Supplement E), which is also an example, how

fluorescence-based study informs on the localization of the protein in the cell with microscopy and at the same time provides insight into the structure of its oligomers.

## 1.7. References

1. Dror, R. O., Dirks, R. M., Grossman, J. P., Xu, H. F. & Shaw, D. E. Biomolecular Simulation: A Computational Microscope for Molecular Biology. *Annu. Rev. Biophys.* **41**, 429-452 (2012).
2. Lucic, V., Rigort, A. & Baumeister, W. Cryo-electron tomography: The challenge of doing structural biology in situ. *J. Cell Biol.* **202**, 407-419 (2013).
3. Woutersen, S., Mu, Y., Stock, G. & Hamm, P. Hydrogen-bond lifetime measured by time-resolved 2D-IR spectroscopy: N-methylacetamide in methanol. *Chem. Phys.* **266**, 137-147 (2001).
4. Skrynnikov, N. R., Millet, O. & Kay, L. E. Deuterium spin probes of side-chain dynamics in proteins. 2. Spectral density mapping and identification of nanosecond time-scale side-chain motions. *J. Am. Chem. Soc.* **124**, 6449-6460 (2002).
5. Bremer, H. & Dennis, P. P. Modulation of chemical composition and other parameters of the cell by growth rate. *Escherichia coli and Salmonella: cellular and molecular biology* **2**, 1553-1569 (1996).
6. Frueh, D. P., Goodrich, A. C., Mishra, S. H. & Nichols, S. R. NMR methods for structural studies of large monomeric and multimeric proteins. *Curr. Opin. Struct. Biol.* **23**, 734-739 (2013).
7. Winkler, J. R. FRETting over the Spectroscopic Ruler. *Science* **339**, 1530-1531 (2013).
8. Hellenkamp, B. *et al.* Precision and accuracy of single-molecule FRET measurements—a multi-laboratory benchmark study. *Nat. Meth.* **15**, 669-+ (2018).
9. Sisamakos, E., Valeri, A., Kalinin, S., Rothwell, P. J. & Seidel, C. A. M. Accurate single-molecule FRET studies using multiparameter fluorescence detection. *Methods Enzymol.* **475**, 455-514 (2010).
10. Eggeling, C., Fries, J. R., Brand, L., Gunther, R. & Seidel, C. A. M. Monitoring conformational dynamics of a single molecule by selective fluorescence spectroscopy. *Proc. Natl. Acad. Sci. USA* **95**, 1556-1561 (1998).
11. Kühnemuth, R. & Seidel, C. A. M. Principles of single molecule multiparameter fluorescence spectroscopy. *Single Mol.* **2**, 251-254 (2001).
12. Felekyan, S., Kalinin, S., Sanabria, H., Valeri, A. & Seidel, C. A. M. Filtered FCS: species auto- and cross-correlation functions highlight binding and dynamics in biomolecules. *ChemPhysChem* **13**, 1036-1053 (2012).
13. Bohmer, M., Wahl, M., Rahn, H. J., Erdmann, R. & Enderlein, J. Time-resolved fluorescence correlation spectroscopy. *Chem. Phys. Lett.* **353**, 439-445 (2002).
14. Peulen, T. O., Opanasyuk, O. & Seidel, C. A. M. Combining graphical and analytical methods with molecular simulations to analyze time-resolved FRET measurements of labeled macromolecules accurately. *J. Phys. Chem. B* **121**, 8211-8241 (2017).
15. Dale, R. E., Eisinger, J. & Blumberg, W. E. Orientational Freedom of Molecular Probes - Orientation Factor in Intra-Molecular Energy-Transfer. *Biophys. J.* **26**, 161-193 (1979).
16. Schneidman-Duhovny, D., Pellarin, R. & Sali, A. Uncertainty in integrative structural modeling. *Curr. Opin. Struct. Biol.* **28**, 96-104 (2014).
17. Ward, A. B., Sali, A. & Wilson, I. A. Integrative Structural Biology. *Science* **339**, 913-915 (2013).
18. Ha, T. *et al.* Probing the interaction between two single molecules: Fluorescence resonance energy transfer between a single donor and a single acceptor. *Proc. Natl. Acad. Sci. USA* **93**, 6264-6268 (1996).
19. Weiss, S. Fluorescence spectroscopy of single biomolecules. *Science* **283**, 1676-1683 (1999).
20. Muschielok, A. *et al.* A nano-positioning system for macromolecular structural analysis. *Nat. Meth.* **5**, 965-971 (2008).
21. Kalinin, S. *et al.* A toolkit and benchmark study for FRET-restrained high-precision structural modeling. *Nat. Meth.* **9**, 1218-1225 (2012).

22. Tompa, P. On the supertertiary structure of proteins. *Nat. Chem. Biol.* **8**, 597-600 (2012).
23. Beckers, M., Drechsler, F., Eilert, T., Nagy, J. & Michaelis, J. Quantitative structural information from single-molecule FRET. *Farad. Discuss.* **184**, 117-129 (2015).
24. Ahmed, A., Rippmann, F., Barnickel, G. & Gohke, H. A normal mode-based geometric simulation approach for exploring biologically relevant conformational transitions in proteins. *J. Chem. Inf. Model.* **51**, 1604-1622 (2011).
25. Berman, H. M. *et al.* The Protein Data Bank. *Nucleic Acids Res.* **28**, 235-242 (2000).
26. Chopra, G., Kalisman, N. & Levitt, M. Consistent refinement of submitted models at CASP using a knowledge-based potential. *Proteins* **78**, 2668-2678 (2010).
27. Ruiz-Blanco, Y. B. *et al.* A physics-based scoring function for protein structural decoys: Dynamic testing on targets of CASP-ROLL. *Chem. Phys. Lett.* **610**, 135-140 (2014).
28. Oldziej, S. *et al.* Physics-based protein-structure prediction using a hierarchical protocol based on the UNRES force field: Assessment in two blind tests. *Proc. Natl. Acad. Sci. USA* **102**, 7547-7552 (2005).
29. Rohl, C. A., Strauss, C. E. M., Misura, K. M. S. & Baker, D. Protein structure prediction using rosetta. *Methods Enzymol.* **383**, 66-+ (2004).
30. Yang, J. Y. *et al.* The I-TASSER Suite: protein structure and function prediction. *Nat. Meth.* **12**, 7-8 (2015).
31. Arnold, K., Bordoli, L., Kopp, J. & Schwede, T. The SWISS-MODEL workspace: a web-based environment for protein structure homology modelling. *Bioinformatics* **22**, 195-201 (2006).
32. Jones, D. T., Buchan, D. W. A., Cozzetto, D. & Pontil, M. PSICOV: precise structural contact prediction using sparse inverse covariance estimation on large multiple sequence alignments. *Bioinformatics* **28**, 184-190 (2012).
33. Ovchinnikov, S. *et al.* Large-scale determination of previously unsolved protein structures using evolutionary information. *Elife* **4** (2015).
34. Morcos, F. *et al.* Direct-coupling analysis of residue coevolution captures native contacts across many protein families. *Proc. Natl. Acad. Sci. USA* **108**, E1293-E1301 (2011).
35. Gansen, A. *et al.* Nucleosome disassembly intermediates characterized by single-molecule FRET. *Proc. Natl. Acad. Sci. USA* **106**, 15308-15313 (2009).
36. Best, R. B., Hofmann, H., Nettels, D. & Schuler, B. Quantitative Interpretation of FRET Experiments via Molecular Simulation: Force Field and Validation. *Biophys. J.* **108**, 2721-2731 (2015).
37. Graen, T., Hoefling, M. & Grubmuller, H. AMBER-DYES: Characterization of Charge Fluctuations and Force Field Parameterization of Fluorescent Dyes for Molecular Dynamics Simulations. *J. Chem. Theory Comput.* **10**, 5505-5512 (2014).
38. Sindbert, S. *et al.* Accurate distance determination of nucleic acids via Förster resonance energy transfer: implications of dye linker length and rigidity. *J. Am. Chem. Soc.* **133**, 2463-2480 (2011).
39. Hellenkamp, B., Wortmann, P., Kandzia, F., Zacharias, M. & Hugel, T. Multidomain structure and correlated dynamics determined by self-consistent FRET networks. *Nat. Meth.* **14**, 174-180 (2017).
40. Steffen, F. D., Sigel, R. K. O. & Borner, R. An atomistic view on carbocyanine photophysics in the realm of RNA. *Phys. Chem. Chem. Phys.* **18**, 29045-29055 (2016).
41. Hofig, H., Gabba, M., Pobleto, S., Kempe, D. & Fitter, J. Inter-Dye Distance Distributions Studied by a Combination of Single-Molecule FRET-Filtered Lifetime Measurements and a Weighted Accessible Volume (wAV) Algorithm. *Molecules* **19**, 19269-19291 (2014).
42. Gregory, P. *Bayesian Logical Data Analysis for the Physical Sciences: A Comparative Approach with Mathematica® Support.* (Cambridge University Press, 2005).

43. Andrae, R., Schulze-Hartung, T. & Melchior, P. Dos and don'ts of reduced chi-squared. *arXiv:1012.3754* (2010).
44. Ye, J. M. On measuring and correcting the effects of data mining and model selection. *J. Amer. Statist. Assoc.* **93**, 120-131 (1998).
45. Berger, J. O. & Sellke, T. Testing a Point Null Hypothesis - the Irreconcilability of P-Values and Evidence. *J. Amer. Statist. Assoc.* **82**, 112-122 (1987).
46. Sellke, T., Bayarri, M. J. & Berger, J. O. Calibration of p values for testing precise null hypotheses. *Am. Stat.* **55**, 62-71 (2001).
47. Delampady, M. & Berger, J. O. Lower Bounds on Bayes Factors for Multinomial Distributions, with Application to Chi-Squared Tests of Fit. *Ann. Stat.* **18**, 1295-1316 (1990).
48. Morey, R. D., Hoekstra, R., Rouder, J. N., Lee, M. D. & Wagenmakers, E. J. The fallacy of placing confidence in confidence intervals. *Psychon. Bull. Rev.* **23**, 103-123 (2016).
49. Greenland, S. *et al.* Statistical tests, P values, confidence intervals, and power: a guide to misinterpretations. *Eur. J. Epidemiol.* **31**, 337-350 (2016).
50. Best, R. B., Hummer, G. & Eaton, W. A. Native contacts determine protein folding mechanisms in atomistic simulations. *Proc. Natl. Acad. Sci. USA* **110**, 17874-17879 (2013).
51. Shakhnovich, E., Farztdinov, G., Gutin, A. M. & Karplus, M. Protein Folding Bottlenecks - a Lattice Monte-Carlo Simulation. *Phys. Rev. Lett.* **67**, 1665-1668 (1991).
52. Zemla, A., Venclovas, C., Moulton, J. & Fidelis, K. Processing and analysis of CASP3 protein structure predictions. *Proteins*, 22-29 (1999).
53. Zhang, Y. & Skolnick, J. Scoring function for automated assessment of protein structure template quality. *Proteins* **57**, 702-710 (2004).
54. Mariani, V., Biasini, M., Barbato, A. & Schwede, T. IDDT: a local superposition-free score for comparing protein structures and models using distance difference tests. *Bioinformatics* **29**, 2722-2728 (2013).
55. International Organization for Standardization. Accuracy (trueness and precision) of measurement methods and results — Part 1: General principles and definitions. **ISO 5725-1:1994**.
56. Barlow, R. J. *Statistics: a guide to the use of statistical methods in the physical sciences*. Vol. 29 (John Wiley & Sons, 1989).
57. Massey, F. J. The Kolmogorov-Smirnov Test for Goodness of Fit. *J. Amer. Statist. Assoc.* **46**, 68-78 (1951).
58. Wlodawer, A. Stereochemistry and Validation of Macromolecular Structures. *Methods Mol. Biol.* **1607**, 595-610 (2017).
59. Read, R. J. *et al.* A New Generation of Crystallographic Validation Tools for the Protein Data Bank. *Structure* **19**, 1395-1412 (2011).
60. Chen, V. B. *et al.* MolProbity: all-atom structure validation for macromolecular crystallography. *Acta Crystallogr. D* **66**, 12-21 (2010).
61. Laskowski, R. A., MacArthur, M. W., Moss, D. S. & Thornton, J. M. Procheck - a Program to Check the Stereochemical Quality of Protein Structures. *J. Appl. Crystallogr.* **26**, 283-291 (1993).
62. Hooft, R. W. W., Vriend, G., Sander, C. & Abola, E. E. Errors in protein structures. *Nature* **381**, 272-272 (1996).
63. Rieping, W., Habeck, M. & Nilges, M. Inferential structure determination. *Science* **309**, 303-306 (2005).
64. Kryshtafovych, A. *et al.* Some of the most interesting CASP11 targets through the eyes of their authors. *Proteins* **84**, 34-50 (2016).
65. Matthews, B. W. & Remington, S. J. The three dimensional structure of the lysozyme from bacteriophage T4. *Proc Natl Acad Sci U S A* **71**, 4178-4182 (1974).



66. Llinas, M., Gillespie, B., Dahlquist, F. W. & Marqusee, S. The energetics of T4 lysozyme reveal a hierarchy of conformations. *Nat. Struct. Biol.* **6**, 1072-1078 (1999).
67. Kuroki, R., Weaver, L. H. & Matthews, B. W. A Covalent Enzyme-Substrate Intermediate with Saccharide Distortion in a Mutant T4 Lysozyme. *Science* **262**, 2030-2033 (1993).
68. Ghosh, A., Praefcke, G. J. K., Renault, L., Wittinghofer, A. & Herrmann, C. How guanylate-binding proteins achieve assembly-stimulated processive cleavage of GTP to GMP. *Nature* **440**, 101-104 (2006).
69. Li, P. *et al.* Ubiquitination and degradation of GBPs by a Shigella effector to suppress host defence. *Nature* **551**, 378-+ (2017).
70. Piro, A. S. *et al.* Detection of cytosolic Shigella flexneri via a C-terminal triple-arginine motif of GBP1 inhibits actin-based motility. *Mbio* **8** (2017).
71. Tietzel, I., El-Haibi, C. & Carabeo, R. A. Human Guanylate Binding Proteins Potentiate the Anti-Chlamydia Effects of Interferon-gamma. *Plos One* **4** (2009).
72. Klare, J. P. & Steinhoff, H. J. Spin labeling EPR. *Photosynth. Res.* **102**, 377-390 (2009).
73. Dimura, M. *et al.* Quantitative FRET studies and integrative modeling unravel the structure and dynamics of biomolecular systems. *Curr. Opin. Struct. Biol.* **40**, 163-185 (2016).
74. Mullner, D. fastcluster: Fast Hierarchical, Agglomerative Clustering Routines for R and Python. *J. Stat. Softw.* **53**, 1-18 (2013).
75. Vöpel, T. *et al.* Triphosphate induced dimerization of human guanylate binding protein 1 involves association of the C-Terminal helices: A joint Double Electron-Electron Resonance and FRET study. *Biochemistry* **53**, 4590-4600 (2014).
76. Kozakov, D. *et al.* Encounter complexes and dimensionality reduction in protein-protein association. *Elife* **3**, e01370 (2014).
77. Pandita, E. *et al.* Tetrameric assembly of hGBP1 is crucial for both stimulated GMP formation and antiviral activity. *Biochem. J.* **473**, 1745-1757 (2016).
78. Schalch, T., Duda, S., Sargent, D. F. & Richmond, T. J. X-ray structure of a tetranucleosome and its implications for the chromatin fibre. *Nature* **436**, 138-141 (2005).
79. Song, F. *et al.* Cryo-EM Study of the Chromatin Fiber Reveals a Double Helix Twisted by Tetranucleosomal Units. *Science* **344**, 376-380 (2014).
80. Robinson, P. J. J., Fairall, L., Huynh, V. A. T. & Rhodes, D. EM measurements define the dimensions of the "30-nm" chromatin fiber: Evidence for a compact, interdigitated structure. *Proc. Natl. Acad. Sci. USA* **103**, 6506-6511 (2006).
81. Grigoryev, S. A., Arya, G., Correll, S., Woodcock, C. L. & Schlick, T. Evidence for heteromorphic chromatin fibers from analysis of nucleosome interactions. *Proc. Natl. Acad. Sci. USA* **106**, 13317-13322 (2009).
82. Wei, Y. Z., Chesne, M. T., Terns, R. M. & Terns, M. P. Sequences spanning the leader-repeat junction mediate CRISPR adaptation to phage in *Streptococcus thermophilus*. *Nucleic Acids Res.* **43**, 1749-1758 (2015).
83. Koopmans, W. J. A., Brehm, A., Logie, C., Schmidt, T. & van Noort, J. Single-pair FRET microscopy reveals mononucleosome dynamics. *J. Fluoresc.* **17**, 785-795 (2007).
84. Li, G. & Widom, J. Nucleosomes facilitate their own invasion. *Nat. Struct. Mol. Biol.* **11**, 763-769 (2004).
85. Poirier, M. G., Oh, E., Tims, H. S. & Widom, J. Dynamics and function of compact nucleosome arrays. *Nat. Struct. Mol. Biol.* **16**, 938-U959 (2009).
86. Li, W. *et al.* FACT Remodels the Tetranucleosomal Unit of Chromatin Fibers for Gene Transcription. *Mol. Cell* **64**, 120-133 (2016).
87. Kruithof, M. *et al.* Single-molecule force spectroscopy reveals a highly compliant helical folding for the 30-nm chromatin fiber. *Nat. Struct. Mol. Biol.* **16**, 534-540 (2009).

88. Pope, L. H. *et al.* Single chromatin fiber stretching reveals physically distinct populations of disassembly events. *Biophys. J.* **88**, 3572-3583 (2005).
89. Cui, Y. & Bustamante, C. Pulling a single chromatin fiber reveals the forces that maintain its higher-order structure. *Proc. Natl. Acad. Sci. USA* **97**, 127-132 (2000).
90. Arya, G., Zhang, Q. & Schlick, T. Flexible histone tails in a new mesoscopic oligonucleosome model. *Biophys. J.* **91**, 133-150 (2006).
91. Arya, G. & Schlick, T. A Tale of Tails: How Histone Tails Mediate Chromatin Compaction in Different Salt and Linker Histone Environments. *J. Phys. Chem. A* **113**, 4045-4059 (2009).
92. Yu, D. D. *et al.* Stereoselective synthesis, biological evaluation, and modeling of novel bile acid-derived G-protein coupled Bile acid receptor 1 (GP-BAR1, TGR5) agonists. *Bioorg. Med. Chem.* **23**, 1613-1628 (2015).
93. Sindhu, T. & Srinivasan, P. Exploring the binding properties of agonists interacting with human TGR5 using structural modeling, molecular docking and dynamics simulations. *RSC Adv.* **5**, 14202-14213 (2015).
94. Macchiarulo, A. *et al.* Probing the Binding Site of Bile Acids in TGR5. *ACS Med. Chem. Lett.* **4**, 1158-1162 (2013).
95. Gertzen, C. G. W. *et al.* Mutational mapping of the transmembrane binding site of the G-protein coupled receptor TGR5 and binding mode prediction of TGR5 agonists. *Eur. J. Med. Chem.* **104**, 57-72 (2015).
96. Simpson, L. M., Taddese, B., Wall, I. D. & Reynolds, C. A. Bioinformatics and molecular modelling approaches to GPCR oligomerization. *Curr. Opin. Pharmacol.* **10**, 30-37 (2010).
97. Filizola, M. & Weinstein, H. The study of G-protein coupled receptor oligomerization with computational modeling and bioinformatics. *FEBS J.* **272**, 2926-2938 (2005).
98. Manglik, A. *et al.* Crystal structure of the mu-opioid receptor bound to a morphinan antagonist. *Nature* **485**, 321-U170 (2012).
99. Salom, D. *et al.* Crystal structure of a photoactivated deprotonated intermediate of rhodopsin. *Proc. Natl. Acad. Sci. USA* **103**, 16123-16128 (2006).
100. Patowary, S. *et al.* The muscarinic M-3 acetylcholine receptor exists as two differently Sized complexes at the plasma membrane. *Biochem. J.* **452**, 303-312 (2013).
101. Huang, J. Y., Chen, S., Zhang, J. J. & Huang, X. Y. Crystal structure of oligomeric beta(1)-adrenergic G protein-coupled receptors in ligand-free basal state. *Nat. Struct. Mol. Biol.* **20**, 419-+ (2013).
102. Fotiadis, D. *et al.* Atomic-force microscopy: Rhodopsin dimers in native disc membranes. *Nature* **421**, 127-128 (2003).

# Chapter 2. Automated and optimally FRET-assisted structural modelling

---

Mykola Dimura<sup>1,2</sup>, Thomas O. Peulen<sup>1</sup>, Hugo Sanabria<sup>1,3</sup>, Dmitro Rodnin<sup>1</sup>, Katherina Hemmen<sup>1</sup>, Claus A.M. Seidel<sup>1,\*</sup>, Holger Gohlke<sup>2,4,\*</sup>

<sup>1</sup> Chair for Molecular Physical Chemistry, Heinrich Heine University Düsseldorf, 40225 Düsseldorf, Germany;

<sup>2</sup> Institute for Pharmaceutical and Medicinal Chemistry, Heinrich Heine University Düsseldorf, 40225 Düsseldorf, Germany;

<sup>3</sup> Department of Physics and Astronomy, Clemson University, Clemson, South Carolina, U.S.A.

<sup>4</sup> John von Neumann Institute for Computing (NIC), Jülich Supercomputing Centre (JSC), and Institute for Complex Systems - Structural Biochemistry (ICS-6), Forschungszentrum Jülich GmbH, 52425 Jülich, Germany

## 2.1. Abstract

FRET experiments can yield state-specific structural information on complex dynamic biomolecular assemblies. However, FRET experiments need to be combined with computer simulations to overcome their sparsity. We introduce (i) an automated FRET experiment design tool determining optimal FRET pairs for structural modelling, (ii) a protocol for efficient FRET-assisted computational structural modelling at multiple scales, and (iii) a quantitative quality estimate for judging the accuracy of determined structures. We tested against simulated and experimental data.

## 2.2. Introduction

Structures of biomacromolecules and their complexes are often key to understanding the molecules' functions and underlying mechanisms, and therefore can be a prerequisite for related biological and medical developments. For certain classes of systems, including multi-domain proteins, biomacromolecular complexes, dynamic systems with unstructured regions, and systems with lowly populated conformational states, experimental structure determination is challenging. For such complex systems, contemporary computational structure prediction tools<sup>1-5</sup> often yield several alternative models, which may contain different domain folds and supertertiary structures, particularly if template structures of homologous proteins are not available. FRET experiments

can alleviate these difficulties in that they yield state-specific structural information on complex constructs, even for very dynamic systems with short-lived states in the microsecond time scale<sup>6-10</sup>. However, FRET experiments need to be combined with computer simulations to solve the issue that FRET data is usually too sparse to cover all structural details<sup>11,12</sup>. The problem of quantitative *accuracy* evaluation (as opposed to *precision*) remained largely unaddressed as well. Here, we introduce (i) methodological developments for an automated design of FRET experiments that aim at obtaining the most informative set of FRET pairs optimal for structural modelling, and (ii) a protocol for efficient structure determination and quantitative quality estimation based on such FRET data and computational modelling at multiple scales.

### 2.3. Results

We devised an iterative workflow for FRET-assisted modelling consisting of six steps (**Fig. 1a**), and developed the related software (see Code Availability below): (1) collection of prior knowledge, (2) generation of an initial structural ensemble, (3) selection of the most informative FRET pairs, (4) acquisition and analysis of the experimental data, (5) FRET screening (a statistical quality assessment using a  $\chi_n^2$  criterion (**eq. section 1.5.8**)), (6) FRET-guided structural sampling. This workflow is exemplified for the *E. coli* YaaA protein (YaaA, **Fig. 1b-h**).

In step 1, prior information is obtained from structures in the PDB of other states of a given target, homology models, or structural models built with other computational structure prediction tools<sup>1-5</sup> (**Fig. 1b**). In step 2, this initial structural ensemble is expanded by conformational sampling (**Fig. 1c**). For this, multiple unrestrained simulations using structures obtained in the first step as seeds are performed using the NMSim approach, which performs normal mode-based geometric simulations for multiscale modelling of protein conformational changes<sup>13</sup> (<http://nmsim.de>). For YaaA, *prior* structures were taken from the computational structure predictions submitted to the CASP 11 experiment (T806)<sup>14</sup> (**section 1.5.1**). For the other proteins, seed structures corresponding to conformational states different from the ‘true’ one were taken from the PDB (**Table 4**). In step 3, we use a novel algorithm for experiment planning to automatically determine a set of most informative FRET pairs (**Fig. 1d, Supplementary Fig. 1, Supplementary Table 1**) optimized for highest model precision that is based on a given *prior* structural ensemble. Additionally, our tool for experimental design can consider user-specified labelling site

accessibility, chemical nature, and influence on function and stability as determined from mutation analysis or sequence coevolution data (section 1.5.4). A higher number of measured FRET pairs results in higher precision, since less diverse structures are found for the ensemble within the confidence level of 68% corresponding to  $\chi_n^2 < 1$  (Fig. 1e). This agrees with the predictions from the pair selection algorithm (Fig. 1f). Notably, for sparser and smaller prior ensembles less FRET measurements are needed to achieve a target precision. In step 4, FRET data is acquired including uncertainty estimates (Supplementary Table 1).

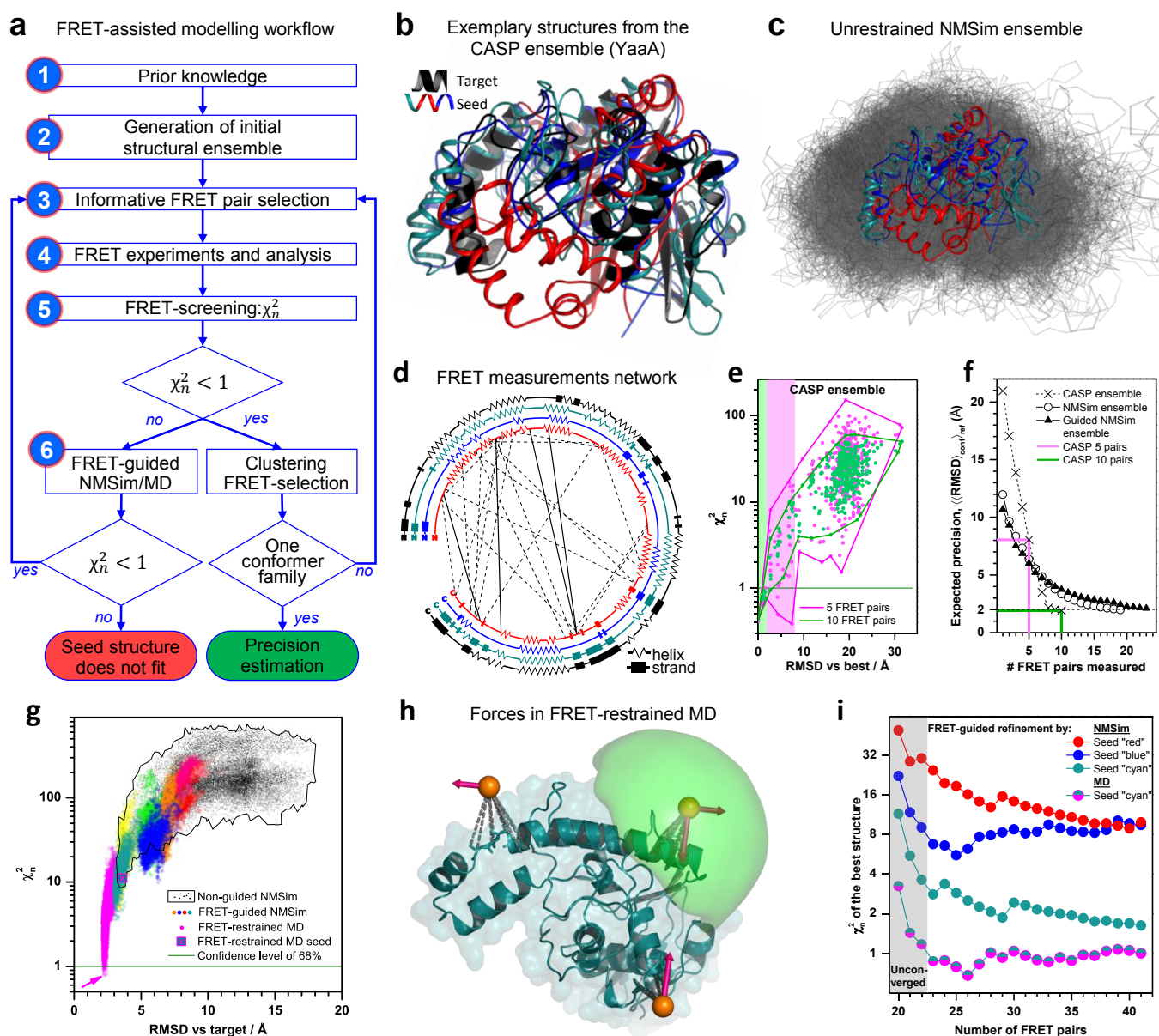


**Figure 1 | Automated FRET-assisted structure prediction on the example of the *E. coli* protein YaaA.** (a) Step-by-step workflow for automated and optimally FRET-assisted structural modelling. (b) Collection of prior information: CASP predictions used as seed structures (red, cyan, blue), and the target crystal structure of YaaA (black, PDB ID: 5caj). Three out of eleven used seed structures are shown for clarity. (c) Generation of initial structural ensemble (grey) by NMSim without any FRET information, using CASP predictions (red, cyan, blue) as seed structures. (d) Network of FRET pairs used for guided NMSim simulations (dashed) and FRET screening (dashed and solid). Secondary structure elements (zigzag –  $\alpha$ -helix,  $3_{10}$ -helix or  $\pi$ -helix; rectangle –  $\beta$ -bridge or  $\beta$ -ladder, line – loop) for three shown seed structures (red, cyan, blue) and the target (black). (e) Impact of the number of selected FRET pairs on the precision of the selected ensemble. The  $\chi_n^2$  values and RMSD against the best structure for the structural ensemble of CASP targets are shown. The diversity of the structures with lower  $\chi_n^2$  defines the precision of the FRET-selected structure. The green and magenta shaded areas correspond to 10 and 5 FRET measurements, respectively. (f) Expected precision of the resulting structural model, depending on the number of used FRET measurements. For the sparser conformational ensemble (CASP ensemble, crosses), the decay is steeper than for the more diverse ensembles generated by NMSim (circles). (g) FRET  $\chi_n^2$  values and RMSD against the crystal structure (target) for different conformations (points). Black points stand for unrestrained NMSim sampling starting from homology models. Colored points represent FRET-guided NMSim simulations. Magenta points represent FRET-restrained MD simulations. Guided simulations stemming from different homology models are shown in different colours. (h) Attachment (dashed grey) of pseudo-atoms (orange spheres) and application of FRET-restraints (pink arrows) in FRET-restrained MD simulations. The accessible volume of a fluorophore is shown as green surface. (i)  $\chi_n^2$  of the best conformers generated by FRET-guided NMSim or FRET-restrained MD simulations using different seed structures.  $\chi_n^2$  starts to converge with  $\sim 23$  selected FRET pairs. Line colours correspond to structure colours in (b).

In step 5 we screen our large ensemble to find those structural models which agree well with the FRET observables corresponding to the ‘true’ structure. To our knowledge, no absolute quality measure exists for this purpose so far. Thus, we introduced a quantitative and reliable accuracy estimation by computing the goodness-of-fit,  $\chi_n^2 = \chi^2 / \chi_{68\%}^2$ , to judge the agreement (eq. 1.5.8).  $\chi_n^2$  is an absolute measurement of quality, it relies on an accurate error estimation and requires

FRET measurements that have not been used for previous optimization steps. Therefore,  $\chi_n^2$  is analogous to cross-validation of the structural model and similar in spirit to  $R_{\text{free}}$  known from X-ray crystallography<sup>15</sup>. For calculating  $\chi_n^2$ , we introduce for the first time a tool for the automatic quantitative estimation of the number of relevant degrees of freedom in FRET-assisted models. The tool can be applied to an arbitrary ensemble of structural models, which opens a convenient interface for integration with third party structural modelling tools. Using the  $\chi_n^2$  criterion ( $\chi_n^2 < 1$ ), the FRET data allow us to extract a set of conformers (**Supplementary Fig. 2**): conformations with  $\chi_n^2$  values  $< 1.0$  are identified as FRET-consistent models. If the diversity within the FRET-selected ensemble is sufficiently low (e.g., root mean square deviation ( $RMSD_{ij}$ )  $< 3$  Å), the workflow is considered to converge. The diversity within the FRET-selected ensemble represents the precision of the obtained model.

However, if no structure with good FRET agreement ( $\chi_n^2 < 1$ ) were found in the initial ensemble (**Fig. 1g**, black points), we establish two new multi-scale structural sampling tools to extend this ensemble by FRET-guided structural sampling (step (6): FRET-guided normal mode-based geometric simulations (NMSim approach<sup>13</sup>, **Supplementary Fig. 3**) employing a Metropolis-Hastings Monte Carlo algorithm and FRET-restrained molecular dynamics simulations (**Fig. 1h**, **Supplementary Fig. 4**), which implement a novel implicit dye representation and experiment-based inter-dye distance restraints, rather than inaccurate atom-atom distance restraints. The additional FRET information allows us to explore areas of phase space inaccessible for purely computational multi-scale simulations, so that novel and experimentally relevant (super-) tertiary structures can be resolved. Strikingly, FRET-guided refinement of different seed structures yields distinct limiting  $\chi_n^2$  levels for the final structural models (**Fig. 1g,i**) with more accurate folds indicated by lower  $\chi_n^2$  values. This allows us to detect errors in the folds of seed conformers that cannot be easily corrected, down to the level of secondary structure (**Fig. 1d**). Note that only four additional FRET-pairs are needed here for reaching a converged  $\chi_n^2$  (grey box, **Fig. 1i**).

The workflow was benchmarked on simulated and experimental data. For that, we used an exemplary set of six proteins that are diverse in their structures, sizes (148 to 409 amino acids), and types of internal interconversion motions (hinge-bending, shear, and twist), and mode of interaction (induced fit or conformational selection<sup>16,17</sup>, **Supplementary Note 1**). Some of these

proteins have been used previously to investigate conformational sampling techniques<sup>18-20</sup>. For each protein, at least one conformation is available in the PDB. This conformation is used as a ‘true’ reference structure for accuracy estimation. For five proteins realistic FRET data was simulated as described previously<sup>8</sup> (**Supplementary Table 1, Supplementary Fig. 5, Supplementary Note 5**). For T4 lysozyme (T4L) a comprehensive experimental data set was acquired in solution, which allowed us to resolve two short (4  $\mu$ s) lived conformers referred to as “C1” and “C2”<sup>21</sup>, which were also observed by X-ray crystallography. Using simulated and experimental datasets, we applied our FRET-guided structural modelling procedure in order to arrive at a target structural model, starting from the seed conformer corresponding to the other state. In this benchmark study, we obtained state-specific structural models with a precision of 2 to 3.5 Å and an accuracy against the target structure between 2 and 3 Å (**Table 4, Fig. 2, Supplementary Fig. 11**) for as few as 13 to 23 FRET measurements, depending on the structural diversity and accuracy of the prior ensemble. This parsimony is attributed to the novel method for automatic determination of a set of optimal FRET pairs (**Supplementary Fig. 1**). These results illustrate that the predictive power and reliability of  $\chi_n^2$  (**Supplementary Fig. 6**) yields target structures with an observed structural heterogeneity for protein backbone conformations at room temperature as found in all-atom MD simulations and NMR experiments<sup>22</sup>. The resolution of experimental FRET studies is sufficient to distinguish between the known conformers C1 and C2 (**Supplementary Fig. 5**) which differ by 4 Å RMSD.

**Table 4** | Summary over the proteins used in the benchmark<sup>(\*\*)</sup>.

Protein name	PDB ID			RMSD / Å				#pairs	
	seed	target	#aa	prior	best	min	max	guiding	+validation
<b><i>E. coli</i> YaaA protein</b>	(*)	5caj	256	4.7-14.6	2.4	2.2	2.5	19	+4
<b>LAO binding protein</b>	2lao	1l1st	238	4.7	2.4	1.8	2.4	12	+3
<b>Calmodulin</b>	1cfd	1ckk	148	9.8	2.4	2.4	3.1	13	+9
<b>Atlastin1</b>	4idn	3q5e	409	18.7	2.5	2.4	3.0	10	+9
<b>Adenylate kinase</b>	4ake	1ake	214	7.2	2.3	2.1	3.2	10	+8
<b><u>T4 lysozyme (C2→C1)</u></b>	3gun	172l	162	4.0	2.8	2.8	3.3	10	+10
<b><u>T4 lysozyme (C1→C2)</u></b>	172l	3gun	162	4.0	2.5	2.0	3.5	10	+10

#aa stands for the no. of amino acids in the protein, as used in the benchmark. The RMSD of the seed structure against the target structure is indicated as  $RMSD_{prior}$ .  $RMSD_{min/best/max}$  of the FRET-selected structures against the target structure are indicated as an accuracy measure for the



obtained ensembles;  $RMSD_{best}$  represents the deviation for the model with the lowest  $\chi_n^2$ ;  $RMSD_{min}$  and  $RMSD_{max}$  correspond to the minimum and maximum RMSD of the structural models within the confidence level. All RMSDs are calculated for  $C_\alpha$  atoms only. For the T4L (underlined) experimental FRET data was used, for other proteins the data was simulated.

(\*)For *E. coli* YaaA protein, 10 seed structures were selected among the predictions submitted for the CASP 11 experiment (target T806). This selection differs from the target crystal structure (RMSD of 4.7 to 14.6 Å) and represents different folds and secondary structures. The number of FRET measurements needed for reliable segregation of models is reported in the “#pairs” column. Initially predicted FRET pairs are used for guiding, while an extended set of FRET pairs is used for cross-validation.

(\*\*)The starting ensembles, FRET networks and optimization cycles are summarized for all proteins in **Supplementary Fig. 7**.

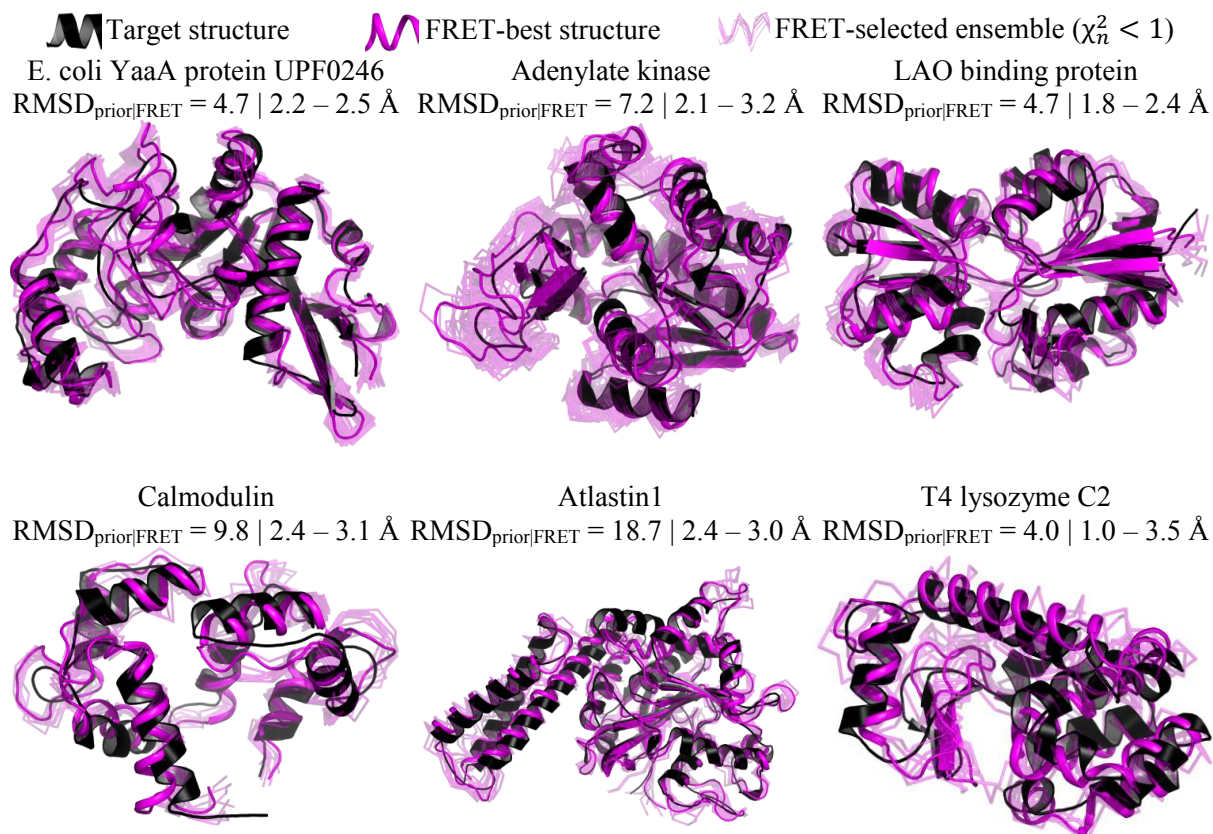


**Figure 2** | Structures obtained by FRET-assisted modelling (magenta) and target X-ray structures (black) are shown for each of the benchmarked proteins. FRET-selected structures are depicted in transparent magenta as a measure for precision; a confidence level of 68% is assumed.

## 2.4. Conclusions

In summary, we demonstrate against simulated and experimental data that accurate, efficient, and largely automated protein structure determination is possible based on optimally designed FRET experiments and structural modelling at multiple scales. In our view, the obtained results provide a major step ahead for quantitative FRET-assisted structural modelling. Furthermore, the approach described here should also be applicable to other label-based techniques such as EPR, paramagnetic relaxation enhancement NMR, vibrational spectroscopy, and their combinations, with minimal changes to the implementation.

## 2.5. Methods

### 2.5.1. Proteins used in the benchmark.

To demonstrate our structural modelling approach and assess its performance, we selected six protein systems: LAO binding protein, adenylate kinase, calmodulin, atlastin1, *E. coli* YaaA protein and T4 lysozyme. The proteins were selected such that the conformational transition between *prior* and target conformer covers different types of internal motions (hinge-bending, shear, bend, and twist). The proteins span a wide range of sizes, from 148 amino acids (calmodulin) to 409 amino acids (atlastin1).

For each of the first four proteins<sup>23-32</sup>, at least two crystal structures are known. One crystal structure is considered the “target” structure, another one of a different conformational state was used as a *prior* (**Table 4**). *E. coli* YaaA protein was one of the targets of the CASP11 experiment<sup>14</sup> (T806). For this protein, 10 homology models provided by the participants of the CASP11 experiment were used as the *prior*. These seed structures were selected from 639 complete protein models submitted to the CASP11 experiment by, first, removing those structures that are similar to the target ( $C_{\alpha}$  atom RMSD  $< 4.6$  Å). The remaining 589 models were clustered into 100 clusters by their secondary structure using Hierarchical agglomerative clustering<sup>33</sup>. From these 100 cluster representatives, 10 were selected by hand such that they represent different tertiary structures and different  $C_{\alpha}$  atom RMSD with respect to the target ( $4.6 \leq \text{RMSD} \leq 14.6$  Å, CASP model ID: Tc806TS041\_1, Tc806TS065\_1, Tc806TS276\_1, Tc806TS345\_1, Tc806TS357\_1, Tc806TS420\_1, Tc806TS428\_1, Tp806TS065\_1, Ts806TS065\_1, Ts806TS276\_1).

### 2.5.2. Quality metric for evaluation of FRET pair sets: $\langle\langle\text{RMSD}\rangle\rangle$ .

To assess, how well certain sets of DA pairs can help resolving a protein structure, we introduce a quality parameter  $\langle\langle\text{RMSD}_{\#conf}\rangle_{\#ref}\rangle$ , or short  $\langle\langle\text{RMSD}\rangle\rangle$ , an estimate for expected precision (uncertainty). Assuming that one unknown structure from the *prior* ensemble is correct,  $\langle\langle\text{RMSD}\rangle\rangle$  is defined to serve as an estimate for what would be the precision if we determined it from experiment (**Supplementary Fig. 8**). Conceptually, first, we take an arbitrary reference model from the prior and assume that it corresponds to the ‘true’ structure of the molecule in experiment. For this reference, a full reference set of FRET observables is simulated. Second, FRET observables are simulated for each conformer in the *prior* and tested against the reference set of observables,  $\chi^2$  and *p*-values are calculated, and the precision  $\langle\text{RMSD}_{\#conf}\rangle$  for this reference is determined. This procedure is repeated for each reference conformer from the prior, and the average over  $\langle\text{RMSD}_{\#conf}\rangle$  is calculated, yielding  $\langle\langle\text{RMSD}_{\#conf}\rangle_{\#ref}\rangle$  (**Supplementary Fig. 8**).

For any given set of  $N$  *prior* conformations,  $\langle\langle\text{RMSD}\rangle\rangle$  is calculated in three stages (**Supplementary Fig. 1**): First, a  $N \times N$  matrix is formed from RMSD values of all pairwise combinations of conformers in the prior:

$$\text{RMSD}_{conf,ref} = \sqrt{\frac{1}{N_{atoms}} \sum_{at=1}^{N_{atoms}} \|\vec{r}_{ref,at} - \vec{r}_{conf,at}\|^2} \quad (2.1)$$

*ref* stands for the reference conformer, *conf* for the tested conformer,  $\vec{r}_{at}$  is the position of an atom in space,  $N_{atoms}$  is the number of atoms in the protein. In this study only  $C_\alpha$  atoms are considered for RMSD estimation. Second, the  $N \times N$  matrix of FRET *p*-values are calculated for the same conformer pairs. To evaluate *p*-values, we start by calculating  $\chi^2_{conf,ref}$ , the  $\chi^2$  of a tested conformation with respect to the reference conformation:

$$\chi^2_{conf,ref} = \sum_{i=1}^{N_{measurements}} \left( \frac{R_{conf}^{(i)} - R_{ref}^{(i)}}{\Delta R_{ref}^{(i)}} \right)^2 \quad (2.2)$$

$R_{conf}^{(i)}$  is the inter-dye distance calculated for FRET pair *i* on a conformational model *conf*,  $R_{ref}^{(i)}$  is the corresponding distance in the reference conformer,  $\Delta R_{ref}^{(i)}$  is the expected experimental error.  $N_{dof}$  is the number of degrees of freedom in  $\chi^2$  test:

$$N_{dof} = N_{measurements} - N_{fit.param}. \quad (2.3)$$

$N_{measurements}$  is the number of FRET measurements (pairs) taken,  $N_{fit.param.}$  is the number of independent relevant coordinates (parameters) for the conformational model (see below). For every conformer pair, we can calculate a  $p$ -value or a probability that a sample  $\chi^2$  will be larger than  $\chi_{conf,ref}^2$ :

$$p_{conf,ref} = p(\chi_{conf,ref}^2, N_{dof}) = \int_{\chi_{conf,ref}^2}^{+\infty} f_{N_{dof}}(\chi^2) d\chi^2 \quad (2.4)$$

$f_{N_{dof}}(\chi^2)$  denotes the chi-squared distribution:

$$f_{N_{dof}}(\chi^2) = \frac{1}{2^{N_{dof}/2} \Gamma(N_{dof}/2)} (\chi^2)^{N_{dof}/2-1} e^{-\chi^2/2} \quad (2.5)$$

$\Gamma$  is the Gamma function. Third,  $\langle\langle \text{RMSD} \rangle\rangle$  is evaluated as a weighted average over the RMSD matrix using the respective  $p$ -values as weights.  $\langle\langle \text{RMSD} \rangle\rangle$  is a double average over all reference conformers as well as all conformers being tested:

$$\langle\langle \text{RMSD} \rangle\rangle = \frac{1}{N_{conf}} \sum_{ref=1}^{N_{conf}} \frac{\sum_{conf=1}^{N_{conf}} p_{conf,ref} \text{RMSD}_{conf,ref}}{\sum_{conf=1}^{N_{conf}} p_{conf,ref}} \quad (2.6)$$

### 2.5.3. FRET screening.

To assess, how well a given structural model or structural ensemble agrees with experimental FRET data, we calculate the  $\chi^2$  value for each structure in the ensemble. To do that, we need to estimate FRET observables corresponding to the specified conformer. We achieve this by simulating the Accessible Volume (AV) of the fluorophore attached to a protein by a flexible linker<sup>12</sup> (see **Supplementary Note 5**).

In general, reduced chi-squared  $\chi_r^2$ , also known as chi-squared per degree of freedom, is used as an absolute quality parameter of a model:

$$\chi_r^2 = \chi^2 / N_{dof} \quad (2.7)$$

However, for values of  $N_{dof} < 30$ , a constant confidence level corresponds to different values of  $\chi_r^2$ . Therefore, using  $\chi_r^2$  to compare models with different  $N_{dof}$  is inconvenient. To overcome this,

we introduce an alternative metric, normalized chi-squared  $\chi_{n,68\%}^2$ , which equals to 1 for  $p = 1 - 68\%$  (one sigma) by definition, independent of the  $N_{dof}$  value (**Supplementary Fig. 9**):

$$\chi_n^2 = \chi_{n,68\%}^2 \equiv \chi^2 / \text{Inv.}\chi^2(p = 1 - 0.68, N_{dof}) \quad (2.8)$$

Where

$$\text{Inv.}\chi^2(p, N_{dof}) = \frac{2^{-N_{dof}/2}}{\Gamma(N_{dof}/2)} p^{-N_{dof}/2-1} e^{-1/(2p)} \quad (2.9)$$

is the inverse chi-squared distribution. To visualize the precision of the generated structural ensembles, we display conformations on two-dimensional plots (**Supplementary Fig. 2**).

Given an ensemble of structural models,  $\chi_n^2$  can be calculated for each conformer. Structures that show better agreement with FRET data have lower  $\chi_n^2$ . If the FRET-selected ensemble ( $\chi_n^2 < 1$ ) is too diverse (e.g.,  $RMSD_{ij} > 3 \text{ \AA}$ ), extra FRET pairs can be selected and measured to improve resolution (see below). In this benchmark reference FRET data ( $R_{ref}^{(i)}, \Delta R_{ref}^{(i)}$ ) were determined from experiment for T4 lysozyme and simulated for other benchmarked proteins using the ‘true’ crystal structure conformations, as described previously<sup>8</sup>. Structures of T4 lysozyme and its homologs from the PDB were screened against the experimental datasets C1 and C2 in order to select reference conformations for each state (**Supplementary Fig. 5**). As a result, PDB ID 172L appears to correspond to C1, and PDB ID 3GUN was selected for C2.

#### 2.5.4. Selection of a set of optimal FRET pairs.

To maximize the precision of FRET-assisted protein structure determination under the condition of a limited number of experimental measurements, we developed a method for automated determination of the most informative labelling sites and donor-acceptor (DA) pairs. We define sets of pairs to be most informative if they lead to the highest expected precision, i.e., lowest  $\langle\langle RMSD \rangle\rangle$ , of a structural model. To find such an optimal DA pair set, we test three different feature selection algorithms (**Supplementary Fig. 10**): greedy forward selection (**Supplementary Note 2**), greedy backward elimination (**Supplementary Note 3**), and an algorithm based on mutual information and inspired by a Minimum Redundancy Maximum Relevance (mRMR) algorithm<sup>34</sup> (**Supplementary Note 4**). FRET pairs are selected among the full set of all possible pairwise combinations of available labelling sites. Labelling sites can be excluded from calculations based on additional prior information provided by the user, e.g. accessibility, chemical nature and

influence on function and stability as determined from mutation analysis or sequence coevolution data. For the proof of principle study with simulated data, we assume that these effects are negligible. However, considering the experimental data sets of T4L, care was taken to avoid these problems. For T4L automated FRET pair selection was performed from only 33 FRET pairs as opposed to theoretically possible  $162^2/2$  residue-residue combinations. These 33 pairs were earlier chosen by authors for a functional study of T4L<sup>21</sup> (see **section 1.5.9**). Despite of this low number of available FRET-pairs, only minor decrease in expected precision was observed as compared to other proteins (**Supplementary Fig. 7**).

In greedy forward feature selection, in the first iteration,  $\langle\langle\text{RMSD}\rangle\rangle$  is calculated for each possible DA pair, and that pair is selected for the DA set that yields the minimal  $\langle\langle\text{RMSD}\rangle\rangle$ . In the next iterations, DA pairs remaining from the previous iteration are probed against the DA set to determine which one leads to the largest decrease in  $\langle\langle\text{RMSD}\rangle\rangle$ ; that DA pair is then added to the DA set. The algorithm stops when a desired  $\langle\langle\text{RMSD}\rangle\rangle$  is reached. Therefore, for conformational ensembles  $< 100,000$  structures, the current implementation converges in less than a day on a 4-core desktop computer.

In greedy backward elimination, in the first iteration,  $\langle\langle\text{RMSD}\rangle\rangle$  is calculated for DA sets containing all possible DA pairs but one. That pair is eliminated for which the remaining DA set yielded the smallest  $\langle\langle\text{RMSD}\rangle\rangle$ ; the remaining DA set is narrowed further in an iterative manner. The algorithm needs to run as many iterations as there are DA pairs available and is therefore slower than the greedy selection algorithm. One run of this algorithm for an ensemble of less than 10,000 conformers completes in about one day on a 4-core desktop computer in the current implementation.

In the mutual information-based DA pair selection algorithm Shannon conditional entropies are calculated for all pairwise combinations of DA pairs. In the first iteration, the DA pair with the highest Shannon entropy is selected. In the next iterations, the DA pair with the highest minimum Shannon conditional entropy with respect to the previous DA pairs is selected (**Supplementary Note 4**). That way, the DA pair providing the highest amount of new information not provided by the previously selected DA pairs is selected. One run of this algorithm for an ensemble of less than 100,000 conformers completes in about one day on a 4-core desktop computer in the current implementation.

### 2.5.5. Estimation of the complexity of the structural model.

Estimation of complexity for a structural model that is used in integrative protein structure determination is essential for quantitative accuracy assessment and automated experiment design. We quantify the complexity of a structural model by the number of relevant independent parameters  $N_{fit.param.}$  needed to describe the corresponding conformational ensemble to a certain precision ( $\langle\langle RMSD \rangle\rangle$ ). If the structural model is simple,  $N_{fit.param.}$  can be calculated analytically, for example, for a rigid body model:

$$N_{fit.param.} = (N_{bodies} - 1) * 6 - N_{bonds}. \quad (2.10)$$

For non-rigid body models, coming from other computational tools, an analytical expression for  $N_{fit.param.}$  is usually unavailable. Examples of such tools are numerous: molecular dynamics simulations (all-atom or coarse-grained), normal mode-based models, homology models, elastic network models, and others.

We thus introduce a heuristic approach for automated  $N_{fit.param.}$  determination, which requires as an input only the user-provided conformational ensemble. Initially, to obtain a  $N_{fit.param.}$  estimate, we start by assuming  $N_{0,fit.param.} = 0$ , and determine a set of DA pairs needed to describe the conformations within an ensemble with a desired precision ( $\langle\langle RMSD \rangle\rangle$ ) employing our DA pair selection algorithm. Each DA pair can be seen as a coordinate, and the number of DA pairs corresponds to our definition of  $N_{fit.param.}$ . Second, we use the number of FRET pairs as predicted by the algorithm at the first stage as the true  $N_{fit.param.}$  and calculate  $\chi_n^2$ . The number of required measurements is always larger than the model's complexity ( $N_{fit.param.}$ ), reflecting that statistical significance can only be properly assigned to an overdetermined model ( $N_{dof} > 0$ , see eq. 3).

For a FRET-restrained structural model (e.g., generated by FRET-guided NMSim or FRET-restrained MD simulations, see below) the same procedure can be used. Presuming that the explored degrees of freedom in the FRET-restrained model cover all FRET restraints, one can conservatively assume  $N_{fit.param.} \geq N_{FRET\ restraints}$ . In this study, we use  $N_{fit.param.} = N_{FRET\ restraints}$  as a complexity estimate for all FRET-restrained models. Hence, FRET-guided structural sampling must be followed by an additional round of pair selection, so that more FRET pairs are measured for cross-validation.

Overall, these approximations lead to good  $N_{fit,param.}$  estimates, and further independent measurements do not change  $\chi_n^2$  significantly (**Fig. 1i**). Reliability of  $N_{fit,param.}$  estimates is also evident from the correlation between  $\chi_n^2$  and accuracy against the target structure (**Supplementary Fig. 6**).

### 2.5.6. Unbiased conformation sampling by NMSim.

Structural ensembles unbiased by experimental FRET data were generated by the NMSim software<sup>13</sup>. Ten independent and unbiased NMSim simulations generating 10,000 conformations each were performed, starting from the *prior* structure and using default parameters for sampling of large-scale motions. These trajectories are clustered and serve as *prior* candidates. NMSim is a normal mode-based geometric simulation approach for multiscale modelling of protein conformational changes that incorporates information about preferred directions of protein motions into a geometric simulation algorithm. NMSim follows a three-step protocol: In the first step, the protein structure is coarse-grained by the software FIRST<sup>35</sup> into rigid parts connected by flexible links<sup>36</sup>. In the second step, low-frequency normal modes are computed by rigid cluster normal mode analysis (RCNMA)<sup>37</sup>. In the third step, a linear combination of the first 10 normal modes was used to bias backbone motions along the low-frequency normal modes, while the side chain motions were biased towards favoured rotamer states. Detailed list of used simulation parameters is given in the **Supplementary Note 6**.

### 2.5.7. FRET-guided NMSim.

To improve the sampling of the conformational space in regions most relevant according to experiment, we extended the NMSim approach by a Markov Chain Monte Carlo step to prioritize conformations lying in such regions (**Supplementary Fig. 3**). In every NMSim iteration, the generated conformation is scored with respect to its agreement with experimental data using the  $\chi_n^2$  metric. Then, according to the Metropolis-Hastings approach,

$$p_{accept} = \exp\left(\frac{\chi_{n,previous}^2 - \chi_{n,current}^2}{kT}\right) \quad (2.11)$$

is computed, and the conformation is accepted and used in the next NMSim iteration if  $p$  is larger than a uniformly distributed random number sampled from the range  $[0, 1]$ ; else, the conformation is discarded, and the previous one is used in the next NMSim iteration. As a result, conformations are generated that are both stereochemically plausible and agree with experimental data. To



improve the sampling and enable the exploration of multiple local minima, an annealing procedure is applied in which  $kT$  is varied from 0 to 1 units of  $\chi_n^2$  and back to 0 (see **Supplementary Note 6**). A single FRET-guided NMSim simulation contains two such annealing cycles. If, models with good FRET agreement ( $\chi_n^2 \rightarrow 1$ ) cannot be obtained from FRET-guided simulations, alternative seed structures should be considered.

### 2.5.8. FRET-restrained MD.

To reconstruct structures to maximum detail, we developed a procedure to incorporate FRET-restraints in atomistic molecular dynamics (MD) simulations (**Supplementary Fig. 4**). To generate the restraints, first Accessible Volume (AV) calculations are performed for each labelling position. Second, pseudo atoms are positioned at the mean position of every accessible volume. These pseudo atoms do not interact with protein or solvent atoms. To keep the pseudo atoms in their initial positions relative to the corresponding part of the back-bone, harmonic restraints are used: Pseudo bonds are created between the pseudo atom and  $C_\alpha$  and  $C_\beta$  atoms of amino acids up to two residues towards the C- or N-termini of the protein from the amino acid, where the fluorophore linker is attached. Thus, each pseudo atom is anchored to ten nearby backbone atoms. The positions of pseudo atoms, the anchoring bonds, and FRET restraints are recalculated every 2 ns during the simulation to account for changes in local structure.

To mimic the measured inter-dye distances, pseudo atoms are restrained with respect to each other using harmonic-linear restraints. If the distance between pseudo atoms corresponds exactly to the measured donor-acceptor distance, no additional force is applied to pseudo atoms. To prevent unphysical unfolding of the protein, the FRET-restraint force is capped at an empirically determined value  $F_{\max} = 50$  pN, which is reached when the bond length ( $R_{DA}$ ) is more than one standard error ( $\Delta_{exp}$ ) away from the optimum ( $R_{exp}$ , **Supplementary Fig. 4D**). The error for each inter-dye distance is determined from experimental data. Force constants for each FRET-restraint are tuned such that for every pseudo atom the magnitude of the total FRET-restraints vector is  $\leq F_{\max}$ , resulting in force constants for FRET restraints in the range from 0.7 to 14 pN / Å, depending on their collinearity. Force constants of the pseudo bonds that attach pseudo atoms to their local backbone atoms are set 10 times higher than those for FRET restraints. FRET restraints are implemented using the AMBER interface for NMR restraints (“DISANG” file).

It is worthwhile to note that, unlike the immediate position of a fluorophore, its *mean* position with respect to the local backbone does not change as quickly. This way, we avoid complications of explicit dye simulations, such as potential inaccuracies of dye force field parametrizations and large convergence times ( $> 100 \text{ ns}^{38}$ ) of fluorophore diffusion. Furthermore, if FRET restraints were applied to explicitly modelled fluorophores directly, the flexible dye linker would become an entropic spring<sup>39</sup> and absorb virtually all of the strain. Finally, FRET observables determined in experiment have a statistical nature: they represent state-specific ensemble averages and underlying distributions, rather than immediate quantities. Therefore, application of ‘statistical’ FRET restraints to pseudo atoms that are constructed to mimic statistically averaged fluorophore positions is more straightforward and effective.

The AMER16 suite of molecular simulation codes<sup>40</sup> was used to perform MD simulations. All co-crystallized waters and ligands were removed from the crystal structures. Hydrogen atoms were removed and re-added by tleap<sup>41</sup> from the AMBER Tools suite. The TIP3P explicit water model<sup>42</sup> was used to solvate proteins in a periodic truncated octahedral box with at least 12 Å of solvent in every direction from the protein surface. Sodium and chloride counter ions were added to neutralize the systems. MD simulations were performed with the ff14SB force field<sup>43</sup> using the GPU version of pmemd<sup>44</sup>. The SHAKE algorithm<sup>45</sup> was used to constrain bond lengths of hydrogen atoms. Long-range electrostatic interactions were evaluated using the particle mesh Ewald method<sup>46</sup>. Hydrogen mass repartitioning<sup>47</sup> and a time step of 4 fs were used. A five-stage equilibration procedure was pursued: First, 100 steps of steepest descent and 400 steps of conjugate gradient minimization were performed, while solute atoms were restrained to their initial positions by harmonic restraints with force constants of  $5 \text{ kcal mol}^{-1} \text{ \AA}^{-2}$ . Second, the temperature of the system was raised from 100 K to 300 K in 50 ps of NVT-MD simulations. Third, 150 ps of NPT-MD simulations were performed to adjust the system density. Finally, the force constants of harmonic restraints were gradually reduced to zero during 2 ns of NVT-MD simulations. Production NVT-MD simulations were carried out at 300 K, using the Berendsen thermostat<sup>48</sup> and a coupling constant of 0.5 ps. Three independent replicas of MD simulations (1  $\mu\text{s}$  per simulation) were performed for each system using different random number generator seeds to assign initial velocities.

### 2.5.9. T4 Lysozyme site specific mutation, purification and labelling.

T4L site directed mutagenesis was performed on the cysteine-less pseudo-wild-type encoded backbone using the pET11a (Life Technologies, Corp) vector as previously described<sup>49-51</sup>. For protein expression and purification, the plasmid containing T4L desired mutations (an unnatural amino acid –p-acetyl-L-phenylalanine or pAcPhe, in the N-terminal subdomain (NTsD) and the replacement to a Cys in the C-terminal subdomain (CTsD)) was co-transformed with pEVOL<sup>50</sup> for the introduction of (pAcPhe) into BL21(DE3) *E. coli* strains (Life Technologies Corp.). Transformed *E. coli* were plated onto LB- agar plates supplemented with ampicillin and chloramphenicol for single colony selection. For each variant, a single colony was inoculated into 100 mL of LB with antibiotics and grown overnight at 37 °C in a shaking incubator, followed by inoculation of a 1 L LB medium supplemented with the respective antibiotics and 0.4 g/L of pAcPhe (SynChem) with 50 mL of the overnight culture. The culture was grown at 37 °C until an OD<sub>600</sub> of 0.5 was achieved, for further induction. The protein production was induced for 6 hours by addition of 1 mM IPTG and 4 g/L of arabinose. Harvested cells were lysed in 50 mM HEPES, 1 mM EDTA, and 5 mM DTT pH 7.5 and purified using a monoS 5/5 column (GE Healthcare) with an eluting gradient from 0 to 1 M NaCl according to standard procedures. High-molecular weight impurities were removed by passing the eluted protein through a 30 kDa Amicon concentrator (Millipore), followed by subsequent concentration and buffer exchange to 50 mM PB, 150 mM NaCl pH 7.5 of the protein flow through with a 10 kDa Amicon concentrator.

Site specific labelling of T4L was accomplished using orthogonal chemistry following manufacturer suggestion. For labelling the Keto functional group of pAcPhe at the NTsD, the Alexa 488 with hydroxylamine linker chemistry was used (Life Technologies Corp.). Cysteine sites were labelled via a thiol reaction with maleimide linkers of Alexa-647. FRET or DA variants were labelled sequentially - first thiol and second the keto handle<sup>51</sup>. A proper Donor Only reference sample was only kept before proceeding with the acceptor labelling. The selected FRET pair has a Förster distance  $R_0$  of 52 Å.

### 2.5.10. FRET Experiments and Analysis.

To resolve the conformational heterogeneity of T4L, Donor only and FRET labelled T4L variants were studied by time-resolved fluorescence spectroscopy using Time Correlated Single Photon Counting (TCSPC) and single-molecules studies with confocal multiparameter fluorescence detection.

Donor only and FRET labelled T4L variants were measured by TCSPC using either an IBH-5000U (IBH, Scotland) or a Fluotime 200 (Picoquant, Germany) system. The excitation source of the IBH machine were a 470 nm diode laser (LDH-P-C470, Picoquant, Germany) operating at 10 MHz for donor excitation and a 635 nm (LDH-P-C635, Picoquant, Germany) for acceptor excitation. The excitation and emission slits were set to 2 nm and 16 nm, respectively. The excitation source of the Fluotime200 system was a white light laser (SuperK extreme, NKT Photonics, Denmark) operating at 20 MHz for both donor (485 nm) and acceptor (635 nm) excitation with excitation and emission slits set to 2 nm and 5 nm, respectively. Additionally, in both systems, cut-off filters were used to reduce the amount of scattered light (>500 nm for donor and >640 nm for acceptor emission).

For green detection, the monochromator was set to 520 nm and for red detection to 665 nm. All measurements were conducted under magic angle conditions (excitation polarizer  $0^\circ$ , emission polarizer  $54.7^\circ$ , VM), except for anisotropy where the position of the emission polarizer was alternately set to  $0^\circ$  (VV) or  $90^\circ$  (VH).

In the IBH system, the TAC-histograms were recorded with a bin width of 14.1 ps within a time window of 57.8 ns, while the Fluotime200 was set to a bin width of 8 ps within a time window of 51.3 ns. The average number of collected photons per sample were  $30 \times 10^6$  photons.

A global joint analysis of the donor only and FRET labelled samples was implemented in order to assure proper donor reference samples, determination of the mean inter-dye distances,  $\langle R_{DA} \rangle$ , and assignment of states by sharing the population parameters on the FRET labelled samples. The analysis and justification of the methods are reported in Sanabria *et al*<sup>21</sup>. In short, the donor only labelled samples were fit with a multiexponential decay model (eq. 25, Peulen *et al*)<sup>52</sup>. All FRET induced donor VM decays were fit using the corresponding donor only decay parameters with a sum of Gaussian distributed states to derive  $\langle R_{DA} \rangle$ . By using a global analysis, we assure conformational states are assigned via the linked population fractions. A  $2\sigma$  statistical uncertainty and an error propagation rule considering  $\kappa^2$  error was used to consider the overall uncertainty (+/- err). The derived distances for two states are presented in in **Supplementary Table 1**. The error estimation considers: (i) upper estimates for the uncertainty of the orientation factor<sup>53</sup>,  $\kappa^2$ , (ii) statistical uncertainties of the analysis<sup>52</sup>, (iii) estimates for systematic errors due to imprecise

reference samples<sup>52</sup>, and (iv) uncertainty estimates for modelling the spatial distribution of the dyes based on the dye's residual anisotropies<sup>9</sup> (see **Supplementary Table 2**).

## 2.6. Acknowledgments

This work was funded in part by the German Research Foundation (DFG) within the Collaborative Research Center SFB 1208 “Identity and Dynamics of Membrane Systems – From Molecules to Cellular Functions” (TP A03 to HG and TP A08 to CS) and by the European Research Council through the Advanced Grant 2014 (number 671208) to CS. HS acknowledges support of the Alexander von Humboldt, NSF-BIO 1749778. We are grateful for computational support and infrastructure provided by the “Zentrum für Informations- und Medientechnologie” (ZIM) at the Heinrich Heine University Düsseldorf and the computing time provided by the John von Neumann Institute for Computing (NIC) to HG on the supercomputer JURECA at Jülich Supercomputing Centre (JSC) (user ID: HKF7). Authors are grateful to Christian Hanke for the help with the preparation of data files for submission to PDB-Dev.

## 2.7. References

1. Kim, D. E., Chivian, D. & Baker, D. Protein structure prediction and analysis using the Robetta server. *Nucleic Acids Res.* **32**, W526-W531 (2004).
2. Kelley, L. A. & Sternberg, M. J. E. Protein structure prediction on the Web: a case study using the Phyre server. *Nature Protocols* **4**, 363-371 (2009).
3. Webb, B. & Sali, A. Protein structure modelling with MODELLER. *Methods Mol. Biol.* **1137**, 1-15 (2014).
4. Zhang, Y. I-TASSER server for protein 3D structure prediction. *BMC Bioinformatics* **9** (2008).
5. Arnold, K., Bordoli, L., Kopp, J. & Schwede, T. The SWISS-MODEL workspace: a web-based environment for protein structure homology modelling. *Bioinformatics* **22**, 195-201 (2006).
6. Henzler-Wildman, K. & Kern, D. Dynamic personalities of proteins. *Nature* **450**, 964-972 (2007).
7. Neudecker, P., Robustelli, P., Cavalli, A., Walsh, P., Lundstrom, P., Zarrine-Afsar, A., Sharpe, S., Vendruscolo, M. & Kay, L. E. Structure of an intermediate state in protein folding and aggregation. *Science* **336**, 362-366 (2012).
8. Dimura, M., Peulen, T. O., Hanke, C. A., Prakash, A., Gohlke, H. & Seidel, C. A. M. Quantitative FRET Studies and Integrative Modelling Unravel the Structure and Dynamics of Biomolecular Systems. *Curr. Opin. Struct. Biol.* **40**, 163-185 (2016).
9. Hellenkamp, B., Wortmann, P., Kandzia, F., Zacharias, M. & Hugel, T. Multidomain Structure and Correlated Dynamics Determined by Self-Consistent FRET Networks. *Nat. Meth.* **14**, 174-180 (2017).
10. Margittai, M., Widengren, J., Schweinberger, E., Schröder, G. F., Felekyan, S., Haustein, E., König, M., Fasshauer, D., Grubmüller, H., Jahn, R. & Seidel, C. A. M. Single-molecule fluorescence resonance energy transfer reveals a dynamic equilibrium between closed and open conformations of syntaxin 1. *Proc. Natl. Acad. Sci. USA* **100**, 15516-15521 (2003).
11. Muschielok, A., Andrecka, J., Jawhari, A., Bruckner, F., Cramer, P. & Michaelis, J. A Nano-Positioning System for Macromolecular Structural Analysis. *Nat. Meth.* **5**, 965-971 (2008).
12. Kalinin, S., Peulen, T., Sindbert, S., Rothwell, P. J., Berger, S., Restle, T., Goody, R. S., Gohlke, H. & Seidel, C. A. M. A toolkit and benchmark study for FRET-restrained high-precision structural modelling. *Nat. Meth.* **9**, 1218-1227 (2012).
13. Ahmed, A., Rippmann, F., Barnickel, G. & Gohlke, H. A normal mode-based geometric simulation approach for exploring biologically relevant conformational transitions in proteins. *J. Chem. Inf. Model.* **51**, 1604-1622 (2011).
14. Kinch, L. N., Li, W. L., Monastyrskyy, B., Kryshtafovych, A. & Grishin, N. V. Evaluation of free modelling targets in CASP11 and ROLL. *Proteins-Structure Function and Bioinformatics* **84**, 51-66 (2016).
15. Brunger, A. T. Free R-Value - a Novel Statistical Quantity for Assessing the Accuracy of Crystal-Structures. *Nature* **355**, 472-475 (1992).

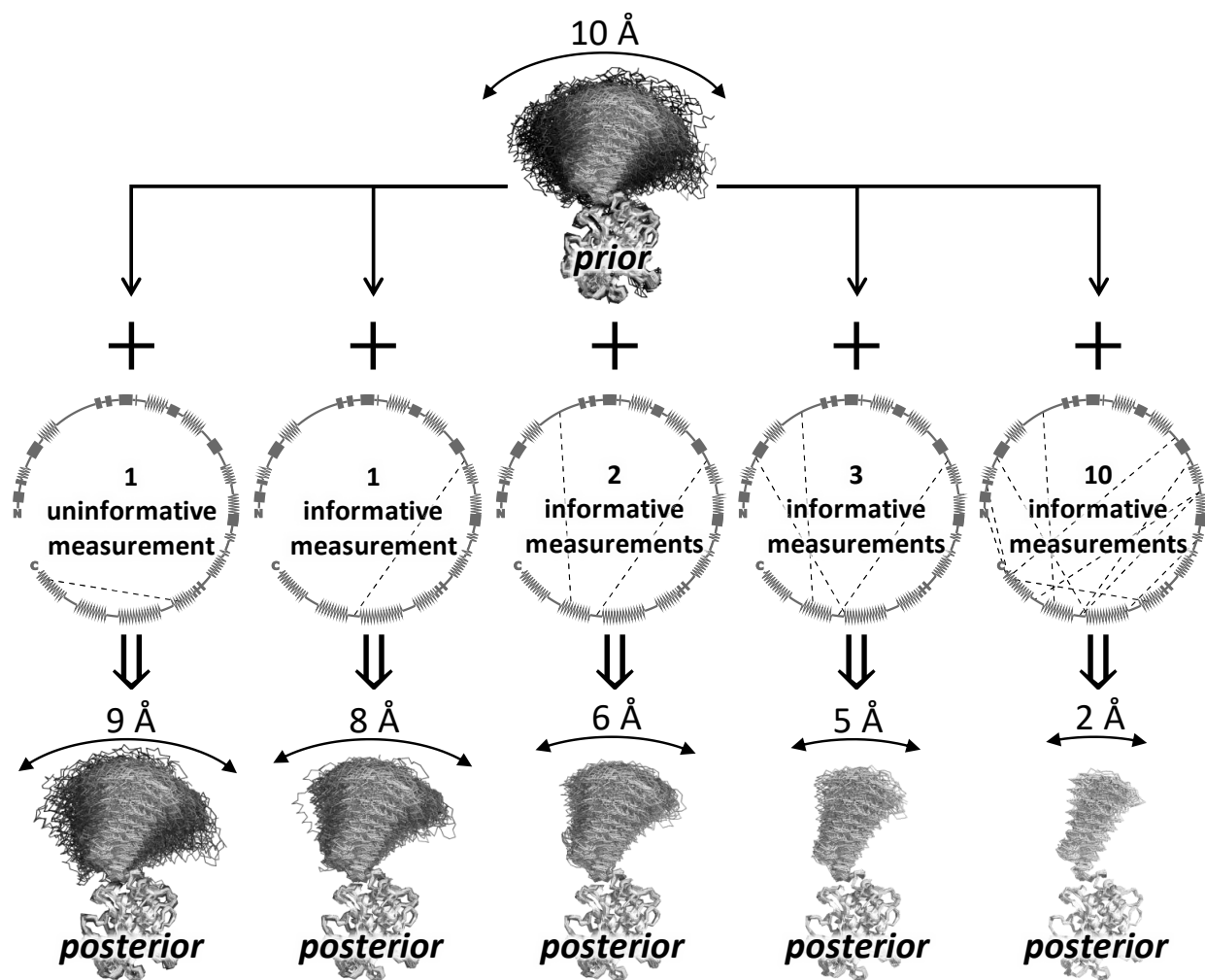
16. Okazaki, K. I. & Takada, S. Dynamic energy landscape view of coupled binding and protein conformational change: Induced-fit versus population-shift mechanisms. *Proc. Natl. Acad. Sci. USA* **105**, 11182-11187 (2008).
17. Hayward, S. Identification of specific interactions that drive ligand-induced closure in five enzymes with classic domain movements. *J. Mol. Biol.* **339**, 1001-1021 (2004).
18. Cavasotto, C. N., Kovacs, J. A. & Abagyan, R. A. Representing receptor flexibility in ligand docking through relevant normal modes. *J. Am. Chem. Soc.* **127**, 9632-9640 (2005).
19. Ahmed, A. & Gohlke, H. Multiscale modelling of macromolecular conformational changes combining concepts from rigidity and elastic network theory. *Proteins-Structure Function and Bioinformatics* **63**, 1038-1051 (2006).
20. Tama, F. & Sanejouand, Y. H. Conformational change of proteins arising from normal mode calculations. *Protein Eng.* **14**, 1-6 (2001).
21. Sanabria, H., Rodnin, D., Hemmen, K., Peulen, T., Felekyan, S., Fleissner, M. R., Dimura, M., Koberling, F., Kühnemuth, R., Hubbell, W. L., Gohlke, H. & Seidel, C. A. Resolving dynamics and function of transient states in single enzyme molecules. *Nat. Commun.* (2018).
22. Berjanskii, M. & Wishart, D. S. NMR: prediction of protein flexibility. *Nature Protocols* **1**, 683-688 (2006).
23. Muller, C. W. & Schulz, G. E. Structure of the complex between adenylate kinase from *Escherichia coli* and the inhibitor Ap5A refined at 1.9 Å resolution. A model for a catalytic transition state. *J. Mol. Biol.* **224**, 159-177 (1992).
24. McPhalen, C. A., Vincent, M. G. & Jansonius, J. N. X-ray structure refinement and comparison of three forms of mitochondrial aspartate aminotransferase. *J. Mol. Biol.* **225**, 495-517 (1992).
25. Kuboniwa, H., Tjandra, N., Grzesiek, S., Ren, H., Klee, C. B. & Bax, A. Solution structure of calcium-free calmodulin. *Nat. Struct. Biol.* **2**, 768-776 (1995).
26. Osawa, M., Tokumitsu, H., Swindells, M. B., Kurihara, H., Orita, M., Shibamura, T., Furuya, T. & Ikura, M. A novel target recognition revealed by calmodulin in complex with Ca<sup>2+</sup>-calmodulin-dependent kinase kinase. *Nat. Struct. Biol.* **6**, 819-824 (1999).
27. Oh, B. H., Pandit, J., Kang, C. H., Nikaido, K., Gokcen, S., Ames, G. F. & Kim, S. H. Three-dimensional structures of the periplasmic lysine/arginine/ornithine-binding protein with and without a ligand. *J. Biol. Chem.* **268**, 11348-11355 (1993).
28. Byrnes, L. J. & Sondermann, H. Structural basis for the nucleotide-dependent dimerization of the large G protein atlastin-1/SPG3A. *Proc. Natl. Acad. Sci. USA* **108**, 2216-2221 (2011).
29. Muller, C. W., Schlauderer, G. J., Reinstein, J. & Schulz, G. E. Adenylate kinase motions during catalysis: an energetic counterweight balancing substrate binding. *Structure* **4**, 147-156 (1996).
30. Byrnes, L. J., Singh, A., Szeto, K., Benvin, N. M., O'Donnell, J. P., Zipfel, W. R. & Sondermann, H. Structural basis for conformational switching and GTP loading of the large G protein atlastin. *EMBO J.* **32**, 369-384 (2013).
31. Prahlad, J. & Wilson, M. A. *Crystal structure of E. coli YaaA, a member of the DUF328/UPF0246 family* (2015).

32. McPhalen, C. A., Vincent, M. G., Picot, D., Jansonius, J. N., Lesk, A. M. & Chothia, C. Domain closure in mitochondrial aspartate aminotransferase. *J. Mol. Biol.* **227**, 197-213 (1992).
33. Mullner, D. fastcluster: Fast hierarchical, agglomerative clustering routines for R and Python. *Journal of Statistical Software* **53**, 1-18 (2013).
34. Peng, H., Long, F. & Ding, C. Feature selection based on mutual information: criteria of max-dependency, max-relevance, and min-redundancy. *IEEE Trans Pattern Anal Mach Intell* **27**, 1226-1238 (2005).
35. Jacobs, D. J., Rader, A. J., Kuhn, L. A. & Thorpe, M. F. Protein flexibility predictions using graph theory. *Proteins* **44**, 150-165 (2001).
36. Hermans, S. M. A., Pflieger, C., Nutschel, C., Hanke, C. A. & Gohlke, H. Rigidity theory for biomolecules: concepts, software, and applications. *Wiley Interdisciplinary Reviews-Computational Molecular Science* **7** (2017).
37. Ahmed, A. & Gohlke, H. Multiscale modelling of macromolecular conformational changes combining concepts from rigidity and elastic network theory. *Proteins* **63**, 1038-1051 (2006).
38. Peulen, T. O., Opanasyuk, O. & Seidel, C. A. M. Combining Graphical and Analytical Methods with Molecular Simulations To Analyze Time-Resolved FRET Measurements of Labelled Macromolecules Accurately. *J. Phys. Chem. B* **121**, 8211-8241 (2017).
39. Gao, J. & Weiner, J. H. Range of Validity of the Entropic Spring Concept in Polymer Melt Relaxation. *Macromolecules* **25**, 3462-3467 (1992).
40. AMBER 2017 (University of California, San Francisco, 2017).
41. Case, D. A., Cheatham, T. E., Darden, T., Gohlke, H., Luo, R., Merz, K. M., Onufriev, A., Simmerling, C., Wang, B. & Woods, R. J. The Amber biomolecular simulation programs. *J. Comput. Chem.* **26**, 1668-1688 (2005).
42. Jorgensen, W. L., Chandrasekhar, J., Madura, J. D., Impey, R. W. & Klein, M. L. Comparison of Simple Potential Functions for Simulating Liquid Water. *J. Chem. Phys.* **79**, 926-935 (1983).
43. Maier, J. A., Martinez, C., Kasavajhala, K., Wickstrom, L., Hauser, K. E. & Simmerling, C. ff14SB: Improving the Accuracy of Protein Side Chain and Backbone Parameters from ff99SB. *J. Chem. Theory Comput.* **11**, 3696-3713 (2015).
44. Salomon-Ferrer, R., Gotz, A. W., Poole, D., Le Grand, S. & Walker, R. C. Routine Microsecond Molecular Dynamics Simulations with AMBER on GPUs. 2. Explicit Solvent Particle Mesh Ewald. *J. Chem. Theory Comput.* **9**, 3878-3888 (2013).
45. Ryckaert, J. P., Ciccotti, G. & Berendsen, H. J. C. Numerical-Integration of Cartesian Equations of Motion of a System with Constraints - Molecular-Dynamics of N-Alkanes. *J. Comput. Phys.* **23**, 327-341 (1977).
46. Darden, T., York, D. & Pedersen, L. Particle Mesh Ewald - an N.Log(N) Method for Ewald Sums in Large Systems. *J. Chem. Phys.* **98**, 10089-10092 (1993).
47. Hopkins, C. W., Le Grand, S., Walker, R. C. & Roitberg, A. E. Long-Time-Step Molecular Dynamics through Hydrogen Mass Repartitioning. *J. Chem. Theory Comput.* **11**, 1864-1874 (2015).



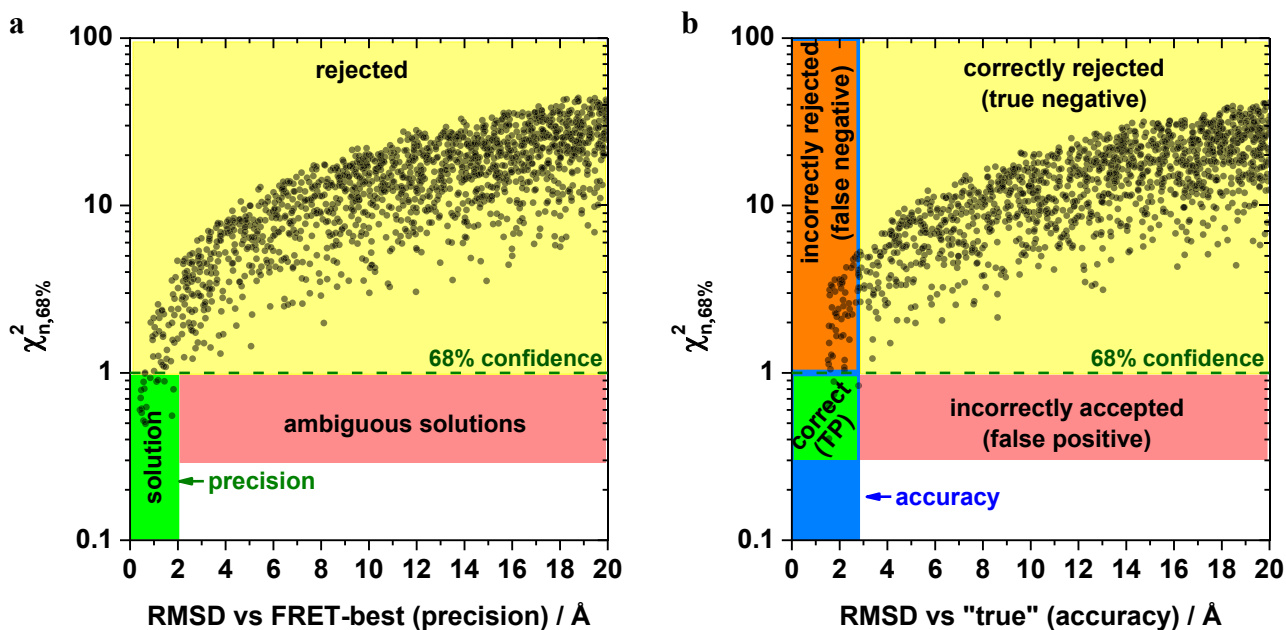
48. Berendsen, H. J. C., Postma, J. P. M., Vangunsteren, W. F., Dinola, A. & Haak, J. R. Molecular-Dynamics with Coupling to an External Bath. *J. Chem. Phys.* **81**, 3684-3690 (1984).
49. Fleissner, M. R., Brustad, E. M., Kalai, T., Altenbach, C., Cascio, D., Peters, F. B., Hideg, K., Peuker, S., Schultz, P. G. & Hubbell, W. L. Site-directed spin labelling of a genetically encoded unnatural amino acid. *Proc. Natl. Acad. Sci. USA* **106**, 21637-21642 (2009).
50. Lemke, E. A. & Schultz, C. Principles for designing fluorescent sensors and reporters. *Nat. Chem. Biol.* **7**, 480-483 (2011).
51. Brustad, E. M., Lemke, E. A., Schultz, P. G. & Deniz, A. A. A General and Efficient Method for the Site-Specific Dual-Labeling of Proteins for Single Molecule Fluorescence Resonance Energy Transfer. *J. Am. Chem. Soc.* **130**, 17664-+ (2008).
52. Peulen, T. O., Opanasyuk, O. & Seidel, C. A. M. Combining Graphical and Analytical Methods with Molecular Simulations To Analyze Time-Resolved FRET Measurements of Labelled Macromolecules Accurately. *J. Phys. Chem. B* **121**, 8211-8241 (2017).
53. Sindbert, S., Kalinin, S., Hien, N., Kienzler, A., Clima, L., Bannwarth, W., Appel, B., Muller, S. & Seidel, C. A. M. Accurate Distance Determination of Nucleic Acids via Förster Resonance Energy Transfer: Implications of Dye Linker Length and Rigidity. *J. Am. Chem. Soc.* **133**, 2463-2480 (2011).

## 2.8. Supplementary information



**Supplementary Figure 1** | Optimal FRET pair selection.

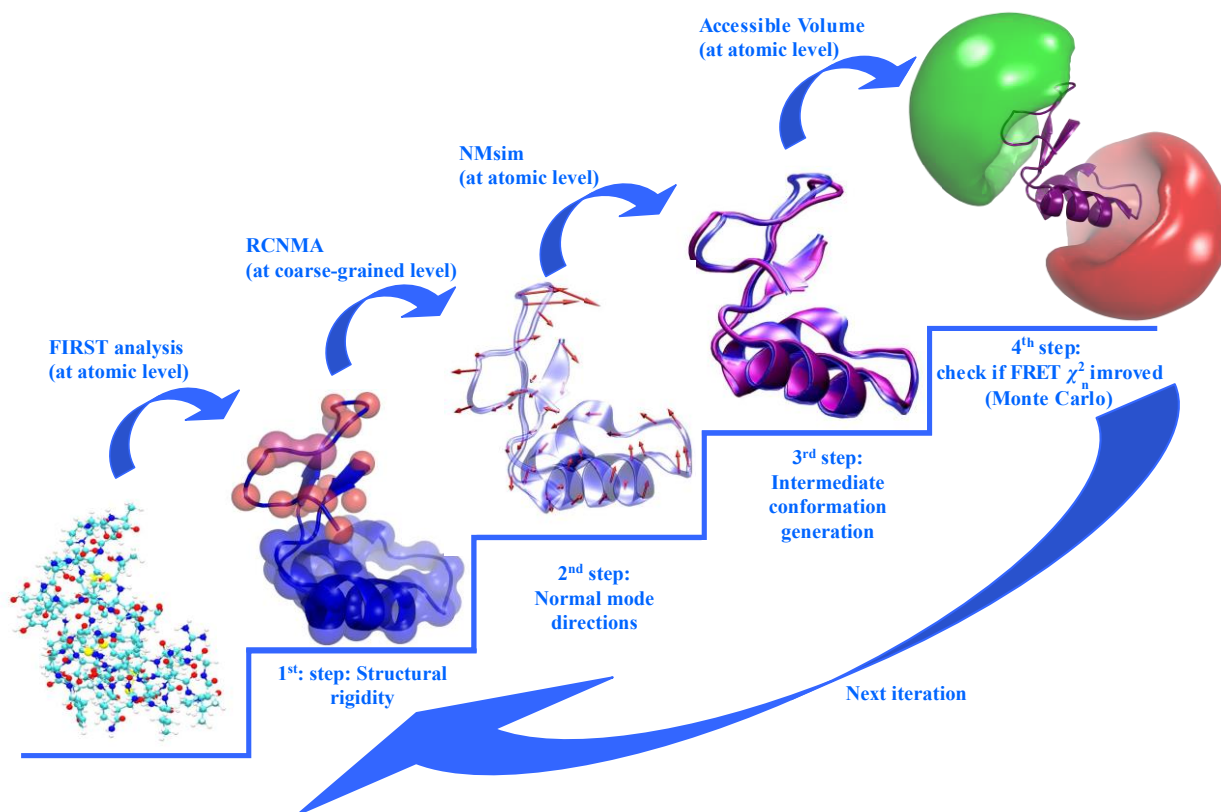
At the top an exemplary prior conformational ensemble is depicted. The arrow over the ensemble reflects its structural diversity, the  $\langle\langle\text{RMSD}\rangle\rangle$  value is shown above. Circles in the middle row represent the secondary structure of the source protein conformation. Inside the circles, the set of FRET pairs is indicated by dashed lines. Given a pair set, the prior ensemble is narrowed (posterior, bottom row). More informative pairs lead to narrower posteriors. A larger pair set generally results in smaller  $\langle\langle\text{RMSD}\rangle\rangle$  as well. In the greedy forward feature selection algorithm, first, all possible donor-acceptor (DA) pairs are tested one by one, and the pair that yields the smallest posterior  $\langle\langle\text{RMSD}\rangle\rangle$  is selected. In the next iterations, remaining DA pairs are tested one by one, in order to determine, which additional pair in combination with pairs selected earlier will yield the smallest  $\langle\langle\text{RMSD}\rangle\rangle$ . Thus, at each iteration, one optimal pair is added to the set, until the desired  $\langle\langle\text{RMSD}\rangle\rangle$  is reached or the number of required measurements is too high.



**Supplementary Figure 2** | Selection of conformers by FRET.

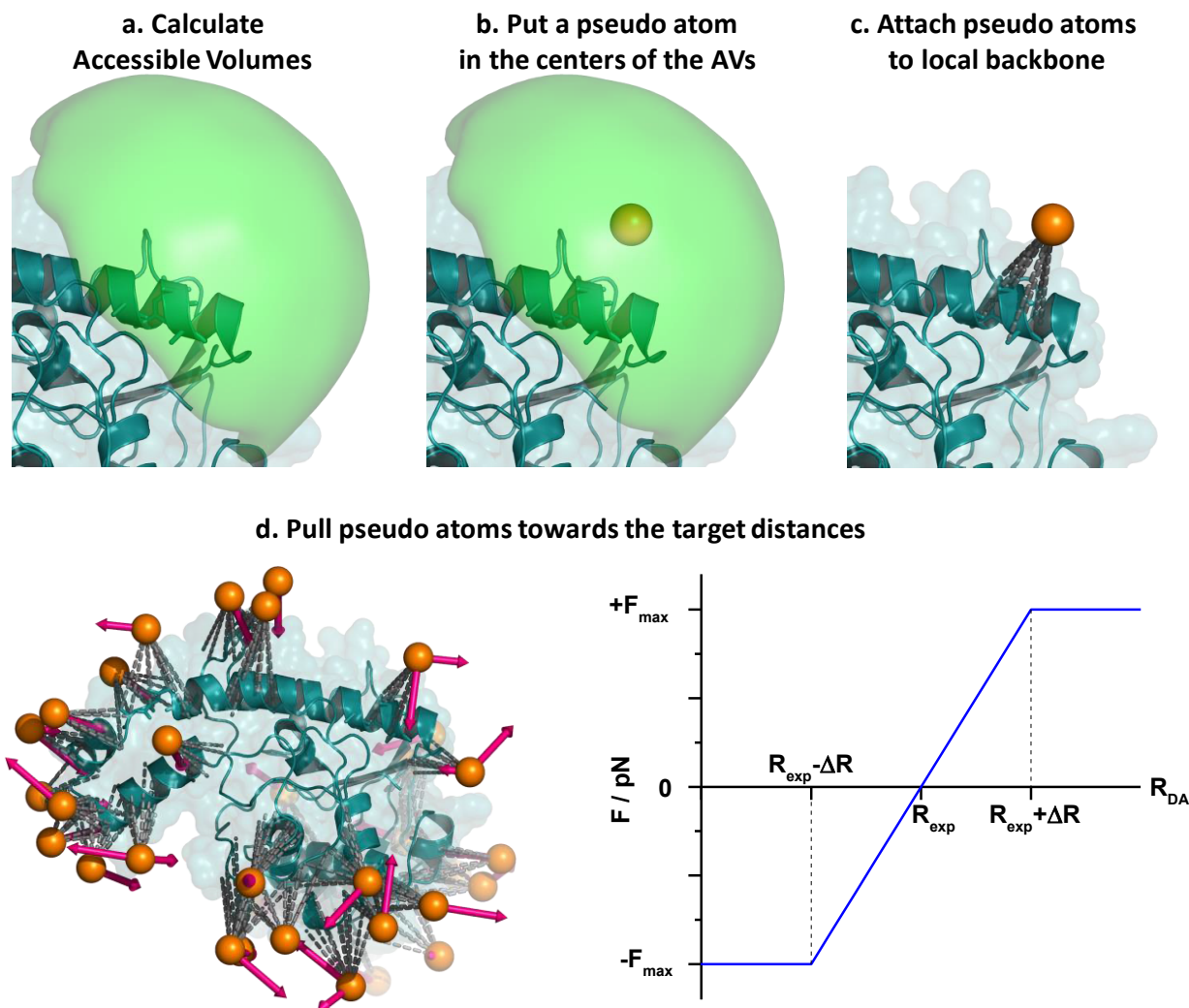
On the y-axis, the normalized chi-squared reduced value,  $\chi_{n,68\%}^2$ , is shown. On the x-axis, the RMSD against the reference conformer is displayed. The horizontal line at  $\chi_n^2 = 1$  indicates the confidence level of 68%.

(a) The structure with the lowest  $\chi_n^2$  is used as the reference for RMSD calculations. The RMSDs of the structures below the  $\chi_n^2 = 1$  threshold define (green box) the precision of the model. (b) The “true” (crystal structure) conformation is used as the reference for RMSD calculations. Here, RMSDs below the threshold define the accuracy of the model. The lower left corner of the plot shows correctly predicted structures (true positives, green box), conformers incorrectly selected by FRET (false positives, red box) would be on the lower right side, correctly discarded models (true negatives, yellow box) on the upper right side, and incorrectly discarded (false negatives, orange box) on the upper left side.



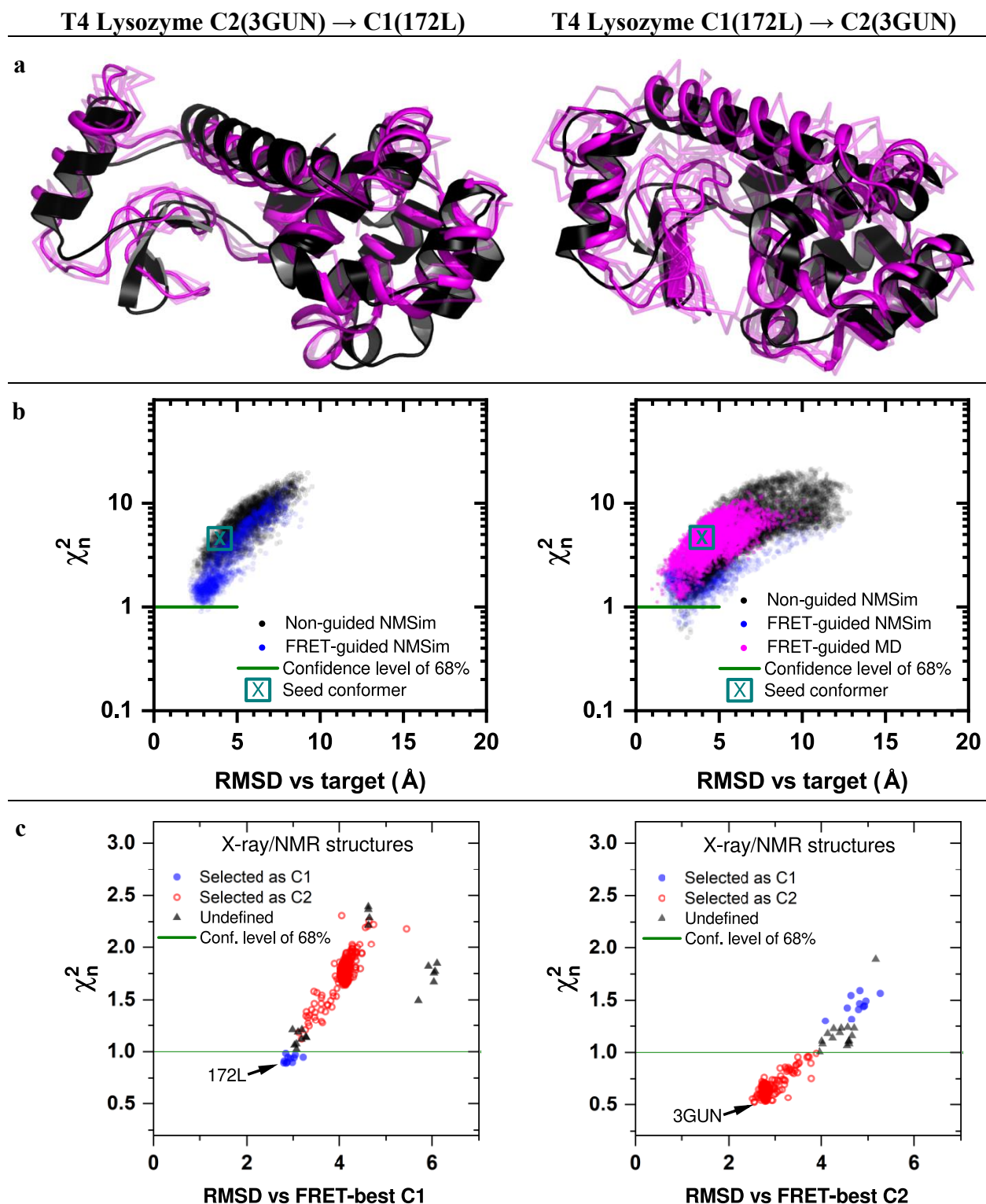
**Supplementary Figure 3** | FRET-guided NMSim simulations workflow.

NMSim is a normal mode-based geometric simulation approach for multiscale modelling of protein conformational changes using three-step iterations: In the first step, the protein structure is coarse-grained by the software FIRST into rigid parts (coloured blobs) connected by flexible links (single spheres). In the second step, low-frequency normal modes are computed by rigid cluster normal mode analysis (RCNMA). In the third step, a linear combination of the first normal modes is used to bias backbone motions along the low-frequency normal modes, while the side chain motions were biased towards favoured rotamer states. The algorithm is here extended by a fourth step – a Markov Chain Monte Carlo step to prioritize conformations lying in most relevant regions according to the FRET  $\chi_n^2$  value. Depiction of steps 1 to 3 was adapted from<sup>1</sup>.



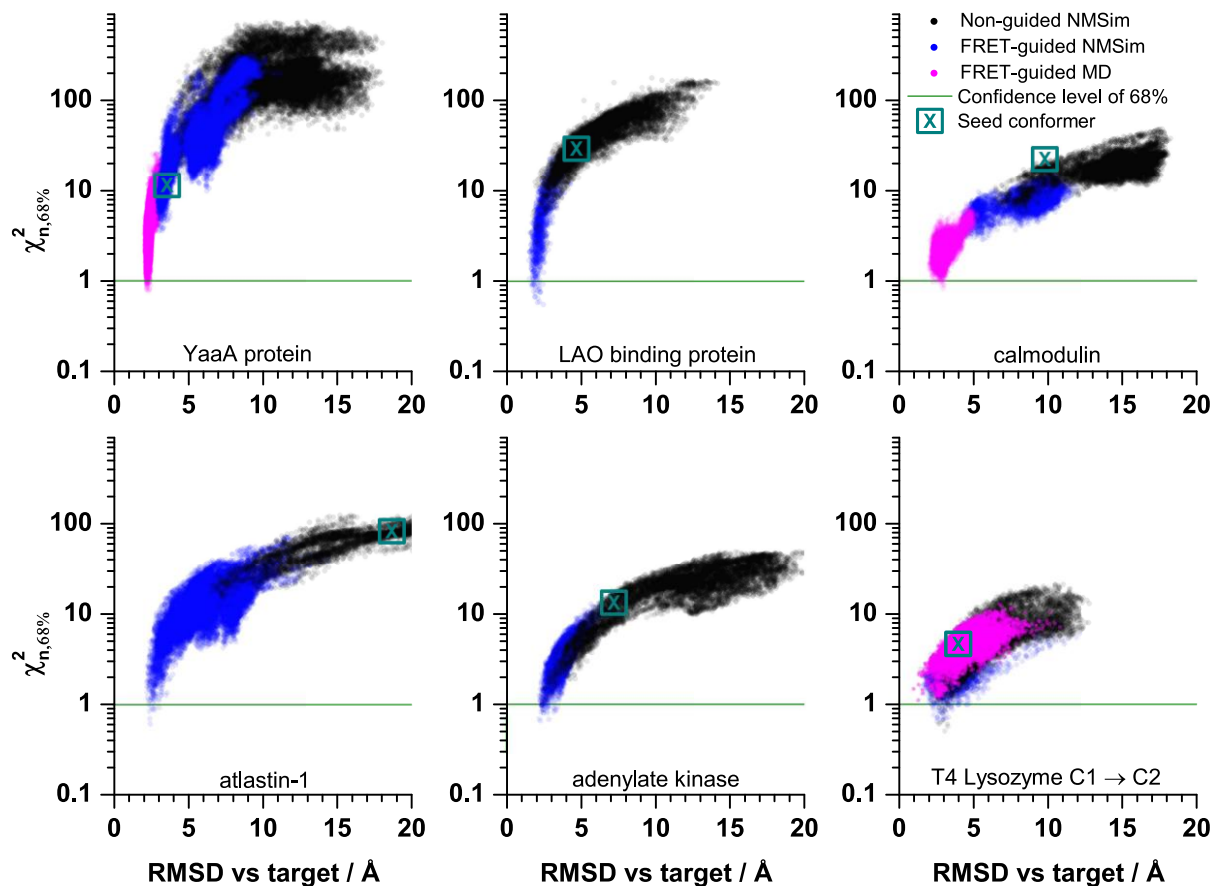
**Supplementary Figure 4** | FRET-guided MD simulations workflow.

We introduce FRET restraints into MD simulations in a four-step approach. **(a)** Accessible Volume (AV) calculations are performed for each labelling position. **(b)** Pseudo atoms are positioned at the mean position of every accessible volume. **(c)** Pseudo bonds (grey dashed lines) are created between the pseudo atom and nearby  $C_\alpha$  and  $C_\beta$  atoms to keep pseudo atoms in their initial positions relative to the corresponding part of the protein backbone. **(d)** Restraints between pseudo atom pairs are applied to mimic measured inter-dye distances. To prevent unphysical unfolding of the protein, the FRET-restraint force is capped at an empirically determined value  $F_{max} = 50$  pN, which is reached when the distance between pseudo atoms  $R_{DA}$  is more than one standard error ( $\delta_{exp}$ ) away from the optimum ( $R_{exp}$ ).



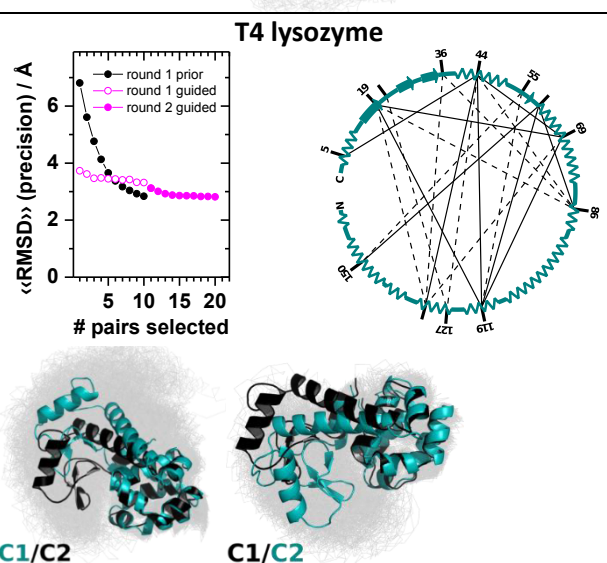
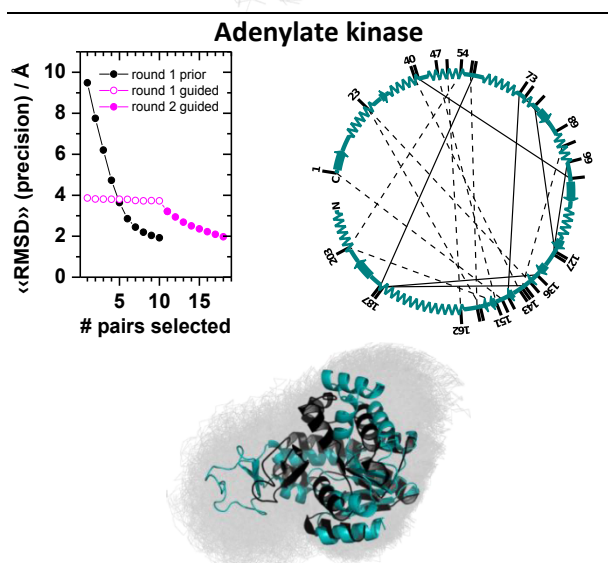
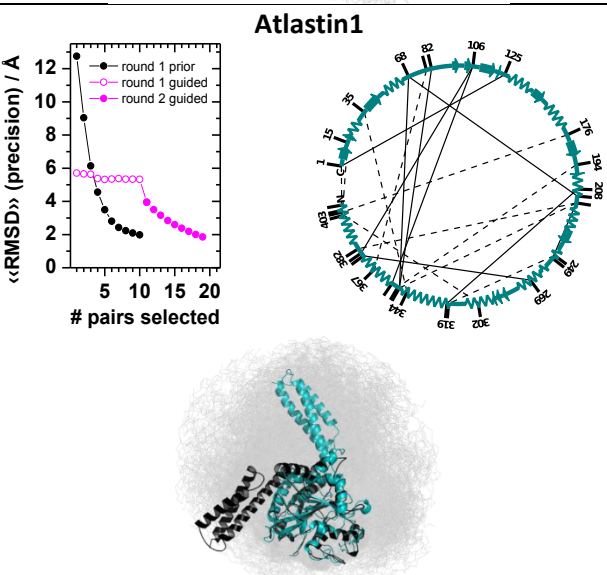
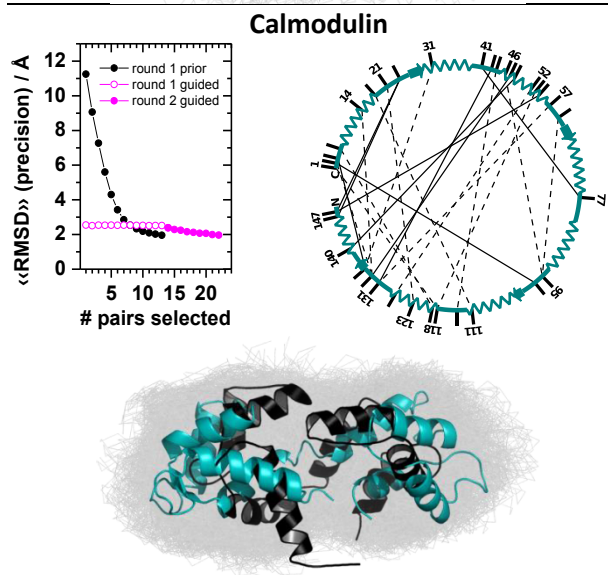
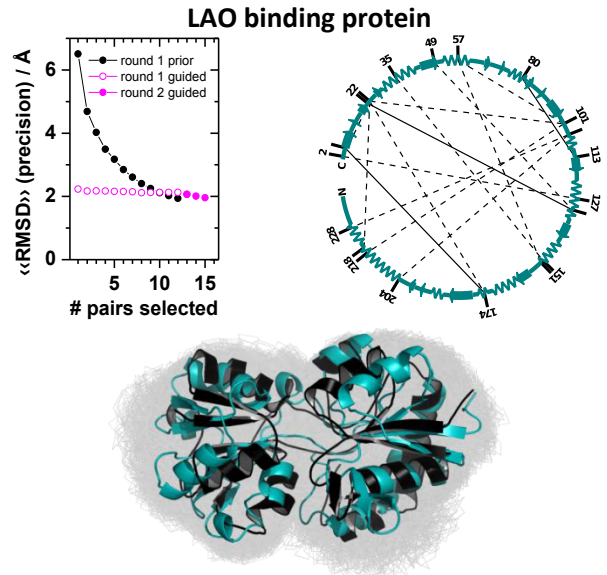
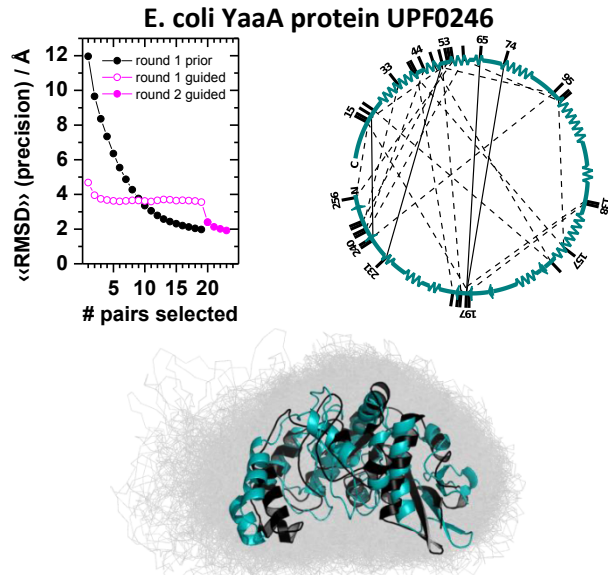
**Supplementary Figure 5** | FRET assisted modelling for two states of T4 Lysozyme. To the left the C1 state obtained by FRET assisted modelling using a C2 crystal structure as a prior (C2→C1). To the right reverse situation (C1→C2) is shown: The C1 crystal structure serves as prior and the C2 conformation is determined by FRET assisted modelling. (a) FRET-selected

ensemble with confidence level of 68%. **(b)** FRET  $\chi_n^2$  values and RMSDs against the crystal structure (target). Each point represents a conformation. Black points stand for unrestrained NMSim sampling starting from homology models. Blue points represent FRET-guided NMSim simulations. Magenta points represent FRET-restrained MD simulations. **(c)** FRET  $\chi_n^2$  values and RMSDs against the best FRET-assisted structure (lowest  $\chi_n^2$ ) for 571 X-ray and NMR structures from the PDB.

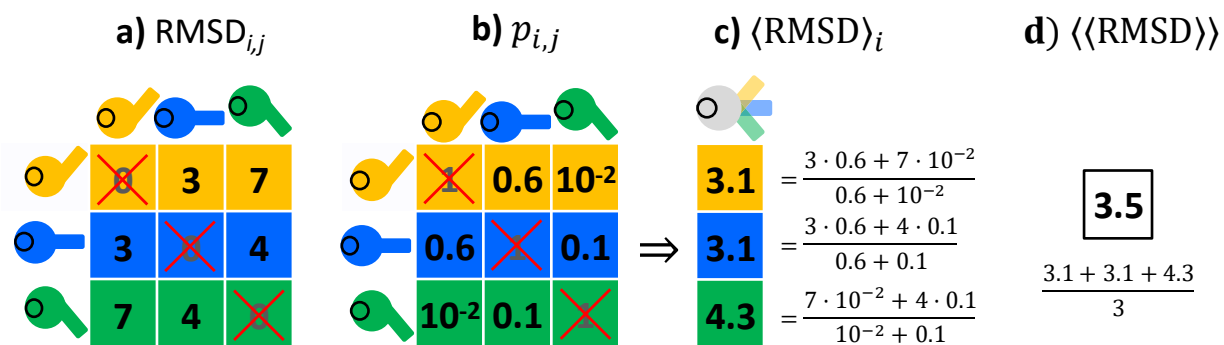


**Supplementary Figure 6** | Correlation between the accuracy (RMSD of Ca atoms) and agreement with FRET ( $\chi^2_n$ ). Structures obtained from unrestrained NMSim simulations are shown as black dots, conformers from FRET-guided NMSim simulations are blue, and magenta represents the results of FRET-guided MD simulations. The confidence level of 68% is indicated by the green horizontal line. Seed conformers for each protein are indicated by cyan crosses.



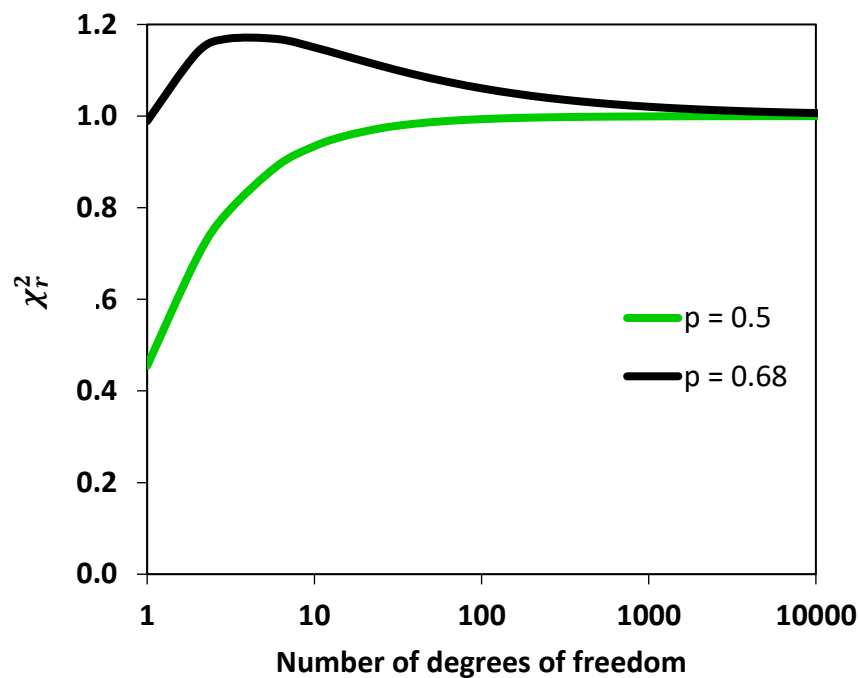


**Supplementary Figure 7** | *Expected precision and FRET pair networks of benchmarked proteins. Scatter plots in the upper left corner of each block show expected precision depending on the number of FRET pairs measured: first round of selection based on prior ensemble is indicated by black circles, second round of selection, based on guided structural ensemble is indicated by full magenta circles, open magenta circles indicate the projection of the pairs selected in the first round onto the structural ensemble obtained during guiding. FRET pair networks and secondary structures of corresponding seed conformers are shown to the upper right. Dashed lines indicate pairs selected in the first round, solid lines stand for the second round of selection. At the bottom prior conformational ensemble is shown in grey. Seed structure is shown in cyan and target conformer is in black.*

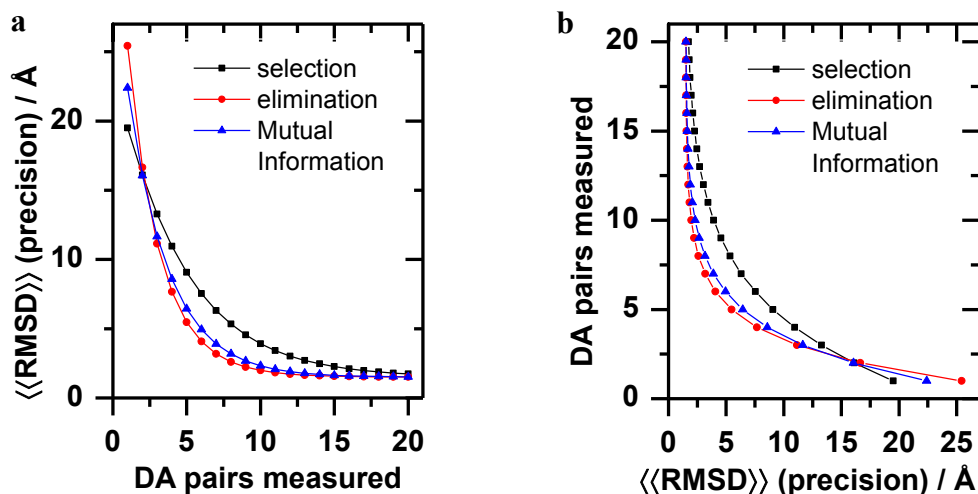


**Supplementary Figure 8** | Calculation of expected precision.

For a given conformational ensemble of  $N$  conformers (here  $N = 3$  for clarity: yellow, blue, green), the measure for expected precision  $\langle \langle \text{RMSD} \rangle \rangle$  is calculated: **(a)** The  $N \times N$  matrix of pairwise RMSD values is computed, as are FRET observables for each conformer and **(b)** expected  $p_{i,j}$  values (see eq. 4). Then, per-row weighted averages are taken to form **(c)**  $\langle \text{RMSD} \rangle_i$ , the elements of which are averaged to obtain **(d)**  $\langle \langle \text{RMSD} \rangle \rangle$ .

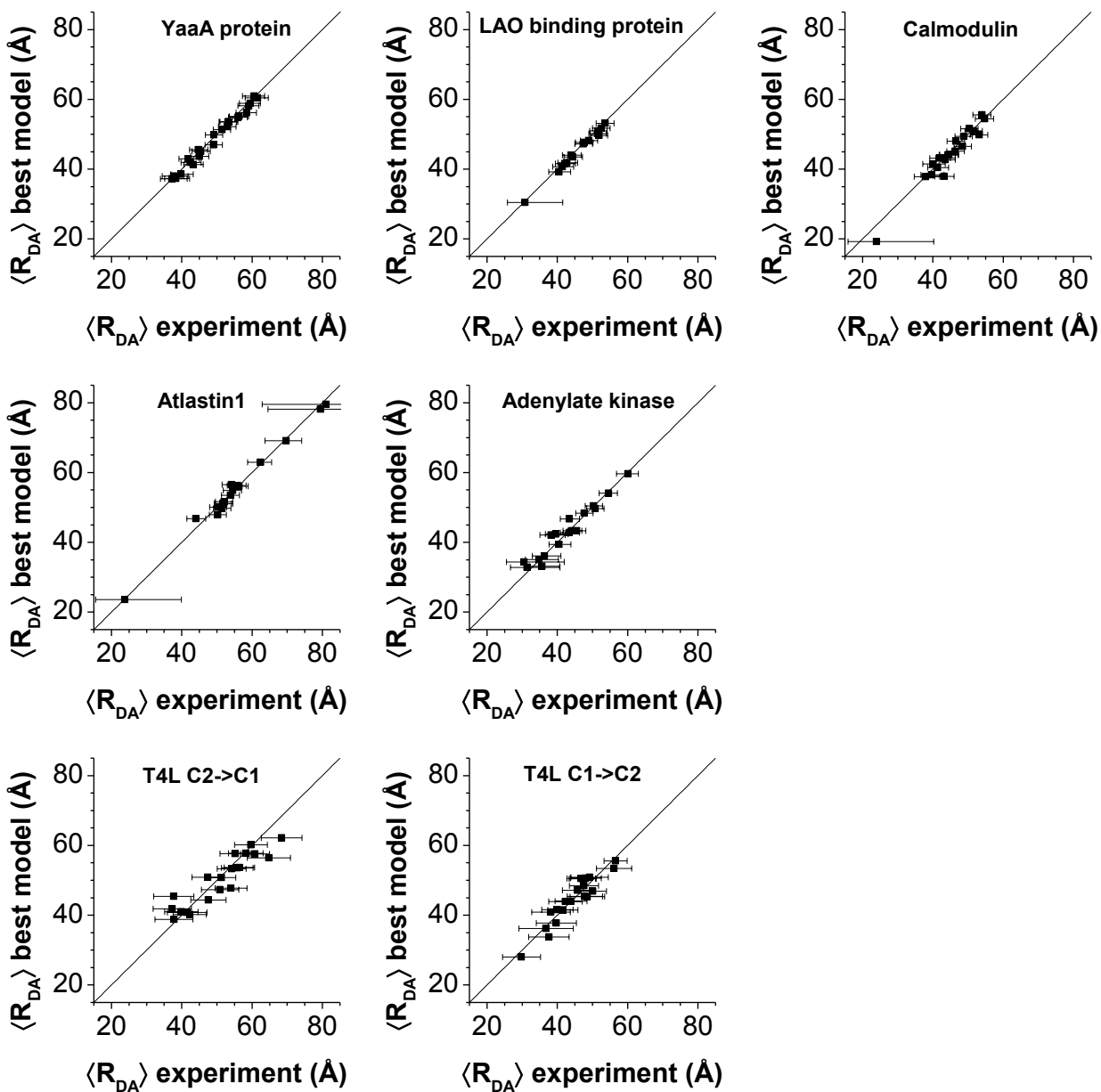


**Supplementary Figure 9** | Dependency of the reduced chi-squared value  $\chi_r^2$  on the number of degrees of freedom for a constant value of confidence level. As illustrated, constant confidence level corresponds to different  $\chi_r^2$  values, depending on the number of degrees of freedom in the test.



**Supplementary Figure 10** | Optimal FRET pair selection algorithms.

(a) Dependence of expected precision on the measurement pair set size for different pair selection algorithms. The greedy pair **selection** algorithm (black, **Supplementary Note 2**) shows the lowest  $\langle\langle\text{RMSD}\rangle\rangle$  at a low number of measurements, although there the actual  $\langle\langle\text{RMSD}\rangle\rangle$  is high. The greedy pair **elimination** algorithm (red, **Supplementary Note 3**) yields the lowest  $\langle\langle\text{RMSD}\rangle\rangle$  except for a low number of measurements, however, this algorithm is also the most computationally demanding. The **mutual information**-based pair selection algorithm (blue, **Supplementary Note 4**) shows an intermediate behaviour to the greedy pair selection and elimination algorithms, however greedy pair elimination algorithm is by an order of magnitude more computationally demanding. (b) Dependence of the measurement count on the desired precision  $\langle\langle\text{RMSD}\rangle\rangle$  (note, these are the inverse functions to those depicted in (a)). The steepness of the curves is system specific. The presented curves illustrate qualitative differences among selection algorithms.



*Supplementary Figure 11* | Measured inter-dye distances against predicted inter-dye distances for the best model (lowest  $\chi_n^2$ ). Error bars depict standard errors (see **section 1.5.10**).

**Supplementary Table 1** | Selected FRET pairs and corresponding donor-acceptor averaged distances and errors for the target.

#	YaaA protein			LAO binding protein			Calmodulin		
	Pair	$\langle R_{DA} \rangle$	[+err, -err] / Å	Pair	$\langle R_{DA} \rangle$	[+err, -err] / Å	Pair	$\langle R_{DA} \rangle$	[+err, -err] / Å
1	138_201	58.4	[+2.7,-3]	49_131	40.4	[+3.3,-2.8]	31_135	48.4	[+2.4,-2.4]
2	139_198	56	[+2.5,-2.7]	57_152	41.4	[+3.1,-2.7]	53_118	54.7	[+2.5,-2.6]
3	15_197	43.2	[+2.8,-2.6]	35_151	44.3	[+2.7,-2.5]	18_111	23.9	[+16.2,-8.1]
4	16_256	45.4	[+2.6,-2.5]	105_228	47.6	[+2.5,-2.4]	21_123	43.5	[+2.8,-2.5]
5	16_54	42.5	[+2.9,-2.6]	105_204	53.6	[+2.4,-2.5]	46_95	39.5	[+3.5,-2.9]
6	18_239	41.9	[+3,-2.7]	23_101	52.5	[+2.4,-2.5]	52_127		
7	20_164	49	[+2.4,-2.4]	2_127	51.8	[+2.4,-2.5]	5_119	43.1	[+2.8,-2.6]
8	33_246	53.4	[+2.4,-2.5]	23_220	42.1	[+3,-2.7]	60_95	51.6	[+2.4,-2.4]
9	40_157	44.7	[+2.7,-2.5]	57_101	51.4	[+2.4,-2.4]	2_133	43.5	[+2.8,-2.5]
10	41_203	39.7	[+3.5,-2.9]	23_174	30.7	[+10.7,-4.9]	44_114	44.5	[+2.7,-2.5]
11	44_244	56.3	[+2.5,-2.8]	101_218	51.6	[+2.4,-2.4]	14_133	46.4	[+2.5,-2.4]
12	48_164	59.5	[+2.8,-3.1]	2_23	42.7	[+2.9,-2.6]	57_131	53.9	[+2.4,-2.6]
13	48_95	53.1	[+2.4,-2.5]	80_113	43.9	[+2.7,-2.5]	1_118	37.8	[+4,-3.2]
14	51_200	37.2	[+4.3,-3.3]	22_131	48.9	[+2.4,-2.4]	47_133	46.5	[+2.5,-2.4]
15	51_231	52.9	[+2.4,-2.5]	5_174	47.4	[+2.5,-2.4]	24_148	50.3	[+2.4,-2.4]
16	53_247	51.4	[+2.4,-2.4]				2_97	48.7	[+2.4,-2.4]
17	55_256	44.9	[+2.6,-2.5]				41_77	40	[+3.4,-2.9]
18	59_243	60.5	[+2.9,-3.3]				43_131	41.8	[+3,-2.7]
19	59_99	49.1	[+2.4,-2.4]				54_148	41.3	[+3.1,-2.7]
20	65_198	59.1	[+2.7,-3.1]				3_135	44.3	[+2.7,-2.5]
21	74_198	61.5	[+3,-3.5]				48_140		
22	95_240	38.3	[+3.9,-3.1]				24_147	53.1	[+2.4,-2.5]
23	98_157	37.6	[+4.1,-3.2]						

#	Atlastin1			Adenylate kinase			T4 lysozyme (C1→C2)			T4 lysozyme (C2→C1)		
	Pair	$\langle R_{DA} \rangle$	[+err, -err] / Å	Pair	$\langle R_{DA} \rangle$	[+err, -err] / Å	Pair	$\langle R_{DA} \rangle$	[+err, -err] / Å	Pair	$\langle R_{DA} \rangle$	[+err, -err] / Å
1	194_350	79.4	[+7.3,-14.9]	47_151	34.7	[+5.5,-3.8]	36_132	37.6	[+5.7,-5.7]	36_86	51.3	[+4,-4]
2	79_367	69.7	[+4.4,-6]	94_142	60.1	[+2.8,-3.2]	36_86	41.6	[+4.2,-4.2]	44_119	59.7	[+4.6,-4.6]
3	35_344	23.7	[+16,-8.2]	1_149	40.4	[+3.3,-2.8]	19_132	39.7	[+5.6,-5.6]	55_150	60.8	[+4.1,-4.1]
4	216_382	54.1	[+2.4,-2.6]	50_162	31.4	[+9.2,-4.7]	44_127	56.1	[+5,-5]	19_119	56.4	[+4.2,-4.2]
5	176_405	55.7	[+2.5,-2.7]	54_203	50.3	[+2.4,-2.4]	44_86	45.8	[+4.3,-4.3]	36_132	50.9	[+5.3,-5.3]
6	249_319	62.4	[+3.1,-3.7]	23_139	35.6	[+5,-3.6]	22_127	36.8	[+7.7,-7.7]	44_86	55.8	[+4.4,-4.4]
7	15_406	56.3	[+2.5,-2.8]	23_156			55_132	46.8	[+4,-4]	55_132	55.2	[+4.3,-4.3]
8	1_409	44	[+2.7,-2.5]	40_143	36.3	[+4.6,-3.4]	19_86	47.2	[+3.8,-3.8]	44_150	58.2	[+4.9,-4.9]
9	216_349	81	[+7.9,-18.1]	57_157	30.5	[+11.3,-5]	69_132	47.8	[+5,-5]	60_150	37.8	[+5.4,-5.4]
10	302_403			151_203	39.5	[+3.5,-2.9]	55_150	47.6	[+4.1,-4.1]	19_86	54.2	[+4,-4]
11	208_320	51.7	[+2.4,-2.4]	141_187	54.5	[+2.5,-2.6]	60_150	48.5	[+4.9,-4.9]	60_86	54	[+4.5,-4.5]
12	269_377	52	[+2.4,-2.5]	79_127	43.4	[+2.8,-2.6]	8_86	38.2	[+5.5,-5.5]	55_119	68.4	[+5.8,-5.8]
13	106_354	54.4	[+2.5,-2.6]	73_147	45.4	[+2.6,-2.4]	44_119	50.1	[+3.8,-3.8]	44_132	64.8	[+6.1,-6.1]
14	82_349	50.3	[+2.4,-2.4]	75_89	44.1	[+2.7,-2.5]	60_86	43.9	[+4.5,-4.5]	69_119	39.9	[+4.7,-4.7]
15	68_212	50.2	[+2.4,-2.4]	41_104	47.6	[+2.5,-2.4]	44_69	29.8	[+5.4,-5.4]	60_119	47.4	[+4.4,-4.4]
16	106_379			136_187	50.8	[+2.4,-2.4]	60_132	49.2	[+5.3,-5.3]	8_86	47.6	[+5,-5]
17	1_125	53.8	[+2.4,-2.6]	58_188	38.2	[+3.9,-3.1]	5_44	42.3	[+4.7,-4.7]	69_132	37.3	[+5.4,-5.4]
18	216_251	52	[+2.4,-2.5]	99_128	43.4	[+2.8,-2.6]	69_119	40	[+4.4,-4.4]	5_44	42.3	[+4.7,-4.7]
19	68_349	51.5	[+2.4,-2.4]				44_150	48.1	[+4.4,-4.4]	60_132	37.7	[+5.7,-5.7]
20							55_119	56.6	[+3.2,-3.2]	22_127	41.5	[+5.6,-5.6]

*Lists of selected FRET pairs for each of the benchmarked proteins. Donor and acceptor residue IDs are indicated for each pair.  $\langle R_{DA} \rangle$  stands for donor-acceptor averaged distance. Pairs are ordered by relevance, starting from the most relevant. Pairs selected additionally for cross-validation are underlined. Reference distances and corresponding errors are provided unless the labelling site is inaccessible in the reference conformer. In the case of T4 lysozyme experimentally measured values are reported, for other proteins simulated data is provided.*



**Supplementary Table 2** | Site-specific residual anisotropies for donor and acceptor dyes of T4 lysozyme.

<b>Donor, Alexa488</b>		<b>Acceptor, Alexa647</b>	
<b>Residue sequence number</b>	<b><math>r_{\infty}/r_0</math></b>	<b>Residue sequence number</b>	<b><math>r_{\infty}/r_0</math></b>
5	0.72	44	0.43
8	0.67	86	0.49
19	0.43	119	0.55
22	0.58	69	0.57
36	0.55	150	0.61
44	0.51	127	0.68
55	0.33	132	0.69
60	0.54		
69	0.44		
70	0.46		

Ratio of the residual anisotropy,  $r_{\infty}$ , determined experimentally by analysis of time- and polarization resolved fluorescence decays of fluorescent labelled T4 lysozyme over fundamental anisotropy  $r_0 = 0.38$  of the dyes.

*Supplementary Note 1: System selection and geometric modelling justification.*

For this benchmark study, we selected systems where similar approaches have been applied<sup>2-4</sup>. These systems are representative molecules of different sizes (148 to 409 aa), they reflect different interconversion motions (hinge bending, shear, twist), and the mode of interaction with target molecules is different (Induced fit or conformational selection).

Because NMSim samples geometrically allowed (considering covalent and non-covalent bond constraints) conformations of proteins, there is less emphasis on the mode of motion or interactions. Hence, even low populated states with high energy and non-physiological states as in the case of induced fit are allowed, because the sampling over these geometric models generates flat energy landscape, reaching to states that traditional MD simulations would not be allowed. The drawback is that the relative energy between states is lost. Therefore, with NMSim, it is possible to reach induced fit configurations even in the absence of ligands; highlighting the predictive nature of NMSim over traditional MD simulations, which require more complex simulations and are more computational expensive. For example, ligand bound form of Calmodulin is reached even when the seed structure corresponds to the Apo-state.

***Supplementary Note 2: Pseudocode for greedy FRET pair selection algorithm.***

```
def greedySelection(RMSD_target=2.0):
    residues = range(1, len(protein))
    pairs = combinations(residues, 2)
    selected = []
    RMSDmin = float("inf")
    while RMSDmin > RMSD_target:
        RMSDmin = float("inf")
        for pair in pairs:
            RMSD = rmsd_ave(ensemble, selected+[pair])
            if RMSD < RMSDmin:
                bestPair = pair
                RMSDmin = RMSD
        selected.append(bestPair)
    print(len(selected), bestPair, RMSDmin)
```

***Supplementary Note 3: Pseudocode for greedy FRET pair elimination algorithm.***

```
def greedyElimination(RMSD_target=2.0):
    residues = range(1, len(protein))
    selected = combinations(residues, 2)
    RMSDmin = float("inf")
    while RMSDmin > RMSD_target:
        RMSDmin = float("inf")
        for pair in selected:
            pairs = copy(selected)
            pairs.remove(pair)
            RMSD = rmsd_ave(ensemble, pairs)
            if RMSD < RMSDmin:
                worstPair = pair
                RMSDmin = RMSD
        selected.remove(worstPair)
    print(len(selected), worstPair, RMSDmin)
```

**Supplementary Note 4: Pseudocode for mutual information-based FRET pair selection algorithm.**

```
def MI_selection(RMSD_target=2.0):
    residues = range(1, len(protein))
    pairs = combinations(residues, 2)
    #Shannon entropies for each pair
    entropies = [entropy(pair) for pair in pairs]
    iBest = argmax(entropies)
    selected = [pairs[iBest]]

    RMSD = rmsd_ave(ensemble, selected)
    print(1, selected[0], RMSD)
    while RMSD > RMSD_target:
        minCHlist = [] #conditional entropies
        for pair in pairs:
            condHlist = []
            for prev in selected:
                condHlist.append(conditionalEntropy(pair, prev))
            minCHlist.append(min(condHlist))
        iMaxCH = minCHlist.index(max(minCHlist))
        bestPair = pairs[iMaxCH]
        selected.append(bestPair)
        RMSD = rmsd_ave(ensemble, selected)
        print(len(selected), bestPair, RMSD)
```

**Supplementary Note 5: Dye models in the simulations**

Accessible volume (AV) simulations were successfully used to estimate the average donor-acceptor distances  $\langle R_{DA} \rangle$  from structural models of RNA and DNA<sup>5</sup>. An AV is the sterically allowed space of the dye molecule attached to the protein as calculated by the FPS program<sup>6</sup>. In proteins dyes can be trapped on the protein surface to a significant extent (see **Supplementary Table 2**). To account for this, we used the Accessible and Contact Volume (ACV) dye model for all simulations<sup>7</sup>. The surface areas of the ACVs were considered separately using the residual anisotropy values determined from experiment. For that, we defined contact volume as the part of the AV which is closer than  $R_{CV} = 3 \text{ \AA}$  from the protein surface. Population fraction of the dye within the contact volume is assigned to a higher value equal to the experimental ratio of residual anisotropy over fundamental anisotropy  $r_{\infty}/r_0$  of the corresponding labelling position as determined from the T4L experiments<sup>7</sup> (see **Supplementary Table 2**).

T4L was labelled by Alexa488 with a C5-hydroxylamine linker (Donor), which is coupled to the unnatural amino acid p-acetylphenylalanine, and Alexa647 with a C2-maleimide linker (Acceptor), which is coupled to cysteine (see **section 1.5.9**). Despite the different coupling chemistry and distinct fluorophores, a single set of dye parameters is most suitable to describe the experiments. In the simulations these dye/linker pairs were approximated as flexible tubes with width of  $L_{width} = 2.5 \text{ \AA}$  and length of  $L_{link} = 21.0 \text{ \AA}$ . The fluorophore moieties were approximated by spheres with a radius of  $R_{dye} = 3.5 \text{ \AA}$ . The same dye parameters were also used for the simulation of FRET data.

In the simulated data constant value of  $r_{\infty}/r_0 = 0.3$  was used to mimic a typical fraction of trapped dye. In the simulated data, the uncertainty level of average FRET efficiency standard error was constant ( $E = E_{ref} \pm 0.06$ ), which corresponds to typical magnitude of the error in such experiments. This leads to asymmetric uncertainties of the average donor-acceptor distances  $\delta_{ref}$ . Depending on the target FRET efficiency  $E_{ref}$ , uncertainties  $\delta_{ref}$  vary in the range from 2.0 to 20  $\text{\AA}$  (see **Supplementary Table 1**).

**Supplementary Note 6: NMSim coarse grained simulations**

Unbiased and FRET-guided structural ensembles were generated by the NMSim software<sup>1</sup> (<http://www.nmsim.de>). For unbiased NMSim simulations ten simulations generating 10,000 conformations (steps) each were performed, starting from the seed structure and using default parameters for sampling of large-scale motions. These trajectories are clustered and serve as *prior* candidates.

In the case of FRET-guided simulations, same NMSim parameters were used. Additionally, Monte Carlo Metropolis-Hastings annealing procedure was applied, in which FRET  $\chi_r^2$  of the conformation is used as the guiding potential. A single FRET-guided NMSim simulation of 10,000 steps contains two annealing cycles, such that effective temperature varies from  $kT = 0$  to  $kT = kT_{max}$  and back to  $kT = 0$ . For each seed structure, five FRET-guided NMSim simulations were performed for  $kT_{max} = 0.1$  units of  $\chi_r^2$  and another five for  $kT_{max} = 1.0$  units of  $\chi_r^2$ .

Parameter	Value
E-cutoff for H-bonds	-1.0
Hydrophobic cutoff	0.35
Hydrophobic method	3
No. of sim. cycles	10000
No. of NMSim cycles	1
NM mode range	1-5
Step size	0.5
C-alpha Cutoff	10
$kT_{max}$	1.0; 0.1

## References

1. Ahmed, A., Rippmann, F., Barnickel, G. & Gohlke, H. A normal mode-based geometric simulation approach for exploring biologically relevant conformational transitions in proteins. *Journal of Chemical Information and Modelling* **51**, 1604-1622 (2011).
2. Cavasotto, C. N., Kovacs, J. A. & Abagyan, R. A. Representing receptor flexibility in ligand docking through relevant normal modes. *Journal of the American Chemical Society* **127**, 9632-9640 (2005).
3. Ahmed, A. & Gohlke, H. Multiscale modelling of macromolecular conformational changes combining concepts from rigidity and elastic network theory. *Proteins-Structure Function and Bioinformatics* **63**, 1038-1051 (2006).
4. Tama, F. & Sanejouand, Y. H. Conformational change of proteins arising from normal mode calculations. *Protein Engineering* **14**, 1-6 (2001).
5. Sindbert, S. *et al.* Accurate Distance Determination of Nucleic Acids via Förster Resonance Energy Transfer: Implications of Dye Linker Length and Rigidity. *Journal of the American Chemical Society* **133**, 2463-2480 (2011).
6. Kalinin, S. *et al.* A toolkit and benchmark study for FRET-restrained high-precision structural modelling. *Nature Methods* **9**, 1218-1227 (2012).
7. Dimura, M. *et al.* Quantitative FRET Studies and Integrative Modelling Unravel the Structure and Dynamics of Biomolecular Systems. *Current Opinion in Structural Biology* **40**, 163-185 (2016).



Supplement A. Quantitative FRET studies and integrative modelling unravel the structure and dynamics of biomolecular system

# Quantitative FRET studies and integrative modeling unravel the structure and dynamics of biomolecular systems

Mykola Dimura<sup>1,2,3</sup>, Thomas O Peulen<sup>1,3</sup>, Christian A Hanke<sup>1</sup>,  
Aiswaria Prakash<sup>1</sup>, Holger Gohlke<sup>2</sup> and Claus AM Seidel<sup>1</sup>



Förster Resonance Energy Transfer (FRET) combined with single-molecule spectroscopy probes macromolecular structure and dynamics and identifies coexisting conformational states. We review recent methodological developments in integrative structural modeling by satisfying spatial restraints on networks of FRET pairs (hybrid-FRET). We discuss procedures to incorporate prior structural knowledge and to obtain optimal distance networks. Finally, a workflow for hybrid-FRET is presented that automates integrative structural modeling and experiment planning to put hybrid-FRET on rails. To test this workflow, we simulate realistic single-molecule experiments and resolve three protein conformers, exchanging at 30  $\mu$ s and 10 ms, with accuracies of 1–3 Å RMSD versus the target structure. Incorporation of data from other spectroscopies and imaging is also discussed.

## Addresses

<sup>1</sup> Chair for Molecular Physical Chemistry, Heinrich Heine University Düsseldorf, 40225 Düsseldorf, Germany

<sup>2</sup> Institute for Pharmaceutical and Medicinal Chemistry, Heinrich Heine University Düsseldorf, 40225 Düsseldorf, Germany

Corresponding author: Seidel, Claus AM ([cseidel@hhu.de](mailto:cseidel@hhu.de))

<sup>3</sup> Contributed equally.

**Current Opinion in Structural Biology** 2016, **40**:163–185

This review comes from a themed issue on **Biophysical and molecular biological methods**

Edited by **Petra Fromme** and **Andrej Sali**

For a complete overview see the [Issue](#) and the [Editorial](#)

<http://dx.doi.org/10.1016/j.sbi.2016.11.012>

0959-440/© 2016 The Authors. Published by Elsevier Ltd. This is an open access article under the CC BY license (<http://creativecommons.org/licenses/by/4.0/>).

## Introduction

The measurement of Förster resonance energy transfer (FRET) [1<sup>\*\*</sup>,2<sup>\*\*</sup>,3] from a donor (D) to an acceptor (A) fluorophore has become a popular biophysical method that can yield unique insights into the structure and the structural exchange dynamics of labeled biomolecular systems. FRET has applications in two major research areas. The first application makes use of the high time resolution and single-molecule capabilities to study the

kinetics and to detect intermediates of exchanging systems with a limited number of DA pairs [4]. The second application utilizes FRET to study structures of biomolecules in solution using a larger number of DA pairs, to obtain detailed structural insights on biomolecules in solution [5]. The first approach is successful in correlating structural dynamics and function by directly mapping the timescales of exchange and the pathways between conformational states with biomolecules on the single-molecule (sm) level [4,6]. Various equilibrium processes were studied such as folding of proteins [7,8] or nucleic acids [9–11], assembly and disassembly of complexes [12–14], and enzymatic cycles [15,16]. A versatile set of single-molecule based measurements and analysis techniques allows one to cover a wide range of time scales ranging from picoseconds [17], tens of nanoseconds [18,19], microseconds [13,20<sup>\*</sup>,21<sup>\*</sup>,22,23<sup>\*</sup>,24<sup>\*</sup>] to milliseconds and seconds [25<sup>\*</sup>,26,27<sup>\*\*</sup>]. Moreover, perturbation techniques such as temperature modulation [28] and microfluidic mixers for non-equilibrium experiments [29<sup>\*</sup>] widen the use of smFRET experiments even further.

In the second approach, FRET is applied as a spectroscopic ruler for quantitative structural studies by measuring a larger set of single-pair DA pairs, which is necessary for interrogating the most important degrees of freedom of the system (i.e., the data sparseness must be sufficiently low [30<sup>\*</sup>]). In the absence of prior structural knowledge, such a set should ideally be a connected network. Pioneering work on the ensemble and single-molecule level determined quantitative FRET-based structural models of essentially static systems such as polyprolines [5,31], various nucleic acids [32–34,35<sup>\*</sup>], and large biomolecular complexes [36,37]. This approach benefits from single-molecule methods, which increase the effective resolution, to discriminate among coexisting states in solution. Combining methodologies of both major application areas harbors the potential to resolve structural models of dynamically exchanging coexisting states.

FRET measurements can only report inter-dye distances, and the number of FRET pairs is limited. Integrated methods can leverage experimental data that by itself would be insufficient to determine structures with satisfactory accuracy [38,39]. Therefore, integrative structural modeling relying on molecular simulations as well as FRET data is essential for achieving FRET-based

atomistic structural models. In the following article, we refer to this hybrid approach as hybrid-FRET modeling. Due to the long-range FRET information (typically 20–100 Å), the hybrid-FRET modeling approach is especially suitable to characterize the tertiary, super-tertiary [40], and quaternary structures of biomolecular systems. Benchmark studies for FRET-restrained structural hybrid modeling of biomolecules and their complexes versus crystal structures have demonstrated the accuracy of the integrative approach [41\*,42\*\*]. A dramatic improvement in the precision and accuracy (root mean square deviation (RMSD) of 0.5 Å) is achieved by explicitly considering spatial distributions of dye positions, which greatly reduces uncertainties due to flexible dye linkers [42\*\*].

There are many reasons for further improving FRET-based structural modeling. In view of the huge dynamic time range from picoseconds to hours that can be covered by fluorescence, smFRET experiments and hybrid-FRET modeling are an especially promising combination to determine structure and dynamics simultaneously. Many other biophysical techniques have shown that a dynamic view on protein structures can give many important insights because the dynamic properties control their functions, as shown for various research areas such as signaling [43], enzymatic catalysis [44], (mis)folding [45,46], and modulation of allostery [47]. Several structured [48–50] and partially unstructured [51,52,53\*] proteins were characterized by the FRET approach. Even dynamic and large biomolecular systems were studied such as ligand-induced conformational changes of the membrane-bound SNARE complex [54] and the conformational dynamics of single HIV-1 envelope trimers on the surface of native virions [55].

The dynamic smFRET experiments combined with integrative modeling should be especially useful to detect and directly characterize the conformational heterogeneity of biomolecules in the presence of thermally excited conformational states with a lifetime in the microsecond time range, which complements recently improved NMR spectroscopy methods [56]. Moreover, there are many reasons (e.g., limited solubility, unsuitable molecular size, limited stability, inadequate purity, or large conformational heterogeneity) why the structures of biological macromolecules often prove intractable to mainstream structural biology methods (i.e., crystallography, NMR spectroscopy, and cryo-electron microscopy) [38]. Exploiting the time resolution, sensitivity, and selectivity of fluorescence, integrative structural modeling, combining FRET experiments with computer simulations and comparative protein structure modeling [57] as prior information is developing into a promising complementary method for structural biology of dynamic biomolecules.

This perspective article focuses on advances in FRET-based structural modeling and the application to dynamic

biomolecular systems. To this end, we first review FRET techniques that can yield information for structural modeling of biomolecules. We then summarize the current state of the art techniques for modeling the FRET dye label behavior, which is important for FRET-based structural modeling. Subsequently, we introduce a typical workflow for hybrid-FRET modeling, which is then applied in a test case. We demonstrate an application of fluorescence methods to a three-state model system to show the potential of FRET-based structural modeling and to assess the currently achievable precision and accuracy. For this test case, we introduce an automated procedure for determining the most informative single-pair FRET labeling sites and simulate experimental data under realistic conditions, which are then used for structural modeling. In the outlook, we discuss the potential directions for future improvements with respect to experimental techniques and computational modeling to improve the precision and accuracy of hybrid models. Finally, we discuss applications of hybrid-FRET methods in imaging to realize an integrated molecular fluorescence microscope combining optical and computational microscopy (i.e., coarse-grained and all-atom molecular (dynamics) simulations) [58] to describe suitably labeled biomolecular systems by atomistic structural models.

## FRET-based structural modeling

### Experimental techniques

Considering the conformational species ( $i$ ), FRET between the tethered fluorophores D and A with the DA-distance  $R_{DA}^{(i)}$  is characterized by the yield of energy transfer from D to A, usually called transfer efficiency  $E^{(i)}$  or FRET efficiency (Eq. (1a)). This yield is the ratio of the rate constant  $k_{RET}^{(i)}$  relative to all other processes depopulating the excited donor with the total rate constant  $k_{D,0}$ . Eq. (1b), derived by Theodor Förster [1\*\*,2\*\*], allows one to compute  $R_{DA}^{(i)}$  in units of the coupling constant  $R_0$  (Förster radius).  $R_0$  is specific for the used dye pair. It depends on the refractive index of the medium  $n$ , the spectral overlap integral of the D fluorescence and the A absorption spectrum  $J$ , the factor  $\kappa^2$  for the relative orientation of the D and A dipole, and the D fluorescence quantum yield in absence of an acceptor,  $\Phi_{F,D(0)}$  [3].

$$\begin{aligned}
 E^{(i)} &= \frac{k_{RET}^{(i)}}{\underbrace{k_{D,0} + k_{RET}^{(i)}}_{(a)}} = \frac{1}{\underbrace{1 + \left(R_{DA}^{(i)}/R_0\right)^6}_{(b)}} \\
 &= \frac{F_A^{(i)}}{\underbrace{\gamma F_D^{(i)} + F_A^{(i)}}_{(c)}} = 1 - \frac{\tau_{D(A)}^{(i)}}{\underbrace{\tau_{D(0)}}_{(d)}}
 \end{aligned}
 \tag{1}$$

The FRET-efficiency  $E$  can be determined by fluorescence intensities of the sensitized acceptor emission  $F_A$  and the quenched donor fluorescence  $F_D$  (Eq. (1c)). The

accuracy of  $E$  relies critically on several factors: (1) the purity of the samples, that is, the Donor-only reference for a correct calibration and the degree of labeling of the FRET sample; and (2) the properties of the labels and the setup. The setup and the samples should be carefully characterized for computing the experimental calibration factor  $\gamma = (x_{b,A} g_A \Phi_{F,A}) / (g_D \Phi_{F,D(0)})$  given by the spectrum-dependent detection efficiencies of the D and A fluorescence ( $g_D$  and  $g_A$ ), and the fluorescence quantum yields  $\Phi_{F,D(0)}$  and  $\Phi_{F,A}$  of D and A respectively. Often  $\Phi_{F,D(0)}$  and  $\Phi_{F,A}$  are assumed to be identical for all conformational species (for details and a more complex analysis, see [59<sup>••</sup>,60<sup>••</sup>,61<sup>•</sup>]). In single-molecule experiments, the excitation irradiances are usually high. Thus, saturation effects of the fluorophores due to formation of long lived dark-states must be considered in the fluorescence quantum yield. For example, the cyanine-based acceptor dyes such as Cy5 and Alexa647, undergo photo-induced cis-trans isomerization [62], such that the fraction of bright trans species  $x_{b,A}$  drops significantly below one.  $x_{b,A}$  can be obtained by analyzing the acceptor autocorrelation function of the FRET experiment [63,64<sup>•</sup>].

Time-resolved measurements of donor fluorescence decays  $f(t)$  by, for example, time-correlated single photon counting (TCSPC) are useful for precise FRET measurements, because they offer three main advantages. (1) The FRET efficiency can be determined without instrumental calibrations via the excited state lifetimes  $\tau$  of the D-only reference sample  $\tau_{D(0)} = 1/k_{D,0}$  and the DA sample  $\tau_{D(A)}^{(i)} = (1/k_{D,0} + 1/k_{RET}^{(i)})$  (Eq. (1d)). These correspond to the slopes of the decay curves (see Box 1, panel 1). (2) The joint decay analysis of the D-only reference  $f_{D(0)}(t)$  and the FRET sample  $f_{D(A)}(t)$  allows relating the FRET rate constant  $k_{RET}^{(i)}$  directly to  $R_{DA}^{(i)}$  (Eq. (2), for details see [65]). (3) The curvature of  $f_{D(A)}(t)$  contains information on the heterogeneity of the FRET sample such that a distance distribution  $x(k_{RET}^{(i)})$  with species fractions  $x^{(i)}$  can directly be resolved (Eq. (2)).

$$f_{D(0)}(t) = e^{-(k_{D,0})t},$$

$$f_{D(A)}(t) = f_{D(0)}(t) \cdot \int_0^\infty x(k_{RET}^{(i)}) \cdot e^{-k_{RET}^{(i)}t} dk_{RET}^{(i)} \text{ with} \quad (2)$$

$$k_{RET}^{(i)} = k_{D,0}(\Phi_{F,D(0)}) \cdot \left( \frac{R_0(n, \kappa^2, \Phi_{F,D(0)})}{R_{DA}^{(i)}} \right)^6$$

Depending on the complexity of the sample, FRET experiments can be performed on the single-molecule, sub-ensemble (selectively averaged single-molecule events), and ensemble levels, where each technique has its advantages. Intensity-based ensemble FRET measurements are relatively easy to perform; however, these

experiments yield only average observables due to ensemble averaging over the mixture of the molecules in the sample (Eq. (3)), and the sample must be well-characterized (purity, degree of labeling, homogeneity, fluorescence quantum yields of D and A) [59<sup>••</sup>]. Ideally, for such a mixture of  $N$  species with fractions  $x^{(i)}$  and transfer efficiencies  $E^{(i)}$ , the average transfer efficiency is given by:

$$E = \sum_{i=1}^N x^{(i)} E^{(i)} \quad (3)$$

Single-molecule measurements are currently the most common type of FRET experiments, because they can resolve distributions of FRET observables and provide kinetic information over 15 orders of magnitude in time. The main advantage of sm fluorescence spectroscopy is the ability to resolve static (multiple distinguishable static states) and dynamic (interconverting states) heterogeneities. There are two main measurement setup types for smFRET which differ significantly in their time resolution: (1) total internal reflection fluorescence (TIRF) microscopy [66<sup>•</sup>] with emCCD camera detection and (2) confocal detection with fast single-photon counting point detectors [67]. TIRF is widely used for immobilized molecules. The experimental time resolution is usually limited by the frame rate ( $\sim 60$  Hz) of the camera. Recently Farooq and Hohlbein [68] presented a generalized excitation scheme (sALEX) that combines the concepts of alternating laser excitation (ALEX) [69,70] and stroboscopic illumination [71,72] to improve the time resolution at least 10 fold. Confocal setups can be used for studying immobilized and freely diffusing molecules. Felekyan *et al.* [73] presented a dead-time free configuration with four detectors and two data acquisition boards, which enables time-resolved measurements over 15 orders of magnitude in time (Box 1). The immobilization of single molecules on a coated glass surface can be either directly accomplished via tags [66<sup>•</sup>] or indirectly via encapsulation in a liposome, which is immobilized afterwards [74].

Sm experiments with confocal detection of freely diffusing molecules are characterized by reproducible and stable detection efficiencies. In combination with pulsed excitation or pulsed interleaved excitation (PIE) [64<sup>•</sup>,75<sup>•</sup>] time-resolved fluorescence spectroscopy with multi-parameter fluorescence detection (MFD) [60<sup>••</sup>,76,77] can be conveniently realized for all FRET relevant fluorescence observables in a single measurement with the same sample. Most importantly, time-resolved anisotropy decay curves are obtained to estimate the uncertainty of the FRET orientation factor  $\kappa^2$  [61<sup>•</sup>]. Additionally, a series of combined 2D fluorescence parameter histograms can be generated, which allows determining all necessary FRET calibration parameters [60<sup>••</sup>,64<sup>•</sup>]. Finally, MFD increases the species selectivity, which is essential for

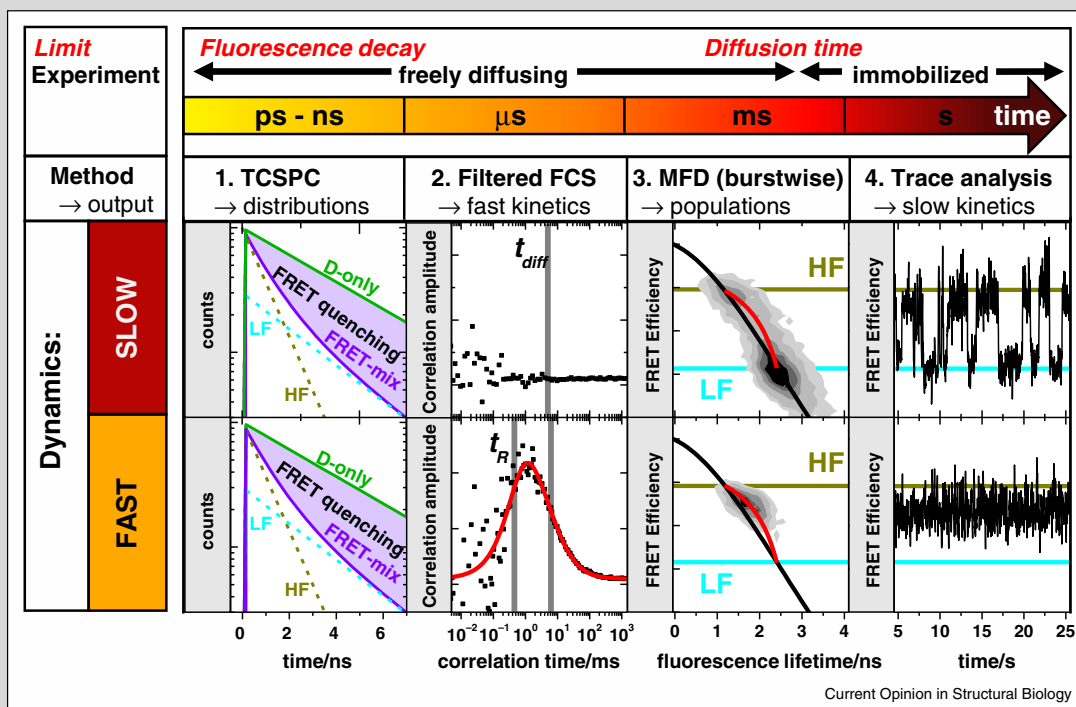
**Box 1** A combination of fluorescence spectroscopy methodologies records dynamics over 15 orders of magnitude in time and captures a large variety of biologically relevant processes such as conformational transitions or folding/unfolding events [22,29\*,60\*\*,150].

The fluorescence lifetime of typical fluorophores decays in the pico-second to nanosecond range and sets the lower limit to interrogate conformational dynamics. The upper limit is set by the time a single molecule can be observed. Immobilized molecules can be studied for seconds while fluorescence bursts due to freely diffusing molecules are observed only for milliseconds in confocal setups.

Experimental information can be obtained by (1) time-correlated single photon counting (TCSPC) histograms, (2) fluorescence correlation spectroscopy (filtered FCS), (3) burst-wise single-molecule analysis, and (4) the analysis of FRET efficiency traces. The influence of the exchange dynamics on the observed data is outlined for a system with two FRET states, Low-FRET (LF) and High-FRET (HF), which are either in fast (sub milliseconds, lower row) or in slow (seconds, upper row) exchange.

- (1) In the analysis, fluorescence decays of FRET rate constants of HF and LF are averaged over the fluorescence lifetime of the dye (nanoseconds). Therefore, a joint analysis of a FRET sample and a D-only sample (shown in green) provides a static picture of a molecular ensemble and decomposes into HF and LF components shown as dashed dark yellow and cyan lines, respectively.
- (2) In FCS, fluorescent photons are correlated to provide kinetic information in the submicro-second to milliseconds regime. Filtered FCS (fFCS) additionally utilizes the photon distribution with respect to an excitation pulse [23\*] to highlight the kinetic exchange between the HF and LF species by the species cross-correlation functions (SCC, black dots). If the kinetic exchange is significantly slower than the observation time ( $t_{diff}$  – diffusion time), no correlation is observed. Otherwise, a pronounced anti-correlation in the SCC is visible, which is analyzed (red curve) to yield the relaxation time ( $t_R$ ) of the HF/LF exchange.
- (3) In burst-wise analysis, fluorescence is integrated over milliseconds to provide the FRET efficiency and fluorescence lifetime of freely diffusing single molecules. A 2D-histogram allows interrogating the kinetics between states and reveals dynamics by changes in the shapes. Theoretical static (black) and dynamic FRET lines (red) serve as references for the location of the FRET populations in the 2D parameter histograms. A shift of the observed population towards longer lifetimes with respect to the static FRET line indicates conformational dynamics.
- (4) By recording fluorescence intensities of immobilized or liposomal encapsulated single molecules over a longer time with a lower time resolution, processes significantly slower than the typical burst duration ( $>ms$ ) are interrogated. FRET efficiency time traces of single molecules reveal stochastic jumps between HF and LF if the integration time of each frame is shorter than the dwell time of the state (upper plot); these jumps are averaged if the dwell time of the states are short (lower plot).

### Box 1



Fluorescence timescales to study molecular kinetics using FRET.

sub-ensemble TCSPC of sub-populations, that is, selective averaging by integrating all single-molecule events of a resolved FRET species to reduce the data noise dramatically (for details, see Box 1).

To perform quantitative FRET measurements, all procedures for determining the calibration factor  $\gamma$  in Eq. (1) (TIRF [66\*,78,79\*,80], confocal [60\*\*,64\*]) rely on well characterized standards, which are usually DNA rulers

labeled with a FRET pair using the dyes of interest. A worldwide consortium of research groups on FRET is currently working to establish a set of common recommendations for measurement procedures, data analysis, and joint reference molecules to maximize the accuracy of the FRET observables measured in different laboratories.

### Description of the labels

Both EPR spectroscopy with the double electron–electron resonance (DEER) method [81] and FRET spectroscopy are frequently used to obtain structural information on proteins by selectively coupling labels via flexible linkers (i.e., nitroxide spin-labels or donor and acceptor dyes, respectively). Thus, the labels can explore a large conformational space, such that a distribution of inter-label distances rather than a single inter-label distance is observed experimentally. In structural analysis, both techniques face the same problem of describing the localization of their respective labels and connecting the measured distances with structural information on the protein. This is a typical inverse problem, where both EPR [81–84] and FRET [42<sup>••</sup>,85<sup>••</sup>,86<sup>••</sup>] spectroscopies have developed similar solution strategies of assuming a structural model to compute a specific distance distribution between the labels and comparing the simulated and experimental values. Analogous to super-resolution microscopy, where the knowledge of the optical point spread function allows for localizing single emitters far beyond the optical resolution limit, a detailed knowledge of the label distribution for a given biomolecular structure is required to maximize the structural resolution of the respective technique. The so far used dye models are reviewed in this section, and their implementation in various toolkits for integrative FRET-based structural modeling is described in Section ‘Procedures for hybrid-FRET modeling’.

All-atom molecular dynamics (MD) simulations [33,87–93] seem to be the most appropriate solution to describe the label localization in integrative modeling (Figure 1a–c). However, while the relevant time-scale of fluorescence and biomolecular dynamics covers picoseconds to hours (Box 1), current MD simulations reach only the micro- to millisecond timescale. Furthermore, MD simulations are time-consuming and limited in their capability to sample the conformational space, in particular since the dye distribution changes with conformational changes of the biomolecule. MD simulations [87,89,94] as well as experimental fluorescence [61<sup>•</sup>,95,96<sup>•</sup>] and EPR [97] studies find long-lived conformational states, where the labels are trapped on the biomolecular surface. Trapping of cyanine dyes is known to change their fluorescence quantum yields [96<sup>•</sup>] such that this process is utilized by others for probing protein–nucleic acid interactions by protein-induced fluorescence enhancement (PIFE) [98,99<sup>•</sup>]. To avoid quenching and mobility reduction

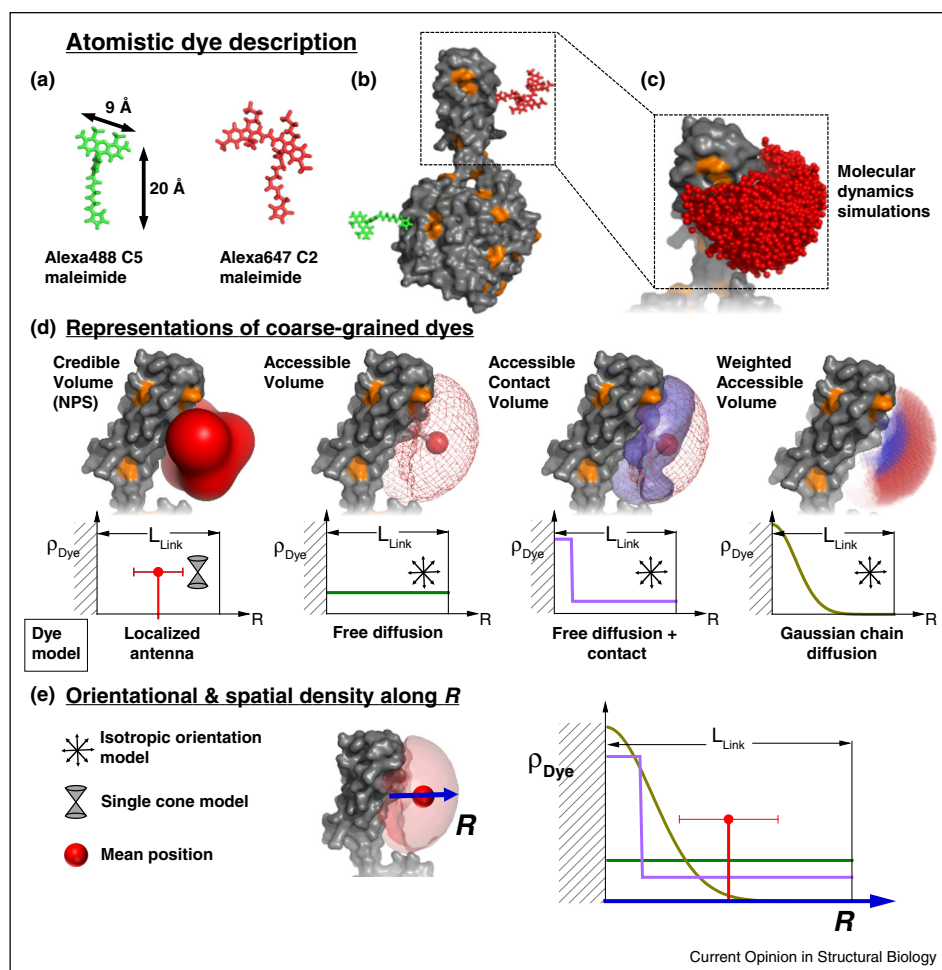
by the surface effects, most commercially available dyes used for FRET experiments have long flexible linkers ( $\sim 20$  Å), and the fluorophore carries sulfonic acid groups for improved solubility. The large flexibility of the linker also ensures a high orientational mobility of the dyes such that the assumption of the isotropic average for the dipole orientation factor (i.e.,  $\kappa^2 = 2/3$ ) is feasible, which is an important factor determining the accuracy of distance calculations by FRET measurements. In conclusion, the atomistic treatment of dye labels, together with the biomolecular system, by MD simulations is helpful for analyzing protein label interactions. However, it is currently not feasible to use MD simulations as a rapid routine method to predict the conformational sampling of the labels, which is needed for finding the structural model within a large ensemble that is most consistent with FRET data, as shown below.

Computationally faster algorithms use a coarse-grained representation, e.g. the label is approximated by a flexibly linked sphere ([83,85<sup>••</sup>], see Figure 1a–c), to compute the sterically allowed accessible volume (AV), which reproduced MD simulations well [61<sup>•</sup>]. The use of a geometric search algorithm reduces the computational time for the AV of a single FRET-label to less than 50 milliseconds on a conventional desktop computer [42<sup>••</sup>]. The computed AV represents uniform population densities  $\rho_{Dye}$  of the spatial dye localizations (Figure 1d). The mesh represents the surface of the dye positions most distant from the attachment point and includes all sterically allowed dye positions. To compute fluorescence observables the spatial population densities  $\rho_{Dye}(x,y,z)$  of the dye localizations is needed.

Two convenient assumptions for limiting cases were initially used for the models describing the spatial and orientational dye density in various hybrid-FRET modeling approaches: (1) The original dye model of the Nano Positioning System (NPS) assumed a label adopting a single position with a defined conformation of the linker and the fluorophore wobbling in a cone (*Localized antenna/Single cone model*) [85<sup>••</sup>]. This means that all fluorophores of an ensemble of molecules are located at the same position (defined by a delta function  $\delta$ ) with respect to the macromolecule:  $\rho_{Dye}(x,y,z) = \delta(x_{Dye},y_{Dye},z_{Dye})$ . Since the position  $(x_{Dye},y_{Dye},z_{Dye})$  of the dye is initially unknown, multiple measurements are used to localize it within a credible volume for a given confidence level (Figure 1d, left). (2) As an approximation of a freely diffusing fast rotating dye all orientations and all positions within the AV are equally populated;  $\rho_{Dye}(x,y,z)$  is constant and the fluorophore is isotropically oriented within the AV (*Free diffusion/Iso model*) [42<sup>••</sup>,61<sup>•</sup>]. The effect of different dye models on the spatial population densities  $\rho_{Dye}(x,y,z)$  along the vector  $R$ , pointing from the linker attachment site to the mean dye position in the AV, is visualized in the lower panel of Figure 1d.



Figure 1



Description of fluorescent labels in simulation. Treatment of dye labels in FRET-based modeling. (a) The donor and acceptor dyes, for example, Alexa488 C5 maleimide (green) and Alexa647 C2 maleimide (red), respectively, are typically attached to the biomolecule via long (~20 Å) flexible linkers. (b) Dye labels attached to the protein Atlastin-1 (grey surface) to give an impression of the sizes. Quenching amino acids on the protein surface are highlighted in orange. (c) Molecular dynamics simulations provide the spatial distribution of dye molecules. (d) Representation of coarse-grained dye labels. On the top different dye representations are shown. On the bottom the spatial density  $\rho_{Dye}$  along a vector  $R$  starting at the attachment point in the direction of the dye mean position is shown for the corresponding dye models. The original Nano Positioning System (NPS) [85\*\*] assumes the accessible volume as *prior* information (uncertainty), which is reduced by a set of FRET measurements with fixed satellites resulting in an uncertainty distribution (red) of a putatively *fixed* localized dye (antenna). The orientation of the dyes follows a diffusion in a cone model highlighted by a pictogram. Following  $R$ , the dye is located at a specific position (vertical red line) with an uncertainty. Accessible volume (AV, mesh) models provide the sterically allowed space of the dye molecule attached to the protein as calculated by the FPS program [42\*\*]. Here, the linkers of Alexa488 and Alexa647 are approximated as flexible tubes with width of  $L_{width} = 4.5 \text{ \AA}$  and length of  $L_{link} = 20.5 \text{ \AA}$  and  $L_{link} = 21.0 \text{ \AA}$ , respectively. Three radii were used to describe the dyes (5.0 Å, 4.5 Å, 1.5 Å) and (11.0 Å, 4.7 Å, 1.5 Å) for Alexa488 and Alexa647, respectively. The large sphere indicates the mean dye position. For a dye freely diffusing inside of its AV a uniform spatial distribution is assumed. The accessible and contact volume (ACV, [102]) provides a similar description as the AV, but defines an area close to the surface as contact volume (violet). In this figure the density  $\rho_{Dye}$  in the contact volume is weighted six times stronger and defined as part of the AV that is closer than 3 Å from the macromolecular surface. For the corresponding model, where a dye freely diffuses within the AV and its diffusion is hindered close to the surface, the spatial density  $\rho_{Dye}$  along  $R$  is approximated by a step function:  $\rho_{Dye}(R < 3 \text{ \AA}) = 6 \cdot \rho_{Dye}(R \geq 3 \text{ \AA})$ . The weighted accessible volume is a modification of AV where  $\rho_{Dye}$  along  $R$  is approximated by a Gaussian chain-inspired empirical weighting function [101]. To illustrate the effect of the proposed weighting of  $\rho_{Dye}$  the weighted AV is colored from blue (high density) to red (low density). (e) Comparison of the normalized spatial population densities  $\rho_{Dye}$  of the above dye models.

More recently, other dye models were suggested [100\*,101,102]. To consider small fractions of fluorescent fluorophores trapped on the biomolecular surface [102], the classical AV description was extended (using the *Free diffusion/Iso model*) by defining an additional interacting surface layer (the contact volume of defined thickness is highlighted in violet in Figure 1d) with a preferential surface residence of the dye, which may be approximated by a step function. This surface preference is specific for the dye and the labeling site. This combination yields the *Free diffusion + Contact/Iso model* for an accessible and contact volume (ACV), which predicts the compaction of the spatial dye distribution due to trapped dye fractions without significant increase of the computational cost. Höfig *et al.* [101] introduced a weighted AV description, where the densities  $\rho_{Dye}$  are enriched by empirical weighting with a Gaussian function leading to a higher local dye surface preference but only close to the attachment point (*Gaussian-chain (GC) diffusion/Iso model*) (Figure 1d,e).

The comparison of the normalized densities  $\rho_{Dye}$  of the four dye models in Figure 1e shows that the mean dye positions of an ACV or a weighted AV are closer to the protein interface as compared to the AV with a uniform density. This dye model specific shift of the mean positions becomes important for the predicted inter-dye distances if the other dye of the FRET pair is attached on the opposite side of the protein. To avoid an arbitrary choice of dye models, it is important to define rational criteria based on experimental evidence through observable fluorescence parameters. For example, time-resolved fluorescence data map the translational and orientational dye diffusion and the resulting DA distance distributions by fluorescence quenching, anisotropy and FRET.

So far we have discussed four dye models that have been developed for synthetic organic fluorescent labels, which are usually not too large (Figure 1a,b) so that their steric requirements are small. However, if the more bulky fluorescent proteins (FPs), such as GFP and mCherry, are used as labels in fusion proteins, we have to account for the significant steric hindrance of the FPs and their linkers. For this case, self-avoiding walk (SAW) weighting of the linker configuration (*SAW-Diffusion/Iso model*) was applied in our group. The scaled weighting factors were determined by computationally tractable MD simulations for sampling configurations of an explicit linker/label combination alone, followed by calculations of conformational free energies to weight each linker/label configuration in the presence of the biomolecule [103]. We applied this dye model in live cell hybrid-FRET studies for analyzing the architecture of biomolecular complexes labeled with FPs ([103,104\*], further details see outlook). Notably, this *SAW-Diffusion/Iso model* has similar effects on the conformational space in the AV as the rotamer

library model that is widely used for the analysis of DEER experiments in EPR spectroscopy [81]. Unlike the weighted AV description, the steric effects in the SAW-weighting lead to a strong reduction of  $\rho_{Dye}$  in proximity to the attachment site so that  $\rho_{Dye}$  has a maximum far away from the surface.

### Error estimation

For quantitative FRET studies, a number of control tasks should be performed for an appropriate analysis and interpretation of the experimental observables [60\*\*]: (1) analysis of the fluorescence properties of D or A by analyzing multiple fluorescence parameters with respect to quenching and trapping [37,60\*\*], which could affect  $R_0$  [105] and the calibration of the intensity-based experiments; (2) interpretation of discrete distributions of FRET efficiency  $E$  and anisotropy in confocal single-molecule experiments by photon distribution analysis, which allows separating structural heterogeneities from stochastic variations [106\*,107]; (3) validation of the chosen dye model by analyzing (i) the linker-induced distance distributions of single FRET states by TCSPC or sub-ensemble TCSPC, (Eq. (2)), and (ii) the time-resolved anisotropy to scrutinize the dye mobility [61\*] for verifying the assumption of  $\kappa^2 = 2/3$ ; (4) verification by sub-ensemble TCSPC and FCS (Box 1) that a population with a single FRET efficiency is indeed a single species and that it is not narrowed by a dynamic exchange (i.e. that it is actually a mixture of fast inter-converting states); and (5) verification by functional assays (e.g. binding constants of ligands, catalytic activity, structural stability sensed by thermal or chemical denaturation) that the label does not disturb the biomolecule.

The analysis of FRET measurements provides the inter-dye distances  $R_{DA}$  as sparse input data. To take advantage of this information, rigorous error estimation is necessary for integrative modeling such that all uncertainties that have been considered correctly propagate to the final structural model [30\*]. According to the error propagation rules, the overall uncertainties of the experimental inputs (the inter-dye distances  $R_{DA}$ ) for the search of structural model contain three major contributions.

- (1) In single photon counting, the statistical relative error is inversely proportional to the square root of the registered photons that translate to the experimental distance uncertainty,  $\Delta R_{DA}^2(E)$ , via the experimentally determined FRET efficiencies  $E$  or FRET rate constants  $k_{RET}$ . Systematic error in  $\Delta R_{DA}^2(E)$  is introduced primarily by two factors: (i) Preprocessing of experimental data by approximate fluorescence models (e.g. Eq. (2)) and (ii) Inaccurate instrumental calibrations and reference samples. Furthermore, if dynamic multi-component systems are studied,  $\Delta R_{DA}^2(E)$  usually also contains the uncertainty due



to data ambiguity and incoherence, resulting in FRET observables being correlated [30<sup>•</sup>]. To obtain a distance set for a specific FRET species (i.e. conformer) from analyzing a large set of studied FRET pairs, species fractions and specific kinetic properties [27<sup>••</sup>], which are global (joint) for the whole data set, are the best choices to assign FRET observables to the corresponding specific FRET species. The reason is that a global analysis of multiple independent datasets by a joint model minimizes the ambiguity by making use of correlations between otherwise independent model parameters. A global analysis procedure will be demonstrated below using a sample test case.

- (2) The uncertainty  $\Delta R_{DA}^2(\kappa^2)$  of using the correct orientation factor  $\kappa^2$  directly influences  $R_0$ , so that the accuracy of the computed distances,  $R_{DA}$ , is affected. The error range of  $\kappa^2$  can be estimated by anisotropy measurements [61<sup>•</sup>].
- (3) The uncertainty  $\Delta R_{DA}^2(\vec{R}_D, \vec{R}_A)$  of using an appropriate dye model describing the spatial positions  $\vec{R}_D, \vec{R}_A$  of D and A, respectively, influences the accuracy of predicting appropriate distances from structural models.

In the end, all the errors above propagate to structural models obtained via sampling of the conformational space and define the accuracy of the structural models with respect to the true structure and the precision of the model ensemble.

### Procedures for hybrid-FRET modeling

Due to the sparse information provided by experimental techniques such as FRET or EPR measurements, given the large number of degrees of freedom in atomistic models of biomolecules, a complete determination of biomolecular models with atomic resolution using only these experimental data is impossible. Fortunately, computational methods can provide complementary information, such as detailed structural features of biomolecules. At the same time, many computational methods also face challenges such as sufficient sampling and correct identification of near-native structures in a structural ensemble. The combination of computational methods with experimental input within a hybrid approach can facilitate generation and verification of the detailed biomolecular structures [108<sup>•</sup>], because experimental FRET data can provide external information on the architecture of proteins and biomolecular complexes to guide the modeling procedure.

Although many FRET-based structural studies were performed since Förster's publication in 1948 [1<sup>••</sup>], the obtained structural models were shown primarily as cartoons. In recent years, a number of integrative computational modeling methods [33,51,85<sup>••</sup>,86<sup>••</sup>,89,109] were developed to derive and present structural models in a

more quantitative manner. The high accuracy and performance of hybrid-FRET modeling was demonstrated in two benchmark studies with static structures [41<sup>•</sup>,42<sup>••</sup>]. In the last decade, many applications for small and large complex biomolecular systems were published, albeit the models remained on a rather descriptive level. Considering flexibly linked dyes, currently three software toolkits, Nano Positioning System (NPS) [85<sup>••</sup>], Crystallography & NMR System (CNS) [88,110] and FRET-restrained positioning and screening (FPS) [42<sup>••</sup>], are publicly available; they implement different methodologies, use partially different assumptions and dye models. Therefore, common standards for FRET analysis, generally available joint toolkits with well-defined workflows and widely accepted procedures should be established to facilitate quantitative hybrid-FRET modeling.

The key to hybrid modeling lies in the fine interplay between the computer simulations and the experiments to accomplish the most effective synergies between the strengths of both sides. On the experimental side, accuracy is achieved by appropriate consideration of spatial dye distributions, while precision estimation stems from rigorous error analysis. Moreover, the establishment of a statistically appropriate quantitative scoring function for judging agreement between the structural models and FRET observables is far from trivial. Three major routes currently exist to find a structural model satisfying FRET observables best. First, in the screening approach used by FPS, computational methods are used to initially generate a conformational ensemble that is subsequently quantitatively evaluated in terms of its agreement with the experimental FRET data. Second, in the multibody docking approach, used by CNS and FPS, the integration of FRET data into the computational modeling is achieved by addition of experiment-based distances with corresponding uncertainties as restraints that define a harmonic potential for the fluorophore center positions treated as pseudoatoms rigidly connected to the biomolecule [42<sup>••</sup>,86<sup>••</sup>]. The defined "FRET-forces" induce the docking process of the labeled domains and molecules. Many iterations (typically > 10 000) with distinct starting conditions (i.e. different randomly assigned orientations of domains and molecules, different relative conformations of flexible domains) are usually performed for each set of FRET distance restraints to cover the configurational space. As a third option, the Markov Chain Monte Carlo (MCMC) [111<sup>••</sup>] approach, among others, allows circumventing the difficulties with geometric restraints. Examples for the use of MCMC guiding in conjunction with data from FRET experiments include the generation of an open conformation of Syntaxin 1 [48] and the determination of structures of large biomolecular complexes, such as a RNAP complex [36].

Appropriate dye models, in combination with quantitative FRET studies, are crucial for the accuracy of

integrative modeling. Previously [37,85\*\*], studies utilizing the toolkit for the Nano Positioning System (NPS) have assumed the *Localized antenna/Single cone model* and have used Bayesian parameter estimation for three dimensional dye localization to extract structural information from a network of FRET measurements. The AV has been used as a *prior*, which is refined by experiments to resolve potential locations of the dyes as credible dye volume (*posterior*). The inclusion of more complex dye models into NPS has been introduced recently [100\*,112]. In its current stage of development, NPS tests the consistency of a given structural model with DA distance sets by comparing the overlap of these credible dye volumes (*posterior*, depicted in Figure 1d) with the AVs (*prior*) of the considered structural model. Initially, CNS and FPS both used the *Free Diffusion/Iso model* to consider the distribution of flexibly linked dyes. In a benchmark study with FPS, docking a DNA primer-template to HIV-1 reverse transcriptase, Kalinin et al. have shown that it is crucial for the accuracy of the docked complex to explicitly consider the spatial dye distribution [42\*\*]. CNS uses fluorophore center positions as pseudoatoms rigidly connected to the biomolecule. The position of the pseudoatom is taken as the average position of the fluorophore relative to the molecule as obtained from a molecular dynamics simulation [86\*\*,88]. Owing to the explicit treatment of the dye distance distributions, FPS can serve as an appropriate interface for this experimental input. Thus additional dye models have been included in FPS meanwhile for improving the accuracy of hybrid-FRET modeling for specific combinations of systems and labels: (1) *Free diffusion/Iso model* for organic fluorophores tethered to nucleic acids [42\*\*,61\*], (2) *Free diffusion + Contact/Iso model* for organic fluorophores tethered to proteins (this work), and (3) *SAW-Diffusion/Iso model* for fusion proteins [103,104\*]. Finally, Preus et al. [35\*] developed the toolkit FRET-matrix for modeling FRET between probes possessing limited diffusional and rotational freedom. This toolkit is especially useful for localized fluorophores in nucleic acids as a replacement for one of the natural bases [113] giving the advantage of reporting from internal sites of interest.

Currently, structural models from hybrid-FRET modeling cannot be deposited in the Worldwide Protein data Bank (wwPDB) [114,115]. At present, the authors have two alternatives to archive the coordinates of suggested structural models: (1) provide them as supplementary information with the publication or (2) deposit them in the Model Archive (MA, [www.modelarchive.org](http://www.modelarchive.org)), which assigns a unique stable accession code (DOI) to each deposited model. The Model Archive is being developed following a community recommendation during a workshop on applications of protein models in biomedical research [57] as part of the Protein Model Portal (<http://www.proteinmodelportal.org>; [116]). Advantageously, it offers

the opportunity to apply consistent assessment and validation criteria to the complete set of structural models available for proteins. Moreover, it allows providing in depth information about the simulations performed and the parameters and constraints used. Therefore we decided to deposit all data of the presented test case study in the Model Archive with the DOI: 10.5452/ma-a2hbq.

Finally, it is important to note that the wwPDB is aware of the need for a large and general repository for structural models of biomolecular systems that have been obtained by integrative modeling using varied types of experimental data and theoretical information [38]. Establishing community-wide accepted standards for measuring, analyzing, and describing FRET data is an additional step necessary for organized data deposition.

### Hybrid-FRET modeling on rails: a case study

#### *Which information can be obtained by a hybrid-FRET study?*

The aim of hybrid-FRET modeling is to describe macromolecules that potentially adopt multiple dynamically exchanging conformations in thermal equilibrium by three-dimensional structural models derived from prior structural knowledge and multiple quantitative FRET measurements [42\*\*,88]. To provide an informative answer, our hybrid-FRET modeling procedure is organized such that a spectrum of possible solutions (structural arrangements) is collected from all structural background information (e.g. X-ray structures, homology/comparative models and/or at least educated guesses) whose suitability is under question. We use this initial information (*prior*) in step I of the workflow considering two perspectives. From the first perspective, experiments are designed to *confirm* our *prior* structural knowledge. If the experiments prove to be inconsistent with this *prior*, we consider the design also from the second perspective that the experimental information can be used to generate a three-dimensional structural model as *posterior* hypothesis. To test our *prior* (i.e. the structural background information), we seek DA pairs with the largest power in proving our null hypothesis that the initial structural information is incorrect (step I of the workflow). We identify such DA pairs by exploring a range of possible conformational motions of the system, given the *prior* knowledge. At this stage, unbiased and extensive coverage of the structural space is more important than the accuracy of structures or the density of the generated ensemble. To extract the most useful information from the system of interest, we established an iterative workflow for hybrid-FRET modeling consisting of five steps:

Step I: Defining specific questions about the biomolecular system of interest and initializing modeling by collecting *prior* knowledge to generate an initial structural ensemble and to determine the most informative DA pairs.

Step II: Performing calibrated FRET measurements and quantitative analysis.

Step III: Computational modeling to improve the sampling density of the initial ensemble guided by the obtained experimental FRET data. Identifying the best structures by screening and computing the precision of the obtained ensemble.

Step IV: Judging the agreement between the modeled structure and experimental data to decide whether the steps I to III should be repeated.

Step V: Assessing the quality of the obtained conformational ensemble with respect to the FRET data (precision and accuracy) and to the structural modeling (judgement by short-range stereochemical criteria).

**Choosing informative DA pairs — an experimental design problem.** The choice of DA pairs for FRET experiments is an essential initial step. It represents a classical experimental design problem [117] which influences the obtained structural model in terms of the precision and accuracy. More explicitly, the question is, which DA pairs should be measured such that the obtained information is maximized with respect to its power to discriminate structures of the initial ensemble. Two cases need to be distinguished for the selection of DA pairs. If structural pre-knowledge is unavailable or not fully considered, the localization of the fluorophores themselves is of interest. Thus, connected networks of DA pairs are needed and the dyes are localized by trilateration approaches [37,100\*].

In the second case, if structural pre-knowledge is available, usually not all DA pairs are equally informative. Therefore it is advantageous to select a small set of most informative DA pairs because in real experiments, acquisition of reliable data is challenging due to the involvement of multiple steps, that is, mutagenesis, protein expression, purification, biochemical activity assays and measurements.

Here, we define distance sets to be the most informative if they lead to the highest expected precision of a structural model. To achieve high precision with a minimum set of DA pairs  $\{DA^{(i)}\}$  for a well-planned experiment, we formalize the design of  $\{DA^{(i)}\}$  to automate generation of FRET-based structural models. Thus, we establish a quality parameter,  $\langle \Delta_{set} \rangle_{ref}$  for a given  $\{DA^{(i)}\}$  by defining its expected precision (uncertainty). First, each conformer is used as a reference to compute the reference-specific precision  $\Delta_{set}$  for  $\{DA^{(i)}\}$ . Here the precision corresponds to the weighted average  $C_\alpha$  atom RMSD over all conformers with respect to the chosen reference conformer. The weight of the conformer is determined by its confidence in being a worse model compared to the reference

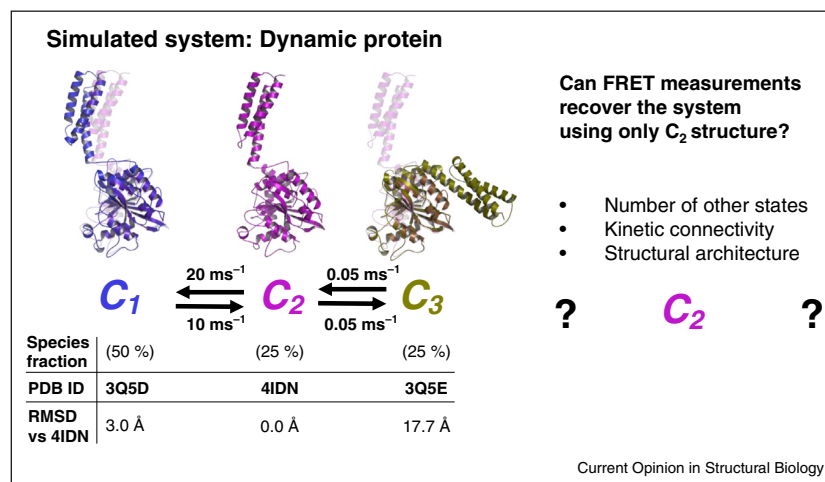
model as judged by squared, error weighted deviations. Second, the average over the reference-specific precisions yields  $\langle \Delta_{set} \rangle_{ref}$ . To find an informative distance set  $\{DA^{(i)}\}$ , we apply a greedy backward elimination feature selection algorithm [118] to minimize  $\langle \Delta_{set} \rangle_{ref}$ . In this algorithm, DA pairs that lead to the smallest decline of  $\langle \Delta_{set} \rangle_{ref}$  (i.e. smallest increase in RMSD) were iteratively excluded from the set. As the set of possible DA pairs is limited to several thousand pairs, the computational burden of this algorithm is low enough to complete within  $\sim 24$  h on a desktop PC.

For the first iteration of the hybrid-FRET modeling workflow (Figure 3), ten distances were selected (Figure 4a). In real experiments, suggested DA pairs might be discarded to minimize errors (see Section ‘Error estimation’). Structural aspects relevant for biochemical activity (binding pockets, stabilizing salt bridges, and so on) and fluorescence properties (quenching amino acids) should be considered in the selection procedure to minimize the effects of the labels on the biomolecular function and to optimize their fluorescence properties.

**Generating hybrid-FRET models for a heterogeneous system in the presence of fast dynamics for the test case Atlantin-1.** To study the accuracy and precision of hybrid-FRET modeling, we designed a test case and simulated a protein with three exchanging conformers. The used structures of the conformers are structurally well-characterized by X-ray crystallography. We simulated typical data traces of single-molecule FRET experiments with multi-parameter fluorescence detection for typical conditions [60\*\*,119]. In this way, the known X-ray structures can serve as unquestioned references for the assessment of the structural models obtained by hybrid-FRET modeling using our FPS toolkit.

We chose to study the cytoplasmic part (residues 1–446) of the large GTPase human Atlantin-1, which belongs to the dynamin superfamily. This part consists of two flexibly connected domains, the N-terminal GTPase domain (G domain) and the C-terminal middle domain, for which three distinct conformations in the functional cycle were found by X-ray crystallography. For the simulations of smFRET experiments, we chose the monomeric subunits of two crystallographic dimers (PDB-IDs 3Q5D [120] and 4IDN [121]) and a tetramer (PDB-ID 3Q5E [120]), depicted in Figure 2, named here  $C_1$ ,  $C_2$ , and  $C_3$ . To the best of our knowledge, nothing is known about conformational dynamics of Atlantin-1 in solution. Thus, in a Gedankenexperiment, we assumed the existence of a putative dynamic exchange equilibrium with the linear reaction scheme  $C_1 \rightleftharpoons C_2 \rightleftharpoons C_3$  (Figure 2). The conformer  $C_3$  differs significantly from the conformers  $C_1$  and  $C_2$ . In contrast, the structures of conformers  $C_1$  and  $C_2$  are similar to each other (RMSD 3.0 Å). Therefore, we simulated a fast exchange between  $C_1$  and  $C_2$  (kinetic

Figure 2



Presentation of the test case Atlastin. Overview of the benchmark test system. For the benchmark test, we used three crystal structures of Atlastin-1, which are termed  $C_1$ ,  $C_2$ , and  $C_3$  (PDB-ID: 3Q5D (chain A) [120], 4IDN (chain A) [121], and 3Q5E (chain A) [120], respectively). We simulate the kinetic exchange between  $C_1$  and  $C_2$  to be fast, and the exchange between  $C_2$  and  $C_3$  to be slow. Our task was to recover the number of other states, their kinetic connectivity, and their structures, given only the structure (PDB-ID: 4IDN) and information from smFRET spectroscopy.

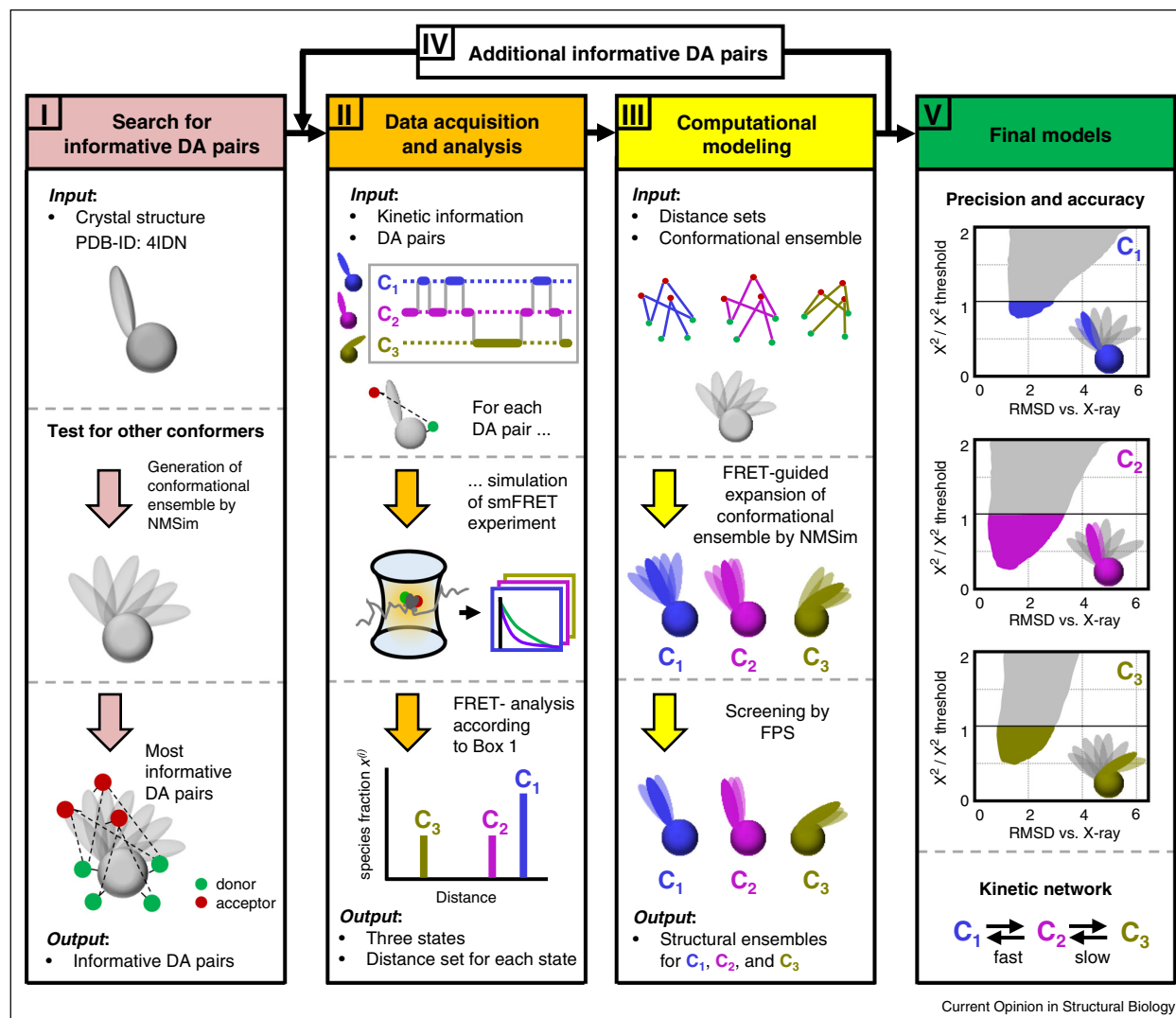
relaxation time  $t_{R,1-2} = 30 \mu\text{s}$ ) and a slow exchange between  $C_2$  and  $C_3$  ( $t_{R,2-3} = 10 \text{ ms}$ ). In the test case, we utilized the crystal structure (PDB-ID: 4IDN) as a *prior* for structural simulations. Note, however, that all experimental FRET observables were simulated from the three “true” crystallographic structures to test whether they could be recovered by hybrid-FRET modeling. Thus, we aimed at finding suitable structural models for  $C_1$ ,  $C_2$ , and  $C_3$  and recovering the kinetic exchange equilibrium by treating the simulated photon traces identical to single-molecule FRET experiments using a data generator (for details see [119]) that generated photon streams of typical single-molecule experiments by Brownian dynamics (BD) simulations.

In real experiments, fluorescence decays are complex due to DA distance distributions, brightness distributions due to the confocal excitation profile and experimental nuisances such as instrumental response function and detector dark counts. All these aspects are reproduced by the simulations of freely diffusing molecules, to generate realistic photon traces. Technical details are given in detail in [119] and are outlined below. As in real single photon counting experiments, the Poissonian statistics determines the experimental noise and thus the statistical errors of the subsequent analysis. The simulations correspond to  $\sim 3$  measurement hours with current instrumentation in the Seidel group. In this test case, we want to study whether the simulated data of typical experimental quality allows us to recover accurate hybrid-FRET models and explore experimental limits on their precision.

**FRET on rails: Step I.** We started our hybrid-FRET modeling (Figure 3) by testing the null hypothesis that our *prior* will *not* be described by experiments. To design an optimal set of DA pairs for this test, we use the toolkit NMSim to generate an ensemble unbiased by experimental FRET data with 400 000 conformers (RMSD from PDB-ID: 4IDN up to 26 Å) as alternative candidates to the *prior*. NMSim is a normal mode-based geometric simulation approach for multiscale modeling of protein conformational changes that incorporates information about preferred directions of protein motions into a geometric simulation algorithm [122,123]. The obtained ensemble was clustered and used to select an optimal set of DA pairs according to three criteria. At first, all residues that are positioned on the protein surface and are located far enough from quenching amino acid residues (Trp, Tyr, His, Met) [124] were selected. Secondly, from all pairwise combinations of these labeling positions, those that result in average inter-dye distances  $>30 \text{ Å}$  were selected. Thirdly, we determined the most informative distances from a matrix of inter-dye distances as described above.

**FRET on rails: Steps II + III.** Next, we have to test the null hypothesis using this initial distance set. In real situations, we have to prepare a set of samples and perform a series of measurements of freely diffusing molecules. However, in this test study, we replace the experimental data acquisition by simulations for a set of 10 hypothetical FRET samples with the mixtures of appropriately labeled Atlastin-1 conformers.

Figure 3



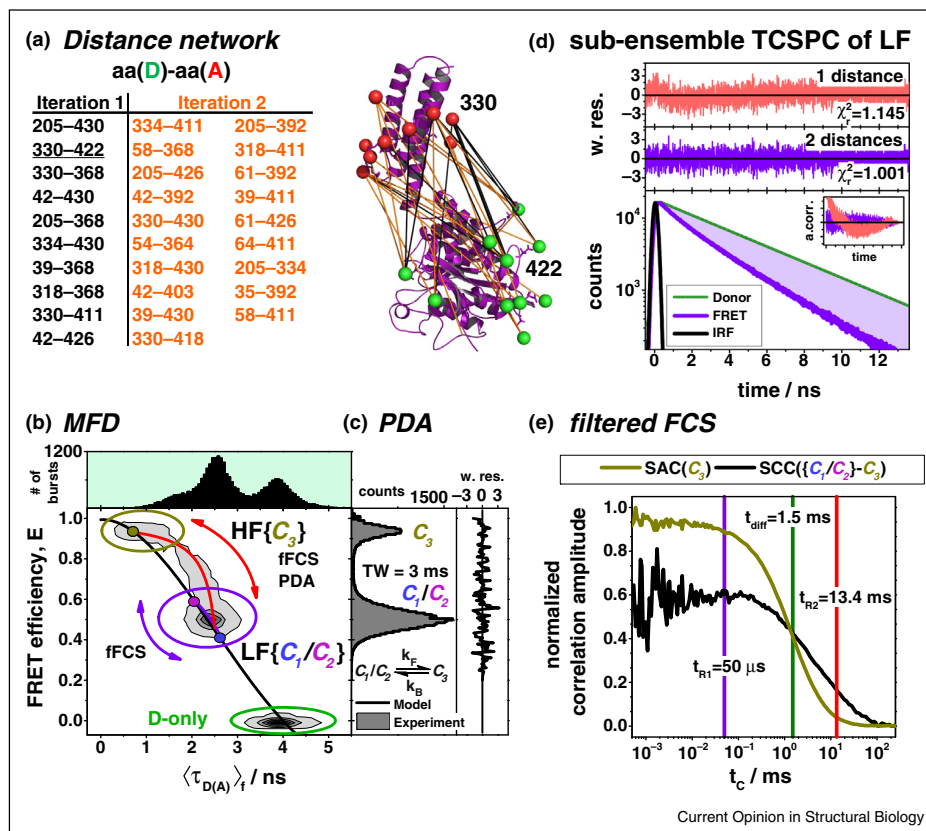
Complete workflow of FRET-restrained structural modeling. Workflow for the benchmark test using three distinct crystal structures of Atlastin-1. **Step I:** Starting from the crystal structure (PDB-ID: 4IDN), we generated a conformational ensemble by NMSim, which was subsequently clustered. From this, we derived the most informative donor-acceptor (DA) pairs, which can distinguish between these clusters. These DA pairs serve as one of the inputs for the next step. **Step II:** The previously determined DA pairs, crystal structures, and the kinetic scheme (Figure 2) were used to simulate smFRET experiments. In the simulations, the molecules randomly exchange their conformation, diffuse freely, and emit fluorescence if they diffuse through the confocal detection volume. The simulated photon trajectories were analyzed according to Box 1 to yield for each DA pair a conformer-specific distance and a species fraction  $x^0$ . This results in a distance set for each of the three conformers, which is used in the next step. **Step III:** Structural modeling was based on the distance sets determined in step II and the conformational ensembles generated in step I. Using fitted distance sets, we applied FRET-guided NMSim to expand the conformational ensemble of each conformer. Subsequently, we screened the resulting conformational ensemble with the FPS software to identify conformers that are in agreement with the simulated experiment. **Step IV:** A second round repeating steps II and III, which considers additional DA pairs, improved the discrimination power and increased the resolution. **Step V:** The final models were chosen by selecting those that are within the 68% confidence level.

In *in silico* MFD-experiments, we simulate: (1) diffusion of individual molecules; (2) dynamic exchange of the states; (3) the confocal excitation profile and observation volume; (4) the photon emission as Poissonian process, which follows the conformer-specific fluorescence decay  $f_{D(A)}(t)$

(Eq. (2)) described by the excited state depopulation with  $k_{D,0}$  and FRET-induced quenching with a distributed  $k_{RET}^{(i)}$  due to flexibly linked dyes; and (5) experimental nuisances such as the instrumental response function (IRF), background fluorescence and experimental calibration



Figure 4



Analysis of simulated FRET data. Fluorescence analysis workflow. **(a)** The distance network used to simulate the fluorescence experiments was constructed in two iterations. After a first analysis round (iteration 1, black), the network was extended by additional distances (iteration 2, orange). The analysis workflow is shown for the highlighted DA pair. **(b)** Confocal sm experiments with pulsed excitation (73.56 MHz) and time-resolved multi-parameter fluorescence detection (i.e. spectral and polarization resolved detection) [60\*\*] were simulated for every DA pair using a data generator as described in detail in [119], that generated photon streams of typical single-molecule experiments by Brownian dynamics (BD) simulations. The fluorescence decay of D and A in absence of FRET was modeled by single exponential decays using a fluorescence lifetime of D of  $\tau_{D(0)} = 4$  ns and A of  $\tau_A = 1$  ns, respectively. Their time-resolved anisotropies were modeled using mean rotational correlation times of 1 ns. The fluorescence signal was modeled to yield  $\gamma = 1$  as calibration parameter. The DA distance distributions were simulated by ACV simulations, which resulted in an average DA distance half-width of 10.4 Å. The optical detection profile of the setup was simulated by a 3D-Gaussian, which decayed at a radius of  $\omega_0 = 0.5 \mu\text{m}$  ( $x, y$  direction) and  $z_0 = 2.25 \mu\text{m}$  ( $z$  direction) to a value of  $1/e^2$ . To assure single-molecule conditions we simulate experiments with a mean number of 0.004 molecules in the focus which diffuse with a diffusion time  $t_{\text{diff}} = 1.5$  ms as defined by FCS. First, single molecule bursts of the interconverting conformers ( $C_1$ ,  $C_2$ , and  $C_3$ ) were classified in 2D frequency histograms by their FRET-efficiency and intensity-weighted average donor fluorescence lifetime  $\langle \tau_{D(A)} \rangle_f$ . The number of molecules (bursts) is scaled from light grey (lowest) to black (highest). The 1D histogram of  $\langle \tau_{D(A)} \rangle_f$  is given as a projection on the top. In the 2D-histogram, three peaks a high FRET (HF, yellow), low FRET (LF, violet) and a peak corresponding to FRET-inactive molecules (D-only, green) are visible. These peaks can be described by static and dynamic FRET lines. The static FRET line (black) describes the theoretical relationships between the FRET efficiency and  $\langle \tau_{D(A)} \rangle_f$  for all molecules in the absence of protein dynamics. Deviation from the static FRET line towards longer fluorescence lifetimes indicates conformational dynamics. Dynamic FRET lines are defined by the limiting states of the dynamic processes. The FRET-efficiencies and  $\langle \tau_{D(A)} \rangle_f$  of the conformers  $C_1$ ,  $C_2$ , and  $C_3$  are shown as yellow, magenta, and blue filled circles, respectively. Dynamic FRET lines of the  $C_1$ - $C_2$  transition and a  $C_3$ - $C_1/C_2$  transition are shown in violet and red, respectively.  $C_1$  and  $C_2$  are in fast exchange (violet arrow) while  $C_3$  exchanges slowly with  $C_2$  (red arrow). Therefore, only an average of  $C_1$  and  $C_2$  LF{ $C_1/C_2$ } is resolved. **(c)** Dynamic PDA (time-window,  $TW = 3$  ms) characterizes the slow  $C_3$ - $C_1/C_2$  exchange by the analysis of FRET-efficiency histograms (data, grey) by a kinetic two-state model (fit, black line) and recovers fluorescence-averaged distances of  $C_3$  (33.6 Å) and  $C_1/C_2$  (52.5 Å). Weighted residuals are shown to the right. **(d)** Sub-ensemble donor fluorescence decay analysis of the LF population resolves  $C_1$  and  $C_2$  as individual components. The donor fluorescence decay in the absence of FRET serves as reference. The instrument response function (IRF) is shown as black line. The magenta region shows the number of photons of the donor quenched due to FRET. On top of the fluorescence decay, the weighted residuals (w.res.) of a one-component (1 distance, red) and a two-component model (2 distances, violet) are shown. As visualized by the auto-correlation of the weighted residuals, the one-component model is significantly worse and is therefore discarded ( $p$  value  $> 0.99$ ) **(e)** Filtered fluorescence correlation spectroscopy (fFCS) computes the species-specific cross-correlation (SCC) between HF{ $C_3$ } and LF{ $C_1/C_2$ }. The species auto correlation (SAC) of  $C_3$  recovers the diffusion time  $t_{\text{diff}}$ . The presence of two anticorrelation terms in the SCC indicates three kinetic states. The analysis of the SCC recovers characteristic relaxation times  $t_{R1}$  and  $t_{R2}$  of the  $C_1$ ,  $C_2$ , and  $C_3$  kinetics.

factors. Finally, to generate brightness  $Q$  and fluorescence decays  $f_{D(A)}(t)$  for each state in the simulated single-molecule experiment, we used the crystal structures as input. This involved two steps. First, DA distance distributions  $x(R_{DA})$  of the selected FRET pair were calculated using two inputs, the crystal structures of  $C_1$ ,  $C_2$ , and  $C_3$ , respectively, and the *Free diffusion+Contact/Iso model* defining the corresponding accessible contact volumes. Second, the obtained respective  $x(R_{DA})$  for  $C_1$ ,  $C_2$ , and  $C_3$  were used to calculate the FRET observables (fluorescence intensity decays  $f(t)$  and transfer efficiencies  $E$ ) according to Eqs. (1)–(3) (the assumed fluorescence parameters of the dyes are compiled in the caption of Figure 4). The transfer efficiencies  $E$  were used to calculate the brightness  $Q$  as described previously [60\*\*]. All simulation parameters are compiled in the caption of Figure 4b.

The analysis of the fluorescence signals of the sm experiments simulated in step II of the workflow follows the procedures described in Box 1. First, the bright fluorescence bursts due to single-molecule events with durations of a few milliseconds were identified and selected in the time trace by separating them from the low background of 1–2 kHz. Second, for each single-molecule burst, all fluorescence parameters were determined as described in [60\*\*]. To check for the presence of exchange dynamics, the FRET indicators, FRET efficiency  $E$  and the donor fluorescence lifetime  $\tau_{D(A)}$  were plotted in two dimensional frequency MFD histograms (Figure 4b) to analyze the location of the bursts using the static (black) and dynamic (red) FRET lines [60\*\*].

The number of conformers and their species fractions were identified as follows. A time window-based analysis by dynamic photon distribution analysis (dynPDA) [24\*] resolved the FRET averaged distances  $\langle R_{DA} \rangle_E$  of a small population ( $\sim 25\%$ ) with high FRET efficiencies, referred to as HF population, which is in slow exchange with a second population with a lower FRET efficiency ( $\sim 75\%$ ), referred to as LF population (Figure 4c). To test whether these populations are homogeneous, we performed a sub-ensemble TCSPC analysis of both populations. While the fluorescence decay of the HF population could be fitted with a single distance distribution (i.e. a single FRET species) (Eq. (2)), two distance distributions (i.e. two FRET species) were needed to describe the decay of the LF population (Figure 4d). The necessity of two FRET species in the LF population was judged by comparing the goodness of the fits for one and two distance distributions using weighted residuals (w.res.), the autocorrelation function (a.corr.) of the residuals, and  $\chi_r^2$ . Overall, sub-ensemble TCSPC and PDA analysis allowed us to resolve three FRET species. PDA identifies two dynamically exchanging populations. One of these populations is resolved into two distinct populations by sub-ensemble TCSPC (seTCSPC). We formally assign the HF population to the conformer ( $C_3$ ) and the LF

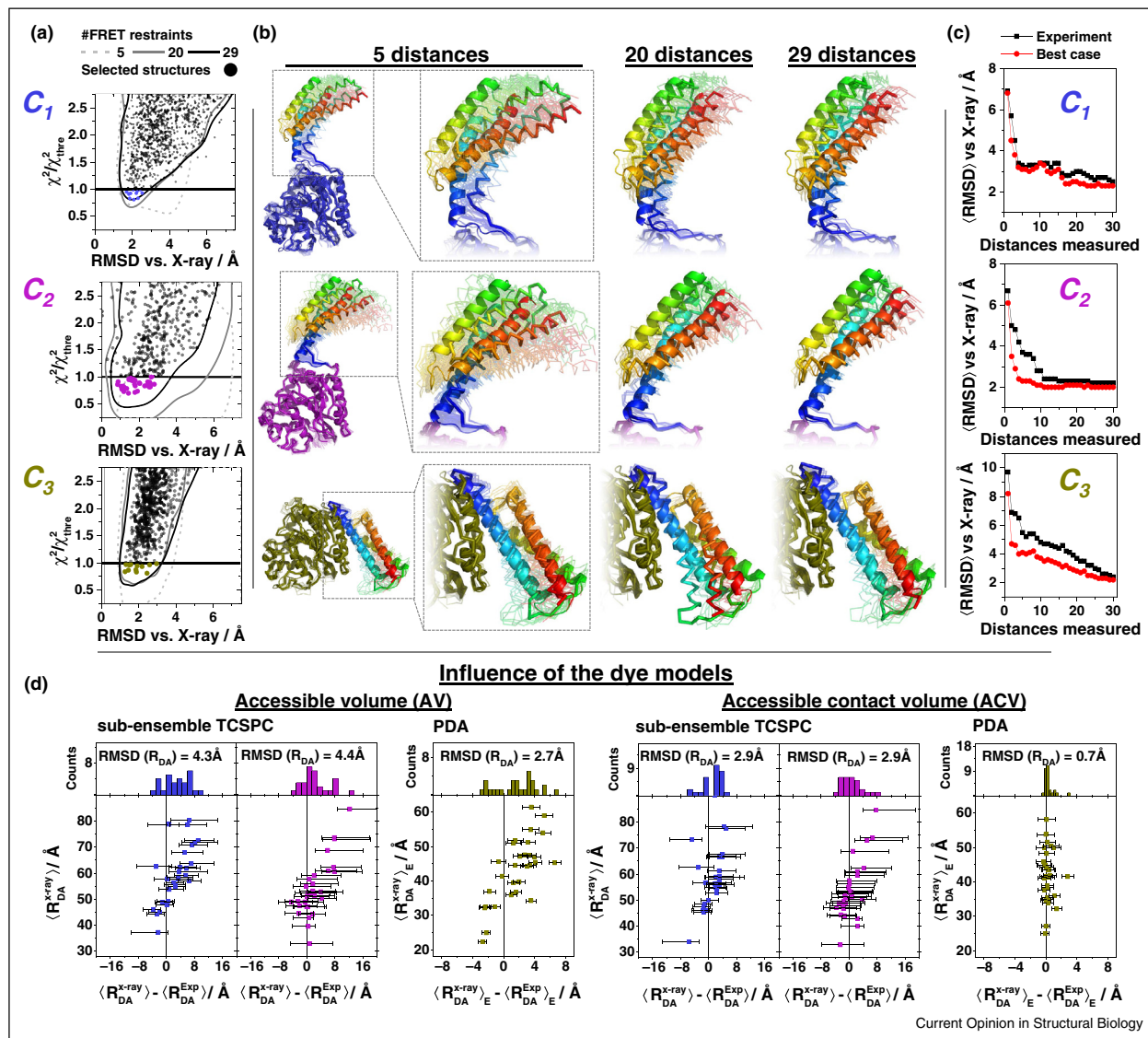
population to a dynamic mixture of  $C_1$  and  $C_2$ , which is separated from  $C_3$  by a large kinetic barrier with a relaxation time of  $\sim 10$  ms.

To resolve the heterogeneity of the averaged  $\{C_1/C_2\}$  population, the fluorescence decays of the respective sub-ensembles for all 10 simulated single-pair FRET experiments were analyzed by a joint model, which assumed global species fractions of the  $\{C_1/C_2\}$  population and Gaussian-distributed distances. Only this joint analysis is capable of recovering the experimental global species fractions  $x_1 = 50\%$  and  $x_2 = 25\%$ , which agree well with input values used in the simulation (Figure 2). The presence of exchange kinetics is independently detected by filtered fluorescence correlation spectroscopy (fFCS) [23\*,119] (Figure 4e) by computing the species cross-correlation function (SCC( $\{C_1/C_2\} - C_3$ )) that analyzes the exchange between the fast interchanging populations  $\{C_1/C_2\}$  and  $C_3$ . The SCC exhibits two relaxation times, which is additional evidence for the existence of three conformational states. The fast relaxation time  $t_{R1} = 50 \mu\text{s}$  exactly corresponds to the one used in the simulations to describe the exchange between  $C_1$  and  $C_2$ . Even though the lifetimes of the conformers  $C_1$  and  $C_2$  are short (100 and 50  $\mu\text{s}$ , respectively), MFD, se-TCSPC and fFCS analysis unequivocally identified three FRET species together with their species fractions, respective distances and corresponding exchange kinetics. The errors of these distances  $\Delta R_{DA}^2(E)$  were determined by propagating the experimental noise to the model parameters. As this analysis revealed three states, we accept the null hypothesis and reject the initial assumption that the crystal structure describes the experimental sample.

Therefore, in step III of the workflow, we explore the information contained in the experiments by screening the entire ensemble using FPS [42\*\*]. This screen selects an ensemble of iteration 1 for the structural models of  $C_1$ ,  $C_2$  and  $C_3$  as *posterior* hypothesis.

**FRET on rails: Step IV.** To improve the precision of our *posterior* model, we performed the iteration step IV by repeating the DA pair selection procedure now using the reduced ensemble of iteration 1. Based on this analysis, we chose 19 additional informative DA pairs (Figure 4a). For these pairs, we again simulated smFRET experiments following step II as described above. After the analysis, our distance set for each conformer contained 29 distances. We then used these expanded distance sets of iterations 1 and 2 to model the respective structures applying FRET-guided NMSim simulations and subsequent screening by FPS (step III). We monitored the improvement of accuracy and precision for each conformer (Figure 5c). Since the RMSD value from the X-ray structure levels off at 25–29 distances for the best-case prediction and the recovered experimental accuracy for

Figure 5



Assessment of the hybrid-FRET structural models. Outcome of hybrid-FRET structural modeling of the three Atlastin-1 conformers. **(a)** The sum of squared deviations weighted by the estimated experimental error  $\chi^2$  relative to a threshold value  $\chi_{\text{threshold}}^2$  estimated for the confidence level of 68% with respect to the best structure is plotted against  $C_{\alpha}$  root-mean-square deviations (RMSD) from the corresponding crystal structure for 5 (dashed contour), 20 (grey contour), and 29 (black contour) measured distances. Black dots represent conformers corresponding to the set of 29 distances. Contours are drawn using a kernel density estimate. Colored dots represent selected conformations for the set of 29 distances. RMSD versus X-ray is calculated excluding flexible loops using the residues 35–99, 122–147, 157–189, 209–237, 257–277, 292–332, and 349–437. **(b)** Overlay of the crystal structures (cartoon representation), selected ensembles (transparent ribbon, 68% confidence), and best ( $\chi_{\text{min}}^2$ ) structures (solid ribbon) for the sets of 5, 20, and 29 distances. **(c)** Improvement of the corresponding accuracy with respect to the number of distances measured. Accuracy is calculated as  $\chi^2$ -weighted average  $C_{\alpha}$  RMSD from the corresponding crystal structure. Black line represents the improvement using experimentally measured distances, the red line represents the best-case scenario where all the distances measured agree perfectly with the ones predicted for the crystal structure. **(d)** Comparison for the deviations between measured distances and distances predicted from the crystal structure by AV and ACV dye models.

all conformers, further measurements would not improve the accuracy of the obtained structures for Atlastin-1. However, in the case of remaining ambiguity for the solutions, additional iterations through steps IV and II

(determining DA pairs, simulating and analyzing smFRET experiments), and step III (structural modeling and subsequent screening) could improve the models even further.



**FRET on rails: Step V (Figure 3).** We screened all generated structures using FPS, which yielded FRET-selected ensembles of iteration 2 for each conformer  $C_1$ ,  $C_2$ , and  $C_3$ , using the confidence level threshold of 68%.

**Accuracy and precision of FRET-derived structural models for the test case Atlastin-1.** The accuracy and precision of the hybrid-FRET structural models obtained by the iterative workflow (Figure 3) is summarized in Figure 5a. We judge the accuracy of the method by plotting the conformer specific  $f$ -value ( $\chi^2/\chi_{threshold}^2$  ratio) versus the  $C_\alpha$  RMSD of the modeled structures from the corresponding target crystal structure. The  $\chi_{threshold}^2$  value is estimated for the confidence level of 68%. For all states, the accuracy of the selected structures at a confidence level of 68% using 29 distances ranges between 1 and 3 Å. As we are interested in large-scale rearrangements of the super-tertiary structures, we exclude minor rearrangements of the sub-domains for the estimation of our accuracy (Figure 5a). To minimize the effect of non-uniform sampling, we use cluster representatives with a RMSD threshold of 1 Å (complete linkage) [125]. Cluster representatives below a confidence level of 68% for 29 distances are shown as colored dots. An overlay of the selected cluster representatives and the best model structure (highlighted by solid ribbons) visualizes the precision, which is given by the structural diversity within the selection (Figure 5b). To emphasize the differences, we aligned the representatives to the rigid G domain of the conformers. Within our precision (confidence level 68%) we can distinguish all three conformers, even  $C_1$  and  $C_2$  (i.e. the conformational ensembles do not overlap).

To capture the general dependence of the accuracy on the number of measured distances, we calculate an average RMSD that is weighted by the probability of agreement with the experimental distances as judged by  $\chi^2$  of the corresponding structural model. In Figure 5c, this average RMSD is used as a measure of accuracy, and shown as a function of the number of measured distances sorted by their information content. Interestingly, this RMSD decays fast with the number of measured distances and levels off in the studied system at an RMSD value of 2 Å. The precision and accuracy of the structural model is expected to depend on three major factors: (1) the noise (uncertainty) of the experimental data, (2) its sparseness and (3) outliers. Indeed, by increasing the number of distances, the effect of noise and data sparseness decrease for all conformers as highlighted in Figure 5c. The precision of the FRET-ensemble (4 to 5 Å) selected by 5 distances improves to 2 Å when 29 distances are measured. The influence of experimental noise and sparseness is seen by comparing the RMSD dependence on the number of measured distances in Figure 5c for the best case with accurate distances (black) and the real case with experimentally determined DA distances (red).

Notably, already small optimally informative set of DA pairs may provide a high accuracy (Figure 5c, red), because in the structural models obtained by NMSim (or any other computer simulation procedure)  $C_\alpha$  atoms are interdependent. Therefore, only 29 FRET measurements with realistic errors (Figure 5c, black) localize the  $C_\alpha$  positions to an RMSD of  $\sim 2$  Å; the accuracy in our test does not improve significantly even if more than 15 measurements are performed. Notably, even for a large optimal experimental dataset, a residual RMSD error will be observed, as intrinsic degrees of backbone freedom within the structural model (relatively small fluctuations of  $C_\alpha$  atoms) are not sensed by FRET. More FRET measurements would not alleviate this problem; that is, this test study reached the maximum possible precision. Finally, the third effect considering the possibility that the measurements might contain a low number of outliers, may be minimized by increasing the number of measurements, reducing the risk of systematic errors.

In crystallography, short range (up to 3 Å) stereo-chemical criteria, that is, deviations of atomic distances, angles, and dihedrals from their mean values, are used as quality criteria for obtained structures. Using such criteria (MolProbity [126]), the FRET-selected models generated by NMSim generally score better than corresponding X-ray structures. Therefore, we assess the overall quality of the structural model by experimental quality measures. As such, deviations between experimentally determined distances ( $R_{DA}^{Exp}$ ) and corresponding model distances ( $R_{DA}^{Model}$ ) are utilized as a quality indicator. Knowing the target structures in our test case, we used this indicator to assess the accuracy of different dye models (Figure 5d). We simulated our experimental information using the ACV dye model (Figure 3, step II) and, accordingly, the ACV model clearly outperformed the alternative AV model with an RMSD( $R_{DA}$ ) that is lower by  $\sim 1.5$ – $2$  Å when comparing  $R_{DA}^{Exp}$  with  $R_{DA}^{Model} = R_{DA}^{X-ray}$  (Figure 5d). Thus, parameters of coarse grained dye models such as the preferential surface residence of the dye (ACV model) may be refined experimentally by calibration studies.

## Outlook

**Hybrid/integrative modeling: Combining FRET spectroscopy with other fluorescence and biophysical methods.** To interrogate different molecular length scales, to address distinct sample properties (e.g. backbone, side chain, shape) and to cover different time scales, hybrid modeling can utilize the complementary information from a multitude of experimental techniques such as small-angle neutron scattering (SANS), small-angle X-ray scattering (SAXS), NMR-spectroscopy, EPR-spectroscopy and FRET-spectroscopy in one study [53<sup>\*</sup>,109,127–129]. Integrative modeling is a thriving direction in methodological development directed towards

a multi-dimensional structural and dynamical description of complex biomacromolecular systems [38]. However, the error assessment of the data can often be treated only semi-quantitatively, because it is difficult, perhaps impossible, to determine specific errors of each method and their relative weights in a joint analysis.

In single photon counting it is straightforward to estimate error of FRET and other fluorescence measurements due to the Poisson statistics for photon noise. Besides FRET, other fluorescence methods are usually convenient and can also provide restraints for structural modeling as described in the following examples. Photo-induced electron-transfer (PET) probes the close proximity of the fluorophore to certain electron-rich quenching amino acid residues [130,131] and hence senses conformational dynamics [132]. Fluorescence polarization senses dye mobility that can be influenced by local and global rotation [133] and by complex formation where the label can be trapped [134]. The fluorescence spectra of polarity-sensitive fluorophores, such as intrinsic fluorescent amino acid tryptophan, sense their exposure to water [135]. FRET between the fluorophores and PET with electron rich amino acid residues are often competing processes in quenching the donor fluorescence, so that this scenario was either judged as valuable information [136] or as experimental nuisance [17]. Both methods can be combined to obtain distance (PET: short range, FCS: long range) [137] as well as kinetic information [138]. Information similar to that from PET can be obtained from protein-induced fluorescence enhancement (PIFE) experiments with cyanine dyes [98,99]. Finally, SAXS and polarization resolved FCS measurements [139,140] contain information on the anisotropic rotational diffusion of macromolecules, which reports on the size and the global shape of the macromolecules.

**Maximizing data utilization by structure-based forward modeling.** In forward modeling [111], the chosen model parameters are verified by a direct comparison to the experimental data. In fluorescence experiments with single photon counting detection, forward modeling of the registered fluorescence decays and FRET efficiency histograms has a long tradition (e.g. convolution of instrument response function instead of deconvolution), because in this way the Poisson statistics of the counted photons is preserved and the experimental noise (shot-noise) is exactly known. However, since structural modeling is typically performed using distance restraints (in backward modeling; i.e. the fit is decoupled from structural model), experimental data is preprocessed by applying fluorescence models (for instance Eqs. (1)–(3)). This can lead to overestimation of the errors, if the model parameters (distances) are correlated. However, to obtain independent errors for the distance restraints, the multi-dimensional uncertainties of the distances are projected

to one dimension (i.e. marginalized). In this process, the valuable information on correlations is lost. Similar to peak assignment problems in NMR spectroscopy [111], correlations can be preserved by forward modeling which utilizes a structural model as a global model for the experimental data, maximizing the recovered information and minimizing ambiguities. Dye models must be applied to directly link the structural model to the fluorescence decay. For this purpose AV, ACV or more complex spatial dye distributions can be used. In this forward fitting approach the structural model is varied for optimal agreement with experiment.

**Hybrid-FRET studies in live cells.** The FRET technique offers unique advantages for characterizing large biomolecules with high specificity and sensitivity in living cells or *in vitro*. Time-resolved FRET studies can deal with heterogeneous samples and make use of the single-molecule advantage so that a quantitative FRET analysis can be combined with normal [141,142] and super-resolution [143] imaging to gain insight into the biological function of biomolecules in their cellular context (e.g. localizing complexes inside of cells [141], quantifying binding to interaction partners [104], and validating structural models [103,144,145]). For example, we could show by detailed hybrid-FRET studies of murine immune defense Guanylate binding proteins with GFP and mCherry fusions that they undergo reversible structural transitions between monomeric, dimeric and oligomeric states as revealed by a quantitative analysis of homo- and hetero-FRET [104]. Notably, the degree of oligomerization is specific to the localization in live cells. Detailed hybrid-FRET studies allowed us to characterize the structures of the dimer and oligomer.

Comparative studies of cell-like environment and dilute solutions were used to extrapolate excluded volume effects from *in vitro* experiments to live-cells [146], and to identify biomolecular stabilization mechanism caused by macromolecular crowding [147]. Microinjection allows one to control the concentration of biomolecules labeled by photostable fluorophores and therefore enables the study of crowding effects in live cells [28]. In this way, single-molecule conditions can be achieved by tracking microinjected *in vitro* purified FRET-labeled proteins to study complex formation and conformational changes of individual proteins [148]. This approach, combined with fast confocal detection, was used to probe protein dynamics from millisecond down to the nanosecond regime [149].

In conclusion, the presented hybrid-FRET methods actually allow realizing an integrated molecular fluorescence microscope combining optical and computational microscopy [58] at a huge spatial and temporal range to display suitably labeled biomolecular systems at unprecedented resolution by atomistic structural models.

## Further information

For the presented test case study on Atlastin-1, all structural models presented in Figure 5, additional detailed information on the applied procedures and the simulated sm FRET data are deposited in the Model Archive with the DOI: 10.5452/ma-a2hbq.

## Conflict of interest

Nothing declared.

## Acknowledgments

We thank Stanislav Kalinin, Jens Michaelis and Oleg Opanasyuk for fruitful discussions on integrative FRET-modeling. We are grateful to Suren Felekyan for supporting the fluorescence simulations and Katherina Hemmen for her support in preparing figures. This work was supported by the European Research Council through the Advanced Grant 2014 hybridFRET (671208). The authors acknowledge the stimulating networking support by the COST Action CM1306 – Understanding Movement and Mechanism in Molecular Machines.

## References and recommended reading

Papers of particular interest, published within the period of review, have been highlighted as:

- of special interest
- of outstanding interest

1. Förster T: **Zwischenmolekulare Energiewanderung und Fluoreszenz.** *Ann Phys* 1948, **437**:55-75.
  - In this seminal paper Förster derived the correct distance and orientation dependence of the FRET-rate constant for the first time. Additionally, energy migration within regular crystallographic lattices (the second part of this paper) is studied, which is still of interest for crystal like structures for instance, formed by membrane associated proteins such as GPCRs.
2. Förster T: **Experimentelle und theoretische Untersuchung des zwischenmolekularen Übergangs von Elektronenanregungsenergie.** *Z Naturforsch A* 1949, **4**:321-327.
  - In this second seminal paper Förster derived experimental observables starting from simple schemes of rate constants. Equations for fluorescence decays of donors randomly surrounded by acceptor fluorophores are presented. In this sense this fundamental paper is the basis for understanding most FRET-experiments with flexibly coupled dyads.
3. van der Meer BW, Cooker G, Chen SY: **Resonance Energy Transfer: Theory and Data.** VCH Publishers; 1994.
4. Weiss S: **Fluorescence spectroscopy of single biomolecules.** *Science* 1999, **283**:1676-1683.
5. Stryer L: **Fluorescence energy transfer as a spectroscopic ruler.** *Annu Rev Biochem* 1978, **47**:819-846.
6. Ha T, Enderle T, Ogletree DF, Chemla DS, Selvin PR, Weiss S: **Probing the interaction between two single molecules: fluorescence resonance energy transfer between a single donor and a single acceptor.** *Proc Natl Acad Sci U S A* 1996, **93**:6264-6268.
7. Pirchi M, Ziv G, Riven I, Cohen SS, Zohar N, Barak Y, Haran G: **Single-molecule fluorescence spectroscopy maps the folding landscape of a large protein.** *Nat Commun* 2011, **2**:493-499.
8. Chung HS, Eaton WA: **Single-molecule fluorescence probes dynamics of barrier crossing.** *Nature* 2013, **502**:685-688.
9. Zhuang XW, Kim H, Pereira MJB, Babcock HP, Walter NG, Chu S: **Correlating structural dynamics and function in single ribozyme molecules.** *Science* 2002, **296**:1473-1476.
10. Kim HD, Nienhaus GU, Ha T, Orr JW, Williamson JR, Chu S: **Mg<sup>2+</sup>-dependent conformational change of RNA studied by fluorescence correlation and FRET on immobilized single molecules.** *Proc Natl Acad Sci U S A* 2002, **99**:4284-4289.
11. Al-Hashimi HM, Walter NG: **RNA dynamics: it is about time.** *Curr Opin Struct Biol* 2008, **18**:321-329.
12. Roy R, Kozlov AG, Lohman TM, Ha T: **SSB protein diffusion on single-stranded DNA stimulates RecA filament formation.** *Nature* 2009, **461**:1092-1097.
13. Olofsson L, Felekyan S, Doumazane E, Scholler P, Fabre L, Zwier JM, Rondard P, Seidel CAM, Pin JP, Margeat E: **Fine tuning of sub-millisecond conformational dynamics controls metabotropic glutamate receptors agonist efficacy.** *Nat Commun* 2014, **5**:e5206.
14. Robb NC, Te Velthuis AJ, Wieneke R, Tampe R, Cordes T, Fodor E, Kapanidis AN: **Single-molecule FRET reveals the pre-initiation and initiation conformations of influenza virus promoter RNA.** *Nucleic Acids Res* 2016, **44**.
15. Diez M, Zimmermann B, Börsch M, König M, Schweinberger E, Steigmiller S, Reuter R, Felekyan S, Kudryavtsev V, Seidel CAM, Gräber P: **Proton-powered subunit rotation in single membrane-bound F<sub>0</sub>F<sub>1</sub>-ATP synthase.** *Nat Struct Mol Biol* 2004, **11**:135-141.
16. Lu HP: **Sizing up single-molecule enzymatic conformational dynamics.** *Chem Soc Rev* 2014, **43**:1118-1143.
17. Winkler JR: **FRETting over the spectroscopic ruler.** *Science* 2013, **339**:1530-1531.
18. Nettels D, Gopich IV, Hoffmann A, Schuler B: **Ultrafast dynamics of protein collapse from single-molecule photon statistics.** *Proc Natl Acad Sci U S A* 2007, **104**:2655-2660.
19. Soranno A, Buchli B, Nettels D, Cheng RR, Muller-Spath S, Pfeil SH, Hoffmann A, Lipman EA, Makarov DE, Schuler B: **Quantifying internal friction in unfolded and intrinsically disordered proteins with single-molecule spectroscopy.** *Proc Natl Acad Sci U S A* 2012, **109**:17800-17806.
20. Gopich I, Szabo A: **Theory of photon statistics in single-molecule Förster resonance energy transfer.** *J Chem Phys* 2005, **122**:014707.
  - Gopich and Szabo describe FRET-efficiency histograms (FEHs) of single-molecule FRET experiments by the photon statistics. As they consider the effect of conformational dynamics on FEH, they set the basis for quantitative time-window analysis of FEHs of dynamically exchanging species.
21. Chung HS, Gopich IV: **Fast single-molecule FRET spectroscopy: theory and experiment.** *Phys Chem Chem Phys* 2014, **16**:18644-18657.
  - In this perspective, the authors demonstrate the improvement of the dynamic range and accuracy of sm fluorescence spectroscopy at a given photon count rate by considering each and every photon and introducing a maximum likelihood (ML) method. By analyzing photon trajectories with recorded photon colors and inter-photon times of smFRET studies (protein folding), their ML method recovers parameters of a kinetic exchange model.
22. Chung HS, McHale K, Louis JM, Eaton WA: **Single-molecule fluorescence experiments determine protein folding transition path times.** *Science* 2012, **335**:981-984.
23. Felekyan S, Sanabria H, Kalinin S, Kühnemuth R, Seidel CAM: **Analyzing Förster Resonance Energy Transfer with fluctuation algorithms.** *Methods Enzymol* 2013, **519**:39-85.
  - This review describes the theory and application of fluorescence correlation spectroscopy (FCS) with different analysis procedures (classical FRET-FCS and FRET-specific species correlation by filtered FCS) to analyze FRET fluctuations in order to distinguish between different species. Filtered FCS is especially useful for systems with complex dynamics.
24. Kalinin S, Valeri A, Antonik M, Felekyan S, Seidel CAM: **Detection of structural dynamics by FRET: a photon distribution and fluorescence lifetime analysis of systems with multiple states.** *J Phys Chem B* 2010, **114**:7983-7995.
  - The authors present a method to analyze FRET efficiency histograms, taking into account shot noise and background contributions. The method can be applied to resolve the dynamically exchanging states and their kinetics. Furthermore, the authors present analysis tools to identify conformational dynamics by comparing the intensity-based and time-resolved FRET indicators  $F_D$ ,  $F_A$  and  $\tau_D$  (Eq. (1)) by calculating FRET-lines for the static and dynamic case, respectively (see Box 1). The provided theory is valuable to investigate dynamic systems.

25. McKinney SA, Joo C, Ha T: **Analysis of single-molecule FRET trajectories using hidden Markov modeling.** *Biophys J* 2006, **91**:1941-1951.  
The authors present a robust and unbiased algorithm to recover kinetic schemes from time-binned sm FRET trajectories. A number of different states and state-to-state transition probabilities can be recovered, together with the corresponding FRET efficiencies for transitions slower than the bin width. This is an effective analysis method for widely applied TIRF measurements.
26. König SLB, Hadzic M, Fiorini E, Börner R, Kowanko D, Blanckenhorn WU, Sigel RKO: **BOBA FRET: Bootstrap-based analysis of single-molecule FRET data.** *PLoS ONE* 2013, **8**:e84157.
27. Keller BG, Kobitski A, Jaschke A, Nienhaus GU, Noe F: **Complex RNA folding kinetics revealed by single-molecule FRET and Hidden Markov Models.** *J Am Chem Soc* 2014, **136**:4534-4543.  
A rigorous hidden Markov Model (HMM) analysis procedure is shown to recover states based on kinetics rather than just FRET efficiencies. For Diels-Alderase ribozyme, a seven state model with fastest interconversion timescale of 3 ms is recovered. The approach enables reconstruction of complex kinetic schemes at high temporal resolution.
28. Gao M, Gnutz D, Orban A, Appel B, Righetti F, Winter R, Narberhaus F, Müller S, Ebbinghaus S: **RNA hairpin folding in the crowded cell.** *Angew Chem Int Ed* 2016, **55**:3224-3228.
29. Schuler B, Hofmann H: **Single-molecule spectroscopy of protein folding dynamics-expanding scope and timescales.** *Curr Opin Struct Biol* 2013, **23**:36-47.  
The authors review a broad spectrum of sm fluorescence methods based on sm FRET and photo-induced electron transfer (PET) that have been developed for probing protein structure and dynamics, especially in structurally heterogeneous systems. They give an excellent overview on the applications of the kinetic experiments by discussing many processes coupled with protein folding such as misfolding, binding, transition path times and interactions with chaperones.
30. Schneidman-Duhovny D, Pellarin R, Sali A: **Uncertainty in integrative structural modeling.** *Curr Opin Struct Biol* 2014, **28**:96-104.  
This review defines the need for standards and tools to assess the input data and resulting models in integrative structural modeling. To tackle problems in integrative structural modeling they define standards for a common terminology. Furthermore, the authors point out possible sources of model uncertainty.
31. Stryer L, Haugland RP: **Energy transfer: a spectroscopic ruler.** *Proc Natl Acad Sci U S A* 1967, **58**:719-726.
32. Murchie AI, Clegg RM, von Kitzing E, Duckett DR, Diekmann S, Lilley DMJ: **Fluorescence energy transfer shows that the four-way DNA junction is a right-handed cross of antiparallel molecules.** *Nature* 1989, **341**:763-766.
33. Wozniak AK, Schröder GF, Grubmüller H, Seidel CAM, Oesterhelt F: **Single-molecule FRET measures bends and kinks in DNA.** *Proc Natl Acad Sci U S A* 2008, **105**:18337-18342.
34. Preus S, Wilhelmsson LM: **Advances in quantitative FRET-based methods for studying nucleic acids.** *ChemBioChem* 2012, **13**:1990-2001.
35. Preus S, Kilsa K, Miannay FA, Albinsson B, Wilhelmsson LM: **FRETmatrix: a general methodology for the simulation and analysis of FRET in nucleic acids.** *Nucleic Acids Res* 2013, **41**:e18.  
The presented methodology addresses the problem of deriving structures using fluorophores with fixed positions and fixed dipoles using information from fluorescence decays combined with fits directed by the structural model. The resulting toolkit FRETmatrix (<http://www.fluortools.com/software/fretmatrix>) is applied to study nucleic acid structures in 3D.
36. Mekler V, Kortkhonja E, Mukhopadhyay J, Knight J, Revyakin A, Kapanidis AN, Niu W, Ebricht YW, Levy R, Ebricht RH: **Structural organization of bacterial RNA polymerase holoenzyme and the RNA polymerase-promoter open complex.** *Cell* 2002, **108**:599-614.
37. Nagy J, Grohmann D, Cheung ACM, Schulz S, Smollett K, Werner F, Michaelis J: **Complete architecture of the archaeal RNA polymerase open complex from single-molecule FRET and NPS.** *Nat Commun* 2015, **6**:e6161.
38. Sali A, Berman HM, Schwede T, Trehwella J, Kleywegt G, Burley SK, Markley J, Nakamura H, Adams P, Bonvin A, Chiu W et al.: **Outcome of the first wwPDB Hybrid/Integrative methods task force workshop.** *Structure* 2015, **23**:1156-1167.
39. Schneider M, Belson A, Rappsilber J, Brock O: **Blind testing of cross-linking/mass spectrometry hybrid methods in CASP11.** *Proteins* 2016, **84**:152-163.
40. Tompa P: **On the supertertiary structure of proteins.** *Nat Chem Biol* 2012, **8**:597-600.
41. Knight JL, Mekler V, Mukhopadhyay J, Ebricht RH, Levy RM: **Distance-restrained docking of rifampicin and rifamycin SV to RNA polymerase using systematic FRET measurements: developing benchmarks of model quality and reliability.** *Biophys J* 2005, **88**:925-938.  
This benchmark study demonstrates positioning accuracies between 7 and 10 Å for small molecules relative to the crystallographically defined binding sites without explicitly considering dye distributions.
42. Kalinin S, Peulen T, Sindbert S, Rothwell PJ, Berger S, Restle T, Goody RS, Gohlke H, Seidel CAM: **A toolkit and benchmark study for FRET-restrained high-precision structural modeling.** *Nat Meth* 2012, **9**:1218-1227.  
The authors present a comprehensive toolkit (FRET Positioning and Screening, FPS, <http://www.mpc.hhu.de/software/fps.html>) for quantitative FRET-restrained modeling for applications in structural biology, which takes the spatial distributions of flexible linked dyes into account. In a benchmark study (docking a DNA primer-template to HIV-1 reverse transcriptase) the RMSD of the structural model to the known X-ray structure was only 0.5 Å. The FPS toolkit has two main functionalities: (1) Planning FRET experiments by calculating fluorescence observables for the given structural models; (2) FRET-based screening and multibody docking determine quantitative structural models.
43. Smock RG, Gierasch LM: **Sending signals dynamically.** *Science* 2009, **324**:198-203.
44. Henzler-Wildman K, Kern D: **Dynamic personalities of proteins.** *Nature* 2007, **450**:964-972.
45. Neudecker P, Robustelli P, Cavalli A, Walsh P, Lundstrom P, Zarrine-Afsar A, Sharpe S, Vendruscolo M, Kay LE: **Structure of an intermediate state in protein folding and aggregation.** *Science* 2012, **336**:362-366.
46. Banerjee PR, Deniz AA: **Shedding light on protein folding landscapes by single-molecule fluorescence.** *Chem Soc Rev* 2014, **43**:1172-1188.
47. Ferreon ACM, Ferreon JC, Wright PE, Deniz AA: **Modulation of allostery by protein intrinsic disorder.** *Nature* 2013, **498**:390-394.
48. Margittai M, Widengren J, Schweinberger E, Schröder GF, Felekyan S, Hausteiner E, König M, Fasshauer D, Grubmüller H, Jahn R, Seidel CAM: **Single-molecule fluorescence resonance energy transfer reveals a dynamic equilibrium between closed and open conformations of syntaxin 1.** *Proc Natl Acad Sci U S A* 2003, **100**:15516-15521.
49. McCann JJ, Zheng LQ, Chiantia S, Bowen ME: **Domain orientation in the N-terminal PDZ tandem from PSD-95 is maintained in the full-length protein.** *Structure* 2011, **19**:810-820.
50. McCann JJ, Zheng L, Rohrbeck D, Felekyan S, Kühnemuth R, Sutton RB, Seidel CAM, Bowen ME: **Supertertiary structure of the synaptic MAGuK scaffold proteins is conserved.** *Proc Natl Acad Sci U S A* 2012, **109**:15775-15780.
51. Merchant KA, Best RB, Louis JM, Gopich IV, Eaton WA: **Characterizing the unfolded states of proteins using single-molecule FRET spectroscopy and molecular simulations.** *Proc Natl Acad Sci U S A* 2007, **104**:1528-1533.
52. Kellner R, Hofmann H, Barducci A, Wunderlich B, Nettels D, Schuler B: **Single-molecule spectroscopy reveals chaperone-mediated expansion of substrate protein.** *Proc Natl Acad Sci U S A* 2014, **111**:13355-13360.
53. Aznauryan M, Delgado L, Soranno A, Nettels D, Huang JR, Labhardt AM, Grzesiek S, Schuler B: **Comprehensive structural and dynamical view of an unfolded protein from the**



- combination of single-molecule FRET, NMR, and SAXS.** *Proc Natl Acad Sci U S A* 2016, **113**:E5389-E5398.
- In this integrative structural study, the authors combine three of the most powerful biophysical methods (NMR spectroscopy, small angle X-ray scattering and smFRET measurements) available to obtain a comprehensive view on the structure and dynamics of the unfolded protein, ubiquitin, that would not be available from any of the individual methods.
54. Choi UB, Zhao ML, Zhang YX, Lai Y, Brunger AT: **Complexin induces a conformational change at the membrane-proximal C-terminal end of the SNARE complex.** *Elife* 2016, **5**:e16886.
  55. Munro JB, Gorman J, Ma XC, Zhou Z, Arthos J, Burton DR, Koff WC, Courter JR, Smith AB, Kwong PD, Blanchard SC *et al.*: **Conformational dynamics of single HIV-1 envelope trimers on the surface of native virions.** *Science* 2014, **346**:759-763.
  56. Kay LE: **New views of functionally dynamic proteins by solution NMR spectroscopy.** *J Mol Biol* 2016, **428**:323-331.
  57. Schwede T, Sali A, Honig B, Levitt M, Berman HM, Jones D, Brenner SE, Burley SK, Das R, Dokholyan NV, Dunbrack RL Jr *et al.*: **Outcome of a workshop on applications of protein models in biomedical research.** *Structure* 2009, **17**:151-159.
  58. Lee EH, Hsin J, Sotomayor M, Comellas G, Schulten K: **Discovery through the computational microscope.** *Structure* 2009, **17**:1295-1306.
  59. Clegg RM: **Fluorescence resonance energy transfer and nucleic acids.** *Methods Enzymol* 1992, **211**:353-388.  
This review provides an introduction to FRET and presents elegant and simple methods to determine absolute FRET efficiencies by steady state fluorimeters. This allows one to obtain structural insights on the ensemble level using standard instrumentation.
  60. Sisamakris E, Valeri A, Kalinin S, Rothwell PJ, Seidel CAM: **Accurate single-molecule FRET studies using multiparameter fluorescence detection.** *Methods Enzymol* 2010, **475**:455-514.  
This review gives an introduction to single-molecule FRET experiments and analyses. It focuses on confocal detection of freely diffusing molecules by multi-parameter fluorescence detection. The authors describe qualitative and quantitative analysis methods for single-molecule FRET measurements and their prerequisites. Quantitative analysis of FRET measurements is the basis for FRET-based structural modeling.
  61. Sindbert S, Kalinin S, Hien N, Kienzler A, Clima L, Bannwarth W, Appel B, Muller S, Seidel CAM: **Accurate distance determination of nucleic acids via Förster Resonance Energy Transfer: implications of dye linker length and rigidity.** *J Am Chem Soc* 2011, **133**:2463-2480.  
This study relates dye linker length flexibilities to experimental FRET observables by measuring the fluorescence lifetimes and anisotropies of donor (Alexa 488) and acceptor (Cy5) dyes, respectively, tethered to dsRNA and dsDNA. For dyes with short linkers and unknown local environments, positional-related and orientational-related uncertainties outweigh better defined dye positions. For FRET-based structure determination of very high accuracy using dyes with long linkers, a procedure (accessible volume simulations) to model the spatial dye distributions is introduced.
  62. Widengren J, Schweinberger E, Berger S, Seidel CAM: **Two new concepts to measure fluorescence resonance energy transfer via fluorescence correlation spectroscopy: theory and experimental realizations.** *J Phys Chem A* 2001, **105**:6851-6866.
  63. Rothwell PJ, Berger S, Kensch O, Felekyan S, Antonik M, Wöhrl BM, Restle T, Goody RS, Seidel CAM: **Multi-parameter single-molecule fluorescence spectroscopy reveals heterogeneity of HIV-1 Reverse Transcriptase:primer/template complexes.** *Proc Natl Acad Sci U S A* 2003, **100**:1655-1660.
  64. Kudryavtsev V, Sikor M, Kalinin S, Mokranjac D, Seidel CAM, Lamb DC: **Combining MFD and PIE for accurate single-pair Förster Resonance Energy Transfer measurements.** *ChemPhysChem* 2012, **13**:1060-1078.  
A combination of multiparameter fluorescence detection (MFD), pulsed interleaved excitation (PIE) and smFRET experiments on freely diffusing molecules is presented. MFD monitors a variety of fluorescence parameters simultaneously while PIE directly excites the acceptor to probe its presence and photoactivity. A single MFD-PIE measurement provides all necessary calibration factors for accurate analysis of smFRET histograms and excludes artifacts due to acceptor blinking or photobleaching. The performance of MFD-PIE measurements is demonstrated studying the interdomain separation in DnaK, the major bacterial heat shock protein 70 (Hsp70).
  65. Vöpel T, Hengstenberg CS, Peulen TO, Ajaj Y, Seidel CAM, Herrmann C, Klare JP: **Triphosphate induced dimerization of human guanylate binding protein 1 involves association of the C-terminal helices: a joint double electron-electron resonance and FRET study.** *Biochemistry* 2014, **53**:4590-4600.
  66. Roy R, Hohng S, Ha T: **A practical guide to single-molecule FRET.** *Nat Meth* 2008, **5**:507-516.  
The majority of the single-molecule FRET community performs total internal reflection (TIRF) experiments. This guide gives an introduction to FRET, TIRF, and discusses potential artifacts relevant for quantitative FRET-based structural modeling.
  67. Rigler R, Mets Ü, Widengren J, Kask P: **Fluorescence correlation spectroscopy with high count rate and low background: analysis of translational diffusion.** *Eur Biophys J* 1993, **22**:169-175.
  68. Farooq S, Hohlbein J: **Camera-based single-molecule FRET detection with improved time resolution.** *Phys Chem Chem Phys* 2015, **17**:27862-27872.
  69. Lee NK, Kapanidis AN, Wang Y, Michalet X, Mukhopadhyay J, Ebright RH, Weiss S: **Accurate FRET measurements within single diffusing biomolecules using alternating-laser excitation.** *Biophys J* 2005, **88**:2939-2953.
  70. Hohlbein J, Craggs TD, Cordes T: **Alternating-laser excitation: single-molecule FRET and beyond.** *Chem Soc Rev* 2014, **43**:1156-1171.
  71. Elf J, Li GW, Xie XS: **Probing transcription factor dynamics at the single-molecule level in a living cell.** *Science* 2007, **316**:1191-1194.
  72. Flors C, Hotta J, Uji IH, Dedecker P, Ando R, Mizuno H, Miyawaki A, Hofkens J: **A stroboscopic approach for fast photoactivation-localization microscopy with Dronpa mutants.** *J Am Chem Soc* 2007, **129**:13970-13977.
  73. Felekyan S, Kühnemuth R, Kudryavtsev V, Sandhagen C, Becker W, Seidel CAM: **Full correlation from picoseconds to seconds by time-resolved and time-correlated single photon detection.** *Rev Sci Instrum* 2005, **76**:083104.
  74. Boukobza E, Sonnenfeld A, Haran G: **Immobilization in surface-tethered lipid vesicles as a new tool for single biomolecule spectroscopy.** *J Phys Chem B* 2001, **105**:12165-12170.
  75. Müller BK, Zaychikov E, Bräuchle C, Lamb DC: **Pulsed interleaved excitation.** *Biophys J* 2005, **89**:3508-3522.  
The authors present the method and analysis procedures of pulsed interleaved excitation (PIE) for the first time. PIE measurements significantly extend the capabilities of multiple-color fluorescence imaging, fluorescence cross-correlation spectroscopy (FCCS), and smFRET measurements.
  76. Kühnemuth R, Seidel CAM: **Principles of single molecule multiparameter fluorescence spectroscopy.** *Single Mol* 2001, **2**:251-254.
  77. Widengren J, Kudryavtsev V, Antonik M, Berger S, Gerken M, Seidel CAM: **Single-molecule detection and identification of multiple species by multiparameter fluorescence detection.** *Anal Chem* 2006, **78**:2039-2050.
  78. McCann JJ, Choi UB, Zheng L, Weninger K, Bowen ME: **Optimizing methods to recover absolute FRET efficiency from immobilized single molecules.** *Biophys J* 2010, **99**:961-970.
  79. Hildebrandt LL, Preus S, Birkedal V: **Quantitative single molecule FRET efficiencies using TIRF microscopy.** *Faraday Discussions* 2015, **184**:131-142.  
The authors introduced new software (<http://www.isms.au.dk>) to determine quantitative FRET efficiencies directly from individual fluorescence time traces of surface immobilized DNA molecules without the need for external calibrants.
  80. Preus S, Hildebrandt LL, Birkedal V: **Optimal background estimators in single-molecule FRET microscopy.** *Biophys J* 2016, **111**:1278-1286.

81. Jeschke G: **DEER distance measurements on proteins.** In *Annual Review of Physical Chemistry*, Vol. 63. Edited by Johnson MA, Martinez TJ. 2012:419-446.
82. Columbus L, Hubbell WL: **A new spin on protein dynamics.** *Trends Biochem Sci* 2002, **27**:288-295.
83. Cai Q, Kusnetzow AK, Hideg K, Price EA, Haworth IS, Qin PZ: **Nanometer distance measurements in RNA using site-directed spin labeling.** *Biophys J* 2007, **93**:2110-2117.
84. Hagelueken G, Abdullin D, Schiemann O: **mtsslSuite: Probing biomolecular conformation by spin-labeling studies.** In *Electron Paramagnetic Resonance Investigations of Biological Systems by Using Spin Labels, Spin Probes, and Intrinsic Metal Ions*, Pt A. 563. Edited by Qin PZ, Warncke K. 2015:595-622.
85. Muschielok A, Andrecka J, Jawhari A, Bruckner F, Cramer P, ● ● Michaelis J: **A nano-positioning system for macromolecular structural analysis.** *Nat Meth* 2008, **5**:965-971.
- The nano positioning system (NPS) methodology (<https://www.uni-ulm.de/nawi/nawi-biophys/forschung/forschung-michaelis/method-development/software/nps/>) determines the spatially distributed uncertainties from a set of FRET experiments, assuming the dyes adopt fixed positions in space. A Bayesian approach to address such a problem is presented which localizes dyes with fixed locations.
86. Brunger AT, Strop P, Vrljic M, Chu S, Weninger KR: **Three-dimensional molecular modeling with single molecule FRET.** *J Struct Biol* 2011, **173**:497-505.
- Technical details on implementing FRET-restraints into modelling techniques originally developed for NMR to FRET are given. The presented implementation is publicly available in the established software CNS (Crystallography and NMR system; <http://cns-online.org/v1.3/>).
87. Klose D, Klare JP, Grohmann D, Kay CWM, Werner F, Steinhoff HJ: **Simulation vs. reality: a comparison of in silico distance predictions with DEER and FRET measurements.** *PLoS ONE* 2012, **7**:e39492.
88. Choi UB, Strop P, Vrljic M, Chu S, Brunger AT, Weninger KR: **Single-molecule FRET-derived model of the synaptotagmin 1-SNARE fusion complex.** *Nat Struct Mol Biol* 2010, **17**:318-324.
89. Hoefling M, Lima N, Haenni D, Seidel CAM, Schuler B, Grubmüller H: **Structural heterogeneity and quantitative FRET efficiency distributions of polyprolines through a hybrid atomistic simulation and Monte Carlo approach.** *PLoS ONE* 2011, **6**:e19791.
90. Graen T, Hoefling M, Grubmüller H: **AMBER-DYES: characterization of charge fluctuations and force field parameterization of fluorescent dyes for molecular dynamics simulations.** *J Chem Theory Comput* 2014, **10**:5505-5512.
91. Best RB, Hofmann H, Nettels D, Schuler B: **Quantitative interpretation of FRET experiments via molecular simulation: force field and validation.** *Biophys J* 2015, **108**:2721-2731.
92. Milas P, Gamari BD, Parrot L, Krueger BP, Rahmanseresht S, Moore J, Goldner LS: **Indocyanine dyes approach free rotation at the 3' terminus of A-RNA: a comparison with the 5' terminus and consequences for Fluorescence Resonance Energy Transfer.** *J Phys Chem B* 2013, **117**:8649-8658.
93. Liao J-M, Wang Y-T, Chen C-L: **Computer simulation to investigate the FRET application in DNA hybridization systems.** *Phys Chem Chem Phys* 2011, **13**:10364-10371.
94. Walczewska-Szewc K, Corry B: **Accounting for dye diffusion and orientation when relating FRET measurements to distances: three simple computational methods.** *Phys Chem Chem Phys* 2014, **16**:12317-12326.
95. Kalinin S, Sisamakias E, Magennis SW, Felekyan S, Seidel CAM: **On the origin of broadening of single-molecule FRET efficiency distributions beyond shot noise limits.** *J Phys Chem B* 2010, **114**:6197-6206.
96. Levitus M, Ranjit S: **Cyanine dyes in biophysical research: the photophysics of polymethine fluorescent dyes in biomolecular environments.** *Q Rev Biophys* 2010:1-29.
- This review focuses on the photophysical and photochemical properties of the most frequently used cyanine dyes in single-molecule FRET studies. Non-fluorescent dark states and methods to enhance dye fluorescence are discussed. Effects of dark states in the context of single-molecule FRET and localization studies are described.
97. Abdullin D, Hagelueken G, Schiemann O: **Determination of nitroxide spin label conformations via dPELDOR and X-ray crystallography.** *Phys Chem Chem Phys* 2016, **18**:10428-10437.
98. Hwang H, Myong S: **Protein induced fluorescence enhancement (PIFE) for probing protein-nucleic acid interactions.** *Chem Soc Rev* 2014, **43**:1221-1229.
99. Lerner E, Ploetz E, Hohlbein J, Cordes T, Weiss S: **A quantitative theoretical framework for protein-induced fluorescence enhancement-Förster-Type Resonance Energy Transfer (PIFE-FRET).** *J Phys Chem B* 2016, **120**:6401-6410.
- Protein-induced fluorescence enhancement (PIFE) serves as a complementary molecular ruler at molecular distances inaccessible to other spectroscopic rulers such as FRET or photoinduced electron transfer (PET). The authors provide experimental evidence that PIFE is proportional to the contact volume of the dye's accessible volume with protein interface.
100. Beckers M, Drechsler F, Eilert T, Nagy J, Michaelis J: **Quantitative structural information from single-molecule FRET.** *Faraday Discuss* 2015, **184**:117-129.
- The classic NPS methodology is extended by assumptions (e.g. dynamic dipole averaging), which drastically increases the precision in locating the position of the dyes by multiple FRET measurements. This study demonstrates that the dye description is essential to achieve a high precision to localize dyes.
101. Höfing H, Gabba M, Poblete S, Kempe D, Fitter J: **Inter-dye distance distributions studied by a combination of single-molecule FRET-filtered lifetime measurements and a weighted accessible volume (wAV) algorithm.** *Molecules* 2014, **19**:19269-19291.
102. Steffen FD, Sigel RKO, Börner R: **An atomistic view on carbocyanine photophysics in the realm of RNA.** *PCCP* 2016, **18** Advance Article.
103. Greife A, Felekyan S, Ma QJ, Gertzen CGW, Spomer L, Dimura M, Peulen TO, Wöhler C, Häussinger D, Gohlke H, Keitel V et al.: **Structural assemblies of the di- and oligomeric G-protein coupled receptor TGR5 in live cells: an MFIS-FRET and integrative modelling study.** *Sci Rep* 2016. Advance Article.
104. Kravets E, Degrandi D, Ma QJ, Peulen TO, Klumpers V, Felekyan S, ● Kühnemuth R, Weidtkamp-Peters S, Seidel CAM, Pfeffer K: **Guanylate binding proteins directly attack *Toxoplasma gondii* via supramolecular complexes.** *eLife* 2016, **5**:e11479.
- The authors use multi-parameter fluorescence image spectroscopy in live cells to validate structural models and determine equilibrium constants to study the role of immuno-proteins in intracellular pathogen defense. This study shows the application of forward modeling using live-cell data.
105. Iqbal A, Arslan S, Okumus B, Wilson TJ, Giraud G, Norman DG, Ha T, Lilley DMJ: **Orientation dependence in fluorescent energy transfer between Cy3 and Cy5 terminally attached to double-stranded nucleic acids.** *Proc Natl Acad Sci U S A* 2008, **105**:11176-11181.
106. Antonik M, Felekyan S, Gaiduk A, Seidel CAM: **Separating structural heterogeneities from stochastic variations in fluorescence resonance energy transfer distributions via photon distribution analysis.** *J Phys Chem B* 2006, **110**:6970-6978.
- The authors established the probability distribution analysis (PDA) method for the quantitative analysis of FRET efficiency (E) histograms to determine with high precision (<1% of the Förster radius) the originating E value of a shot-noise-limited distribution. Any deviations can be assigned to static and/or dynamic heterogeneities of the molecular system.
107. Kalinin S, Felekyan S, Antonik M, Seidel CAM: **Probability distribution analysis of single-molecule fluorescence anisotropy and resonance energy transfer.** *J Phys Chem B* 2007, **111**:10253-10262.
108. Raval A, Piana S, Eastwood MP, Shaw DE: **Assessment of the utility of contact-based restraints in accelerating the prediction of protein structure using molecular dynamics simulations.** *Protein Sci* 2016, **25**:19-29.
- An excellent demonstration of how sparse restraints similar to those provided by FRET, enable MD-based protein structure determination.

109. Boura E, Rozycki B, Chung HS, Herrick DZ, Canagarajah B, Cafiso DS, Eaton WA, Hummer G, Hurley JH: **Solution structure of the ESCRT-I and -II supercomplex: Implications for membrane budding and scission.** *Structure* 2012, **20**:874-886.
110. Brunger AT: **Version 1.2 of the crystallography and NMR system.** *Nat Protocols* 2007, **2**:2728-2733.
111. Rieping W, Habeck M, Nilges M: **Inferential structure determination.** *Science* 2005, **309**:303-306.  
The authors describe a forward modeling Bayesian approach to improve the structural quality of a model by taking into account indirect structural data, such as NMR data. Similar to NMR, ambiguous experimental data poses a challenge to structural modeling by FRET
112. Muschielok A, Michaelis J: **Application of the nano-positioning system to the analysis of fluorescence resonance energy transfer networks.** *J Phys Chem B* 2011, **115**:11927-11937.
113. Dumat B, Larsen AF, Wilhelmsson LM: **Studying Z-DNA and B-to Z-DNA transitions using a cytosine analogue FRET-pair.** *Nucleic Acids Res* 2016, **44**:e101.
114. Berman H, Henrick K, Nakamura H: **Announcing the worldwide Protein Data Bank.** *Nat Struct Biol* 2003, **10** 980-980.
115. Berman HM, Burley SK, Kleywegt GJ, Markley JL, Nakamura H, Velankar S: **The archiving and dissemination of biological structure data.** *Curr Opin Struct Biol* 2016, **40**:17-22.
116. Haas J, Roth S, Arnold K, Kiefer F, Schmidt T, Bordoli L, Schwede T: **The Protein Model Portal – a comprehensive resource for protein structure and model information.** *Database* 2013:bat031.
117. NIST/SEMATECH: *e-Handbook of Statistical Methods*. 2016: <http://www.itl.nist.gov/div898/handbook/>.
118. Guyon I, Elisseeff A: **An introduction to variable and feature selection.** *J Mach Learn Res* 2003, **3**:1157-1182.
119. Felekyan S, Kalinin S, Sanabria H, Valeri A, Seidel CAM: **Filtered FCS: species auto- and cross-correlation functions highlight binding and dynamics in biomolecules.** *ChemPhysChem* 2012, **13**:1036-1053.
120. Byrnes LJ, Sondermann H: **Structural basis for the nucleotide-dependent dimerization of the large G protein atlastin-1/SPG3A.** *Proc Natl Acad Sci U S A* 2011, **108**:2216-2221.
121. Byrnes LJ, Singh A, Szeto K, Benveniste NM, O'Donnell JP, Zipfel WR, Sondermann H: **Structural basis for conformational switching and GTP loading of the large G protein atlastin.** *EMBO J* 2013, **32**:369-384.
122. Ahmed A, Gohlke H: **Multiscale modeling of macromolecular conformational changes combining concepts from rigidity and elastic network theory.** *Proteins* 2006, **63**:1038-1051.
123. Ahmed A, Rippmann F, Barnickel G, Gohlke H: **A normal mode-based geometric simulation approach for exploring biologically relevant conformational transitions in proteins.** *J Chem Inf Model* 2011, **51**:1604-1622.
124. Chen HM, Ahsan SS, Santiago-Berrios MB, Abruna HD, Webb WW: **Mechanisms of quenching of Alexa fluorophores by natural amino acids.** *J Am Chem Soc* 2010, **132**:7244-7245.
125. Mullner D: **fastcluster: fast hierarchical, agglomerative clustering routines for R and Python.** *J Stat Softw* 2013, **53**:1-18.
126. Chen VB, Arendall WB, Headd JJ, Keedy DA, Immormino RM, Kapral GJ, Murray LW, Richardson JS, Richardson DC: **MolProbity: all-atom structure validation for macromolecular crystallography.** *Acta Crystallogr Sect D: Biol Crystallogr* 2010, **66**:12-21.
127. Delaforge E, Milles S, Bouvignies G, Bouvier D, Boivin S, Salvi N, Maurin D, Martel A, Round A, Lemke EA, Jensen MR *et al.*: **Large-scale conformational dynamics control H5N1 influenza polymerase PB2 binding to Importin alpha.** *J Am Chem Soc* 2015, **137**:15122-15134.
128. Choudhury AR, Sikorska E, van den Boom J, Bayer P, Popenda L, Szutkowski K, Jurga S, Bonomi M, Sali A, Zhukov I, Passamonti S *et al.*: **Structural model of the bilitranslocase transmembrane domain supported by NMR and FRET data.** *PLoS ONE* 2015:10.
129. Boura E, Rozycki B, Herrick DZ, Chung HS, Vecer J, Eaton WA, Cafiso DS, Hummer G, Hurley JH: **Solution structure of the ESCRT-I complex by small-angle X-ray scattering, EPR, and FRET spectroscopy.** *Proc Natl Acad Sci U S A* 2011, **108**:9437-9442.
130. Doose S, Neuweiler H, Sauer M: **Fluorescence quenching by photoinduced electron transfer: a reporter for conformational dynamics of macromolecules.** *ChemPhysChem* 2009, **10**:1389-1398.
131. Noe F, Doose S, Daidone I, Lollmann M, Sauer M, Chodera JD, Smith JC: **Dynamical fingerprints for probing individual relaxation processes in biomolecular dynamics with simulations and kinetic experiments.** *Proc Natl Acad Sci U S A* 2011, **108**:4822-4827.
132. Schulze A, Beliu G, Helmerich DA, Schubert J, Pearl LH, Prodromou C, Neuweiler H: **Cooperation of local motions in the Hsp90 molecular chaperone ATPase mechanism.** *Nat Chem Biol* 2016, **12**:628-635.
133. Schröder GF, Alexiev U, Grubmüller H: **Simulation of fluorescence anisotropy experiments: Probing protein dynamics.** *Biophys J* 2005, **89**:3757-3770.
134. Cristovao M, Sisamakias E, Hingorani MM, Marx AD, Jung CP, Rothwell PJ, Seidel CAM, Friedhoff P: **Single-molecule multiparameter fluorescence spectroscopy reveals directional MutS binding to mismatched bases in DNA.** *Nucleic Acids Res* 2012, **40**:5448-5464.
135. Lakowicz JR: *Principles of Fluorescence Spectroscopy*. Springer Science & Business Media; 2013.
136. Yang H, Luo GB, Karnchanaphanurach P, Louie TM, Rech I, Cova S, Xun LY, Xie XS: **Protein conformational dynamics probed by single-molecule electron transfer.** *Science* 2003, **302**:262-266.
137. Mansoor SE, DeWitt MA, Farrens DL: **Distance mapping in proteins using fluorescence spectroscopy: the tryptophan-induced quenching (TrIQ) method.** *Biochemistry* 2010, **49**:9722-9731.
138. Haenni D, Zosel F, Reymond L, Nettels D, Schuler B: **Intramolecular distances and dynamics from the combined photon statistics of single-molecule FRET and Photoinduced Electron Transfer.** *J Phys Chem B* 2013, **117**:13015-13028.
139. Kask P, Piksarv P, Pooga M, Mets Ü, Lippmaa E: **Separation of the rotational contribution in fluorescence correlation experiments.** *Biophys J* 1989, **55**:213-220.
140. Pieper CM, Enderlein J: **Fluorescence correlation spectroscopy as a tool for measuring the rotational diffusion of macromolecules.** *Chem Phys Lett* 2011, **516**:1-11.
141. Stahl Y, Grabowski S, Bleckmann A, Kuhnemuth R, Weidtkamp-Peters S, Pinto KG, Kirschner GK, Schmid JB, Wink RH, Hulsewede A, Felekyan S *et al.*: **Moderation of Arabidopsis root stemness by CLAVATA1 and ARABIDOPSIS CRINKLY4 receptor kinase complexes.** *Curr Biol* 2013, **23**:362-371.
142. Somssich M, Ma QJ, Weidtkamp-Peters S, Stahl Y, Felekyan S, Bleckmann A, Seidel CAM, Simon R: **Real-time dynamics of peptide ligand-dependent receptor complex formation in planta.** *Sci Signal* 2015:8.
143. Blom H, Widengren J: **STED microscopy – towards broadened use and scope of applications.** *Curr Opin Chem Biol* 2014, **20**:127-133.
144. Bonomi M, Pellarin R, Kim SJ, Russel D, Sundin BA, Riffle M, Jaschob D, Ramsden R, Davis TN, Muller EGD, Sali A: **Determining protein complex structures based on a Bayesian model of in vivo Förster Resonance Energy Transfer (FRET) data.** *Mol Cell Proteomics* 2014, **13**:2812-2823.
145. Vogel SS, van der Meer BW, Blank PS: **Estimating the distance separating fluorescent protein FRET pairs.** *Methods* 2014, **66**:131-138.
146. Gnutt D, Gao M, Bryliski O, Heyden M, Ebbinghaus S: **Excluded-volume effects in living cells.** *Angew Chem Int Ed* 2015, **54**:2548-2551.

The effect of macromolecular crowding inside living cells is studied by a FRET based sensor. This study is of relevance to relate *in vitro* FRET-studies to live-cell measurements.

147. Senske M, Tork L, Born B, Havenith M, Herrmann C, Ebbinghaus S: **Protein stabilization by macromolecular crowding through enthalpy rather than entropy**. *J Am Chem Soc* 2014, **136**:9036-9041.
148. Sakon JJ, Weninger KR: **Detecting the conformation of individual proteins in live cells**. *Nat Meth* 2010, **7**:203-205.
149. König I, Zarrine-Afsar A, Aznauryan M, Soranno A, Wunderlich B, Dingfelder F, Stuber JC, Pluckthun A, Nettels D, Schuler B: **Single-molecule spectroscopy of protein conformational dynamics in live eukaryotic cells**. *Nat Meth* 2015, **12**:773-779.
150. Ratzke C, Mickler M, Hellenkamp B, Buchner J, Hugel T: **Dynamics of heat shock protein 90 C-terminal dimerization is an important part of its conformational cycle**. *Proc Natl Acad Sci U S A* 2010, **107**:16101-16106.










## Supplement B. Resolving dynamics and function of transient states in single enzyme molecules

## ARTICLE

<https://doi.org/10.1038/s41467-020-14886-w>

OPEN

# Resolving dynamics and function of transient states in single enzyme molecules

Hugo Sanabria <sup>1,2,8</sup>✉, Dmitro Rodnin<sup>1,8</sup>, Katherina Hemmen <sup>1,8</sup>, Thomas-Otavio Peulen <sup>1</sup>, Suren Felekyan <sup>1</sup>, Mark R. Fleissner<sup>3,7</sup>, Mykola Dimura <sup>1,4</sup>, Felix Koberling<sup>5</sup>, Ralf Kühnemuth<sup>1</sup>, Wayne Hubbell<sup>3</sup>, Holger Gohlke <sup>4,6</sup> & Claus A.M. Seidel <sup>1</sup>✉

We use a hybrid fluorescence spectroscopic toolkit to monitor T4 Lysozyme (T4L) in action by unraveling the kinetic and dynamic interplay of the conformational states. In particular, by combining single-molecule and ensemble multiparameter fluorescence detection, EPR spectroscopy, mutagenesis, and FRET-positioning and screening, and other biochemical and biophysical tools, we characterize three short-lived conformational states over the ns-ms timescale. The use of 33 FRET-derived distance sets, to screen available T4L structures, reveal that T4L in solution mainly adopts the known open and closed states in exchange at 4  $\mu$ s. A newly found minor state, undisclosed by, at present, more than 500 crystal structures of T4L and sampled at 230  $\mu$ s, may be actively involved in the product release step in catalysis. The presented fluorescence spectroscopic toolkit will likely accelerate the development of dynamic structural biology by identifying transient conformational states that are highly abundant in biology and critical in enzymatic reactions.

<sup>1</sup>Institut für Physikalische Chemie, Lehrstuhl für Molekulare Physikalische Chemie, Heinrich-Heine-Universität, Düsseldorf, Germany. <sup>2</sup>Department of Physics and Astronomy, Clemson University, Clemson, SC, USA. <sup>3</sup>Jules Stein Eye Institute and Department of Chemistry and Biochemistry, University of California, Los Angeles, CA, USA. <sup>4</sup>Institut für Pharmazeutische und Medizinische Chemie, Heinrich-Heine-Universität, Düsseldorf, Germany. <sup>5</sup>PicoQuant GmbH, Berlin, Germany. <sup>6</sup>John von Neumann Institute for Computing (NIC), Jülich Supercomputing Centre (JSC) & Institute of Biological Information Processing (IBI-7: Structural Biochemistry), Forschungszentrum Jülich GmbH, 52425 Jülich, Germany. <sup>7</sup>Present address: Avanir Pharmaceuticals Inc., Aliso Viejo, CA, USA. <sup>8</sup>These authors contributed equally: Hugo Sanabria, Dmitro Rodnin, Katherina Hemmen. ✉email: [hsanabr@clemson.edu](mailto:hsanabr@clemson.edu); [cseidel@hhu.de](mailto:cseidel@hhu.de)

Enzymes adopt distinct conformational states during catalysis<sup>1,2</sup>, where transiently populated (“excited”) states are often of critical importance in the enzymatic cycle. These states are short-lived and therefore “hidden” to many experimental techniques. Classical structural biology methods often struggle to fully capture enzymes during catalytic action because the conformational rearrangements often span several decades in time (ns–ms)<sup>3–8</sup>. Hence, there is an urgent need to develop experimental and analysis methods to overcome this challenge. Recently, we demonstrated by simulated experiments that a new analysis toolkit (“FRET on rails”) combined with molecular simulations can resolve short-lived conformational states of proteins<sup>9</sup>.

Here, we apply and extend the fluorescence analysis toolkit<sup>9,10</sup>, developed for dynamic structural biology, to interrogate the catalytic cycle of an enzyme<sup>11</sup>. In particular, the analysis (1) captures an excited, short-lived state and (2) identifies its potential relevance in the enzyme’s catalytic cycle. The presented approach may serve as a blueprint for future enzymologic studies with the well-established single-molecule multiparameter fluorescence detection (MFD) experiments in that it enables detecting hidden states by the unique time-resolution (picoseconds) and sensitivity (single-molecule) of fluorescence.

We use lysozyme (T4L) of the bacteriophage T4 as development platform and probe its conformational dynamics and structural features. Structurally, T4L<sup>12</sup> consists of two interrelated subdomains, the N-terminal subdomain (NTsD) and the C-terminal subdomain (CTsD), differing in their folding behavior and stability<sup>13</sup>. A long  $\alpha$ -helix (helix c) links the two subdomains (Fig. 1a). To date, more than 500 structural models of T4L are available within the Protein Data Bank (PDB). In this ensemble, T4L adopts several opening angles corresponding to a classic hinge-bending motion of the NTsD with respect to the CTsD. The enzymatic function of T4L is to cleave the glycosidic bond between N-acetylmuramic acid and N-acetylglucosamine of the saccharides of the bacterial cell wall<sup>14</sup>.

T4L in solution is thought to adopt conformations that are open to various degrees, and a covalent adduct of the protein and its processed enzymatic product can crystallize in a closed conformation<sup>14–16</sup>. Therefore, T4L is thought to follow a classical Michaelis–Menten mechanism (MMm) characterized as a two-state system (Fig. 1b). Here, an open and closed conformational state fulfils unique functions of substrate binding and substrate cleavage, respectively<sup>17</sup>. In a MMm, the product dissociates stochastically from the enzyme. For other enzymes, e.g. the Horseradish peroxidase<sup>18</sup>, an “active” product release state was identified. Recent experimental findings for T4L suggest the involvement of more than two states in catalysis<sup>19,20</sup>, where the turnover rate was estimated between 10 and 50 ms<sup>20–23</sup>, while the conformational dynamics fell within the ns to sub-ms range<sup>4,15,20–29</sup>. Such complex cases, with distinct interconverting conformational states, open additional reaction paths and yield disperse kinetics<sup>30</sup>.

For a full description of an enzymological cycle, the number of enzymatic states, their connectivity, the conformational structures of the states, and the states’ chemical function have to be unraveled. Technically, we achieve these objectives by a hybrid approach combining classic biochemical methods (mutagenesis & HPLC), probe-based spectroscopy, and molecular simulations. Förster resonance energy transfer (FRET) and electron paramagnetic resonance (EPR) spectroscopy probe distances between bioorthogonally introduced probes through dipolar coupling. In FRET spectroscopy, the coupling is measured between a donor (D) and acceptor (A) fluorophore.

In confocal MFD single-molecule FRET (smFRET) experiments, freely diffusing molecules are repeatedly excited by a pulsed light source, and the emitted fluorescence photon is

detected with picosecond time-resolution by time-correlated single photon counting (TCSPC) for several milliseconds per molecule (diffusion time,  $t_{diff}$ )<sup>31</sup> (Fig. 1c). smFRET experiments are ideal to study kinetics because no sophisticated strategies are necessary to synchronize molecules prior to the analysis. Consequently, it is possible to probe reliably protein kinetics over seven decades in time (sub ns–ms).

Distinct features of photon streams are highlighted by different representations (Fig. 1d). (1) A MFD-histogram is particularly valuable to reveal the number of states, identify dynamics, and to inform on state connectivities. A MFD-histogram is generated by analyzing two complementary FRET-indicators, the average intensity-based FRET-efficiency,  $E$ , and the fluorescence-averaged donor lifetime in the presence of acceptor,  $\langle \tau_{D(A)} \rangle_F$ , for individual single-molecule events<sup>31–33</sup>. (2) Filtered fluorescence correlation spectroscopy (fFCS) quantifies exchange dynamics among the states by determining relaxation times<sup>34,35</sup>. (3) The analysis of fluorescence decays reveals populations of states and equilibrium distance distributions. (4) Finally, these experimental distances can be translated to structural models by molecular simulations<sup>10,36,37</sup>.

Following the concepts that were established for simulated data to resolve the structure and dynamics of proteins by integrative studies with FRET experiments<sup>8,9</sup> (Fig. 1e and more detailed in Supplementary Fig. 1), we start out with a systematic design of a FRET network for T4L to simultaneously monitor its dynamics and structural features. In step II, we use a combination of MFD to resolve the conformational states stable at the ns timescales. In step III, we quantify the conformational dynamics by employing fFCS and Monte Carlo simulations to resolve the connectivity of the conformational states. Following this, we perform a statistical analysis to further substantiate the existence of a hidden conformational state of T4L that was clearly identified above. In step IV, we identify structural models by using three distinct distance sets to screen an ensemble of structural models and to compare our identified states with models in the PDB. In the final step V, we derive an experimental energy landscape of T4L’s enzymatic cleavage cycle, based on shifting equilibrium, by mutating key active site residues that mimic functional enzyme states at various steps during substrate hydrolysis. Overall, our results demonstrate the potential of fluorescence spectroscopy to go beyond traditional experimental methods for obtaining a dynamic structural picture of enzymes in action. The existence of the identified hidden/excited conformational state is also corroborated by other analytical tools such as chromatography and EPR spectroscopy.

## Results

**Detecting T4L’s states by MFD.** In our smFRET-experiments, we monitor the distance between a donor (D) and acceptor (A) attached to specific amino acids of a T4L variant (see Methods). We designed a network of 33 distinct T4L variants to probe hinge-bending motions of T4L from different spatial directions (Fig. 2a) that cover the whole protein.

In Fig. 2b, c, we present MFD-histograms with the two FRET-indicators for two exemplary variants of our FRET network. Three peaks are identified in the MFD-histogram. In both histograms, a major and a minor FRET peak are present. The peak located at a low FRET-efficiency  $E$  corresponds to molecules without, or with an inactive acceptor, fluorophore (DOnly).

For an open (PDB ID: 172L, blue) and a closed (PDB ID: 148L, magenta) conformation, FRET efficiencies  $E$  are predicted by experimentally calibrated dye models (see Methods, section 5.5)<sup>9,38</sup>. These  $E$  values are shown as horizontal lines in the marginal distributions of Fig. 2b, c. A comparison with the major peak (Fig. 2b:  $0.3 < E < 0.7$ , Fig. 2c:  $E > 0.7$ ) demonstrates that they are

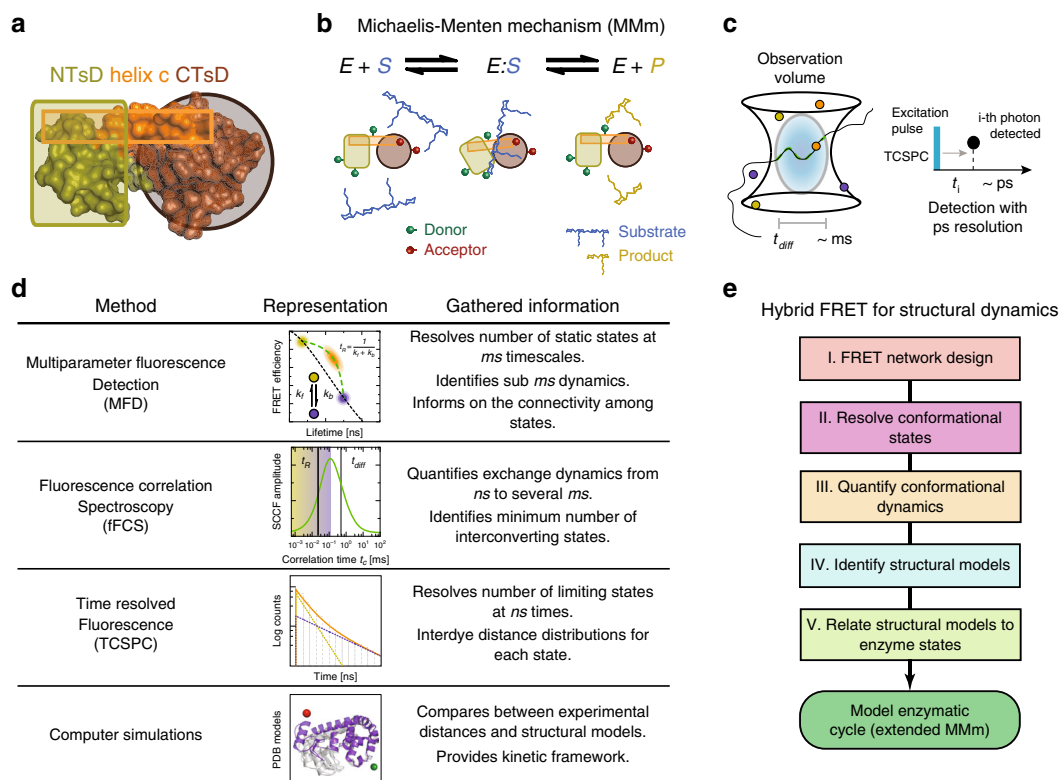


**Fig. 1 Schematic of the high precision FRET and fluctuation analysis toolkit.** **a** Subdomain architecture of Phage T4 Lysozyme (T4L). **b** Upon cleavage of its substrate peptidoglycan (blue), the N-terminal lobe (green) and the C-terminal lobe (brown) of T4L exhibit a change of closure, which can be observed via the induced change in the FRET indicators<sup>14,15</sup>. **c** In MFD-experiments of freely diffusing single molecules, the emitted fluorescent photons (“bursts”) are detected with ps resolution (with respect to the exciting laser pulse) during the diffusion (on the ms time scale) of the molecule through the observation volume (diffusion time,  $t_{diff}$ ). **d** The labeled T4L molecules are studied with different experimental methods. In single-molecule multiparameter fluorescence detection (MFD) experiments, the fluorescence bursts—averaged over *ms*—are analyzed e.g. with respect to their fluorescence lifetime ( $\tau_D$ ,  $\langle A \rangle_F$ ) or FRET-efficiency  $E$  and displayed in multidimensional frequency histograms (2D MFD-histogram). Molecules that adopt a stable conformation during burst duration are located along the static FRET-line (black) (Supplementary Methods). Assuming that the two limiting states (yellow and blue) exchange on timescales faster than *ms* with exchange rate constants  $k_f$  and  $k_b$ , we find only a single population (orange) shifted towards a longer fluorescence lifetime that is located on the dynamic FRET-line (green) connecting these two limiting states. Thus, FRET-lines serve as a visual guide to interpret 2D MFD-histograms, with deviations from the static FRET-line being indicative for the dynamic averaging and dynamics at the sub-*ms* and *ms* timescales. Filtered fluorescence correlation spectroscopy (fFCS) computes the species-specific cross-correlation function (sCCF (green), Supplementary Methods). The observed anti-correlation reveals a characteristic relaxation time  $t_R$  related to the inverse of the sum of the exchange rate constants,  $k_f$  and  $k_b$ . In eTCSPC, the distribution of the fluorescent photons (yellow/blue—individual states, orange—mixture) is detected with respect to an excitation pulse with ps resolution to reveal populations stable on the *ns* timescale (Supplementary Methods). Finally, in molecular simulations, the experimental results are compared to available structural models. **e** Flowchart for the hybrid FRET toolkit for determining structural dynamics. Based on a network of FRET variants, the conformational states and their exchange dynamics are determined, which are then used to identify the structural models. T4L variants with mutations altering their enzymatic activity relate the structural models to enzymatic states. Based on the gathered information, the enzymatic cycle can be modeled.

similar but not identical to known structural models. Next, we will show how dynamic exchange explains the observed peaks.

In MFD-histograms, FRET-lines (Supplementary Methods) serve as a unique guide to visualize conformational dynamics by peak shifts and splitting like in NMR relaxation dispersion measurements. A static FRET-line relates  $E$  and  $\langle \tau_{D(A)} \rangle_F$  for molecules in the absence of dynamics (magenta line, Fig. 2b, c). States that exchange on a time scale much slower than the observation time (quasi-static case) are separated in a MFD-histogram and follow the static FRET-line. However, a shift of a peak to the right with respect to the static FRET-line is a model-free indication for sub-*ms* dynamics<sup>31</sup>, because the FRET-efficiencies in a MFD-histogram are averaged over the observation time of the molecules ( $\sim$ ms). Thus, very fast exchanging states result in a single average peak that is shifted to the right of the static FRET-line. These peaks can be described by dynamic FRET-lines, which connect the exchanging states. For a visual representation of the possible transitions, the dynamic FRET-

lines of the identified exchanging states are displayed in the MFD-diagrams (dark green, cyan, and light green). A dynamic FRET-line connecting high FRET states with the DOnly population (gray) demonstrates the lack of significant photobleaching or blinking of acceptor dyes.

In the presented data, the major populations are shifted to the right of the static FRET-line (Fig. 2b, c). This gives clear evidence for a dynamic exchange faster than *ms*. For molecules in very rapid ( $\mu$ s) exchange between an open and a closed conformation, we expected to detect a single averaged peak in MFD-histograms. Hence, taking fast exchange into account, the major peak of the smFRET data is in agreement with known X-ray structures<sup>14,39</sup> and kinetic data<sup>4,13,20,21,23,24,29,40–42</sup>, most likely corresponding to the dynamic averaging of the hinge bending mechanism.

However, in 18 out of 33 MFD-histograms, we visually identify additional minor populations, which are in slow exchange with the major populations. Surprisingly, these minor populations ( $E > 0.8$ , Fig. 2b) and ( $0.2 < E < 0.6$ , Fig. 2c) can neither be assigned to the

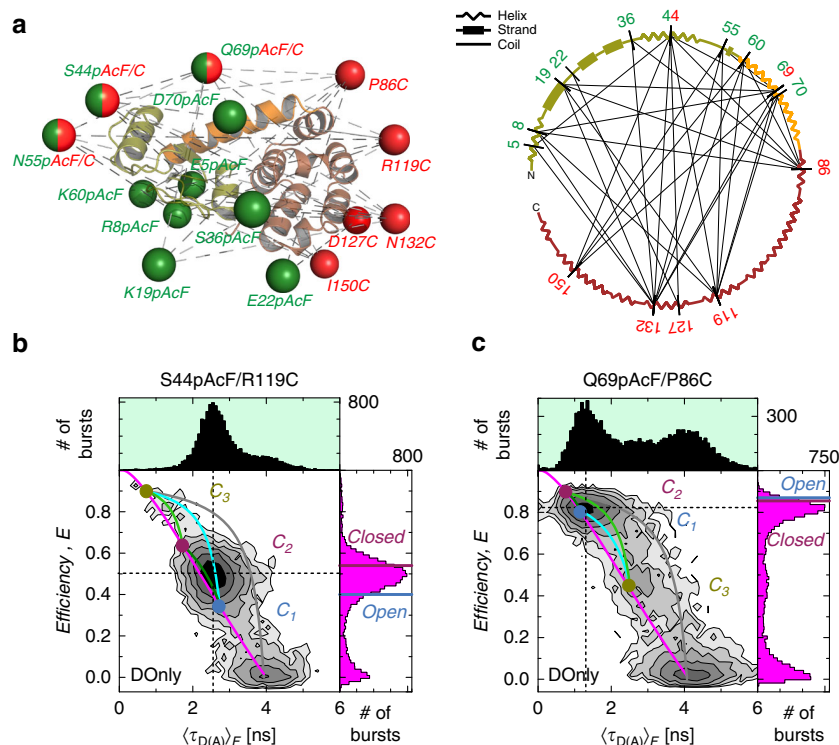


**Fig. 2 FRET studies probe T4L structure and dynamics.** **a** Network representing 33 measured distinct FRET-variants of T4L. The donor (D) Alexa488-hydroxylamine and acceptor (A) Alexa647-maleimide are coupled to *para*-acetylphenylalanine (pAcF) and cysteine (C), respectively. The spheres in the left panel represent the average donor (green) and acceptor (red) position for a structure of T4L (PDB ID: 172L) that is determined by the FRET Positioning System (FPS)<sup>10</sup>. Positions 44, 55, and 69 are used for donor and acceptor labeling. Right panel shows the secondary structure elements (helix, strand or coil) of T4L. The labeling positions are indicated and network pairs are connected. The N-terminal lobe is shown in green, the connecting helix c in orange and the C-terminal lobe in brown. **b, c** The FRET-efficiency,  $E$ , and fluorescence lifetime of D in the presence of A,  $\langle \tau_{D(A)} \rangle_F$ , of the DA-labeled T4L variants **(b)** S44pAcF/R119C and **(c)** Q69pAcF/P86C are shown in two-dimensional MFD-histograms (center) with one-dimensional projections of  $E$  (right) and  $\langle \tau_{D(A)} \rangle_F$  (top). The magenta lines (static FRET-line) describe those molecules with a single conformational state. The limiting states (circles) of the dynamic FRET-lines ( $C_1$ , blue;  $C_2$ , purple;  $C_3$ , yellow) are identified by eTCSPC (Supplementary Methods, Supplementary Note 4). The dynamic FRET-lines are shown in dark green ( $C_1$ - $C_2$ ), cyan ( $C_1$ - $C_3$ ), and light green ( $C_2$ - $C_3$ ) (Supplementary Methods). The gray lines trace molecules of high FRET-efficiency with a bleaching A. For comparison, the FRET-efficiencies of the X-ray structures for an open (blue, PDB ID: 172L) and closed (violet, 148L) state (determined by FPS) are shown as horizontal lines in the FRET-efficiency histograms (magenta) in the left 1D projection; for S44pAcF/R119C  $E(\text{open}) = 0.40$  and  $E(\text{closed}) = 0.54$  and for Q69pAcF/P86C  $E(\text{open}) = 0.87$  and  $E(\text{closed}) = 0.86$ . Black dashed lines mark the center of the main peak.

predicted average open and closed conformation (Supplementary Fig. 2). This is a first indicative for the existence of a third, conformationally excited, structurally distinct conformer.

In conclusion, MFD-histograms identify three conformers in T4L referred to as  $C_1$ ,  $C_2$ , and  $C_3$ . The conformers  $C_1$  and  $C_2$  are likely in fast exchange, while  $C_3$  is in slow exchange with  $C_1$  or  $C_2$ . These conformers may represent limiting states in the exchange dynamics<sup>43,44</sup>.

Following the workflow presented in Fig. 1e, we next determine the kinetic signatures via fFCS and resolve remaining ambiguities by simulations of MFD-experiments.

**Connectivity of states in a kinetic network.** To construct a reaction scheme of T4L's enzymatic cycle, the variant S44pAcF/I150C is used as pseudo-wildtype ("wt\*\*"). At first, we carry out control experiments by comparing for this variant (DA)-labeled and reversely (AD)-labeled T4L variants. In this way, we could exclude potential dye artifacts (Supplementary Fig. 3a-c, Supplementary Note 1) because the kinetic behavior was independent of the labeling scheme. The MFD-histogram of S44pAcF/I150C (Fig. 3a) reveals a typical pattern: a major population  $C_1/C_2$  ( $0.2 < E < 0.6$ ) and a minor  $C_3$  population ( $E > 0.8$ ) similar to the variants presented in Fig. 2b, c.

To unravel the kinetic behavior of an enzyme, one has to be aware that an enzymatic cycle with multiple states can be described by a transition rate matrix, which contains all exchange rate constants of the states. To recover T4L's transition rate matrix, we determine a set of relaxation times by fFCS (see next paragraph) and the species fractions of the states by analysis of the fluorescence decays (for details see the section below). This analysis results in ambiguous solutions, which are resolved by simulating MFD experiments making use of the information contained in smFRET experiments.

**Kinetic network of conformational states resolved by fFCS.** By fFCS, we probe transitions in T4L on all relevant timescales<sup>34,35</sup> to resolve the kinetic network of conformational states. fFCS uses species-specific information encoded as a characteristic pattern within the ns-regime of the polarization-resolved fluorescence decays<sup>34,45</sup>. This amplifies the contrast compared to conventional FCS for resolving relaxation times with high precision. We find very good agreement between the normalized species cross-correlation functions (sCCF) of the (AD)- and (DA)-labeled molecules. A global analysis of the sCCFs and the species auto-correlation functions (sACF) requires at least two relaxation times ( $\tau_{R1} = 4 \mu\text{s}$  and  $\tau_{R2} = 230 \mu\text{s}$ , Fig. 3b, Supplementary Note 2).

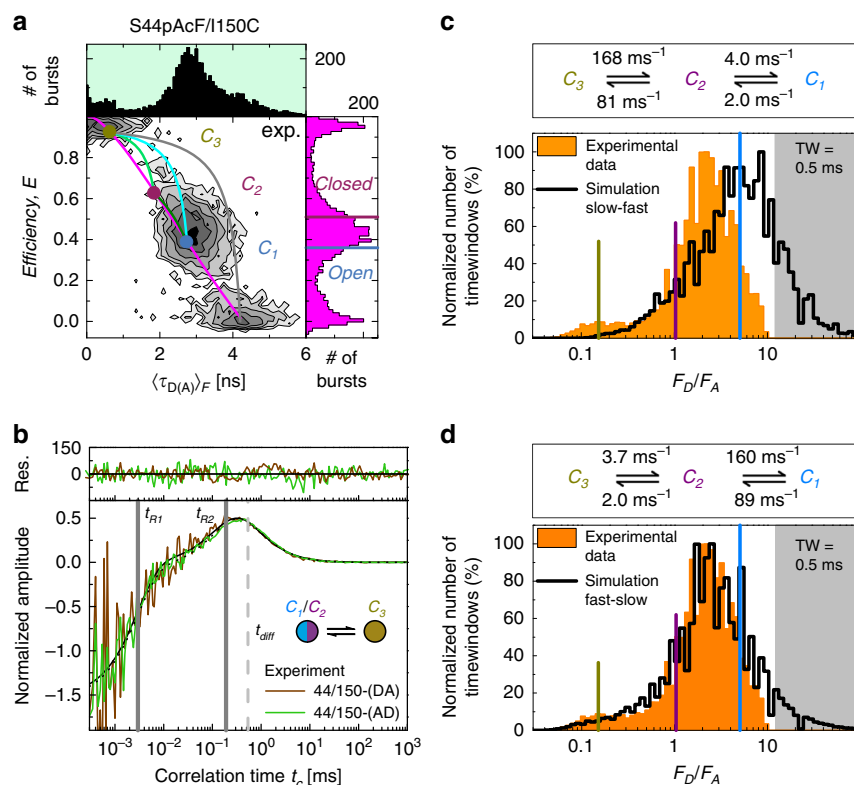


**Fig. 3 Kinetic connectivity.** **a** The FRET-efficiency,  $E$ , and fluorescence lifetime of D in the presence of A,  $\langle \tau_{D(A)} \rangle_F$ , of the DA-labeled T4L variant S44pAcF/I150C (or wt\*\*) is shown in the two-dimensional MFD-histograms (center) with the one-dimensional projections of  $E$  (right) and  $\langle \tau_{D(A)} \rangle_F$  (top). The magenta line (static FRET-line) represents the molecules with a single conformation. The dynamic FRET-lines represent the molecules changing their conformational state under monitoring. The limiting states (circles) of the dynamic FRET-lines ( $C_1$ , blue;  $C_2$ , purple;  $C_3$ , yellow) are identified by eTCSPC (see Fig. 4). The dynamic FRET-lines are shown in dark green ( $C_1$ - $C_2$ ), cyan ( $C_1$ - $C_3$ ), and light green ( $C_2$ - $C_3$ ) (Supplementary Methods). The gray line represents the trace molecules of high FRET-efficiency with a bleaching A. The FRET-efficiencies of X-ray structures for an open (blue, PDB ID: 172L) and closed (violet, 148L) state (determined by FPS) are shown for comparison and represented as horizontal lines in the FRET-efficiency histograms. **b** Overlay of the normalized sCCFs (Supplementary Methods Equation (17)) of S44pAcF/I150C-(DA) and S44pAcF/I150C-(AD). The global fit with other variants shows two relaxation times ( $t_{R1} = 4.0 \pm 2.3 \mu\text{s}$ ,  $t_{R2} = 230 \pm 28 \mu\text{s}$ ) and a diffusion time  $t_{\text{diff}} = 0.54 \text{ ms}$ . **c, d** Overlay of time-window analysis, slow-fast in **c** and fast-slow in **d**, respectively. The shaded area in gray indicates the region of donor only. See Supplementary Note 3 for data on the model and the simulation.

In summary, the two relaxation times obtained by sCCFs independently support the hypothesis of the interconversion between three states at sub-ms timescales. Moreover, in line with the MFD-histograms, we find a fast and a slow relaxation time.

Simulation of the kinetic network of T4 Lysozyme. The three identified conformers  $C_1$ ,  $C_2$ , and  $C_3$  are assigned by their characteristic species fractions (see below) to the corresponding structural states open, closed, and excited, respectively.

Three distinct kinetic linear reaction schemes are possible:  $C_1 \rightleftharpoons C_2 \rightleftharpoons C_3$ ,  $C_2 \rightleftharpoons C_1 \rightleftharpoons C_3$ ,  $C_1 \rightleftharpoons C_3 \rightleftharpoons C_2$  while the cycle scheme  $C_1 \rightleftharpoons C_2 \rightleftharpoons C_3 \rightleftharpoons C_1$  is unlikely due to the lack of burst across all FRET variants that connect  $C_3 \rightleftharpoons C_1$  with an effective slower rate to satisfy equilibrium. These bursts would follow the dynamic FRET-lines as guides between states in the MFD-diagram (Fig. 3a and Supplementary Fig. 2). Nonetheless, the sequential closing, from the most open (lowest FRET-efficiency in the variant S44pAcF/I150C) state to the most compact (highest FRET-efficiency in the variant S44pAcF/I150C) is depicted by  $C_1 \rightleftharpoons C_2 \rightleftharpoons C_3$ , so that we can discard the models  $C_1 \rightleftharpoons C_3 \rightleftharpoons C_2$  and  $C_2 \rightleftharpoons C_1 \rightleftharpoons C_3$ . With the relaxation times determined by fFCS and the species fractions obtained by analysis of the fluorescence decays (see next section), we calculate the exchange rate constants and find two competing solutions (Supplementary Note 3, Equation (36)). The exchange between  $C_1$  and  $C_2$  can be either slow (Fig. 3c) or fast (Fig. 3d).

To solve this ambiguity, we simulate sm-experiments of the two possible solutions<sup>43</sup> (Supplementary Note 3). The obtained simulations are compared with experimental histograms and fFCS (Fig. 3c, d, Supplementary Fig. 4). The corresponding  $p$ -values ( $C_1$ - $C_2$  fast vs.  $C_1$ - $C_2$  slow) of the respective 1D ( $p = 1$  for  $\langle \tau_{D(A)} \rangle_F$ ,  $p = 0.734$  for  $E$ ) and 2D MFD-histograms ( $p = 1$ ) clearly demonstrate a better agreement of the experimental data with a fast exchange between  $C_1$  and  $C_2$  (Supplementary Note 3, Supplementary Table 1a, b).

To conclude, we experimentally determine all reaction rate constants that define the reaction network, and the resulting species fractions. This description covers  $\mu\text{s}$  –  $\text{ms}$  and captures the relevant global motions of T4L.

**Characterization of the third conformer by eTCSPC.** As demonstrated by fFCS analysis, T4L is highly dynamic. Hence, the FRET-efficiencies in smFRET-histograms only represent dynamic averages of states<sup>46</sup>. Therefore, for resolving the limiting states of the system, we record high-precision fluorescence decays by eTCSPC and analyze the distribution of the photon arrival times,  $t$ , with respect to the excitation pulse in fluorescence decays. This analysis benefits from polarization-free effects resulting from measuring at magic-angle detection, low background fluorescence, and the absence of photobleaching.



Moreover, it can reveal DA-distance distributions and species populations<sup>47</sup>. To dissect the donor quenching by FRET (i.e., FRET-induced donor decay), we jointly analyze the DA- and DOnly-dataset, where the fluorescence lifetime distribution is shared with the DA-dataset. For physically meaningful analysis results, we explicitly consider the DA-distribution broadening due to the linkers by normal distributions<sup>47</sup>.

The analysis results of all 33 FRET-datasets are discussed using the variant S36pAcF/P86C shown in Fig. 4a (for other variants see Supplementary Note 4, Supplementary Fig. 5a). We display the experimental data by fluorescence decays of the DA- and the corresponding DOnly-sample (Fig. 4a). In agreement with the MFD-histograms and the fFCS data, 1-component models result in broad DA-distributions and/or are insufficient to describe the data (Fig. 4a, weighted residuals, violet). For S36pAcF/P86C, we obtain both, an unphysical distribution width and significant deviations in the weighted residuals, a strong indication that more than one conformer is found.

The analysis of the fluorescence decays by a 2-component model yields an inconsistent assignment by the species fractions (Supplementary Fig. 5b, c). This is evident by significant differences among the species fractions (Supplementary Table 2b). Moreover, the DA-distances disagree with known structural models (compare Supplementary Table 2d, e).

In our effort to seek a consistent description of all measured fluorescence decays, we develop a joint/global model function. For such description, we treated all fluorescence decays as a single dataset sharing common species fractions for the states. This reduces the number of free parameters and dramatically stabilizes the optimization algorithm. Because the global 2-component model (Fig. 4, cyan, Supplementary Table 2c) shows no agreement with the data, we consequently used a 3-component model (Fig. 4a orange, Supplementary Table 2d–f) to describe the data.

To analyze the precision of this fit, the uncertainties  $\Delta R_{DA}$  of the obtained distances,  $\langle R_{DA} \rangle$ , from the 3-component model need to be determined.  $\Delta R_{DA}$  depends on statistical uncertainties and systematic errors. We use the known shot noise of the fluorescence decays to estimate the statistical uncertainties,  $\Delta R_{DA}(k_{FRET})$ , of the FRET-rate constant  $k_{FRET}$  (Fig. 4b, Supplementary Table 2g). Moreover, we record polarization-resolved fluorescence decays of the donor and acceptor by eTCSPC to analyze the time-resolved anisotropy (Supplementary Table 3a, b) for estimating systematic errors,  $\Delta R_{DA}(\kappa^2)$ , due to the orientation factor  $\kappa^2$ . In conclusion, we can demonstrate that  $\Delta R_{DA}(\kappa^2)$  dominates the overall uncertainty of  $\Delta R_{DA}$  (Eq. (5), Supplementary Table 2d–g).

Moreover, we sample the model parameters of a 3-component model for individual datasets by a Markov chain Monte Carlo (MCMC) method. This demonstrates that, for given state populations, the mean distances  $\langle R_{DA,1} \rangle$ ,  $\langle R_{DA,2} \rangle$ , and  $\langle R_{DA,3} \rangle$  are very well defined (compare red to black in Fig. 4b). This also shows that a global model, which interrelates the state populations among datasets, improves the capability to resolve interdy distances.

A global 3-component model has too many degrees of freedom (Supplementary Methods) to be exhaustive when sampling by MCMC. Hence, we vary the state population of the minor state,  $x$  ( $C_3$ ), while optimizing all other model parameters (support plane analysis). This way, we determine the dependency of  $x(C_3)$  on the quality parameter  $\chi^2_r$  of all measurements (Fig. 4c). This analysis (1) shows that the minor state population is in the range of 0.1–0.27 and best agrees with the data for 0.21 (Fig. 4c,  $p$ -value = 0.68), (2) provides an estimate for  $\Delta R_{DA}(k_{FRET})$  (Supplementary Table 2d–f), and (3) demonstrates that  $\Delta R_{DA}(\kappa^2)$  dominates  $\Delta R_{DA}$  (Eq. (5)).

In summary, only a 3-component analysis describes all FRET samples and reference samples in a global model. This analysis recovers a set of physically meaningful average DA-distances that are grouped automatically and unbiased by their state populations. Additionally, the 3-component model is consistent with the fFCS data and with the dynamic FRET-lines displaying dynamically averaged sm-subpopulations in MFD (Fig. 2, Supplementary Fig. 2).

The integrated results are consistent with a view that T4L adopts three states ( $C_1$ ,  $C_2$ , and  $C_3$ ), as opposed to the expected two conformational states based on structural pre-knowledge.

**Structural features of conformational states.** To compare the experimental distances  $\langle R_{DA,exp} \rangle$  obtained from the fluorescence decays—under consideration of their respective uncertainties  $\Delta R_{DA}$ —to the structural models deposited in the PDB, we cluster all available 578 structures of T4L and aligned them. We observed that the structural models of T4L group into open, ajar, and closed clusters (based on the proximity of the CTsD and NTsD, Supplementary Table 4) with an intra-cluster root mean-squared displacement of less than 1.8 Å. The representative structures of these clusters are given by PDB IDs 172L, 1JQU, and 148L for the open, ajar, and closed conformations, respectively (Fig. 5a).

Next, we apply the FRET positioning system (FPS)<sup>34</sup> to compute an error function ( $\chi^2_{r,FPS}$ ) that compares the three sets of 33 distances  $\langle R_{DA,exp} \rangle$  to the modeled distances  $\langle R_{DA,model} \rangle$  by FPS. In  $\chi^2_{r,FPS}$ , we consider explicitly the uncertainties,  $\Delta R_{DA}$ , of the distance  $\langle R_{DA,exp} \rangle$ <sup>9</sup>. The overall agreement (minimum  $\chi^2_{r,FPS}$ ) for the distance sets for  $C_1$  and  $C_2$  is best for 172L and 148L, respectively (Fig. 5b). In Fig. 5c,  $\langle R_{DA,model} \rangle$  for 172L and 148L are compared to  $\langle R_{DA,exp} \rangle$  of  $C_1$  and  $C_2$ , respectively. A linear regression (red line) with a slope close to one demonstrates the absence of significant systematic deviations.

Structurally, the ajar state is more closed than the open state and more open than the closed state, most likely representing an intermediate conformation or it could arise from structural instabilities introduced by specific mutations such as W158L<sup>48</sup>. The deviation from the open and closed state is clearly reflected in the elevated  $\chi^2_{r,FPS}$ . Consequently, within our precision we can safely assign  $C_1$  as open and  $C_2$  as closed state. Screening results of other structures in the PDB against the FRET data are very similar to the results for the discussed cluster representatives, as expected (Supplementary Fig. 6). However, none of the structures can be assigned to the  $C_3$  state as judged by the disagreement with the data (Fig. 5b,  $\chi^2_{r,FPS}$ ). Thus, we conclude that  $C_3$  is an excited conformational state of currently unknown structure.

#### Relevant functional states in the enzymatic cleavage cycle.

Detection of  $C_3$  by EPR. We use double electron-electron resonance (DEER) to provide additional support for the  $C_3$  state. Multiple DEER studies on T4L have shown interspin distributions for wt T4L<sup>49,50</sup>. Here, we show the distribution of interspin distances of the adduct form of the variant T26E/S44pAcF/I150C labeled with the appropriate spin label MTSSL to produce the variant T26E(+)-44R1/150R1, which displays a satellite population with interspin distance of  $\sim 35$  Å resembling the enzyme-product-complex EP within the catalytic cleavage cycle of T4L (Fig. 6a, Supplementary Fig. 5d). The most frequently observed distance falls at interspin distances of 42 Å with another less populated state at interspin distances of  $>50$  Å. These may correspond to the various sub-states of the closed ( $C_2$ ) and open ( $C_1$ ) states, respectively. To ensure that this small population is not an artifact of the Tikhonov regularization algorithm<sup>51,52</sup> or due to the rotamer populations of the spin label-carrying side chain, we lower the pH to influence the conformational equilibrium of the

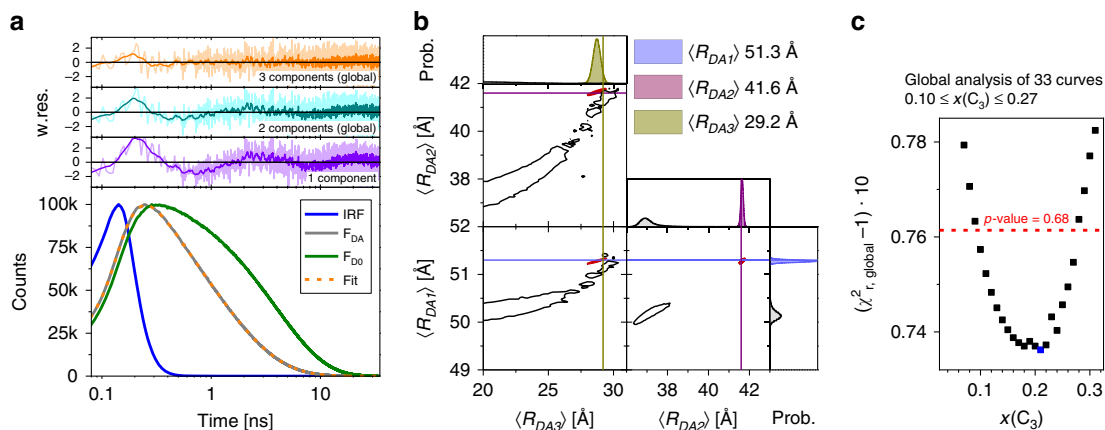


**Fig. 4 Uncovering the third conformational state by eTCSPC.** The eTCSPC measurements of all FRET variants are analyzed by superposition of normal distributed DA-distances (due to the coupling of dyes with long and flexible linkers, details see Supplementary Methods). **a** Experimental fluorescence decay of the variant S36pAcF/P86C ( $F_{DA}$ , gray, overlaid in orange with best fit), the corresponding DOnly-reference sample ( $F_{DO}$ , green), and instrumental response function (IRF, blue). At the top, the weighted residuals (w.res.) of different analyses by models with DA-distance distributions composed of one (violet), two (cyan), and three (orange) normal distributions are shown in corresponding colors. In the 2- and 3-component analysis, all FRET-measurements are jointly analyzed (global), and the species fractions of the states are shared among all 33 datasets. For the 1-component model of the variant S36pAcF/P86C, we find a mean DA-distance of 45.7 Å with a width of 17.6 Å. The analysis results of the 3-component model are summarized in Supplementary Table 2d-g. **b** Uncertainties,  $\Delta R_{DA}(k_{FRET})$ , of the 3-component analysis for the variant S36pAcF/P86C. Other contributions to the total uncertainty,  $\Delta R_{DA}$ , i.e.  $\chi^2$ , are not shown for clarity. To the sides, the marginalized (projected) histograms of the sampled model parameters are shown (black: individual fit; red: global fractions). The lines highlight the most likely combination of distances. **c** Uncertainty estimation of the species fraction of the third (minor) state,  $x(C_3)$ , for the three-component analysis. The fraction  $x(C_3)$  was varied from 0-0.32 followed by a subsequent minimization of all other model parameters. This yields the global, reduced  $\chi^2_{r,global}$  of all 33 FRET eTCSPC measurements in dependence of  $x(C_3)$ . This curve has a minimum at  $x(C_3) = 0.21$  ( $\chi^2_{r,min} = 1.074$ ). Points above the red line ( $\chi^2_r = 1.0761$ ,  $p$ -value = 0.68) are significantly worse than the best analysis result as judged by an  $F$ -test (225 parameters, 100,000 channels).

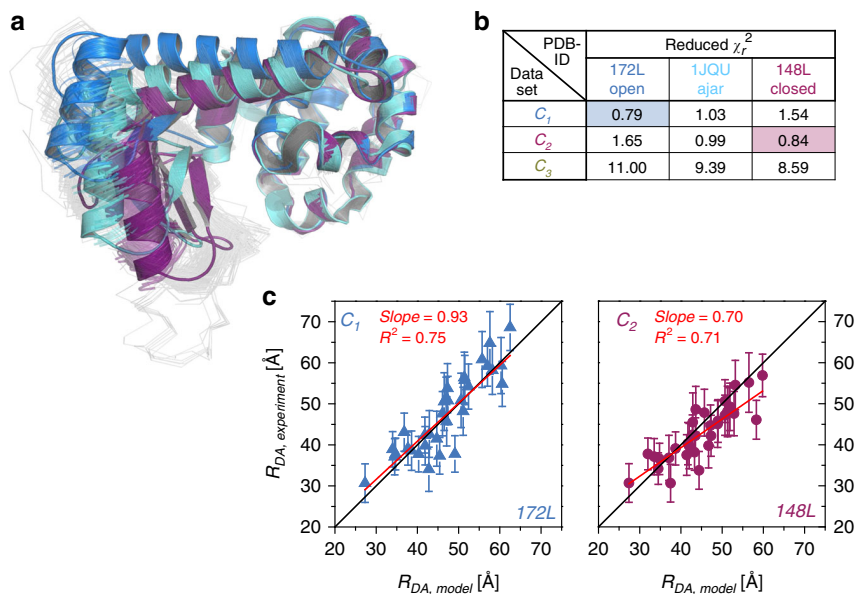


**Fig. 5 PDB screening.** **a** Overlay of the PDB structures used for screening. Blue, light blue and violet cartoons show the cluster representative of the open (172L), ajar (1JQU), and closed (148L) conformation of T4L. **b** Reduced  $\chi^2_r$  for each distance set compared to the expected distances from the selected cluster representative. **c** The experimental distances  $R_{DA,experimental}$  of the  $C_1$  and  $C_2$  dataset are plotted against the model distances  $R_{DA,Model}$  from the best PDB structure representative and fitted linearly (red lines). The black lines show a 1:1-relationship. Error bars shown are determined from the support plane analysis (95% confidence interval) shown in Fig. 4 and described in the text.

states<sup>53</sup>. The FRET-experiment with the variant S44pAcF/I150C shows an increase in the population of  $C_3$  at pH 2 (Fig. 6b), and the analogous DEER experiment at pH 3 shows a remarkably similar redistribution of interspin distances. Compared to

physiological pH conditions (Fig. 6a, dashed trace), these distances exhibit a shortening that is consistent with the  $C_3$  state, thus validating our conclusion that EPR and FRET do show the excited state  $C_3$ .



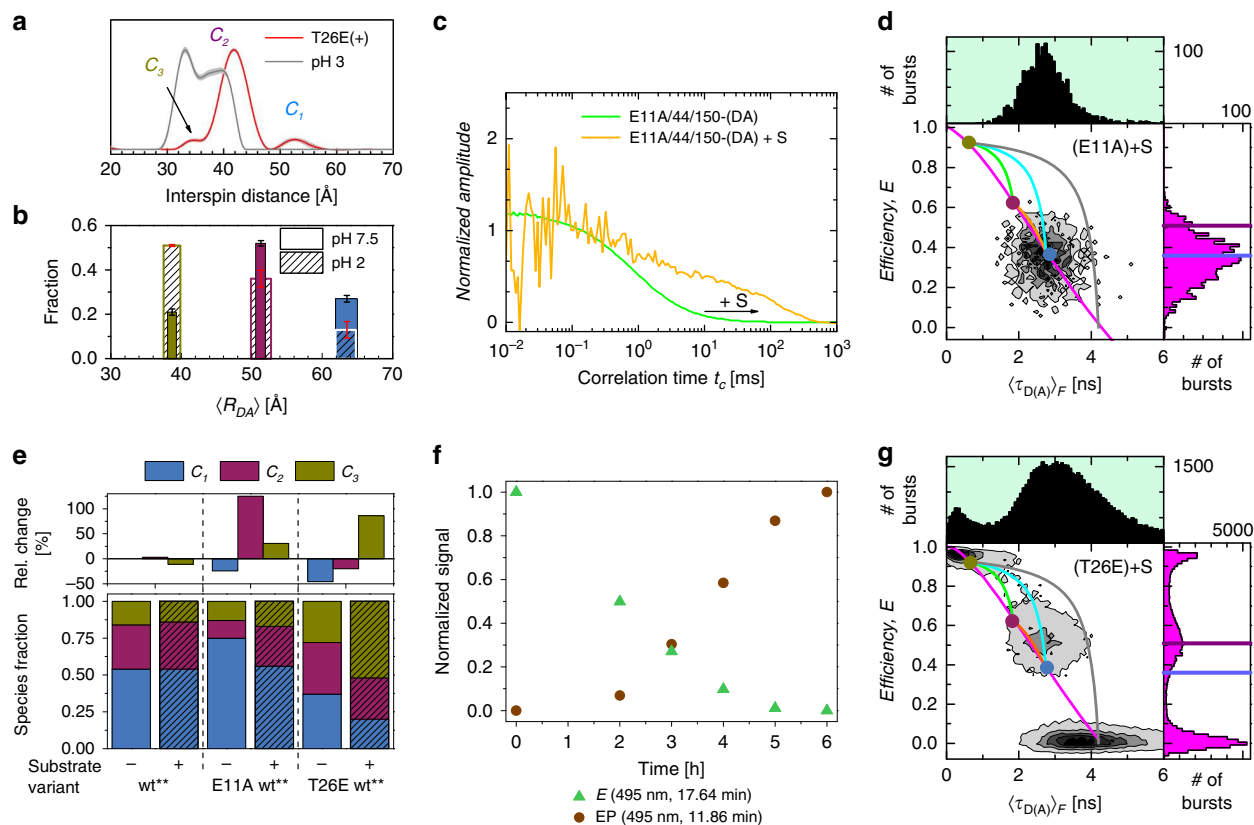


**Fig. 6 Functional states of T4L.** **a** Interspin distribution of T26E(+)-44R1/150R1 and 44R1/150R1 at pH 3.0 from DEER experiments. Gray area surrounding the distribution corresponds to error estimates. **b** Population fraction of S44pAcF/I150C from eTCSPC at pH 7.0 (solid colors) and at pH 2.0 (dashed rectangles). The width of the bar represents the uncertainty in distance (filled bars: pH 7.5, hatched bars: pH 2). The error bars represent the statistical uncertainty in the amplitudes (black: pH 7.5, red: pH 2).  $C_3$  increases in population at low pH. Similar effect is shown in EPR DEER experiments (Supplementary Fig. 5d) error estimates are 95% confidence intervals as determined by support plane analysis (Supplementary Methods). **c, d** The effects of the substrate on E11A/S44C/I150C: **c** Overlay of normalized sCCF of E11A/S44C/I150C with and without substrate. Consistent with the larger rotational correlation, we observe a shift of  $t_{diff}$  towards longer times for the variant E11A/S44C/I150C when incubated with the substrate; **d** MFD-histograms for the variant E11A/S44C/I150C with substrate. Upon addition of the substrate, we observe a shift towards lower  $E$  values. **e** Species fractions of the variants S44pAcF/I150C (wt\*\*), E11A/S44C/I150C (E11A wt\*\*), and T26E/S44pAcF/I150C (T26E wt\*\*) used to mimic free enzyme (E), enzyme-substrate complex (ES), and enzyme-product bound state (EP) without (–) and with (+) peptidoglycan. At the top, the relative change in fractions upon addition of peptidoglycan is shown. **f, g** Effects of the substrate on the variant T26E/S44pAcF/I150C: **f** Reverse-phase HPLC is used to monitor the adduct formation of the labeled T4L with peptidoglycan via plotting of the normalized signal at 17.64 min (E, green) and 11.86 min (EP, brown) after background subtraction; **g** MFD-histograms for the variant T26E/S44pAcF/I150C with substrate. An accumulation of the high FRET state is observed. The color code and FRET-lines for 2D and 1D MFD histograms (**d**) and **g** are as in Fig. 2.

**Trapped reaction states of T4L.** To mimic functional enzymatic states, we mutated the residues E11 and T26 at the active site using the backbone of the S44pAcF/I150C variant, also named wt\*\*<sup>14,39,54</sup>. We use wt\*\* because of the advantage in clearly resolving all three conformations of the free enzyme (E) by FRET. These mutations help identifying the role of  $C_3$  during enzyme catalysis: E11A, which inactivates T4L, causes the enzyme to bind its substrate S (peptidoglycan from *Micrococcus luteus*) while obviating the expected hydrolysis reaction<sup>54</sup>. Thus, in the presence of excess substrate, this mutation mimics the enzyme-substrate complex (ES). We monitor the effect of the substrate binding for the E11A mutation by FCS and compare the characteristic translational diffusion times,  $t_{diff}$ , in both the absence and presence of substrate. While  $t_{diff}$  is small (0.54 ms, Fig. 6c, green curve) without the substrate, it increases by several orders of magnitude when the large substrate is introduced (Fig. 6c, yellow curve). Moreover, the shift towards the larger donor anisotropy values upon incubation with substrate also provides additional evidence for substrate binding without cleavage (Supplementary Fig. 6e).

Sub-ensemble TCSPC analysis of the DA-subpopulation of the ES state (E11A/wt\*\* in the presence of substrate, Fig. 6d, Supplementary Fig. 7a–d, Supplementary Note 5) reveals an increase of 125% in the population corresponding to  $C_2$  compared to the free enzyme state E, with a concomitant reduction of  $C_1$ . In contrast, no effect of substrate binding for wt\*\*-(DA) is observed because ES is not trapped (Fig. 6e).

Although the variant T26E cleaves the substrate, the formation of a covalent adduct (PDB ID 148L) prevents a release of the formed product<sup>14</sup>. Therefore, we use this intermediate adduct to mimic the product-bound enzyme state (EP). To confirm the adduct formation under our measurement conditions, we monitor the adduct formation of labeled T4L (T26E/wt\*\* variant) by HPLC (Fig. 6f). T4L without substrate (E) elutes at ~18 min. After incubation with the substrate, the peak of E drops, and a new elution peak at ~12 min is detected with increasing incubation time (Fig. 6f, Supplementary Fig. 8), indicative of the adduct form of T4L (EP). Both ensemble (Fig. 6e) and sm MFD-measurements (Fig. 6g, Supplementary Fig. 7e–h) show a significant increase of the relative fraction of the  $C_3$  state, an effect

also observed in the EPR measurements (Fig. 6a). In the T26E variant, the accumulation of the  $C_3$  state is connected to the inability of this variant to release a part of the product<sup>14</sup>. We conclude that the new excited conformational state must be involved in this step.

## Discussion

In the following, we present the experimental evidence for the  $C_3$  state and its structural properties. To corroborate the existence of  $C_3$ , we discuss our experiments in four aspects: (1) the kinetic behavior in sm-experiments, (2) the error statistics of data analysis, (3) the structural validation of the obtained FRET parameters, and (4) the effect of specific mutations.

**Aspect 1: Kinetic behavior.** Considering 18 out of 33 variants with FRET-pairs, the sm-experiments directly show the presence of an additional DA-subpopulation in the MFD-histograms, which differs significantly from  $C_1$  and  $C_2$  (Figs. 2, 3, Supplementary Fig. 2). This DA-subpopulation is either populated or depopulated with specific mutations that alter the overall catalytic activity of T4L. Moreover, our global fluctuation analysis recovers at least two relaxation times that are shared throughout all studied variants (Fig. 3, Supplementary Fig. 9). Applying kinetic theory, two relaxation times indicate at least three states in equilibrium, which are reproduced by Brownian dynamics simulations (Supplementary Fig. 4).

**Aspect 2: Error statistics.** Key to the analysis and determination of  $C_3$  by ensemble fluorescence decays is the use of global analysis of all 33 variants, which reduces the number of free parameters, increases fitting quality (Supplementary Methods), and gives a consistent description with sm-experiments. Moreover, assuming that CTsD and NTsD are rigid, there are six independent degrees of freedom in the system, which we significantly oversample by measuring 33 variants.

**Aspect 3: Structural validation.** In contrast to our 3-component model, the global analysis of eTCSPC data using a 2-component model yields two distance sets, which cannot describe the expected interdyer distances of the known conformers ( $C_1$  (172L) and  $C_2$  (148L)). Furthermore, for the 2-component model, we do not observe the expected linear correlation between the modeled and experimental interdyer distances, as shown in Supplementary Fig. 5b, c.

**Aspect 4: Specific mutations.** The final point to corroborate the existence of  $C_3$  are the results of a few specific mutations. The variant Q69pAcF/P86C is especially informative, as the donor is placed in the middle of helix c (Orange Fig. 1a), which connects both domains, while the acceptor is located in the middle of helix d, which is part of the CTsD (Brown Fig. 1a). According to FPS, the interdyer distances for  $C_1$  (172L) and  $C_2$  (148L) states are hardly distinguishable by FRET,  $\langle R_{DA} \rangle$  of 34 and 35 Å, respectively. Assuming that both domains preserve their secondary structure, the compaction of T4L in  $C_3$  can only proceed by kinking the helix c. This conclusion is consistent with previous studies that identify V75 as the subdomain boundary and critical in protein stability of the pseudo-wild-type construct wt\* with a boundary for the local stability to unfolding around residue N68<sup>13,55</sup>. Given the location of the dyes and the extension of the dye linkers, expected dye orientations will lead to an increase of the interdyer distance for  $C_3$ , i.e., a greater interdyer distance is expected for  $C_3$  compared to the experimental distances for  $C_1$  (39 Å) and  $C_2$  (37 Å). The additional observed distance of 52.4 Å agrees with this hypothesis (Supplementary Table 2f, Fig. 2c).

An additional inactive variant (R137E)<sup>56,57</sup>, which disturbs the salt bridge between residues 22 and 137, reduces the population of  $C_3$  by ~50% (Supplementary Fig. 10d, Supplementary Table 2h), a

phenotype also observed for the inactive variant E11A/S44C/I150C.

In conclusion, the existence of  $C_3$  demonstrates a greater level of complexity of the domain motions of T4L than a single hinge-bending motion, which is in agreement with recent indirect observations<sup>20,24,29</sup>. The complex exchange dynamics between the conformations with relaxation times of 4 and 230 μs and the small population of  $C_3$  may explain the difficulties of other experimental biophysical methods and MD simulations in identifying this exchange, and some heterogeneity in interspin distances observed in previous studies for similar conditions<sup>49</sup>.

**Relating conformational states and enzyme function.** A three-step process characterizes the T4L hydrolysis of peptidoglycans. First, the glycosidic bond of the substrate (S) is protonated by E11 followed by the simultaneous nucleophilic attack of water molecules, which are hydrogen-bonded to residues D20 and T26, on the C-1 carbon of S. As a result, the covalent adduct (ES) is observed in PDB ID 148L<sup>14</sup>. Second, the proton is presumably returned from D20 to E11 via solvent transfer. The third and final step is the product release from the active site to regenerate the enzyme to the original state.

In view of the structural dynamics and to link T4L's functional cycle to our three observed conformations, we use an extended MMm (eMMm) scheme as suggested by Kou et al.<sup>30</sup> (Fig. 7a).

Here, this model considers a sequential succession of three steps to go from a free enzyme via a product bound state back to the relaxed free enzyme state. The substrate S binds reversibly to the enzyme E to form an enzyme-substrate complex ES and is converted to the product P, resulting in an EP complex with the product still bound to the enzyme. A transition of E to an excited state  $E^*$  then releases P from the complex, followed by a relaxation of the free enzyme  $E^*$  to E.

Next, we consider our results in the light of the eMMm framework. First, by using the S44/I150C backbone and two key functional T4L variants (E11A, T26E), we create the relationship between the conformational ( $C_1$ ,  $C_2$ , and  $C_3$ ) and the above-described reaction states (E, ES, and EP) for purposes of elucidating the functional role of  $E^*$  (Fig. 7). We observed a significant difference of the populations of the conformers (Fig. 6) between the three reaction states.

To connect conformational equilibria with catalysis, we monitor the relative changes in species fractions observed across the functional variants in both the absence and presence of substrate (upper panel of Fig. 6e) by generating a  $3 \times 3$  state matrix (Fig. 7b). As indicated in the matrix, specific conformational states are favored in each enzyme reaction state (Fig. 7c,d). For this representation, we use the relative population changes as compared to the wt\*\* to monitor the conformational populations of the different enzyme states.

In the free enzyme state E, the open conformation  $C_1$  is mostly populated to enable substrate binding, which initiates the catalytic cycle through the formation of ES. Through this cycle, the closed conformation  $C_2$  now becomes the most abundant conformation<sup>14</sup>. In this conformation, the glycosidic bond can be cleaved such that  $C_2$  connects both ES and EP. In our studies, we determine that the product release may occur in the compact conformation  $C_3$ , a population that is greatly increased in EP. Thus,  $C_3$  links EP and E so that the original enzyme E is regenerated from EP, which closes the enzymatic cycle. Consequently, the compact state  $C_3$  now corresponds to the excited conformational state  $E^*$  (Fig. 7a–d), the function of which is to disperse the product<sup>18,29</sup> (Fig. 7b, d). These series of events show a sequential closing from the most open conformation  $C_1$  to the most compact form  $C_3$  along two coordinates: the reaction state and the conformational state.

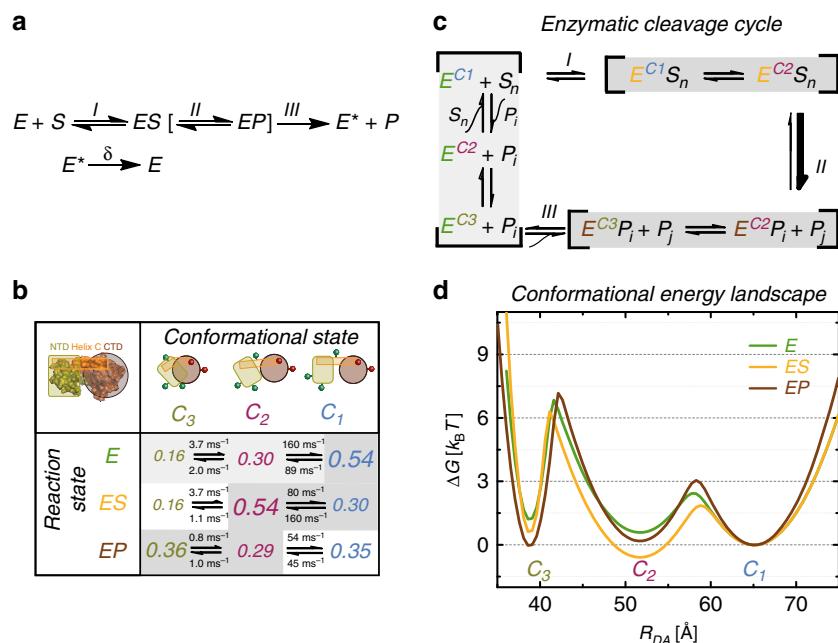


**Fig. 7 Energy landscape of T4L.** **a** Extended Michaelis-Menten scheme. **b** T4L interconverts between three major  $C_1$ ,  $C_2$ , and  $C_3$  conformational states. The population fractions of  $C_1$ ,  $C_2$ , and  $C_3$  are normalized to the variant S44pAcF/I150C in the absence of substrate using the relative changes in Fig. 6e to correct for the influence of specific mutations in that absence. The different font sizes represent the species fractions  $x_i$  for each conformer according to Supplementary Table 2h and satisfy  $x_1 + x_2 + x_3 = 1$ . The three enzyme states are monitored via the following three enzyme variants: (i) the free enzyme state E via S44pAcF/I150C; (ii) the enzyme-substrate state ES via the inactive E11A/S44C/I150C with bound substrate; and (iii) the enzyme product state EP via the product adduct with T26E/S44pAcF/I150C after substrate cleavage. The reaction rate constants are calculated according to the process detailed in Supplementary Note 3, the confidence intervals of which are shown in Supplementary Table 4c. **c** The peptidoglycan chain with  $n$  subunits ( $S_n$ ) is cleaved into two products ( $P_i$  and  $P_j$  with  $n = i + j$ ) by T4L, both of which can be further processed by T4L until only the dimer of *N*-acetylglucosamine and *N*-acetylmuramic acid remains. The gray shaded steps indicate the conformational/reaction states observed. **d** Relative Gibbs free energy landscapes are calculated using  $\Delta G^0 = -k_B T \ln \left( \frac{k_{ij}}{k_{ji}} \right)$ , where  $k_B$  is the Boltzmann constant and  $T$  is the temperature;  $k_{ij}$  are the reaction rate constants between states  $C_i$  and  $C_j$  for the data presented in (a). The activation energies are calculated according to  $\Delta G^{0+} = -k_B T \ln \left( \frac{k_{ij}}{k_0} \right)$  assuming  $k_0 = 10^3 \text{ ms}^{-1}$  as an arbitrary constant. The distributions consider  $C_1$ ,  $C_2$ , and  $C_3$  to follow a Gaussian distribution as a function of the interdyne distance  $R_{DA}$ . The Gaussian widths ( $\sigma_i$ ) are adjusted to satisfy the energy differences and calculated activation energies. Each energy landscape is independently normalized to  $C_1$ .

Most strikingly, even under saturating conditions, which favor the ES and EP states, the enzyme was observed to remain in dynamic equilibrium between the conformational states, rather than transforming entirely into a single conformational state.

To visualize the relative energetic changes of the enzyme during the various steps of the catalytic cycle, we use the species fractions and reaction rate constants to compute the relative energy landscape based on the Arrhenius equation (Fig. 7d, Supplementary Fig. 11). We observe a sequential closing of the enzyme to populate  $C_3$ . This is consistent with a ratchet model for providing directionality on the reaction<sup>58–60</sup> beyond the directionality introduced by the excess of S. This also corroborates with our Monte Carlo simulations (Fig. 3) that are incompatible with the unlikely off pathway from  $C_1$  to  $C_2$  through  $C_3$  due to steric hindrances and with the fast hinge bending motion (4  $\mu\text{s}$ ) expected from structural models (PDB ID 172L and 148L).

All our evidence suggests that the conformational state  $C_3$ , which appears to be more compact than any other structure known of T4L, is compulsory after rather than before catalytic cleavage. Thus, the compact nature of this structure suggests a functional role that is related to product release via an excited state  $E^*$  (Fig. 7a). This mechanism can be an evolutionary advantage when directionality is required for function. On the contrary, considering a system with only two conformational states and without an active cleaning mechanism, the stochastic dissociation of the product can become rate-limiting given a high affinity of the product to the enzyme in the EP state. Indeed, a

large surfeit of substrate is always characteristic of the *in vivo* conditions for T4L. Thus, the use of a three-state system to decouple the substrate access and product release can mitigate the occurrence of substrate inhibition in a two-state system when the route to the active site is clogged by excess substrate concentrations<sup>61</sup>.

In summary, we studied 33 distinct FRET-pairs to effectively oversample the anticipated simple hinge-bending motion of T4L. Due to the high precision, we identified three substrate-dependent fluorescence states that are in fast kinetic exchange. Inverting the positions of the dyes, e.g. S44pAcF/I150C-DA vs. S44pAcF/I150C-AD (Fig. 3b), rules out specific interactions of the dyes with T4L.

Functional variants change the relative populations of the fluorescence states that are determined in a substrate-dependent manner (Fig. 6). Given successive compaction via three conformational states ( $C_1$ ,  $C_2$ , and  $C_3$ ), and three reaction states (E, ES, and EP), we considered an eMM reaction scheme (Fig. 7a, c) to provide a meaningful description of the data. Mutagenesis and stability studies indicate the stability of CTsD and a flexibility of the NTsD<sup>4,13,40–42,62</sup>, which may be a necessary principle for the construction of enzymes undergoing conformational changes during catalysis. The combination of known structural models and fluorescence data is used to create a proposed novel structural state in the catalytic cycle of T4L involving a rearrangement of the reactive NTsD with respect to the CTsD, which is deemed consistent with the eMM for enzyme kinetics. For a complete



structural insight, we are now using the obtained FRET-restraints to present a potential model of  $C_3$ , which is left for a future report.

We anticipate that the presented integrative approach combining the fluorescence spectroscopic toolkit and computational information can accelerate the development of dynamic structural biology<sup>63</sup> by resolving the behaviors of long- and short-lived excited states for purposes of characterizing their functional relevance. This approach is highly relevant as we move towards understanding biomolecular dynamics in situ, where “invisible” molecular effects (i.e., ionic, viscous, and crowding effects<sup>64</sup>) have the potential to modulate weak interactions with important repercussions in biological systems. The elucidation of excited conformational states is necessary for a thorough in-depth understanding of the mechanisms of enzymes. Thus, a comprehensive description of a dynamic molecular system contains intertwined kinetic and structural information, which is often difficult to obtain by traditional methods. Such information can be archived in the data bank PDB-dev<sup>65</sup> so that excited conformational states gain the urgently needed visibility.

## Methods

**Sample preparation.** T4L cysteine and amber (TAG) mutants are generated via site-directed mutagenesis in the pseudo-wild-type construct containing the mutations C54T and C97A (wt\*), which was subsequently cloned into the pET11a vector (Life Technologies Corp.)<sup>66–68</sup>. All primer sequences are listed in Supplementary Table 6. The plasmid containing the gene with the desired mutant was co-transformed with pEVOL<sup>66</sup> into BL21(DE3) *E. coli* (Life Technologies Corp.) and plated onto LB-agar plates supplemented with the respective antibiotics, ampicillin and chloramphenicol. A single colony was inoculated into 100 mL of LB medium containing the above-mentioned antibiotics and grown overnight at 37 °C in a shaking incubator. 50 mL of the overnight culture are used to inoculate 1 L of LB medium supplemented with the respective antibiotics and 0.4 g/L of pAcF (SynChem) and grown at 37 °C until an OD<sub>600</sub> of 0.5 was reached. The protein production was induced for 6 h by addition of 1 mM IPTG and 4 g/L of arabinose.

Cells are harvested, lysed in 50 mM HEPES, 1 mM EDTA, and 5 mM DTT at pH 7.5 and purified using a monoS 5/5 column (GE Healthcare) with an eluting gradient from 0 to 1 M NaCl according to standard procedures. High-molecular weight impurities are removed by passing the eluted protein through a 30 kDa Amicon concentrator (Millipore), followed by subsequent concentration and buffer exchange to 50 mM PB, 150 mM NaCl pH 7.5 of the protein flow through with a 10 kDa Amicon concentrator. For the double cysteine mutant containing E11A, the temperature was reduced to 20 °C after induction and the cells are grown additional 20 h to increase the fraction of soluble protein. This mutant was produced and purified as described above, except that only ampicillin for selection and IPTG for induction are needed.

Site-specific labeling of T4L was accomplished using orthogonal chemistry. To probe T4L structure by FRET studies (Fig. 2a) we labeled the Keto group of the *p*-acetyl-L-phenylalanine (pAcF) amino acid at the N-terminal subdomain, hydroxylamine linker chemistry was used for the donor dye Alexa488 (Life Technologies Corp.). Cysteine mutants were labeled via a thiol reaction with maleimide linkers of the Alexa647 acceptor dye.

In one exceptional case of the sample S44pAcF/I150C-AD, the labeling was reversed in order to test the reproducibility of the filtered FCS (Fig. 3b) and FRET measurements with different dyes. Acceptor dye Alexa647 with hydroxylamine linker was used to label the pAcF and the Alexa488 donor dye with maleimide linker was used to label the cysteine residue of the mutant S44pAcF/I150C-AD.

For spin labeling, the S44C/I150C double mutant was diluted to a final concentration of ~10 μM in labeling buffer (50 mM MOPS, 25 mM NaCl, pH 6.8) and a 10-fold molar excess of a methanethiosulfonate nitroxide (MTSSL) was added overnight<sup>68</sup>. Next day, excess spin reagent was removed using a desalting column (HiPrep 26/10, GE Healthcare) according to the manufacturer's instructions and concentrated with a 15 kDa Amicon concentrator (Millipore).

Binding of labeled T4L mutants to peptidoglycan from *Micrococcus luteus* (Sigma-Aldrich) was monitored by reverse phase chromatography using a C-18 column out of ODS-A material (4 × 150 mm, 300 Å) (YMC Europe GmbH, Dinslaken, Germany). The labeled protein (1 μM) was incubated with the substrate at 1 mg/mL in PBS. At various points of the reaction, 25 μL of mixed sample injected and further eluted with a gradient from 0 to 80% acetonitrile containing 0.01% trifluoroacetic acid for 25 min at a flow rate of 0.5 ml/min. The labeled complex elution was monitored by absorbance at 495 nm.

**Single-molecule experiments.** For single-molecule measurements with multi-parameter fluorescence detection, we added 40 μM TROLOX to the measurement buffer to minimize the acceptor blinking and 1 μM unlabeled T4L to prevent any

adsorption to the cover glass. A custom-built confocal microscope with a dead time-free detection scheme using 8 detectors (four green (τ-SPAD, PicoQuant, Germany) and four red channels (APD SPCM-AQR-14, Perkin Elmer, Germany)) was used for MFD and fFCS measurements. A time-correlated single photon counting (TCSPC) module with 8 synchronized input channels (HydraHarp 400, PicoQuant, Germany) was used to register the detected photon counts in the Time-Tagged Time-Resolved (TTTR) mode. For more details on TTTR please read<sup>69</sup>. The data was analyzed by established MFD procedures<sup>31,33,43</sup> and software, a more detailed description is given in Supplementary Methods. Exemplary data analysis is shown in Supplementary Fig. 3 and Supplementary Note 1, MFD-histograms of all measurements are collected in Supplementary Fig. 2 and Supplementary Fig. 10.

**Filtered FCS.** Filtered FCS (fFCS) is a derivative of fluorescence correlation spectroscopy (FCS). In fFCS, the information on the fluorescent species contained in the time- and polarization- resolved fluorescence decays (exemplary shown in Supplementary Fig. 9a, c) was used to amplify the transitions between the species of interest<sup>32,34,45</sup>. For this, we arbitrarily constructed species-selective filters (exemplary shown in Supplementary Fig. 9b, d) based on the major and minor population in the smFRET experiment and calculated species-selective auto-(sACF) and cross-correlation functions (sCCF). The in total four curves (two sACF's and two sCCF's) are analyzed jointly using established fitting models (Supplementary Methods Equations (15–17))<sup>32,34,45</sup>. For more details see Supplementary Methods.

**Fluorescence decay analysis.** Fluorescence decays of all samples and single-labeled reference samples are collected on either an IBH-5000U (IBH, Scotland) or a Fluotime 200 (Picoquant, Germany) system. We collected high-precision fluorescence decays histograms with 30 million photons to precisely determine the FRET parameters of limiting states together with their corresponding structural properties. eTCSPC has the advantage of better photon statistics, polarization-free measurements due to magic-angle detection, a keenly evolved instrumental response function (IRF), low background fluorescence, and the absence of photobleaching at low excitation powers. As the fluorophores are coupled via long and flexible linkers, this resulted in a DA-distance distribution even for single protein conformations. For our data analysis, we assumed that the dyes rotate quickly ( $\kappa^2 = 2/3$ ) and diffuse slowly compared to the fluorescence lifetime (~ns)<sup>38</sup>. We validated the assumption of fast rotating dyes by time-resolved anisotropy measurements (Supplementary Table 3a–c). Moreover, we interpret the broadening of the DA-distance distributions, beyond what is expected from flexible linkers, as evidence for conformational heterogeneity of the host molecule. To dissect the donor-quenching by FRET (i.e., FRET-induced donor decay), we jointly analyzed the DA- and DOnly-dataset, where the donor fluorescence lifetime distribution was shared with the DA-dataset (Supplementary Methods, Supplementary Equations (20, 24–S27))<sup>47</sup>. We compared three different fit models (Supplementary Table 5). The results are summarized in Supplementary Table 2. We estimated the statistical uncertainty of the model parameters by making use of the known shot noise of the fluorescence decays. We randomly sampled the model parameters by a Markov chain Monte Carlo (MCMC) method to estimate their uncertainties for a single dataset (Supplementary Methods)<sup>70</sup>. The applied joint, global fit significantly reduced the overall dimensionality of the analysis but still left too many degrees of freedom (Supplementary Methods) for an exhaustive sampling by MCMC. Hence, we applied a support plane analysis to estimate the model parameter uncertainties, in which we systematically varied  $x_3$  while minimizing all other parameters.

**Electron paramagnetic resonance.** For double electron electron resonance (DEER) measurements of doubly spin labeled proteins, ~200 μM spin-labeled T4L containing 20% glycerol (v/v) was placed in a quartz capillary (1.5 mm i.d. × 1.8 mm o.d.; VitroCom) and then flash-frozen in liquid nitrogen. Sample temperature was maintained at 80 K. The four-pulse DEER experiment was conducted on a Bruker Elexys 580 spectrometer fitted with an MS-2 split ring resonator. Pulses of 8 ns ( $\pi/2$ ) and 16 ns ( $\pi$ ) are amplified with a TWT amplifier (Applied Engineering Systems). Pump frequency was set at the maximum of the central resonance, and the observe frequency was 70 MHz less than the pump frequency. Dipolar data are analyzed by using a custom program, LongDistances<sup>71</sup>, written in LabVIEW (National Instruments Co.). Distance distributions are acquired using Tikhonov regularization<sup>51</sup>.

**Recovering the reaction network by Brownian dynamics simulations.** To solve the ambiguity in the connectivity of states and kinetics of T4L, i.e. between the two possible analytical solutions of the transition rate matrix (Supplementary Methods Equation (31)), we used Brownian dynamics simulation of single-molecule and fFCS experiments. Simulations of single-molecule measurements are done via Brownian dynamics<sup>72–75</sup>. The spatial intensity distribution of the observation volume was assumed a 3D Gaussian. In contrast to other simulators, freely diffusing molecules in an “open” volume are used. Transition kinetics is modeled by allowing  $i \rightarrow j$  transitions. The time that molecules spend in  $i$  and  $j$  states ( $t_i$  and  $t_j$ ,

respectively) are exponentially distributed with

$$P(t_i) = k_i^{-1} \exp(-k_i t_i) \text{ and } P(t_j) = k_j^{-1} \exp(-k_j t_j). \quad (1)$$

Simulated photon counts are saved in SPC-132 data format (Becker & Hückel GmbH, Berlin, Germany) and treated as experimental data. To quantify the difference between the two possible, simulated models and the experimental data, we calculated the relative  $\chi^2$  for the one-dimensional and two-dimensional MFD-histograms (Supplementary Note 3, Supplementary Table 1a, b).

**Simulation of inter-dye distances and structural modelling.** Accessible contact volume (ACV) simulations and inter-dye distances. The accessible volume (AV) considers dyes as hard sphere models connected to the protein via flexible linkers (modeled as a flexible cylindrical pipe)<sup>38</sup>. The overall dimension (width and length) of the linker is based on their chemical structures. For Alexa488 the five carbon linker length was set to 20 Å, the width of the linker is 4.5 Å and the dye radii  $R_1 = 5$  Å,  $R_2 = 4.5$  Å and  $R_3 = 1.5$  Å. For Alexa647 the dimensions used are: length = 22 Å, width = 4.5 Å and three dye radii  $R_1 = 11$  Å,  $R_2 = 3$  Å and  $R_3 = 3.5$  Å. Here, the dye distribution was modeled by the accessible contact volume approach (ACV)<sup>9</sup>, which is similar to the accessible volume (AV)<sup>38</sup>, but defines an area close to the surface as contact volume.

Similar approaches have been introduced before to predict possible positions for EPR and FRET labels<sup>10,36,37</sup>. The dye is assumed to diffuse freely within the AV and its diffusion is hindered close to the surface. The part of AV which is closer than 3 Å from the macromolecular surface (contact volume) is defined to have higher dye density  $\rho_{\text{Dye, trapped}}$ . The spatial density  $\rho_{\text{Dye}}$  along  $R$  is approximated by a step function:  $\rho_{\text{Dye}} = [\rho_{\text{Dye, free}}, R < 3$  Å;  $\rho_{\text{Dye, trapped}}, R \geq 3$  Å]. The  $\rho_{\text{Dye, trapped}}/\rho_{\text{Dye, free}}$  ratio is calculated from the fraction of the trapped dye  $x_{\text{Dye, trapped}}$  for each labeling position separately:  $\rho_{\text{Dye, free}}/\rho_{\text{Dye, trapped}} = V_{\text{Dye, trapped}}(1 - x_{\text{Dye, trapped}})/(x_{\text{Dye, trapped}} V_{\text{Dye, free}})$ . For this, the fraction  $x_{\text{Dye, trapped}}$  was approximated by the ratio of the residual,  $r_{\text{res}}$ , and fundamental anisotropy,  $r_0$ , determined by the time-resolved anisotropy decay of the directly excited dyes (Supplementary Table 3).

To account for dye linker mobility, we generated a series of ACV's for donor and acceptor dyes attached to T4L placing the dyes at multiple separation distances. For each pair of ACV's, we calculated the distance between dye mean positions ( $R_{\text{mp}}$ )

$$R_{\text{mp}} = \left| \langle \vec{R}_{\text{D}(i)} \rangle - \langle \vec{R}_{\text{A}(j)} \rangle \right| = \left| \frac{1}{n} \sum_{i=1}^n \vec{R}_{\text{D}(i)} - \frac{1}{m} \sum_{j=1}^m \vec{R}_{\text{A}(j)} \right|, \quad (2)$$

where  $\vec{R}_{\text{D}(i)}$  and  $\vec{R}_{\text{A}(j)}$  are all the possible positions that the donor fluorophore and the acceptor fluorophore can take. However, in ensemble TCSPC (eTCSPC) the mean donor-acceptor distance is observed:

$$\langle R_{\text{DA}} \rangle = \left| \langle \vec{R}_{\text{D}(i)} - \vec{R}_{\text{A}(j)} \rangle \right| = \frac{1}{nm} \sum_{i=1}^n \sum_{j=1}^m \left| \vec{R}_{\text{D}(i)} - \vec{R}_{\text{A}(j)} \right|, \quad (3)$$

which can be modeled with the accessible volume calculation.

The relationship between  $R_{\text{mp}}$  and  $\langle R_{\text{DA}} \rangle$  can be derived empirically following a third order polynomial from many different simulations. The  $\langle R_{\text{DA}} \rangle$  is not directly related to the distance between atoms on the backbone (Ca-Ca), except through the use of a structural model.

FRET positioning and Screening (FPS). FPS is done in four steps, and its flow is based on the recent work by Kalinin et al.<sup>10</sup>. In order to do our experimental design using the available PDB structures of T4L with respect to our FRET data, FPS calculates the donor and acceptor accessible volumes for each donor-acceptor labeling scheme. We then compute an error function for each conformational state  $C^{(i)}$

$$\chi_{r, \text{FPS}}^2 = \frac{1}{N} \sum_{i=1}^N \frac{\left( \langle R_{\text{DA}} \rangle_{\text{experiment}}^{(i)} - \langle R_{\text{DA}} \rangle_{\text{model } j}^{(i)} \right)^2}{\left( \Delta R_{\text{DA, tot}}^{(i)} \right)^2}, \quad (4)$$

where  $N = 33$  is the total number of FRET distances ( $\langle R_{\text{DA}} \rangle$ ) and the overall theoretically computed absolute uncertainty  $\Delta R_{\text{DA, tot}}^{(i)}$  (see next section).

In order to compare the structural models currently available in the PDB to our experimental results, we clustered all PDB models using the RMSD (Root Mean Squared Deviation) of Ca atoms as the similarity measure. Clustering allowed us to sort all PDB models into three distinct groups based on the similarity of their backbone shapes. We found that the structural models of T4L group into open, ajar, and closed clusters (based on the proximity of the CTsD and NTsD) with an intra-cluster RMSD of less than 1.8 Å. Representative structures of these clusters are given by PDB IDs 172L, 1JQU, and 148L for the open, ajar, and closed conformations, respectively (Fig. 5a). This was done using the agglomerative hierarchical complete-linkage clustering of the "fastcluster"<sup>76</sup> software.

In Supplementary Table 4 we provide the complete breakdown of the three clusters. In Supplementary Fig. 6 we display the complete FRET-screening of the three clusters.

**Calculation of uncertainties.** The overall theoretically computed absolute uncertainty  $\Delta R_{\text{DA, tot}}^{(i)}$  of the average inter-dye distance for the pair ( $i$ ) is determined

by the error-propagation rule:

$$\Delta R_{\text{DA, tot}}^{(i)} = \sqrt{\left( \delta R_{\text{dye model}} \cdot R_{\text{DA}}^{(i)} \right)^2 + \left( \delta R_{R_0} \left( r(t)_{\text{dye}} \right) \cdot R_{\text{DA}}^{(i)} \right)^2 + \left( \Delta R_{\text{Reference}} \right)^2 + \left( \Delta R_{\text{noise-},+}^{(i)} \right)^2} \quad (5)$$

In the following, we describe the computation of the four individual contributions expressed as absolute and relative distance uncertainties,  $\Delta R$  and  $\delta R$ , respectively.

(1) Dye model. The relative distance error  $\delta R_{\text{dye model}}$  usually considers the asymmetry of the AVs for random labeling of two equivalent labeling sites (in general two cysteines) with  $\delta R_{\text{dye model}} \approx 1.5\%$ <sup>47</sup>. However, in this work we labeled T4L specifically (one cysteine, one p-acetylphenylalanine) so that  $\Delta R_{\text{dye model}} = 0$ .

(2) Uncertainty of the Förster Radius  $R_0$ . The relative distance error  $\delta R_{R_0} \left( r(t)_{\text{dye}} \right)$  considers the uncertainty of the Förster Radius  $R_0$  that is usually dominated by  $\kappa^2$  errors related to the mutual orientation of donor and acceptor. At first, we use the experimental anisotropy decays  $r(t)_{\text{dye}}$  recorded by eTCSPC and MFD and the wobbling in a cone (WIC) model to compute possible distribution of orientational factors,  $p(\kappa^2)$ <sup>38,77</sup>. As input we determined the residual anisotropies of the donor fluorescence  $r_{3, \text{D}}$  (Supplementary Table 3a), the directly excited acceptor fluorescence  $r_{3, \text{A}}$  (Supplementary Table 3b) and the FRET-sensitized acceptor fluorescence  $r_{2, \text{A(D)}}$  (Supplementary Table 3c). Based on these limits, we computed the distribution of the orientation factor  $p(\kappa^2)$  (Supplementary Table 3d) for each FRET pair as described in Sindbert et al.<sup>38</sup>. Next, we compute how  $p(\kappa^2)$  affects the experimentally observed inter-dye distance. Following the approach of Sindbert et al.<sup>38</sup>, we can assume that a DA pair is characterized by a single "true" DA distance  $R_{\text{DA}}$  with  $\kappa^2 \neq 2/3$ . As we calculate the DA distance assuming  $\kappa^2 = 2/3$ , we only recover an apparent DA distance,  $R_{\text{app}}$ . Obviously,  $R_{\text{app}}$  differs from  $R_{\text{DA}}$ ,  $R_{\text{app}}/R_{\text{DA}} = \left( \frac{2}{3} \cdot \kappa^2 \right)^{-1/6}$ . A distribution of  $\kappa^2$  relates for a single  $R_{\text{DA}}$  to a distribution of apparent  $R_{\text{app}}$ . For each FRET pair the distribution  $p(\kappa^2)$  compiled in Supplementary Table 3d is transformed to a distribution of the relative distances  $R_{\text{app}}/R_{\text{DA}} = \xi$ . The standard deviation of the distribution  $p(\xi)$  is used as a relative approximate for the precision of the distance  $R_{\text{DA}}$ .

$$\delta R_{\text{DA, precision}}(\kappa^2) \approx (\text{Var}[\xi])^{1/2} \quad \text{with } \xi = R_{\text{app}}/R_{\text{DA}} \quad (6)$$

The expectation value of  $p(\xi)$  can be used as an estimate of the accuracy:

$$\delta R_{\text{DA, accuracy}}(\kappa^2) \approx \langle \xi \rangle - 1 \quad \text{with } \langle \xi \rangle = \int \xi \cdot p(\xi) d\xi \quad (7)$$

For the WIC model with the given residual anisotropies, the precision  $\delta R_{\text{DA, precision}}(\kappa^2)$  dominates the relative uncertainty. Estimates for  $\delta R_{\text{DA, accuracy}}(\kappa^2)$  are very close to one. Hence, we estimate the overall uncertainty attributed to  $\kappa^2$  by

$$\delta R_{R_0} \approx \delta R_{\text{DA}}(\kappa^2) = \delta R_{\text{DA, precision}}(\kappa^2) = \left( \int (\xi - \langle \xi \rangle)^2 \cdot p(\xi) d\xi^{1/2} \right) \quad (8)$$

(3) Uncertainty of the D-only reference. The absolute uncertainty of the Donor-only reference  $\Delta R_{\text{reference}}$  considers the discrepancy between the photophysical properties of the donor in the FRET sample and the properties determined from the donor-only sample. This discrepancy is typically caused by unspecific labeling of the biomolecule and thus unknown fraction of donor-acceptor molecules with respect to acceptor-donor molecules (see also Peulen et al.<sup>47</sup>, Fig. 12). In this work,  $\Delta R_{\text{reference}}$  was set to zero, since specific labeling was used and the donor position is known exactly and accurate donor only sample was measured (Supplementary Table 2a).

(4) Statistical uncertainty (error of the fit). The state-specific asymmetric absolute statistical uncertainty  $\Delta \langle R_{\text{noise-},+}^{(i)} \rangle$  is caused by the shot noise of the lifetime measurements (listed in Supplementary Table 2g).  $\Delta \langle R_{\text{noise-},+}^{(i)} \rangle$  is calculated from the spread of obtained distances for the three states of the global fit using the shortest ( $\langle R_{\text{noise-}} \rangle$ ) and longest distance ( $\langle R_{\text{noise+}} \rangle$ ) below the 1 $\sigma$ -threshold (Supplementary Table 2g). As the distance  $\langle R_{\text{DA}} \rangle$  of the global fit with the lowest  $\chi^2$  ( $x_3 = 0.18$ ) is not necessarily the average of  $\langle R_{\text{noise-}} \rangle$  and  $\langle R_{\text{noise+}} \rangle$ , both  $\Delta \langle R_{\text{noise-},+}^{(i)} \rangle$  and the resulting  $\Delta R_{\text{DA, tot}}^{(i)}$  are not symmetric:

$$\Delta \langle R_{\text{noise-},+}^{(i)} \rangle = \left| \langle R_{\text{noise-},+}^{(i)} \rangle - \langle R_{\text{DA}}^{(i)} \rangle \right|.$$

For example, considering a 1 $\sigma$ -confidence interval, the fraction  $x_3$  of  $\langle R_{\text{DA}}^{(3)} \rangle$  varies between 0.1 and 0.27 (see Fig. 4c). The corresponding  $\langle R_{\text{noise-}}^{(i)} \rangle$  and  $\langle R_{\text{noise+}}^{(i)} \rangle$  are the shortest and longest distance below the 1 $\sigma$ -threshold. The minimal  $\chi^2_{r, \text{global}}$  for this distribution fit model is 1.0736 with the species fraction  $x_3 = x_{\text{middle}} = 0.18$  with  $x_1 = 0.44$  and  $x_2 = 0.38$  and the state-specific mean distances  $\langle R_{\text{DA}}^{(i)} \rangle$  are listed in the Supplementary Table 2d-f.

**Controls for the FRET analysis.** Since the problems inherent in the use of smFRET studies are connected with complexities related to the labels, we performed ten controls to check for any potential label artifacts. Please refer to the

Supplementary Information for additional data and extended controls (Supplementary Note 6).

1. The labeling does not alter enzyme function with the labeled T26E variant indicating an expected adduct formation (Fig. 6, Supplementary Fig. 8).
2. Local quenching of the donor dye is considered when calculating distances and cross correlations (Supplementary Table 2).
3. The triplet state quenchers do not affect the observed relaxation times and amplitudes on the species cross-correlation (Supplementary Fig. 12).
4. The acceptor cis-trans isomerization does not contribute to the signal on the species correlation analysis (Supplementary Fig. 12).
5. The  $\kappa^2$  distributions indicated the validity of our assumption of  $\kappa^2 = 2/3$ . Supplementary Table 3 summarizes the residual anisotropies ( $r_{\infty}$ ) of D—donor, A—acceptor and A(D) by the FRET-sensitized emission of acceptor used for calculating  $\kappa^2$  distributions<sup>31</sup>.
6. The existence and the population fraction of the new conformational state  $C_3$  with a confidence rate of 68% between 10 and 27% is consistent across our library of 33 variants with  $x_3 = 21\%$ . The variation of the experimental uncertainty is consistent with the determination in the literature that mutations slightly affect the conformational stability of T4L, which was measured in chemical denaturation experiments<sup>62</sup>. We thus attribute this variability of the species fractions to mutation effects.
7. All 33 variants provide a consistent view of the T4L conformational states, in which we determined after X-ray crystallography a consistency with the two limiting structures determined by T4L without outliers (Fig. 5, Supplementary Table 2d–f).
8. We oversample the FRET restraints to reduce the uncertainty introduced from each point mutation (Fig. 5, Supplementary Table 2d–f).
9. The thermodynamic stability and proper folding of our variants are verified by chemical denaturation with urea and by measuring CD spectra for both unlabeled and labeled T4L.
10. We fit time resolved fluorescence decays with various models to provide a consistent view of the conformational space (Supplementary Methods).

**Reporting summary.** Further information on research design is available in the Nature Research Reporting Summary linked to this article.

### Data availability

The source data for all variants and all used techniques and screening results for the PDB structures were uploaded to Zenodo under DOI 10.5281/zenodo.3376527 and are described in Supplementary Note 7. The Zenodo archive contains subfolders for all eTCSPEC FRET data including reference measurements used for derivation of DA distances (eTCSPEC\_wildtype.zip; e.g. Figures 4, 5, and Supplementary Fig. 5), single-molecule raw data used for filtered FCS and MFD analysis (Single\_molecule\_wildtype.zip; e.g. Figures 2, 3, Supplementary Figs. 2, 4, and 9), single molecule data of functional variants used for derivation of the kinetic scheme (Single\_molecule\_functional\_variants.zip; e.g. Figure 6, Supplementary Figs. 6, 7, 9, and 11), EPR data (EPR\_wildtype.zip; e.g. Figure 6 and Supplementary Fig. 5), and an overview on the FRET screening of PDB structures (FRET\_screening\_of\_PDB\_structures.zip). The source data underlying Supplementary Fig. 8c is shown in the Source Data File. Further datasets of processed data and the analysis are available from the corresponding authors on reasonable request.

### Code availability

Most general custom-made computer code is directly available from <http://www.mpc.hhu.de/en/software>. Additional computer code custom-made for this publication is available upon request from the corresponding authors. In-house programs are used (1) in the confocal multiparameter fluorescence detection experiments, (2) to elucidate the filtered fluorescence correlation spectroscopy curves, and (3) to analyze the fluorescence lifetime measurements. Software for analysis of single-molecule measurements and fluorescence correlation analysis and their simulation is available at <http://www.mpc.uni-duesseldorf.de> and software for analysis of fluorescence decays can be downloaded from <http://www.fret.at/tutorial/chisurf/>.

Received: 8 June 2018; Accepted: 8 February 2020;

Published online: 06 March 2020

### References

1. Smock, R. G. & Gierasch, L. M. Sending signals dynamically. *Science* **324**, 198–203 (2009).
2. Hammes, G. G. Mechanism of enzyme catalysis. *Nature* **204**, 342–343 (1964).
3. Kleckner, I. R. & Foster, M. P. An introduction to NMR-based approaches for measuring protein dynamics. *Biochim. Biophys. Acta* **1814**, 942–968 (2011).
4. McHaourab, H. S., Lietzow, M. A., Hideg, K. & Hubbell, W. L. Motion of spin-labeled side chains in T4 lysozyme. Correlation with protein structure and dynamics. *Biochemistry* **35**, 7692–7704 (1996).
5. Henzler-Wildman, K. & Kern, D. Dynamic personalities of proteins. *Nature* **450**, 964–972 (2007).
6. Mulder, F. A., Mittermaier, A., Hon, B., Dahlquist, F. W. & Kay, L. E. Studying excited states of proteins by NMR spectroscopy. *Nat. Struct. Biol.* **8**, 932–935 (2001).
7. Kilic, S. et al. Single-molecule FRET reveals multiscale chromatin dynamics modulated by HP1 alpha. *Nat. Commun.* **9**, 235 (2018).
8. Hellenkamp, B., Wortmann, P., Kandzia, F., Zacharias, M. & Hugel, T. Multidomain structure and correlated dynamics determined by self-consistent FRET networks. *Nat. Meth.* **14**, 174–180 (2017).
9. Dimura, M. et al. Quantitative FRET studies and integrative modeling unravel the structure and dynamics of biomolecular systems. *Curr. Opin. Struct. Biol.* **40**, 163–185 (2016).
10. Kalinin, S. et al. A toolkit and benchmark study for FRET-restrained high-precision structural modeling. *Nat. Meth.* **9**, 1218–1225 (2012).
11. van den Bedem, H. & Fraser, J. S. Integrative, dynamic structural biology at atomic resolution—it's about time. *Nat. Meth.* **12**, 307–318 (2015).
12. Matthews, B. W. & Remington, S. J. The three dimensional structure of the lysozyme from bacteriophage T4. *Proc. Natl Acad. Sci. USA* **71**, 4178–4182 (1974).
13. Llinas, M., Gillespie, B., Dahlquist, F. W. & Marqusee, S. The energetics of T4 lysozyme reveal a hierarchy of conformations. *Nat. Struct. Biol.* **6**, 1072–1078 (1999).
14. Kuroki, R., Weaver, L. H. & Matthews, B. W. A covalent enzyme-substrate intermediate with saccharide distortion in a mutant T4 lysozyme. *Science* **262**, 2030–2033 (1993).
15. Goto, N. K., Skrynnikov, N. R., Dahlquist, F. W. & Kay, L. E. What is the average conformation of bacteriophage T4 lysozyme in solution? A domain orientation study using dipolar couplings measured by solution NMR. *J. Mol. Biol.* **308**, 745–764 (2001).
16. Zhang, X. J., Wozniak, J. A. & Matthews, B. W. Protein flexibility and adaptability seen in 25 crystal forms of T4 lysozyme. *J. Mol. Biol.* **250**, 527–552 (1995).
17. Michaelis, L., Menten, M. L., Johnson, K. A. & Goody, R. S. The original Michaelis constant: translation of the 1913 Michaelis-Menten paper. *Biochemistry* **50**, 8264–8269 (2011).
18. Zheng, D. & Lu, H. P. Single-molecule enzymatic conformational dynamics: spilling out the product molecules. *J. Phys. Chem. B* **118**, 9128–9140 (2014).
19. Lu, M. & Lu, H. P. Revealing multiple pathways in T4 Lysozyme substep conformational motions by single-molecule enzymology and modeling. *J. Phys. Chem. B* **121**, 5017–5024 (2017).
20. Akhterov, M. V. et al. Observing lysozyme's closing and opening motions by high-resolution single-molecule enzymology. *ACS Chem. Biol.* **10**, 1495–1501 (2015).
21. Lu, H. P. Revealing time bunching effect in single-molecule enzyme conformational dynamics. *Phys. Chem. Chem. Phys.* **13**, 6734–6749 (2011).
22. Tsugita, A. & Inouye, M. Purification of bacteriophage T4 lysozyme. *J. Biol. Chem.* **243**, 391–397 (1968).
23. Choi, Y. et al. Single-molecule lysozyme dynamics monitored by an electronic circuit. *Science* **335**, 319–324 (2012).
24. Yirdaw, R. B. & McHaourab, H. S. Direct observation of T4 lysozyme hinge-bending motion by fluorescence correlation spectroscopy. *Biophys. J.* **103**, 1525–1536 (2012).
25. de Groot, B. L., Hayward, S., van Aalten, D. M., Amadei, A. & Berendsen, H. J. Domain motions in bacteriophage T4 lysozyme: a comparison between molecular dynamics and crystallographic data. *Proteins* **31**, 116–127 (1998).
26. Lange, O. F. & Grubmüller, H. Full correlation analysis of conformational protein dynamics. *Proteins* **70**, 1294–1312 (2008).
27. Zacharias, M. Combining elastic network analysis and molecular dynamics simulations by hamiltonian replica exchange. *J. Chem. Theory Comput.* **4**, 477–487 (2008).
28. Bouvignies, G. et al. Solution structure of a minor and transiently formed state of a T4 lysozyme mutant. *Nature* **477**, 111–114 (2011).
29. Lu, M. & Lu, H. P. Probing protein multidimensional conformational fluctuations by single-molecule multiparameter photon stamping spectroscopy. *J. Phys. Chem. B* **118**, 11943–11955 (2014).
30. Kou, S. C., Cherayil, B. J., Min, W., English, B. P. & Xie, X. S. Single-molecule Michaelis-Menten equations. *J. Phys. Chem. B* **109**, 19068–19081 (2005).
31. Sisamakos, E., Valeri, A., Kalinin, S., Rothwell, P. J. & Seidel, C. A. M. Accurate single-molecule FRET studies using multiparameter fluorescence detection. *Methods Enzymol.* **475**, 455–514 (2010).
32. Egginger, C., Fries, J. R., Brand, L., Günther, R. & Seidel, C. A. M. Monitoring conformational dynamics of a single molecule by selective fluorescence spectroscopy. *Proc. Natl Acad. Sci. USA* **95**, 1556–1561 (1998).



33. Kühnemuth, R. & Seidel, C. A. M. Principles of single molecule multiparameter fluorescence spectroscopy. *Single Mol.* **2**, 251–254 (2001).
34. Felekyan, S., Kalinin, S., Sanabria, H., Valeri, A. & Seidel, C. A. M. Filtered FCS: species auto- and cross-correlation functions highlight binding and dynamics in biomolecules. *ChemPhysChem* **13**, 1036–1053 (2012).
35. Böhmer, M., Wahl, M., Rahn, H. J., Erdmann, R. & Enderlein, J. Time-resolved fluorescence correlation spectroscopy. *Chem. Phys. Lett.* **353**, 439–445 (2002).
36. Cai, Q. et al. Nanometer distance measurements in RNA using site-directed spin labeling. *Biophys. J.* **93**, 2110–2117 (2007).
37. Muschiellok, A. et al. A nano-positioning system for macromolecular structural analysis. *Nat. Meth.* **5**, 965–971 (2008).
38. Sindbert, S. et al. Accurate distance determination of nucleic acids via Förster resonance energy transfer: implications of dye linker length and rigidity. *J. Am. Chem. Soc.* **133**, 2463–2480 (2011).
39. Shoichet, B. K., Baase, W. A., Kuroki, R. & Matthews, B. W. A relationship between protein stability and protein function. *Proc. Natl Acad. Sci. USA* **92**, 452–456 (1995).
40. McHaourab, H. S., Oh, K. J., Fang, C. J. & Hubbell, W. L. Conformation of T4 lysozyme in solution. Hinge-bending motion and the substrate-induced conformational transition studied by site-directed spin labeling. *Biochemistry* **36**, 307–316 (1997).
41. Cellitti, J. et al. Exploring subdomain cooperativity in T4 lysozyme I: structural and energetic studies of a circular permutant and protein fragment. *Protein Sci.* **16**, 842–851 (2007).
42. Llinas, M. & Marqusee, S. Subdomain interactions as a determinant in the folding and stability of T4 lysozyme. *Protein Sci.* **7**, 96–104 (1998).
43. Kalinin, S., Valeri, A., Antonik, M., Felekyan, S. & Seidel, C. A. Detection of structural dynamics by FRET: a photon distribution and fluorescence lifetime analysis of systems with multiple states. *J. Phys. Chem. B* **114**, 7983–7995 (2010).
44. Gopich, I. V. & Szabo, A. Theory of the energy transfer efficiency and fluorescence lifetime distribution in single-molecule FRET. *Proc. Natl Acad. Sci. USA* **109**, 7747–7752 (2012).
45. Felekyan, S., Sanabria, H., Kalinin, S., Kühnemuth, R. & Seidel, C. A. M. Analyzing Förster resonance energy transfer with fluctuation algorithms. *Methods Enzymol.* **519**, 39–85 (2013).
46. Gopich, I. V. & Szabo, A. Single-macromolecule fluorescence resonance energy transfer and free-energy profiles. *J. Phys. Chem. B* **107**, 5058–5063 (2003).
47. Peulen, T. O., Opanasyuk, O. & Seidel, C. A. M. Combining graphical and analytical methods with molecular simulations to analyze time-resolved FRET measurements of labeled macromolecules accurately. *J. Phys. Chem. B* **121**, 8211–8241 (2017).
48. Sagermann, M., Martensson, L. G., Baase, W. A. & Matthews, B. W. A test of proposed rules for helix capping: implications for protein design. *Protein Sci.* **11**, 516–521 (2002).
49. Islam, S. M., Stein, R. A., McHaourab, H. S. & Roux, B. Structural refinement from restrained-ensemble simulations based on EPR/DEER data: application to T4 lysozyme. *J. Phys. Chem. B* **117**, 4740–4754 (2013).
50. Stein, R. A., Beth, A. H. & Hustedt, E. J. A straightforward approach to the analysis of double electron-electron resonance data. *Methods Enzymol.* **563**, 531–567 (2015).
51. Chiang, Y. W., Borbat, P. P. & Freed, J. H. The determination of pair distance distributions by pulsed ESR using Tikhonov regularization. *J. Magn. Reson.* **172**, 279–295 (2005).
52. Chiang, Y. W., Borbat, P. P. & Freed, J. H. Maximum entropy: a complement to Tikhonov regularization for determination of pair distance distributions by pulsed ESR. *J. Magn. Reson.* **177**, 184–196 (2005).
53. Klein-Seetharaman, J. et al. Long-range interactions within a nonnative protein. *Science* **295**, 1719–1722 (2002).
54. Hu, D. & Lu, H. P. Placing single-molecule T4 lysozyme enzymes on a bacterial cell surface: toward probing single-molecule enzymatic reaction in living cells. *Biophys. J.* **87**, 656–661 (2004).
55. Xue, M. et al. How internal cavities destabilize a protein. *Proc. Natl Acad. Sci. USA* **116**, 21031–21036 (2019).
56. Rennell, D., Bouvier, S. E., Hardy, L. W. & Poteete, A. R. Systematic mutation of bacteriophage T4 lysozyme. *J. Mol. Biol.* **222**, 67–88 (1991).
57. Chen, Y., Hu, D. H., Vorpapel, E. R. & Lu, H. P. Probing single-molecule T4 lysozyme conformational dynamics by intramolecular fluorescence energy transfer. *J. Phys. Chem. B* **107**, 7947–7956 (2003).
58. Fersht, A. *Structure and Mechanism in Protein Science: A Guide to Enzyme Catalysis and Protein Folding*. First edn. (W. H. Freeman, 1998).
59. Ratzke, C., Hellenkamp, B. & Hugel, T. Four-colour FRET reveals directionality in the Hsp90 multicomponent machinery. *Nat. Commun.* **5**, 4192 (2014).
60. Vale, R. D. & Oosawa, F. Protein motors and Maxwell's demons: does mechanochemical transduction involve a thermal ratchet? *Adv. Biophys.* **26**, 97–134 (1990).
61. Gohlke, H. et al. Binding region of alanine dehydrogenase predicted by unbiased molecular dynamics simulations of ligand diffusion. *J. Chem. Inf. Model.* **53**, 2493–2498 (2013).
62. Cellitti, J., Bernstein, R. & Marqusee, S. Exploring subdomain cooperativity in T4 lysozyme II: uncovering the C-terminal subdomain as a hidden intermediate in the kinetic folding pathway. *Protein Sci.* **16**, 852–862 (2007).
63. Lerner, E. et al. Toward dynamic structural biology: Two decades of single-molecule Förster resonance energy transfer. *Science* **359**, 288 (2018). –+.
64. Ross, J. L. The dark matter of biology. *Biophys. J.* **111**, 909–916 (2016).
65. Vallat, B., Webb, B., Westbrook, J. D., Sali, A. & Berman, H. M. Development of a prototype system for archiving integrative/hybrid structure models of biological macromolecules. *Structure* **26**, 894–904 (2018).
66. Lemke, E. A. Site-specific labeling of proteins for single-molecule FRET measurements using genetically encoded ketone functionalities. *Methods Mol. Biol.* **751**, 3–15 (2011).
67. Brustad, E. M., Lemke, E. A., Schultz, P. G. & Deniz, A. A. A general and efficient method for the site-specific dual-labeling of proteins for single molecule fluorescence resonance energy transfer. *J. Am. Chem. Soc.* **130**, 17664–17665 (2008).
68. Fleissner, M. R. et al. Site-directed spin labeling of a genetically encoded unnatural amino acid. *Proc. Natl Acad. Sci. USA* **106**, 21637–21642 (2009).
69. Picoquant. [https://www.picoquant.com/images/uploads/page/files/14528/technote\\_ttrr.pdf](https://www.picoquant.com/images/uploads/page/files/14528/technote_ttrr.pdf) (2019).
70. Goodman, J. & Weare, J. Ensemble samplers with affine invariance. *Comm. Appl. Math. Comp. Sci.* **5**, 65–80 (2010).
71. Altenbach, C. <https://sites.google.com/site/altenbach/labview-programs/epi-programs/long-distances> (2019).
72. Kask, P., Palo, K., Ullmann, D. & Gall, K. Fluorescence-intensity distribution analysis and its application in biomolecular detection technology. *Proc. Natl Acad. Sci. USA* **96**, 13756–13761 (1999).
73. Dix, J. A., Hom, E. F. & Verkman, A. S. Fluorescence correlation spectroscopy simulations of photophysical phenomena and molecular interactions: a molecular dynamics/monte carlo approach. *J. Phys. Chem. B* **110**, 1896–1906 (2006).
74. Enderlein, J., Robbins, D. L., Ambrose, W. P., Goodwin, P. M. & Keller, R. A. Statistics of single-molecule detection. *J. Phys. Chem. B* **101**, 3626–3632 (1997).
75. Laurence, T. A., Kapanidis, A. N., Kong, X. X., Chemla, D. S. & Weiss, S. Photon arrival-time interval distribution (PAID): a novel tool for analyzing molecular interactions. *J. Phys. Chem. B* **108**, 3051–3067 (2004).
76. Müllner, D. fastcluster: Fast hierarchical, agglomerative clustering routines for R and Python. *J. Stat. Softw.* **53**, 1–18 (2013).
77. Dale, R. E., Eisinger, J. & Blumberg, W. E. The orientational freedom of molecular probes. The orientation factor in intramolecular energy transfer. *Biophys. J.* **26**, 161–193 (1979).

## Acknowledgements

We wish to acknowledge the support of Marina Rodnina, Philipp Neudecker, and M. Neal Waxham for their comments and suggestions on the paper, and Daniel Rohrbeck for support on the mutagenesis. We acknowledge the support of Christian A. Hanke for helping in organizing the data deposition at Zenodo. We also wish to acknowledge Evan Brooks for generating several of the T4L variants and in assisting with the DEER sample preparation. This research was supported by the European Research Council through the Advanced Grant 2014 hybridFRET (671208) (to C.A.M.S.), by the NIH (grant R01EY05216 to W.L.H. and grant 1P20GM121342 to HS), NSF CAREER MCB (grant 1749778 to H.S.) and the Jules Stein Professorship Endowment (to W.L.H.). H.S. wishes to acknowledge the support from the Alexander von Humboldt foundation and the Clemson Start-up funds. K.H. wishes to acknowledge the support of the NRW Research School BioStruct and the iGRASP<sub>seed</sub> International Graduate School of Protein Science & Technology.

## Author contributions

H.S. and K.H. purified and labeled the protein. H.S., T.P., K.H., and D.R. measured and analyzed the FRET experiments. T.P., M.D., and H.G. performed structural screening. M.R.F. performed and analyzed EPR experiments. W.H. performed study design and EPR analysis. S.F. developed fluorescence analysis tools. F.K. and R.K. developed fluorescence instrumentation and gave technical support. All authors discussed the results and commented on the paper. H.S., K.H., W.H., and C.A.M.S. wrote the paper. H.G. contributed to the writing of the paper. C.A.M.S. supervised the project.

## Competing interests

The authors declare no competing interests.

**Additional information**

**Supplementary information** is available for this paper at <https://doi.org/10.1038/s41467-020-14886-w>.

**Correspondence** and requests for materials should be addressed to H.S. or C.A.M.S.

**Peer review information** *Nature Communications* thanks the anonymous reviewer(s) for their contribution to the peer review of this work. Peer reviewer reports are available.

**Reprints and permission information** is available at <http://www.nature.com/reprints>

**Publisher's note** Springer Nature remains neutral with regard to jurisdictional claims in published maps and institutional affiliations.



**Open Access** This article is licensed under a Creative Commons Attribution 4.0 International License, which permits use, sharing, adaptation, distribution and reproduction in any medium or format, as long as you give appropriate credit to the original author(s) and the source, provide a link to the Creative Commons license, and indicate if changes were made. The images or other third party material in this article are included in the article's Creative Commons license, unless indicated otherwise in a credit line to the material. If material is not included in the article's Creative Commons license and your intended use is not permitted by statutory regulation or exceeds the permitted use, you will need to obtain permission directly from the copyright holder. To view a copy of this license, visit <http://creativecommons.org/licenses/by/4.0/>.

© The Author(s) 2020



## Supplementary Information

### Resolving dynamics and function of transient states in single enzyme molecules

Hugo Sanabria<sup>1,2,8,\*</sup>, Dmitro Rodnin<sup>1,8</sup>, Katherina Hemmen<sup>1,8</sup>, Thomas Peulen<sup>1</sup>, Suren Felekyan<sup>1</sup>, Mark R Fleissner<sup>3,7</sup>, Mykola Dimura<sup>1,4</sup>, Felix Koberling<sup>5</sup>, Ralf Kühnemuth<sup>1</sup>, Wayne Hubbell<sup>3</sup>, Holger Gohlke<sup>4,6</sup>, Claus A.M. Seidel<sup>1\*</sup>

<sup>1</sup>Institut für Physikalische Chemie, Lehrstuhl für Molekulare Physikalische Chemie, Heinrich-Heine-Universität, Düsseldorf, Germany.

<sup>2</sup>Department of Physics and Astronomy, Clemson University, Clemson, South Carolina, U.S.A.

<sup>3</sup>Jules Stein Eye Institute and Department of Chemistry and Biochemistry, University of California, Los Angeles, U.S.A.

<sup>4</sup>Institut für Pharmazeutische und Medizinische Chemie, Heinrich-Heine-Universität, Düsseldorf, Germany.

<sup>5</sup>PicoQuant GmbH, Berlin, Germany.

<sup>6</sup>John von Neumann Institute for Computing (NIC), Jülich Supercomputing Centre (JSC) & Institute of Biological Information Processing (IBI-7: Structural Biochemistry), Forschungszentrum Jülich GmbH, 52425 Jülich, Germany

<sup>7</sup>Present address: Avanir Pharmaceuticals Inc., Aliso Viejo, California, U. S. A.

<sup>8</sup>These authors contributed equally: Hugo Sanabria, Dmitro Rodnin, Katherina Hemmen

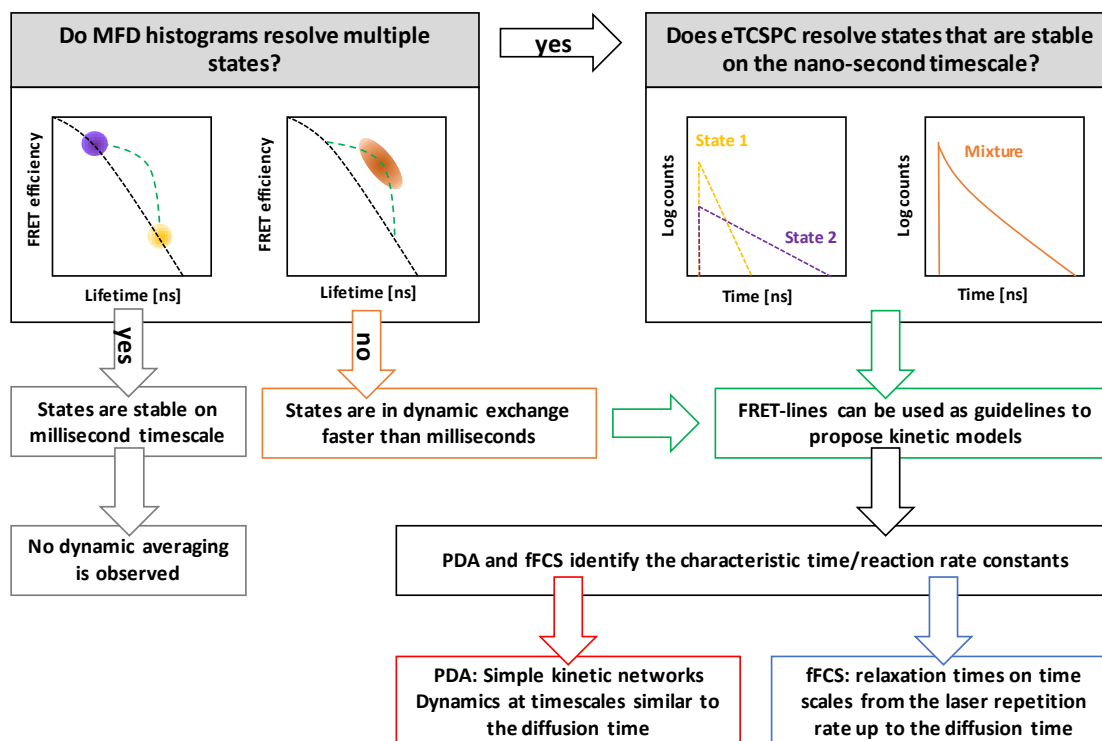
\*Correspondence and requests for materials should be addressed to C.A.M.S.(email: [cseidel@hhu.de](mailto:cseidel@hhu.de)) or to H.S. (email: [hsanabr@clemson.edu](mailto:hsanabr@clemson.edu))

## Table of contents

	Title	Page
<b>Supplementary Figure 1</b>	Detecting protein dynamics with our fluorescence spectroscopic toolkit	<b>3</b>
<b>Supplementary Figure 2</b>	MFD analysis of all 33 variants of the T4L network	<b>4</b>
<b>Supplementary Figure 3</b>	Exemplary data analysis for variant K60pAcF I150C-(DA)	<b>7</b>
<b>Supplementary Figure 4</b>	Brownian Dynamic Simulations of S44pAcF/I150C-(DA)	<b>8</b>
<b>Supplementary Figure 5</b>	eTCSPC and EPR results of T4L	<b>9</b>
<b>Supplementary Figure 6</b>	Reduced FRET chi-squared values of the NMR and X-ray structures.	<b>12</b>
<b>Supplementary Figure 7</b>	Single-molecule experiments of functional variants	<b>13</b>
<b>Supplementary Figure 8</b>	T4L binding to peptidoglycan as observed by reverse phase HPLC and cleavage at low pH	<b>14</b>
<b>Supplementary Figure 9</b>	Exemplary filters for fFCS analysis and fFCS curves	<b>15</b>
<b>Supplementary Figure 10</b>	MFD analysis of further samples	<b>17</b>
<b>Supplementary Figure 11</b>	Total energy landscape of the hydrolysis of T4L on a generalized reaction coordinate	<b>18</b>
<b>Supplementary Figure 12</b>	Triplet or dark states do not influence the $sCCF$ on the variant S44pAcF/I150C-(DA)	<b>19</b>
<b>Supplementary Table 1</b>	States description for the vector $p$ , equilibrium fraction vector $p_{eq}$ and the rate matrix $K$	<b>20</b>
<b>Supplementary Table 2</b>	eTCSPC fit results	<b>21</b>
<b>Supplementary Table 3</b>	Analysis of time-resolved fluorescence anisotropies $r(t)$	<b>30</b>
<b>Supplementary Table 4</b>	Conformational clusters of T4L PDB structures	<b>35</b>
<b>Supplementary Table 5</b>	List of evaluated fit models	<b>36</b>
<b>Supplementary Table 6</b>	List of primers used for cloning	<b>37</b>
<b>Supplementary Note 1</b>	Single-molecule and fluorescence correlation spectroscopy	<b>38</b>
<b>Supplementary Note 2</b>	Species Cross Correlation Function -(DA) and -(AD) labeled samples.	<b>39</b>
<b>Supplementary Note 3</b>	Analyzing the kinetic network of conformational states in T4L	<b>40</b>
<b>Supplementary Note 4</b>	Fluorescence decay analysis of single and double labeled T4 Lysozyme	<b>43</b>
<b>Supplementary Note 5</b>	Characterization of functional T4L variants	<b>44</b>
<b>Supplementary Note 6</b>	Challenges of smFRET measurements and their solutions	<b>44</b>
<b>Supplementary Note 7</b>	Original data available on Zenodo	<b>47</b>
<b>Supplementary Methods</b>	<ul style="list-style-type: none"> <li>• Multiparameter Fluorescence Detection (MFD)</li> <li>• MFD burst analysis: Multiparameter FRET histograms and FRET-lines</li> <li>• Guidelines for reading MFD histograms</li> <li>• Filtered Fluorescence Correlation Spectroscopy</li> <li>• Ensemble Time Correlated Single Photon Counting with high precision</li> <li>• Donor and Acceptor fluorescence quantum yields</li> <li>• Time-resolved fluorescence decay analysis</li> </ul>	<b>50</b>

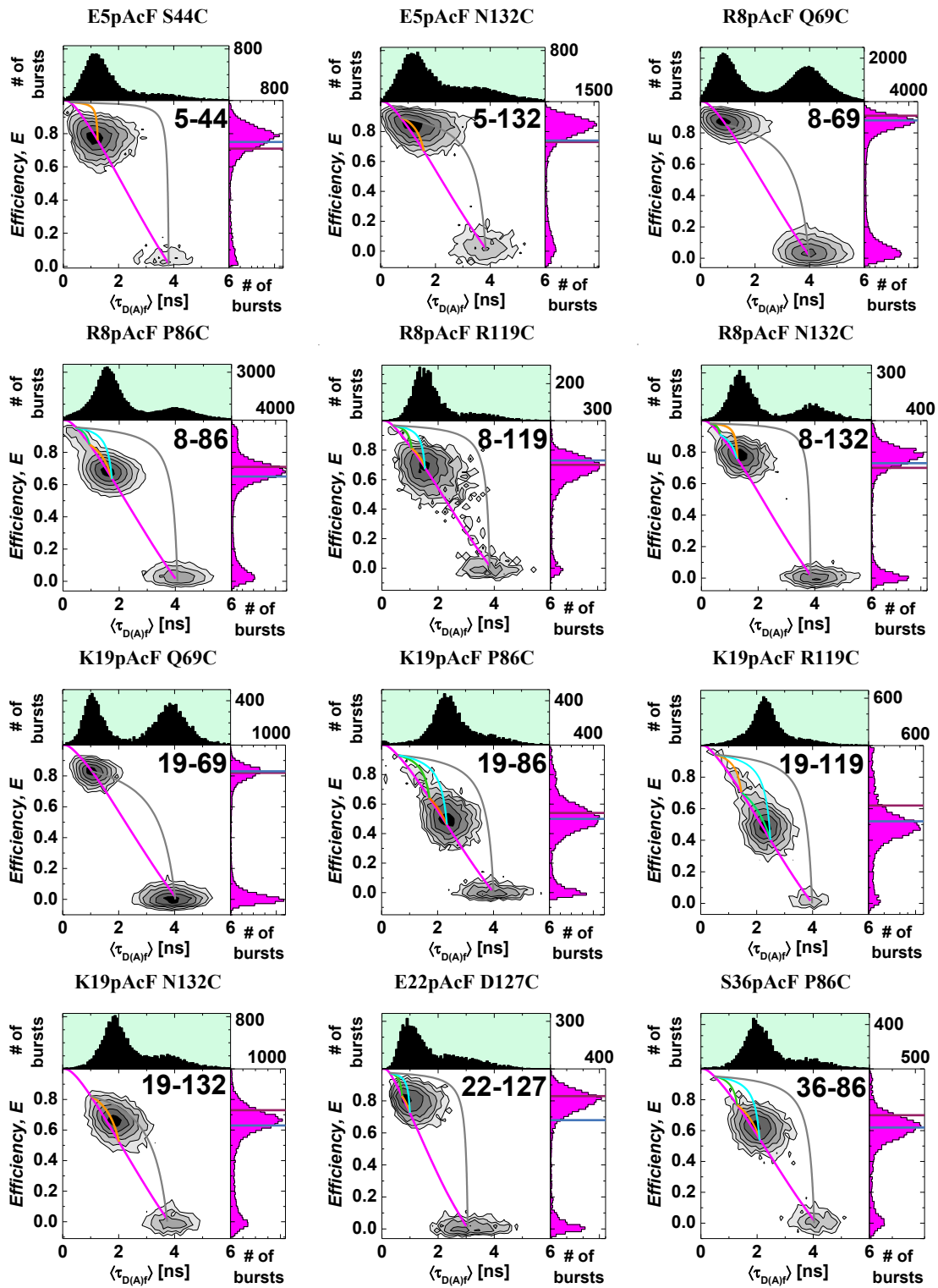
## Supplementary Figures

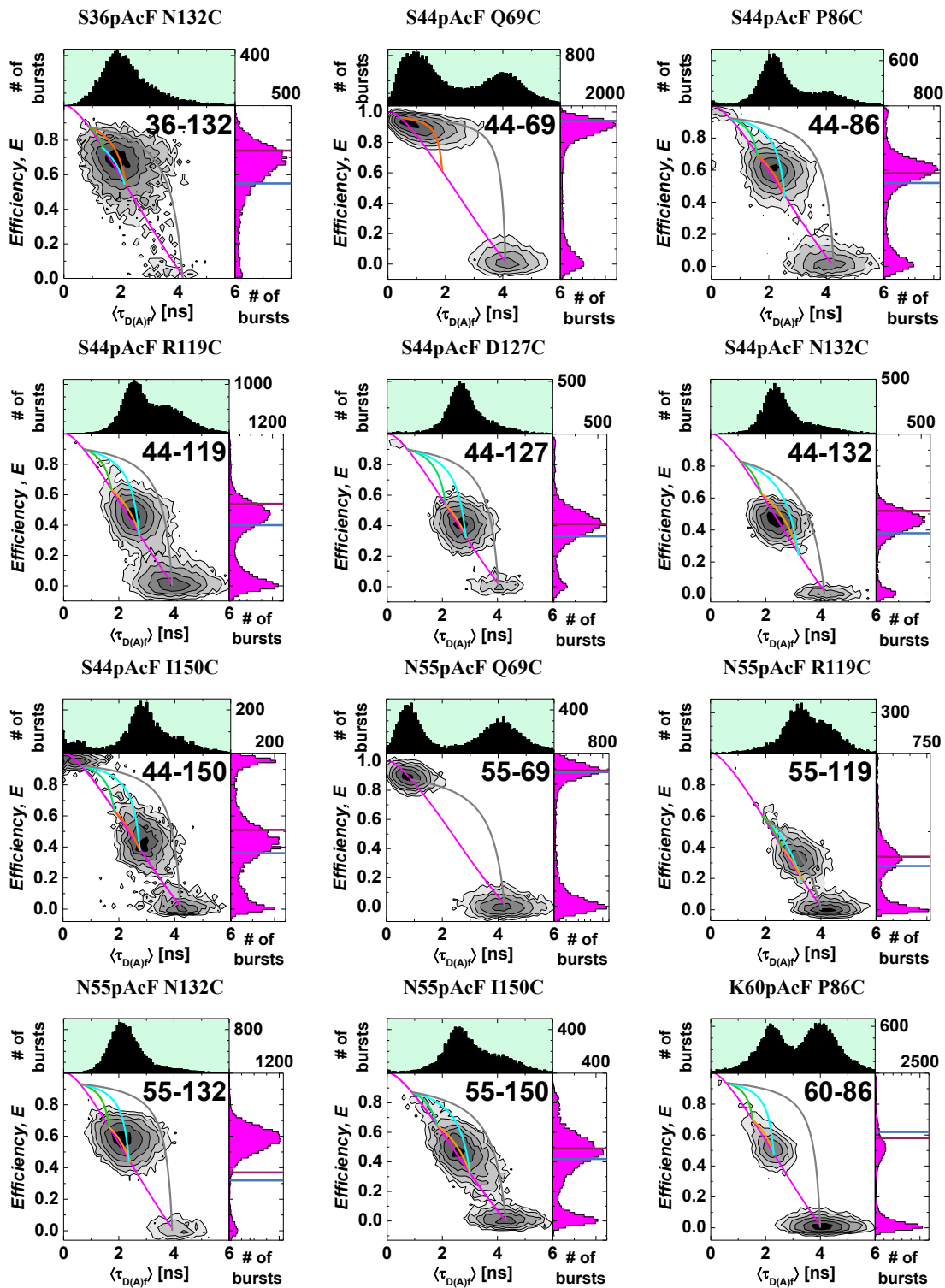
### Supplementary Figure 1

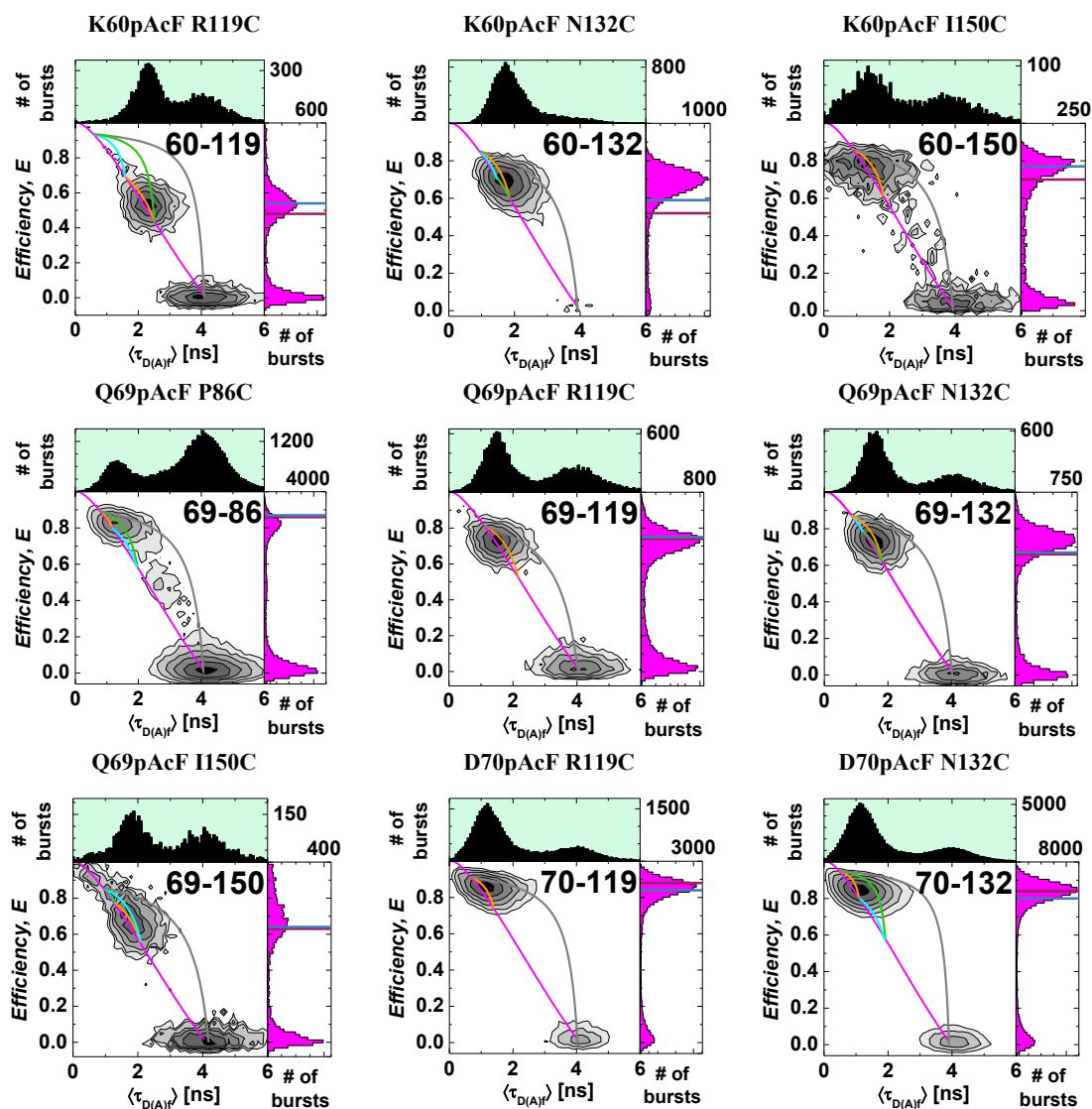


**Supporting Figure 1** How to identify and analysis dynamics with our fluorescence spectroscopic toolkit. Multiparameter Fluorescence Detection (MFD) immediately shows whether a sample undergoes dynamic exchange and the timescale of dynamics can be estimated by the position of the population(s) with respect to the static FRET line. Populations, which are stable on the nanosecond timescale are resolved ensemble time-correlated single-photon counting (TCSPC). These states obtained in TCSPC can be used to generate static and dynamic FRET lines, which serve as guidelines to propose kinetic models. (Filtered) Fluorescence correlation spectroscopy is good in identifying the relaxation times on time scales from the laser repetition rate up to the diffusion time, providing a broader dynamic range, while Photon Distribution Analysis (PDA) is useful for simple and kinetic networks and for dynamics that occur at timescales similar to the diffusion time.

Supplementary Figure 2

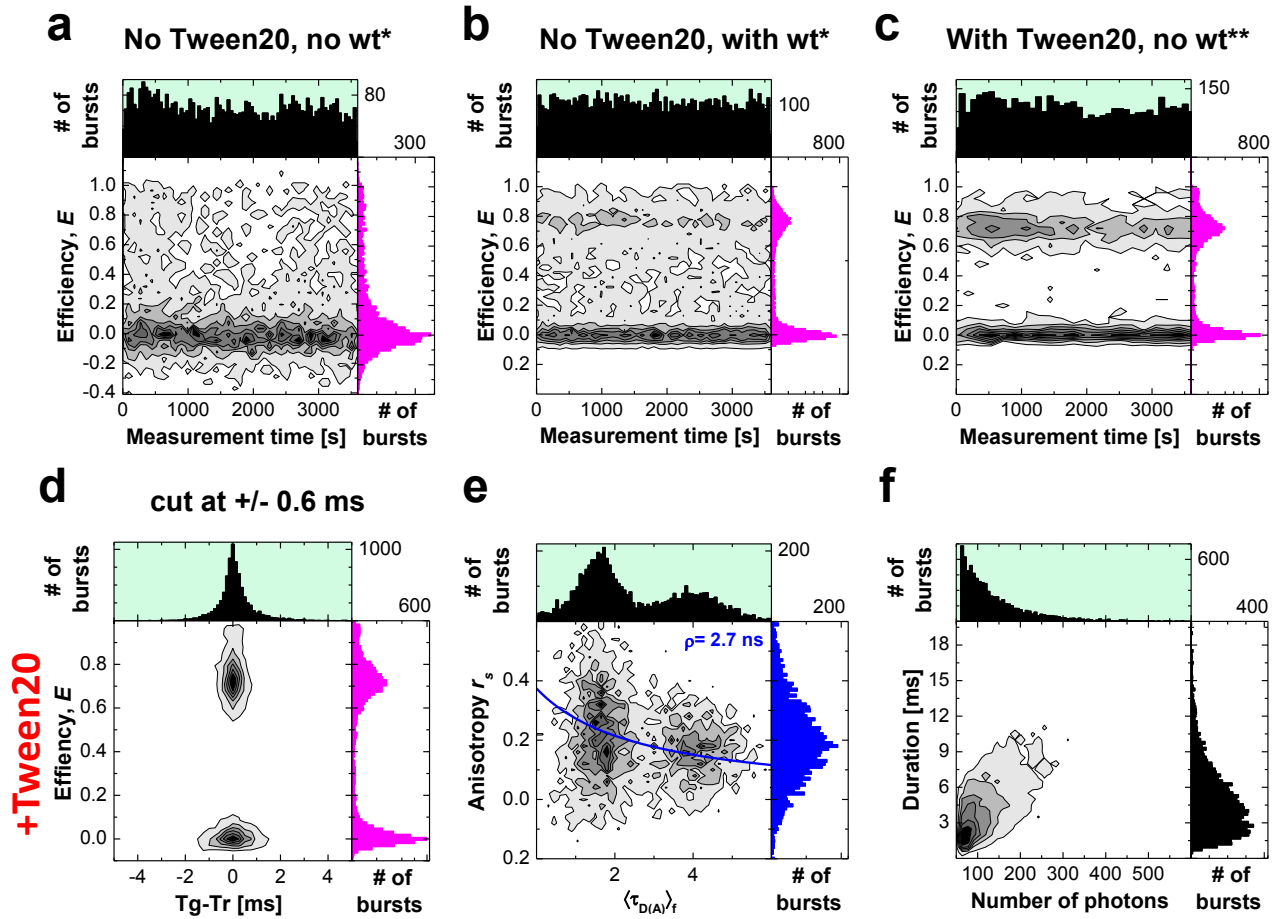






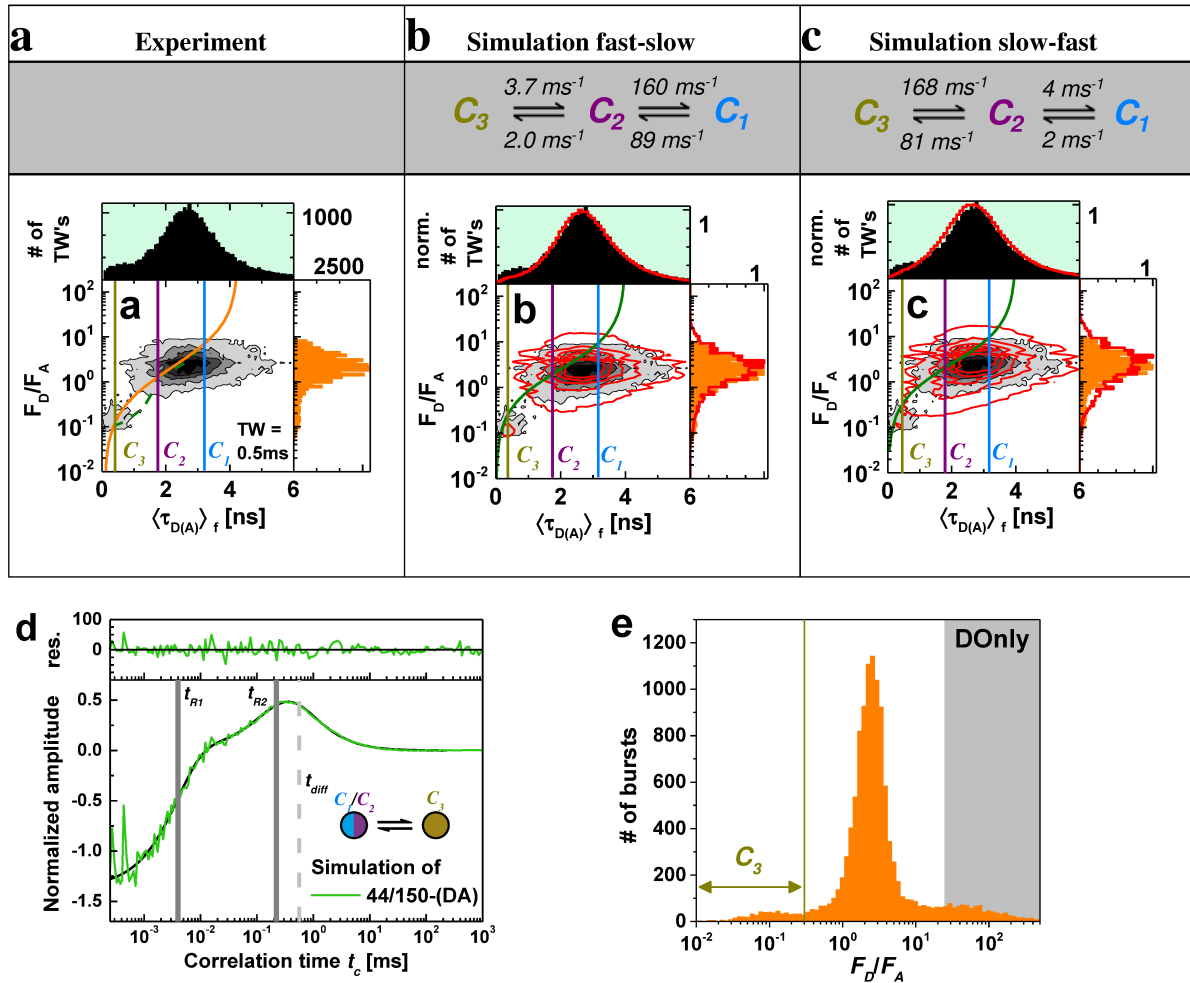
**Supplementary Figure 2. MFD analysis of all 33 variants of the T4L network.** Two dimensional histogram of FRET efficiency  $E$  vs. lifetime of donor in the presence of acceptor  $\langle \tau_{D(A)F} \rangle$ . One dimensional projections for  $E$  and  $\langle \tau_{D(A)F} \rangle$  are also shown. Static (magenta) and dynamic FRET lines connecting states  $C_1$ - $C_2$  (orange),  $C_1$ - $C_3$  (cyan) and  $C_2$ - $C_3$  (bright green) are also shown (Supplementary Methods, Supplementary Equations (19-21)). Solid horizontal lines show the FRET efficiency expected from known X-ray structures for the *open* (blue, PDB ID 172L) and *closed* (violet, 148L) state from T4L.

## Supplementary Figure 3



**Supplementary Figure 3. Exemplary data analysis for variant K60pAcF I150C-(DA).** (a-c) FRET efficiency  $E$  vs. the measurement time for 60-150 in the absence of coating (A), coating of the measurement chamber with 0.1 % (v/v) Tween20 (b), or 1  $\mu$ M unlabeled protein (c). (d) In the case of acceptor photobleaching, the green signal trace will be longer (Tg) than the red signal trace (Tr). The difference  $|Tg-Tr|$  is in ideal case randomly and sharply distributed around 0. Molecules, in which  $|Tg-Tr|$  exceeds 0.6 are removed from further analysis. (e) Free dye molecules can be recognized by a low anisotropy  $\sim 0$ , labeled single molecules follow the Perrin equation. (f) Aggregates will show a high brightness and long burst duration, which do not scale linearly.

Supplementary Figure 4

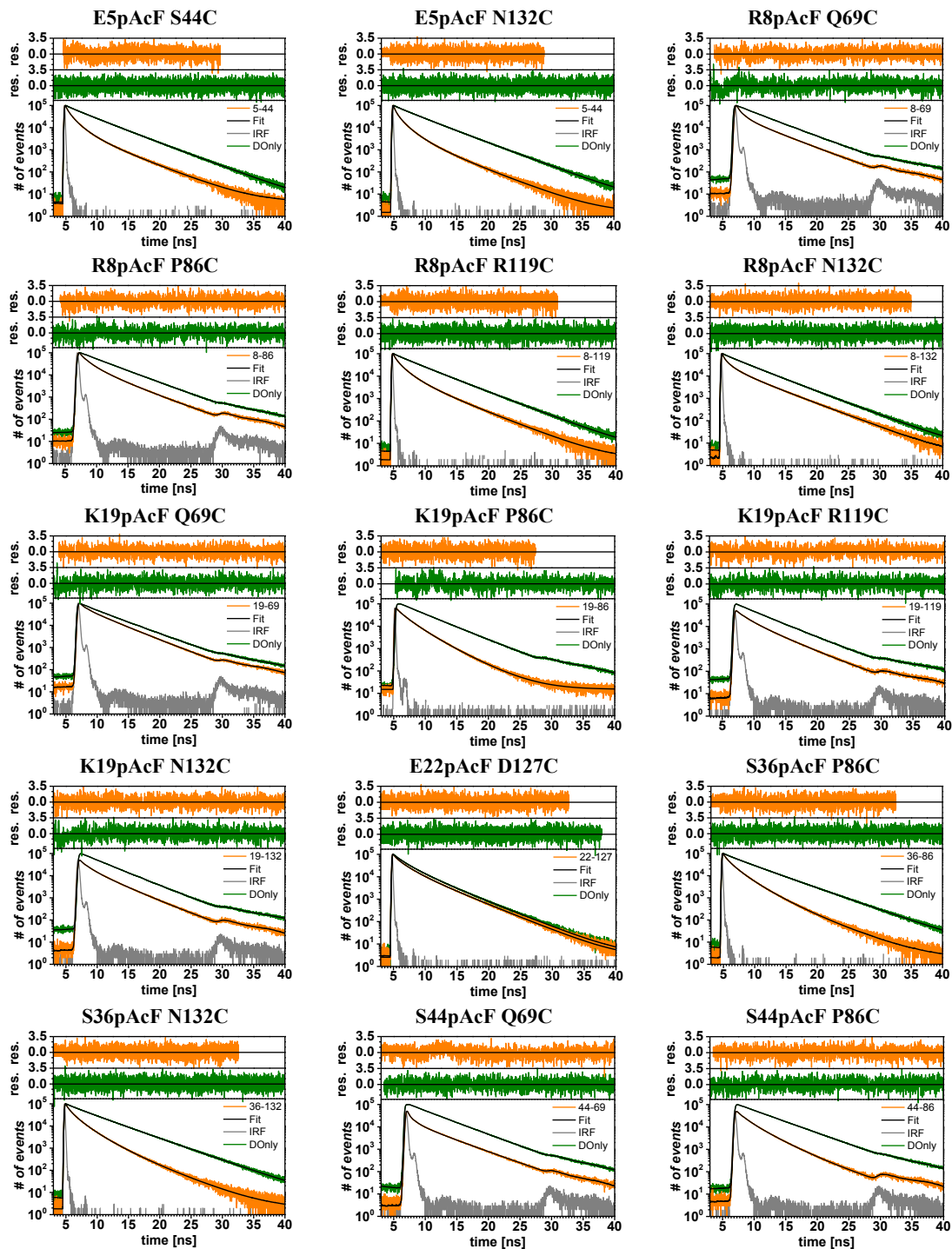


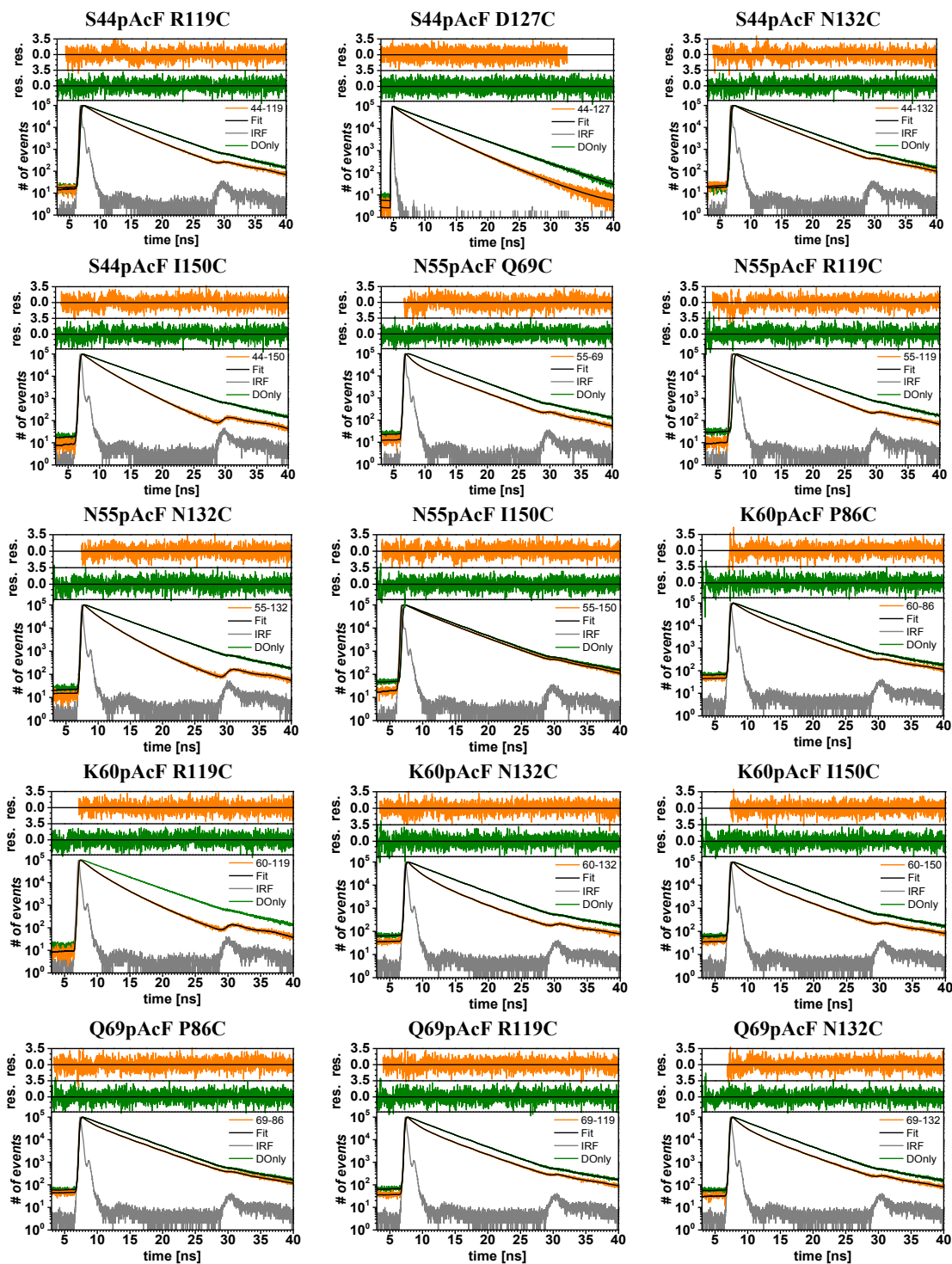
**Supplementary Figure 4. Brownian Dynamics (BD) Simulations of S44pAcF/I150C-(DA).** (a-c) The experimental data (a) are compared with data from BD simulation for the depicted kinetic schemes (b,c). (a) Two dimensional histograms from smFRET analysis ( $F_D/F_A$  vs. fluorescence lifetime ( $\langle \tau_{D(A)} \rangle_f$ ) of the raw data from the S44pAcF/I150C-(DA) variant at pH 7.5 selected with 0.5 ms time-windows (TW's). FRET lines, static and dynamic are shown as orange solid and green dashed lines.  $\langle B_G \rangle = 1.6$  kHz,  $\langle B_R \rangle = 0.8$  kHz, spectral crosstalk  $\alpha = 1.2\%$  and ratio of green and red detection efficiencies  $g_G/g_R = 0.77$  are used for corrections. (b, c) Brownian dynamics simulation using the rates from Figure 3b, c was processed as the experimental data (overlaid red contours). Simulated parameters ( $\langle B_G \rangle$ ,  $\langle B_R \rangle$ ,  $\alpha$ ,  $g_G/g_R$ ) were the same as in the experiment. In addition, we considered a rotational correlation of  $\rho = 2.2$  ns for conformational state. Analysis results of simulated data are presented in the same fashion as in panel (a). The experimental data agree best with simulated data for the case "fast-slow" (b). (d)  $sCCF$  between the pseudo-species consisting of the  $C_1/C_2$  mix and the  $C_3$  for simulated data. Fit of this  $sCCF$  curve returns two relaxation times of 4  $\mu$ s and 220  $\mu$ s, consistent with our input parameters. (e) One dimensional histogram of the raw data from the S44pAcF/I150C-(DA) variant at pH 7.5 analyzed in burstwise mode to illustrate the region of  $C_3$ , D-Only and the dynamically mixed state.

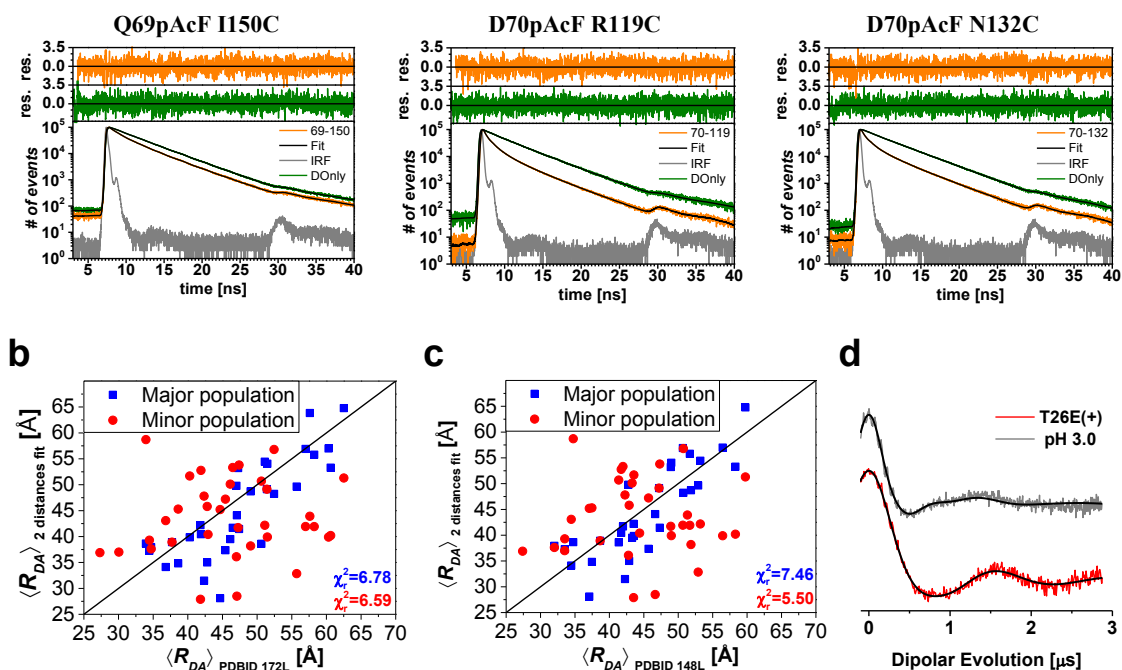


## Supplementary Figure 5

a

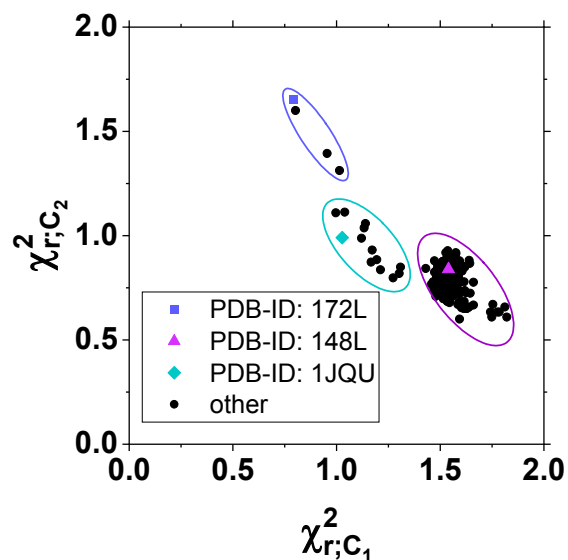






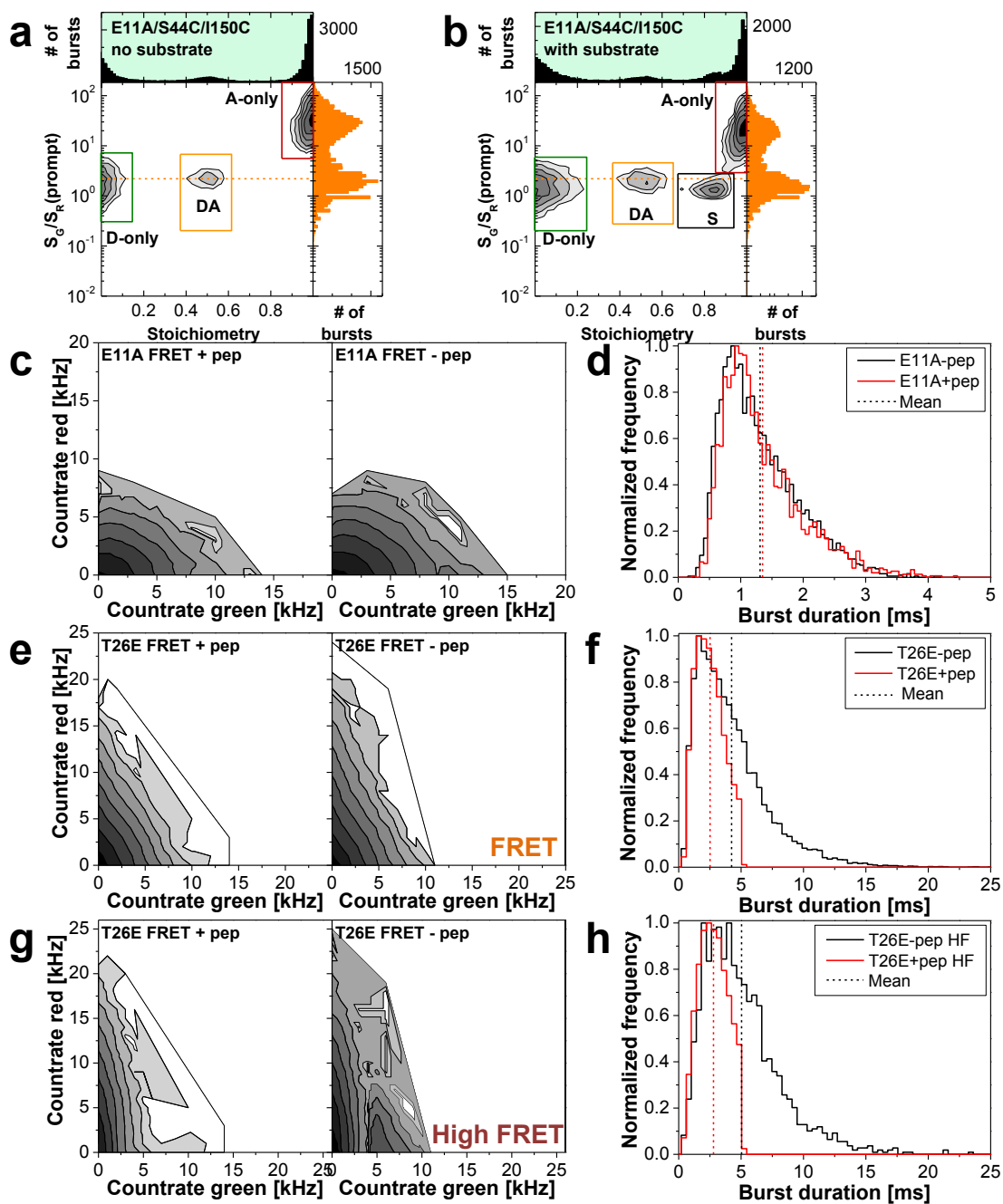
**Supplementary Figure 5. eTCSPC results of T4L.** (a) Fit (black) of the experimental data of double-labeled sample (orange) and respective Donor-only labeled sample (green), weighted residuals are shown on top. Fit parameter are given in Table S2a (D-Only) and S2d-f (double-labeled sample). Instrument response function (IRF) is shown in gray. (b) Fitted distances of two distributed states (Table S2b) fit plotted versus the distances calculated for the model X-ray structure of the open state (PDBID: 172L). “Major state” is the distance having the higher amplitude in fraction, while “minor state” is the distance with the lower fraction. (c) Same as (b), only for the model X-ray structure of the closed state (PDBID 148L). (d) Experimental DEER time traces of the dipolar evolution, which were used to calculate the distance distributions shown in the main text Figure 6a. For pH 3.0 data (grey) the modulation depth was 0.33, the maximum time 2.87  $\mu\text{s}$ , the upper distance limit 56  $\text{\AA}$ , and the upper shape limit 45  $\text{\AA}$ . For the T26E adduct data (red), the modulation depth was 0.39, the maximum time 2.88  $\mu\text{s}$ , the upper distance limit also 56  $\text{\AA}$ , and the upper shape limit also 45  $\text{\AA}$ . Fits are overlaid.

Supplementary Figure 6



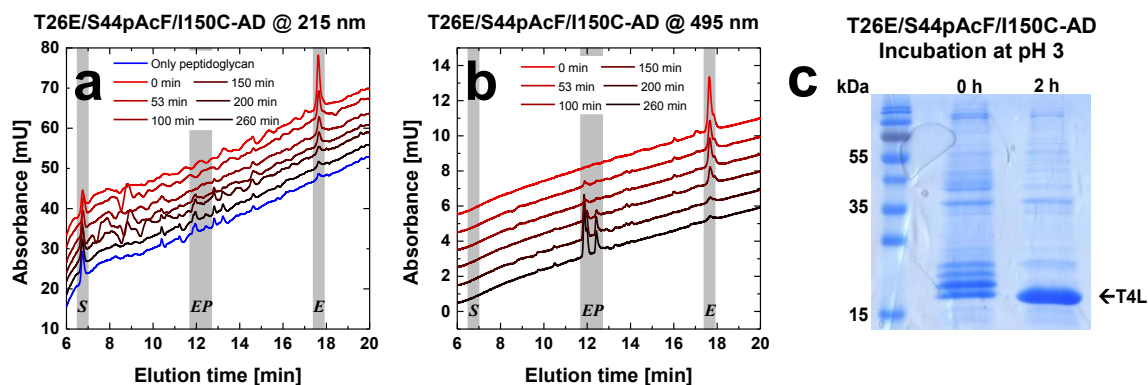
**Supplementary Figure 6. Reduced FRET chi-squared values of the NMR and X-ray structures.** The X axis represents the  $\chi_{r,C_1}^2$  of the PDB structures against the FRET dataset  $C_1$ , the Y axis represents the  $\chi_{r,C_2}^2$ . The  $C_1$  representative structure (open, PDB-ID: 172L) is shown as blue rectangle, similar structures -are highlighted by the blue ellipse. The  $C_2$  representative is shown as violet triangle (closed, PDB-ID: 148L), similar structures are highlighted by the violet ellipse. The ajar structure (PDB-ID: 1JQU) is shown as a light blue diamond, similar structures are highlighted by the light blue ellipse. The data are available at Zenodo (see Supplementary Note 7) in the file FRET\_screening\_of\_PDB\_structures.zip.

## Supplementary Figure 7



**Supplementary Figure 7. Single-molecule experiments of functional variants.** (a,b) PIE experiments identify burst stemming from single and double labeled E11A/S44C/I150C and substrate alone. (c) Brightness distribution of bursts from double-labeled E11A/S44C/I150C. (d) Burst duration distribution of bursts from double-labeled E11A/S44C/I150C. (e-h) Same as (c,d) for the variant T26E/S44pAcF/I150C-(DA).

## Supplementary Figure 8

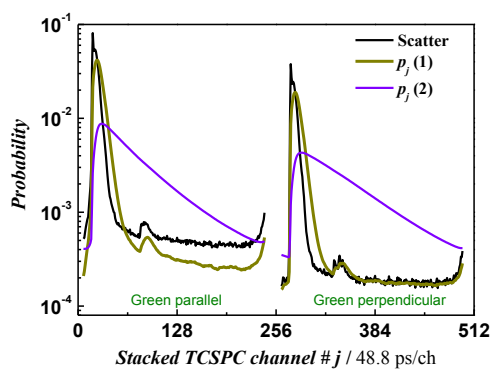


**Supplementary Figure 8. T4L binding to peptidoglycan as observed by reverse phase HPLC and cleavage at low pH.** (a) The elution profile measured at 215 nm of reverse phase chromatography for T26E/S44pAcF/I150C-(AD). Samples were taken at different times during the incubation with peptidoglycan. First line shows only the elution of peptidoglycan. Note different peaks of the heterogeneity on the peptidoglycan. Offset between lines was added for clarity. Gray lines represent the free enzyme population (*e*), the product bound enzyme (*EP*) and the substrate alone (*S*). (b) Elution of the same sample as in (a) but monitored at 495 nm, which corresponds to the absorbance of Alexa488. Saturation of T26E/S44pAcF/I150C-(AD) with substrate is reached at ~ 4 hours of incubation. (c) Purification of T26E/S44pAcF/I150C from the *E. coli* cell pellet yielded a mixture of free and to cell wall pieces of different sizes bound protein. After incubation for 2 hrs at pH 3, nearly all bound peptidoglycan had been cleaved and the free enzyme could now be used for labeling and further experiments after adjusting the conditions to neutral pH again. Source Data are provided by a source data file.

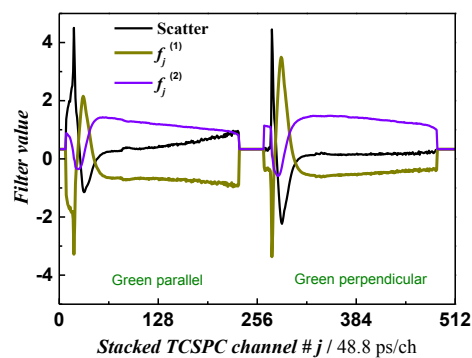
Supplementary Figure 9

S44pAcF/I150C-DA

**a**

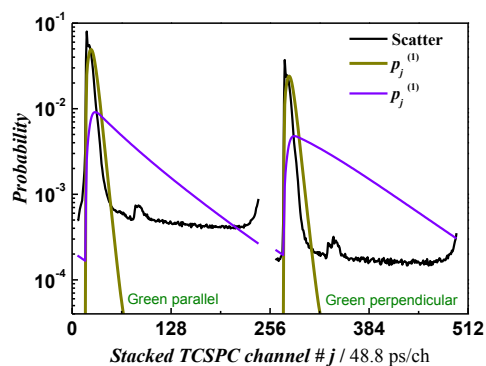


**b**

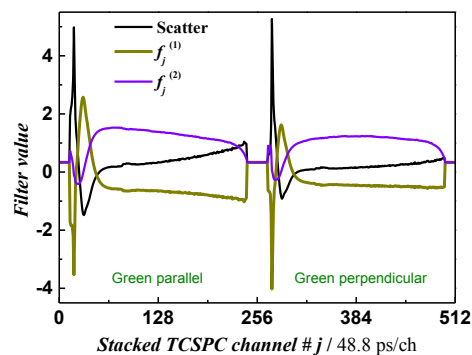


S44pAcF/I150C-AD

**c**

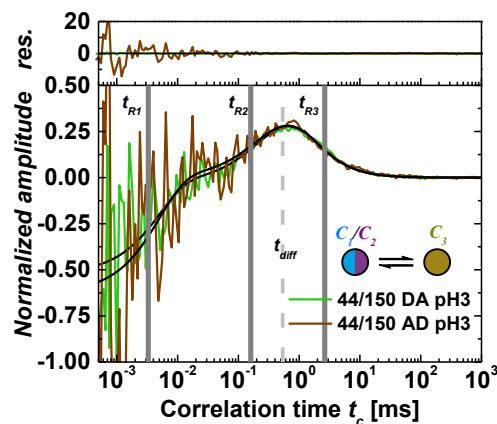


**d**



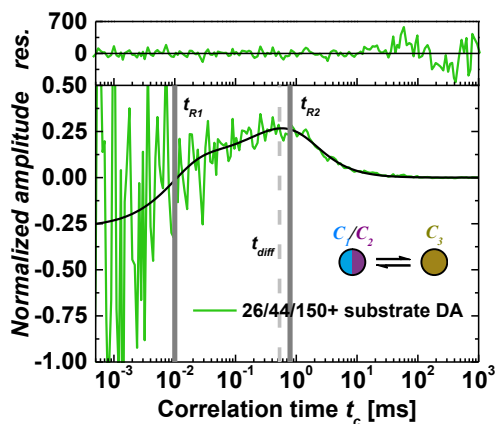
**e**

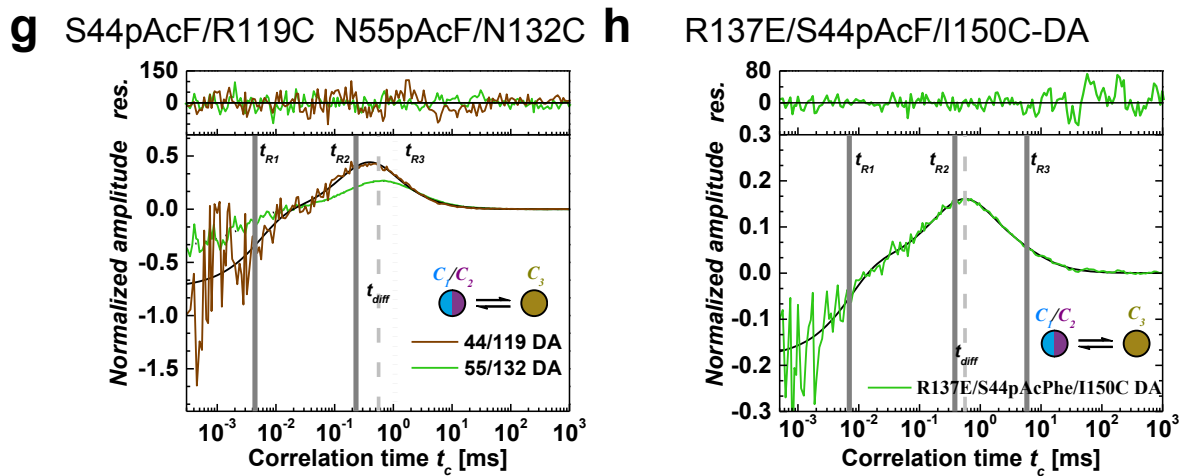
S44pAcF/I150C pH 3



**f**

T26E/S44pAcF/I150C-DA

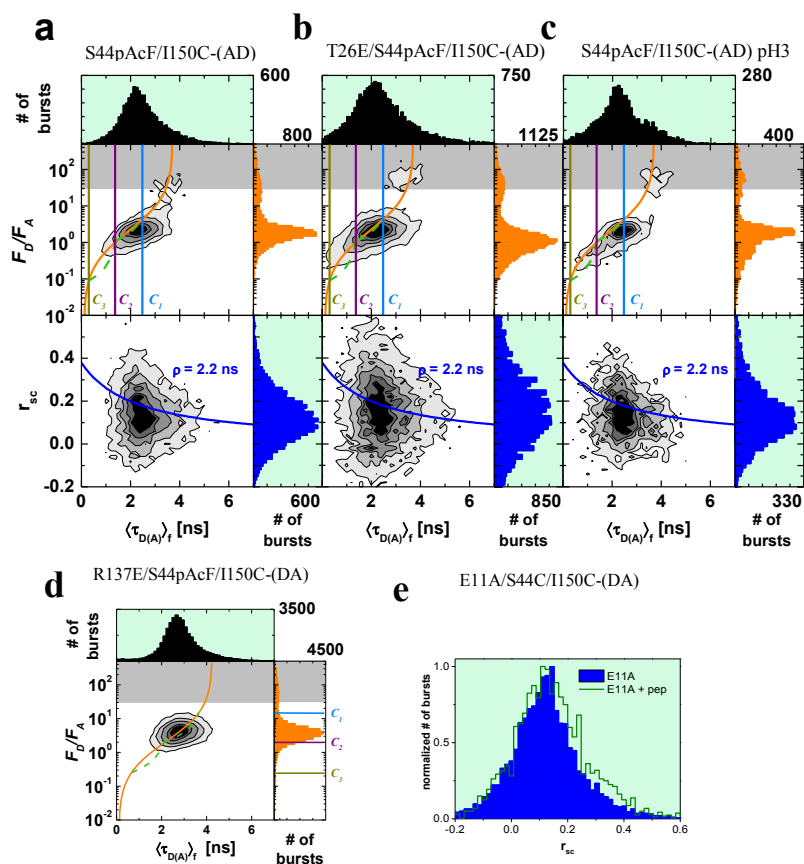




**Supplementary Figure 9. ffCS results.** (a) Generated decays for two pseudo-species of S44pAcF/I150C-DA in addition to the scatter profile. The parameters of the decay generation for the first pseudo-species were  $\tau_1 = 0.25$  ns, and rotational correlation time of  $\rho_1 = 3.3$  ns. The second pseudo-species had a lifetime of  $\tau_2 = 2.97$  ns and the same rotational correlation time. (b) Filters  $f_j^{(i)}$  were calculated according to Supplementary Equation 26 using the decays from graph (A). (c, d) Decay patterns and the corresponding filters for the S44pAcF/I150C-AD with first pseudo species lifetime  $\tau_1 = 0.25$  ns, and rotational correlation time  $\rho_1 = 3.3$  ns. The second pseudo species was generated with  $\tau_2 = 3.25$  ns and same rotational correlation time. (e) *sCCF* between the mix  $C_1/C_2$  and  $C_3$  at pH 3.0 for the two configurations of labeling –(DA) and –(AD). The fit with the Supplementary Equations (27-28) required three relaxation times. The diffusion time was fixed to  $t_{diff} = 0.54$  ms. (f) *sCCF* between the mix  $C_1/C_2$  and  $C_3$  for T26E/S44pAcF/I150C-(DA) incubated with substrate. Two relaxation times are found ( $t_{R1} = 10$   $\mu$ s, and  $t_{R2} = 0.790$  ms). (g) Overlay of the normalized *sCCF* of S44pAcF/R119C-DA and N55pAcF/N132C-(DA). Global fit shows two common relaxation times ( $t_{R1} = 4 \pm 2.4$   $\mu$ s,  $t_{R2} = 230 \pm 28$   $\mu$ s). The variant N55pAcF/N132C-(DA) requires an additional rate  $t_{R3} \sim 1.1$  ms. (h) *sCCF* for variant R137E/S44pAcF/I150C-(DA). Three relaxation times were needed to fit the curve ( $t_{R1} = 7$   $\mu$ s,  $t_{R2} = 0.38$  ms and  $t_{R3} = 5.84$  ms). The diffusion time was fixed to  $t_{diff} = 0.54$  ms.

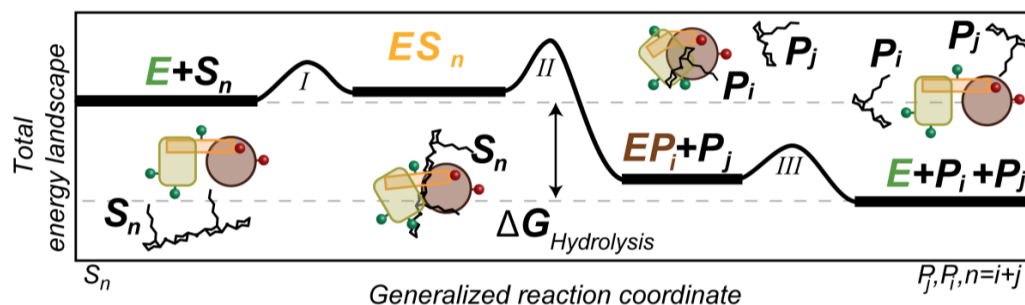


## Supplementary Figure 10



**Supplementary Figure 10. MFD analysis of further samples.** (a) MFD histogram of S44pAcF/I150C-(AD) labeled T4L. Two dimensional histogram  $F_D/F_A$  vs. lifetime of donor in the presence of acceptor  $\langle \tau_{D(A)} \rangle_f$  and anisotropy vs.  $\langle \tau_{D(A)} \rangle_f$  for S44pAcF/I150C-(AD). One dimensional projections for  $F_D/F_A$ ,  $\langle \tau_{D(A)} \rangle_f$  and anisotropy are also shown. Static FRET line is shown in orange. Pure donor and acceptor fluorescence ( $F_D$  and  $F_A$ ) are corrected for background ( $\langle B_G \rangle = 1.8$  kHz,  $\langle B_R \rangle = 0.7$  kHz), spectral cross-talk ( $\alpha = 1.3\%$ ) and detection efficiency ratio ( $g_G/g_R = 0.77$ ). Shaded area in gray is the region of donor only. On the anisotropy vs.  $\langle \tau_{D(A)} \rangle_f$  histograms the Perrin's equation with rotational correlation  $\rho = 2.2$  ns is shown as blue line. Vertical guidelines for states  $C_1$ ,  $C_2$ , and  $C_3$  according to the eTCSPC results of the same sample are added as references. Ignoring the donor only population a single unimodal distribution is observed in all  $F_D/F_A$  vs.  $\langle \tau_{D(A)} \rangle_f$  similarly to what was observed in the -(DA) sample. Two slight differences can be observed: the tilt towards the state  $C_3$  is more evident and the accumulation of the  $C_3$  is not visible. (b) MFD histograms for the variant T26E/S44pAcF/I150C-(AD) without substrate. We observe a more pronounced broadening along the FRET-line in direction to  $C_3$ . (c) At pH 3.0, the MFD histograms for the S44pAcF/I150C-(AD) show very similar characteristics as the variant T26E. (d) Functional mutant of T4L. MFD histograms for R137E/S44pAcPh/I150C-(DA). (e) Effect of substrate on E11A/S44C/I150C. Upon addition of substrate we observe a higher anisotropy (green line). All samples were corrected for background, cross talk, and detection efficiencies according to experimentally determined parameters.

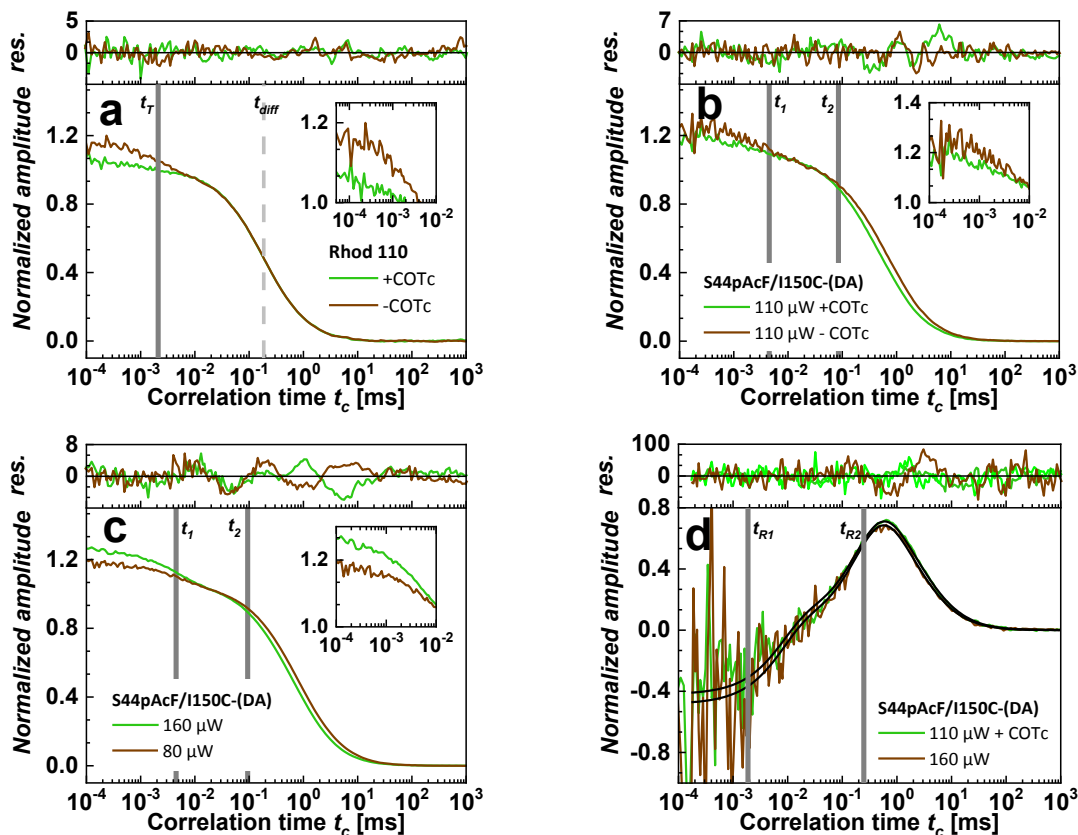
## Supplementary Figure 11



**Supplementary Figure 11. Total energy landscape of the hydrolysis of T4L on a generalized reaction coordinate.** T4L cleaves the polymer chain peptidoglycan, the substrate  $S$ , of length  $n$  ( $S_n$ ) between the alternating residues of  $\beta$ -(1,4) linked N-acetylglucosamine and N-acetylmuramic acid into two shorter peptidoglycan chains, the product  $P$  of chain length  $i$  and  $j$  ( $P_i$  and  $P_j$ ). Here,  $n = i + j$ .

The enzymatic pathway of the extended Michaelis-Menten mechanism (Fig. 7a in main text) consists of three distinct reaction steps. *I*) The substrate  $S$  binds reversibly to the enzyme  $E$  to form an enzyme-substrate complex  $ES$ . *II*) In the  $ES$  complex,  $S$  is converted to the product  $P$ , resulting in the  $EP$  complex with the product still bound to the enzyme. *III*)  $P$  is released from the complex via a transition of  $E$  to an excited state  $E^*$ . Finally, the free enzyme  $E^*$  relaxes to  $E$ . Our observations demonstrate that a fine-tuned shift of the conformational equilibrium favors motions of active product release in T4L where the energy of product formation in step II defines the directionality of the reaction<sup>1</sup>. This hydrolysis reaction is irreversible and thus can be denoted as “ratchet mechanism”<sup>2</sup>.

Supplementary Figure 12



**Supplementary Figure 12. Triplet or dark states do not influence the  $sCCF$  on the variant S44pAcF/I150C-(DA).** (a) The addition of the triplet quencher COTc into Rhod110 solution significantly reduces triplet fraction (see in inset). (b) Overlay of the standard auto/cross-correlation curves from signals in the green channels for the variant S44pAcF/I150C-(DA) without (-COTc) and with (+COTc) triplet quencher COTc in solution. Inset shows the regime where triple kinetics is observed. (c) Overlay of standard auto/cross-correlation of the green signals at 80  $\mu\text{W}$  and at 160  $\mu\text{W}$  power at objective. Two bunching terms are needed to fit the data ( $t_T = 4.5 \mu\text{s}$ , and  $t_b = 60 \mu\text{s}$ ). The triplet fraction changes from 10 % at 80  $\mu\text{W}$  to 15 % at 160  $\mu\text{W}$  power at objective. Also changes in diffusion times are observed from 0.8 ms at 80  $\mu\text{W}$  to 0.6 ms at 160  $\mu\text{W}$  power at objective. Photobleaching can account for this change. Inset shows the reduction of the triplet fraction by COTc quencher. (d)  $sCCF$  of the variant S44pAcF/I150C-(DA) between pseudo-species  $C_1/C_2$  and  $C_3$  at different power at 80  $\mu\text{W}$  and at 160  $\mu\text{W}$  power at the objective. The relaxation times fitted globally are  $t_{R1} = 6 \mu\text{s}$  and  $t_{R2} = 240 \mu\text{s}$ , that are within the errors presented on Table S4c. Note that the amplitudes do not change as in the case of the standard auto-correlation.

## Supplementary Tables

### Supplementary Table 1

**Supplementary Table 1a.** States description for the vector  $p$ , equilibrium fraction vector  $p_{eq}$  and the rate matrix  $K$ .

Kinetic state $i$	State name	Efficiency $E$	Fluorescence lifetime $\tau$ , ns <sup>[a]</sup>	Equilibrium fraction $p_{eq,i}$
1	$C_1$	0.2	3.2	0.51
2	$C_2$	0.5	2.0	0.29
3	$C_3$	0.9	0.5	0.14
4	$C_{3d}$	0.9	0.5	0.06

$$K_{fastslow} = \begin{pmatrix} -158.1 & 90.8 & 0 & 0 \\ 158.1 & -94.5 & 1.8 & 0 \\ 0 & 3.7 & -1.808 & 0.003 \\ 0 & 0 & 0.008 & -0.003 \end{pmatrix} \quad K_{slowfast} = \begin{pmatrix} -3.5 & 2 & 0 & 0 \\ 3.5 & -169.7 & 81.1 & 0 \\ 0 & 167.7 & -81.108 & 0.003 \\ 0 & 0 & 0.008 & -0.003 \end{pmatrix}$$

**Supplementary Table 1b.** Parameters used in the evaluation of the statistical significance of different simulations.

Type of analysis	$\chi^2$ fast-slow	$\chi^2$ slow-fast	Degrees of freedom	$F$ -value	$p(C_1-C_2$ fast vs. $C_1-C_2$ slow)
1D $\langle \tau_{D(A)} \rangle_f$ histogram	68.6	187.2	10	2.72	1
1D $E$ histogram	85.1	95.5	10	1.12	0.734
2D $\langle \tau_{D(A)} \rangle_f$ vs $E$ histogram	0.4551	0.6069	10	1.33	1

**Supplementary Table 1c.** Calculated reaction rates for several variants using Supplementary Equation (8). Confidence intervals ( $2\sigma$ ) are shown in squared brackets and the corresponding renormalized fractions shown below  $x_1+x_2+x_{3d}=1^*$ .

Samples	$k_{12}$ [ $ms^{-1}$ ]	$k_{21}$ [ $ms^{-1}$ ]	$k_{23}$ [ $ms^{-1}$ ]	$k_{32}$ [ $ms^{-1}$ ]
44/150-(DA)	89 [45.5-175.6]	160 [74.1-312.7]	2.0 [1.5-2.3]	3.7 [3.1-4.3]
11/44/150-(DA)+pept	217 [134.8-535.4]	33 [19.0-86.38]	0.8 [0.6-1.1]	3.7 [3.1-4.3]
26/44/150-(DA) + pept	79 [49.2-193.3]	21 [13.0-52.6]	0.5 [0.4-0.6]	0.9 [0.8-1.0]
The relaxations times used were: $t_{R1} = 4 \pm 2.3 \mu s$ ; $t_{R2} = 230 \pm 28.4 \mu s$ for 44/150-(DA) and 11/44/150-(DA)+pept. $t_{R1} = 10 \mu s$ ; $t_{R2} = 790 \mu s$ (Fig. S6F) was used for 26/44/150-(DA) + pept.				
Chemical State	Samples	$x_1$	$x_2$	$x_{3d}$
$E$	44/150-(DA)	0.54	0.30	0.16
$ES$	11/44/150-(DA)+pept	0.30	0.54	0.16
$EP$	26/44/150-(DA) + pept	0.35	0.29	0.36
* Rounded to 2 digits. Renormalized fractions based on the relative changes observed in all states in the presence of substrate (Fig. 6E). Only the amino acid number of the mutagenesis is shown.				

## Supplementary Table 2

**Supplementary Table 2a.** Fluorescence properties of the dyes without FRET. The table lists the parameters of the multi-exponential fits (Supplementary Equation 32) of Donor-only labeled variants and of the direct acceptor excitation of double labeled FRET samples. Fluorescence lifetimes  $\tau_i$  and corresponding species fractions  $x_i$  and fluorescence quantum yields of the donor ( $\Phi_{\text{FD}(0)}$ , Alexa488) and acceptor ( $\Phi_{\text{FA}}$ , Alexa647) are listed. Empty cells represent parameters that are not applicable. The donor fluorophore was attached to the unnatural amino acid pAcF, the acceptor fluorophore to the Cysteine residue.

Variant	$\tau_1$ [ns]	$x_1$	$\tau_2$ [ns]	$x_2$	$\tau_3$ [ns]	$x_3$	$\langle \tau \rangle_{x, \text{D}(0)}$ [ns]	$\Phi_{\text{FD}(0)}^\dagger$	$\langle \tau \rangle_{x, \text{A}}$ [ns]	$\Phi_{\text{FA}}$
E5pAcF/S44C	4.10	0.77	2.44	0.17	0.43	0.06	3.59	0.78	1.24	0.36
E5pAcF/N132C	4.11	0.78	2.33	0.16	0.34	0.06	3.59	0.78	1.25	0.37
R8pAcF/Q69C	4.10	0.89	1.60	0.11			3.83	0.78	1.23	0.34
R8pAcF/P86C	4.16	0.92	1.89	0.08			3.98	0.79	1.35	0.40
R8pAcF/R119C	4.03	0.77	2.43	0.17	0.38	0.05	3.54	0.75	1.26	0.34
R8pAcF/N132C	4.08	0.79	2.27	0.14	0.34	0.07	3.55	0.76	1.25	0.34
K19pAcF/Q69C	4.25	0.78	2.22	0.13	0.65	0.09	3.60	0.80	1.22	0.33
K19pAcF/P86C	3.90	0.77	2.56	0.15	0.32	0.08	3.39	0.73	1.30	0.38
K19pAcF/R119C	3.91	0.74	2.51	0.15	0.52	0.11	3.27	0.73	1.32	0.39
K19pAcF/N132C	3.91	0.81	2.66	0.14	0.32	0.05	3.54	0.74	1.20	0.33
E22pAcF/D127C	3.83	0.36	1.83	0.47	0.67	0.17	2.25	0.60	1.24	0.34
S36pAcF/P86C	4.40	0.81	2.28	0.14	0.49	0.05	3.89	0.83	1.30	0.39
S36pAcF/N132C	4.39	0.83	2.23	0.13	0.46	0.05	3.91	0.83	1.25	0.34
S44pAcF/Q69C	4.32	0.94	1.75	0.06			4.17	0.83	1.25	0.34
S44pAcF/P86C	4.32	0.94	1.75	0.06			4.17	0.83	1.26	0.35
S44pAcF/R119C	4.32	0.96	1.44	0.04			4.20	0.84	1.27	0.35
S44pAcF/D127C	4.28	0.85	2.25	0.10	0.39	0.05	3.85	0.81	1.28	0.35
S44pAcF/N132C	4.32	0.96	1.44	0.04			4.20	0.84	1.37	0.37
S44pAcF/I150C	4.32	0.96	1.44	0.04			4.20	0.84	1.34	0.40
N55pAcF/Q69C	4.14	0.92	1.48	0.08			3.93	0.79	1.32	0.39
N55pAcF/R119C	4.26	0.78	2.31	0.15	0.24	0.07	3.67	0.80	1.35	0.41
N55pAcF/N132C	4.28	0.94	1.49	0.06			4.11	0.82	1.33	0.39
N55pAcF/I150C	4.32	0.69	3.08	0.25	0.72	0.06	3.75	0.79	1.48	0.40
K60pAcF/P86C	4.12	0.94	2.07	0.06			4.00	0.79	1.40	0.41
K60pAcF/R119C	4.26	0.91	1.81	0.09			4.04	0.81	1.34	0.37
K60pAcF/N132C	4.15	0.89	1.78	0.11			3.89	0.79	1.30	0.36
K60pAcF/I150C	4.09	0.88	1.76	0.12			3.81	0.77	1.35	0.37
Q69pAcF/P86C	4.20	0.94	1.52	0.06			4.04	0.81	1.36	0.37
Q69pAcF/R119C	4.20	0.88	1.64	0.12			3.89	0.79	1.37	0.38
Q69pAcF/N132C	4.20	0.89	1.47	0.11			3.90	0.80	1.40	0.38
Q690pAcF/I150C	4.20	0.89	1.88	0.11			3.94	0.80	0.94	0.35
D70pAcF/R119C	4.14	0.68	2.61	0.23	0.82	0.09	3.42	0.76	1.18	0.32
D70pAcF/N132C	4.08	0.88	1.12	0.12			3.72	0.78	1.33	0.36

$^\dagger$  Fluorescence quantum yields are calculated from the species averaged lifetimes  $\langle \tau \rangle_x = \sum_{i=0}^n x_i \tau_i^{(i)}$ , where  $x_i$ 's are the species fractions with reference values of quantum yield  $\Phi_{\text{FD}(0)} = 0.8$  and lifetime  $\langle \tau_{\text{D}(0)} \rangle_x = 4.0$  ns for Alexa488; and  $\Phi_{\text{FA}} = 0.32$  and lifetime  $\langle \tau_{\text{A}} \rangle_x = 1.17$  ns for Alexa647 (see the section "Donor and acceptor fluorescence quantum yields" in Supplementary Methods).

**Supplementary Table 2b.** Table of state-specific mean distances ( $\langle R_{DA_{major}} \rangle$ ,  $\langle R_{DA_{minor}} \rangle$ ) and corresponding fractions ( $x_{major}$ ,  $x_{minor}$ ) for the distribution fit with a 2-component model and individual species fractions ( $N=2$ , Supplementary Equation 36). Species with a higher fraction is assigned to as *major*. Donor only fraction ( $x_{D(0)}$ ) is fitted individually. Fit specific chi-squared reduced values ( $\chi^2_r$ ) are given for each fit. Average  $\chi^2_r$  for this fit model is 1.0825. The results were not used for structural modeling.

Variant	$\langle R_{DA_{major}} \rangle$ [Å]	$x_{major}^{\ddagger}$	$\langle R_{DA_{minor}} \rangle$ [Å]	$x_{minor}^{\ddagger}$	$x_{D(0)}^*$	$\chi^2_r$
E5pAcF/S44C	42.2	0.94	27.9	0.06	0.074	1.12
E5pAcF/N132C	35.0	0.63	45.8	0.37	0.041	1.01
R8pAcF/Q69C	38.0	0.56	37.6	0.44	0.206	1.07
R8pAcF/P86C	39.5	0.68	50.1	0.32	0.178	1.06
R8pAcF/R119C	44.1	0.65	28.5	0.36	0.082	1.03
R8pAcF/N132C	17.9	0.84	40.4	0.16	0.053	1.02
K19pAcF/Q69C	38.9	0.62	38.9	0.38	0.513	1.07
K19pAcF/P86C	48.2	0.62	56.8	0.39	0.068	1.02
K19pAcF/R119C	49.1	0.55	49.1	0.45	0.425	1.05
K19pAcF/N132C	41.7	0.71	53.3	0.29	0.336	1.10
E22pAcF/D127C	28.1	0.65	45.2	0.35	0.581	0.99
S36pAcF/P86C	49.8	0.62	36.1	0.38	0.029	1.03
S36pAcF/N132C	38.6	0.54	50.7	0.46	0.031	0.96
S44pAcF/Q69C	20.9	0.78	36.9	0.22	0.068	1.05
S44pAcF/P86C	54.1	0.62	39.9	0.39	0.082	1.05
S44pAcF/R119C	56.9	0.68	41.9	0.32	0.215	1.12
S44pAcF/D127C	57.0	0.83	39.9	0.17	0.101	1.03
S44pAcF/N132C	63.8	0.55	43.9	0.45	0.357	1.14
S44pAcF/I150C	55.8	0.73	41.9	0.27	0.027	1.09
N55pAcF/Q69C	37.3	0.79	39.3	0.21	0.231	1.16
N55pAcF/R119C	64.8	0.63	51.3	0.37	0.196	1.09
N55pAcF/N132C	53.3	0.68	40.2	0.32	0.042	1.04
N55pAcF/I150C	49.6	0.97	32.9	0.04	0.723	1.13
K60pAcF/P86C	53.2	0.59	41.7	0.41	0.338	1.11
K60pAcF/R119C	54.5	0.61	42.2	0.39	0.263	1.12
K60pAcF/N132C	48.7	0.52	38.2	0.48	0.164	1.04
K60pAcF/I150C	39.8	0.74	51.7	0.26	0.196	1.05
Q69pAcF/P86C	38.6	0.87	58.7	0.14	0.396	1.09
Q69pAcF/R119C	40.5	0.87	52.8	0.13	0.306	1.10
Q69pAcF/N132C	37.4	0.55	47.2	0.45	0.236	1.10
Q690pAcF/I150C	41.5	0.64	53.8	0.37	0.400	1.09
D70pAcF/R119C	34.1	0.56	43.1	0.44	0.115	1.04
D70pAcF/N132C	34.8	0.68	45.3	0.32	0.142	1.07

<sup>‡</sup> Values for the FRET populations are normalized such that  $x_{minor} + x_{major} = 1$ . \*Donor decay was fixed and  $x_{D(0)}$  represents the fraction of donor only from the total.

**Supplementary Table 2c.** Table of state-specific mean distances ( $\langle R_{DA\text{major}} \rangle$ ,  $\langle R_{DA\text{minor}} \rangle$ ) and corresponding fractions ( $x_{\text{major}}$ ,  $x_{\text{minor}}$ ) for the distribution fit with a 2-component model sharing global species fractions for the states ( $N=2$ , Supplementary Equation 36),  $x_{\text{minor}} = 0.466$ ,  $x_{\text{major}} = 0.534$ . Species with higher fraction is assigned as *major*. Donor only fraction ( $x_{D(0)}$ ) is fitted individually. Fit specific chi-squared reduced values ( $\chi^2_{\text{r}}$ ) are given for each fit. Average  $\chi^2_{\text{r}}$  for this fitting model is 1.0985. The results were not used for structural modeling.

Variant	$\langle R_{DA\text{minor}} \rangle$ [Å]	$\langle R_{DA\text{major}} \rangle$ [Å]	$x_{D(0)}$ *	$\chi^2_{\text{r}}$
E5pAcF/S44C	40.3	43.4	0.08	1.16
E5pAcF/N132C	44.4	32.8	0.04	1.05
R8pAcF/Q69C	37.8	37.8	0.21	1.08
R8pAcF/P86C	35.7	47.0	0.17	1.09
R8pAcF/R119C	37.3	45.8	0.10	1.07
R8pAcF/N132C	28.2	41.4	0.17	0.97
K19pAcF/Q69C	39.1	39.1	0.05	1.05
K19pAcF/P86C	46.2	55.5	0.06	1.00
K19pAcF/R119C	49.1	49.1	0.04	1.07
K19pAcF/N132C	38.2	49.2	0.03	1.11
E22pAcF/D127C	29.7	43.4	0.07	1.03
S36pAcF/P86C	39.3	51.1	0.03	1.10
S36pAcF/N132C	36.8	49.6	0.03	1.00
S44pAcF/Q69C	29.0	38.6	0.18	1.38
S44pAcF/P86C	42.8	55.6	0.08	1.06
S44pAcF/R119C	45.9	59.8	0.20	1.15
S44pAcF/D127C	49.4	61.7	0.07	1.11
S44pAcF/N132C	43.4	61.7	0.42	1.14
S44pAcF/I150C	46.7	58.6	0.01	1.13
N55pAcF/Q69C	37.2	37.2	0.23	1.17
N55pAcF/R119C	52.7	67.7	0.17	1.13
N55pAcF/N132C	43.7	55.2	0.04	1.10
N55pAcF/I150C	49.5	49.5	0.73	1.13
K60pAcF/P86C	41.2	53.9	0.32	1.17
K60pAcF/R119C	55.6	44.6	0.05	1.14
K60pAcF/N132C	49.2	39.1	0.17	1.06
K60pAcF/I150C	47.2	36.7	0.20	1.04
Q69pAcF/P86C	34.4	42.8	0.42	1.11
Q69pAcF/R119C	45.8	37.0	0.30	1.12
Q69pAcF/N132C	47.0	37.4	0.23	1.12
Q690pAcF/I150C	51.8	39.8	0.39	1.09
D70pAcF/R119C	31.7	42.1	0.11	1.04
D70pAcF/N132C	31.1	42.6	0.14	1.14

<sup>†</sup> Values for the FRET populations are normalized such that  $x_{\text{major}} + x_{\text{minor}} = 1$ . \*Donor decay was fixed and  $x_{D(0)}$  represents the fraction of donor only from the total.

**Supplementary Table 2d.** Table of determined state-specific mean distances ( $\langle R_{DA}^{(1)} \rangle$ ) and total absolute distance uncertainties  $\Delta R_{DA,tot-+}^{(1)}$  for the state  $C_1$  obtained by the distribution fit with a 3-component model ( $N=3$ , Supplementary Equation (36)) with globally shared species fractions  $x_1 = 0.44$ ,  $x_2 = 0.38$  and  $x_3 = 0.18$  and free donor-only fraction ( $x_{D(\theta)}$ ). Minimal  $\chi^2_{r,global}$  for this fit model is 1.0736. The total distance uncertainties  $\Delta R_{DA,tot-}$  and  $\Delta R_{DA,tot+}$  are calculated according to Equation 5 (main text) using the contributions of individual uncertainties listed in Supplementary Table 2g. The distances were used for FPS in Fig. 5 b,c. We present the weighted residuals (w.res.) of the conformation  $C_j$  against the model structure (PDB-ID 172L).  $C_i-C_j$  represents the distances between the  $C_\alpha$  atoms of the labeled residues in the model structure, and  $\langle R_{D,i} \rangle$  represents the corresponding average inter-dye distances. The donor fluorophore was attached to the unnatural amino acid p-acetyl-L-phenylalanine (pAcF), the acceptor fluorophore to the Cysteine residue (C). The results were used for structural modeling in Figure 5.

Variant	$\langle R_{DA}^{(1)} \rangle$ [Å]	$\Delta R_{DA,tot-}^{(1)}$ [Å]	$\Delta R_{DA,tot+}^{(1)}$ [Å]	$C_i-C_j$ X-ray* [Å]	$\langle R_{D,i} \rangle$ X-ray [Å]	w.res. *** [Å/Å]	$x_{D(\theta)}$ °	$\chi^2_r$	Class
E5pAcF/S44C	42.3	4.4	4.4	27.3	41.8	-0.13	0.07	1.09	$R_1 = R_2, R_3$ var.
E5pAcF/N132C	34.7	5.4	5.4	25.7	42.8	1.62	0.04	1.01	$R_1 = R_2, R_3$ var.
R8pAcF/Q69C	37.8	3.9	3.9	15.1	34.7	-0.80	0.21	1.08	$R_1 = R_2 = R_3$
R8pAcF/P86C	47.6	5.4	5.3	26.8	46.1	-0.28	0.16	1.08	$R_2 = R_3, R_1$ var.
R8pAcF/R119C	45.9	6.0	6.0	28.2	47.1	0.23	0.09	1.04	$R_1 > R_2 > R_3$
R8pAcF/N132C	42.4	5.7	5.7	26.0	42.9	0.16	0.04	0.97	$R_1 > R_3 > R_2$
K19pAcF/Q69C	39.1	4.0	4.0	20.2	37.7	-0.35	0.53	1.05	$R_1 = R_2 = R_3$
K19pAcF/P86C	54.2	5.5	5.5	35.9	52.4	-0.33	0.04	1.00	$R_1 > R_2 > R_3$
K19pAcF/R119C	56.4	6.2	6.2	37.5	51.4	-0.81	0.25	1.07	$R_1 = R_2 = R_3$
K19pAcF/N132C	50.4	7.0	7.0	35.3	46.5	-0.58	0.33	1.11	$R_2 = R_3, R_1$ var.
E22pAcF/D127C	41.5	6.7	6.7	37.3	44.7	0.48	0.53	1.01	$R_3 > R_1 > R_2$
S36pAcF/P86C	51.3	5.2	5.2	37.4	47.0	-0.83	0.03	1.06	$R_1 > R_2 > R_3$
S36pAcF/N132C	50.9	6.6	6.6	41.0	50.6	-0.04	0.03	0.96	$R_2 = R_3, R_1$ var.
S44pAcF/Q69C	29.8	4.7	4.7	18.4	27.3	-0.72	0.13	1.14	$R_1 = R_2, R_3$ var.
S44pAcF/P86C	55.8	6.0	6.0	39.3	51.5	-0.72	0.07	1.05	$R_1 = R_2, R_3$ var.
S44pAcF/R119C	59.7	4.9	4.9	44.2	57.0	-0.45	0.21	1.13	$R_1 > R_2 > R_3$
S44pAcF/D127C	58.4	6.8	6.8	47.6	60.3	0.14	0.10	1.01	$R_1 > R_2 > R_3$
S44pAcF/N132C	64.8	7.7	7.7	45.2	57.6	-0.94	0.40	1.14	$R_1 > R_2 > R_3$
S44pAcF/I150C	58.2	5.9	5.8	38.9	58.2	0.00	0.03	1.10	$R_1 > R_2 > R_3$
N55pAcF/Q69C	37.1	4.4	4.4	20.9	34.5	-0.59	0.23	1.17	$R_1 = R_2 = R_3$
N55pAcF/R119C	68.4	5.6	5.6	46.5	62.5	-1.09	0.18	1.13	$R_1 > R_2 > R_3$
N55pAcF/N132C	55.2	5.5	5.5	46.2	60.6	1.05	0.04	1.08	$R_1 > R_2 > R_3$
N55pAcF/I150C	60.8	6.8	6.8	38.7	55.7	-0.75	0.48	1.13	$R_1 = R_2, R_3$ var.



K60pAcF/P86C	54.0	6.0	6.0	32.7	47.3	-1.09	0.30	1.15	$R_1 > R_2 > R_3$
K60pAcF/R119C	47.4	5.9	5.9	36.4	51.1	0.50	0.06	1.09	$R_2 > R_1 > R_3$
K60pAcF/N132C	37.7	4.4	4.4	35.9	49.1	2.54	0.17	1.06	$R_2 = R_3, R_1$ var.
K60pAcF/I150C	37.8	4.3	4.3	27.1	40.3	0.59	0.20	1.03	$R_1 = R_3, R_2$ var.
Q69pAcF/P86C	38.6	4.3	4.3	22.0	34.0	-1.15	0.42	1.11	$R_1 = R_2, R_3$ var.
Q69pAcF/R119C	39.9	4.7	4.7	27.9	41.9	0.45	0.30	1.10	$R_1 = R_2, R_3$ var.
Q69pAcF/N132C	37.3	4.5	4.5	31.0	45.4	1.81	0.24	1.12	$R_1 = R_3, R_2$ var.
Q690pAcF/I150C	50.8	5.9	5.9	24.7	47.4	-0.58	0.36	1.09	$R_1 = R_3, R_2$ var.
D70pAcF/R119C	43.1	4.6	4.6	25.8	36.8	-1.36	0.12	1.04	$R_2 = R_3, R_1$ var.
D70pAcF/N132C	38.8	4.8	4.8	28.2	38.6	0.00	0.13	1.07	$R_3 > R_1 > R_2$

**Supplementary Table 2e.** Table of determined state-specific mean distances ( $\langle R_{DA}^{(2)} \rangle$ ) and total absolute distance uncertainties  $\Delta R_{DA,tot-+}^{(2)}$  for the state  $C_2$  obtained by the distribution fit with a 3-component model ( $N=3$ , Supplementary Equation (36)) with globally shared species fractions  $x_1 = 0.44$ ,  $x_2 = 0.38$  and  $x_3 = 0.18$  and free donor-only fraction ( $x_{D(0)}$ ). Minimal  $\chi^2_{\text{global}}$  for this fit model is 1.0736. The total distance uncertainties  $\Delta R_{DA,tot-}^{(2)}$  and  $\Delta R_{DA,tot+}^{(2)}$  are calculated according to Equation 5 (main text) using the contributions of individual uncertainties listed in Supplementary Table 2g. The distances were used for FPS in Fig. 5 b,c. We present the weighted residuals ( $w.res.$ ) of the conformation  $C_2$  against the model structure (PDB-ID 148L).  $C_\alpha-C_\alpha$  represents the distances between the  $C_\alpha$  atoms of the labeled residues in the model structure, and  $\langle R_{D,i} \rangle$  represents the corresponding average inter-dye distances. The results were used for structural modeling in Figure 5.

Variant	$\langle R_{DA}^{(2)} \rangle$ [Å]	$\Delta R_{DA,tot-}^{(2)}$ [Å]	$\Delta R_{DA,tot+}^{(2)}$ [Å]	$C_\alpha-C_\alpha$ X-ray* [Å]	$\langle R_{D,i} \rangle$ X-ray [Å]	$w.res.***$ [Å/Å]	$x_{D(0)}^*$	$\chi^2_r$	Class
E5pAcF/S44C	42.3	4.4	4.4	28.9	43.5	0.30	0.07	1.09	$R_1 = R_2, R_3$ var.
E5pAcF/N132C	45.6	7.2	7.2	25.7	42.9	-0.37	0.04	1.01	$R_1 = R_3, R_2$ var.
R8pAcF/Q69C	37.8	3.9	3.9	14.3	32.0	-1.49	0.21	1.08	$R_1 = R_2 = R_3$
R8pAcF/P86C	38.2	4.4	4.4	26.6	43.3	1.16	0.16	1.08	$R_2 = R_3, R_1$ var.
R8pAcF/R119C	39.5	5.4	5.4	28.3	46.7	1.27	0.09	1.04	$R_1 > R_2 > R_3$
R8pAcF/N132C	31.1	4.6	4.6	25.6	44.4	2.31	0.17	0.97	$R_1 > R_3 > R_2$
K19pAcF/Q69C	39.1	4.0	4.0	20.9	38.7	-0.10	0.53	1.05	$R_1 = R_2 = R_3$
K19pAcF/P86C	47.2	4.9	4.9	34.4	50.7	-0.33	0.04	1.00	$R_1 > R_2 > R_3$
K19pAcF/R119C	44.7	5.0	5.0	33.5	47.2	0.50	0.25	1.07	$R_1 = R_2 = R_3$
K19pAcF/N132C	39.7	5.5	5.5	28.4	42.0	0.42	0.33	1.11	$R_2 = R_3, R_1$ var.
E22pAcF/D127C	36.8	5.5	5.5	28.7	37.1	0.05	0.53	1.01	$R_3 > R_1 > R_2$
S36pAcF/P86C	41.6	4.9	4.9	34.3	42.8	0.08	0.03	1.06	$R_1 > R_2 > R_3$
S36pAcF/N132C	37.6	5.0	5.0	30.5	41.4	0.78	0.03	0.96	$R_2 = R_3, R_1$ var.
S44pAcF/Q69C	29.8	4.7	4.7	18.9	27.4	-0.70	0.13	1.14	$R_1 = R_2, R_3$ var.
S44pAcF/P86C	45.8	5.2	5.2	37.5	49.0	0.62	0.07	1.05	$R_1 = R_3, R_2$ var.
S44pAcF/R119C	50.1	5.2	5.2	40.0	50.7	0.01	0.21	1.13	$R_1 > R_2 > R_3$
S44pAcF/D127C	56.1	7.2	7.2	43.8	56.5	0.18	0.10	1.01	$R_1 > R_2 > R_3$
S44pAcF/N132C	47.8	6.2	6.2	38.3	51.3	0.52	0.40	1.14	$R_1 > R_2 > R_3$
S44pAcF/I150C	48.1	5.8	5.8	35.0	51.7	0.62	0.03	1.10	$R_1 > R_2 > R_3$
N55pAcF/Q69C	37.1	4.4	4.4	21.5	33.5	-0.82	0.23	1.17	$R_1 = R_2 = R_3$
N55pAcF/R119C	56.6	5.2	5.2	44.8	59.8	0.56	0.18	1.13	$R_1 > R_2 > R_3$
N55pAcF/N132C	46.8	4.7	4.7	42.1	58.3	2.58	0.04	1.08	$R_1 > R_2 > R_3$
N55pAcF/I150C	47.6	5.4	5.4	37.1	52.9	-0.75	0.48	1.13	$R_1 = R_2, R_3$ var.
K60pAcF/P86C	43.9	5.7	5.7	35.6	48.9	0.67	0.30	1.15	$R_1 > R_2 > R_3$

K60pAcF/R119C	55.0	6.0	6.0	39.3	53.2	-0.22	0.06	1.09	$R_2 > R_l > R_3$
K60pAcF/N132C	49.2	5.8	5.8	37.4	51.9	0.46	0.17	1.06	$R_2 = R_3, R_l$ var.
K60pAcF/I150C	48.5	5.6	5.6	29.9	43.6	-0.90	0.20	1.03	$R_l = R_3, R_2$ var.
Q69pAcF/P86C	36.7	3.8	3.8	23.2	34.8	-0.46	0.42	1.11	$R_l = R_2, R_3$ var.
Q69pAcF/R119C	40.0	5.1	5.1	28.9	41.7	0.28	0.30	1.10	$R_l = R_2, R_3$ var.
Q69pAcF/N132C	47.8	5.7	5.7	30.1	45.7	-0.38	0.24	1.12	$R_l = R_3, R_2$ var.
Q690pAcF/I150C	42.2	5.0	5.0	24.7	47.3	-0.58	0.36	1.09	$R_l = R_3, R_2$ var.
D70pAcF/R119C	34.1	3.8	3.8	26.2	34.5	0.08	0.12	1.04	$R_2 = R_3, R_l$ var.
D70pAcF/N132C	30.4	3.6	3.6	26.6	37.5	1.92	0.13	1.07	$R_3 > R_l > R_2$

**Supplementary Table 2f.** Table of determined state-specific mean distances  $\langle R_{DA}^{(3)} \rangle$  and total absolute distance uncertainties  $\Delta R_{DA,tot-,+}^{(3)}$  for the state  $C_3$  obtained by the distribution fit with a 3-component model ( $N=3$ , Supplementary Equation (36)) with globally shared species fractions  $x_1 = 0.44$ ,  $x_2 = 0.38$  and  $x_3 = 0.18$  and free donor-only fraction ( $x_{D(0)}$ ). Minimal  $\chi^2_{r,global}$  for this fit model is 1.0736. The total distance uncertainties  $\Delta R_{DA,tot-}^{(3)}$  and  $\Delta R_{DA,tot+}^{(3)}$  are calculated according to Equation 5 (main text) using the contributions of the individual uncertainties listed in Supplementary Table 2g. The distances were used for FPS in Fig. 5 b,c. The results were used for structural modeling in Figure 5.

Variant	$\langle R_{DA}^{(3)} \rangle$ [Å]	$\Delta R_{DA,tot-}^{(3)}$ [Å]	$\Delta R_{DA,tot+}^{(3)}$ [Å]	$x_{D(0)}^*$	$\chi^2_r$	Class
E5pAcF/S44C	25.1	3.6	3.6	0.07	1.09	$R_1 = R_2, R_3$ var.
E5pAcF/N132C	35.3	5.9	5.9	0.04	1.01	$R_1 = R_3, R_2$ var.
R8pAcF/Q69C	37.8	3.9	3.9	0.21	1.08	$R_1 = R_2 = R_3$
R8pAcF/P86C	30.0	4.6	4.6	0.16	1.08	$R_2 = R_3, R_1$ var.
R8pAcF/R119C	27.9	3.7	3.7	0.09	1.04	$R_1 > R_2 > R_3$
R8pAcF/N132C	25.2	4.8	4.8	0.17	0.97	$R_1 > R_3 > R_2$
K19pAcF/Q69C	39.1	4.0	4.0	0.53	1.05	$R_1 = R_2 = R_3$
K19pAcF/P86C	32.3	5.0	5.2	0.04	1.00	$R_1 > R_2 > R_3$
K19pAcF/R119C	31.0	4.6	4.6	0.25	1.07	$R_1 = R_2 = R_3$
K19pAcF/N132C	39.7	5.7	5.7	0.33	1.11	$R_2 = R_3, R_1$ var.
E22pAcF/D127C	25.4	4.1	4.1	0.53	1.01	$R_3 > R_1 > R_2$
S36pAcF/P86C	29.2	4.3	4.3	0.03	1.06	$R_1 > R_2 > R_3$
S36pAcF/N132C	41.6	5.8	5.8	0.03	0.96	$R_2 = R_3, R_1$ var.
S44pAcF/Q69C	42.8	6.1	6.1	0.13	1.14	$R_1 = R_2, R_3$ var.
S44pAcF/P86C	54.0	5.8	5.8	0.07	1.05	$R_1 = R_3, R_2$ var.
S44pAcF/R119C	38.5	4.4	4.4	0.21	1.13	$R_1 > R_2 > R_3$
S44pAcF/D127C	41.4	7.1	7.1	0.10	1.01	$R_1 > R_2 > R_3$
S44pAcF/N132C	38.9	4.7	4.7	0.40	1.14	$R_1 > R_2 > R_3$
S44pAcF/I150C	33.4	4.4	4.4	0.03	1.10	$R_1 > R_2 > R_3$
N55pAcF/Q69C	37.8	4.5	4.5	0.23	1.17	$R_1 = R_2 = R_3$
N55pAcF/R119C	49.0	4.2	4.2	0.18	1.13	$R_1 > R_2 > R_3$
N55pAcF/N132C	34.4	4.0	4.0	0.04	1.08	$R_1 > R_2 > R_3$
N55pAcF/I150C	37.3	8.1	8.1	0.48	1.13	$R_1 = R_2, R_3$ var.
K60pAcF/P86C	29.7	4.5	4.5	0.30	1.15	$R_1 > R_2 > R_3$
K60pAcF/R119C	34.1	4.7	4.7	0.06	1.09	$R_2 > R_1 > R_3$
K60pAcF/N132C	45.7	5.6	5.6	0.17	1.06	$R_2 = R_3, R_1$ var.
K60pAcF/I150C	38.0	4.4	4.4	0.20	1.03	$R_1 = R_3, R_2$ var.
Q69pAcF/P86C	52.4	5.2	5.2	0.42	1.11	$R_1 = R_2, R_3$ var.
Q69pAcF/R119C	50.7	7.0	7.0	0.30	1.10	$R_1 = R_2, R_3$ var.
Q69pAcF/N132C	41.0	5.0	5.0	0.24	1.12	$R_1 = R_3, R_2$ var.
Q690pAcF/I150C	38.0	4.5	4.5	0.36	1.09	$R_1 = R_3, R_2$ var.
D70pAcF/R119C	34.1	3.7	3.7	0.12	1.04	$R_2 = R_3, R_1$ var.
D70pAcF/N132C	47.1	5.9	5.9	0.13	1.07	$R_3 > R_1 > R_2$

**Supplementary Table 2g.** Table of uncertainty contributions of mean distances: the state-specific absolute statistical uncertainty  $\langle R_{noise-+}^{(i)} \rangle$  and the  $R_0$  related relative uncertainty  $\delta R_{R_0}(r(t)_{dye})$ , for the distribution fit with a 3-component model ( $N=3$ , Supplementary Equation (36)) with globally shared species fractions  $x_1 = 0.44$ ,  $x_2 = 0.38$  and  $x_3 = 0.18^*$ . The relative uncertainty  $\delta R_{R_0}(r(t)_{dye})$ , which is equal for all states, is computed as described as in the Methods Section "Simulation of interdye distances and structural modelling" in the main text following the procedures in Ref.<sup>3</sup> using the limiting anisotropies of the donor fluorescence  $r_{3,D}$  (Supplementary Table 3a), directly excited acceptor fluorescence  $r_{3,A}$  (Supplementary Table 3b) and FRET-sensitized acceptor fluorescence  $r_{2,A(D)}$  (Supplementary Table 3c) to compute the  $\kappa^2$  distributions compiled in Supplementary Table 3d. The results were used for structural modeling in Figure 5.

Variant	$\langle R_{noise-}^{(1)} \rangle$ [Å]	$\langle R_{noise+}^{(1)} \rangle$ [Å]	$\langle R_{noise-}^{(2)} \rangle$ [Å]	$\langle R_{noise+}^{(2)} \rangle$ [Å]	$\langle R_{noise-}^{(3)} \rangle$ [Å]	$\langle R_{noise+}^{(3)} \rangle$ [Å]	$\delta R_{R_0}(r(t)_{dye})$ [%]
E5pAcF/S44C	42.3	42.5	42.1	42.3	23.1	28.1	10.3
E5pAcF/N132C	33.4	34.7	45.0	46.0	33.9	37.7	15.7
R8pAcF/Q69C	37.8	37.8	37.8	37.8	37.8	37.8	10.2
R8pAcF/P86C	46.9	48.2	37.3	39.1	29.3	30.7	10.7
R8pAcF/R119C	45.6	45.9	38.3	41.3	27.2	28.6	13.1
R8pAcF/N132C	43.0	42.7	35.4	33.8	27.1	26.2	13.6
K19pAcF/Q69C	39.1	39.1	39.1	39.1	39.1	39.1	10.3
K19pAcF/P86C	54.2	54.2	47.2	47.2	28.7	36.1	9.80
K19pAcF/R119C	56.4	56.4	44.7	44.7	31.0	31.0	10.7
K19pAcF/N132C	49.8	51.3	39.0	40.4	39.0	41.6	13.8
E22pAcF/D127C	37.1	45.9	33.6	40.0	22.9	27.8	11.6
S36pAcF/P86C	51.2	51.4	40.2	44.7	27.2	33.2	10.1
S36pAcF/N132C	50.3	51.4	36.6	38.4	38.1	42.8	13.0
S44pAcF/Q69C	29.0	32.4	29.0	32.4	40.9	48.7	10.6
S44pAcF/P86C	55.3	56.2	44.1	47.5	51.2	54.9	10.3
S44pAcF/R119C	58.6	59.8	47.5	53.8	34.7	40.9	8.21
S44pAcF/D127C	58.0	60.6	51.5	58.9	35.0	45.7	11.3
S44pAcF/N132C	63.3	66.3	45.5	50.8	38.1	40.5	11.6
S44pAcF/I150C	57.2	59.1	44.9	51.2	30.7	36.1	9.58
N55pAcF/Q69C	37.1	37.1	37.1	37.1	37.6	38.2	11.9
N55pAcF/R119C	68.0	69.2	54.6	59.2	47.6	50.3	8.16
N55pAcF/N132C	54.5	55.2	45.0	47.2	29.7	34.4	9.97
N55pAcF/I150C	60.3	61.3	47.2	48.1	30.4	44.2	10.9
K60pAcF/P86C	53.6	54.0	42.4	47.8	28.9	34.6	11.1
K60pAcF/R119C	45.6	50.8	53.6	55.5	32.0	37.6	10.9
K60pAcF/N132C	37.3	38.3	48.8	49.7	44.7	47.8	11.7
K60pAcF/I150C	37.3	38.2	47.8	49.5	37.2	38.8	11.3
Q69pAcF/P86C	37.2	40.7	35.6	37.5	57.5	54.7	10.1
Q69pAcF/R119C	39.1	40.5	38.1	42.4	48.4	55.5	11.6
Q69pAcF/N132C	36.8	37.8	47.5	48.2	38.3	41.5	11.9
Q690pAcF/I150C	50.2	51.5	41.4	42.9	37.3	38.7	11.1
D70pAcF/R119C	42.6	43.6	33.0	35.3	33.0	34.8	10.7
D70pAcF/N132C	36.9	40.3	30.2	31.0	45.7	49.6	11.6

\* Considering a  $1\sigma$ -confidence interval, the fraction  $x_3$  of  $\langle R_{DA}^{(3)} \rangle$  varies between 0.1 – 0.27 (see Fig. 4c). The corresponding  $\langle R_{noise-}^{(i)} \rangle$  and  $\langle R_{noise+}^{(i)} \rangle$  are the shortest and longest distance below the  $1\sigma$ -threshold. The minimal  $\chi^2_{r,global}$  for this distribution fit model is 1.0736 with the species fraction  $x_3 = x_{middle} = 0.18$  with  $x_1 = 0.44$  and  $x_2 = 0.38$  and the state-specific mean distances  $\langle R_{DA}^{(i)} \rangle$  a listed in the Supplementary Tables 2d-f.

**Supplementary Table 2h. Results of determined state-specific mean distances  $\langle R_{DA}^{(i)} \rangle$ , relative uncertainties  $\delta R_{DA,tot-,+}^{(i)}$  and species fractions  $x_i$  for the distribution fit for functional variants of the S44/I150C FRET pair.** Globally shared parameters are highlighted in gray cells (Supplementary Equations (36-39)).

Variant	$\langle R_{DA}^{(1)} \rangle$ [Å]	$\delta R_{DA,tot-,+}^{(1)}$ [%]	$x_1^{\dagger}$	$\langle R_{DA}^{(2)} \rangle$ [Å]	$\delta R_{DA,tot-,+}^{(2)}$ [%]	$x_2^{\dagger}$	$\langle R_{DA}^{(3)} \rangle$ [Å]	$\delta R_{DA,tot-,+}^{(3)}$ [%]	$x_3^{\dagger}$	$x_{D(0)}^*$	$\chi_r^2$
S44pAcF/I150C(-)	65.1	8.0	0.25	51.7	8.0	0.55	38.8	3.0	0.20	0.01	1.06
S44pAcF/I150C(+)**	65.1	12.3	0.25	51.7	12.3	0.57	38.8	3.9	0.18	-	1.52**
T26E/S44pAcF/I150C(-)**	65.1	4.7	0.37	51.7	3.0	0.35	34.9	9.0	0.28	0.62	1.21
T26E/S44pAcF/I150C(+)**	65.1	1.9	0.20	51.7	1.0	0.28	34.9	13.0	0.52	0.74	1.08
E11A/S44C/I150C(-)**	65.1	7.8	0.75	51.7	7.8	0.12	38.8	11.8	0.13	-	1.98**
E11A/S44C/I150C(+)**	65.1	4.9	0.56	51.7	4.9	0.27	38.8	17.4	0.17	-	2.00**
R137E/S44pAcF/I150C	59.3	7.3	0.52	49.3	2.6	0.37	36.2	9.1	0.11	0.24	1.07

<sup>†</sup> Values for the FRET populations are normalized such that  $x_1+x_2+x_3=1$ . \*Donor decay was fixed and  $x_{D(0)}$  represents the fraction of donor only from the total. \*\* Data from single molecule experiments shows higher  $\chi_r^2$  when compared to eTCSPC, due to low photon statistics. \*\*\*Sub-ensemble fit from burst analysis. For E11A/S44C/I150C, it was not possible to measure in eTCSPC due to high donor-only (double Cys variant).

### Supplementary Table 3

**Supplementary Table 3a. Donor anisotropies.** Analysis of time-resolved donor fluorescence anisotropies  $r_D(t)$ \* for donor only labeled samples obtained by ensemble time-resolved fluorescence decays as described in <sup>3</sup>. The table lists the rotation correlation times ( $\rho_{i,D}$ ) and corresponding fractions ( $r_{i,D}$ ).

Samples	$r_{1,D}$	$\rho_{1,D}$ [ns]	$r_{2,D}$	$\rho_{2,D}$ [ns]	$r_{3,D}$	$\rho_{3,D}$ [ns]
5/44-(D(0))	0.049	0.18	0.080	1.92	0.246	12.30
5/132-(D(0))	0.036	0.15	0.041	1.12	0.298	8.58
8/69-(D(0))	0.082	0.17	0.063	1.47	0.230	9.76
8/86-(D(0))	0.078	0.18	0.066	1.24	0.231	9.09
8/119-(D(0))	0.04	0.11	0.042	1.08	0.293	8.15
8/132-(D(0))	0.049	0.10	0.047	0.97	0.279	7.85
19/69-(D(0))	0.122	0.26	0.116	1.84	0.137	8.47
19/86-(D(0))	0.122	0.26	0.116	1.84	0.137	8.47
19/119-(D(0))	0.122	0.26	0.116	1.84	0.137	8.47
19/132-(D(0))	0.082	0.16	0.057	1.15	0.237	10.39
22/127-(D(0))	0.054	0.14	0.120	1.78	0.201	16.32
36/86-(D(0))	0.095	0.17	0.089	1.44	0.192	12.00
36/132-(D(0))	0.078	0.13	0.074	0.91	0.223	8.12
44/69-(D(0))	0.093	0.15	0.089	1.17	0.193	9.32
44/86-(D(0))	0.113	0.19	0.067	1.26	0.195	8.60
44/119-(D(0))	0.113	0.19	0.067	1.26	0.195	8.60
44-127-(D(0))	0.093	0.15	0.089	1.17	0.193	9.32
44/132-(D(0))	0.113	0.19	0.067	1.26	0.195	8.60
44/150-(D(0))	0.113	0.19	0.067	1.26	0.195	8.60
55/69-(D(0))	0.268	0.10	0.107	0.73	0.071	7.61
55/119-(D(0))	0.134	0.17	0.084	1.27	0.157	10.89
55/132-(D(0))	0.245	0.05	0.130	0.58	0.120	6.93
55/150-(D(0))	0.144	0.20	0.082	1.22	0.150	9.52
60/86-(D(0))	0.096	0.18	0.081	1.24	0.198	8.24
60/119-(D(0))	0.077	0.16	0.067	1.17	0.231	9.00
60/132-(D(0))	0.096	0.18	0.081	1.24	0.198	8.24
60/150-(D(0))	0.096	0.18	0.081	1.24	0.198	8.24
69/86-(D(0))	0.115	0.18	0.092	1.07	0.167	8.26
69/119-(D(0))	0.115	0.18	0.092	1.07	0.167	8.26
69/132-(D(0))	0.115	0.18	0.092	1.07	0.167	8.26
69/150-(D(0))	0.115	0.18	0.092	1.07	0.167	8.26
70/119-(D(0))	0.108	0.23	0.094	1.38	0.173	8.42
70/132-(D(0))	0.108	0.23	0.094	1.38	0.173	8.42

\* The fluorescence anisotropy decay  $r_D(t)$  can be described as a sum of three exponentials:  
 $r_D(t) = r_{1,D} \exp(-t/\rho_{1,D}) + r_{2,D} \exp(-t/\rho_{2,D}) + r_{3,D} \exp(-t/\rho_{3,D})$  with anisotropy fractions  $r_{1,D} + r_{2,D} + r_{3,D} \leq r_0$ .  
 For Alexa488-hydroxylamine the fundamental anisotropy  $r_{0,D}$  is 0.375.

**Supplementary Table 3b. Acceptor anisotropies (direct excitation).** Analysis of time-resolved fluorescence anisotropies  $r_A(t)$ \* for direct acceptor excitation of double labeled samples obtained by ensemble time-resolved fluorescence decays as described in <sup>3</sup>. The table lists rotation correlation times ( $\rho_{i,A}$ ) and corresponding fractions ( $r_{i,A}$ ).

Samples	$r_{1,A}$	$\rho_{1,A}$ [ns]	$r_{2,A}$	$\rho_{2,A}$ [ns]	$r_{3,A}$	$\rho_{3,A}$ [ns]
5/44-(DA)	0.081	0.03	0.144	0.70	0.165	10.68
5/132-(DA)	0.030	0.14	0.119	0.84	0.241	12.11
8/69-(DA)	0.060	0.08	0.116	0.57	0.214	13.96
8/86-(DA)	0.051	0.05	0.108	0.73	0.231	12.53
8/119-(DA)	0.035	0.08	0.134	0.66	0.221	13.12
8/132-(DA)	0.059	0.10	0.152	0.79	0.178	11.26
19/69-(DA)	0.066	0.04	0.155	0.71	0.169	12.58
19/86-(DA)	0.036	0.17	0.141	0.87	0.214	11.38
19/119-(DA)	0.042	0.09	0.142	0.79	0.206	10.73
19/132-(DA)	0.061	0.09	0.173	0.78	0.156	19.93
22/127-(DA)	0.062	0.05	0.151	0.91	0.177	14.09
36/86-(DA)	0.042	0.12	0.131	0.80	0.217	11.18
36/132-(DA)	0.030	0.03	0.148	0.80	0.212	17.19
44/69-(DA)	0.094	0.02	0.151	0.99	0.145	14.80
44/86-(DA)	0.039	0.16	0.142	0.90	0.209	14.11
44/119-(DA)	0.030	0.17	0.133	0.82	0.227	11.47
44-127-(DA)	0.105	0.35	0.099	1.72	0.186	19.97
44/132-(DA)	0.046	0.06	0.073	0.73	0.271	10.13
44/150-(DA)	0.031	0.14	0.096	0.82	0.263	10.36
55/69-(DA)	0.036	0.07	0.096	0.71	0.257	11.24
55/119-(DA)	0.030	0.09	0.072	0.74	0.288	10.84
55/132-(DA)	0.031	0.07	0.107	0.63	0.252	11.14
55/150-(DA)	0.037	0.16	0.078	0.96	0.275	10.37
60/86-(DA)	0.026	0.09	0.074	0.76	0.290	10.10
60/119-(DA)	0.067	0.12	0.056	0.67	0.267	10.45
60/132-(DA)	0.100	0.12	0.075	0.78	0.215	11.38
60/150-(DA)	0.045	0.02	0.067	0.53	0.278	8.61
69/86-(DA)	0.110	0.23	0.063	2.86	0.216	11.06
69/119-(DA)	0.054	0.07	0.069	0.75	0.267	9.80
69/132-(DA)	0.064	0.21	0.147	1.05	0.179	13.87
69/150-(DA)	0.157	0.70	0.233	24.87		
70/119-(DA)	0.039	0.10	0.087	0.70	0.264	11.08
70/132-(DA)	0.054	0.14	0.080	0.69	0.256	8.66

\* The fluorescence anisotropy decay  $r_A(t)$  can be described as a sum of three exponentials:  $r_A(t) = r_{1,A} \exp(-t/\rho_{1,A}) + r_{2,A} \exp(-t/\rho_{2,A}) + r_{3,A} \exp(-t/\rho_{3,A})$  with anisotropy fractions  $r_{1,A} + r_{2,A} + r_{3,A} \leq r_0$ . For Alexa647-maleimide  $r_{0,A}$  is 0.39.



**Supplementary Table 3c. Acceptor anisotropies (FRET-sensitized).** Analysis of time-resolved fluorescence anisotropies  $r_{A(D)}(t)$ \* for FRET-sensitized emission of acceptor of double labeled samples obtained by ensemble time-resolved fluorescence decays as described in <sup>3</sup> except for <sup>1</sup> and <sup>2</sup>. The table lists the rotation correlation times ( $\rho_{i,A(D)}$ ) and corresponding fractions ( $r_{i,A(D)}$ ).

Samples	$r_{1,A(D)}$	$\rho_{1,A(D)}$ [ns]	$r_{2,A(D)}$	$\rho_{2,A(D)}$ [ns]	$\Sigma r_{i,A(D)}$
5/44-(DA)	0.052	0.192	0.010	8.126	0.062
5/132-(DA)	0.087	0.320	0.026	10.008	0.113
8/69-(DA)	0.025	0.509	0.041	$\infty$	0.066
8/86-(DA)	0.032	0.438	0.049	380	0.081
8/119-(DA)	0.061	0.127	0.012	$\infty$	0.073
8/132-(DA)	0.091	0.280	0.020	4.163	0.111
19/69-(DA)	0.081	0.398	0.105	48.063	0.186
19/86-(DA) <sup>1</sup>	0.209	0.756	0.0561	19.901	0.265
19/119-(DA)	0.041	0.512	0.091	202	0.132
19/132-(DA)	0.1	0.373	0.112	88.561	0.212
22/127-(DA)	0.044	0.702	0.018	$\infty$	0.062
36/86-(DA)	0.087	0.243	0.007	9.393	0.094
36/132-(DA)	0.086	0.241	0.020	2.095	0.106
44/69-(DA)	0.033	0.282	0.019	7.958	0.052
44/86-(DA) <sup>2</sup>	<0.06				
44/119-(DA) <sup>2</sup>	<0.09				
44-127-(DA)	0.179	0.326	0.017	8.815	0.196
44/132-(DA)	0.054	0.246	0.115	23.934	0.169
44/150-(DA)	0.087	0.563	0.048	101.937	0.135
55/69-(DA)	0.036	0.405	0.069	63.43	0.105
55/119-(DA)	0.067	1.31	0.089	136.651	0.156
55/132-(DA)	0.064	1.039	0.016	14.346	0.080
55/150-(DA)	0.065	0.512	0.061	150.739	0.126
60/86-(DA)	0.103	0.483	0.104	127.327	0.207
60/119-(DA)	0.079	0.501	0.086	114.851	0.165
60/132-(DA)	0.054	1.035	0.058	74.739	0.112
60/150-(DA)	0.038	1.102	0.067	77.378	0.105
69/86-(DA)	0.038	0.604	0.073	$\infty$	0.111
69/119-(DA)	0.045	0.603	0.059	84.864	0.104
69/132-(DA)	0.039	0.294	0.049	72.456	0.088
69/150-(DA)	0.049	0.595	0.048	210.295	0.097
70/119-(DA) <sup>2</sup>	<0.04	0.2416			
70/132-(DA) <sup>2</sup>	<0.04	0.2471			

\* The fluorescence anisotropy decay  $r_{A(D)}(t)$  can be described as a sum of two exponentials:

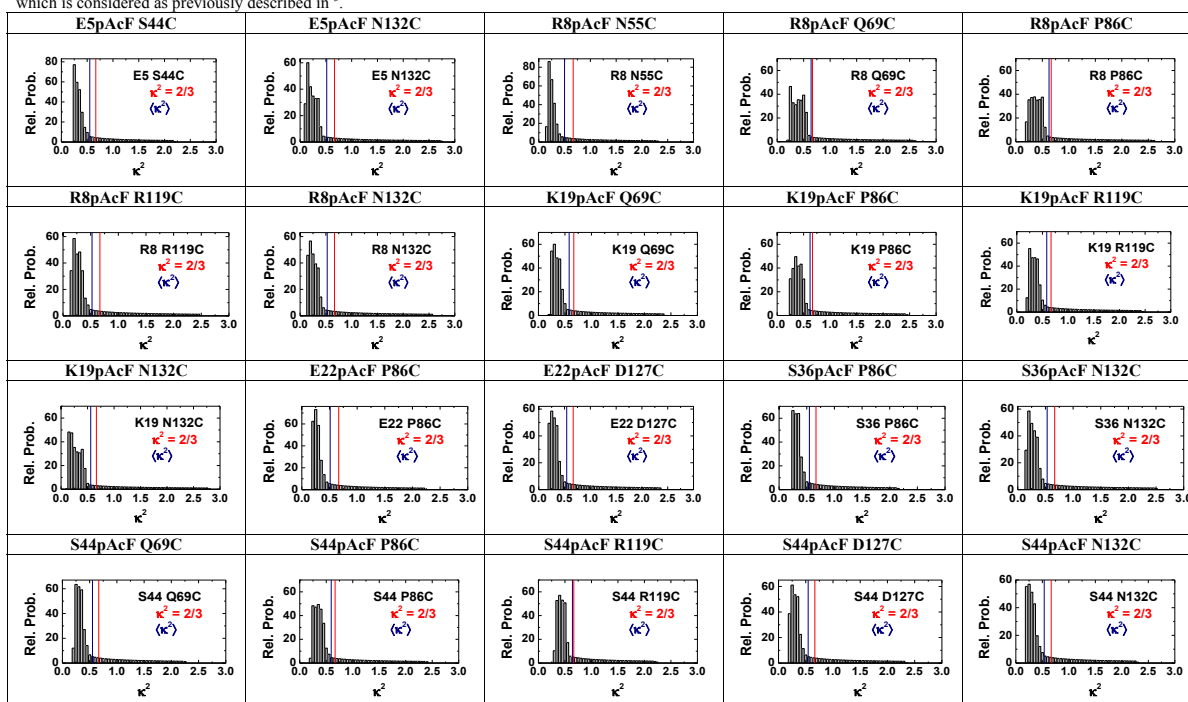
$$r_{A(D)}(t) = r_{1,A(D)} \exp(-t/\rho_{1,A(D)}) + r_{2,A(D)} \exp(-t/\rho_{2,A(D)}) \text{ with anisotropy fractions } r_{1,A(D)} + r_{2,A(D)} \leq r_0.$$

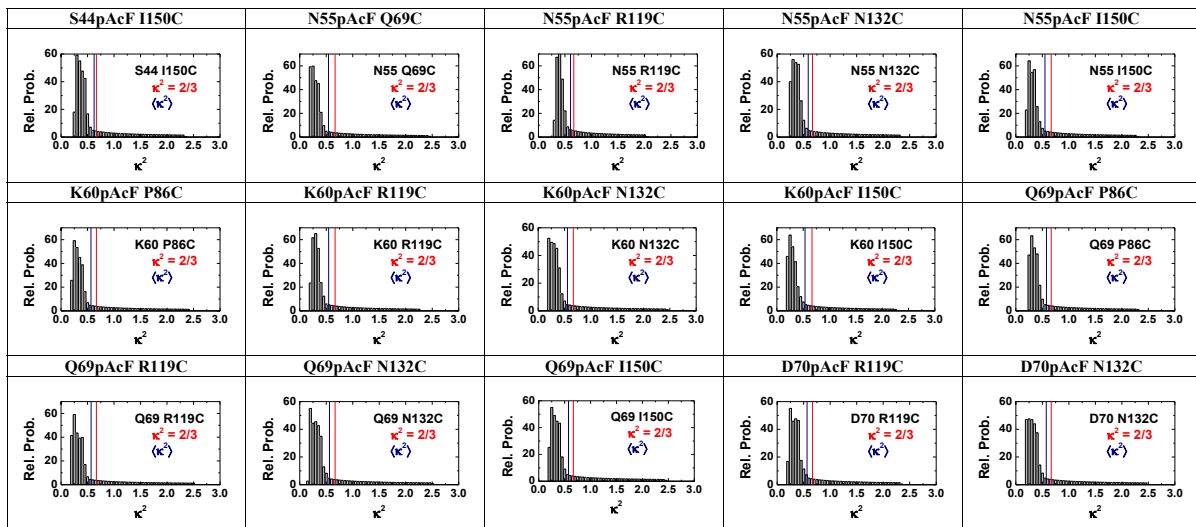
For FRET-sensitized anisotropy decay of Alexa647-maleimide  $r_{0,A(D)}$  is 0.38.

<sup>1</sup> eTCSPC data not available. Fluorescence anisotropy decay was fitted from sub-ensemble single-molecule MFD data of the FRET population.

<sup>2</sup> eTCSPC data not available. Considering variants with a very high FRET efficiency, no satisfactory anisotropy decays from sub-ensemble single-molecule MFD data were obtainable due the short donor fluorescence lifetime. Here, steady-values anisotropies were taken as upper limit from single-molecule MFD measurements.

**Supplementary Table 3d.  $\kappa^2$  distributions for the 33 DA samples.** Donor positions are labeled on green and acceptor positions on red. The mean  $\kappa^2$  ( $\langle \kappa^2 \rangle$ ) is shown as a solid bar in blue, and  $\kappa^2 = 2/3$  is shown in red. Therefore, the assumption of  $\kappa^2 = 2/3$  is justified. Nevertheless, the  $\kappa^2$  distribution adds to the uncertainty on our distances, which is considered as previously described in <sup>3</sup>.





## Supplementary Table 4

**Supplementary Table 4. Groups of structure models for T4L in PDB.** All 578 structural models could be grouped in three clusters: *Open* (19 structures), *ajar* (26 structures) and *closed* (535 structures).

Cluster-name	PDB-ID
<i>Open</i> (19)	172L, 151L, 168L, 169L, 173L, 174L, 178L, 1L97, 2HUK, 3EML, 3JR6, 3OE8, 3QAK, 3RZE, 3SB5, 4ARJ, 4IAP, 4K5Y, 4O09.
<i>Ajar</i> (26)	1JQU, 149L, 150L, 189L, 1P5C, 1P7S, 1QTH, 1SSY, 218L, 2HUM, 2QAR, 2QBO, 2RH1, 3PBL, 3SB9, 3SBA, 3SBB, 3SN6, 3UON, 3V2W, 3V2Y, 3VW7, 4DJH, 4EPI, 4EXM, 4GBR
<i>Closed</i> (535)	148L, 102L, 103L, 104L, 107L, 108L, 109L, 110L, 111L, 112L, 113L, 114L, 115L, 118L, 119L, 120L, 122L, 123L, 125L, 126L, 127L, 128L, 129L, 130L, 131L, 137L, 138L, 139L, 140L, 141L, 142L, 143L, 144L, 145L, 146L, 147L, 152L, 155L, 156L, 157L, 158L, 159L, 160L, 161L, 162L, 163L, 164L, 165L, 166L, 167L, 170L, 171L, 175L, 176L, 177L, 180L, 181L, 182L, 183L, 184L, 185L, 186L, 187L, 188L, 190L, 191L, 192L, 195L, 196L, 197L, 198L, 199L, 1B6I, 1C60, 1C61, 1C62, 1C63, 1C64, 1C65, 1C66, 1C67, 1C68, 1C69, 1C6A, 1C6B, 1C6C, 1C6D, 1C6E, 1C6F, 1C6G, 1C6H, 1C6I, 1C6J, 1C6K, 1C6L, 1C6M, 1C6N, 1C6P, 1C6Q, 1C6T, 1CTW, 1CU0, 1CU2, 1CU3, 1CU5, 1CU6, 1CUP, 1CUQ, 1CV0, 1CV1, 1CV3, 1CV4, 1CV5, 1CV6, 1CVK, 1CX6, 1CX7, 1D2W, 1D2Y, 1D3F, 1D3J, 1D3M, 1D3N, 1D9W, 1DYA, 1DYB, 1DYC, 1DYD, 1DYE, 1DYF, 1DYG, 1EPI, 1G06, 1G07, 1G0G, 1G0J, 1G0K, 1G0L, 1G0M, 1G0P, 1G0Q, 1G1V, 1G1W, 1I6S, 1JTM, 1JTN, 1KNI, 1KS3, 1KW5, 1KW7, 1KY0, 1KY1, 1L00, 1L01, 1L02, 1L03, 1L04, 1L05, 1L06, 1L07, 1L08, 1L09, 1L0J, 1L0K, 1L10, 1L11, 1L12, 1L13, 1L14, 1L15, 1L16, 1L17, 1L18, 1L19, 1L20, 1L21, 1L22, 1L23, 1L24, 1L25, 1L26, 1L27, 1L28, 1L29, 1L30, 1L31, 1L32, 1L33, 1L34, 1L35, 1L36, 1L37, 1L38, 1L39, 1L40, 1L41, 1L42, 1L43, 1L44, 1L45, 1L46, 1L47, 1L48, 1L49, 1L50, 1L51, 1L52, 1L53, 1L54, 1L55, 1L56, 1L57, 1L58, 1L59, 1L60, 1L61, 1L62, 1L63, 1L64, 1L65, 1L66, 1L67, 1L68, 1L69, 1L70, 1L71, 1L72, 1L73, 1L74, 1L75, 1L76, 1L77, 1L79, 1L80, 1L81, 1L82, 1L83, 1L84, 1L85, 1L86, 1L87, 1L88, 1L89, 1L90, 1L91, 1L92, 1L93, 1L94, 1L95, 1L96, 1L98, 1L99, 1L9U, 1L9V, 1L9W, 1L9X, 1L9Y, 1L9Z, 1L9AA, 1L9AB, 1L9AC, 1L9AD, 1L9AE, 1L9AF, 1L9AG, 1L9AH, 1L9AI, 1L9AJ, 1L9AK, 1L9AL, 1L9AM, 1L9AN, 1L9AO, 1L9AP, 1L9AQ, 1L9AR, 1L9AS, 1L9AT, 1L9AU, 1L9AV, 1L9AW, 1L9AX, 1L9AY, 1L9AZ, 1L9BA, 1L9BB, 1L9BC, 1L9BD, 1L9BE, 1L9BF, 1L9BG, 1L9BH, 1L9BI, 1L9BJ, 1L9BK, 1L9BL, 1L9BM, 1L9BN, 1L9BO, 1L9BP, 1L9BQ, 1L9BR, 1L9BS, 1L9BT, 1L9BU, 1L9BV, 1L9BW, 1L9BX, 1L9BY, 1L9BZ, 1L9CA, 1L9CB, 1L9CC, 1L9CD, 1L9CE, 1L9CF, 1L9CG, 1L9CH, 1L9CI, 1L9CJ, 1L9CK, 1L9CL, 1L9CM, 1L9CN, 1L9CO, 1L9CP, 1L9CQ, 1L9CR, 1L9CS, 1L9CT, 1L9CU, 1L9CV, 1L9CW, 1L9CX, 1L9CY, 1L9CZ, 1L9DA, 1L9DB, 1L9DC, 1L9DD, 1L9DE, 1L9DF, 1L9DG, 1L9DH, 1L9DI, 1L9DJ, 1L9DK, 1L9DL, 1L9DM, 1L9DN, 1L9DO, 1L9DP, 1L9DQ, 1L9DR, 1L9DS, 1L9DT, 1L9DU, 1L9DV, 1L9DW, 1L9DX, 1L9DY, 1L9DZ, 1L9EA, 1L9EB, 1L9EC, 1L9ED, 1L9EE, 1L9EF, 1L9EG, 1L9EH, 1L9EI, 1L9EJ, 1L9EK, 1L9EL, 1L9EM, 1L9EN, 1L9EO, 1L9EP, 1L9EQ, 1L9ER, 1L9ES, 1L9ET, 1L9EU, 1L9EV, 1L9EW, 1L9EX, 1L9EY, 1L9EZ, 1L9FA, 1L9FB, 1L9FC, 1L9FD, 1L9FE, 1L9FF, 1L9FG, 1L9FH, 1L9FI, 1L9FJ, 1L9FK, 1L9FL, 1L9FM, 1L9FN, 1L9FO, 1L9FP, 1L9FQ, 1L9FR, 1L9FS, 1L9FT, 1L9FU, 1L9FV, 1L9FW, 1L9FX, 1L9FY, 1L9FZ, 1L9GA, 1L9GB, 1L9GC, 1L9GD, 1L9GE, 1L9GF, 1L9GG, 1L9GH, 1L9GI, 1L9GJ, 1L9GK, 1L9GL, 1L9GM, 1L9GN, 1L9GO, 1L9GP, 1L9GQ, 1L9GR, 1L9GS, 1L9GT, 1L9GU, 1L9GV, 1L9GW, 1L9GX, 1L9GY, 1L9GZ, 1L9HA, 1L9HB, 1L9HC, 1L9HD, 1L9HE, 1L9HF, 1L9HG, 1L9HH, 1L9HI, 1L9HJ, 1L9HK, 1L9HL, 1L9HM, 1L9HN, 1L9HO, 1L9HP, 1L9HQ, 1L9HR, 1L9HS, 1L9HT, 1L9HU, 1L9HV, 1L9HW, 1L9HX, 1L9HY, 1L9HZ, 1L9IA, 1L9IB, 1L9IC, 1L9ID, 1L9IE, 1L9IF, 1L9IG, 1L9IH, 1L9II, 1L9IJ, 1L9IK, 1L9IL, 1L9IM, 1L9IN, 1L9IO, 1L9IP, 1L9IQ, 1L9IR, 1L9IS, 1L9IT, 1L9IU, 1L9IV, 1L9IW, 1L9IX, 1L9IY, 1L9IZ, 1L9JA, 1L9JB, 1L9JC, 1L9JD, 1L9JE, 1L9JF, 1L9JG, 1L9JH, 1L9JI, 1L9JJ, 1L9JK, 1L9JL, 1L9JM, 1L9JN, 1L9JO, 1L9JP, 1L9JQ, 1L9JR, 1L9JS, 1L9JT, 1L9JU, 1L9JV, 1L9JW, 1L9JX, 1L9JY, 1L9JZ, 1L9KA, 1L9KB, 1L9KC, 1L9KD, 1L9KE, 1L9KF, 1L9KG, 1L9KH, 1L9KI, 1L9KJ, 1L9KK, 1L9KL, 1L9KM, 1L9KN, 1L9KO, 1L9KP, 1L9KQ, 1L9KR, 1L9KS, 1L9KT, 1L9KU, 1L9KV, 1L9KW, 1L9KX, 1L9KY, 1L9KZ, 1L9LA, 1L9LB, 1L9LC, 1L9LD, 1L9LE, 1L9LF, 1L9LG, 1L9LH, 1L9LI, 1L9LJ, 1L9LK, 1L9LL, 1L9LM, 1L9LN, 1L9LO, 1L9LP, 1L9LQ, 1L9LR, 1L9LS, 1L9LT, 1L9LU, 1L9LV, 1L9LW, 1L9LX, 1L9LY, 1L9LZ, 1L9MA, 1L9MB, 1L9MC, 1L9MD, 1L9ME, 1L9MF, 1L9MG, 1L9MH, 1L9MI, 1L9MJ, 1L9MK, 1L9ML, 1L9MN, 1L9MO, 1L9MP, 1L9MQ, 1L9MR, 1L9MS, 1L9MT, 1L9MU, 1L9MV, 1L9MW, 1L9MX, 1L9MY, 1L9MZ, 1L9NA, 1L9NB, 1L9NC, 1L9ND, 1L9NE, 1L9NF, 1L9NG, 1L9NH, 1L9NI, 1L9NJ, 1L9NK, 1L9NL, 1L9NM, 1L9NO, 1L9NP, 1L9NQ, 1L9NR, 1L9NS, 1L9NT, 1L9NU, 1L9NV, 1L9NW, 1L9NX, 1L9NY, 1L9NZ, 1L9OA, 1L9OB, 1L9OC, 1L9OD, 1L9OE, 1L9OF, 1L9OG, 1L9OH, 1L9OI, 1L9OJ, 1L9OK, 1L9OL, 1L9OM, 1L9ON, 1L9OO, 1L9OP, 1L9OQ, 1L9OR, 1L9OS, 1L9OT, 1L9OU, 1L9OV, 1L9OW, 1L9OX, 1L9OY, 1L9OZ, 1L9PA, 1L9PB, 1L9PC, 1L9PD, 1L9PE, 1L9PF, 1L9PG, 1L9PH, 1L9PI, 1L9PJ, 1L9PK, 1L9PL, 1L9PM, 1L9PN, 1L9PO, 1L9PP, 1L9PQ, 1L9PR, 1L9PS, 1L9PT, 1L9PU, 1L9PV, 1L9PW, 1L9PX, 1L9PY, 1L9PZ, 1L9QA, 1L9QB, 1L9QC, 1L9QD, 1L9QE, 1L9QF, 1L9QG, 1L9QH, 1L9QI, 1L9QJ, 1L9QK, 1L9QL, 1L9QM, 1L9QN, 1L9QO, 1L9QP, 1L9QQ, 1L9QR, 1L9QS, 1L9QT, 1L9QU, 1L9QV, 1L9QW, 1L9QX, 1L9QY, 1L9QZ, 1L9RA, 1L9RB, 1L9RC, 1L9RD, 1L9RE, 1L9RF, 1L9RG, 1L9RH, 1L9RI, 1L9RJ, 1L9RK, 1L9RL, 1L9RM, 1L9RN, 1L9RO, 1L9RP, 1L9RQ, 1L9RR, 1L9RS, 1L9RT, 1L9RU, 1L9RV, 1L9RW, 1L9RX, 1L9RY, 1L9RZ, 1L9SA, 1L9SB, 1L9SC, 1L9SD, 1L9SE, 1L9SF, 1L9SG, 1L9SH, 1L9SI, 1L9SJ, 1L9SK, 1L9SL, 1L9SM, 1L9SN, 1L9SO, 1L9SP, 1L9SQ, 1L9SR, 1L9SS, 1L9ST, 1L9SU, 1L9SV, 1L9SW, 1L9SX, 1L9SY, 1L9SZ, 1L9TA, 1L9TB, 1L9TC, 1L9TD, 1L9TE, 1L9TF, 1L9TG, 1L9TH, 1L9TI, 1L9TJ, 1L9TK, 1L9TL, 1L9TM, 1L9TN, 1L9TO, 1L9TP, 1L9TQ, 1L9TR, 1L9TS, 1L9TT, 1L9TU, 1L9TV, 1L9TW, 1L9TX, 1L9TY, 1L9TZ, 1L9UA, 1L9UB, 1L9UC, 1L9UD, 1L9UE, 1L9UF, 1L9UG, 1L9UH, 1L9UI, 1L9UJ, 1L9UK, 1L9UL, 1L9UM, 1L9UN, 1L9UO, 1L9UP, 1L9UQ, 1L9UR, 1L9US, 1L9UT, 1L9UU, 1L9UV, 1L9UW, 1L9UX, 1L9UY, 1L9UZ, 1L9VA, 1L9VB, 1L9VC, 1L9VD, 1L9VE, 1L9VF, 1L9VG, 1L9VH, 1L9VI, 1L9VJ, 1L9VK, 1L9VL, 1L9VM, 1L9VN, 1L9VO, 1L9VP, 1L9VQ, 1L9VR, 1L9VS, 1L9VT, 1L9VU, 1L9VV, 1L9VW, 1L9VX, 1L9VY, 1L9VZ, 1L9WA, 1L9WB, 1L9WC, 1L9WD, 1L9WE, 1L9WF, 1L9WG, 1L9WH, 1L9WI, 1L9WJ, 1L9WK, 1L9WL, 1L9WM, 1L9WN, 1L9WO, 1L9WP, 1L9WQ, 1L9WR, 1L9WS, 1L9WT, 1L9WU, 1L9WV, 1L9WW, 1L9WX, 1L9WY, 1L9WZ, 1L9XA, 1L9XB, 1L9XC, 1L9XD, 1L9XE, 1L9XF, 1L9XG, 1L9XH, 1L9XI, 1L9XJ, 1L9XK, 1L9XL, 1L9XM, 1L9XN, 1L9XO, 1L9XP, 1L9XQ, 1L9XR, 1L9XS, 1L9XT, 1L9XU, 1L9XV, 1L9XW, 1L9XX, 1L9XY, 1L9XZ, 1L9YA, 1L9YB, 1L9YC, 1L9YD, 1L9YE, 1L9YF, 1L9YG, 1L9YH, 1L9YI, 1L9YJ, 1L9YK, 1L9YL, 1L9YM, 1L9YN, 1L9YO, 1L9YP, 1L9YQ, 1L9YR, 1L9YS, 1L9YT, 1L9YU, 1L9YV, 1L9YW, 1L9YX, 1L9YY, 1L9YZ, 1L9ZA, 1L9ZB, 1L9ZC, 1L9ZD, 1L9ZE, 1L9ZF, 1L9ZG, 1L9ZH, 1L9ZI, 1L9ZJ, 1L9ZK, 1L9ZL, 1L9ZM, 1L9ZN, 1L9ZO, 1L9ZP, 1L9ZQ, 1L9ZR, 1L9ZS, 1L9ZT, 1L9ZU, 1L9ZV, 1L9ZW, 1L9ZX, 1L9ZY, 1L9ZZ, 200L, 201L, 205L, 206L, 209L, 210L, 211L, 212L, 213L, 214L, 215L, 216L, 217L, 219L, 220L, 221L, 222L, 223L, 224L, 225L, 226L, 227L, 228L, 229L, 230L, 231L, 232L, 233L, 234L, 235L, 236L, 237L, 238L, 239L, 240L, 241L, 242L, 243L, 244L, 245L, 246L, 247L, 248L, 249L, 250L, 251L, 252L, 253L, 254L, 255L, 256L, 257L, 258L, 259L, 260L, 261L, 262L, 2A4T, 2B6T, 2B6W, 2B6X, 2B6Y, 2B6Z, 2B70, 2B72, 2B73, 2B74, 2B75, 2B7X, 2CUU, 2F2Q, 2F32, 2F47, 2HUL, 2IGC, 2L78, 2LC9, 2LCB, 2LZM, 2NTG, 2NTH, 2O4W, 2O79, 2O7A, 2OE4, 2OE7, 2OE9, 2OEA, 2OTY, 2OTZ, 2OU0, 2OU8, 2OU9, 2Q9D, 2Q9E, 2RAY, 2RAZ, 2RB0, 2RB1, 2RB2, 2RBN, 2RBO, 2RBP, 2RBQ, 2RBR, 2RBS, 3C7W, 3C7Y, 3C7Z, 3C80, 3C81, 3C82, 3C83, 3C8Q, 3C8R, 3C8S, 3CDO, 3CDQ, 3CDR, 3CDT, 3CDV, 3DKE, 3DMV, 3DMX, 3DMZ, 3DN0, 3DN1, 3DN2, 3DN3, 3DN4, 3DN6, 3DN8, 3DNA, 3F8V, 3F9L, 3FA0, 3FAD, 3FI5, 3G3V, 3G3W, 3G3X, 3GUI, 3GUJ, 3GUK, 3GUL, 3GUM, 3GUN, 3GUO, 3GUP, 3HH3, 3HH4, 3HH5, 3HH6, 3HT6, 3HT7, 3HT8, 3HT9, 3HTB, 3HTD, 3HTF, 3HTG, 3HU8, 3HU9, 3HUA, 3HUK, 3HUQ, 3HWL, 3K2R, 3L2X, 3L64, 3LZM, 3NY8, 3NY9, 3NYA, 3RUN, 3SB6, 3SB7, 3SB8, 4DAJ, 4DKL, 4E97, 4EJ4, 4EKP, 4EKQ, 4EKR, 4EKS, 4GRV, 4I7J, 4I7K, 4I7L, 4I7M, 4I7N, 4I7O, 4I7P, 4I7Q, 4I7R, 4I7S, 4I7T, 4LDE, 4LDL, 4LDO, 4LZM, 4PHU, 4TN3, 5LZM, 6LZM, 7LZM

### Supplementary Table 5

**Supplementary Table 5. List of evaluated fit models.** The fit models are differentiated by their number of states and free parameters. The average  $\chi^2_r$  and the table with the listed results is given.

N-states	parameter		Constraints	free parameters		Table	Average $\chi^2_r$
	local	global		per sample	total		
2	$\langle R_{DA}^{(1)} \rangle, x_{DA}^{(1)}$ $\langle R_{DA}^{(2)} \rangle, x_{DA}^{(2)}$		$x_{DA}^{(1)} +$ $x_{DA}^{(2)} = 1$	<b>3</b>	<b>101</b> $= (33 \cdot 3 + 3 - 1)$	S2b	1.0825
2	$\langle R_{DA}^{(1)} \rangle,$ $\langle R_{DA}^{(2)} \rangle$	$x_{DA}^{(1)},$ $x_{DA}^{(2)}$	$x_{DA}^{(1)} + x_{DA}^{(2)} = 1$	<b>2</b>	<b>67</b> $= (33 \cdot 2 + 2 - 1)$	S2c	1.0985
3	$\langle R_{DA}^{(1)} \rangle,$ $\langle R_{DA}^{(2)} \rangle,$ $\langle R_{DA}^{(3)} \rangle$	$x_{DA}^{(1)},$ $x_{DA}^{(2)},$ $x_{DA}^{(3)}$	$x_{DA}^{(1)} + x_{DA}^{(2)} +$ $x_{DA}^{(3)} = 1$	<b>3</b>	<b>101</b> $= (33 \cdot 3 + 3 - 1)$	S2d- S2f	1.0736

## Supplementary Table 6

**Supplementary Table 6. List of primers used within this work.** T4Lfor and T4Lrev were used for subcloning into the pet11a vector. Note that T4Lfor lies within the backbone of pet11a to have sufficient distance to the first mutation site (amino acid residue 5).

Primer*	Sequence (5'→3')
T4Lfor	GGAATGGTGCATGCAAGGAGATGG
T4Lend**	GCCGGATCCTTATAGATTTTATACGC
E5Amber for	ATGAATATATTTTAGATGTTACGTATAGAT
E5Amber rev	ATCTATACGTAAC <u>T</u> ACTAAAATATATTCAT
R8Amber for	AATATATTTGAAATGTTATAGATAGATGAACGTCTTAGA
R8Amber rev	TCTAAGACGTTTCTATCTATAACATTTCAAATATATT
E11A for	GAAATGTTACGTATAGATGCTGGTCTTAGACTTAAAATC
E11A rev	GATTTTAAGTCTAAGACCAGCATCTATACGTAACATTTT
T26E for	GACACAGAAGGCTATTACGAGATTGGCATCGGTCATTTG
T26E rev	CAAATGACCGATGCCAATCTCGTAATAGCCTTCTGTGTC
K19Amber for	CTTAGACTTAAAATCTATTAGGACACAGAAGGCTATTAC
K19Amber rev	GTAATAGCCTTCTGTGTCCTAATAGATTTTAAGTCTAAG
E22Amber for	AAAATCTATAAAGACACATAGGGCTATTACACTATTGGC
E22Amber rev	GCCAATAGTGTAAATAGCCCTAGTGTCTTTATAGATTTT
S36Amber for	GGTCATTTGCTTACAAAAATAGCCATCACTTAATGCTCT
S36Amber rev	AGCAGCATTAAAGTGATGGCTATTTTGTAAGCAAATGACC
S44Amber for	TCACTTAATGCTGCTAAATAGGAATTAGATAAAAGCTATT
S44Amber rev	AATAGCTTTATCTAATTCCTATTTAGCAGCATTAAAGTGA
S44C for	TCACTTAATGCTGCTAAATGTGAATTAGATAAAAGCTATT
S44C rev	AATAGCTTTATCTAATTCACATTTAGCAGCATTAAAGTGA
N55Amber for	GCTATTGGGCGTAATACTTAGGGTGAATTACAAAAGAT
N55Amber rev	ATCTTTTGTAATTACACCCTAAGTATTACGCCCAATAGC
K60Amber for	ACTAATGGTGTAAATTACATAGGATGAGGCTGAAAAACTC
K60Amber rev	GAGTTTTTCAGCCTCATCCTATGTAATTACACCATTAGT
Q69Amber for	GCTGAAAAACTCTTTAATTAGGATGTTGATGCTGCTGTT
Q69Amber rev	AACAGCAGCATCAACATCCTAATTAAAGAGTTTTTCAGC
Q69C for	GCTGAAAAACTCTTTAATTGTGATGTTGATGCTGCTGTT
Q69C rev	AACAGCAGCATCAACATCACAAATTAAGAGTTTTTCAGC
D70Amber for	GAAAAACTCTTTAATCAGTAGGTTGATGCTGCTGTTTCGC
D70Amber rev	GCGAACAGCAGCATCAACCTACTGATTAAAGAGTTTTTC
P86C for	AGAAATGCTAAATAAAAATGTTGTTTATGATTCTCTTGAT
P86C rev	ATCAAGAGAATCATAAACACATTTTAATTTAGCATTCT
R119C for	GGATTTACTAACTCTTTATGTATGCTTCAACAAAAACGC
R119C rev	GCGTTTTTGTGAAGCATACATAAAGAGTTAGTAAATCC
D127C for	CTTCAACAAAAACGCTGGTGTGAAGCAGCAGTTAACTTA
D127C rev	TAAGTTAACTGCTGCTTACACCAGCGTTTTTGTGAAG
N132C for	TGGGATGAAGCAGCAGTTTGTTTAGCTAAAAGTAGATGG
N132C rev	CCATCTACTTTTAGCTAAACAACCTGCTGCTTCATCCCA
R137E for	CAATTGAATCGATTTTCACTTACCATATTAGTTTGTGGA
R137E rev	GTAACTTAGCTAAAAGTGAATGGTATAATCAAACACCT
I150C for	AATCGCGAAAAACGAGTCTGTACAACGTTTAGAAGTGGC
I150C rev	GCCAGTTCTAAACGTTGTACAGACTCGTTTTGCGCGATT

\*The underlined nucleotides mark the mutation side.

\*\*The italic nucleotides mark the restriction enzyme recognition site

## Supplementary Notes

### Supplementary Note 1

#### Single-molecule and fluorescence correlation spectroscopy

##### 1-1. Example data analysis of MFD experiments

The smFRET data analysis is done in accordance to previously published methods e.g. Kalinin *et al.*, Sisamakias *et al.* or Kudryavtsev *et al.*<sup>4 5</sup>.

Briefly, the photons emitted from single molecules traversing through the confocal detection volume are selected from background photons using the inter-photon time and a threshold for the maximum inter photon time<sup>6</sup>. Additionally, only burst containing a minimum number of 60 photons were selected for further analysis.

After burst selection, our MFD histograms are checked for e. g. signal stability (Supplementary Figure 3a-c), photobleaching (Supplementary Figure 3d), contamination with free dye (Supplementary Figure 2e), multimolecule events (Supplementary Figure 3d, f) or aggregates (Supplementary Figure 3f). Without coating the measurement chamber either with the tensile Tween20 (Supplementary Figure 3b) or unlabeled protein (Supplementary Figure 3c), the signal of our FRET-labeled molecules is lost within the 10 min needed to start the experiment (Supplementary Figure 3a). Photobleaching of the acceptor will appear as tilting in the 1D projection of  $|Tg-Tr|$  (Supplementary Figure 3d); the photon trace of the acceptor will be shorter than for the donor and thus, shift the – in ideal case sharp and randomly around 0 distributed – plot. Fluorophores coupled to a biomolecule have high anisotropy a follow the Perrin equation (Supplementary Figure 3e), free dye has a very low anisotropy  $\sim 0$ . Thus, it be visible below the biomolecule population. The presence of multimolecule events or aggregates can (i) be detected during burst selection, (ii) large  $|Tg-Tr|$  and/or (iii) by a large number of photons within the burst and a long burst duration, respectively (Supplementary Figure 3f).

##### 1-2. Additional SMD and fFCS

To test for possible influences of the dyes on the protein, two distinct labeling configurations (DA) and (AD) were prepared as previously described. In the sub- $\mu$ s to ms range the dynamics of T4L is independent of the labeling-configuration. However, we can see some small differences in the two samples. For example, the species fractions in eTCSPC for S44pAcF/I150C-(DA) and -(AD) are not identical; although, one can clearly identify the same conformers corresponding to the states  $C_1$ ,  $C_2$ , and  $C_3$ .

Slight differences were observed when comparing experiments for -(DA) and -(AD) at the single-molecule level. When comparing the mutant S44pAcF/I150C-(DA), shown in Figure S8a, to the -(AD) labeling scheme shown in Figure S2, we observe the following: i) There is more "donor-only" fraction in the -(AD) labeling scheme than in the -(DA), this is part of the variability in labeling. ii) There is no accumulation of a high FRET state in the -(AD) scheme.

However, in this situation the elongation toward higher FRET or state  $C_3$  is slightly more pronounced. This elongation is also present in the T26E/S44pAcF/I150C-(AD) mutant (Supplementary Figure 10b). This resembles the accumulation found in the sample T26E/S44pAcF/I150C-(DA) (Figure 6g, main text). Regardless of these differences, the 2D

histograms and eTCSPC show similar states. This is clear evidence that the three conformational states are present independent of the fluorophores.

In summary, the kinetic scheme might change slightly, but not significantly given the conserved effect on the *sCCF* curves (Figure 3b, main text). The *sCCF* shows unequivocally that the transition times are present in both labeling schemes. Therefore, the specific dye-protein interactions are not responsible for the transition times between sub- $\mu$ s and ms.

The major difference between the  $-(DA)$  and  $-(AD)$  is the state  $C_{3r}$ . This state seems to accumulate for the  $-(DA)$  configuration. However, at low pH the  $-(AD)$  shows a similar elongation towards the  $C_3$  state similar as T26E/S44pAcF/I150C- $-(AD)$ , also consistent with the data presented for the S44pAcF/I150C- $-(DA)$  at low pH.

Additional MFD histograms for further functional mutants are shown in Supplementary Figure 7. A summary of the ensemble or sub-ensemble fits for these mutants is shown in Supplementary Table 2h. Supplementary Figure 2 shows MFD histograms for all 33 variants used within the T4L network.

### Supplementary Note 2

#### Species Cross Correlation function of $-(DA)$ and $-(AD)$ labeled samples

Theoretically, the species cross-correlation function (*sCCF*), as defined in Supplementary Equation (25), can be extended to more than two species in solution. Practically, this suffers of technical limitations. The more species one has in solution, the more photons are required to differentiate between them. Therefore, we selected two pseudo-species that represent mixtures of the states found in solution. In addition, we added a third pseudo species that takes into consideration the contribution of scatter photons<sup>7</sup>. In this approach, the meaning of specific amplitudes and their relationships is lost; however, *sCCF* can extract the relaxation times as kinetic signatures of conformational transitions between all possible states.

For all data presented, we generated two pseudo-species, plus the addition of the scatter-filter. Decays were generated accordingly to Supplementary Equations (30)-(31), based on sub-ensemble burst analysis and eTCSPC data. In some cases, lifetimes of the pseudo-species were adjusted by 100's of ps to properly cross the y-axis of the correlation at a predetermined time for visual comparison. This procedure does not affect the recovered relaxation times.

Considering the case of the double labeled mutants S44pAcF/I150C- $-(DA)$  and  $-(AD)$ , the patterns  $p_j^{(i)}$  that correspond to the normalized probability distributions for the  $-(DA)$  and  $-(AD)$  samples are shown on Supplementary Figure 9a, c. The parameters used on the decay generation are shown in the caption. From these patterns, the filters  $f_j^{(i)}$  (Supplementary Equation (26)) were calculated. These are shown in panels B and D of Supplementary Figure 9. These filters are then used to compute the *sCCF* by multiplying each photon and weighting its contribution to each state as in Supplementary Equation (25). The patterns that are shown in Supplementary Figure 9 correspond to only half of the detectors. The other half shows similar patterns. The need of another set of detectors with similar patterns and decays is to increase the amount of pair correlations and to exclude detector after-pulsing related artifacts from calculations. Finally, a full correlation containing all relaxation times and the characteristic diffusion time can be extracted. The reproducibility of the methodology is observed by the overlap of the two species cross-correlations (Figure 3b, main text), even with the fact that different parameters were used on the generation of the filters. Similar



overlap is shown for the mutant S44pAcF/I150C-(DA) and -(AD) at pH 3.0 (Supplementary Figure 9e). For the functional mutants (E11A, T26E, R137E), we show the  $sCCF$  (Supplementary Figure 9f-h).

### Supplementary Note 3

#### Analyzing the kinetic network of conformational states in T4L

##### 3-1. Detection of distinct $C_3$ species

The eTCSPC fluorescence decay of S44pAcF/I150C-(DA) was fit with a model containing three different conformational states ( $C_1$ ,  $C_2$  and  $C_3$ ). The total population of  $C_3$  corresponds to 20 % (Supplementary Table 2h). From the single molecule MFD histograms it was clear to observe burst accumulation at the location where  $C_3$  lies. To quantify the amount of bursts corresponding to this, we computed the area under the curve for the region of  $10^{-2} < F_D/F_A < 0.3$  (Supplementary Figure 4e) corresponding to 564 burst of the total 10139 burst of all single molecule events (subtracting 893 bursts from molecules missing an active acceptor). Thus, the burst accumulation of this state is 5.3% of the total number of bursts. We called this population  $C_{3t}$  because it is a static accumulation of the population  $C_3$  observed by eTCSPC. In order to account for the missing 15 % of  $C_3$ , there has to be an additional population, which exchanges with  $C_1$  and  $C_2$  at timescales faster than the burst duration. We called this population  $C_{3d}$ . Therefore; the total contribution of equals to the sum of the static plus the dynamic subpopulations of  $C_3$  ( $C_3 = 20 \% = C_{3t} + C_{3d} = 5 \% + 15 \%$ ). Because in fFCS we only observe two relaxation times from  $\mu\text{s}$  to  $\text{ms}$ , we ignore for the time being the existence of the 5 % of  $C_{3t}$ , as it is not needed to discuss the connectivity between  $C_1$ ,  $C_2$  and  $C_3$  at faster timescales.

##### 3-2. Consolidated model of T4L

To construct the best kinetic model that describes the free enzyme in solution let us consider the experimental facts: *i*) eTCSPC resolves three different FRET states. *ii*) fFCS shows two transition times faster than 10 ms. *iii*) smFRET diagrams are better described by a unimodal distribution mixed with a small population ( $\sim 5\%$ ) with very high FRET only for the S44pAcF/I150C-(DA) variant.

Unimodal distributions in single-molecule experiments can occur due to time-averaging. Ignoring the donor only population, the free enzyme (S44pAcF/I150C-(DA)) samples four conformational states ( $C_1$ ,  $C_2$ ,  $C_{3d}$  and  $C_{3t}$ ), where the  $C_{3t}$  is a static population at very high FRET, and  $C_1$ ,  $C_2$ ,  $C_{3d}$  mix at the observed times of  $\sim 4 \mu\text{s}$  and  $\sim 230 \mu\text{s}$ .

Putting aside the state  $C_{3t}$ , the simplest model of conformational transitions that one can build from experimental observables is



where  $C_1$  corresponds to the most open conformer,  $C_2$  is similar to the substrate-enzyme complex and  $C_3$  has an interdy distance much shorter than  $C_2$ . With this in mind we disregarded the cyclic model



due to the sequential closing of the enzyme from the most open to the most closed state, due to the unseen number of slow transitions along the  $C_3$  to  $C_1$ , and physical restraints observed in the structural models (PDB ID 172L and 148L). This limits the return process of  $[C_1] \rightleftharpoons [C_3]$ , because there is no evidence of other intermediate states. The only remaining possibility is the unlikely scenario that after reaching the compact state, the enzyme unfolds and refolds very fast, so that we do not capture the process. Thus, given this unlikely set of events, we maintain the assumption of the successive closing of the enzyme.

Our goal is to extract the reaction rates ( $k_{12}$ ,  $k_{21}$ ,  $k_{23}$ ,  $k_{32}$ ) from our experimental observables. To solve this, first we need to write the rate matrix  $K$  for the system described in Supplementary Equation (3).

$$K = \begin{pmatrix} -k_{12} & k_{21} & 0 \\ k_{12} & -(k_{21} + k_{23}) & k_{32} \\ 0 & k_{23} & -k_{32} \end{pmatrix}. \quad (3)$$

The two eigenvalues of  $K$  correspond to the two observables measured by fFCS.

$$\frac{1}{t_{R1,2}} = \frac{1}{2} \cdot (k_{12} + k_{21} + k_{23} + k_{32}) \pm \sqrt{(k_{12} + k_{21} + k_{23} + k_{32})^2 - 4 \cdot (k_{12}k_{23} + k_{12}k_{32} + k_{21}k_{32})}. \quad (4)$$

The time evolution of the system on Supplementary Equation (3) is defined by

$$\frac{d}{dt}[C_i](t) = K_{ij}[C_j](t), \quad (5)$$

which has an analytical solution on the form of

$$[C_i](t) = C_0 \exp(K_{ij}t), \quad (6)$$

where  $C_0$  is the  $i$ -th eigenvector. At equilibrium, or  $t \rightarrow \infty$ , the equilibrium fractions for each conformer can be obtained analytically and are given by

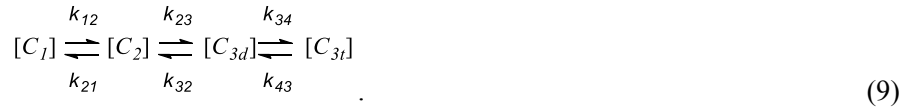
$$[C_i] = \begin{pmatrix} \frac{k_{21} \cdot k_{32}}{k_{21} \cdot k_{32} + k_{12} \cdot (k_{23} + k_{32})} \\ \frac{k_{12} \cdot k_{32}}{k_{21} \cdot k_{32} + k_{12} \cdot (k_{23} + k_{32})} \\ \frac{k_{12} \cdot k_{23}}{k_{21} \cdot k_{32} + k_{12} \cdot (k_{23} + k_{32})} \end{pmatrix}. \quad (7)$$

Note that  $[C_3] = 1 - ([C_1] + [C_2])$ . These fractions are obtained by fluorescence decay analysis as done in Supplementary Methods. The reaction rates ( $k_{12}$ ,  $k_{21}$ ,  $k_{23}$ ,  $k_{32}$ ) can be expressed in terms of the equilibrium fractions ( $x_1 = [C_1]$ ,  $x_2 = [C_2]$ ,  $x_3 = [C_3]$ ) and the relaxation times ( $t_{R1}$  and  $t_{R2}$ ).

The analytical solution of this system has two solutions:

$$\begin{aligned}
k_{12}^{(\pm)} &= \frac{[C_2] \cdot \left( \frac{1}{t_{R1}} + \frac{1}{t_{R2}} \right) \pm \left( [C_2] \cdot \left( \frac{4 \cdot ([C_1] - 1) \cdot ([C_1] + [C_2])}{t_{R1} \cdot t_{R2}} + [C_2] \cdot \left( \frac{1}{t_{R1}} + \frac{1}{t_{R2}} \right)^2 \right) \right)^{\frac{1}{2}}}{2 \cdot ([C_1] + [C_2])}, \\
k_{21}^{(\pm)} &= \frac{[C_1] \cdot \left( [C_2] \cdot \left( \frac{1}{t_{R1}} + \frac{1}{t_{R2}} \right) \pm \left( [C_2] \cdot \left( \frac{4 \cdot ([C_1] - 1) \cdot ([C_1] + [C_2])}{t_{R1} \cdot t_{R2}} + [C_2] \cdot \left( \frac{1}{t_{R1}} + \frac{1}{t_{R2}} \right)^2 \right) \right)^{\frac{1}{2}} \right)}{2 \cdot [C_2] \cdot ([C_1] + [C_2])}, \\
k_{23}^{(\pm)} &= \frac{([C_1] + [C_2] - 1) \cdot \left( [C_2] \cdot \left( \frac{1}{t_{R1}} + \frac{1}{t_{R2}} \right) \mp \left( [C_2] \cdot \left( \frac{4 \cdot ([C_1] - 1) \cdot ([C_1] + [C_2])}{t_{R1} \cdot t_{R2}} + [C_2] \cdot \left( \frac{1}{t_{R1}} + \frac{1}{t_{R2}} \right)^2 \right) \right)^{1/2} \right)}{2 \cdot [C_2] \cdot ([C_1] - 1)}, \\
k_{32}^{(\pm)} &= \frac{-[C_2] \cdot \left( \frac{1}{t_{R1}} + \frac{1}{t_{R2}} \right) \pm \left( [C_2] \cdot \left( \frac{4 \cdot ([C_1] - 1) \cdot ([C_1] + [C_2])}{t_{R1} \cdot t_{R2}} + [C_2] \cdot \left( \frac{1}{t_{R1}} + \frac{1}{t_{R2}} \right)^2 \right) \right)^{1/2}}{2 \cdot ([C_1] - 1)}. \quad (8)
\end{aligned}$$

To complete the model we need to add the static fraction of  $\sim 5\%$ . We assigned this static fraction to conformer  $C_{3s}$ , which is identical in FRET to the state  $C_{3d}$ . We split the fraction of  $C_3$  into these two populations. The final reaction model can be expressed as



Where  $k_{34} = 0.003 \text{ ms}^{-1}$  and  $k_{43} = 0.008 \text{ ms}^{-1}$  were empirically determined but satisfy the condition that they have to be smaller than  $0.01 \text{ ms}^{-1}$ .

We justify the existence of the  $C_{3t}$  population because this state accumulated in MFD histograms over the observation time ( $\sim$ ms), and the population of this state lies over the static FRET line. We note that  $C_{3t}$  does not increase over the period of the experiment. Hence, this state must be in slow equilibrium ( $>10 \text{ ms}$ ) with the rest of the network as reflected by ffCS.

With all the determined rates, we did Brownian dynamics simulations as described in main text. The single-molecule MFD histograms for the simulated data shown in Supplementary Figure 4 and corresponds to the experimental data shown in Figure 3.

Note that if the full cycle were used, this analytical formalism would not have been possible, because there are more parameters unknown than experimental observables.

### 3-3. Simulation of the FRET data in complex kinetic schemes

To describe the experimental 2D histogram a four-state scheme was used. First, we calculated FRET histograms<sup>8</sup> where a kinetic model with discrete conformations was assumed. The transition between the states is described by rate equations. The probability for the system to be in state  $i$  at time  $t$ ,  $\mathbf{p}_i(t)$ , satisfies a set of rate equations, which can be written in matrix notation as:

$$\frac{d\mathbf{p}}{dt} = \mathbf{K} \cdot \mathbf{p} \quad (10)$$

where  $\mathbf{p}$  is a column vector with the components  $\mathbf{p}_i(t)$  and  $\mathbf{K}$  is a transition rate matrix representing the rate constants for the transitions between states  $i$  and  $j$ . At long times,  $\mathbf{p}(t)$

approaches its equilibrium value,  $\mathbf{p}_{eq}$ . The vector of the equilibrium populations  $\mathbf{p}_{eq}$  is normalized to 1 and satisfies  $\mathbf{K} \cdot \mathbf{p}_{eq} = 0$ . For each burst, the mean averaged efficiency  $\langle E \rangle$  and the average fluorescence weighted lifetime  $\langle \tau_{D(A)} \rangle_f$  can be calculated by:

$$\langle E \rangle = \frac{\sum t_i \cdot E_i}{t_{burst}} \quad (11) \quad \text{and} \quad \langle \tau_{D(A)} \rangle_f = \frac{\sum t_i(\mathbf{K}) \cdot \tau_i^2}{\sum t_i(\mathbf{K}) \cdot \tau_i} \quad (12)$$

where  $t_i(\mathbf{K})$  is time spent by a molecule in state  $i$  within the duration of the burst and depends on the transition rate matrix  $\mathbf{K}$ ;  $E_i$  is the FRET efficiency of the  $i$ -th state;  $t_{burst}$  is the duration of the burst and  $\tau_i$  is the fluorescence lifetime of the  $i$ -th state. Practically, each burst has certain duration and number of photons, which were chosen arbitrary from experimentally measured  $t_{burst}$  (duration time) vs.  $N$  (number of photons) 2D histogram. The residence times by each molecule in different states were calculated using Gillespie algorithm for continuous-time Markov Chain. Then, the average fluorescence lifetime  $\langle \tau_{D(A)} \rangle_f$  for each burst was calculated by Monte-Carlo simulation of fluorescence emission given FRET efficiencies of each state. Stationary (equilibrium) populations of states were obtained by solving interstate transition dynamics matrix and the residence times obtained on previous step. The descriptions for the vector  $\mathbf{p}$  and the rate matrix  $\mathbf{K}$  (resulting into the equilibrium fractions for the state  $i$ ,  $\mathbf{p}_{eq,i}$ ) and the experimental observables,  $E$  and  $\tau$ , used in the simulations are shown in the Table S4a. For plotting,  $E$  was converted to  $F_D/F_A$  ratio. The simulation procedure was repeated for a high number of bursts to generate  $F_D/F_A$  vs  $\langle \tau_{D(A)} \rangle_f$  2D histogram (Supplementary Figure 4b-c). The resulting 1D and 2D histograms were compared to the experimental data, yielding a  $\chi^2$  parameter for each simulation and histogram. To test the significance of the difference in  $\chi^2$ , we performed F-test as described above. The resulting values are combined in the Table S4b.

To estimate our errors on determining the rates we considered the  $2\sigma$  confidence interval in determining the population fractions (Supplementary Table 2h) and the  $2\sigma$  confidence interval in determining the relaxation times by fFCS (Table S4c). Taking those extremes we estimated the error and computed the reaction rate constants for Figure 7 in the main text according to Supplementary Equation (8).

#### Supplementary Note 4

##### Fluorescence decay analysis of single and double labeled T4 lysozyme

Selected mutants were labeled in two configurations (DA) and (AD), D for donor (Alexa488) and A for acceptor fluorophore (Alexa647). The order of the letters represents the position of the fluorophore. The first letter represents the label of the keto handle in the N-terminal subdomain and the second position corresponds to the thiol reaction for labeling in the C-terminus, except for the double cysteine mutant.

Each sample was measured in eTCSPC as described in the materials and methods section and analyzed with three different models. As the fluorophores are connected to T4L by long and flexible linkers (Supplementary Methods) the assumption of a static, fixed interdye distance does not reflect the actual sample property. In fact, the flexible linkers assure a free rotational motion of the fluorophore, which allows to assume  $\langle \kappa^2 \rangle = 2/3$  (verified by corresponding anisotropy measurements of each dye, see Supplementary Table 5a-d). Yet, this conformational flexibility leads to a distribution of interdye distances on the timescale of

FRET. A proper model for describing our sample properties has to consider this distribution. Here, we modeled this interdyer distance distribution  $\langle R_{DA} \rangle$  with a Normal distribution (Supplementary Equations (36)) (Supplementary Table 2b-f). The best consistent model based on our experimental data and statistical analysis is that three continuous distance distributions are needed to describe all T4L variants.

To reach to the conclusion that three continuous distance distributions are needed to describe all T4L variants, first we needed to characterize the donor and acceptor fluorescence quantum yield  $\Phi_{FD(0)}$  and  $\Phi_{FA}$ , respectively. A summary table of these is shown in Supplementary Table 2a. Table S2b summarizes the result of the two continuous distance distribution model with free amplitudes. The best fit with three continuous distance distribution is summarized in Supplementary Table 2d-g; decays are shown in Supplementary Figure 5a. The fit results for the functional variants are summarized in Supplementary Table 2h.

Using only the two-state model and comparing the modeled distances using PDBID 172L and 148L for the two states showed that our data cannot be correlated with the structural information from the two crystallographic structures (Supplementary Figure 5b, c).

## Supplementary Note 5

### Characterization of functional T4L variants

#### 5-1. Catalytic activity of S44pAcF I150C T26E

The ability to process the selected substrate (peptidoglycan from *Micrococcus luteus*) of the mutants was monitored by reverse phase chromatography. Prior to use, the purchased peptidoglycan (Sigma-Aldrich, Switzerland) was purified as described by Maeda in 1980<sup>9</sup> to remove minor fluorescent impurities. Double-labeled mutants (1  $\mu$ M) were incubated with 3 mg/mL of substrate and allowed to react for several hours in 50 mM sodium phosphate buffer, 150 mM NaCl at pH 7.5. Samples at different times were monitored under a reverse phase HPLC at 495 nm. In this way we can identify the labeled lysozyme. Typical examples for the processing of substrate are shown in Supplementary Figure 8. Supplementary Figure 8a shows the elution profile of the peptidoglycan monitored at 215 nm. Multiple peaks from 10 to 14 min appear. In the same panel the elution of the T26E/S44pAcF/I150C-(AD) monitored at 215 nm is shown as incubated with the peptidoglycan. For better contrast of the shift in populations the absorbance was measured at the maximum for the AlexaFluor488 (495 nm). This is shown in Supplementary Figure 8b. After 260 minutes this mutant is fully saturated with the substrate.

#### 5-2. Single-molecule experiments in the presence of substrate

For the variant E11A/S44C/I150C we carried out two-color excitation experiments, in which we alternately excited the donor and the acceptor fluorophore (PIE)<sup>5</sup>. Thus, we could sort out the molecules carrying only one type of fluorophore, a disadvantage of the unspecific labeling. However, this allowed us also directly identifying the bursts stemming from the peptidoglycan. Supplementary Figure 7a-b show the green to red fluorescence signal vs. the stoichiometry  $S$  of E11A/S44C/I150C in the absence and presence of substrate. D-Only labeled molecules are located at  $S = 0$ , A-Only molecules at  $S = 1$  and DA labeled molecules are centered at  $S = 0.5$ . The peptidoglycan appears as an additional population at  $S = 0.8$ .

Supplementary Figure 7c shows that the brightness and burst duration distribution of this variant are nearly identical in the absence and presence of substrate.

For the variant T26E/S44pAcF/I150C only single-color excitation experiments were performed. The brightness and burst duration distributions of the FRET and the subset of high-FRET bursts are shown in Supplementary Figure 7e-h. To avoid the contamination with bursts from aggregates, we selectively only considered bursts shorter than 5 ms in the further analysis.

### Supplementary Note 6

#### Challenges of smFRET measurement and their solution

Most of the potential problems with smFRET come from the complexities associated with the labels. We list the solution for potential label artifacts, and how our approaches and considerations allow us to draw conclusions, artifact free, of our data.

1) Labeling influence on enzymatic work: HPLC on the T26E/S44pAcF/150C-(DA) and –(AD) mutants show that they can process the peptidoglycan to keep the substrate bound. Non-functional mutants stayed non-functional after labeling (E11A/S44C/I150C-(DA) and R137E/S44pAcF/I150C-(DA)).

2) Local quenching of Donor:

eTCSPC: In ensemble measurements, local quenching is observed by changes in the average lifetime of the donor. The multi-exponential fluorescence decays of the donor only labeled variants reflect the presence of quenched states. At these states, the fluorophore senses a different environment. Most likely these differences represent various conformations of the protein.

smFRET: Donor quenching, as in the case of eTCSPC, shifts the average donor lifetime towards shorter lifetimes. FRET lines are corrected for the multi-exponential properties of the donor decay.

fFCS: We use the multi-exponential time-resolved fluorescence decay information to generate different filters to calculate the species cross-correlation. Although, protein dynamics can be extracted from single label variants, the structural information is lost. This is only possible from the FRET labeled samples.

3) Triplet-state of Donor:

eTCSPC: Triplet state are long lived compared to the fluorescence lifetime. Therefore, on ensemble time-resolved fluorescence decays this effect is not visible.

smFRET: Triplet or dark states kinetics are short-lived compared to the burst duration.

fFCS: In a classical FCS experiment triplet or dark states appear as a “bunching” term in the correlation function. In fFCS we do not correlate fluctuations on signal, but rather we correlate fluctuations of species. In our case, they correspond to different conformations of T4L. We assume that triplet/dark states are not coupled to the conformations or the selected pseudo species. In other words, the photo-physics of the dye is independent of the conformation in which the molecule is. With this in mind, the *sCCF* will have positive and negative contributions from each species resulting in the fact that the “bunching” term is not present. We know that increasing the power can increase the triplet amplitude. To test this, we measured the *sCCF* of T4L-(DA) at different powers at objective and we did not observe any major differences in the relaxation times  $t_{R1}$  and  $t_{R2}$  (Supplementary Figure 12) or shape

of the *sCCF*. We also tested the addition of triplet quenchers Cycloocta-1,3,5,7-tetraenecarboxylic acid (COTc) but did not observe major deviations (Supplementary Figure 12a-d).

4) Acceptor cis-trans isomerization:

eTCSPC: If FRET to *cis* and *trans* is different the donor decay would reflect the *cis-trans* population. We assume that this effect is small therefore not visible.

smFRET: This effect can be observed as acceptor quenching. The reason is that the *cis* state is dark. Spending more time in the *cis* state will reduce the overall counts observed from the acceptor. This effect can be seen in the two dimensional histograms as a vertical shift of the islands position on  $F_D/F_A$  vs. lifetime  $\langle \tau_{D(A)} \rangle_f$  representation.

fFCS: For fFCS we correlate only photons emitted by the donor fluorophore. Changes in the brightness of the acceptor are not correlated. However, something that can happen is that the absorption of the energy transferred from the donor can be different for *cis* and *trans* states. This is something that was not tested. But as in the case of the donor triplet we assume that, even in the case in which this occurs, the photophysics dynamics of the acceptor dye is decoupled from the conformational dynamics of the molecule.

5) Dye mobility:

eTCSPC: Dye mobility occurs at slower timescales than the time-resolved fluorescence decay of the fluorophore. For this reason, it is better to consider FRET due to all configurations of fluorophore positions during time-resolved fluorescence decays. We take this into consideration by having a distribution of distances instead of single lifetimes to identify each conformational state. These are included in the treatment of the FRET lines. In order to do so, ensemble time resolved anisotropy decays were measured. We assumed that fluorophore mobility follows the “wobble in a cone” model<sup>10</sup>. Table S5a-c summarizes the residual anisotropies ( $r_\infty$ ) of D - donor, A - acceptor and A(D) - the sensitized by FRET emission of acceptor that were used to calculate dye order parameters and  $\kappa^2$  distributions (Table S5d) according to refs.<sup>3 10</sup> (Eq. 9 and 10 in Sindbert *et al.*). The assumption is that fluorophores move according to the “wobble in a cone” model. According to all distributions the assumption of  $\kappa^2 = 2/3$  is very well justified.

smFRET: In smFRET one can inspect the anisotropy  $r_{sc}$  vs. lifetime  $\langle \tau_{D(A)} \rangle_f$  histograms. If anisotropy is too high then one would expect that the dye can have restricted mobility.

fFCS: The mobility of the dye alone is better resolved using a complete FCS technique<sup>11</sup>.

6) FPS provides also a consistent view of the conformational states of T4L. Each distinct set of conformer specific FRET restrains are within the expected uncertainty of our tools. In addition, the kinetics found in all our variants are consistent with two global relaxation time ( $t_{R1} = \sim 4 \mu\text{s}$ ,  $t_{R2} = \sim 230 \mu\text{s}$ ) and the expected three conformational states.

7) Thermodynamic stability and proper folding of our mutants were verified by chemical denaturation using urea.

8) Fluorescence intensity decay were fit with various models and gave a consistent view of three FRET induced donor lifetimes or two FRET induced donor lifetimes where only one would be expected if the conformer  $C_3$  did not exist.

9) Limitations on hybrid FRET: Current limitations of hybrid FRET include the introduction of labels via site directed mutagenesis. Not all systems are resistant to extensive mutations

and maintain their stability. In terms of the size of molecules under study, the limitations will be determined by the level of resolution that it is desired. Larger molecules would require a larger set of FRET measurements and bigger markers, including the inclusion of fluorescent proteins would cause larger uncertainties. Although, nothing limits the ability to do measurements in complex environments (crowder or viscous solutions and even in live cells), one must assure that proper controls are satisfied. Of particular interest are measurements in living cells, where the labeled molecules have to be introduced without damaging the liability of the cells.<sup>12</sup>



### Supplementary Note 7

#### Original data available on Zenodo

The following files are available on Zenodo under DOI 10.5281/zenodo.3376527:

- eTCSPC\_wildtype.zip contains all eTCSPC FRET data including reference measurements used for derivation of DA distances.
- Single\_molecule\_wildtype.zip contains raw single-molecule data used for filtered FCS and MFD analysis: calibration measurements (e.g. for detection efficiency, instrument response function (IRF), background, and g-factor calibration) and measurement data.
- Single\_molecule\_functional\_variants.zip contains raw single-molecule data for derivation of the kinetic scheme.
- EPR\_wildtype.zip contains EPR data.
- FRET\_screening\_of\_PDB\_structures.zip contains a table of experimental distances and errors for each DA pair (corresponding to Supplementary Table 2), and a file with an overview on the FRET screening of the PDB structures.

Each of the subfolders in eTCSPC\_wildtype.zip, Single\_molecule\_wildtype.zip and Single\_molecule\_functional\_variants.zip for a DA pair X-Y contain a X-Y.yml file describing the setup and referencing all data relevant for the analysis of the measurement.

Filename of meta file on Zenodo	description
eTCSPC\5-44\5-44.yml	eTCSPC data for variant E5pAcF/S44C
eTCSPC\5-132\5-132.yml	eTCSPC data for variant E5pAcF/N132C
eTCSPC\8-69\8-69.yml	eTCSPC data for variant R8pAcF/Q69C
eTCSPC\8-86\8-86.yml	eTCSPC data for variant R8pAcF/P86C
eTCSPC\8-119\8-119.yml	eTCSPC data for variant R8pAcF/R119C
eTCSPC\8-132\8-132.yml	eTCSPC data for variant R8pAcF/N132C
eTCSPC\19-69\19-69.yml	eTCSPC data for variant K19pAcF/Q69C
eTCSPC\19-86\19-86.yml	eTCSPC data for variant K19pAcF/P86C
eTCSPC\19-119\19-119.yml	eTCSPC data for variant K19pAcF/R119C
eTCSPC\19-132\19-132.yml	eTCSPC data for variant K19pAcF/N132C
eTCSPC\22-127\22-127.yml	eTCSPC data for variant E22pAcF/D127C
eTCSPC\36-86\36-86.yml	eTCSPC data for variant S36pAcF/P86C
eTCSPC\36-132\36-132.yml	eTCSPC data for variant S36pAcF/N132C
eTCSPC\44-69\44-69.yml	eTCSPC data for variant S44pAcF/Q69C
eTCSPC\44-86\44-86.yml	eTCSPC data for variant S44pAcF/P86C
eTCSPC\44-119\44-119.yml	eTCSPC data for variant S44pAcF/R119C
eTCSPC\44-127\44-127.yml	eTCSPC data for variant S44pAcF/D127C
eTCSPC\44-132\44-132.yml	eTCSPC data for variant S44pAcF/N132C
eTCSPC\44-150\44-150.yml	eTCSPC data for variant S44pAcF/I150C
eTCSPC\55-69\55-69.yml	eTCSPC data for variant N55pAcF/Q69C
eTCSPC\55-119\55-119.yml	eTCSPC data for variant N55pAcF/R119C
eTCSPC\55-132\55-132.yml	eTCSPC data for variant N55pAcF/N132C
eTCSPC\55-150\55-150.yml	eTCSPC data for variant N55pAcF/I150C
eTCSPC\60-86\60-86.yml	eTCSPC data for variant K60pAcF/P86C
eTCSPC\60-119\60-119.yml	eTCSPC data for variant K60pAcF/R119C
eTCSPC\60-132\60-132.yml	eTCSPC data for variant K60pAcF/N132C
eTCSPC\60-150\60-150.yml	eTCSPC data for variant K60pAcF/I150C
eTCSPC\69-86\69-86.yml	eTCSPC data for variant Q69pAcF/P86C
eTCSPC\69-119\69-119.yml	eTCSPC data for variant Q69pAcF/R119C
eTCSPC\69-132\69-132.yml	eTCSPC data for variant Q69pAcF/N132C

eTCSPC\69-150\69-150.yml	eTCSPC data for variant Q69pAcF/I150C
eTCSPC\70-119\70-119.yml	eTCSPC data for variant D70pAcF/R119C
eTCSPC\70-132\70-132.yml	eTCSPC data for variant D70pAcF/N132C

Filename of meta file on Zenodo	description
Single_molecule_wildtype\5-44\5-44.yml	Single-molecule data for variant E5pAcF/S44C
Single_molecule_wildtype\5-44\5-44.yml	Single-molecule data for variant E5pAcF/S44C
Single_molecule_wildtype\5-132\5-132.yml	Single-molecule data for variant E5pAcF/N132C
Single_molecule_wildtype\8-69\8-69.yml	Single-molecule data for variant R8pAcF/Q69C
Single_molecule_wildtype\8-86\8-86.yml	Single-molecule data for variant R8pAcF/P86C
Single_molecule_wildtype\8-119\8-119.yml	Single-molecule data for variant R8pAcF/R119C
Single_molecule_wildtype\8-132\8-132.yml	Single-molecule data for variant R8pAcF/N132C
Single_molecule_wildtype\19-69\19-69.yml	Single-molecule data for variant K19pAcF/Q69C
Single_molecule_wildtype\19-86\19-86.yml	Single-molecule data for variant K19pAcF/P86C
Single_molecule_wildtype\19-119\19-119.yml	Single-molecule data for variant K19pAcF/R119C
Single_molecule_wildtype\19-132\19-132.yml	Single-molecule data for variant K19pAcF/N132C
Single_molecule_wildtype\22-127\22-127.yml	Single-molecule data for variant E22pAcF/D127C
Single_molecule_wildtype\36-86\36-86.yml	Single-molecule data for variant S36pAcF/P86C
Single_molecule_wildtype\36-132\36-132.yml	Single-molecule data for variant S36pAcF/N132C
Single_molecule_wildtype\44-69\44-69.yml	Single-molecule data for variant S44pAcF/Q69C
Single_molecule_wildtype\44-86\44-86.yml	Single-molecule data for variant S44pAcF/P86C
Single_molecule_wildtype\44-119\44-119.yml	Single-molecule data for variant S44pAcF/R119C
Single_molecule_wildtype\44-127\44-127.yml	Single-molecule data for variant S44pAcF/D127C
Single_molecule_wildtype\44-132\44-132.yml	Single-molecule data for variant S44pAcF/N132C
Single_molecule_wildtype\44-150\44-150.yml	Single-molecule data for variant S44pAcF/I150C
Single_molecule_wildtype\55-69\55-69.yml	Single-molecule data for variant N55pAcF/Q69C
Single_molecule_wildtype\55-119\55-119.yml	Single-molecule data for variant N55pAcF/R119C
Single_molecule_wildtype\55-132\55-132.yml	Single-molecule data for variant N55pAcF/N132C
Single_molecule_wildtype\55-150\55-150.yml	Single-molecule data for variant N55pAcF/I150C
Single_molecule_wildtype\60-86\60-86.yml	Single-molecule data for variant K60pAcF/P86C
Single_molecule_wildtype\60-119\60-119.yml	Single-molecule data for variant K60pAcF/R119C
Single_molecule_wildtype\60-132\60-132.yml	Single-molecule data for variant K60pAcF/N132C
Single_molecule_wildtype\60-150\60-150.yml	Single-molecule data for variant K60pAcF/I150C
Single_molecule_wildtype\69-86\69-86.yml	Single-molecule data for variant Q69pAcF/P86C
Single_molecule_wildtype\69-119\69-119.yml	Single-molecule data for variant Q69pAcF/R119C
Single_molecule_wildtype\69-132\69-132.yml	Single-molecule data for variant Q69pAcF/N132C
Single_molecule_wildtype\69-150\69-150.yml	Single-molecule data for variant Q69pAcF/I150C
Single_molecule_wildtype\70-119\70-119.yml	Single-molecule data for variant D70pAcF/R119C
Single_molecule_wildtype\70-132\70-132.yml	Single-molecule data for variant D70pAcF/N132C
Single_molecule_functional_variants\44-150\44-150.yml	Single-molecule data for function variant S44pAcF/I150C (identical to Single_molecule_wildtype\44-150\44-150.yml)
Single_molecule_functional_variants\44-150+pep\44-150+pep.yml	Single-molecule data for function variant S44pAcF/I150C with peptidoglycan
Single_molecule_functional_variants\44-150-E11A\44-150-E11A.yml	Single-molecule data for function variant S44pAcF/I150C/E11A
Single_molecule_functional_variants\44-150-E11A+pep\44-150-E11A+pep.yml	Single-molecule data for function variant S44pAcF/I150C/E11A with peptidoglycan
Single_molecule_functional_variants\44-150-R137E\44-150-R137E.yml	Single-molecule data for function variant S44pAcF/I150C/R137E
Single_molecule_functional_variants\44-150-T26E\44-150-T26E.yml	Single-molecule data for function variant S44pAcF/I150C/T26E
Single_molecule_functional_variants\44-150-T26E+pep\44-150-T26E+pep.yml	Single-molecule data for function variant S44pAcF/I150C/T26E with peptidoglycan

The subfolders for eTCSPC measurements for DA pair X-Y contain the following files:

Filename	Purpose
----------	---------

X-Y_DA.dat	Data for measurement of the FRET sample
X-Y_D0.dat	Data for donor-only reference measurement
IRF_DA.dat	Instrument response function for FRET measurement
IRF_D0.dat	Instrument response function for donor-only reference measurement

The subfolders for a single-molecule measurement for DA pair X-Y contain the following subfolders:

Folder name <sup>1</sup>	Content
"X-Y smd 0M" or "X Y DA sm" or "X_Y_0murea_sm" or "T4L_X_Y_FRET" or "T4L-X-Y-DA-smd" or "X_Y_da_sm"	Measurement data
"IRF" or "irf" or "H2O" or "water" or "h2o"	Instrument response function (IRF)
"DNA" or "dna"	Calibration measurement for detection efficiency
"pbs0M" or "pbs" or "buffer" or "buffer_HS" or "PBS" or "buffer_tween20" or "buff_0m" or "Buffer 00M"	Calibration measurement for background
"Rh101" and "Rh110" or "Rhod101" and "Rhod110" or "Rhod110thick" or "rho101" and "rho110"	Measurements of G-factors for the calibration of the anisotropy in the red (Rh101) and green (Rh110) detection channels

<sup>1</sup> Folder names might vary between subfolders

## Supplementary Methods

### Multiparameter Fluorescence Detection (MFD)

MFD for confocal single molecule Förster Resonance Energy Transfer (smFRET) measurements was done using a 485 nm diode laser (LDH-D-C 485 PicoQuant, Germany, operating at 64 MHz, power at objective 110  $\mu$ W) exciting freely diffusing labeled T4L molecule that passed through a detection volume of the 60X, 1.2 NA collar (0.17) corrected Olympus objective. The emitted fluorescence signal was collected through the same objective and spatially filtered using a 100  $\mu$ m pinhole, to define an effective confocal detection volume. Then, the signal was divided into parallel and perpendicular components at two different colors (“green” and “red”) through band pass filters, HQ 520/35 and HQ 720/150, for green and red respectively, and split further with 50/50 beam splitters. In total eight photon-detectors are used- four for green ( $\tau$ -SPAD, PicoQuant, Germany) and four for red channels (APD SPCM-AQR-14, Perkin Elmer, Germany). A time correlated single photon counting (TCSPC) module (HydraHarp 400, PicoQuant, Germany) with a 1ps resolution in Time Tagged Time Resolved (TTTR – an application note regarding this data acquisition setting is found in Ref <sup>13</sup> ([https://www.picoquant.com/images/uploads/page/files/14528/technote\\_ttr.pdf](https://www.picoquant.com/images/uploads/page/files/14528/technote_ttr.pdf)) was used for data registration.

For smFRET measurements samples were diluted (buffer used 50 mM sodium phosphate, pH 7.5, 150 mM NaCl, 40  $\mu$ M TROLOX and 1  $\mu$ M unlabeled T4L) to pM concentration assuring  $\sim$  1 burst per second. Collection time varied from several minutes up to 10 hours. To avoid drying out of the immersion water during the long measurements an oil immersion liquid with refraction index of water was used (Immersionol, Carl Zeiss Inc., Germany). NUNC chambers (Lab-Tek, Thermo Scientific, Germany) were used with 500  $\mu$ L sample volume. Standard controls consisted of measuring water to determine the instrument response function (IRF), buffer for background subtraction and the nM concentration green and red standard dyes (Rh110 and Rh101) in water solutions for calibration of green and red channels, respectively. To calibrate the detection efficiencies, we used a mixture solution of double labeled DNA oligonucleotides with known distance separation between donor and acceptor dyes.

### MFD burst analysis: Multiparameter FRET histograms and FRET-lines

Bursts were selected by  $2\sigma$  criteria out of the mean background value with cut off times that vary from sample to sample with a minimum of 60 photons for each burst. Each burst was then processed and fitted using a maximum likelihood algorithm <sup>14</sup> using in house developed software (LabVIEW, National Instruments Co.). Fluorescent bursts were plotted in 2D histograms (Origin 8.6, OriginLab Co).

The relation FRET-efficiency  $E$  and the species weighted average donor lifetimes  $\langle\tau\rangle_x$  depends on the fluorescence quantum yields of the dyes ( $\Phi_{FD(0)}$  and  $\Phi_{FA}$  for donor and acceptor respectively) and implicitly on background ( $\langle B_G \rangle$  and  $\langle B_R \rangle$  for green and red channels), detection efficiencies ( $g_G$  and  $g_R$  for green and red respectively) and crosstalk ( $\alpha$ ):

$$E = \frac{1}{1 + \frac{F_D/\Phi_{FD(0)}}{F_A/\Phi_{FA}}} = 1 - \frac{\langle \tau_{D(A)} \rangle_x}{\langle \tau_{D(0)} \rangle_x} \quad (13)$$

The corrected fluorescence ( $F_D$  and  $F_A$ ) depends on the detection efficiencies of green ( $g_G$ ) and red ( $g_R$ ) channels as follows:

$$F_D = \frac{S_G - \langle B_G \rangle}{g_G}, \quad (14)$$

$$F_A = \frac{S_R - \alpha F_G - \langle B_R \rangle}{g_R}, \quad (15)$$

where the total signal in green and red channels are  $S_G$  and  $S_R$ , respectively. The ratio ( $F_D/F_A$ ) is weighted by the species fractions.

In Supplementary Equation (13), brackets  $\langle \dots \rangle_x$  represent averaging over all lifetime components. For the species  $\tau^{(i)}$  weighted by its population fraction  $x^{(i)}$ , these averages are given by:

$$\langle \tau_{D(0)} \rangle_x = \sum_i x^{(i)} \tau_{D(0)}^{(i)} \quad \text{and} \quad \langle \tau_{D(A)} \rangle_x = \sum_i x^{(i)} \tau_{D(A)}^{(i)} \quad (16)$$

Above  $\langle \tau_{D(A)} \rangle_x$  and  $\langle \tau_{D(0)} \rangle_x$  are the species averaged fluorescence lifetimes of the donor in presence and absence of an acceptor, respectively.

In sm FRET experiments approximately  $\sim 100$  green photons per burst are detected. Hence, only the average time since excitation is reliably determined experimentally by the maximum likelihood estimators (MLE) for individual bursts. This time is weighted by the fluorescence intensity and hence, relates to the fluorescence lifetime components by:

$$\langle \tau_{D(0)} \rangle_f = \frac{\sum_i x^{(i)} \tau_{D(0)}^{(i)2}}{\sum_i x^{(i)} \tau_{D(0)}^{(i)}} \quad \text{and} \quad \langle \tau_{D(A)} \rangle_f = \frac{\sum_i x^{(i)} \tau_{D(A)}^{(i)2}}{\sum_i x^{(i)} \tau_{D(A)}^{(i)}} \quad (17)$$

We call these lifetimes fluorescence weighted average lifetimes.

The two averaged observables  $E$  (in Supplementary Equations (13)) and  $\langle \tau_{D(A)} \rangle_f$  can be related to each other. We call a line describing a theoretical relation of the two a ‘‘FRET-line’’. Such FRET-lines are projections of a parametrization of a multi-dimensional lifetime distribution to a two-dimensional plane using either the transfer-efficiency  $E$  or  $F_D/F_A$  as one and  $\langle \tau_{D(A)} \rangle_f$  as second axis.

Fluorophores are moving entities coupled to biomolecules at specific places via flexible linkers. Therefore, for single protein conformations a DA-distance distribution has to be considered. For simplicity, we use normal distributions to describe the DA-distance distributions. If the donor and acceptor interfluorophore average distance is  $\langle R_{DA} \rangle$ , the corresponding DA-distance distribution is:

$$p(R_{DA}) = \frac{1}{w_{DA} \sqrt{\pi/2}} \exp \left( -2 \left[ \frac{R_{DA} - \langle R_{DA} \rangle}{w_{DA}} \right]^2 \right), \quad (18)$$

Here,  $w_{DA}$  is the width of the DA-distance distribution attributed to the broadening due to the linker-flexibility set to a physical meaningful value of  $12 \text{ \AA}^3$ . Using the Förster-relationship

$\tau_{D(A)}(R_{DA}) = \tau_{D(0)} \cdot \left(1 + (R_0/R_{DA})^6\right)^{-1}$  and the following integrals:

$$\langle \tau_{D(A)} \rangle_x = \int \tau_{D(A)}(R_{DA}) p(R_{DA}) dR_{DA}, \quad (19)$$

$$\langle \tau_{D(A)} \rangle_f = \frac{\int (\tau_{D(A)}(R_{DA}))^2 p(R_{DA}) dR_{DA}}{\langle \tau_{D(A)} \rangle_{x,L}}, \quad (20)$$

This (Supplementary Equation (18)) distribution can be projected to a point in the  $E$ - $\langle \tau_{D(A)} \rangle_f$  plane. If the average DA distance  $\overline{\langle R_{DA} \rangle}$  is varied within a given range (i.e.  $[0, \infty]$ ) a line within the  $E$ - $\langle \tau_{D(A)} \rangle_f$  plane is obtained. Such a line we call a static FRET-line, as it is valid for all molecules with given (single) conformation, irrespectively of the mean DA-separation,  $\overline{\langle R_{DA} \rangle}$ .

To describe molecules, which are interconverting between two states with mean distances  $\overline{\langle R_{DA} \rangle}^{(1)}$  and  $\overline{\langle R_{DA} \rangle}^{(2)}$  and fractions  $x^{(1)}$  and  $x^{(2)} = 1 - x^{(1)}$ , by a line in the  $E$ - $\langle \tau_{D(A)} \rangle_f$  plane we use the following distance distribution:

$$p(R_{DA}) = \frac{x_{DA}^{(1)}}{w_{DA} \sqrt{\pi/2}} \exp\left(-2 \left[\frac{R_{DA} - \overline{\langle R_{DA} \rangle}^{(1)}}{w_{DA}}\right]^2\right) + \frac{1 - x_{DA}^{(1)}}{w_{DA} \sqrt{\pi/2}} \exp\left(-2 \left[\frac{R_{DA} - \overline{\langle R_{DA} \rangle}^{(2)}}{w_{DA}}\right]^2\right) \quad (21)$$

To obtain a “dynamic” FRET-line, which is valid for a molecule in exchange between these two states, the fraction  $x^{(1)}$  is varied within the range  $[0, 1]$  and the position in the  $E$ - $\langle \tau_{D(A)} \rangle_f$  plane is calculated using the Supplementary Equations (19), (20) and (13).

### Guidelines for reading MFD histograms

Several guidelines are needed to properly read MFD histograms. A short list is presented here.

- I) Donor only population is shown at low  $E$  with lifetime  $\sim 4$  ns (donor-only for Alexa488).
- II) High FRET appears at shorter lifetimes when the fluorescence of acceptor is high ( $E \rightarrow 1$ ).
- III) Static FRET states follow a theoretical line that accounts for dye linker mobility called “static FRET line”<sup>15</sup>.
- IV) A molecule that exchanges conformations at timescales faster than the diffusion time emits a burst of photons whose mixed fluorescence is characterized by the fluorescence average lifetime. Elongation of peaks in  $E$ - $\langle \tau_{D(A)} \rangle_f$ -histograms and deviation from static FRET-lines are an indication for slow conformational dynamics processes on the hundreds of microseconds.

We inspect the signal over the duration of the measurement. Typically, we find stable signal over 1 hr and 10 hrs. Additionally, we minimize unlikely effects of multimolecule events by comparing the difference in the burst duration in donor and acceptor channels ( $|T_G| - |T_R|$ ) or aggregates (e. g. via burst duration or the diffusion time component of the correlated

molecular bursts) and impurities due to e.g. free, unattached fluorophores (e.g. by plotting the scatter-corrected anisotropy vs.  $\langle \tau_{D(A)} \rangle_f$ ).

### Filtered Fluorescence Correlation Spectroscopy

In fluorescence correlation spectroscopy (FCS) information on fluctuating systems is obtained by calculating the correlation function<sup>16,17</sup>:

$${}^{A,B}G(t_c) = 1 + \frac{\langle \delta^A S(t) \cdot \delta^B S(t+t_c) \rangle}{\langle {}^A S(t) \rangle \cdot \langle {}^B S(t) \rangle}. \quad (22)$$

where  $t_c$  is the correlation time,  ${}^{A,B}S(t)$  represents the detected intensity signal (number of detected photons per time interval) at channels  $A$  or  $B$ , and  $\delta^{A,B}S(t)$  corresponds to the deviation of the signal from the time average signal denoted as  $\langle {}^{A,B}S(t) \rangle$ .  ${}^{A,B}G(t_c)$  is an auto-correlation function (ACF) if  $A = B$  otherwise  ${}^{A,B}G(t_c)$  is a cross-correlation (CCF).

The correlation function<sup>18-19</sup> of a mixture of  $n$  molecular static species is given by an weighted average:

$$G(t_c) = 1 + \frac{1}{N} \cdot \frac{\sum_i^n x^{(i)} \cdot (Q^{(i)})^2 \cdot G_{diff}^{(i)}(t_c)}{\left( \sum_i^n x^{(i)} \cdot Q^{(i)} \right)^2}, \quad (23)$$

where  $G_{diff}^{(i)}(t_c)$  describes molecular diffusion. For a 3-dimensional Gaussian detection probability,  $W(x, y, z) = \exp(-2(x^2 + y^2)/\omega_0^2) \cdot \exp(-2z^2/z_0^2)$ ,  $G_{diff}^{(i)}(t_c)$  is given by:

$$G_{diff}^{(i)}(t_c) = \left( 1 + \frac{t_c}{t_{diff}^{(i)}} \right)^{-1} \cdot \left( 1 + \left( \frac{\omega_0}{z_0} \right)^2 \cdot \frac{t_c}{t_{diff}^{(i)}} \right)^{-\frac{1}{2}}, \quad (24)$$

The  $1/e^2$  radii in  $x$  and  $y$  or in  $z$  direction are denoted by  $\omega_0$  and  $z_0$ , respectively. The characteristic diffusion time  $t_{diff}^{(i)}$  relates to the diffusion coefficient of each species  $i$   $t_{diff}^{(i)} = \omega_0^2 / 4D^{(i)}$ . The amplitude of the correlation is scaled with the reciprocal of the average number of fluorescent particles  $N$  in the confocal volume. Each molecular fraction  $x^{(i)} = c^{(i)} / \sum_i c^{(i)}$  has a concentration  $c^{(i)}$ , and brightness  $Q^{(i)}$ .

To separate species, we use filtered FCS (fFCS)<sup>7,20</sup>. fFCS differs from standard FCS<sup>16</sup> and FRET-FCS<sup>21</sup> by interrogating the “species” (conformational states) fluctuations instead of photon count rates<sup>21</sup>. We define the species cross-correlation function (sCCF) as

$$G^{(i,m)}(t_c) = \frac{\langle F^{(i)}(t) \cdot F^{(m)}(t+t_c) \rangle}{\langle F^{(i)}(t) \rangle \cdot \langle F^{(m)}(t+t_c) \rangle} = \frac{\left\langle \left( \sum_{j=1}^{d-L} f_j^{(i)} \cdot S_j(t) \right) \cdot \left( \sum_{j=1}^{d-L} f_j^{(m)} \cdot S_j(t+t_c) \right) \right\rangle}{\left\langle \sum_{j=1}^{d-L} f_j^{(i)} \cdot S_j(t) \right\rangle \cdot \left\langle \sum_{j=1}^{d-L} f_j^{(m)} \cdot S_j(t+t_c) \right\rangle}, \quad (25)$$

where  $(i)$  and  $(m)$  are two selected “species” or “pseudospecies” in a mixture, where pseudospecies correspond to the equilibrium of two or more mixed species that are in fast exchange. A set of filters  $f_j^{(i)}$  that depend on the arrival time of each photon after each excitation pulse is used. The signal  $S_j(t)$ , obtained via pulsed excitation, is recorded at each  $j$

= 1 ...  $L$  TCSPC-channel. The signal and filters per detector,  $d$ , are stacked in a single array with dimensions  $d \cdot L$  for global minimization according to <sup>7</sup>. Filters are defined in such a way that the relative “error” difference between the photon count per species ( $w^{(i)}$ ) and the weighted histogram  $f_j^{(i)} \cdot H_j$  is minimized as defined in Supplementary Equation (26).

$$\left\langle \left( \sum_{j=1}^{d \cdot L} f_j^{(i)} \cdot H_j - w^{(i)} \right)^2 \right\rangle \rightarrow \min, \quad (26)$$

where brackets represent time averaging.

The requirement is that the decay histogram  $H_j$  can be expressed as a linear combination of the conditional probability distributions  $p_j^{(i)}$ , such as  $H_j = \sum_{i=1}^{n(=2)} w^{(i)} p_j^{(i)}$ , with  $\sum_{j=1}^{d \cdot L} p_j^{(i)} = 1$ .

Here,  $p_j^{(i)}$  corresponds to the time resolved fluorescence decay of each selected pseudo-species  $i$  (Supplementary Figure 9a, c). Using the definition of the fluorescence decays in Equation 26 it is then possible to find a weight value  $w^{(i)}$  to satisfy the experimental observable fluorescence decay characteristic of the mixture  $H_j$ , and the corresponding filters per species  $f_j^{(i)}$ . Examples are plotted in Supplemental Figure 9b, d.

Hence, the species cross- correlation  $G^{(i,m)}(t_c)$  provides maximal contrast for intercrossing dynamics <sup>7</sup>. One major advantage of *sCCF* is that, if photophysical properties are decoupled from species selection, the intercrossing dynamics <sup>21</sup> is recovered with great fidelity.

To properly fit the species cross-correlation function, we used <sup>7</sup>

$$G(t_c) = 1 + \frac{1}{N} \cdot G_{diff}(t_c) \cdot [1 - G_K(t_c)], \quad (27)$$

where  $G_K(t_c)$  is

$$G_K(t_c) = \sum_{t_{Ri}}^{t_{Rn}} A_{Ki} \exp(-t_c/t_{Ri}). \quad (28)$$

In Supplementary Equation (28) the summation is over  $n$  reaction times  $t_{Rn}$ .

The same 3-dimensional Gaussian shaped volume element is assumed. We assume that

$G_{diff}(t_c) = G_{diff}^{(i)}(t_c) = G_{diff}^{(m)}(t_c)$  take the form of Supplementary Equation (27). The

normalized correlation function is presented as:

$$g(t_c) = N \cdot (G(t_c) - 1). \quad (29)$$

Filtered FCS requires prior knowledge of the time-resolved fluorescence and polarization decays for each species or pseudospecies. For a mixture of more than two species, we generated two decays corresponding to two “pseudo-species”. Using the scatter profile as the excitation pulse, the parallel and perpendicular decay components ( $F_{\parallel}(t)$  and  $F_{\perp}(t)$ ) for each “pseudo-species” were generated as

$$\begin{aligned} F_{\parallel}(t) &= F(t) \cdot (1 + (2 - 3l_1) \cdot r(t)) / 3 \\ F_{\perp}(t) &= F(t) \cdot (1 - (1 - 3l_2) \cdot r(t)) / 3 \end{aligned} \quad (30)$$



where  $F(t)$  is the time-resolved fluorescence decay at magic angle, and  $l_1 = 0.01758$  and  $l_2 = 0.0526$  are correction factors<sup>22 23</sup>. The anisotropy decay  $r(t)$  is given by

$$r(t) = r_{0,ov} \exp(-t / \rho_{overall}) + r_{0,ba} \exp(-t / \rho_{backbone}) + r_{0,li} \exp(-t / \rho_{linker}). \quad (31)$$

Background signal consists of dark counts (uniformly distributed over TCSPC channels) and scatter contribution.

### Ensemble Time Correlated Single Photon Counting with high precision

Ensemble Time Correlated Single Photon Counting (eTCSPC) measurements were performed using either an IBH-5000U (IBH, Scotland) or a Fluotime 200 (Picoquant, Germany) system.

The excitation source of the IBH machine were a 470 nm diode laser (LDH-P-C470, Picoquant, Germany) operating at 10 MHz for donor excitation and a 635 nm (LDH-P-C635, Picoquant, Germany) for acceptor excitation. The excitation and emission slits were set to 2 nm and 16 nm, respectively. The excitation source of the Fluotime200 system was a white light laser (SuperK extreme, NKT Photonics, Denmark) operating at 20 MHz for both donor (485 nm) and acceptor (635 nm) excitation with excitation and emission slits set to 2 nm and 5 nm, respectively. Additionally, in both systems, cut-off filters were used to reduce the amount of scattered light (>500 nm for donor and >640 nm for acceptor emission).

For green detection, the monochromator was set to 520 nm and for red detection to 665 nm. All measurements were conducted under magic angle conditions (excitation polarizer 0°, emission polarizer 54.7°), except for anisotropy where the position of the emission polarizer was alternately set to 0° (VV) or 90° (VH).

In the IBH system, the TAC-histograms were recorded with a bin width of 14.1 ps within a time window of 57.8 ns, while the Fluotime200 was set to a bin width of 8 ps within a time window of 51.3 ns. Photons were collected up to a peak count of 100'000 corresponding in average to a total number of  $30 \cdot 10^6$  photons. The instrument response function IRF (~230 ps FWHM for the IBH, ~ 150 ps for the Fluotime200) was collected under the same recording settings at the excitation wavelength of the sample without cutoff-filters using a scattering Ludox-dispersion, which yielded a comparable count rate as the later on measured samples.

For the IBH system, it was needed was performed before each measurement session a reference measurement with a continuous light signal to account for the differential non-linearity of the counting electronics. The recorded uncorrelated photons yield a reference histogram that is ideally constant. After recording of this measurement, the average number of photons in each time-bin is calculated. Next, the measurement was smoothed by a window function using a Hanning-filter with a window-size of 17 bins. The smoothed decay histogram was normalized to the previously calculated average number of photons. Instead of correcting the experimental histogram the model function is multiplied by the smoothed and normalized reference histogram to preserve the Poissonian statistics of the measured fluorescence intensity histograms of interest.

### Donor and acceptor fluorescence quantum yields

Depending on the labeling position, the donor and acceptor fluorescence quantum yields vary and have been estimated for each sample (Supplementary Table 2a). We estimate  $\Phi_{FD(0)}$  and  $\Phi_{FA}$  of the fluorescent species by the species-averaged fluorescence lifetime  $\langle \tau \rangle_x$  of donor or

acceptor, respectively. As reference samples we used Alexa488-labeled DNA  $\langle \tau_{D(0)} \rangle_x = 4.0$  ns,  $\Phi_{FD(0)} = 0.8$  and for the acceptor Alexa647, we used the similar dye Cy5 at Cy5-labeled DNA with  $\langle \tau_A \rangle_x = 1.17$  ns and  $\Phi_{FA} = 0.32$ <sup>24</sup>. This FRET pair has a Förster distance of 52 Å.

### Time-resolved fluorescence decay analysis

#### Model

We model the fluorescence decay of the donor in the absence of FRET  $F_{D(0)}(t)$  by a multi-exponential decay to account for sample specific differences of the donor reference samples

$$F_{D(0)}(t) = \sum_i x_{D(0)}^{(i)} \exp(-t / \tau_{D(0)}^{(i)}). \quad (32)$$

Here,  $\tau_{D(0)}^{(i)}$  is the donor fluorescence lifetime and  $x_{D(0)}^{(i)}$  are the pre-exponential factors.

Sample specific differences were considered in the analysis of the FRET samples by joint analysis where all donor species are quenched by the same FRET rate constant  $k_{RET}$ . Such model is correct if quenching does not change the donor radiative lifetime and if FRET is uncorrelated with quenching of the donor by its local environment. Under these conditions the donor fluorescence intensity decay in the presence of FRET  $F_{D(A)}(t)$  factorizes into the donor fluorescence decay in absence of FRET and the FRET-induced donor quenching  $\varepsilon_{D(A)}(t)$

$$F_{D(A)}(t) = F_{D(0)}(t) \cdot \varepsilon_{D(A)}(t). \quad (33)$$

We relate the FRET-induced donor quenching to the DA-distance distribution by the rate-constant of energy transfer as defined by Förster

$$k_{RET} = k_F \cdot \kappa^2 \cdot \left( \frac{R_{0J}}{R_{DA}} \right)^6 \quad (34)$$

Here,  $R_{0J}$  is a reduced Förster-radius,  $k_F$  is the radiative rate constant of fluorescence and  $\kappa^2$  is the orientation-factor. This reduced Förster-radius is given by

$$R_{0J} = \left[ \frac{9(\ln 10)}{128\pi^5 \cdot N_A} \cdot \frac{J}{n^4} \right]^{\frac{1}{6}} = 0.2108 \cdot \text{Å} \cdot \left[ \frac{1}{n^4} \cdot \left( \frac{J(\lambda)}{\text{mol}^{-1} \cdot \text{dm}^3 \cdot \text{cm}^{-1} \cdot \text{nm}^4} \right) \right]^{\frac{1}{6}}, \quad (35)$$

where  $N_A$  is Avogadro's constant,  $n$  is the refractive index of the medium and  $J = \int f_D(\lambda) \cdot \varepsilon_A(\lambda) \cdot \lambda^4 \cdot d\lambda$  is the overlap integral between  $f_D(\lambda)$ , the donor emission spectrum and  $\varepsilon_A(\lambda)$ , the acceptor absorption spectrum. The FRET-induced donor decay relates to the distance distribution  $p(R_{DA})$  by

$$\varepsilon_{D(A)}(t) = \int p(R_{DA}) \cdot \exp\left(-t \cdot \langle \kappa^2 \rangle \cdot k_F \left[ 1 + (R_{0J} / R_{DA})^6 \right]\right) dR_{DA}. \quad (36)$$

We use an average orientation factor of  $\langle \kappa^2 \rangle \approx 2/3$  (justified by the anisotropy studies compiled in Supplementary Tables 3A-D). We used a reduced Förster-radius of  $R_{0J} = 56.4$  Å which was determined for the donor with a radiative rate constant  $k_F = 0.224$  ns<sup>-1</sup>. As previously described<sup>25</sup> we propagate potential errors of the  $\langle \kappa^2 \rangle \approx 2/3$  approximation to our experimental distances (Supplementary Table 5d).

We use a superposition of normal distributions to describe a mixture of states:

$$p(R_{DA}) = \sum_{i=1}^N x_{DA}^{(i)} \frac{1}{w_{DA} \sqrt{\pi/2}} \exp\left(-2 \left[ \frac{R_{DA} - \langle R_{DA}^{(i)} \rangle}{w_{DA}} \right]^2\right). \quad (37)$$

Here,  $N$  is the number of states (2 or 3) with  $\langle R_{DA}^{(i)} \rangle$  being the mean of the state ( $i$ ) distance distribution with species fraction  $x_{DA}^{(i)}$  and a width  $w_{DA}$  set to a physical meaningful value of 12 Å (flexible dye-linkers)<sup>3</sup>.

We analyze our data by substituting Supplementary Equation (37) into (36). Next, Supplementary Equation (36) is inserted into Supplementary Equations (33). Finally, we analyze the fluorescence intensity decay of the donor in presence and absence of FRET (Supplementary Equation (38) or (39)) in a joint fit, in which the fluorescence lifetimes and corresponding species fractions of the donor only reference sample were identical to the respective parameters in the FRET sample. By this procedure the photon counting statistics of both the reference- and fluorescence-decay in presence of FRET is preserved. Thus, the counting statistics are clearly defined (Poisson distribution). This allows for an analysis with proper error-estimates. By the global (joint) analysis of the reference sample and the FRET-sample the photophysical properties (dynamic quenching) are taken into account. To further reduce the number of free model parameters, we combined the donor only and FRET measurements of all 33 FRET samples into a joint single data set, in which the species fractions of the DA-distance distribution were shared among all 33 variants. The so achieved reduction in degrees of freedom of a joint/global fit stabilizes the fit dramatically.

#### *Ensemble Time Correlated Single Photon Counting*

The experimental fluorescence intensity decays were fitted using the iterative re-convolution approach, where the model-decay curves are convoluted with the experimental instrument response function (*IRF*). Additionally, we consider a constant offset  $c$  of the fluorescence intensity and correct the instrumental differential non-linearity by a time-dependent function  $Lin(t)$ . With these corrections, the experimental time-resolved fluorescence intensities of the FRET-sample and the donor reference sample are proportional to:

$$\begin{aligned} F_{\text{FRET}}(t) &= (N_0 \cdot [(1 - x_{\text{DOnly}})F_{\text{D(A)}}(t) + x_{\text{DOnly}}F_{\text{D(0)}}(t)] \otimes IRF + sc \cdot IRF + c) \cdot Lin(t) \\ F_{\text{Ref}}(t) &= (N_0 \cdot F_{\text{D(0)}}(t) \otimes IRF + sc \cdot IRF + c) \cdot Lin(t) \end{aligned} \quad (38)$$

Here,  $sc$  is due to scattered light from the sample. The model fluorescence intensity histograms were scaled to the experimental measured number of photons to reduce the number of free fitting parameters (the initial amplitude  $N_0$  is not fitted).

#### *Sub-ensemble Time Correlated Single Photon Counting*

In sm-measurements we determine the number of fluorescent photons  $N_F$  and the number of background photons  $N_{BG}$  using buffer reference measurements as reference. Given the known number of fluorescence and background photons the fluorescence decays were modeled by:

$$\begin{aligned} F_{\text{FRET}}(t) &= N_F \cdot [(1 - x_{\text{DOnly}})F_{\text{D(A)}}(t) + x_{\text{DOnly}}F_{\text{D(0)}}(t)] \otimes IRF + N_{BG} \cdot IRF \\ F_{\text{Ref}}(t) &= N_F \cdot F_{\text{D(0)}}(t) \otimes IRF + N_{BG} \cdot IRF \end{aligned} \quad (39)$$

This procedure reduced the number of the number of free parameters compared to the eTCSPC measurements.

#### *Summary fit models*

In total, we used three different fit models to describe our data. They differ in their number of states and the number of joint (global) and free relevant parameters, which are given in Supplementary Table 5. The fit of the two globally linked states was obtained within the procedure to estimate the fraction of the third state (see below).

#### *Fitting of functional variants*

Functional variants were fitted globally, i. e. distances for states  $C_1$  and  $C_2$  were linked over all three variants used to mimic free enzyme  $E$ , enzyme-substrate complex  $ES$  and enzyme product complex  $EP$  while the distance for  $C_3$  was only linked for  $E$  and  $ES$  to allow for the different (covalent) nature of this state in  $EP$ . The experimental fluorescence decays were fitted by the conventional Levenberg–Marquardt minimization algorithm using custom software written in Python.

#### *Uncertainty estimation*

The statistical errors of the DA-distances were determined by sampling the parameter space<sup>26,27</sup> and applying the F-distribution at a confidence level of 95% ( $2\sigma$ ) given the minimum determined  $\chi^2$ . The maximum allowed  $\chi_{r,\max}^2$  for a given confidence-level ( $P$ ; e.g. for  $2\sigma$   $P = 0.95$ ) was calculated by

$$\chi_{r,\max}^2(P) = \chi_{r,\min}^2 \cdot \left[ 1 + n/\nu \cdot \text{cdf}^{-1}(F(n,\nu,P)) \right], \quad (40)$$

where  $\text{cdf}^{-1}(F(n,\nu,P))$  is the inverse of the cumulative distribution function of the  $F$ -distribution for  $n$  number of free parameters, and with  $\nu$  degrees of freedom.  $\chi_{r,\min}^2$  is the minimum determined  $\chi_r^2$ <sup>28</sup>.

To estimate the species fraction  $x_3$  of the third state, we performed a support plane analysis for the global fit<sup>29</sup>.

### **Supplementary References**

1. Ratzke, C., Hellenkamp, B. & Hugel, T. Four-colour FRET reveals directionality in the Hsp90 multicomponent machinery. *Nat. Commun.* **5**, 4192 (2014).
2. Vale, R. D. & Oosawa, F. Protein motors and Maxwell's demons: does mechanochemical transduction involve a thermal ratchet? *Adv. Biophys.* **26**, 97-134 (1990).
3. Sindbert, S. *et al.* Accurate distance determination of nucleic acids via Forster resonance energy transfer: implications of dye linker length and rigidity. *J. Am. Chem. Soc.* **133**, 2463-2480 (2011).

4. Sisamakias, E., Valeri, A., Kalinin, S., Rothwell, P. J. & Seidel, C. A. Accurate single-molecule FRET studies using multiparameter fluorescence detection. *Methods Enzymol.* **475**, 455-514 (2010).
5. Kudryavtsev, V. *et al.* Combining MFD and PIE for accurate single-pair Forster resonance energy transfer measurements. *ChemPhysChem* **13**, 1060-1078 (2012).
6. Widengren, J. *et al.* Single-molecule detection and identification of multiple species by multiparameter fluorescence detection. *Anal. Chem.* **78**, 2039-2050 (2006).
7. Felekyan, S., Kalinin, S., Sanabria, H., Valeri, A. & Seidel, C. A. Filtered FCS: species auto- and cross-correlation functions highlight binding and dynamics in biomolecules. *ChemPhysChem* **13**, 1036-1053 (2012).
8. Gopich, I. V. & Szabo, A. Theory of the energy transfer efficiency and fluorescence lifetime distribution in single-molecule FRET. *Proc. Natl. Acad. Sci. USA* **109**, 7747-7752 (2012).
9. Maeda, H. A new lysozyme assay based on fluorescence polarization or fluorescence intensity utilizing a fluorescent peptidoglycan substrate. *J Biochem* **88**, 1185-1191 (1980).
10. Dale, R. E., Eisinger, J. & Blumberg, W. E. The orientational freedom of molecular probes. The orientation factor in intramolecular energy transfer. *Biophys. J.* **26**, 161-193 (1979).
11. Felekyan, S. *et al.* Full correlation from picoseconds to seconds by time-resolved and time-correlated single photon detection. *Rev. Sci. Instrum.* **76** (2005).
12. Sustarsic, M. & Kapanidis, A. N. Taking the ruler to the jungle: single-molecule FRET for understanding biomolecular structure and dynamics in live cells. *Curr. Opin. Struct. Biol.* **34**, 52-59 (2015).
13. Picoquant.  
<[https://www.picoquant.com/images/uploads/page/files/14528/technote\\_tttr.pdf](https://www.picoquant.com/images/uploads/page/files/14528/technote_tttr.pdf)>
14. Maus, M. *et al.* An experimental comparison of the maximum likelihood estimation and nonlinear least-squares fluorescence lifetime analysis of single molecules. *Anal. Chem.* **73**, 2078-2086 (2001).
15. Kalinin, S., Sisamakias, E., Magennis, S. W., Felekyan, S. & Seidel, C. A. On the origin of broadening of single-molecule FRET efficiency distributions beyond shot noise limits. *J. Phys. Chem. B* **114**, 6197-6206 (2010).
16. Elson, E. L. & Magde, D. Fluorescence correlation spectroscopy. I. Conceptual basis and theory. *Biopolymers* **13**, 1-27 (1974).

17. Magde, D., Elson, E. L. & Webb, W. W. Fluorescence correlation spectroscopy. II. An experimental realization. *Biopolymers* **13**, 29-61 (1974).
18. Kim, S. A., Heinze, K. G., Bacia, K., Waxham, M. N. & Schwille, P. Two-photon cross-correlation analysis of intracellular reactions with variable stoichiometry. *Biophys. J.* **88**, 4319-4336 (2005).
19. Schwille, P. Vol. 65 (ed R. Rigler E.L. Elson) 360-378 (Springer, Berlin, 2001).
20. Böhmer, M., Wahl, M., Rahn, H. J., Erdmann, R. & Enderlein, J. Time-resolved fluorescence correlation spectroscopy. *Chem. Phys. Lett.* **353**, 439-445 (2002).
21. Felekyan, S., Sanabria, H., Kalinin, S., Kuhnemuth, R. & Seidel, C. A. Analyzing Förster resonance energy transfer with fluctuation algorithms. *Methods Enzymol.* **519**, 39-85 (2013).
22. Koshioka, M., Sasaki, K. & Masuhara, H. Time-Dependent Fluorescence Depolarization Analysis in Three-Dimensional Microspectroscopy. *Appl. Spectrosc.* **49**, 224-228 (1995).
23. Schaffer, J. *et al.* Identification of single molecules in aqueous solution by time-resolved fluorescence anisotropy. *J. Phys. Chem. A* **103**, 331-336 (1999).
24. Woźniak, A. K., Schröder, G., Grubmüller, H., Seidel, C. A. M. & Oesterhelt, F. Single molecule FRET measures bends and kinks in DNA. *Proc.Natl.Acad.Sci.USA.* **105**, 18337-18342 (2008).
25. Kalinin, S. *et al.* A toolkit and benchmark study for FRET-restrained high-precision structural modeling. *Nat. Meth.* **9**, 1218-1225 (2012).
26. Goodman, J. & Weare, J. Ensemble Samplers with Affine Invariance. *Comm. App. Math. Comp. Sci.* **5**, 65-80 (2010).
27. Foreman-Mackey, D., Hogg, D. W., Lang, D. & Goodman, J. emcee: The MCMC Hammer. *Publications of the Astronomical Society of the Pacific* **125**, 306-312 (2013).
28. Lakowicz, J. R. *Principles of Fluorescence Spectroscopy*. Third edn, (Springer, 2006).
29. Straume, M., Frasier-Cadoret, S. G. & Johnson, M. L. Topics in Fluorescence Spectroscopy, Principles. Vol. 2 (ed Joseph R Lakowicz) Ch. Least-Squares Analysis of Fluorescence Data, 177-240 (Plenum Press, 1991).

Supplement C. Integrative dynamic structural biology  
unveils conformers essential for the oligomerization of a  
large GTPase

## **Integrative dynamic structural biology unveils conformers essential for the oligomerization of a large GTPase**

**Thomas-Otavio Peulen<sup>2,9†</sup>, Carola S. Hengstenberg<sup>1†</sup>, Ralf Biehl<sup>3</sup>, Mykola Dimura<sup>2,4</sup>, Charlotte Lorenz<sup>3,7</sup>, Alessandro Valeri<sup>2,10</sup>, Semra Ince<sup>1</sup>, Tobias Vöpel<sup>1</sup>, Bela Faragó<sup>5</sup>, Holger Gohlke<sup>4,8</sup>, Johann P. Klare<sup>6\*</sup>, Andreas M. Stadler<sup>3,7\*</sup>, Claus A. M. Seidel<sup>2\*</sup>, Christian Herrmann<sup>1\*</sup>**

<sup>1</sup>Physical Chemistry I, Faculty of Chemistry and Biochemistry, Ruhr-University Bochum, Universitätsstr. 150, 44780 Bochum, Germany; <sup>2</sup>Chair for Molecular Physical Chemistry, Heinrich-Heine-University Düsseldorf, Universitätsstr. 1, 40225 Düsseldorf, Germany; <sup>3</sup>Jülich Centre for Neutron Science JCNS and Institute for Complex System ICS, Forschungszentrum Jülich GmbH, 52425 Jülich, Germany; <sup>4</sup>Institut für Pharmazeutische und Medizinische Chemie, Heinrich-Heine-Universität Düsseldorf, Universitätsstr. 1, 40225 Düsseldorf, Germany; <sup>5</sup>Institut Laue-Langevin, CS 20156, 38042 Grenoble, France; <sup>6</sup>Macromolecular Structure Group, Department of Physics, University of Osnabrück, Barbarastr. 7, 49076 Osnabrück, Germany; <sup>7</sup>Institute of Physical Chemistry, RWTH Aachen University, Landoltweg 2, 52056 Aachen, Germany; <sup>8</sup>John von Neumann Institute for Computing, Jülich Supercomputing Centre, Institute for Complex Systems-Structural Biochemistry (ICS-6), Forschungszentrum Jülich GmbH, Wilhelm-Johnen-Str., 52425 Jülich, Germany; <sup>9</sup>Present Address: Department of Bioengineering and Therapeutic Sciences, University of California, San Francisco, Mission Bay Byers Hall, 1700 4th Street, San Francisco, CA 94143, USA; <sup>10</sup>Present address: Geomatys, 1000 Avenue Agropolis, 34000 Montpellier, France.

**† Contributed equally, \* Corresponding authors**

Guanylate binding proteins (GBPs) are soluble dynamin-like proteins with structured domains that undergo a conformational transition for GTP-controlled oligomerization to exert their function as part of the innate immune system of mammalian cells - attacking intra-cellular parasites by disrupting their membranes. The structural basis and mechanism of this process is unknown. Therefore, we apply neutron spin echo, X-ray scattering, fluorescence, and EPR spectroscopy as techniques for integrative dynamic structural biology to human GBP1 (hGBP1). We mapped hGBP1's essential dynamics from nanoseconds to milliseconds by motional spectra of sub-domains. We find a GTP-independent flexibility of the C-terminal effector domain in the  $\mu$ s-regime and structurally characterize conformers being essential that hGBP1 can open like a pocketknife for oligomerization. This unveils the intrinsic flexibility, a GTP-triggered association of the GTPase-domains and assembly-dependent GTP-hydrolysis as functional design principles of hGBP1 that control its reversible oligomerization in polar assemblies and the subsequent formation of condensates.

**Teaser:** How a pocketknife works on the molecular level



## Introduction

The biological function of proteins is directly linked to their structure, conformational heterogeneity, and their associated conformational dynamics. It is well known that structural flexibilities, heterogeneities, and polymorphisms can enable interactions among biomolecules, promote promiscuity with different binding partners, and are often essential for enzymatic activity.<sup>(1,2)</sup> For a molecular understanding of such biological processes (1) the players of the biological process need to be described by structures, and (2) the associated conformational dynamics need to be characterized in detail. However, if taken out of context the structures of individual macromolecules are often uninformative about function. X-ray crystallography and electron microscopy provide detailed insights on snapshots of conformational states revealing secondary structures of individual domains and domain arrangements. However, to relate structures with their associated function it is imperative to study their conformational dynamics and for a molecular understanding of a biological process all conformational states need to be mapped, ideally watching single molecules move along their transition paths.<sup>(3)</sup>

The relevance of dynamic structural biology is most evident for motor proteins such as myosin or dynamin, where cyclic structural changes are the molecular mechanism for their function. A widespread mechanism exerting such biomolecular function is the binding and cleavage of a suitable substrate to switch between at least two distinct states. Mostly hydrolyzable substrates such as the nucleotides ATP or GTP control structural changes by introducing the substrate hydrolysis as a quasi-irreversible step. Notably, the molecular mechanisms of the functionally relevant dynamics are mostly unknown because structurally flexible intermediates cannot be crystallized. Thus, NMR spectroscopy is often employed to map conformationally excited states and intermediates.<sup>(4)</sup>

For larger proteins the determination of dynamic biomolecular structures is extremely challenging, as there is no single technique that can in parallel observe conformational transitions in biomolecules and determine structures with close to atomistic resolution. To overcome the disadvantages of the individual experimental methods, we employ a new integrative approach that unveils dynamic conformers and domain motions of large multi-domain proteins.<sup>(5,6)</sup> By combining multiple experimental techniques we simultaneously probe protein structures and dynamics and cover time scales from nanoseconds to seconds for dynamic structural biology.

We apply this approach to study molecular mechanisms and design principles of large GTPases, a class of soluble proteins that are important for the innate cell-autonomous immunity

in multicellular organisms. These large GTPases, namely guanylate binding proteins (GBPs), belong to the dynamin superfamily and more specifically to the class of interferon- $\gamma$  induced effector molecules of first cell-autonomous defense.(7) GBPs have efficient antimicrobial activity against a wide range of intracellular pathogens such as viruses(8,9), bacteria(10-12) by assembling of inflammasomes(13,14) and by directly attacking the parasites(15). In living cells GBP isoforms form polar homo- and hetero-oligomers in different subcellular localizations,(16,17) that are involved in the intracellular immune response such as: defense against the vesicular stomatitis virus and the encephalomyocarditis virus,(8) suppression of Hepatitis C virus replication,(9) promotion of oxidative killing and the delivery of antimicrobial peptides to autophagolysosomes.(18)

As a prime example for a GBP we study the human guanylate binding protein 1 (hGBP1). hGBP1 is biochemically well characterized and shows nucleotide-dependent oligomerization.(19) In vitro studies demonstrated GTP regulated polymerization of hGBP1 and the formation of polar supramolecular structures.(20) Noteworthy, a homolog GBP in mice translocates from the cytosol to endomembranes and attacks the plasma membrane of eukaryotic cellular parasites by the formation of supramolecular complexes during infection.(15) An additional feature of GBPs is the GTP induced formation of multimeric complexes in mesoscopic droplet-shaped protein condensates (referred to as vesicle-like structures, VLS) and on parasite membranes. VLS potentially facilitate the controlled formation of productive and supramolecular complexes(20) that attack intra-cellular parasites in living cells(15).

X-ray crystallography on the full-length hGBP1 revealed a folded and fully structured protein with the typical architecture of a dynamin superfamily member. hGBP1 consists of a large GTPase domain (LG domain), an alpha-helical middle domain, and an elongated, also purely alpha-helical, effector domain comprising the helices  $\alpha$ 12 and  $\alpha$ 13, with an overall length of around 120 Å (**Fig. 1A**).<sup>(21)</sup> X-ray crystallography (19) and biochemical experiments (7) identified the LG domains as interfaces for GTP-analogue induced homo-dimerization. Like for other membrane associated dynamins that form tubular shaped condensates to fuse membranes in cells (22,23), cylindrical and tubular structure have been observed for hGBP1 (20,22). For hGBP1 neither molecular structures of these tubules nor precursor structures in solution that inform on the assembly mechanism are known. FRET and DEER experiments on the hGBP1-dimer identified two conformers. In the majorly populated hGBP1 dimer, the two C-terminal  $\alpha$ 13 helices associate.<sup>(24)</sup> This is in line with live-cell experiments that highlight the relevance of helix  $\alpha$ 13 for the immune response (12,25,26). However, an association of the two  $\alpha$ 13

helices in a hGBP1 dimer requires large-scale structural rearrangements that cannot be explained by the GppNHp bound X-ray crystal structures.<sup>(19)</sup> This highlights the necessity for structural flexibility on the formation pathway of a fully bridged hGBP1 dimer (b-hGBP1:L)<sub>2</sub>, where nucleotide ligands L (GTP) are bound and the effector domains *and* the LG domains are both associated (**Fig. 1B**). On the formation pathway of the fully bridged hGBP1 dimer, there are at least two intermediates - the ligand complex hGBP1:L and the flexible dimer (f-hGBP1:L)<sub>2</sub> (**Fig. 1B**).

We address the question at which step of this pathway hGBP1 becomes flexible (red arrows, **Fig. 1B**). There are three options: either hGBP1's flexibility is substrate independent (*i*), induced by the ligand (*ii*), or induced by the dimerization (*iii*). Consequently, three potential dimerization scenarios could describe the required structural rearrangements (**Fig. 1B**). In the first pathway (**Fig. 1B, i**) the structural flexibility is an intrinsic property of the free monomer and already in the absence of substrate; although the flexibility is only needed for the dimerization at a later step. In the second pathway (**Fig. 1B, ii**) the free monomer is predominantly stiff; the binding and/or the hydrolysis of the substrate in the complex hGBP1:L increases the flexibility needed at a later stage for the dimerization. In the third alternative pathway (**Fig. 1B, iii**) GTP binds to hGBP1 to enable dimerization of the LG domains and the LG domain dimerization triggers an internal rearrangement for effector domains to associate. To sum up, the pathways could be distinguished if one studies the monomeric hGBP1 that has either a single (pathways *ii, iii*) or multiple conformations in dynamic exchange (pathway *i*). Otherwise, the different mechanisms are indistinguishable. Hence, to differentiate these pathways, we map the structure and dynamics of the free and the ligand bound hGBP1.

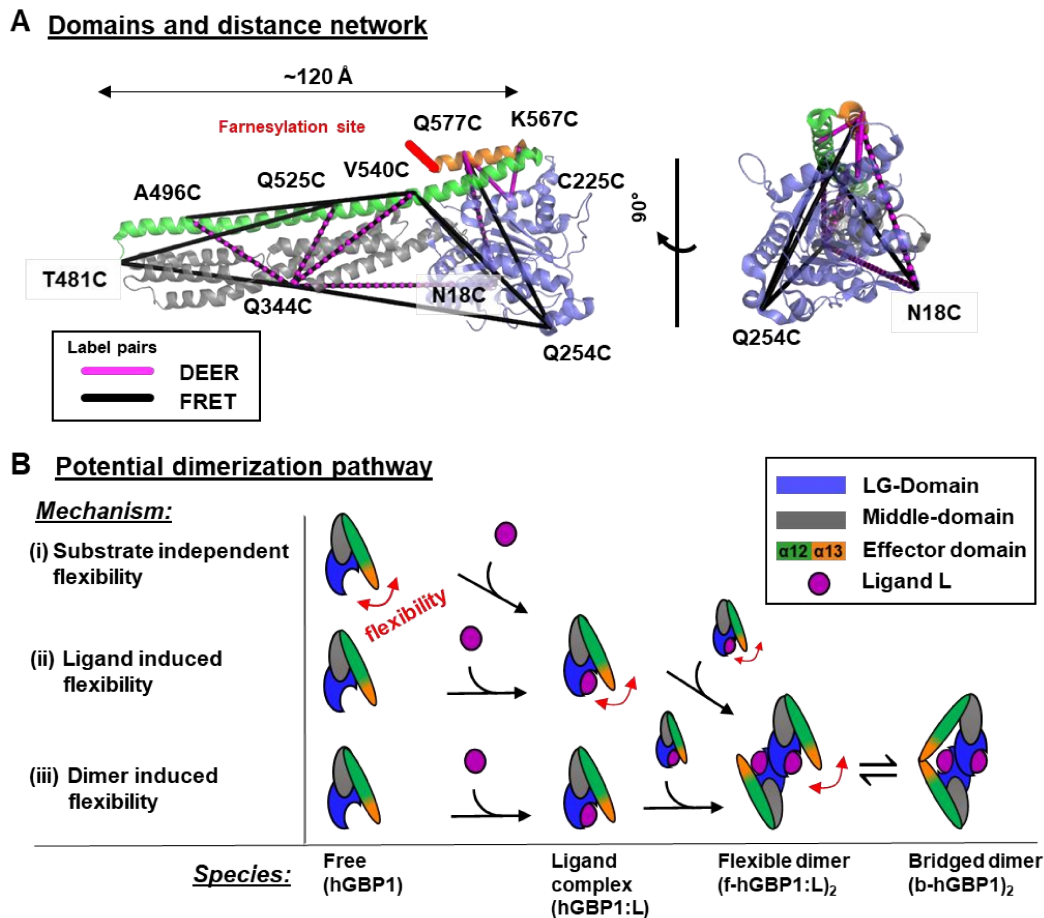


**Figure 1 | Network of pair-wise mutations for DEER and FRET measurements to probe the structural arrangement of the human guanylate binding protein 1 (hGBP1) and potential dimerization pathways. (A)** The network is shown on top of the crystal structure (hGBP1, PDB-ID: 1DG3). hGBP1 consists of three domains: the LG domain (blue), a middle domain (gray) and the helices  $\alpha 12/13$  (green/orange). The amino acids highlighted by the labels were used to attach spin-labels and fluorophores for DEER-EPR and FRET experiments, respectively. Magenta and black lines connect the DEER pairs and FRET-pairs, respectively. In hGBP1 the C-terminus is post-translationally modified and farnesylated for insertion into parasite membranes (red). **(B)** Potential different pathways for the formation of a functional hGBP1 dimer where the substrate binding LG domains and the helix  $\alpha 13$  associate. The association of the helix  $\alpha 13$  requires flexibility (highlighted by red arrows). This flexibility could be induced at different stages of a dimerization pathway.

We employ an integrative modeling toolkit for dynamic structural biology to address two objectives: (1) mapping the motions of the monomeric hGBP1 in the absence and the presence of a ligand and (2) resolving the structures of potential hGBP1 conformers in solution. This way, we study the molecular prerequisites for hGBP1 dimerization. We use structural information from small-angle X-ray scattering (SAXS), electron paramagnetic resonance (EPR) spectroscopy by site-directed spin labeling(27), ensemble and single-molecule fluorescence spectroscopy(28) and dynamic information from neutron spin-echo spectroscopy (NSE) and filtered fluorescence correlation spectroscopy (fFCS)(5). We mapped exchange kinetics from nanoseconds to milliseconds and detected at least two new conformational states in hGBP1.

Moreover, interrogating hGBP1's conformational dynamics by a network of 12 FRET pairs (**Fig. 1A**), we generated a temporal spectrum of hGBP1's internal motions. Finally, we discuss potential implications of the detected protein flexibility and conformers controlling the formation of multimers. This allows us to understand the mechanisms excreting the function of this large multi-domain system, i.e., the programmed and controlled oligomerization.

We expect that our findings on the so far unresolved intrinsic flexibility of nucleoside triphosphate processing enzymes will sharpen our view on the importance of conformational dynamics for ligand-controlled allosteric regulation of multi-domain proteins and enzymes far beyond GBPs.

## Results

### Experimental equilibrium distributions

We combined SAXS, DEER, and FRET experiments to probe distinct structural features of hGBP1 expressed and labeled for DEER and FRET by standard procedures (**Methods 1**). Size exclusion chromatography SAXS (SEC-SAXS) measurements (**Methods 2**) were performed at different protein concentrations (**Fig. S1A**). SEC-SAXS assures the data quality by discriminating aggregates and oligomeric species in the sample immediately before the SAXS data acquisition. A Kratky-plot of the SAXS data (**Fig. 2A**, middle) visualizes that hGBP1's conformation in solution clearly disagrees with the crystal structure of the full-length protein (PDB-ID: 1DG3). *Ab initio* modeling of the SAXS data (**Methods 2**) revealed a shape that suggests an additional kink between the LG and the middle domain (**Fig. 2A**, right).

Orthogonal information to the SAXS data were obtained by DEER (**Methods 3**) and FRET experiments (**Methods 4**), which specifically probe distances between labeling sites (**Fig. 1A**). The results of the DEER and FRET measurements and analyses are exemplified for the dual cysteine variant Q344C/A496C labeled by MTSSL spin probes for DEER experiments (**Fig. 2B**) and by the fluorophores Alexa488 and Alexa647 for ensemble FRET experiments

(Fig. 2C).

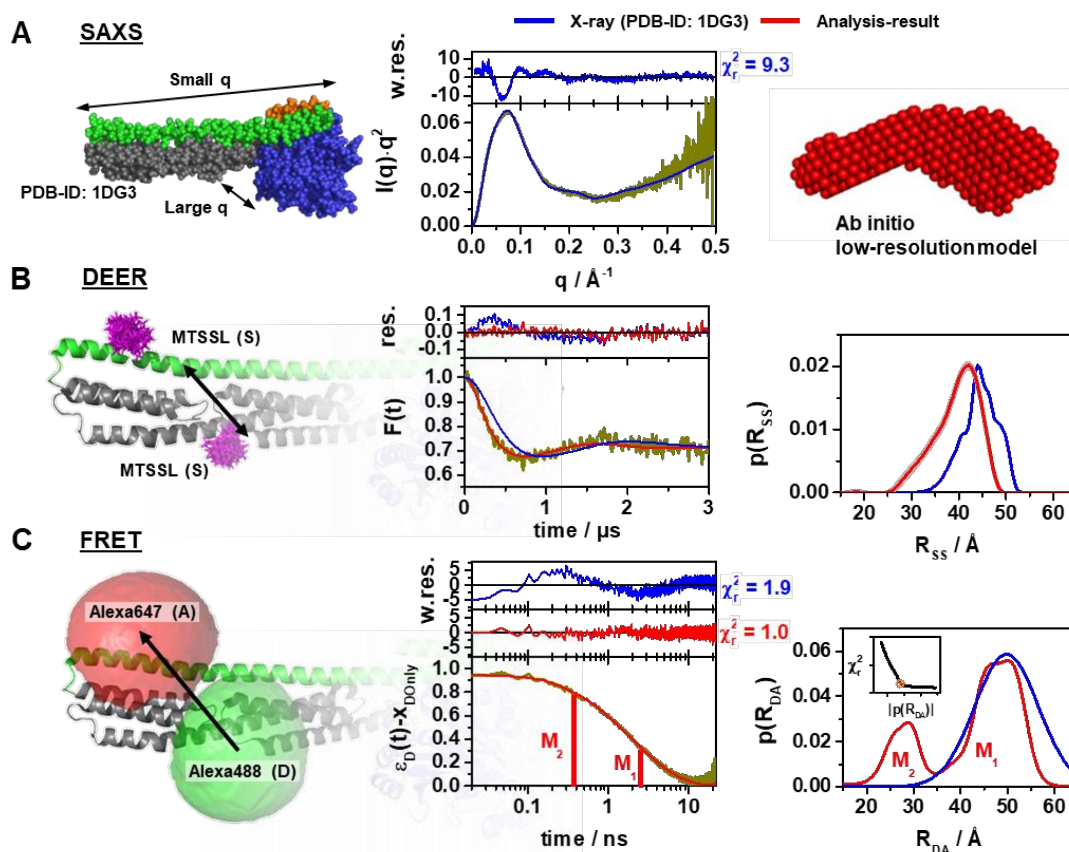


**Figure 2 | Probing the structure of hGBP1 in solution experimentally.** The left panels illustrate the characteristic properties probed by the experimental techniques – (A) small angle X-ray scattering (SAXS), (B) double electron-electron resonance spectroscopy (DEER), and (C) Förster resonance energy transfer spectroscopy (FRET); the middle panels display representations of the experimental ensemble data (dark yellow curves), and the right panels show analysis results thereof. Model-free analyses of the data are presented in red. Predicted experimental data based on a full-length X-ray crystal structure of hGBP1 (PDB-ID: 1DG3) are shown in blue. To the top of the experimental curves, either data noise weighted, w.res., or unweighted residuals, res., are shown (middle panels). In SAXS the scattered intensity  $I(q)$  is measured as a function of the scattering vector  $q$ . For better illustration,  $I(q)$  is presented in a Kratky-plot (A: middle). SAXS *ab initio* bead modeling determines an average shape of hGBP1 in solution (A: right). DEER and FRET experiments sense distances between labels that are flexibly coupled to specific labeling sites (exemplified for the double cysteine variant Q344C/A496C). The DEER experiments measured the dipolar coupling between two MTSSL spin-labels (left panel, magenta). FRET experiments measure the energy transfer from a donor fluorophore (D, Alexa488, green) to an acceptor fluorophore (Alexa647, red). In DEER (center) and time-resolved FRET experiments (middle), time-dependent responses of the sample inform on the inter-label distance distributions (right panels). Recovered distance distributions are compared to structural models by simulating the spatial distribution of the labels around their attachment point (left panels). The spatial distributions of the MTSSL-labels (B: left), as well as the donor and acceptor dye (c: left), are shown in magenta, green, and red, respectively. DEER-traces,  $F(t)$ , analyzed by Tikhonov regularization (red curve) recover inter-spin distance distributions,  $p(R_{SS})$ . Fluorescence intensity decays of the donor analyzed by the maximum entropy method (MEM) recover donor-acceptor distance distributions,  $p(R_{DA})$ . The inset displays the L-curve criterion of the MEM reconstruction for the presented data set. The FRET-induced donor decay,  $\varepsilon_D(t)$ , represents the fluorescence decays.<sup>(29)</sup>  $\varepsilon_D(t)$  is corrected for the fraction of FRET-inactive molecules,  $x_{DOnly}$ , in the sample. The shape of  $\varepsilon_D(t)$  reveals characteristic times (labeled  $M_1$  and  $M_2$ ) that correspond to peaks in  $p(R_{DA})$ . To the right inter-label distance distributions for DEER and FRET are shown.

A model free analysis of the Q344C/A496C DEER data by Tikhonov regularization (**Methods 3**) revealed a clear shift of  $\sim 2.5 \text{ \AA}$  towards shorter distances for the experimental inter-spin distance distribution  $p(R_{SS})$  compared to the average distance simulated for an X-ray structure (PDB-ID: 1DG3) using a rotamer library analysis approach (RLA)(30) to account for the conformational space of the spin label side chain (**Fig. 2B**, right, **Methods 3**). This indicates that the protein exhibits conformations, where the spin-labels come closer than suggested by the crystal structure. Overall, the  $p(R_{SS})$  of all eight DEER measurements were unimodal (**Fig. S2**). Their experimental average distances,  $\langle R_{SS,exp} \rangle$ , differ from the RLA-predicted distances,  $\langle R_{SS,sim} \rangle$ , by  $1.0 \text{ \AA}$  to  $3.6 \text{ \AA}$  (**Tab. S1A**). The RLA approach does not account for protein backbone dynamics. Thus, we anticipated finding narrower  $p(R_{SS})$  in the simulations than in the experiments. Yet, for the variants Q344C/Q525C and Q344C/V540C the experimental  $p(R_{SS})$  are even narrower than the  $p(R_{SS})$  predicted by RLA for the crystal structure (**Tab. S1A**). This reduced spread of possible inter-spin distances indicates a reduced conformational freedom of the spin-labeled side chains due to a denser packing of the spin label(s) with the neighboring side chains and/or backbone elements than predicted from the crystal structure.

Our ensemble and single-molecule FRET measurements (**Methods 4**) were paralleled by the following control studies confirming that the probes can accurately report on inter-fluorophore distance distributions,  $p(R_{DA})$ , of a molecular ensemble representative for the wild-type protein (**Supplementary Note 1**). (i) Single-molecule anisotropy measurements (**Fig. S3A**, **Tab. S1A**) and control samples in the absence of FRET (**Tab. S1B**) validate the model of a mobile dye only weakly quenched by its local environment. (ii) Activity assays demonstrate that the dyes and the introduced Cys mutations only weakly affect the protein function (**Supplementary Note 1**, **Fig. S4**). To recover inter-fluorophore distance distributions,  $p(R_{DA})$ , we applied ensemble time-correlated single photon counting (eTCSPC) to record high-precision fluorescence intensity decays  $f_{DD}^{(DA)}(t)$  and  $f_{DD}^{(D0)}(t)$  of donor (D) fluorophores in the presence (DA) and the absence (D0) of acceptor (A) fluorophores, respectively.(29) The measured fluorescence decays are available in a public data repository (**Data availability**). We computed the FRET-induced donor decay  $\varepsilon_D(t) \equiv f_{DD}^{(DA)}(t)/f_{DD}^{(D0)}(t)$  to directly visualize  $p(R_{DA})$  in a semi-logarithmic plot of  $\varepsilon_D(t)$  where the position (time) and the height (amplitude) of steps recover DA distances and species fractions, respectively.(29)  $\varepsilon_D(t)$  of the variant Q344C/A496C clearly revealed two distances - a hallmark for hGBP1's conformational heterogeneity. (**Fig. 2C**, center). An analysis of  $f_{DD}^{(DA)}(t)$  by the maximum-entropy method (MEM) resolved a

bimodal distance distribution  $p(R_{DA})$  (**Fig. 2C**, right) with a *major* and *minor* subpopulation. To associated conformational states are referred to as  $M_1$ , and  $M_2$ , respectively (**Fig. 2C**, right). For an unambiguous assignment of the experimental distances to the conformational states, all 12 datasets (**Fig. 1**) were analyzed by a joint/global quasi-static homogeneous FRET-model (29)) for all samples with shared species fractions of  $M_1 = 0.61$  and  $M_2 = 0.39$  (**Tab. S1A**) at room temperature.

To compare theoretical and experimental average DA distances  $\langle R_{DA} \rangle$  and distance distributions  $p(R_{DA})$ , we need (1) a dye model that predicts the spatial distributions of the flexibly linked dyes for given structural models(31,32) and (2) reliable uncertainty estimates of the experimental distances (**Supplementary Note 1**). To account for variable interactions of the dyes with the protein surface, we performed accessible contact volume (ACV) simulations of the dye, that consider both, the accessible volume of free dye and the fraction of dye bound at the protein's surface.(33) ACV simulations have the attractive feature that the fraction of surface bound dyes needed for calibration is a direct experimental observable registered in the time-resolved anisotropy decays via the residual anisotropies (**Tab. S1A**). Moreover, we validated the ACV approach by confirming that the fluorescence decays of the donor exhibited no significant additional quenching beyond the quenching anticipated for a dye freely diffusing within an ACV (**Supplementary Note 1**).

Overall, in the FRET measurements,  $M_1$  agreed better with the X-ray structure than  $M_2$  (**Fig. 2C**, right, **Tab. S1A**) - the sum of uncertainty weighted squared deviations,  $\chi_{FRET}^2$ , for  $M_1$  is significantly smaller than for  $M_2$  ( $\chi_{FRET}^2(M_1, 1DG3) \sim 17$  vs.  $\chi_{FRET}^2(M_2, 1DG3) \sim 1500$ ). In an F-test, this corresponds to a p-value > 0.999. Thus, considering statistical uncertainties, potential systematic errors, uncertainties of the orientation factor, and uncertainties of the ACVs due to the differences of the donor and acceptor linker length, (**Supplementary Note 1**), we conclude that  $M_1$  is more like the X-ray structure than  $M_2$ . Remarkably, an analysis of the fluorescence decays for the variants A496C/V540C and T481C/Q525C, which were designed to test the stability of helix  $\alpha 12$ , revealed identical distances for  $M_1$  and  $M_2$  (**Tab. S1A**). Hence, we corroborate that helix  $\alpha 12$  is predominantly extended, like the helix found in the solved crystal structures (e.g., PDB-ID: 1DG3). The variants N18C/Q344C and Q254C/Q344C, probing distances between the middle- to the LG domain, revealed only relatively minor differences between  $M_1$  and  $M_2$ , while for the variants designed to interrogate motions from the middle- to the helices  $\alpha 12/13$ ,  $M_1$  and  $M_2$  were significantly different.



To sum up, EPR-DEER at cryogenic temperatures detected small deviations to the crystal structure while SAXS and FRET detected clear deviations at room temperature. Presumably, due to the longer linkers used in the FRET experiments leveraging differences, we resolved the experimental DA-distance distributions  $p(R_{DA})$  into two states. Temperature dependent measurements revealed that these states found at room temperature are similarly populated at higher intracellular temperatures (**Supplementary Note 1 (section 2), Fig. S4D**).

### Identification and quantification of molecular kinetics

To probe the conformational dynamics of hGBP1, we performed single-molecule (sm) FRET experiments with Multiparameter Fluorescence Detection (MFD) (**Methods 4**) and Neutron Spin Echo (NSE) experiments (**Methods 5**),<sup>(34,35)</sup> While the NSE experiments are most sensitive up to a correlation time of 200 ns, the filtered fluorescence correlation spectroscopy (fFCS) analyses of our MFD experiments are most sensitive from sub-microseconds to milliseconds. Thus, by combining NSE with MFD-fFCS, we effectively probe for conformational dynamics from nano- to milliseconds.

An analysis result of the NSE data is visualized in **Fig. 3A**, which displays the scattering vector,  $q$ , dependent effective diffusion coefficient  $D_{eff}$  extracted from the initial slope of the NSE spectra measured up to 200 ns (**Fig. S5A**). The translational diffusion coefficient  $D_T$  of the protein was obtained from dynamic light scattering (DLS) at the same concentration (**Methods 5**). The diffusion coefficient of a single protein increases from the translational diffusion  $D_T$  measured at low  $q$  (DLS) due to contributions from rotational diffusion  $D_R(q)$  and contributions related to internal protein dynamics  $D_{int}(q)$  as the observation length scale  $2\pi/q$  covers the protein size. The translational and rotational diffusion coefficients  $D_T$  and  $D_R(q)$  were calculated and corrected for hydrodynamic interactions and interparticle effects to result in the expected  $D_0(q)$  for a rigid body (**Fig. 3A**, black line, **eq. 18**). The measured  $D_{eff}(q)$  agrees well with the theoretical calculations accounting for rigid body diffusion alone. A significant additional contribution of internal protein dynamics to the measured effective diffusion coefficients cannot be identified. The same result was obtained by directly optimizing the parameters of an analytical model describing rigid protein-diffusion (**eq. 19**) to the NSE spectra (**Fig. S5B**). Hence, the overall internal protein dynamics may only result in negligible amplitude, i.e., minor overall shape changes, within the observation time up to 200 ns.

To study structure and dynamics from sub- $\mu$ s to ms we performed MFD smFRET experiments on freely diffusing molecules briefly (milliseconds) diffusing through a confocal detection volume. We performed a burst-wise analysis of the MFD data for each detected molecule to

determine the fluorescence weighted average lifetime of the donor,  $\langle\tau_{D(A)}\rangle_F$ , and the intensity-based FRET efficiency,  $E$  (**Methods 4**).<sup>(35)</sup> MFD diagrams, which are multidimensional frequency histograms of parameters determined for single molecules, directly visualize heterogeneities among the molecules. In a MFD-diagram of  $E$  and  $\langle\tau_{D(A)}\rangle_F$  the “static FRET-line” serves as a reference to detect fast conformational dynamics.<sup>(36)</sup> A shift of a peak from the static FRET line towards longer  $\langle\tau_{D(A)}\rangle_F$  indicates fast conformational dynamics within the observation time of the molecules ( $\sim$ ms) (**Methods 4**).<sup>(35,36)</sup> In all 12 FRET variants, only single peaks were visible in the 2D-histograms for the DA labeled molecules (**Fig. 3B**, **Fig. S3A**). In 8 out of 12 variants, we found clear indications of dynamics by a peak shift of the FRET molecules off the static FRET-line towards longer  $\langle\tau_{D(A)}\rangle_F$  (**Fig. S3A**). Analogous to relaxation dispersion experiments in NMR, such shifts confirm that  $M_1$  and  $M_2$  are in an exchange faster than the integration time of the molecules ( $\sim$ milliseconds).<sup>(35,36)</sup> A detailed analysis of the fluorescence decays of the FRET sub-ensembles (**Fig. S3B**) by a two-component model revealed limiting states (**Tab. S1C**) agreeing with the eTCSPC measurements (**Tab. S1A**). Hence, the peak positions in the MFD histograms are consistent with the eTCSPC analysis and are captured by dynamic FRET-lines, which describe the mixing of the two states (**Fig. 3B**, **Fig. S3A**).

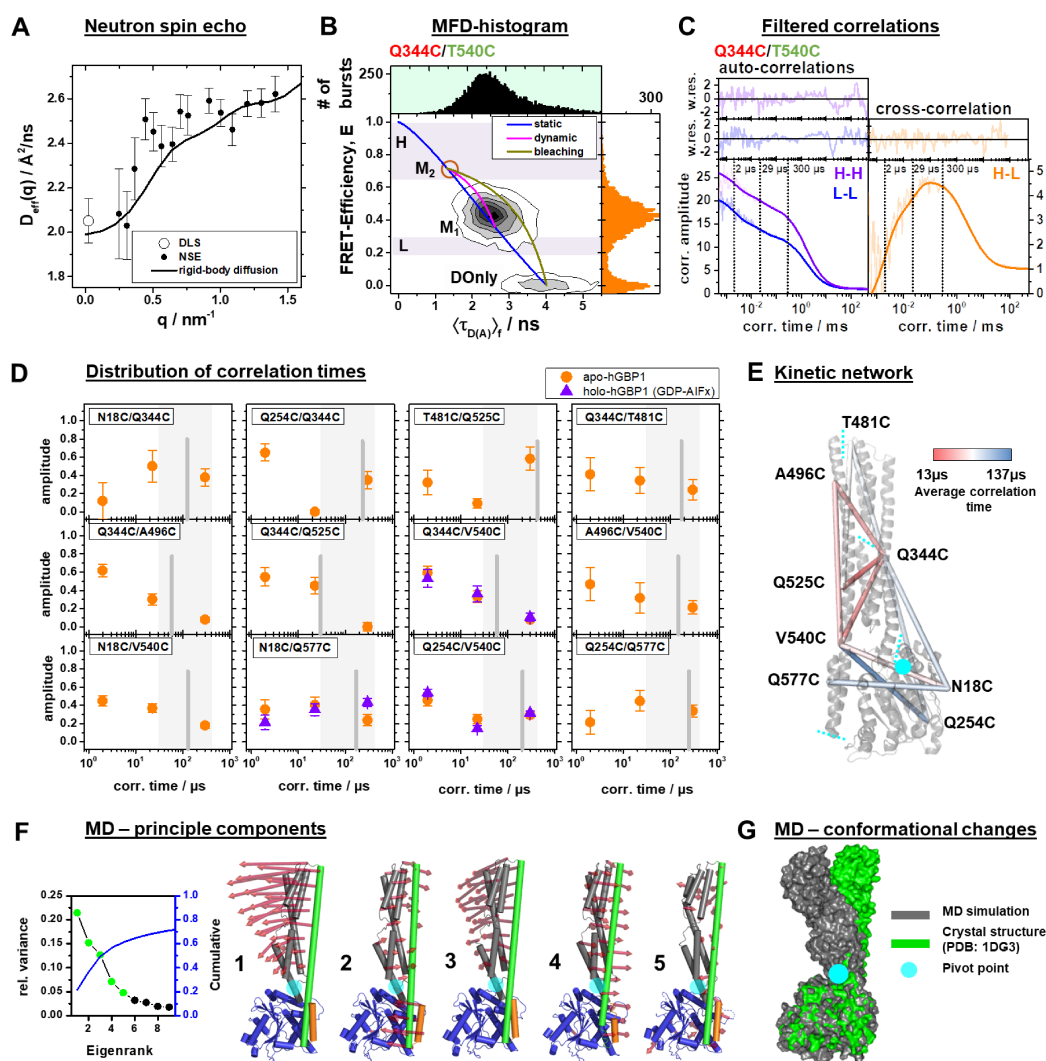


**Figure 3 | Conformational dynamics of hGBP1 studied by NSE, smFRET with multi-parameter fluorescence detection (MFD), and molecular dynamics (MD) simulations.** (A) NSE studies of effective diffusion coefficients of hGBP1,  $D_{eff}$ , determined by NSE and DLS compared to a model describing only the translational and rotational diffusion of the protein by a rigid-body as a function of the scattering vector,  $q$ . The agreement of the measured effective diffusion coefficients with the calculated values demonstrates insignificant shape changes of hGBP1 as sensed by NSE on fast time scales up to 200 ns. (B) A two-dimensional single-molecule histogram displays absolute FRET-efficiencies,  $E$ , and the fluorescence weighted average lifetimes of the donor in the presence of FRET,  $\langle\tau_{D(A)}\rangle$ , for the FRET-labeled double cysteine variant Q344C/V540C. The one-dimensional histograms are projections of the 2D histogram. The color of the variant's name indicates the location of the donor (green) and acceptor (red) determined by analysis of time-resolved anisotropy decays. The static-FRET line (blue) relates  $E$  and  $\langle\tau_{D(A)}\rangle$  for static proteins with a single conformation. The dynamic FRET line (magenta) describes molecules changing their state from  $M_1$  to  $M_2$  (brown circles) and *vice-versa* while being observed. The states  $M_1$  and  $M_2$  were identified by  $\epsilon$ TCSPC (Tab. S1A) and sub-ensemble TCSPC (Fig. S3B, Tab. S1C). Molecules in the state  $M_2$  with bleaching acceptors are described by a dark yellow line, which describes the transitions from  $M_2$  to the donor only population (DOnly). The highlighted areas refer to the groups of molecules (H for high FRET, L for low FRET) selected for the generation of fluorescence lifetime filters for filtered FCS (fFCS). (C) fFCS Q344C/T540C with H and L filters. To the left the species autocorrelation functions ( $sACF$ ) and to the right, a species cross-correlation function ( $sCCF$ ) are shown as semitransparent lines overlaid by model functions shown as solid lines (eq. 17). The fFCS model parameters were determined by a joint/global analysis of all 12 FRET-pairs (Fig. S3C, Tab. S2) revealing at least three correlation times (vertical dotted lines). The weighted residuals for the global analysis are shown to the top. (D) The analysis of the fFCS curves assigned to every variant

amplitudes and correlation times shown for the GTP free apo- (orange circles) and GDP-AIF<sub>x</sub> bound holo-state (violet triangles). The average correlation times for the variants are shown as gray vertical lines. The gray box highlights the minimum and maximum of the average correlation times for all variants. **(E)** For visualization, the average correlation times of the apo-state were mapped to a crystal structure (PDB-ID: 1DG3, see G) by color-coded bars connecting the C $\alpha$ -atoms of labeled amino acids. The sections of the five derived rigid bodies are displayed by cyan dashed lines. **(F)** First five principle components of molecular dynamics (MD) and accelerated molecular dynamics (aMD) simulations starting from the crystal structure (PDB-ID: 1DG3). The LG domain, the middle domain, and the helix  $\alpha$ 12, and  $\alpha$ 13 are colored in blue, gray, green, and orange, respectively. The red arrows indicate the direction of the motion. The components were scaled by a factor of 1.5 for better visibility. The semi-transparent cyan circle corresponds to a pivot point located at the LG domain. To identify correlated motions in the MD and aMD simulations, we performed principal component analysis (PCA, **Supplementary Note 2**). The first five principal components (PCs) sorted by the magnitude of the eigenvalues, contribute to 60% of the total variance of all simulations. **(G)** Superposition of a MD trajectory frame (gray) deviating the most in RMSD ( $\sim$ 8 Å) from the crystal structure (green). Both structural models were aligned to the LG domain.

For two states in dynamic exchange ( $M_1 \rightleftharpoons M_2$ ) under equilibrium conditions, we expected to find a single correlation time. To quantify the precise time-scale(s) of the exchange among the conformers detected by FRET, we analyzed the species cross-correlation functions (*sCCF*) and the species autocorrelation functions (*sACF*) determined by ffCS (**Fig. S3C**) and displayed the results as relaxation time spectra, where the normalized amplitudes are plotted versus the correlation time (**Fig. 3D**). Surprisingly, each individual set of *sCCF* and *sACF* of the 12 FRET pairs required at least two correlation times to be fully described. This is an indication for more complex kinetics or more (kinetic) states, which are unresolved by the analysis of the fluorescence decays. In a global analysis of all 12 variants (**eq. 17**), where we treat all 48 ffCS curves (two *SACF* and *SCCF* per variant) as a single dataset and we recovered three joint correlation times of 2, 23 and 297  $\mu$ s (**Fig. 3C**). However, the amplitudes of the relaxation times differ significantly so that the average relaxation time varies approximately by one order of magnitude (gray bars in **Fig. 3D**). Intriguingly, this global analysis reveals a variant-specific amplitude distribution of correlation times and highlights significant differences among the variants (**Fig. 3D**, **Fig. S3C**, **Tab. S2**). In most cases, the shortest correlation time has the highest amplitude. This is consistent with the MFD histograms, because we detected shifted/dynamic unimodal peaks. To visualize the dynamics detected by ffCS, we mapped the average correlation times color coded to the FRET network shown on top of a protein X-ray structure (**Fig. 3E**). This visualization highlights that the fast dynamics is mainly associated with the helices  $\alpha$ 12/13 and the middle domain, while the slow dynamics is predominantly linked to the LG domain.

Referring to the sketch in **Fig. 1B**, we hypothesize that the states  $M_1$  and  $M_2$  and the transition among them are of functional relevance (pathway *i*). Therefore, we studied the effect on the dynamics exerted by the ligand GDP-AIF<sub>x</sub> as a substrate that mimics the holo-state hGBP1:L. The GDP-AIF<sub>x</sub> concentration was sufficiently high (100  $\mu$ M) to fully induce dimerization for hGBP1 at  $\mu$ M concentrations.<sup>(15)</sup> For comparison, the affinity of hGBP1 for mant-GDP is  $\sim$ 3.5

$\mu\text{M}$  and much higher for GDP-AIF<sub>x</sub>.<sup>(37)</sup> Hence, in the sm-measurements GDP-AIF<sub>x</sub> was bound to the LG domain while hGBP1 (20 pM) was still monomeric. We refer to this as the holo-form of the protein and selected a set of variants (N18C/Q577C, Q254C/V540C, Q344C/V540C) for which we found large substrate induced effects at higher hGBP1 concentrations due to oligomerization. Surprisingly, the amplitude distribution of the correlation times is within errors indistinguishable from the measurements of the nucleotide-free apo forms (**Fig. 3D**). Moreover, the FRET observables did not change either.

In conclusion, our integrative study on the structure and dynamics yielded the four major results: (1) We identified heterogeneous conformational ensemble that can be approximated by two majorly populated conformers  $M_1$  and  $M_2$ .  $M_1$  is similar to the crystal structure. (2) NSE detects no significant shape changes of hGBP1 on a time-scale up to 200 ns. (3) For the exchange  $M_1 \rightleftharpoons M_2$  probed by fFCS, we expected to find a single correlation time but found a complex distribution of correlation times spanning the  $\mu\text{s}$ -range. Therefore, we propose for the motion of  $\alpha 12/13$  relative to the LG and the middle domain additional intermediate conformational states, resolved by their kinetic fingerprint captured by fFCS. (4) hGBP1's kinetics between the middle domain and  $\alpha 12/13$  is unaffected by the presence of a nucleotide analog as a substrate.

### **Essential motions determined by molecular dynamics simulations**

We performed molecular dynamics (MD) simulations without experimental restraints to assess the structural dynamics of the full-length crystal structure at the atomistic level and to capture potential motions of hGBP1 (**Methods 6, Supplementary Note 2**). The apo (PDB-ID: 1DG3) and a GTP bound holo-form of hGBP1 were simulated in three replicas by conventional MD simulations for 2  $\mu\text{s}$  each (**Fig. S6A**). Additionally, accelerated molecular dynamics (aMD) simulations, which proved to sample the free-energy landscape of a small protein (58 amino acids) 2000-fold more efficiently<sup>(38)</sup>, were performed in two replicas of 200 ns each. Autocorrelation analysis of the RMSD vs. the average structure of the MD simulations reveals fast correlation times. The average correlation time in the presence and the absence of GTP were 11 ns and 17 ns (**Fig. S6B**). However, note that the amplitude of the fluctuations is, on average, below an RMSD of 3 Å, which is below the resolution limit of our NSE measurements. In the MD simulations, larger conformational changes (RMSD > 7 Å) with considerable shape changes were very rare events. A principle component analysis revealed kinking motions of the middle domain and helix  $\alpha 12/13$  around a pivot point as most dominant motions in the MD simulations (**Fig. 3F**). A visual inspection of structures deviating most from the mean reveals a

kink at the connector of the LG and the middle domain (**Fig. 3G**) consistent with rearrangements required for average shape as recovered by SAXS (**Fig. 2**).

To sum up, the MD simulations cover only time-scales of a few microseconds. Nevertheless, they indicated potential directions of motions and identified a pivot point between the LG and the middle domain. In agreement with NSE on the simulation time-scale, the overall shape is majorly conserved, and large conformational changes are rare events. The helices  $\alpha_{12/13}$  were mobile and exhibited a limited “rolling” motion along the LG and middle domain that could connect the conformers  $M_1$  and  $M_2$  as suggested by our FRET studies.

### **Experimentally guided structural modeling**

We integrate the experimental evidence for alternative conformations beyond the crystal structure into structural models of hGBP1 (**Methods 7**). Considering the specific requirements of label-based methods(31,32) we previously demonstrated using synthetic data the reliability of MFD measurements for resolving short-lived conformational states by structural models of a large GTPase.(33) Here, we additionally integrate DEER and SAXS data in a joined framework for an unbiased meta-analysis (**Methods 7**) and generate quantitative structural models for hGBP1 in three major steps: (i) “*Data acquisition*”, (ii) “*Model generation*”, and (iii) “*Model discrimination*” (**Fig. 4A**). In a previous *in silico* benchmark study on the GTPase Alastin, we needed only 29 optimal chosen FRET pairs to achieve an accuracy vs. the target structures and a precision below 2 Å.(33) For the given set of 12 FRET and 8 DEER pairs of hGBP1 we expect to recover low-resolution models with an average RMSDs in the range of 8-15 Å, and aim to resolve hGBP1’s shape, domain arrangement, and topology.

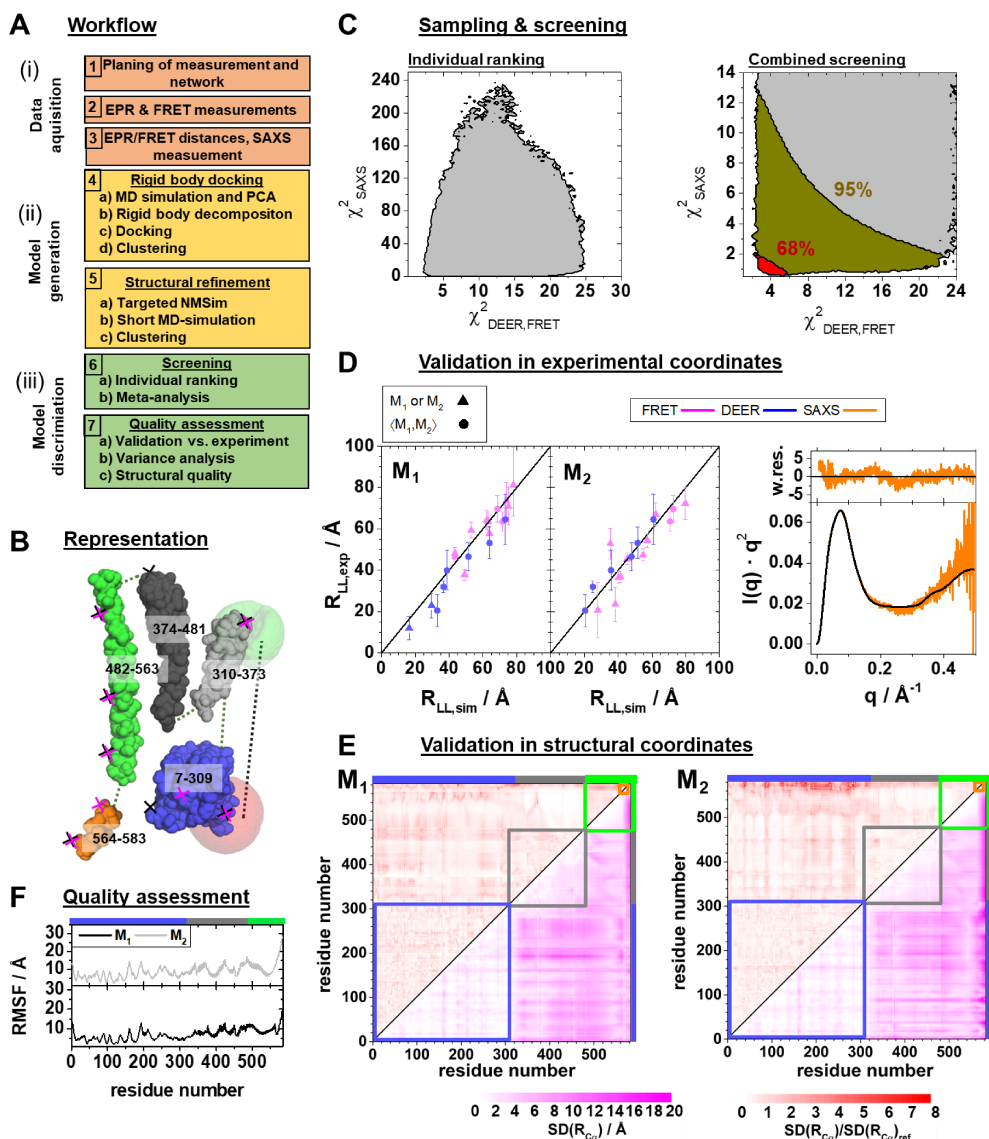


**Figure 4 | Generation and validation of structural models of hGBP1 by integrative modeling using DEER, ensemble FRET, and SAXS data.** (A) The applied workflow creates structural models in three steps: “Data acquisition”, “Model generation”, and a final “Model discrimination” step. The protocol for the generation of structural models combines a coarse-grained rigid body docking (RBD) approach<sup>(32)</sup> with a structural refinement step by NMSim<sup>(39)</sup> and molecular dynamics (MD) simulations. Rigid domains are identified for RBD by MD simulations and principal components analysis (PCA) thereof (**Supplementary Note 2**). Finally, the generated structural models are ranked and discriminated (screening) by the experimental data. (B) Representation of hGBP1 by a set of rigid bodies: LG-domain (blue), the middle domain (gray), helix  $\alpha_{12}$  (green), helix  $\alpha_{13}$  (orange). The middle domain was decomposed into two separate bodies. The amino acid ranges of the rigid bodies are given by the shown numbers. The crosses indicate the labeling positions for the FRET (black) and the EPR (magenta) experiments. The average fluorophore positions of an example FRET pair are shown as spheres within the accessible volumes of the dyes which are shown as semi-transparent green (donor) and red (acceptor) surfaces. (C) To the left a histogram of  $\chi^2_{SAXS}$  (eq. 22) and  $\chi^2_{DEER,FRET}$  (eq. 23) and for all pair of structural models ( $M_1, M_2$ ) is shown.  $\chi^2_{DEER,FRET}$  and  $\chi^2_{SAXS}$  are sums of weighted squared deviations and rank the pairs of structural models. To the right, a meta-analysis (eq. 25) fuses the probabilities derived from  $\chi^2_{DEER,FRET}$  and  $\chi^2_{SAXS}$  to discriminate pairs ( $M_1, M_2$ ). The red and the dark yellow areas highlight regions below a p-value of 0.68 and 0.95, respectively. For a given p-value all pairs of structural models with smaller p-values need to be accepted. (D) Comparisons of the individual experiments with the pair of structural models best agreeing with all experiments validate the model

by the data. Left diagrams (values see Tab. S3A): Experimental  $R_{LL,exp}$  (for DEER  $\langle R_{LL,exp} \rangle$  and FRET  $\bar{R}_{DA,exp}$ ) are compared to modeled average inter-label distances  $R_{LL,sim}$  (for DEER  $\langle R_{LL,sim} \rangle$  and FRET  $\bar{R}_{DA,sim}$ ). We use specific symbols to display inter-label distances  $R_{LL,exp}$  for label pairs with distinct ( $\blacktriangle$ ) and equal ( $\bullet$ ) values for  $M_1$  and  $M_2$ , respectively. For EPR  $R_{LL,exp}$  represents the average inter-label distance  $\langle R_{LL,exp} \rangle$  and for FRET  $R_{LL,exp}$  represents the central donor-acceptor distance  $\bar{R}_{DA,exp}$ . Right diagram: For SAXS, the theoretical scattering curve (black line) is directly compared to the experimental data (orange line) with weighted residuals to the top. (E) The standard deviation, SD, of the pair-wise C $\alpha$ -C $\alpha$  distance  $SD(R_\alpha)$  of the experimentally determined conformational ensemble with a p-value  $< 0.68$  (lower triangles) highlights the variability with possible models for  $M_1$  (left) and  $M_2$  (right). The  $SD(R_\alpha)$  normalized by the smallest possible  $SD(R_\alpha)_{ref}$  for the given set of distances and experimental noise (Methods 7) validates the selected models in structural coordinates. (F) For the structural models with a p-value  $< 0.68$ , the root mean square fluctuations of the C $\alpha$  atoms are displayed for the globally aligned ensemble.

**Data acquisition.** We initially assumed as prior knowledge that the crystal structure of hGBP1 corresponded to the solution structure and designed the above experiments to test this assumption (Fig. 4A, steps 1-3). **Model generation.** As we disproved this initial assumption, we employed the experimental data to generate new structural models by modifying our initial model (Fig. 4A, steps 4-5). For that, we sampled the experimentally allowed conformational space as vastly as possible by combining simulations of different granularity and computational complexity (Methods 7). First, we identify a set of rigid bodies (RBs) (Fig. 4B, Supplementary Note 4) using the information on the motions observed in the MD simulations (Fig. 3F), an order-parameter based rigidity analysis (Fig. S6C), knowledge on the individual domains within the dynamin family (40,41), position dependence of FRET and DEER properties (Tab. S1A) and SAXS experiments suggesting a kink in hGBP1's middle domain. To this RB assembly, we applied DEER and ensemble FRET restrains for guided rigid body docking (RBD) (Methods 7, Supplementary Note 5).(32) In this docking step, DEER and FRET restrains were treated by AV and ACV simulations, respectively. Next, all generated RBD structures were corrected for their stereochemistry using NMSim.(39) This was achieved by guiding the crystal structure in NMSim towards the RBD structures as templates minimizing the root mean squared deviation (RMSD) taking the uncertainties into account (Methods 7, Tab. S1A, D). These refined models were clustered into 343 and 414 groups for the states  $M_1$  and  $M_2$ , respectively (Methods 7). Group representatives were used as seeds for short (1-2 ns) MD-simulations of all 343 and 414 group representatives. The MD trajectories were clustered into 3395 and 3357 groups for  $M_1$  and  $M_2$ , respectively, before the model discrimination step by the DEER, FRET, and SAXS data (Methods 7).

**Model discrimination.** First, the structural models were ranked by their agreement with the individual techniques, using the quality measures  $\chi_{SAXS}^2$  and  $\chi_{DEER,FRET}^2$ , which capture deviations between the model and the data for SAXS and for the combined DEER and FRET



datasets, respectively (**Methods 7**). For maximum parsimony with respect to the modelled conformational states, the DEER, FRET and SAXS measurements were described by two states  $M_1$  and  $M_2$ . Theoretical SAXS curves for all structural models of  $M_1$  and  $M_2$  were calculated using the computer program CRY SOL. Using the theoretical SAXS curves all possible combinations of structural models for  $M_1$  and  $M_2$  were ranked by their agreement with the SAXS data in an ensemble analysis (**Fig. 4A**, step 6a; **Fig. 4C**, eq. 21). Like in the model free bead modeling of the SAXS data (**Fig. 2**), for the pair of structural models best agreeing with SAXS the middle domain is kinked towards the LG domain (**Fig. S1C**). The SAXS ensemble analysis reveals species population fractions for  $M_1$  in the range of  $\sim 0.1$ - $0.7$  (**Fig. S1D**, p-value = 0.68). For DEER and FRET measurements,  $M_1$  and  $M_2$  representatives were ranked by comparing the average simulated inter-label distances  $\langle R_{SS, sim} \rangle$  and  $\langle R_{DA, sim} \rangle$  with the corresponding experimental distances. The simulated average inter-label distances for  $M_1$  and  $M_2$  were determined by simulating the distribution of the labels around their attachment point (**Methods 7**).<sup>(30-32,42)</sup> Next, a meta-analysis by Fisher's method fused the experimental data and analysis to rank and discriminate the generated structural models in a statistically meaningful manner (**Fig. 4A**, step 6b). In this step, the meta-analysis considers estimates for the degrees of freedom (dof) of the model and the data (**Methods 7**). This way, we select well-balanced structural models and fully avoid fudge factors equalizing experimental contributions to the model (**Fig. 4C**, Combined screening). A stability test demonstrates that reasonably chosen dofs have only a minor influence on the results (**Fig. S6D**). In the final analysis, a p-value of 0.68 discriminated more than 95% of all structural models (**Fig. 4C**, red area; **Fig. S6E**), leaving 99 and 105 models with average RMSDs of 11.2 Å and 14.5 Å for  $M_1$  and  $M_2$ , respectively. For these structures, uncertainties are largest for  $\alpha 12/13$  (**Fig. 4E**).

**Quality assessment.** As the last step, we assessed the quality of the selected structures (**Fig. 4A**, step 7). For DEER and FRET, the consistency of the model with the experiment is demonstrated by comparing simulated distances to the analysis result of the experiment. This is visualized for the pair of structural models best agreeing with DEER, FRET and SAXS combined (**Fig. 4D**, left). For DEER such comparison was used to identify outliers (**Supplementary Note 1**, **Fig. S4E**). The SAXS measurements were compared to the model by calculated theoretical scattering curve (**Fig. 4D**, right). These representations demonstrate that the models capture the essential features of the experiments within the experimental uncertainties. The experimental uncertainties were propagated to model uncertainties through an exhaustive sampling of the model's conformational space. The model uncertainties are visualized by the experimental standard deviation of pair-wise  $C_\alpha$  distances,  $SD(R_{C_\alpha})$ , (**Fig. 4E**, lower triangles). This

representation reveals regions of low and high variability in the structural models. To assess the local quality of the models and check if their variabilities are larger than statistically expected, we compared the experimental precision  $SD(R_{C\alpha})$  to a reference precision  $SD(R_{C\alpha})_{ref}$  by computing the weighted (normalized) precision,  $SD(R_{C\alpha})/SD(R_{C\alpha})_{ref}$  (Methods 7, Fig. 4E upper triangles). The weighting reference  $SD(R_{C\alpha})_{ref}$  is the expected precision of "ideal and perfect" model ensembles, determined using the experimental uncertainties under the assumption, that the best experimentally determined model is the ground truth.

For  $M_1$ , this procedure yields a rather uniform distribution for the weighted precision of the recovered structural models that fluctuates around unity, the theoretical optimum (Fig. 4E, left). The distribution of the weighted precision for  $M_2$  looks also fine, except close to the C-terminus (end of helix  $\alpha_{12}$  and  $\alpha_{13}$ ) where the precision of the ensemble is worse than expected (Fig. 4E, right), presumably due to granularity of the model or systematic experimental errors.

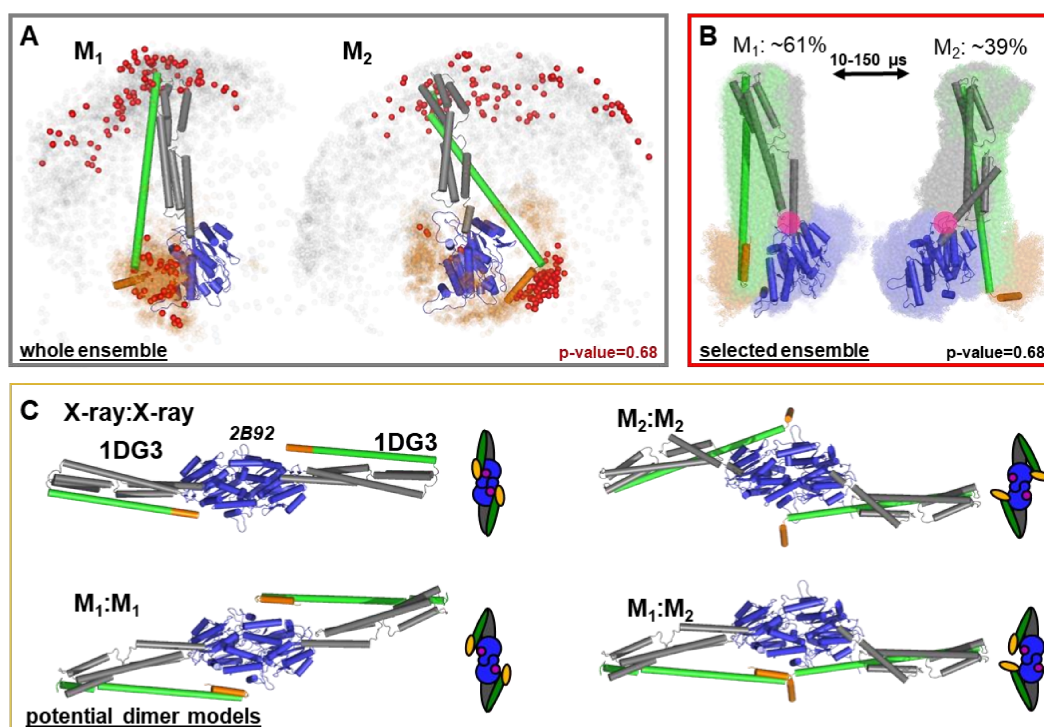


**Figure 5 | Selected conformers and potential dimer models of hGBP1 based on structures generated by integrative modeling of DEER, FRET, and SAXS data.** (A) All structural models for  $M_1$  and  $M_2$  were aligned to the LG domain and are represented by orange and gray dots, indicating the  $C\alpha$  atoms of the amino acids F565 and T481, respectively. The structural model best agreeing with all experiments is shown as cartoon representation. Non-rejected conformations ( $p$ -value = 0.68) are shown as red spheres. (B) Global alignment of all selected structural models ( $p$ -value = 0.68). In the center, the structure best representing the average of the selected ensembles is shown. The conformational transition from  $M_1$  to  $M_2$  with average correlation times in the range of 10 to 150  $\mu$ s can be described by a rotation around the connecting region of the LG and the middle domain (pivot point PP, shown as a magenta circle). (C) Potential hGBP1:hGBP1 dimer structures constructed by superposing the head-to-head interface of the LG domain (PDB-ID: 2B92) to the full-length crystal structure (1DG3), and both models of the states  $M_1$  and  $M_2$ . The LG and middle domain are colored in blue and gray, respectively. Helices

$\alpha_{12}$  and  $\alpha_{13}$  are colored in green and orange, respectively. As structural models for  $M_1$  and  $M_2$ , the structures best representing the ensemble of possible conformers are shown.

The heterogeneity of the structural ensembles is judged by their root mean square fluctuations (RMSF) (**Fig. 4F**). The RMSF values of both conformers  $M_1$  and  $M_2$  depend on the residue number and fluctuate around the expected range of  $\sim 7$  and  $\sim 9$  Å, respectively. To visualize differences among the structural models, we aligned the selected conformers to the LG domain. This demonstrates that in  $M_1$  and  $M_2$   $\alpha_{12/13}$  binds at two distinct regions of the LG domain (**Fig. 5A**, red spheres). In  $M_1$   $\alpha_{12/13}$  binds to the same side of the LG domain as in the full-length crystal structure (PDB-ID: 1DG3). In  $M_2$   $\alpha_{12/13}$  is bound to the opposing side of the LG domain. A global alignment of the conformations  $M_1$  to  $M_2$  and the best representatives of the ensembles visualize the transition between the two states. In our model a rearrangement of residues 306-312 results in a rotation of the middle domain around a pivot point (**Fig. 5B**, magenta circle). Such model describes the experimental data, the relocation of  $\alpha_{12/13}$ , and agrees well with global motions identified by PCA of the MD simulations. For the transitions from  $M_1$  to  $M_2$   $\alpha_{12/13}$  “rolls” along the LG domain, while the middle domain rotates towards the LG domain. Starting in  $M_1$ , which is comparable to the crystal structure except for a slight kink of the middle towards the LG domain, the movement of  $\alpha_{12/13}$  stops on the opposite side of the LG domain.

## Discussion

Our experimental findings on the structure of hGBP1 in solution can be approximated by two major conformations  $M_1$  and  $M_2$ , which are in dynamic exchange. We mapped the dynamics of hGBP1 by NSE spectroscopy and fFCS. NSE showed that hGBP1 is a protein without significant detectable shape changes on the ns-timescale up to 200 ns. However, fFCS that analyzed a network of FRET-pairs revealed considerable dynamics on slower time scales (2-300  $\mu$ s, **Fig. 3**). The distribution of dynamics over such a wide range are indicative for a frustrated potential energy landscape. Structural models for  $M_1$  and  $M_2$  based on SAXS, DEER and FRET data revealed that the middle domain kinks towards the LG domain and that the helices  $\alpha_{12/13}$  are bound on opposite sides of the LG domain. These findings are self-consistent, as (1) the conformational transition from  $M_1$  to  $M_2$  and vice versa is complex and may result in a distribution of relaxation times, indicating a rough energy landscape with several intermediates, and (2) the dynamics is mainly associated to  $\alpha_{12/13}$ . Analogous to protein folding, where Chung *et al.*(43) monitored the transition from the unfolded to the folded state and defined a transition path time, it would be intriguing to define an effective time for the conformational transition from  $M_1$  to  $M_2$ . The conformational transition time would be

definitively a convolute between all observed relaxation times (**Fig. 3, Tab. S2**) and is expected to be in the sub-millisecond time range. To sum up, the experiments can be described by two conformational states separated by a rugged energy landscape, resulting in slow transition invisible on the NSE timescale. The smFRET measurements demonstrate that this transition is an intrinsic property of hGBP1 that does not depend on the presence of substrate (pathway (i) in **Fig.1B**).

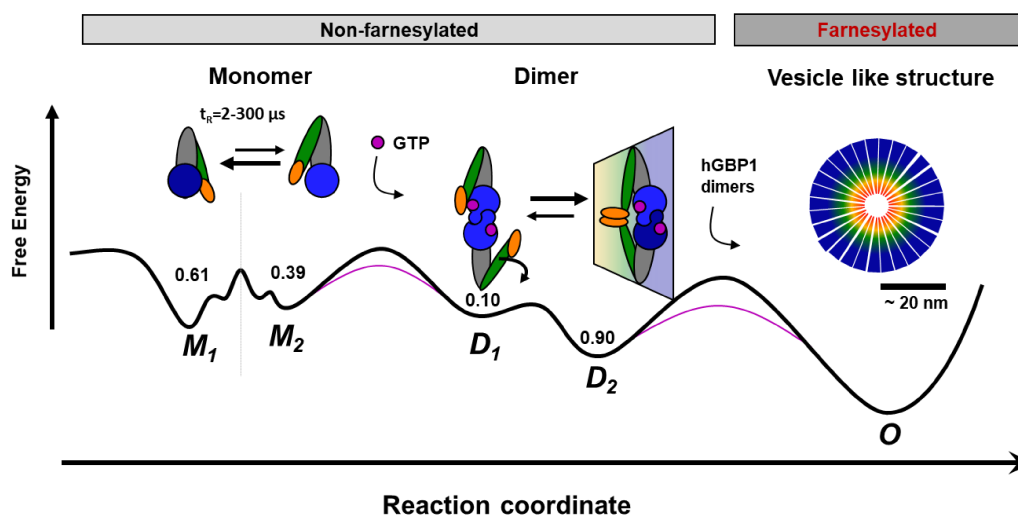


**Figure 6 | Potential oligomerization pathways of the human guanylate binding protein 1 (hGBP1) summarizing current experimental findings (15,17,20,24).** In the presence and absence of a nucleotide, hGBP1 is in a conformational exchange between at least two conformational states  $M_1$  and  $M_2$  with a correlation time of 2-300  $\mu$ s. Binding of a nucleotide to the LG domain activates hGBP1 for dimerization. After hGBP1 dimerization via the LG domains conformational changes of the middle domains and the helices  $\alpha_{12/13}$  lead to an association of both helices  $\alpha_{13}$ . The species fractions for respective populations are given as numbers on top of the wells of a schematic energy landscape (black line). The substrate GTP lowers the activation barrier (red line). Under turnover of GTP, farnesylated hGBP1 further self-assembles to form highly ordered, micelle-like polymers.

To understand the potential functional relevance of  $M_1$  and  $M_2$ , various observations should be considered. First, the oligomerization of hGBP1 is an important feature that demands flexibility of the structure as deduced from major structural rearrangements described so far.(20,24,44) In particular, large movements of the LG, the middle domain and helices  $\alpha_{12/13}$  against each other are required to establish the elongated building blocks of the polymer.(20) It is also most conceivable that various dynamically interchanging configurations of the sub-domains need to be sampled to assemble the highly ordered polymer. Dynamins and farnesylated hGBP1 are known to form highly ordered oligomers (20) requiring at least two binding sites. We previously showed that non-farnesylated hGBP1 forms dimers via the LG domains (in a head-to-head manner) and via helix  $\alpha_{13}$ (24) in the presence of a GTP analog. This finding is inconsistent with the crystal structures of the full-length protein (PDB-ID: 1DG3 and 1F5N) and for dimers formed by two hGBP1s in the same conformations, as within such dimers the helices  $\alpha_{13}$  are

on opposite sides and thus could not associate (**Fig. 5**). However, in a dimer formed of two distinct conformers ( $M_1:M_2$ ), the helices  $\alpha_{13}$  are located on the same side of their LG domains. Thus, in line with previous studies, which identified preferred pathways to increase the association yield of protein-protein complexes,<sup>(45)</sup> we suggest that, owing to the conformational flexibility, precursors necessary for oligomerization are already formed spontaneously before binding of the oligomerization-inducing substrate GTP. Remarkably, we detected virtually no substrate induced differences in the amplitude distribution of the correlation times demonstrating that the flexibility is independent of the bound nucleotide. Overall, the findings strongly suggest that the GTP induced dimerization of the GTPase domains and a substrate independent flexibility are needed for a dimerization of the effector domains (pathway *i* in **Fig. 1B**). The substrate solely facilitates hGBP1 association by increasing the affinity of the LG domain as a hub for dimerization.

Structure-wise, we found that the middle domain is kinked with respect to the LG domain as found for other dynamins <sup>(40,41)</sup>. Moreover, our data supports two conformations with distinct binding sites of helix  $\alpha_{12/13}$  that can be explained by major rearrangements of the region connecting the middle and the LG domain. Prakash et al. <sup>(21)</sup> described already the interconnecting region of LG and middle domain, which comprise residues 279-310 including a small  $\beta$ -sheet and  $\alpha$ -helix 6. The packing of helix  $\alpha_6$  (residues 291 to 306) against  $\alpha_1/\beta_1$  of the LG domain and against helix  $\alpha_7$  of the middle domain was hypothesized to stabilize the relative location of LG and middle domain against each other. Most intriguingly, the Sau group reported on the importance of helix  $\alpha_6$  for full catalytic activity of hGBP1 and for oligomer formation. They could also clearly establish the relationship between oligomer formation and defensive activity against hepatitis C virus showing that impairing catalytic activity and oligomer formation by mutations leads also to a decreased antiviral activity.<sup>(46)</sup> These observations support our conclusions as to the importance of the movements around the pivot point located close to  $\alpha$ -helix 6. Similar movements have been reported for other dynamin-like proteins, where the GTPase domain rearranges with respect to the middle domain along the catalytic cycle.<sup>(23,47)</sup>

Previous data<sup>(15,17,20,24)</sup> and our new findings in this work lead to a common model which describes the reaction pathway of hGBP1 from a monomer to the formation of mesoscale droplets *in vitro* and living cells (**Fig. 6**). All structural requirements for this multi-step conformational rearrangement for positioning the two interaction sites and defining the molecular polarity are already predefined in the monomeric hGBP1 molecule. In the absence of substrate and other GBP molecules, hGBP1 adopts at least two distinct conformational states.

Upon addition of GTP the LG domain is capable of binding to another protomer, whilst the conformational dynamics appear to remain unchanged. When two GTP bound hGBP1s associate, a head-to-head dimer either in a  $M_1:M_1$ ,  $M_2:M_2$  or a  $M_1:M_2$  configuration is formed. As the  $M_1:M_2$  dimer has a higher stability, in  $M_1:M_2$  the  $\alpha 13$  helices of the two subunits associate, the equilibrium is shifted towards the  $M_1:M_2$  dimers.(24)

Notably, *in vivo* helix  $\alpha 13$  is farnesylated at the end of a “CaaX” motif(7). Thus, hGBP1 provides a membrane anchor and now, hGBP1 dimers supposedly act as amphiphilic particles in the build-up of supramolecular structures. (20) This suggests, in line with the common knowledge that amphiphilic Janus particles can form liquid phases(48), that hGPB1 forms protein condensates and droplets, also referred to as vesicle like structures (VLS) in living cells. (15) *In vitro* studies (20) of farnesylated hGBP1 showed that the polymerization is driven by the GTP-dependent high-affinity association of the N-termini and the association of the lipophilic C-terminus. For hGBP1, the amphiphilicity depends on the presence of GTP. Beyond pure affinity driven phase separations in living cells(49), the time-dependent hydrolysis of GTP affects the lifetime of the GPB multimers and is responsible for their dynamic formation and dissolution. This allows for a fine controlled and orchestrated attack on a parasite by GPBs in response to the signaling cascade in activated cells (15).

It is also interesting to compare these features of hGBP1 with properties of proteins that exhibit phase separation and form condensates. The recent literature for phase separation (50) especially discusses proteins that form assemblies composed of modular interaction domains or large intrinsically disordered regions (IDR), which introduce flexibility to the scaffold of the condensate. An additional important factor for phase separation are multivalent interactions. If one compares these findings with the behavior of the well-folded hGBP1, it becomes obvious that hGBP1's intrinsic flexibility, multivalency and amphiphilicity after opening might be analogously essential for the formation of condensates. To conclude: (1) hGBP1 is multivalent with interaction sites of distinct affinities that define the polarity of the formed molecular assembly. The high affinities of LG domains ensure formation of a dimeric encounter complex already at low concentrations in the first step. The conformational flexibility of hGBP1's effector domain promotes the second key step for multimerization - the association of helices  $\alpha 13$  that makes the dimer amphiphilic. (2) The affinity of hGBP1 for membranes might be increased by a polybasic sequence directly adjacent to the CaaX box (<sup>582</sup>KMRRRK<sup>587</sup>). (16,51) Thus, an association of the  $\alpha 13$  helices does not only further stabilize the hGBP1 dimer, but also increase amphiphilicity and promote membrane association. (3) The GTP hydrolysis by

the LG domain controls the formation of the reversible formation of multimeric complexes by GBPs.

In a more general view, our results on hGBP1 demonstrate that the exchange between distinct protein conformations is usually encoded in its design (pathway *i*, **Fig. 1A**). Thus, the conformational flexibility of a protein can already be a characteristic of the apo form although this property is only relevant for a later stage of the protein's functional cycle, for example in a complex with its ligand, substrates and other proteins, respectively. Considering, for example, the movement of the substrate-dependent conformational transitions in the finger subdomain of a DNA polymerase,(52) it is obvious that these opening and closing movements are essential for catalyzing polymerization under ambient conditions. The rule that functionally relevant conformational equilibria may be predefined by protein design also applies to other steps in protein function. In future, when considering additional quantitative live-cell studies such integrative approaches may provide a molecular picture on complex biological processes like intracellular immune response.

## Materials and Methods

### 1 Protein expression and labeling

*Expression and purification.* All cysteine variants are based on cysteine-free hGBP1 (C12A/ C82A/ C225S/ C235A/ C270A/ C311S/ C396A/ C407S/ C589S) and were constructed in a pQE80L vector (Qiagen, Germany) following the instructions of the QuikChange site-directed mutagenesis kit (Stratagene, USA) according to (24,53). Previously, these mutations were shown to only weakly affect hGBP1's function.(24,53) New cysteines were introduced at various positions of interest (N18C, Q254C, Q344C, T481C, A496C, Q525C, 540C, Q577C). The mutagenesis was verified by DNA sequencing with a 3130xl sequencer (Applied Biosystems, USA). hGBP1 was expressed in *E. coli* BL21(DE3) and purified following the protocol described previously.(37) A Cobalt-NTA-Superflow was used for affinity chromatography. No glycerol was added to any buffer as it did not make any detectable differences. To not interfere with the following labeling reactions, the storage buffer did not contain DTT or DTE. Protein concentrations were determined by absorption at 280 nm according Gill and Hippel using an extinction coefficient of 45,400 M<sup>-1</sup> cm<sup>-1</sup>. Tests of enzyme activity and function demonstrate that the effect of mutations and labeling on hGBP1's function is small (**Supplementary Note 1**, section 2).

*Protein labeling.* FRET labeling was performed in two steps. First, the protein was incubated with a deficit amount of Alexa647N maleimide C2 (Alexa647) (Invitrogen, Germany). To start the first labeling reaction, a solution with a hGBP1 concentration 100-300  $\mu\text{M}$  in labeling buffer containing 50 mM Tris-HCl (pH 7.4), 5 mM  $\text{MgCl}_2$ , 250 mM NaCl was gently mixed with a 1.5-fold molar excess of Alexa647. After 1 hour incubation on ice, the unbound dye was removed using a HiPrep 26/20 S25 desalting column (GE Healthcare, Germany) with a flow rate of 0.5 ml/min. After this first labeling step, double, single and unlabeled proteins were separated based on the charge difference introduced by the coupled dyes using anion exchange chromatography on a ResourceQ column (GE Healthcare, Germany) and a salt gradient running from 0-500 mM NaCl over 120 ml at a pH of 7.4 and flow rate of 2.0 ml/min. The peaks in the elugram were analyzed for their degree of labeling (dol) by measuring their absorption by UV/Vis spectroscopy at a wavelength of 280 nm and 651 nm. The fraction with the highest, single-acceptor labeled protein amount was labeled with a 4-fold molar excess of Alexa488 C5 maleimide (Alexa488). The unreacted dye was separated as described for the first labeling step. Finally, the dol for both dyes was determined (usually 70-100% for each dye). The dols were determined by absorption using  $71,000 \text{ M}^{-1} \text{ cm}^{-1}$  and  $265,000 \text{ M}^{-1} \text{ cm}^{-1}$  as extinction coefficients for Alexa488 and Alexa647, respectively. The labeled proteins were aliquoted into buffer containing 50 mM Tris-HCl (pH 7.9), 5 mM  $\text{MgCl}_2$ , 2 mM DTT, shock-frozen in liquid nitrogen and stored at  $-80^\circ\text{C}$ .

The spin labeling reactions were conducted at  $4^\circ\text{C}$  for 3 hours using an 8-fold excess of (1-Oxyl-2,2,5,5-tetramethylpyrroline-3-methyl) methanethiosulfonate (MTSSL) as a spin label (Enzo Life Sciences GmbH, Germany). The reaction was performed in 50 mM Tris, 5 mM  $\text{MgCl}_2$  dissolved in  $\text{D}_2\text{O}$  at pH 7.4. Unbound spin labels were removed with Zeba Spin Desalting Columns (Thermo Fisher Scientific GmbH, Germany) equilibrated with 50 mM Tris, 5 mM  $\text{MgCl}_2$  dissolved in  $\text{D}_2\text{O}$  at pH 7.4. Concentrations were determined as described before. Labeling efficiencies were determined by double integration of CW room temperature (RT) EPR spectra by comparison of the EPR samples to samples of known concentration. In all cases, the labeling efficiencies were  $\sim 90\text{-}100\%$ .

## 2 Small angle X-ray scattering

*Experimental methods.* Small-angle X-ray scattering (SAXS) was measured on the beamlines X33 at the Doris III storage ring, DESY and on BM29 at the ESRF(54) using X-ray wavelengths of  $1.5 \text{ \AA}$  and  $1 \text{ \AA}$ , respectively. On BM29 a size exclusion column (Superdex 200 10/300 GL, GE Healthcare) coupled to the SAXS beamline was used (SEC-SAXS). The scattering vector  $q$  is defined as  $q = 4\pi/\lambda \cdot \sin(\theta/2)$  with the incident wavelength  $\lambda$  and the scattering angle  $\theta$ .



The measurements cover an effective  $q$  range from 0.015 to 0.40  $\text{\AA}^{-1}$  for X33 data and 0.006 to 0.49  $\text{\AA}^{-1}$  for BM29 data.

SAXS allows determining the shape and low-resolution structure of proteins in solution by the measured scattering intensity  $I(q)$ , which is proportional to the form factor  $F(q)$  multiplied by the structure factor  $S(q)$ .<sup>(55)</sup>  $F(q)$  informs about the electron distribution in the protein, while  $S(q)$  contains  $q$ -dependent modulations due to protein-protein interactions occurring at higher protein concentration. At sufficiently low protein concentrations (in the limit of  $c \rightarrow 0$ ) the structure factor converges towards unity. A concentration series (hGBP1 concentrations of 1.1, 2.1, 5.0, 11.5 and 29.9 mg/mL) was recorded on X33, whereas on BM29 two SEC-SAXS runs using protein concentrations of 2 mg/mL and 16 mg/mL that were loaded on the SEC column (used buffer for both SAXS and SEC-SAXS experiments: 50 mM TRIS, 5 mM  $\text{MgCl}_2$ , 150 mM NaCl at pH 7.9) have been performed. The SEC-SAXS data were averaged over the elution peak. The obtained SEC-SAXS data of the used high and low protein solutions were overlapping validating the infinite dilution limit. Therefore, the SEC-SAXS data recorded at the high protein concentration were used for further data analysis. An automated sample changer was used for sample loading and cleaning of the sample cell on X33. The storage temperature of the sample changer and the temperature during X-ray exposure in the sample cell were 10°C. The buffer was measured before and after each protein sample as a check of consistency. For each sample, eight frames with an exposure time of 15 sec each were recorded to avoid radiation damage. The absence of radiation damage was verified by comparing the measured individual frames. The frames without radiation damage were merged. On BM29 X-ray frames with exposure time of 1 sec were continuously recorded. The scattering contribution of the buffer and the sample cell was subtracted from the measured protein solutions. Measured background corrected SAXS intensities  $I(q,c)$  of the hGBP1 solutions are shown in **Fig. S1A**.  $I(q,c)$  were scaled by the protein concentration  $c$  and extrapolated ( $c \rightarrow 0$ ) to determine the form factor  $I(q,0)$  of the protein at infinite dilution. At larger  $q$ -values, where the structure factor equals unity, the extrapolated form factor overlapped with the SAXS data of the highest protein concentration within the error bars. Therefore, for better statistics the extrapolated form factor at small  $q$ -values and the data of the 29.9 mg/mL solution at larger scattering vectors were merged. The structure factor  $S(q,c)$  (**Fig. S1B**) was extracted by  $S(q,c) = I(q,c) / (c \cdot I(q,0))$  and fitted by a Percus-Yevik structure factor including the correction of Kotlarchyk *et al.* for asymmetric particles resulting in an effective hard sphere radius of 2.2 nm.<sup>(56)</sup>

*Analysis methods.* Data was analyzed using the ATSAS software package.<sup>(57)</sup> Theoretical scattering curves of the crystallographic and the simulated structures of the monomer were

calculated and fitted to the experimental SAXS curves using the computer program CRY SOL. The distance distribution function  $P(r)$  was determined using the program DATGNOM. *Ab initio* models were generated using the program DAMMIF. In total 20 *ab initio* models were generated, averaged and the filtered model was used. Normalized spatial discrepancy (NSD) values of the different DAMMIF models were between 0.8 and 0.9 indicative of good agreement between generated *ab initio* models. The resolution of the obtained *ab initio* model is  $29 \pm 2$  Å as evaluated by the resolution assessment algorithm.

### 3 EPR spectroscopy

*Experimental methods.* Pulse EPR (DEER) experiments were performed at X-band frequencies ( $\sim 9.4$  GHz) with a Bruker Elexsys 580 spectrometer equipped with a split-ring resonator (Bruker Flexline ER 4118X-MS3) in a continuous flow helium cryostat (CF935; Oxford Instruments) controlled by an Oxford Intelligent Temperature Controller ITC 503S adjusted to stabilize a sample temperature of 50 K. Sample conditions for the EPR experiments were 100  $\mu$ M protein in 100 mM NaCl, 50 mM Tris-HCl, 5 mM MgCl<sub>2</sub>, pH 7.4 dissolved in D<sub>2</sub>O with 12.5 % (v/v) glycerol-d<sub>8</sub>. Further details are described by Vöpel et al. (24).

DEER inter spin-distance measurements were performed using the four-pulse DEER sequence (58,59):

$$\frac{\pi}{2}(v_{obs}) - \tau_1 - \pi(v_{obs}) - t' - \pi(v_{pump}) - (\tau_1 + \tau_2 - t') - \pi(v_{obs}) - echo \quad (1)$$

with observer pulse ( $v_{obs}$ ) lengths of 16 ns for  $\pi/2$  and 32 ns for  $\pi$  pulses and a pump pulse ( $v_{pump}$ ) length of 12 ns. A two-step phase cycling (+  $\langle x \rangle$ , -  $\langle x \rangle$ ) was performed on  $\pi/2(v_{obs})$ . Time  $t'$  was varied with fixed values for  $\tau_1$  and  $\tau_2$ . The dipolar evolution time is given by  $t = t' - \tau_1$ . Data were analyzed only for  $t > 0$ . The resonator was overcoupled to  $Q \sim 100$ . The pump frequency  $v_{pump}$  was set to the center of the resonator dip (coinciding with the maximum of the EPR absorption spectrum). The observer frequency  $v_{obs}$  was set  $\sim 65$  MHz higher, at the low field local maximum of the EPR spectrum. Deuterium modulation was averaged by adding traces recorded with eight different  $\tau_1$  values, starting at  $\tau_{1,0} = 400$  ns and incrementing by  $\Delta\tau_1 = 56$  ns. Data points were collected in 8 ns time steps or, if the absence of fractions in the distance distribution below an appropriate threshold was checked experimentally, in 16 ns time steps. The total measurement time for each sample was 4 - 24 h.

*Analysis methods.* The DEER data was analyzed using the software DeerAnalysis which implements a Tikhonov regularization.(60) Background correction of the DEER signal dipolar evolution function  $V(t)$  (normalized to unity at the time  $t = 0$ )

$$V(t) = F(t) \cdot V_{background}(t), \quad (2)$$

was performed assuming an isotropic distribution of the spin-labeled hGBP1 molecules in frozen solution that is described by

$$V_{background}(t) = \exp(-k \cdot t). \quad (3)$$

Briefly, the resulting form factor  $F(t)$  is modulated with the dipolar frequency

$$\omega_{DD}(R_{SS}, \theta) = \frac{1}{4\pi} \cdot \frac{g^2 \mu_B^2 \mu_0}{\hbar} \cdot \frac{1}{R_{SS}^3} \cdot (3 \cos^2 \theta - 1), \quad (4)$$

that is proportional to the cube of the inverse of the inter-spin distance  $R_{SS}$  ( $\mu_B$ : Bohr magneton;  $\mu_0$ : magnetic field constant;  $\theta$ : angle between the external magnetic field and the vector connecting the two spins, for nitroxide spin labels the  $g$  values of both spins can be approximated with the isotropic value  $g \approx 2.006$ ). Analysis of the form factor  $F(t)$  in terms of a distance distribution  $p(R_{SS})$  was performed by a Tikhonov regularization. A simulated time domain signal

$$S(t) = K(t, R_{SS}) \cdot p(R_{SS}) \quad (5)$$

from a given distance distribution  $p(R_{SS})$  was calculated by means of a kernel function

$$K(t, R_{SS}) = \int_0^1 \cos[(3x^2 - 1) \cdot \omega_{DD} \cdot t] dx \quad (6)$$

with  $\omega_{DD}(R_{SS}) = \frac{2\pi \cdot 52.04 \text{ MHz nm}^{-3}}{R_{SS}^3}$  for nitroxide spin labels.

The optimum  $p(R_{SS})$  was found by minimizing the objective function

$$G_\alpha(P) = \|S(t) - V_{local}(t)\|^2 + \alpha \cdot \left\| \frac{d^2}{dr^2} p(R_{SS}) \right\|^2. \quad (7)$$

The regularization parameter  $\alpha$  was varied to find the best compromise between smoothness, i.e., the suppression of artifacts introduced by noise, and resolution of  $p(R_{SS})$ . The optimum regularization parameter was determined by the L-curve criterion, where the logarithm of the smoothness  $\left\| \frac{d^2}{dr^2} p(R_{SS}) \right\|^2$  of  $p(R_{SS})$  is plotted against the logarithm of the mean square deviation  $\|S(t) - V_{local}(t)\|^2$ , allowing to choose the distance distribution with maximum smoothness representing a good fit to the experimental data.

Theoretical inter spin label distance distributions for MTS spin labels attached to structural models have been calculated using the rotamer library analysis (RLA) implemented in the freely available software MMM (30).

#### 4 Fluorescence spectroscopy

*Experimental methods - eTCSPC.* Ensemble time-correlated single-photon-counting (eTCSPC) measurements of the donor fluorescence decay histograms were either performed on an IBH-5000U (HORIBA Jobin Yvon IBH Ltd., UK) equipped with a 470 nm diode laser LDH-P-C 470 (Picoquant GmbH, Germany) operated at 8 MHz or on a EasyTau300 (PicoQuant, Germany) equipped with an R3809U-50 MCP-PMT detector (Hamamatsu) and a BDL-SMN 465 nm diode laser (Becker & Hickl, Germany) operated at 20 MHz. The donor fluorescence was detected at an emission wavelength of 520 nm using a slit-width that resulted in a spectral resolution of 16 nm in the emission path of the machines. A cut-off filter (495 nm) in the detection path additionally reduced the contribution of the scattered light. All measurements were conducted at room temperature under magic-angle conditions. Typically,  $14 \cdot 10^6$  to  $20 \cdot 10^6$  photons were recorded at TAC channel-width of 14.1 ps (IBH-5000U) or 8 ps (EasyTau300). When needed, the analysis considers differential non-linearities of the instruments by multiplying the model function with a smoothed and normalized instrument response of uncorrelated room light. The fits cover the full instrument response function (IRF) and 99.9% of the total fluorescence. The IRFs had typically FWHM of 254 ps (IBH-5000U) or 85 ps (PicoQuant EasyTau300).

*Experimental methods - Single-molecule (sm) spectroscopy.* A beam of linearly polarized pulsed argon-ion laser (Sabre®, Coherent) was used to excite freely diffusing molecules through a corrected Olympus objective (UPLAPO 60X, 1.2 NA collar (0.17)). The laser was operated at 496 nm and 73.5 MHz. An excitation power of 120  $\mu$ W at the objective has been used during experiments. The fluorescence light was collected through the same objective and spatially filtered by a 100  $\mu$ m pinhole which defines an effective confocal detection volume of  $\sim 3$  fl. A polarizing beam-splitter divided the collected fluorescence light into its parallel and perpendicular components. Next, the fluorescence light passed a dichroic beam splitter that defines a “green” and “red” wavelength range (below and above 595 nm, respectively). After passing through band pass filters (AHF, HQ 520/35 and HQ 720/150) single photons were detected by two “green” (either  $\tau$ -SPADs, PicoQuant, Germany or MPD-SPADs, Micro Photon Devices, Italy) and two “red” detectors (APD SPCM-AQR-14, Perkin Elmer, Germany). Two SPC 132 single photon counting boards (Becker & Hickel, Berlin) have recorded the detected

photons stream. Thus, for each detected photon the arrival time after the laser pulse, the time since the last photon and detection channel number (so, polarization and color) were recorded.

*Conditions.* All ensemble and single-molecule FRET experiments were performed at room temperature in 50 mM Tris-HCl buffer (pH 7.4) containing 5 mM MgCl<sub>2</sub> and 150 mM NaCl. All ensemble measurements were performed at concentrations of labeled protein of approximately 200 nM. The single-molecule (sm) measurements were performed at concentrations of labeled protein of approximately 20 pM to assure that only single-molecules were detected. All sm MFD-measurements probing the hGBP1 apo state were performed under two conditions: (i) without unlabeled protein, and (ii) with 7.5 μM unlabeled protein to minimize the loss of labeled molecules due to adsorption in the measurement chamber. Both conditions gave comparable results. Due to the higher counting statistics, all results of the apo state reported in this work have been obtained for condition ii. To study also the ligand bound holo state hGBP1:L (Fig. 1B) by fFCS in Fig. 4D, we used the ligand GDP-AIF<sub>x</sub> as a non-hydrolyzable substrate. The ligand GDP -AIF<sub>x</sub> is formed *in situ* by diluting a stock solution with 30 mM AlCl<sub>3</sub> and 1 M NaF by 1:100 in the standard buffer containing 100 μM GDP and 20 pM labeled protein without unlabeled protein (condition i). All fFCS measurements of the hGBP1 apo and holo state, respectively, were performed under condition i.

*Fluorescence decay analysis.* Fluorescence intensity decays of the donor in the presence,  $f_{D|D}^{(DA)}(t)$ , and the absence of FRET,  $f_{D|D}^{(D0)}(t)$ , inform on DA distance distributions,  $p(R_{DA})$ . However, the local environment of the dyes may result in complex fluorescence decays of the donor  $f_{D|D}^{(D0)}(t)$  and the acceptor  $f_{A|A}^{(AD)}(t)$  even in the absence of FRET. Such sample-specific fluorescence properties were accounted for by donor and acceptor reference samples using single cysteine variants.  $f_{D|D}^{(D0)}(t)$  and  $f_{A|A}^{(A0)}(t)$  were formally described by multi-exponential model functions:

$$f_{D|D}^{(D0)}(t) = \sum_i x_D^{(i)} \exp\left(-\frac{t}{\tau_D^{(i)}}\right) \quad (8)$$

$$f_{A|A}^{(DA)}(t) = \sum_i x_A^{(i)} \exp\left(-\frac{t}{\tau_A^{(i)}}\right)$$

Here  $D|D$  refers to the donor fluorescence under the condition of donor excitation and  $A|A$  refers to the acceptor fluorescence under acceptor excitation. The individual species fractions  $x_D^{(i)}$  and  $x_A^{(i)}$  and lifetimes of the donor  $\tau_D^{(i)}$  and the acceptor  $\tau_A^{(i)}$  are summarized in **Tab. S1**.

We assume that the same distribution of FRET-rate constants quenches all fluorescent states of the donor (quasi-static homogeneous model (29)). Thus,  $f_{D|D}^{(DA)}(t)$  can be expressed by:

$$f_{D|D}^{(DA)}(t) = f_{D|D}^{(D0)}(t) \cdot \sum_i x_{RET}^{(i)} \exp(-t \cdot k_{RET}^{(i)}) = f_{D|D}^{(D0)}(t) \cdot \epsilon_D(t). \quad (9)$$

Where  $\epsilon_D(t)$  is the FRET-induced donor decay. The MFD measurements demonstrate that the major fraction of the dyes is mobile (**Supplementary Note 1**). Therefore, we approximate the  $\kappa^2$  by 2/3 and relate  $\epsilon_D(t)$  to the  $p(R_{DA})$  by:

$$\epsilon_D(t) = \int_{R_{DA}} p(R_{DA}) \cdot \exp\left(-t \cdot k_0 \cdot \left(\frac{R_0}{R_{DA}}\right)^6\right) dR_{DA} + x_{DOnly}. \quad (10)$$

Here,  $R_0$  is the Förster-radius ( $R_0 = 52 \text{ \AA}$ ) and  $k_0 = 1/\tau_0$  is the radiative rate constant of the unquenched dye ( $\tau_0 = 4 \text{ ns}$ ). In  $\epsilon_D(t)$  incomplete labeled molecules lacking an acceptor and molecules with bleached acceptors are considered by the fraction of FRET-inactive,  $x_{DOnly}$ .

For rigorous uncertainty estimates  $p(R_{DA})$  was modeled by a linear combination of normal distributions. Overall, a superposition of two normal distributions with a central distance  $\bar{R}_{DA}^{(1,2)}$  and a width  $w_{DA}$  was sufficient to describe the data:

$$p(R_{DA}) = \frac{1}{\sqrt{\frac{\pi}{2}} w_{DA}} \left[ x_1 e^{-\left(\frac{2(R_{DA} - \bar{R}_{DA}^{(1)})}{w_{DA}}\right)^2} + (1 - x_1) e^{-\left(\frac{2(R_{DA} - \bar{R}_{DA}^{(2)})}{w_{DA}}\right)^2} \right] \quad (11)$$

In the analysis of the seTCSPC data, the FRET-sensitized emission of the acceptor,  $f_{A|D}^{DA}(t)$ , was considered to reduce the overall photon noise and a typical width of 12  $\text{\AA}$  was consistent with the data.  $f_{A|D}^{(DA)}(t)$  was described by the convolution of  $f_{A|A}^{(DA)}(t)$ , and  $f_{D|D}^{(DA)}(t)$ :

$$f_{A|D}^{(DA)}(t) = f_{D|D}^{(D0)}(t) \cdot \epsilon_D(t) \otimes f_{A|A}^{(DA)}(t) \quad (12)$$

All  $f(t)$ s were fitted by model functions using the iterative re-convolution approach.(61) Here, the parameters of a model function  $g(t)$  were optimized to the data by using the modified Levenberg–Marquardt algorithm. The model function  $g(t)$  considers experimental nuisances as scattered light and a constant background:

$$g(t) = N_F \cdot f(t) \otimes IRF(t) + N_{BG} \cdot IRF(t) + bg \quad (13)$$

$N_F$  is the number of fluorescence photons,  $N_{BG}$  is the number of background photons due to Rayleigh or Raman scattering and  $bg$  is a constant offset attributed to detector dark counts and

afterpulsing. In seTCSPC, the fraction of scattered light and the constant background was calculated by the experimental integration time and the buffer reference measurements. In eTCSPC, the fraction of scattered light and the constant offset were free fitting parameters. Finally,  $g(t)$  was scaled to the data by the experimental number of photons and fitted to the experimental data.

All fluorescence decays were fitted by ChiSurf, a custom software package tailored for the global analysis of multiple fluorescence experiments (<https://github.com/Fluorescence-Tools/ChiSurf>).<sup>(29)</sup> Statistical errors were estimated by sampling the parameter space<sup>(62)</sup> and applying an F-test at a confidence level of 95%.

*Burst-wise analysis.* Briefly, as the first step in the burst-wise analysis, fluorescence bursts were discriminated from the background signal of 1–2 kHz of the single-molecule measurements by applying an intensity threshold criterion. Next, the anisotropy and the fluorescence averaged lifetime,  $\langle \tau_{D(A)} \rangle_F$ , were determined for each burst. Moreover, the background, the detection efficiency-ratio of the “green” and “red” detectors, and the spectral cross-talk were considered to determine the FRET efficiency,  $E$ , of every burst.<sup>(35)</sup> The species averaged fluorescence lifetime of the donor in the absence of an acceptor  $\langle \tau_{D(0)} \rangle_x$ ,  $\langle \tau_{D(A)} \rangle_F$ , and the FRET efficiency estimate the mean  $\langle \tau_{D(A)} \rangle_x = (1 - E) \cdot \langle \tau_{D(0)} \rangle_x$  and variance  $var(\tau_{D(A)}) = \langle \tau_{D(A)} \rangle_F \cdot \langle \tau_{D(A)} \rangle_x - \langle \tau_{D(A)} \rangle_x^2$  of the burst averaged fluorescence lifetimes distribution. This highlights conformational dynamics by a non-zero variance (**Fig. S3A**). For a detailed analysis of the sub-ensemble the fluorescence photons of multiple burst were integrated into joint fluorescence decay histograms (seTCSPC, **Fig. S3B**). The seTCSPC fluorescence decays were analyzed as described above.

*FRET-lines.* By relating fluorescence parameters, FRET lines serve as a visual guide to interpret histograms of MFD parameters determined for individual molecules. The fluorescence weighted lifetime of the donor,  $\langle \tau_{D(A)} \rangle_F$ , and the FRET efficiency  $E$  were related by FRET-lines by a methodology similar as previously described.<sup>(36)</sup> First, FRET-rate constant distributions,  $p(k_{RET})$ , were calculated for a given set of model parameters. Next,  $p(k_{RET})$  was converted to the averages  $\langle \tau_{D(A)} \rangle_F$  and  $E$ . This results in a parametric relation between  $\langle \tau_{D(A)} \rangle_F$  and  $E$ , called a FRET-line. We use two types of FRET-lines: dynamic and static FRET-lines. Dynamic FRET-lines describe the mixing of typically two states. A static FRET-line relates  $\langle \tau_{D(A)} \rangle_F$  to  $E$  for all molecules that are static within their observation time (the burst duration). Static molecules are identified by populations in a MFD histogram located on the static FRET-line. The FRET-lines

were calculated using the scripting capability of ChiSurf assuming states with normal distributed distance and are calibrated for sample-specific fluorescence properties, i.e., donor and acceptor fluorescence quantum yields, the fraction of acceptor in power dependent dark states (cis-state in Alexa647), and complex fluorescence decays of the donor in the absence of FRET.

*Filtered species cross-correlations.* Filtered FCS increases the contrast by a set of state-specific filters applied to the recorded photon stream. For every FRET pair a specific set of filters,  $w_j^{(i)}$ , was generated using experimental fluorescence bursts for high (H) and low (L) FRET states as previously described and listed in Tab. S2.(5) Using these filters species cross correlation functions  $G^{(n,m)}(t_c)$  were calculated by weighted signal intensities  $S_j(t)$ :

$$G^{(n,m)}(t_c) = \frac{\langle F^{(n)}(t) \cdot F^{(m)}(t+t_c) \rangle}{\langle F^{(n)}(t) \rangle \cdot \langle F^{(m)}(t+t_c) \rangle} \text{ with } F^{(n)}(t) = \left( \sum_{j=1}^{d \cdot L} w_j^{(n)} \cdot S_j(t) \right) \quad (14)$$

Herein  $n$  and  $m$  are the two species (either H or L),  $d$  is the number of detectors,  $L$  is the number of TAC channels, and  $S_j(t)$  is the signal recorded in the TAC-channel  $j$ . The choice of  $n$  and  $m$  defines the type of the correlation function. If  $n$  equals  $m$ ,  $G^{(n,n)}(t_c)$  is a species autocorrelation function (*sACF*), otherwise  $G^{(n,m)}(t_c)$  is a species cross-correlation function (*sCCF*).<sup>(5)</sup> Overall four correlation curves were generated per sample: two species auto -  $sACF^{H,H}(t_c)$ ,  $sACF^{L,L}(t_c)$  and two species cross -  $sCCF^{H,L}(t_c)$ ,  $sCCF^{L,H}(t_c)$  correlation curves. All curves were fitted by a model which factorizes  $G^{(n,m)}(t_c)$  into a diffusion-,  $G_{diff}^{(n,m)}(t_c)$ , and a kinetic- term  $G_{kin}^{(n,m)}(t_c)$ :

$$G^{(n,m)}(t_c) = 1 + \frac{1}{N_{eff}^{(n,m)}} \cdot G_{Diff}^{(n,m)}(t_c) \cdot G_{kin}^{(n,m)}(t_c). \quad (15)$$

Here,  $N^{(n,m)}$  is the effective number of molecules. The *sACFs* were fitted by individual effective numbers of molecules. The two *sCCFs* shared a single effective number of molecules.

We assume that the same diffusion term can describe all correlation curves of a sample and that the molecules diffuse in a 3D Gaussian illumination/detection profile. Under these assumptions  $G_{diff}^{(n,m)}(t_c)$  is

$$G_{Diff} = \left( 1 + \frac{t_c}{t_{diff}} \right)^{-1} \left( 1 + \left( \frac{\omega_0}{z_0} \right)^2 \left( \frac{t_c}{t_{diff}} \right) \right)^{-1/2}, \quad (16)$$

where  $t_{diff}$  the characteristic diffusion time and  $\omega_0$  and  $z_0$  are the radii of the focal and the axial plane, respectively, where the intensity decayed to  $1/e^2$  of the maximum's intensity.

The kinetic terms of the *sACF* and the *sCCF* were formally described by:



$$\begin{aligned}
G_{kin}^{LH}(t_c) &= \left(1 - A_0^{LH} \cdot (A_1 \cdot e^{-t_c/t_{c,1}} + A_2 \cdot e^{-t_c/t_{c,2}} + A_3 \cdot e^{-t_c/t_{c,3}})\right) \\
G_{kin}^{HL}(t_c) &= \left(1 - A_0^{HL} \cdot (A_1 \cdot e^{-t_c/t_{c,1}} + A_2 \cdot e^{-t_c/t_{c,2}} + A_3 \cdot e^{-t_c/t_{c,3}})\right) \cdot (1 - A_b^{HL} \cdot e^{-t_c/t_b}) \\
G_{kin}^{LL}(t_c) &= \left(1 + A_1^{LL} (e^{-t_c/t_{c,1}} - 1) + A_2^{LL} (e^{-t_c/t_{c,2}} - 1) + A_3^{LL} (e^{-t_c/t_{c,3}} - 1)\right) \\
G_{kin}^{HH}(t_c) &= \left(1 + A_1^{HH} (e^{-t_c/t_{c,1}} - 1) + A_2^{HH} (e^{-t_c/t_{c,2}} - 1) + A_3^{HH} (e^{-t_c/t_{c,3}} - 1)\right) \cdot (1 + A_b^{HH} (e^{-t_c/t_b} - 1))
\end{aligned} \tag{17}$$

Here,  $A_0$  defines the amplitude of the anti-correlation;  $A_b$  accounts for acceptors bleaching in the high-FRET state;  $t_b$  is the characteristic bleaching time of the acceptor (under the given conditions typically 5-10 ms);  $A_1$ ,  $A_2$  and  $A_3$  together with  $t_{c,1}$ ,  $t_{c,2}$  and  $t_{c,3}$  define the anti-correlation time spectrum of the H to L and L to H transitions. The sum of  $A_1$ ,  $A_2$  and  $A_3$  was constrained to unity. The correlation times  $t_{c,1}$ ,  $t_{c,2}$  and  $t_{c,3}$  were global parameters shared among all samples.  $A_1$ ,  $A_2$  to  $A_3$  were sample specific. The amplitudes  $A_1^{HH}$ ,  $A_2^{HH}$ ,  $A_3^{HH}$  and  $A_1^{LL}$ ,  $A_2^{LL}$ ,  $A_3^{LL}$  of the sACFs were non-global parameters optimized for every curve individually. Overall 48 correlation curves of 12 samples were analyzed as a joint dataset. The uncertainties of the amplitudes and correlation times were determined by support plane analysis that considers the mean and the standard deviation of the individual correlation channels. Estimates for the mean and the standard deviation of the correlation channels were determined by splitting individual measurements. The global data analysis of the FCS curves was performed using ChiSurf.

## 5 Neutron spin-echo spectroscopy

NSE was measured on IN15 at the Institut Laue-Langevin, Grenoble, France. Four incident neutron wavelengths with 8, 10, and 12.2, and 17.5 Å were used. The buffer composition for NSE experiments was 50 mM TRIS, 5 mM MgCl<sub>2</sub>, 150 mM NaCl at pD 7.9 in heavy water (99.9 atom % D). The protein concentration was 30 mg/mL. The measured NSE spectra are shown in **Fig. S5A**. Effective diffusion coefficients  $D_{eff}$  were determined from the initial slope of the NSE spectra by using a cumulant analysis  $\frac{I(q,t)}{I(q,0)} = \exp\left(K_1 t + \frac{1}{2} K_2 t^2\right)$  with  $D_{eff} = -\frac{K_1}{q^2}$ .

The rigid body diffusion  $D_0(q)$  of a structural model at infinite dilution was calculated according to (34):

$$D_0(q) = \frac{1}{q^2 F(q)} \sum_{j,k} \left( b_j \exp(-i\vec{q}\vec{r}_j) \left( \vec{q} \times \vec{r}_j \right) \widehat{D} \left( \vec{q} \times \vec{r}_k \right) b_k \exp(i\vec{q}\vec{r}_k) \right) \tag{18}$$

where  $\widehat{D}$  is the 6x6 diffusion tensor, which was calculated using the HYDROPRO program.(63)  $D_0(q)$  was calculated for the hGBP1 crystal structure (PDB-ID: 1DG3) and the best representing

M<sub>2</sub> structure. The population values have been determined from fits to the SAXS data with 69% best representing M<sub>2</sub> structure and 31% crystal structure at the temperature of 10°C.

The full NSE spectra were described by rigid body diffusion and internal protein dynamics according to (64):

$$I(q, t)/I(q, 0) = [(1 - A(q)) + A(q) \exp(-\Gamma t)] \cdot \quad (19)$$

$$\exp\left(-q^2 D_t \frac{H_t}{S(q)} t\right) \left(\sum_{l=0}^{15} S_l(q) \exp(-l(l+1) D_r H_r t)\right) / \sum_{l=0}^{15} S_l(q) \text{ with } S_l(q) = \sum_m \left| \sum_i b_i j_l(qr_i) Y_{l,m}(\Omega_i) \right|^2$$

where  $D_t$  and  $D_r$  are the calculated scalar translational and rotational diffusion coefficients found in the trace of  $\widehat{D}$  of the rigid protein at infinite dilution from the structural models. Rotational diffusion of the rigid protein were expressed in spherical harmonics with spherical Bessel functions  $j_l(qr_i)$ , spherical harmonics  $Y_{l,m}$  and scattering length densities  $b_i$  of atoms at positions  $r_i$ . Here the crystal structure was used as a base.  $D_t$  and  $D_r$  were chosen according to the mixture of crystal structure and best representing M<sub>2</sub> structure. Direct interaction and hydrodynamic interactions were accounted for by the corrections  $D_{t,eff}(q) = D_t H_t/S(q)$  and  $D_{r,eff} = H_r D_r$ . Interparticle interactions were considered by the structure factor  $S(q)$  as measured by SANS.  $H_t$  and  $H_r$  reduce the effective translational and rotational diffusion coefficients.  $H_t$  is related to the intrinsic viscosity  $[\eta]$  by  $H_t = 1 - c[\eta]$  and  $H_r$  can be approximated by  $1 - H_r = (1 - H_t)/3$  for spherical particles,(65) which might underestimate  $H_r$  for large asymmetric particles. Internal protein dynamics was described by an exponential decay with a  $q$ -independent rate  $\Gamma$ , and a  $q$ -dependent contribution  $A(q)$  of internal dynamics to the NSE spectra.

The parameters  $H_t$ ,  $H_r$ , the relaxation time  $\lambda$  and the amplitudes  $A(q)$  (eq. 19) were simultaneously optimized to all NSE spectra (Fig. S5). The fits show a small contribution of internal dynamics with amplitudes close to the error bars and seemingly long relaxation times, but not strong enough to be determined unambiguously. Fitting the spectra without additional internal dynamics shows an excellent description of the data (Fig. S5) with  $H_t = 0.61 \pm 0.01$  and  $H_r = 0.72 \pm 0.03$  as the only fitting parameters.

Dynamic light scattering was measured on a Zetasizer Nano ZS instrument (Malvern Instruments, Malvern, United Kingdom) in D<sub>2</sub>O buffer identical to that used in the NSE experiment. Autocorrelation functions were analyzed by the CONTIN like algorithm (66).

## 6 Simulations

*MD simulations & principal component analysis.* We performed molecular dynamics (MD) and accelerated MD (aMD) simulations to identify collective degrees of freedom, essential movements, and correlated domain motions of hGBP1 by Principal Component Analysis (PCA) (all references for the methodology are given in **Supplementary Note 2**). The simulations were started from a known crystal structure of the full-length protein (PDB code: 1DG3) protonated with the program PROPKA at a pH of 7.4, neutralized by adding counter ions and solvated in an octahedral box of TIP3P water with a water shell of 12 Å around the solute. The obtained system was used to perform unbiased MD simulations and aMD simulations. The Amber14 package of molecular simulation software(67) and the ff14SB force field were used to perform five unrestrained all-atom MD simulations. Three of the five simulations were conventional MD (2 μs each) and two aMD simulations (200 ns each). The “Particle Mesh Ewald” method was utilized to treat long-range electrostatic interactions; the SHAKE algorithm was applied to bonds involving hydrogen atoms. For all MD simulations, the mass of solute hydrogen atoms was increased to 3.024 Da and the mass of heavy atoms was decreased respectively according to the hydrogen mass repartitioning method.(68) The time step in all MD simulations was 4 fs with a direct-space, non-bonded cutoff of 8 Å. For initial minimization, 17500 steps of steepest descent and conjugate gradient minimization were performed; harmonic restraints with force constants of 25 kcal·mol<sup>-1</sup> Å<sup>-2</sup>, 5 kcal·mol<sup>-1</sup>·Å<sup>-2</sup>, and zero during 2500, 10000, and 5000 steps, respectively, were applied to the solute atoms. Afterwards, 50 ps of NVT simulations (MD simulations with a constant number of particles, volume, and temperature) were conducted to heat up the system to 100 K, followed by 300 ps of NPT simulations (MD simulations with a constant number of particles, barostat and temperature) to adjust the density of the simulation box to a pressure of 1 atm and to heat the system to 300 K. A harmonic potential with a force constant of 10 kcal·mol<sup>-1</sup> Å<sup>-2</sup> was applied to the solute atoms at this initial stage. In the following 100 ps NVT simulations the restraints on the solute atoms were gradually reduced from 10 kcal·mol<sup>-1</sup> Å<sup>-2</sup> to zero. As final equilibration step 200 ps of unrestrained NVT simulations were performed. Boost parameters for aMD were chosen by the method as previously suggested.(38)

## 7 Integrative modeling

The generation of structural models follows the workflow (**Fig. 4A**) presented in the main text. A key prerequisite for integrative modeling is the simulation of experimental observables for a given set of structural models. To generate an integrative structural model, the degrees of freedom, i.e., the model needs to be defined, structural models need to be generated, the

structural models need to be ranked, i.e., evaluated against the experimental data, and experiments need to be combined in a meta-analysis.

#### Simulation of experimental parameters

Theoretical SAXS scattering curves for the structural models were calculated using the established software CRYSOLO(55) DEER and the FRET inter-label distance distributions  $p_{sim}(R_{LL}, M)$  were simulated by accessible volume (AV) simulations. The experimental inter-label distances were compared to the simulated average distances (**Fig. 4D**). For a given protein conformation M the average simulated distance for all label linker conformations  $\langle R_{LL,sim} \rangle$  is

$$\langle R_{LL,sim} \rangle(M) = \int R_{LL} \cdot p_{sim}(R_{LL}, M) dR_{LL}. \quad (20)$$

Because of the different meaning of the experimental DEER and FRET inter-label distances, the modeled average inter-spin distances  $\langle R_{LL,sim} \rangle$  and the center to center inter-dye distances  $\bar{R}_{DA,sim}$  are denoted in Fig. 4D with the general symbol  $R_{LL,sim}$ .

The DEER AV simulations were calibrated against established rotamer library approaches (**Fig. S2B**). The AV simulations of the fluorophores were refined using experimental anisotropies to account for dyes bound to the molecular surface in accessible contact volume (ACV) simulations. The model for the fluorescent dyes and the transferability of the results were validated by reference measurements and protein activity measurements (**Supplementary Note 1**).

In detail, the spatial distribution of the labels was modeled by accessible volume (AV) simulations weighted by the fraction of dyes in contact with the protein – accessible contact volume (ACV).(31,69,70) The used ACV simulations determine all sterically allowed positions of a label, which is approximated by ellipsoids, using a geometric search algorithm, and weight the fraction of dyes in contact with the protein by experimental anisotropies (**Supplementary Note 1**).(33) The center of the ellipsoid was connected by a linker to the C $_{\beta}$ -atoms of the reactive amino-acid. The linker extends from the reactive group to the center of the dipole of the labels. The fluorophores were simulated with previously published parameters determined by the spatial dimensions of the dyes.(31,32) The donor (Alexa Fluor 488 C5 maleimide, Alexa488) and the acceptor fluorophore (Alexa Fluor 647 C2 maleimide, Alexa647) were modeled using a linker width  $L_{width}$  of 4.5 Å and linker-length  $L_{link}$  of 20.5 Å and 22 Å for Alexa488 and Alexa647, respectively. The radii of the ellipsoids ( $R_{dye1}$ ,  $R_{dye2}$  and  $R_{dye3}$ ) for Alexa488 were 5.0 Å, 4.5 Å and 1.5 Å and for Alexa647 11.0 Å, 4.7 Å and 1.5 Å, respectively. The residual anisotropy was used as an estimate for the fraction of dyes bound to the surface of the protein

for screening by accessible surface volume simulations.(33) The parameters for the methanethiosulfonate (MTSSL) spin labels were determined by comparing ACV simulated  $p(R_{SS})$  to established simulation approaches(30,42) resulting in linker-length of 8.5 Å, a linker-width of 4.5 Å, and an ellipsoid radius of 4.0 Å (**Fig. S2B**).

The analysis of the fluorescence data provided per variant two central distances  $\bar{R}$  that were assigned based on their relative population to the identified conformations  $M_1$  and  $M_2$  (**eq. 11**) while the model free DEER analysis yields distance distributions (**eqs. 5, 6**) that were considered by their average distance  $\langle R_{LL,exp} \rangle$ . Note, contrary to the simulated average distance, the experimental average is a linear combination of the distances of the two co-existing conformations.

#### Definition of an integrative structural model

In the model definition, the experimental constraints and the constraints imposed by the model need to be defined. To describe our experimental observables, we use in the first step a decomposition of the protein into rigid bodies (RB). The used RBD-framework represents proteins as an assembly of flexible linked rigid bodies interacting via a very soft repulsion (clash) potential which tolerates atomic overlaps to a certain degree.(32) Essential steps for the generation of structural models by rigid body docking (RBD) is the segmentation of the protein into rigid bodies (RB). Consistent with MD simulations and the biochemical pre-knowledge on the existence of different domain, hGBP1 was decomposed into its individual domains: the LG domain (aa 1-309), the middle domain (aa 310-481) and the helices  $\alpha_{12}$  (aa 482-563) and  $\alpha_{13}$  (aa 564-583) for RBD (**Supplementary Note 3, Fig. S6C, Fig. 4B**). To allow for internal reorganization the middle domain is represented by two rigid bodies (aa 310-373, aa 374-481). The N- to the C-terminal parts of the rigid bodies were connected via bonds with a weak quadratic potential. Such reduced model does not allow for bending of the individual domains. Therefore, we used a very soft clash-potential (**Supplementary Note 4**).

#### Generation of structural models

We use in a first step coarse-grained rigid-body (RB) models and experimental constraints from DEER and FRET, to sample the experimentally allowed conformational space as vast as possible. As first step to generate structural models we use RB docking (RBD) with DEER and FRET restrains. Here, average distances between the labels were determined by modeling their spatial distribution of the labels around their attachment point by accessible volume (AV) simulations.(32) Deviations between the modeled and the experimental FRET and DEER distances were minimized by driving initial random configurations the rigid-body assembly

towards an optimal conformation (**Supplementary Note 4**). The restraints are compiled in the supplement (**Tab. S3**). This docking procedure was repeated 20,000 times for  $M_1$  and  $M_2$  to generate structural models refined by subsequent NMSim and MD simulations (**Fig. 4A**).

Next, the structural models generated by RBD were refined by the computationally more demanding normal mode based all-atom multiscale NMSim. NMSim generates representations with stereochemical accurate conformations by a three-step protocol and incorporates information about preferred directions of protein motions into a geometric simulation algorithm.<sup>(39)</sup> We used the RBD structures as a target for NMSim to optimize the stereochemistry. In targeted NMSim the conformational change vector is formulated as a linear combination of the modes calculated for the starting structure (the crystal structure) weighted by the proximity to the target structure (the RBD structure). This way, the normal modes that overlap best with the direction of conformational change contribute more to the direction of motion in NMSim.

Next, the structural models refined by NMSim were clustered into 343 and 414 groups by their  $C_\alpha$  RMSD for the states  $M_1$  and  $M_2$ , respectively, using hierarchical agglomerative clustering with complete linkage and distance threshold of 5 Å. As final step, conventional MD simulations on the group representatives were performed for 2 ns (**Methods 6**). The MD trajectories were clustered using hierarchical agglomerative clustering with complete linkage and distance threshold of 2 Å into 3395 and 3357 groups for  $M_1$  and  $M_2$ , respectively.

#### Individual ranking of structural models

To filter (screen) structural models, the calculation of probabilities, the (dis)agreement of the model with the data needs to be measured. Here, the disagreement of the simulated and experimental data was measured by weighted sums of squared deviations,  $\chi^2$ . The structural models were compared to the SAXS and to the combined DEER and FRET dataset by  $\chi_{SAXS}^2$  and  $\chi_{DEER,FRET}^2$ , respectively.

For a consistent description of the FRET, DEER, and the SAXS experiments, the experimental scattering curve was described by a mixture of the conformations. Here, as a first step, theoretical scattering curves for all proposed conformations were calculated using the program CRY SOL. Next, model functions  $I_{model}(q, M_1, M_2)$  for all possible combinations of structural models for the states  $M_1$  and  $M_2$  were calculated. The model functions were linear combinations of  $F_{M_1}(q)$  and  $F_{M_2}(q)$ , the theoretical scattering curves for  $M_1$  and  $M_2$ , respectively.

$$I_{model}(q, M_1, M_2) = x_{M_1} \cdot F_{M_1}(q) + (1 - x_{M_1}) \cdot F_{M_2}(q) \quad (21)$$

To determine the initially unknown fraction of molecules in the  $M_1$  state,  $x_{M_1}$ , the sum of weighted squared deviations between the experiment and the data  $\chi_{SAXS}^2$  to the measured data,  $I_{\text{exp}(q)}$  was minimized.

$$\chi_{SAXS}^2(M_1, M_2) = \frac{1}{N} \sum_{i=1}^N \left( \frac{I_{\text{exp}(q_i)} - I_{\text{model}(q_i, M_1, M_2)}}{\sigma(q_i)} \right)^2 \quad (22)$$

Above,  $\sigma(q_i)$  is the noise of the experimental scattering curve and  $N$  is the number of detection channels.

For the combined DEER and FRET dataset,  $\chi_{DEER,FRET}^2$  measures the disagreement between simulated distances and experimental distances considering the asymmetric (deviation dependent) uncertainty of the distances. For a pair of structural models ( $M_1, M_2$ ) we approximate  $\chi_{DEER,FRET}^2$  by:

$$\begin{aligned} \chi_{DEER}^2(M_1, M_2) &\approx \sum_i \left( \frac{\langle R_{LL,exp}^{(i)} \rangle(M_1) - \langle R_{LL,sim}^{(i)} \rangle(M_1)}{w^{(i)}(M_1)/2} \right)^2 \\ &+ \sum_i \left( \frac{\langle R_{LL,exp}^{(i)} \rangle(M_2) - \langle R_{LL,sim}^{(i)} \rangle(M_2)}{w^{(i)}(M_2)/2} \right)^2 \\ \chi_{FRET}^2(M_1, M_2) &\approx \sum_i \left( \frac{\bar{R}_{DA,exp}^{(i)}(M_1) - \langle R_{DA,sim}^{(i)} \rangle(M_1)}{\Delta^{(i)}(M_1)} \right)^2 + \sum_i \left( \frac{\bar{R}_{DA,exp}^{(i)}(M_2) - \langle R_{DA,sim}^{(i)} \rangle(M_2)}{\Delta^{(i)}(M_2)} \right)^2 \\ \chi_{DEER,FRET}^2(M_1, M_2) &= \chi_{DEER}^2(M_1, M_2) + \chi_{FRET}^2(M_1, M_2). \end{aligned} \quad (23)$$

Here,  $\bar{R}_{DA,exp}^{(i)}(M_1)$  and  $\bar{R}_{DA,exp}^{(i)}(M_2)$  are the central experimental donor-acceptor FRET distances assigned to  $M_1$  and  $M_2$ .  $\langle R_{LL,exp}^{(i)} \rangle(M_{\{1,2\}})$  is the average label-label distance in DEER experiments. Modeled average inter-label distances  $\langle R_{LL,sim}^{(i)} \rangle(M_{\{1,2\}})$  correspond to the average simulated label-label distance  $\langle R_{LL,sim} \rangle$  for DEER and average simulated donor-acceptor distance and  $\langle R_{DA,sim}^{(i)} \rangle(M_{\{1,2\}})$  for FRET, which is a good approximation for the central donor-acceptor distance  $\bar{R}_{DA,exp}$  of a symmetric distance distribution being used for analysis (**eq. 11**). Uncertainties that depend on the sign of the deviation between the model and the data were considered by the half width of the distance distribution  $w^{(i)}(M_{\{1,2\}})/2$  for DEER and estimate for the uncertainty of the central distance  $\Delta^{(i)}(M_{\{1,2\}})$  for FRET.

#### Model discrimination & quality assessment

The experimental technique assesses different structural aspects with uncertainties thereof, e.g. inter-label distance distributions in DEER, FRET *vs.* average shapes in SAXS. Thus, the balance of the techniques for modeling and screening, captured by relative weights, will affect the final model. A well-balanced model weights the different experiments by estimates of their relative information content. This way balanced absolute probabilities, which depend on accurate estimates of the degrees of freedom for the model and the data, for a structural model can be calculated. By combining these probabilities in a meta-analysis, a well-balanced structural model combining diverse techniques can be recovered. Here, we combined the label-based FRET, DEER measurements with SAXS measurements to a well-balanced integrative structural model.

The values for  $\chi_{DEER,FRET}^2$  and  $\chi_{SAXS}^2$  assess the quality in a pair of structural models with respect to the experiment. We use these  $\chi^2$  values to identify/filter models that are significantly worse than the best possible pair of structures for the respective methods. For that, we compare pairs of  $\chi^2$  values for structural models by an F-test (The ratio  $x := \chi_1^2/\chi_2^2$  is F-distributed). For two  $\chi^2$ -values with corresponding degrees of freedom  $d_1$  and  $d_2$  the cumulative F distribution is:

$$F(x, d_1, d_2) = \mathbf{I} \frac{d_1 x}{d_1 x + d_2} \left( \frac{d_1}{2}, \frac{d_2}{2} \right). \quad (24)$$

Here,  $\mathbf{I}$  is the regularized incomplete beta function. To relate the F-value  $x$  to a probability  $\alpha$ , for given  $\chi_1^2$  and  $\chi_2^2$  and significantly different  $d_1$ , and  $d_2$ , we must compute the inverse of the cumulative F distribution.

Here, we compare the  $\chi^2$  value of all possible combinations of structural models ( $M_1, M_2$ ) and experimental techniques DEER/FRET and SAXS F-values to the  $\chi^2$  value of best pair of structures ( $x = \chi^2 / \min(\chi^2)$ ). These models have the same dofs ( $d_1 = d_2 = \text{dof}$ ). Hence, we first identify the best model and compute  $x$  for all pairs of models. Next, we determine the degrees of freedom, dof, that are calculated by the degrees of freedom of the data, dof<sub>d</sub>, and the degrees of freedom of the model, dof<sub>m</sub>, i.e. dof=dof<sub>m</sub>-dof<sub>d</sub>. With  $x$  and dof we compute the probability  $\alpha$  that a model is significantly worse than the best model.

The dof<sub>m</sub> was estimated by a PCA applied to all structural models. PCA revealed that 10 principal components explain more than 90% of the total variance. Hence, we conclude that dof<sub>m</sub> ~ 10. For DEER/FRET, dof<sub>d,DEER/FRET</sub> was estimated by correcting the total number of inter-label distances (see **Tab. S3A**: 22 FRET, 8 DEER) for duplicates and for redundant mutual information content. This was accomplished by determining the number of informative distances via a greedy backward elimination feature selection algorithm for our total ensemble



((33), see Fig. 5) so that the precision of the obtained corresponded to our experimental one. In this way, we obtained a  $\text{dof}_{\text{d,DEER/FRET}} = 22$  (**Fig. S6D**) - a value that is close to the number of independent label-pair positions of 23. For SAXS measurements the number of Shannon channels is typically in the range of 10 to 23. For our measurements, the number of Shannon channels approximately 18-22 (71,72). We used the number of Shannon channels as an initial estimate for the dof of the SAXS measurements,  $\text{dof}_{\text{d,SAXS}}$ , and we varied  $\text{dof}_{\text{d,SAXS}}$  in the range of 10 to 24. We found only minor effects of  $\text{dof}_{\text{d,SAXS}}$  on  $\alpha_{\text{SAXS}}$ , the SAXS discrimination power of the models, and used  $\text{dof}_{\text{d,SAXS}} = 17$  to discriminate structural models (for details see **Fig. S6D**). Using these estimates of  $\text{dof}_{\text{m}}$  and  $\text{dof}_{\text{d}}$ ,  $\alpha$  for DEER/FRET,  $\alpha_{\text{DEER,FRET}}$ , and SAXS,  $\alpha_{\text{SAXS}}$ , were calculated for all pairs ( $M_1, M_2$ ). Next,  $\alpha_{\text{DEER,FRET}}$  and  $\alpha_{\text{SAXS}}$  were combined in a meta-analysis to a joint probability of discriminating a pair.

$\alpha_{\text{DEER,FRET}}$  and  $\alpha_{\text{SAXS}}$  measure how likely a pair ( $M_1, M_2$ ) is dissimilar from the best pair for DEER/FRET and SAXS, respectively. To combine DEER/FRET and SAXS we used the probability  $p$  that a pair is similar,  $p = 1 - \alpha$ . Note,  $p$  for DEER/FRET,  $p_{\text{DEER,FRET}}$ , and for SAXS,  $p_{\text{SAXS}}$ , considers the degrees of freedom for the system and data. Moreover,  $p_{\text{DEER,FRET}}$  and  $p_{\text{SAXS}}$  are independent. Thus, Fisher's method was applied to fuse datasets in a meta-analysis. Fisher's method combines probabilities of  $k$  independent tests (here  $k = 2$ ) into a combined  $\chi_{2k}^2$  with  $2k$  degrees of freedom. For  $p_{\text{DEER,FRET}}$  and  $p_{\text{SAXS}}$ , the combined probability is

$$\begin{aligned} \chi_{2k}^2 &\sim -2 \cdot \sum_{i=1}^k \ln(p_i) = -2 \cdot \ln\left(\prod_{i=1}^k p_i\right) \\ &= -2 \cdot \ln(p_{\text{DEER,FRET}} \cdot p_{\text{SAXS}}). \end{aligned} \quad (25)$$

Thus,  $\chi_{2k}^2$  is chi-squared distributed with 4 combined degrees of freedom. In this way a  $\chi_{2k}^2$  value was determined for every ( $M_1, M_2$ ), and pairs ( $M_1, M_2$ ) were discriminated by a chi-squared test with 4 degrees of freedom.

#### Assessment of model precision & quality in Fig 4E

To assess the local quality of the models, the inter-residue distances between all  $C_\alpha$  atoms,  $R_{C_\alpha}$ , and the standard deviation,  $SD(R_{C_\alpha})$ , of the distribution of  $R_{C_\alpha}$  were calculated for all models as a measure for the experimental model precision (**Fig. 4E**, lower triangles). Next, we checked if these variabilities are larger than statistically expected. For this, we compared the experimental precision  $SD(R_{C_\alpha})$  to the precision  $SD(R_{C_\alpha})_{\text{ref}}$  of a ground truth model ensemble as an "ideal and perfect" reference by computing the weighted (normalized) precision,  $SD(R_{C_\alpha})/SD(R_{C_\alpha})_{\text{ref}}$ . Due to (i) the incomplete experimental information on the model, (ii)

the uncertainties of the experiments, and (iii) imprecisions of the model, we anticipate a limited resolution of the model even for ideal experiments. We calculated the reference precision of the ground truth ensembles in two steps. At first, we use the models for  $M_1$  and  $M_2$  of the experimental ensemble that describe our FRET and EPR data best. Next, we use the distances corresponding to the best models and our experimental errors in **Tab. S3A** to generate the ideal reference ensemble by our structural modeling pipeline (**Fig. 4A**) so that we could compute the theoretical inter-residue distance distributions and precisions. The finally computed distributions of the weighted precisions,  $SD(R_{C_\alpha})/SD(R_{C_\alpha})_{ref}$  allow us to test whether the modeled conformational ensemble approaches the theoretical optimum ratios around unity or whether systematic deviations indicate problems in the modelling.

Please note that the above procedure provides only an estimate for the reference model precision and corresponding variability of  $R_{C_\alpha}$ . For a correctly estimated model precision with the corresponding  $SD(R_{C_\alpha})_{ref}$ , the weighted precision  $SD(R_{C_\alpha})/SD(R_{C_\alpha})_{ref}$  theoretically has the meaning of an F-value. Such an F-value for pair-wise estimates of the model precision as  $SD(R_{C_\alpha})$  could be used for estimating the probability that the model insufficiently describes the data within their experimental noise. This procedure could yield such estimates for residue pairs that facilitate the detection of the model defects and limitations.

### Data availability

The following material is available at Zenodo (doi 10.5281/zenodo.1490101): (i) fluorescence decays recorded by eTCSPC used to compute the distance restraints in Tab. S3A, (ii) single-molecule multiparameter fluorescence data: raw data, fluorescence decays of FRET sub-ensembles (seTCSPC), fFCS curves, (iii) scripts for structural modeling of conformational ensembles through integrative/hybrid (I/H) methods using FRET, DEER and SAXS. The experimental SAXS data and the *ab initio* analysis thereof are available in the SASBDB at <https://www.sasbdb.org/data/SASDDD6/e1d68arhp4/>. The generated conformational ensembles will be uploaded to Zenodo and later deposited at the PDB-Dev. Further datasets generated during and/or analyzed during the current study are available from the corresponding author on reasonable request.

### Code availability

Most general custom-made software is directly available from <http://www.mpc.hhu.de/en/software>. General algorithms and source code is published under

<https://github.com/Fluorescence-Tools>. Additional computer code custom-made for this publication is available upon request from the corresponding authors.

### Competing Interests

All authors declare that they have no competing interests.

### References

1. Tompa, P. & Fuxreiter, M. Fuzzy complexes: polymorphism and structural disorder in protein-protein interactions. *Trends Biochem. Sci.* **33**, 2-8 (2008).
2. Hensen, U., Meyer, T., Haas, J., Rex, R., Vriend, G. & Grubmüller, H. Exploring protein dynamics space: The dynasome as the missing link between protein structure and function. *Plos One* **7** (2012).
3. Lerner, E., Cordes, T., Ingargiola, A., Alhadid, Y., Chung, S., Michalet, X. & Weiss, S. Toward dynamic structural biology: Two decades of single-molecule Forster resonance energy transfer. *Science* **359**, 288+ (2018).
4. Neudecker, P., Robustelli, P., Cavalli, A., Walsh, P., Lundstrom, P., Zarrine-Afsar, A., Sharpe, S., Vendruscolo, M. & Kay, L. E. Structure of an Intermediate State in Protein Folding and Aggregation. *Science* **336**, 362-366 (2012).
5. Felekyan, S., Kalinin, S., Sanabria, H., Valeri, A. & Seidel, C. A. M. Filtered FCS: species auto- and cross-correlation functions highlight binding and dynamics in biomolecules. *ChemPhysChem* **13**, 1036-1053 (2012).
6. Kilic, S., Felekyan, S., Doroshenko, O., Boichenko, I., Dimura, M., Vardanyan, H., Bryan, L. C., Arya, G., Seidel, C. A. M. & Fierz, B. Single-molecule FRET reveals multiscale chromatin dynamics modulated by HP1 alpha. *Nat. Commun.* **9** (2018).
7. Praefcke, G. J. K. & McMahon, H. T. The dynamin superfamily: Universal membrane tubulation and fission molecules? *Nat. Rev. Mol. Cell Biol.* **5**, 133-147 (2004).
8. Anderson, S. L., Carton, J. M., Lou, J., Xing, L. & Rubin, B. Y. Interferon-induced guanylate binding protein-1 (GBP-1) mediates an antiviral effect against vesicular stomatitis virus and encephalomyocarditis virus. *Virology* **256**, 8-14 (1999).
9. Itsui, Y. *et al.* Antiviral effects of the interferon-induced protein guanylate binding protein 1 and its interaction with the Hepatitis C Virus NS5B protein. *Hepatology* **50**, 1727-1737 (2009).
10. MacMicking, J. D. Interferon-inducible effector mechanisms in cell-autonomous immunity. *Nat. Rev. Immunol.* **12**, 367-382 (2012).
11. Kim, B. H., Shenoy, A. R., Kumar, P., Das, R., Tiwari, S. & MacMicking, J. D. A Family of IFN-gamma-Inducible 65-kD GTPases Protects Against Bacterial Infection. *Science* **332**, 717-721 (2011).
12. Li, P., Jiang, W., Yu, Q., Liu, W., Zhou, P., Li, J., Xu, J. J., Xu, B., Wang, F. C. & Shao, F. Ubiquitination and degradation of GBPs by a Shigella effector to suppress host defence. *Nature* **551**, 378-383 (2017).
13. Shenoy, A. R., Wellington, D. A., Kumar, P., Kassa, H., Booth, C. J., Cresswell, P. & MacMicking, J. D. GBP5 Promotes NLRP3 Inflammasome Assembly and Immunity in Mammals. *Science* **336**, 481-485 (2012).
14. Randow, F., MacMicking, J. D. & James, L. C. Cellular Self-Defense: How Cell-Autonomous Immunity Protects Against Pathogens. *Science* **340**, 701-706 (2013).
15. Kravets, E., Degrandi, D., Ma, Q., Peulen, T., Felekyan, S., Kühnemuth, R., Weidtkamp-Peters, S., Seidel, C. A. M. & Pfeffer, K. Guanylate binding proteins (GBPs) directly attack *T. gondii* via supramolecular complexes. *eLife*, e11479 (2016).

16. Britzen-Laurent, N., Bauer, M., Berton, V., Fischer, N., Syguda, A., Reipschlager, S., Naschberger, E., Herrmann, C. & Sturzl, M. Intracellular trafficking of guanylate-binding proteins is regulated by heterodimerization in a hierarchical manner. *Plos One* **5** (2010).
17. Kravets, E., Degrandi, D., Weidtkamp-Peters, S., Ries, B., Konermann, C., Felekyan, S., Dargazanli, J. M., Praefcke, G. J. K., Seidel, C. A. M., Schmitt, L., Smits, S. H. J. & Pfeffer, K. The GTPase activity of murine guanylate-binding protein 2 (mGBP2) controls the intracellular localization and recruitment to the parasitophorous vacuole of *Toxoplasma gondii*. *J. Biol. Chem.* **287**, 27452-27466 (2012).
18. Lee, C. S., Kim, Y. J., Kim, W. & Myung, S. C. Guanylate cyclase activator YC-1 enhances TRAIL-induced apoptosis in human epithelial ovarian carcinoma cells via activation of apoptosis-related proteins. *Basic Clin. Pharm. Toxicol.* **109**, 283-291 (2011).
19. Ghosh, A., Praefcke, G. J. K., Renault, L., Wittinghofer, A. & Herrmann, C. How guanylate-binding proteins achieve assembly-stimulated processive cleavage of GTP to GMP. *Nature* **440**, 101-104 (2006).
20. Shydlovskiy, S. *et al.* Nucleotide-dependent farnesyl switch orchestrates polymerization and membrane binding of human guanylate-binding protein 1. *Proc. Natl. Acad. Sci. USA* **114**, E5559-E5568 (2017).
21. Prakash, B., Praefcke, G. J. K., Renault, L., Wittinghofer, A. & Herrmann, C. Structure of human guanylate-binding protein 1 representing a unique class of GTP-binding proteins. *Nature* **403**, 567-571 (2000).
22. Reubold, T. F. *et al.* Crystal structure of the dynamin tetramer. *Nature* **525**, 404-+ (2015).
23. Faelber, K., Held, M., Gao, S., Posor, Y., Haucke, V., Noe, F. & Daumke, O. Structural Insights into Dynamin-Mediated Membrane Fission. *Structure* **20**, 1621-1628 (2012).
24. Vöpel, T., Hengstenberg, C. S., Peulen, T. O., Ajaj, Y., Seidel, C. A. M., Herrmann, C. & Klare, J. P. Triphosphate induced dimerization of human guanylate binding protein 1 involves association of the C-Terminal helices: A joint Double Electron-Electron Resonance and FRET study. *Biochemistry* **53**, 4590-4600 (2014).
25. Piro, A. S., Hernandez, D., Luoma, S., Feeley, E. M., Finethy, R., Yirga, A., Frickel, E. M., Lesser, C. F. & Coers, J. Detection of cytosolic *Shigella flexneri* via a C-terminal triple-arginine motif of GBP1 inhibits actin-based motility. *Mbio* **8** (2017).
26. Tietzel, I., El-Haibi, C. & Carabeo, R. A. Human guanylate binding proteins potentiate the anti-chlamydia effects of interferon-gamma. *PLoS One* **4**, e6499 (2009).
27. Klare, J. P. & Steinhoff, H. J. Spin labeling EPR. *Photosynth. Res.* **102**, 377-390 (2009).
28. Hellenkamp, B. *et al.* Precision and accuracy of single-molecule FRET measurements—a multi-laboratory benchmark study. *Nat. Meth.* **15**, 669-676 (2018).
29. Peulen, T. O., Opanasyuk, O. & Seidel, C. A. M. Combining graphical and analytical methods with molecular simulations to analyze time-resolved FRET measurements of labeled macromolecules accurately. *J. Phys. Chem. B* **121**, 8211-8241 (2017).
30. Polyhach, Y., Bordignon, E. & Jeschke, G. Rotamer libraries of spin labelled cysteines for protein studies. *Phys. Chem. Chem. Phys.* **13**, 2356-2366 (2011).
31. Sindbert, S., Kalinin, S., Nguyen, H., Kienzler, A., Clima, L., Bannwarth, W., Appel, B., Müller, S. & Seidel, C. A. M. Accurate distance determination of nucleic acids via Förster resonance energy transfer: implications of dye linker length and rigidity. *J. Am. Chem. Soc.* **133**, 2463-2480 (2011).
32. Kalinin, S., Peulen, T., Sindbert, S., Rothwell, P. J., Berger, S., Restle, T., Goody, R. S., Gohlke, H. & Seidel, C. A. M. A toolkit and benchmark study for FRET-restrained high-precision structural modeling. *Nat Methods* **9**, 1218-1225 (2012).

33. Dimura, M., Peulen, T. O., Hanke, C. A., Prakash, A., Gohlke, H. & Seidel, C. A. M. Quantitative FRET studies and integrative modeling unravel the structure and dynamics of biomolecular systems. *Curr. Opin. Struct. Biol.* **40**, 163-185 (2016).
34. Biehl, R., Monkenbusch, M. & Richter, D. Exploring internal protein dynamics by neutron spin echo spectroscopy. *Soft Matter* **7**, 1299-1307 (2011).
35. Sisamakris, E., Valeri, A., Kalinin, S., Rothwell, P. J. & Seidel, C. A. M. Accurate single-molecule FRET studies using multiparameter fluorescence detection. *Methods Enzymol.* **475**, 455-514 (2010).
36. Kalinin, S., Valeri, A., Antonik, M., Felekyan, S. & Seidel, C. A. M. Detection of structural dynamics by FRET: A photon distribution and fluorescence lifetime analysis of systems with multiple states. *J. Phys. Chem. B* **114**, 7983-7995 (2010).
37. Praefcke, G. J. K., Geyer, M., Schwemmle, M., Kalbitzer, H. R. & Herrmann, C. Nucleotide-binding characteristics of human guanylate-binding protein 1 (hGBP1) and identification of the third GTP-binding motif. *J. Mol. Biol.* **292**, 321-332 (1999).
38. Pierce, L. C. T., Salomon-Ferrer, R., de Oliveira, C. A. F., McCammon, J. A. & Walker, R. C. Routine access to millisecond time scale events with accelerated molecular dynamics. *J. Chem. Theory Comput.* **8**, 2997-3002 (2012).
39. Ahmed, A. & Gohlke, H. Multiscale modeling of macromolecular conformational changes combining concepts from rigidity and elastic network theory. *Proteins Struct. Funct. Bioinform.* **63**, 1038-1051 (2006).
40. Chen, Y., Zhang, L., Graf, L., Yu, B., Liu, Y., Kochs, G., Zhao, Y. & Gao, S. Conformational dynamics of dynamin-like MxA revealed by single-molecule FRET. *Nat. Commun.* **8**, 15744 (2017).
41. Low, H. H. & Löwe, J. Dynamin architecture—from monomer to polymer. *Curr. Opin. Struct. Biol.* **20**, 791-798 (2010).
42. Hagelueken, G., Ward, R., Naismith, J. H. & Schiemann, O. MtsslWizard: In Silico spin-labeling and generation of distance distributions in PyMOL. *Appl. Magn. Reson.* **42**, 377-391 (2012).
43. Chung, H. S., McHale, K., Louis, J. M. & Eaton, W. A. Single-molecule fluorescence experiments determine protein folding transition path times. *Science* **335**, 981-984 (2012).
44. Ince, S., Kutsch, M., Shydlovskiy, S. & Herrmann, C. The human guanylate-binding proteins hGBP-1 and hGBP-5 cycle between monomers and dimers only. *FEBS J.* **284**, 2284-2301 (2017).
45. Kozakov, D., Li, K., Hall, D. R., Beglov, D., Zheng, J., Vakili, P., Schueler-Furman, O., Paschalidis, I., Clore, G. M. & Vajda, S. Encounter complexes and dimensionality reduction in protein-protein association. *Elife* **3**, e01370 (2014).
46. Pandita, E., Rajan, S., Rahman, S., Mullick, R., Das, S. & Sau, A. K. Tetrameric assembly of hGBP1 is crucial for both stimulated GMP formation and antiviral activity. *Biochem. J.* **473**, 1745-1757 (2016).
47. Kalia, R., Wang, R. Y. R., Yusuf, A., Thomas, P. V., Agard, D. A., Shaw, J. M. & Frost, A. Structural basis of mitochondrial receptor binding and constriction by DRP1. *Nature* **558**, 401-405 (2018).
48. Bergeron-Sandoval, L. P., Safaei, N. & Michnick, S. W. Mechanisms and consequences of macromolecular phase separation. *Cell* **165**, 1067-1079 (2016).
49. Brangwynne, C. P., Tompa, P. & Pappu, R. V. Polymer physics of intracellular phase transitions. *Nature Physics* **11**, 899-904 (2015).
50. Banani, S. F., Lee, H. O., Hyman, A. A. & Rosen, M. K. Biomolecular condensates: organizers of cellular biochemistry. *Nat. Rev. Mol. Cell Biol.* **18**, 285-298 (2017).

51. Hancock, J. F., Paterson, H. & Marshall, C. J. A polybasic domain or palmitoylation is required in addition to the Caax motif to localize P21ras to the plasma-membrane. *Cell* **63**, 133-139 (1990).
52. Rothwell, P. J., Allen, W. J., Sisamakias, E., Kalinin, S., Felekyan, S., Widengren, J., Waksman, G. & Seidel, C. A. M. dNTP-dependent Conformational Transitions in the Fingers Subdomain of KlenTaq1 DNA Polymerase insights into the role of the "nucleotide-binding" state. *J. Biol. Chem.* **288**, 13575-13591 (2013).
53. Vöpel, T., Kunzelmann, S. & Herrmann, C. Nucleotide dependent cysteine reactivity of hGBP1 uncovers a domain movement during GTP hydrolysis. *FEBS Lett.* **583**, 1923-1927 (2009).
54. Pernot, P. *et al.* Upgraded ESRF BM29 beamline for SAXS on macromolecules in solution. *Journal of Synchrotron Radiation* **20**, 660-664 (2013).
55. Svergun, D., Barberato, C. & Koch, M. H. J. CRY SOL - A program to evaluate X-ray solution scattering of biological macromolecules from atomic coordinates. *Journal of Applied Crystallography* **28**, 768-773 (1995).
56. Wertheim, M. S. Exact solution of the Percus-Yevick integral equation for hard spheres. *Phys. Rev. Lett.* **10**, 321-323 (1963).
57. Petoukhov, M. V., Franke, D., Shkumatov, A. V., Tria, G., Kikhney, A. G., Gajda, M., Gorba, C., Mertens, H. D. T., Konarev, P. V. & Svergun, D. I. New developments in the ATSAS program package for small-angle scattering data analysis. *Journal of Applied Crystallography* **45**, 342-350 (2012).
58. Martin, R. E., Pannier, M., Diederich, F., Gramlich, V., Hubrich, M. & Spiess, H. W. Determination of end-to-end distances in a series of TEMPO diradicals of up to 2.8 nm length with a new four-pulse double electron electron resonance experiment. *Angew. Chem. Int. Ed.* **37**, 2834-2837 (1998).
59. Pannier, M., Schädler, V., Schops, M., Wiesner, U., Jeschke, G. & Spiess, H. W. Determination of ion cluster sizes and cluster-to-cluster distances in ionomers by four-pulse double electron electron resonance spectroscopy. *Macromolecules* **33**, 7812-7818 (2000).
60. Jeschke, G., Chechik, V., Ionita, P., Godt, A., Zimmermann, H., Banham, J., Timmel, C. R., Hilger, D. & Jung, H. DeerAnalysis2006 - a comprehensive software package for analyzing pulsed ELDOR data. *Appl. Magn. Reson.* **30**, 473-498 (2006).
61. Straume, M., Frasier-Cadoret, S. G. & Johnson, M. L. Least-Squares Analysis of Fluorescence Data. in *Topics in Fluorescence Spectroscopy* Vol. 2 (ed J.R. Lakowicz) 177-239 (2002).
62. Foreman-Mackey, D., Hogg, D. W., Lang, D. & Goodman, J. emcee: The MCMC Hammer. *Publications of the Astronomical Society of the Pacific* **125**, 306-312 (2013).
63. Ortega, A., Amoros, D. & de la Torre, J. G. Prediction of hydrodynamic and other solution properties of rigid proteins from atomic- and residue-level models. *Biophys. J.* **101**, 892-898 (2011).
64. Inoue, R., Biehl, R., Rosenkranz, T., Fitter, J., Monkenbusch, M., Radulescu, A., Farago, B. & Richter, D. Large domain fluctuations on 50-ns timescale enable catalytic activity in Phosphoglycerate Kinase. *Biophys. J.* **99**, 2309-2317 (2010).
65. Degiorgio, V., Piazza, R. & Jones, R. B. Rotational diffusion in concentrated colloidal dispersions of hard-spheres. *Phys.Rev.E* **52**, 2707-2717 (1995).
66. Provencher, S. W. Contin - A general-purpose constrained regularization program for inverting noisy linear algebraic and integral-equations. *Comput. Phys. Commun.* **27**, 229-242 (1982).
67. D.A. Case, J. T. B., R.M. Betz, D.S. Cerutti, T.E. Cheatham, III, T.A. Darden, R.E. Duke, T.J. Giese, H. Gohlke, A.W. Goetz, N. Homeyer, S. Izadi, P. Janowski, J. Kaus, A. Kovalenko, T.S. Lee, S. LeGrand, P. Li, T. Luchko, R. Luo, B. Madej, K.M. Merz,

- G. Monard, P. Needham, H. Nguyen, H.T. Nguyen, I. Omelyan, A. Onufriev, D.R. Roe, A. Roitberg, R. Salomon-Ferrer, C.L. Simmerling, W. Smith, J. Swails, R.C. Walker, J. Wang, R.M. Wolf, X. Wu, D.M. York and P.A. Kollman. *Amber*, <<http://ambermd.org/>> (2015).
68. Hopkins, C. W., Le Grand, S., Walker, R. C. & Roitberg, A. E. Long-time-step molecular dynamics through hydrogen mass repartitioning. *J. Chem. Theory Comput.* **11**, 1864-1874 (2015).
  69. Cai, Q., Kusnetzow, A. K., Hideg, K., Price, E. A., Haworth, I. S. & Qin, P. Z. Nanometer distance measurements in RNA using site-directed spin labeling. *Biophys. J.* **93**, 2110-2117 (2007).
  70. Muschielok, A., Andrecka, J., Jawhari, A., Brückner, F., Cramer, P. & Michaelis, J. A nano-positioning system for macromolecular structural analysis. *Nat. Meth.* **5**, 965-971 (2008).
  71. Moore, P. B. Small-Angle Scattering - Information-content and error analysis. *J. Appl. Crystallogr.* **13**, 168-175 (1980).
  72. Mertens, H. D. T. & Svergun, D. I. Combining NMR and small angle X-ray scattering for the study of biomolecular structure and dynamics. *Arch. Biochem. Biophys.* **628**, 33-41 (2017).
  73. Kotlarchyk, M. & Chen, S. H. Analysis of Small-Angle Neutron-Scattering spectra from polydisperse interacting colloids. *J. Chem. Phys.* **79**, 2461-2469 (1983).
  74. Tsodikov, O. V., Record, M. T., Jr. & Sergeev, Y. V. Novel computer program for fast exact calculation of accessible and molecular surface areas and average surface curvature. *J. Comput. Chem.* **23**, 600-609 (2002).
  75. Kunzelmann, S., Praefcke, G. J. K. & Herrmann, C. Transient kinetic investigation of GTP hydrolysis catalyzed by interferon-gamma-induced hGBP1 (human guanylate binding protein 1). *J. Biol. Chem.* **281**, 28627-28635 (2006).
  76. Hengstenberg, C. S. *Structural dynamics and implications for dimer formation of human guanylate-binding protein 1* Dr. rer. nat. thesis, Ruhr University Bochum, (2013).
  77. Dale, R. E., Eisinger, J. & Blumberg, W. E. Orientational Freedom of Molecular Probes - Orientation Factor in Intra-Molecular Energy-Transfer. *Biophys. J.* **26**, 161-193 (1979).
  78. Hamelberg, D., Mongan, J. & McCammon, J. A. Accelerated molecular dynamics: A promising and efficient simulation method for biomolecules. *J. Chem. Phys.* **120**, 11919-11929 (2004).
  79. Bas, D. C., Rogers, D. M. & Jensen, J. H. Very fast prediction and rationalization of pK(a) values for protein-ligand complexes. *Proteins Struct. Funct. Bioinform.* **73**, 765-783 (2008).
  80. Jorgensen, W. L., Chandrasekhar, J., Madura, J. D., Impey, R. W. & Klein, M. L. Comparison of simple potential functions for simulating liquid water. *J. Chem. Phys.* **79**, 926-935 (1983).
  81. Wang, J. M., Cieplak, P. & Kollman, P. A. How well does a restrained electrostatic potential (RESP) model perform in calculating conformational energies of organic and biological molecules? *J. Comput. Chem.* **21**, 1049-1074 (2000).
  82. Darden, T., York, D. & Pedersen, L. Particle Mesh Ewald - An nLog(n) method for Ewald Sums in large systems. *J. Chem. Phys.* **98**, 10089-10092 (1993).
  83. Ryckaert, J. P., Ciccotti, G. & Berendsen, H. J. C. Numerical-integration of cartesian equations of motion of a system with constraints - molecular-dynamics of N-alkanes. *J. Comput. Phys.* **23**, 327-341 (1977).

## Acknowledgments

This work was supported by DFG grants RESOLV (EXC 1069) and HE 2679/6-1 to CH, SE 1195/17-1 to CAMS, KL2077/1-2 to JPK and STA 1325/2-1 to AS. TOP and CL wish to acknowledge the support of the International Helmholtz Research School of Biophysics and Soft Matter (BioSoft). A part of this research was supported by the European Research Council through the Advanced Grant 2014 hybridFRET (671208) to CAMS. We are grateful for computational support and infrastructure provided by the “Zentrum für Informations- und Medientechnologie” (ZIM) at the Heinrich Heine University Düsseldorf and the computing time provided by the John von Neumann Institute for Computing (NIC) to HG on the supercomputer JURECA at Jülich Supercomputing Centre (JSC) (user ID: HKF7). This work is based upon experiments performed on the instruments BM29 at the European Synchrotron Radiation Facility (ESRF), X33 at the Doris III storage ring, DESY, and IN15 at the Institut Laue-Langevin (ILL). We acknowledge the ESRF, the EMBL and the ILL for provision of synchrotron and neutron radiation facilities and we would like to thank Drs. Martha Brennich and Clement Blanchet for assistance in using BM29 and X33.

### **Author contributions**

TOP, CSH, RB, MD, CL, HG, JPK, AS, CAMS, and CH wrote the manuscript. MD performed the molecular simulations under the supervision of HG. CSH prepared samples for smFRET and performed protein activity assays. SI and CL prepared samples for SAXS measurements. TV prepared sampled for EPR measurements. CL and AS performed and analyzed SAXS measurements. RB, AS and BF performed NSE measurements and analysis. TOP, CSH, and AV performed the smFRET measurements under the supervision of CAMS. TOP analyzed the smFRET measurements. JPK performed and analyzed the EPR measurements. TOP combined the FRET, EPR, and SAXS measurements in a meta-analysis for integrative modeling. CH, CAMS, JPK and AS planned and supervised the research project.

### **Additional information**

Supplementary Information accompanies this paper.



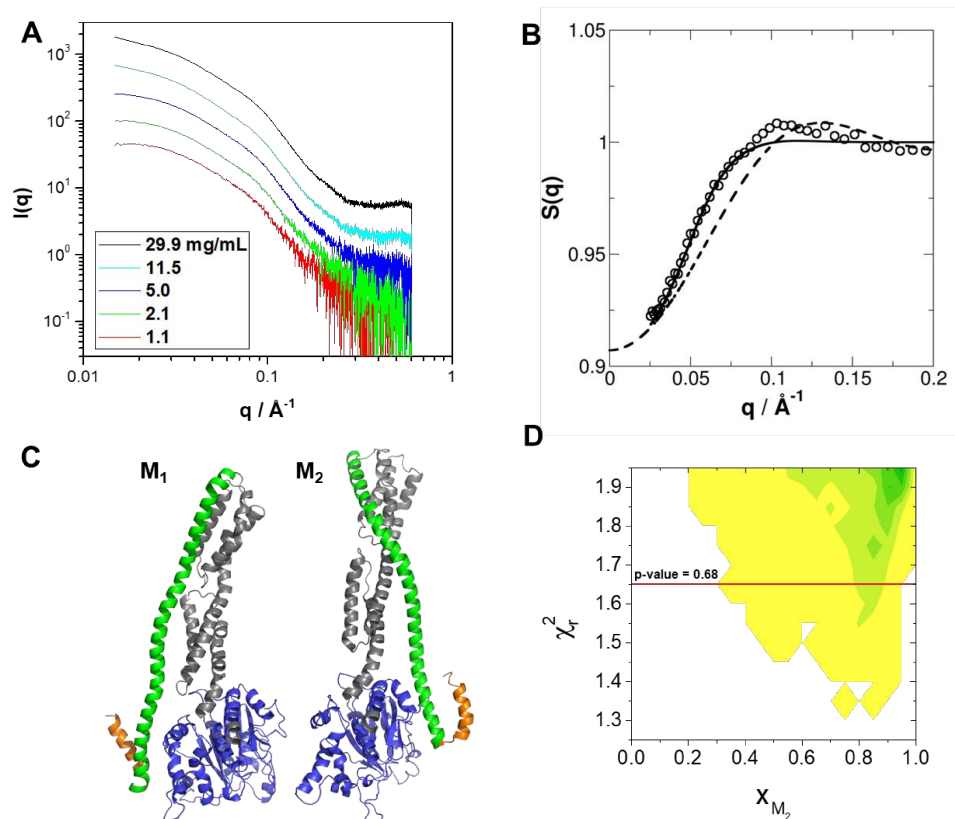
## Supplementary Information

### Integrative dynamic structural biology unveils conformers essential for the oligomerization of a large GTPase

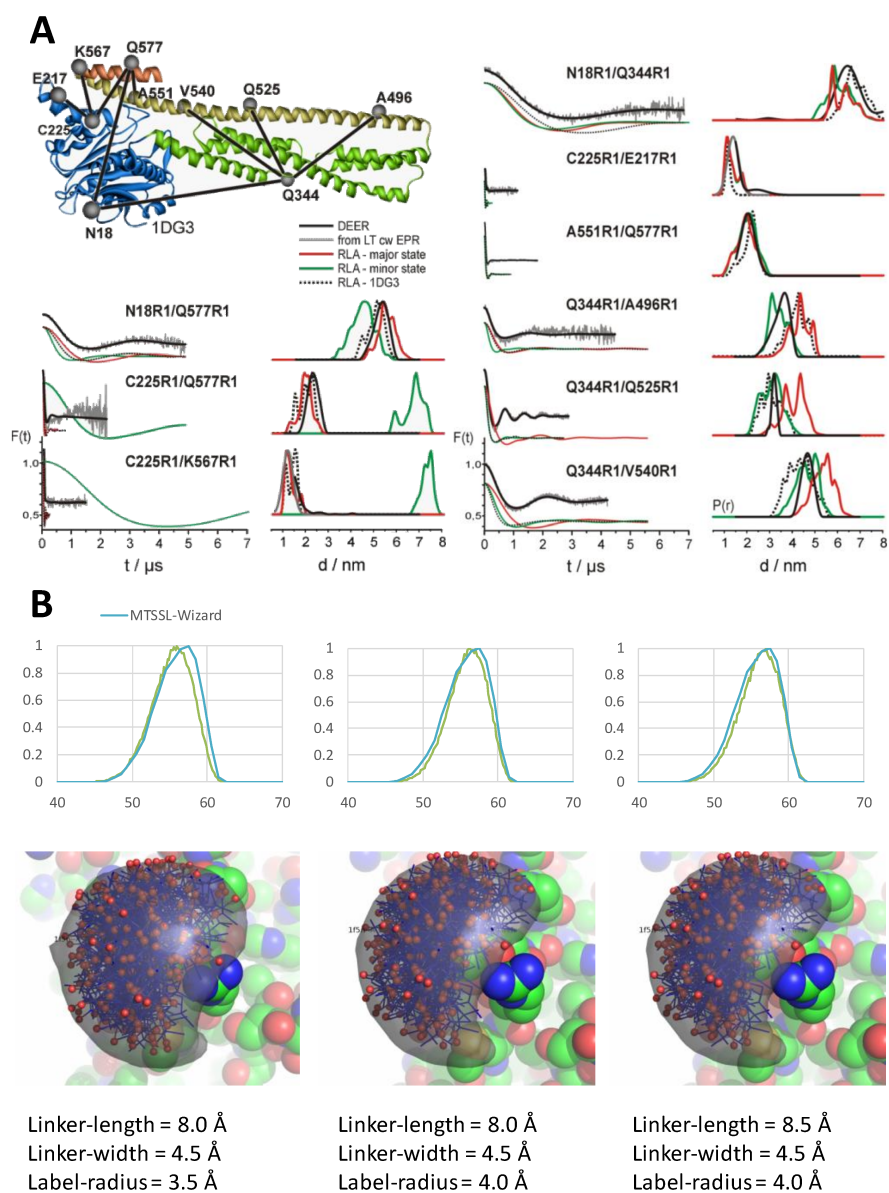
Thomas-Otavio Peulen, Carola S. Hengstenberg et al.

Supplementary Figure 1	Small-angle X-ray scattering measurements on the nucleotide free hGBP1. <b>(A)</b> Measured SAXS data of hGBP1 at different protein concentrations. <b>(B)</b> Structure factor extracted from the SAXS data. <b>(C)</b> Pair of structural models selected corresponding best to the SAXS scattering data. <b>(D)</b> Fitted species fractions.
Supplementary Figure 2	DEER-spectroscopy on a network of MTSSL spin-labeled pairs resolves pairwise inter-label distance distributions.
Supplementary Figure 3	Single-molecule fluorescence measurements and analysis <b>(A)</b> Multi-parameter fluorescence detection histograms. <b>(B)</b> Sub-ensemble fluorescence decays. <b>(C)</b> Filtered fluorescence correlation spectroscopy.
Supplementary Figure 4	Quality controls for labeling based methods. <b>(A)</b> Protein activity measurements <b>(B)</b> dye model consistency <b>(C)</b> temperature dependent state population <b>(D)</b> dimerization activity of labeled species <b>(E)</b> state assignment consistency.
Supplementary Figure 5	Internal dynamics on the nanosecond time-scale by Neutron spin echo spectroscopy (NSE).
Supplementary Figure 6	<b>(A, B)</b> Analysis of molecular dynamics simulations. <b>(C)</b> Identification of flexible regions. <b>(D, E)</b> Stability and significance analysis of integrative models.
Supplementary Figure 7	Assessment of the conformers within the conformational space covered by MD simulations using FRET- and EPR-data.
Supplementary Table 1	Inter-label distance analysis of DEER and ensemble fluorescence decay measurements (eTCSPC). <b>(A)</b> Analysis results of the DEER, FRET ensemble fluorescence decays measurements, and residual anisotropies. <b>(B)</b> Reference fluorescence lifetimes of Alexa647 and Alexa488 maleimide coupled to different single cysteine hGBP1 variants. <b>(C)</b> Complementary inter-dye distance analysis of donor and sensitized acceptor fluorescence decays of sub-ensemble (seTCSPC) obtained from of single-molecule FRET experiments. <b>(D)</b> Uncertainties of the average inter-dye distances determined by eTCSPC measurements.
Supplementary Table 2	Filtered fluorescence correlation spectroscopy analysis results.
Supplementary Table 3	<b>(A)</b> Experimental restraints for rigid body docking. <b>(B)</b> Additional restraints used for rigid body docking.
Supplementary Note 1	Quality assessment of labeled samples for fluorescence spectroscopy, uncertainty estimation, and consistency analysis.
Supplementary Note 2	MD simulations and PC Analysis
Supplementary Note 3	Identification of rigid domain and rigid body decomposition
Supplementary Note 4	Rigid body docking

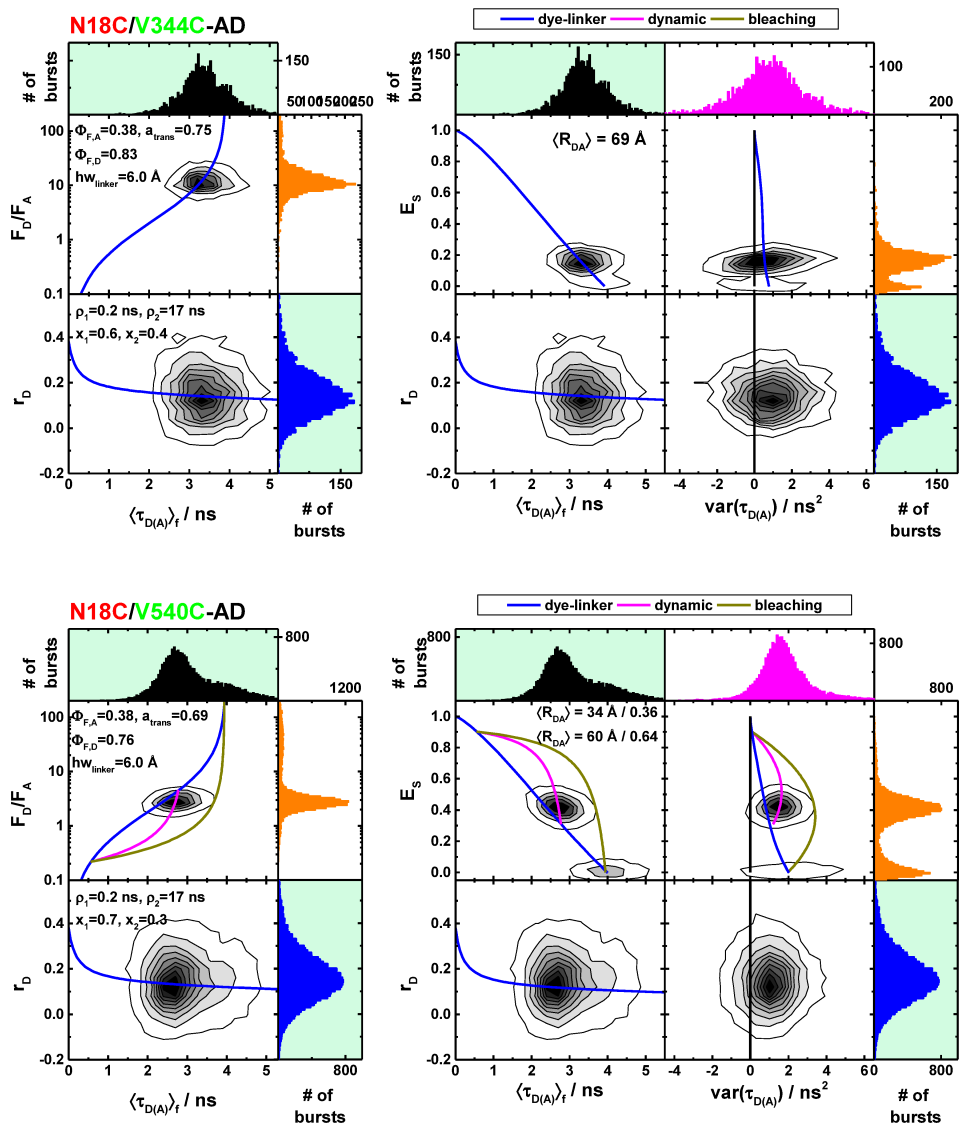
## Supplementary Figures

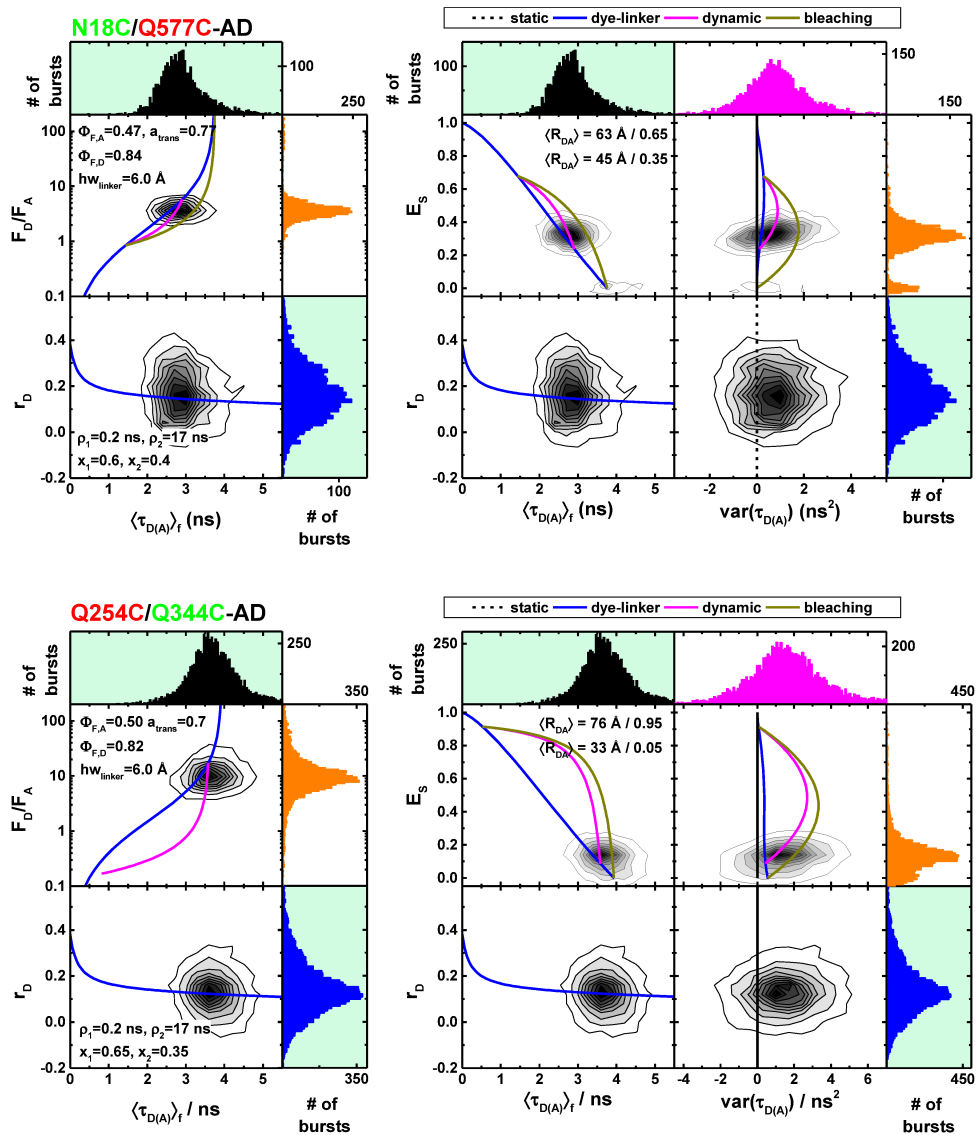


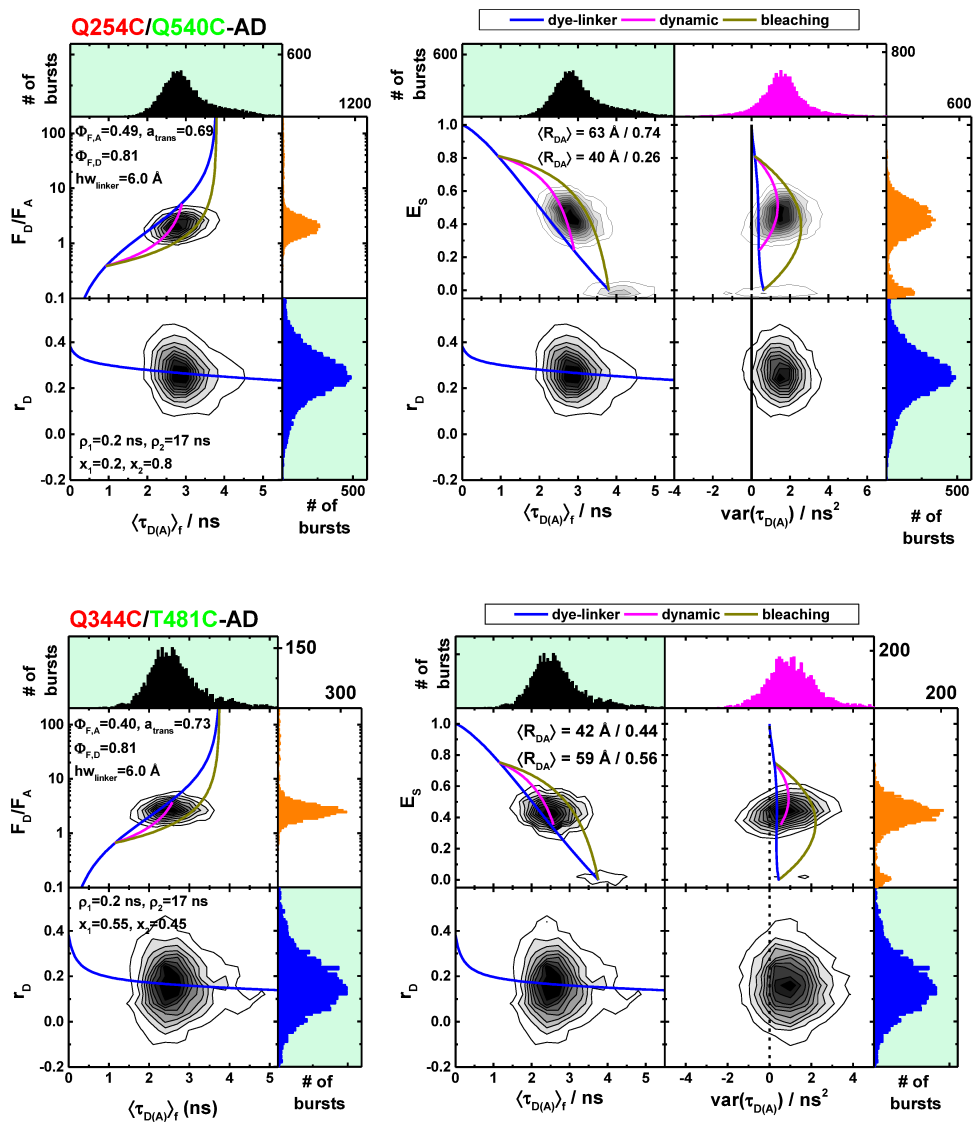
**Supplementary Figure 1** | Small-angle X-ray scattering measurements on the nucleotide-free hGBP1. **(A)** Measured SAXS data of hGBP1 at different protein concentrations. The scattering curves are not normalized by the protein concentration. **(B)** Structure factor of the 29.9 mg/mL solution extracted from the SAXS data. The structure factor is obtained by the background corrected SAXS curves at highest concentration scaled through division by the form factor (empty circles). The fitted structure factors according to the Percus-Yevik structure factor include the correction for the protein asymmetry factor *beta* (full line) (58,75). For comparison the uncorrected structure factor without asymmetry factor is given (stitched line). Data are averaged at larger wave vectors to reduce noise. **(C)** The pair of structural models ( $M_1$ ,  $M_2$ ) selected from the structural ensemble generated by DEER- and FRET-measurements best corresponding to the SAXS scattering data is shown in a cartoon representation. Both structural models are aligned to the LG domain. **(D)** The fitted fractions of the conformer  $M_2$ ,  $x_{M_2}$ , for all combinations ( $M_1$ ,  $M_2$ ) generated by rigid body docking (RBD) using the DEER and FRET constraints are shown in dependence of the reduced sum of the squared deviation,  $\chi_r^2$ , in a 2D histogram. The red line corresponds to a p-value of 0.68. Pairs of structural models above the red line are discriminated.

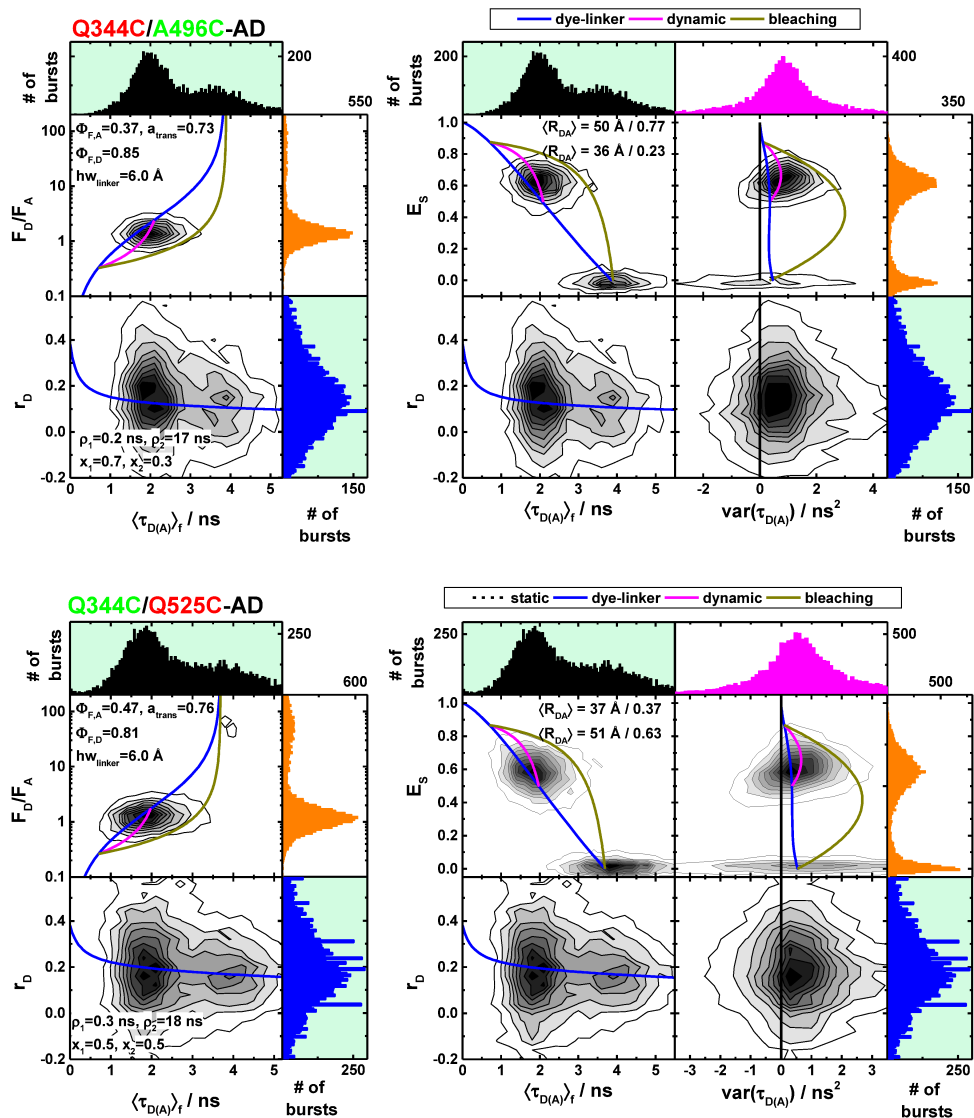


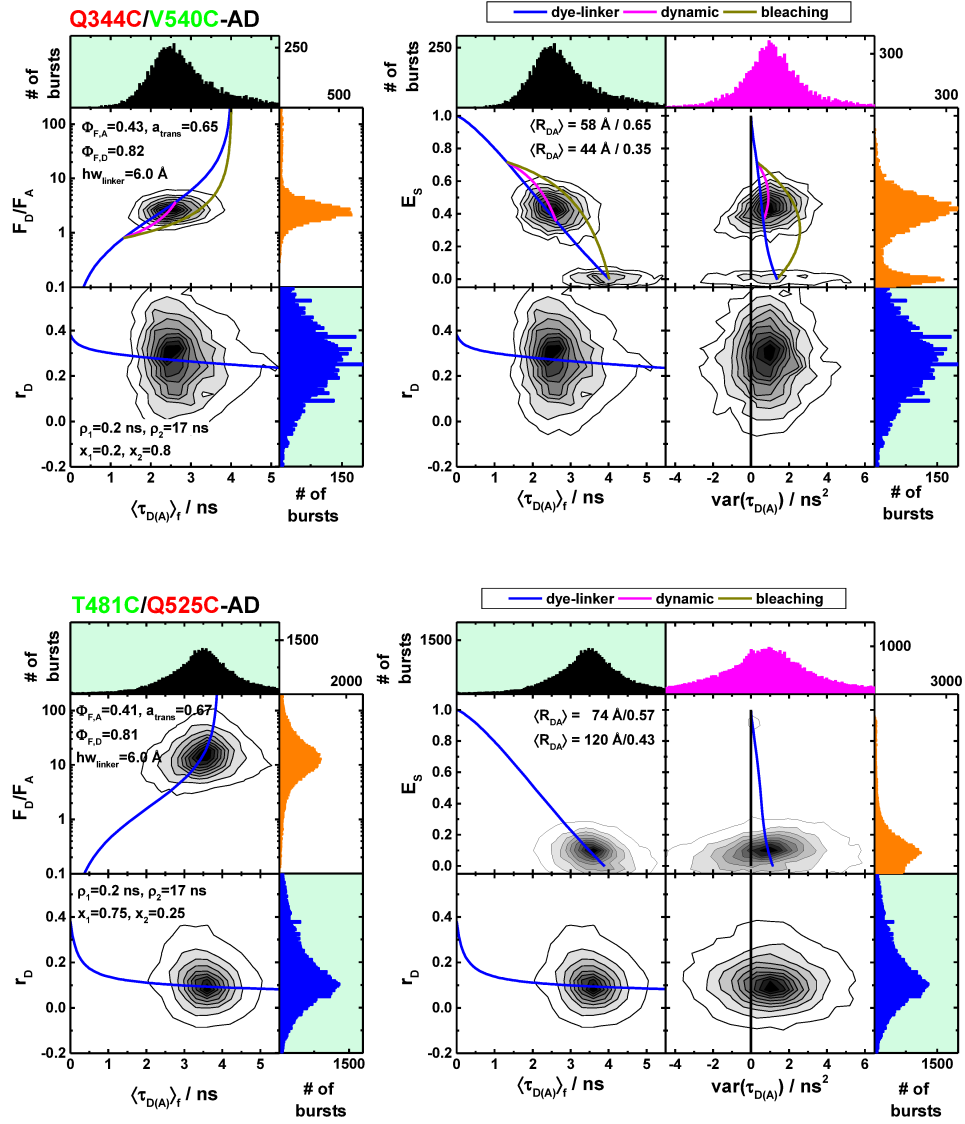
**Supplementary Figure 2 |** DEER-spectroscopy on a network of MTSSL spin-labeled pairs of the hGBP1 resolves pairwise inter-label distance distributions. **(A)** At the top, the network of spin-labeled hGBP1 is shown superposed to a crystal structure of hGBP1. A rotamer library analysis (RLA) simulates for the crystal structure (PDB-ID: 1DG3), the FRET major state ( $M_1$ ), the minor state ( $M_2$ ) inter-spin distance distributions. To the left, experimental background corrected DEER-traces and simulated DEER-traces based on a RLA of different structural models; to the right, inter-spin distance distribution as determined by Tikhonov regularization of the experimental DEER-trace. **(B)** Parametrization of the EPR-MTSSL label for accessible volume calculations. Top the distance distributions for the spin-pair N18C/Q577C of the hGBP1 crystal structure (PDB-ID: 1DG3) as calculated by the MTSSL-Wizard (43) is overlaid by the distance distribution as calculated by accessible volume calculations with the parameter set as provided below. For visual comparison, the rotamers are overlaid with the accessible volume calculated for the labeling position N18C. To parameterize the MTSSL-label we used the variant N18C/Q577C as reference and optimized the simulated linker-length, the label-radius and the linker-width until the distance distribution as determined by the AV-calculations agrees best with the distance distributions as determined by the MTSSL-Wizard(43) and MMM(30). The best agreement was found using a linker-length of 8.5 Å, a linker-width of 4.5 Å and a label-radius of 4.0 Å. All rigid body dockings were performed using this parameter set.



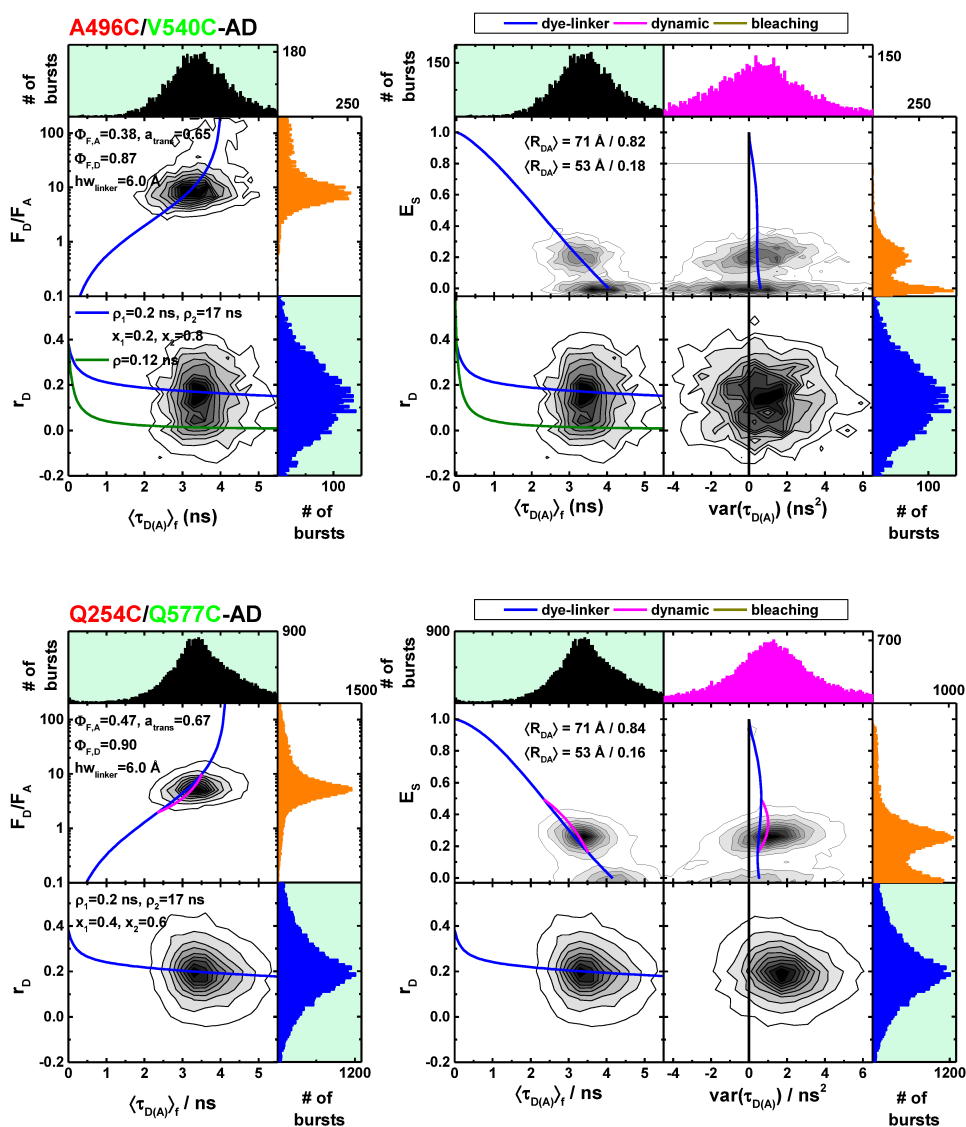




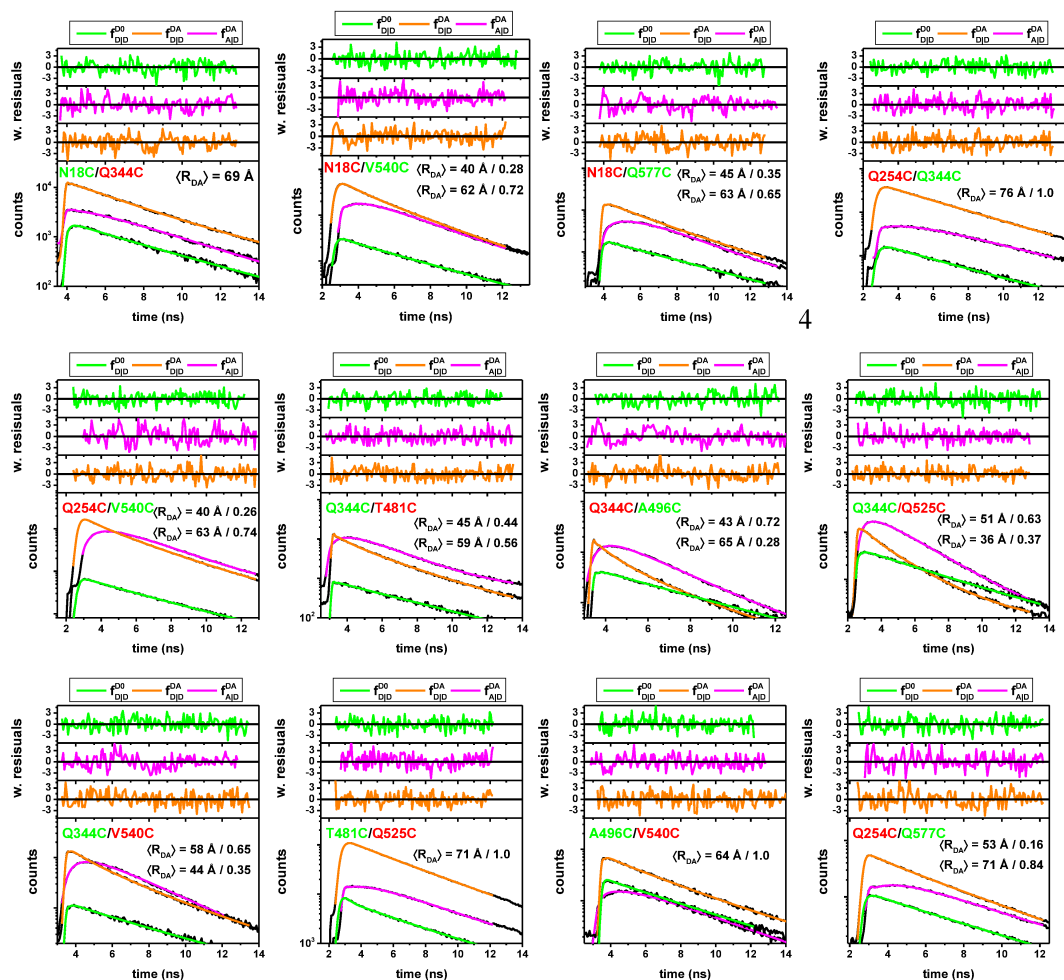




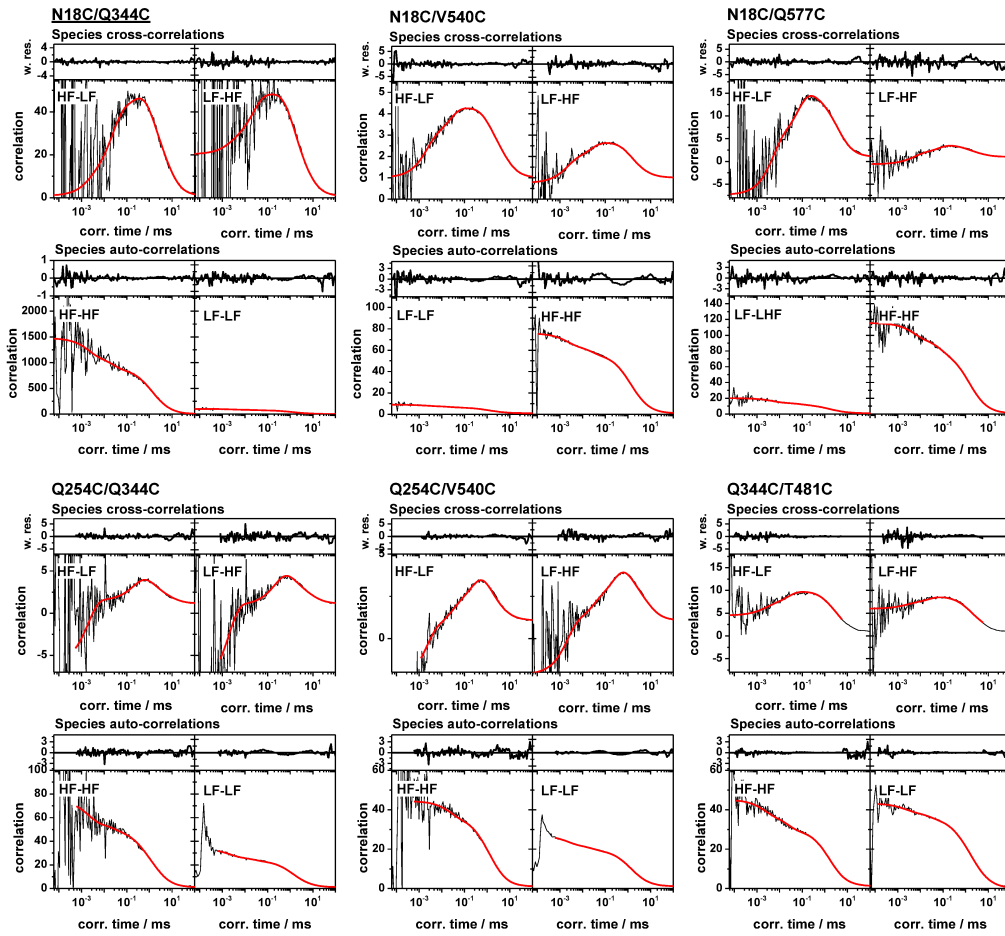


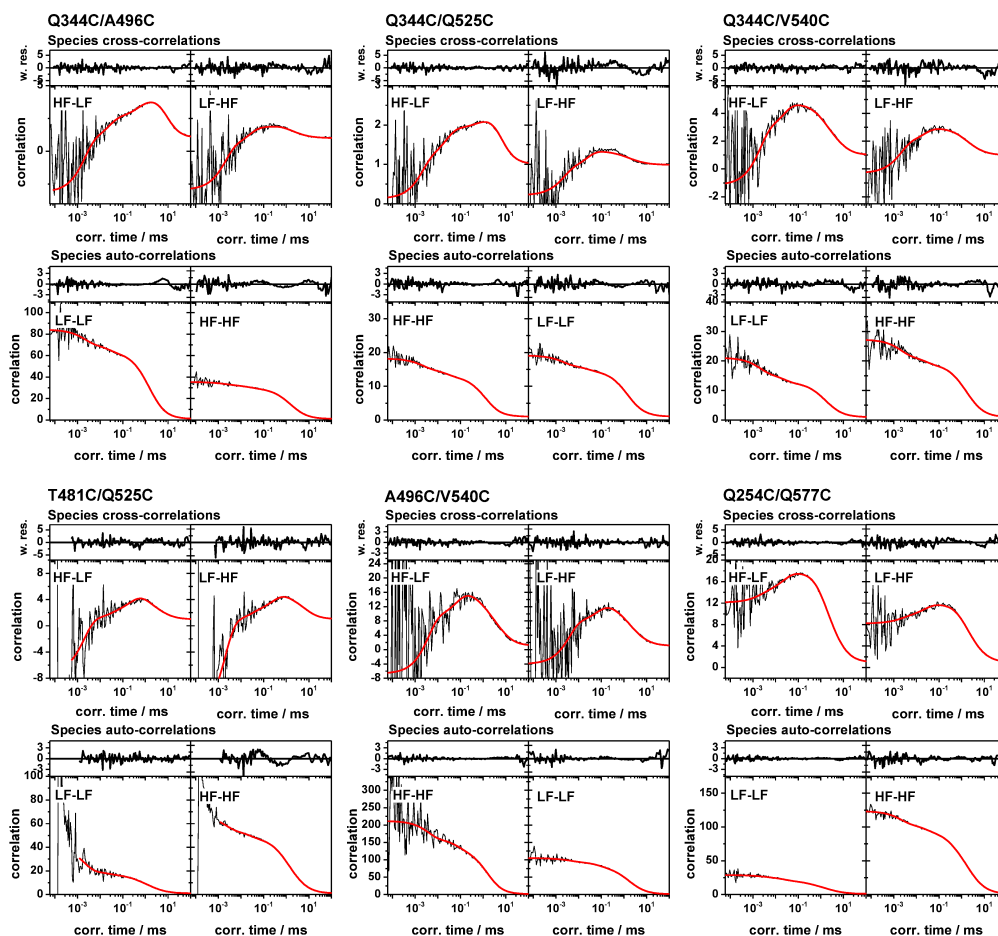


**Supplementary Figure 3A | Single-molecule fluorescence measurements.** Multi-parameter fluorescence detection histograms of different variants of Alexa488 and Alexa647 labeled human guanylate binding protein 1. The dashed blue lines are either static FRET-lines considering linker broadening (top panels) or Perrin-equations for a dye with two rotational correlation times (bottom panels, **Supplementary Note 1, eq. 1**).  $x_1$  and  $x_2$  refer to the fraction of fast and slow rotating dyes, respectively. For variants with states of different FRET efficiencies, dynamic FRET-lines connecting these states are shown as magenta solid line. The dark-yellow lines describe the acceptor bleaching from high-FRET states. The data are displayed in histograms of the donor-acceptor fluorescence intensity-ratio,  $F_D/F_A$ , the steady-state transfer-efficiency,  $E_s$ , and the mean fluorescence averaged lifetime of the donor in the presence of the acceptor  $\langle \tau_{D(A)} \rangle_f$ . The variance of the donor-acceptor lifetime  $var(\tau_{D(A)})$  was calculated for every detected fluorescence burst. The color of the FRET-pair name indicated the most probable position of the donor (green) and acceptor dye (red); as inset the fluorescence quantum yield of the acceptor  $\Phi_{F,A}$  and the donor  $\Phi_{F,D}$  are shown. The fraction of the acceptor Alexa647 in trans-conformation,  $a_{trans}$ , was determined by FCS and is shown as inset.

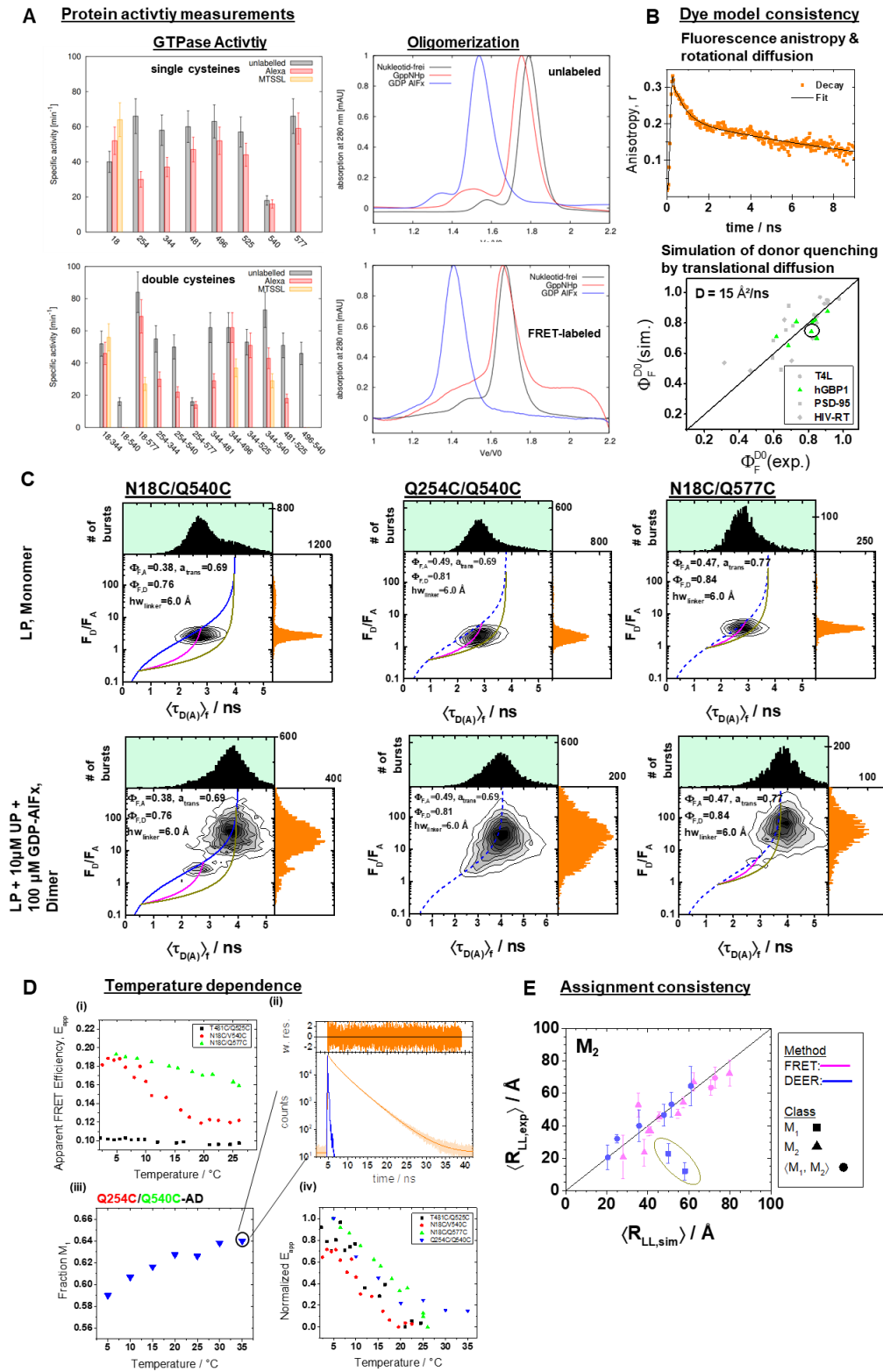


**Supplementary Figure 3B** | Sub-ensemble fluorescence intensity decays of single-molecule FRET measurements on different FRET-labeled (Alexa488, Alexa647) variant of the human guanylate binding protein 1. In green the fluorescence intensity decay of the donor-only fraction of the respective sample are shown. The donor-only fraction was selected by the acceptor intensity. In orange the time-resolved fluorescence intensity of the donor in the presence of the acceptor is shown. In magenta the FRET-sensitized acceptor emission is displayed. The fluorescence decays were jointly analyzed by a weighted combination of normal distributed donor-acceptor distances. The mean and the fractions of the normal distributions are reported by the insets, e.g., the variant Q254C/Q577C was described by two normal distributions, with average distances of 53 Å and 71 Å with fractions of 0.16 and 0.84, respectively.



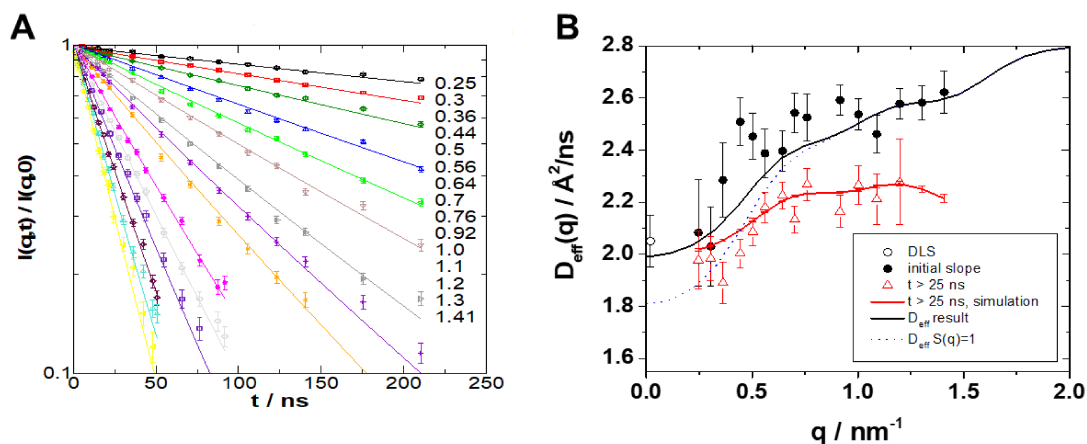


**Supplementary Figure 3C** | Filtered fluorescence correlation spectroscopy of FRET-labeled variants for the human guanylate binding protein 1 probing hGBP1's internal dynamics from  $\mu$ s to ms. In the MFD histograms high FRET, H, and low FRET, L, species were identified to generate a variant specific set of filters. These filters were used to calculate two species cross-correlation functions, *sCCFs*, and two species autocorrelation functions, *sACFs*. For every variant the *sCCFs* and the *sACFs* are shown to the top and bottom, respectively. The *sACFs* and the *sCCFs* of all variants were analyzed by a global model (red lines, **Methods 4, eq. 19**) with three correlation times. The weighted residuals of the model and the data are shown to the top of the *sACFs* and the *sCCFs*. The displayed correlation curves correspond to the fluorescence intensity weighted average correlation curves obtained by subsetting the measurement. The fluorescence intensity weighted averages correspond to the displayed mean correlation amplitudes of the individual correlation channels.

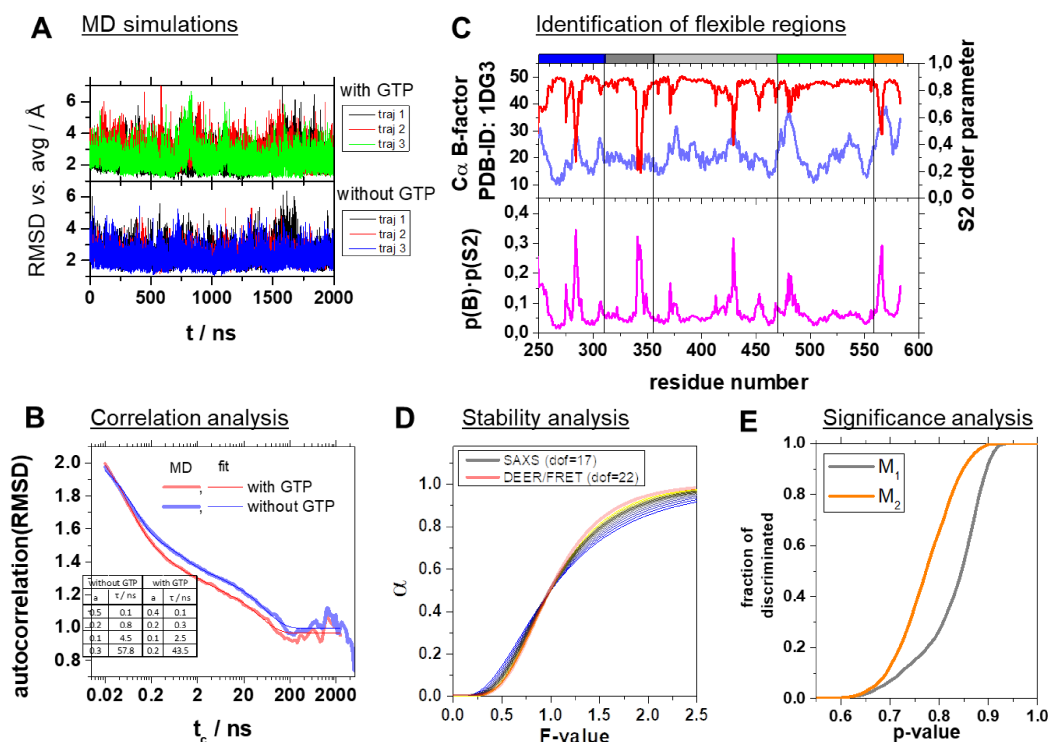


**Supplementary Figure 4 |** Quality controls for labeling based methods. (A) Assessment of the labeling on the protein activity by comparison of the GTPase activity (left) and the self-oligomerization of hGBP1. The effect of labeling on GTPase activity of hGBP1 as measured by the specific activities of  $1\mu\text{M}$  single cysteine hGBP1

mutants at 25°C, either unlabeled or modified by Alexa488 or MTSSL at their free cysteines. Specific activities of the hGBP1 variants labeled by Alexa488 and Alexa647. The effect of the labels on the oligomerization of hGBP1 was assessed by size exclusion chromatography of 20 µM of unlabeled (top, right) and double labelled hGBP1 Cys9 (bottom, right) in the presence of 150 to 200 µM GppNHp or GDP AIFx or in the absence of any nucleotide. **(B)** The fluorescence properties of the dye were studied by time-resolved anisotropies (left). The donor Alexa488 was predominantly freely rotating. This is highlighted by the fast-initial decay of the time-resolved anisotropy,  $r(t)$ . **(C)** Temperature dependent FRET measurements: (i) apparent FRET efficiency  $E_{app} = 1/(1 + S_G/S_R)$  ( $S_G$  and  $S_R$  are the measured (uncorrected) green and red fluorescence intensities) as measured on a steady-state fluorometer. (ii) Time-resolved fluorescence decay of the hGBP1 variant Q254C/Q540C for a temperature of 35 °C. (iii) Temperature dependence of the population of the state M1 for the variant Q254C/Q540C as determined by an analysis of the associated time-resolved fluorescence decays. (iv) Normalized changes of the fluorescence observables in dependence of the temperature. **(D)** Multiparameter single-molecule fluorescence measurements of a set of comparable hGBP1 variants that is weakly affected in their GTP hydrolysis to different extent by the introduced mutations and labels. The Labeling positions N18C and Q254C are on opposing sites of the molecule. LP and UP refer to labeled protein and unlabeled protein, respectively. In the presence of UP and GDP-AIFx hGBP1 forms a dimer and undergoes significant conformational changes. These conformational changes were detected for the variants with weakly (N18C/Q577C) and variants stronger affected in their GTP hydrolysis (Q254C/Q540C) & (N18C/Q577C). The mutation Q577C has for the labeled and the unlabeled hGBP1 no effect on the specific activity. The mutation Q540C affects GTP hydrolysis activity of the labeled and the unlabeled hGBP1 equally strong. The mutation Q254C affects the GTP hydrolysis activity only the presence of a dye. **(E)** A consistency analysis reveals that two DEER datasets (encircled in yellow) resolve  $M_1$  instead of an averaged state of the two states,  $\langle M_1, M_2 \rangle$ . The deviation between the simulated and the experimental observables beyond the noise of the other measurements identify two distances assigned to  $M_2$  as a mis-assignment.

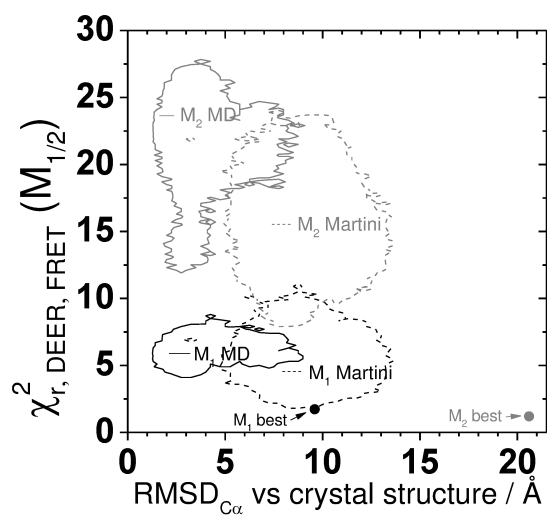


**Supplementary Figure 5** | Neutron spin echo spectroscopy (NSE) on the hGBP1 resolves internal dynamics on the nanosecond time-scale. **(A)** Intermediate scattering function as measured by NSE with fits according to the rigid body models (**Methods 5**). The numbers to the right show the respective wave-vectors from top down with  $q$  in  $\text{nm}^{-1}$ . **(B)** Effective diffusion coefficients determined by NSE together with rigid body diffusion calculated from the protein structure. Circles and black line correspond to values derived from the initial slope of the NSE spectra and for rigid body diffusion at infinite dilution. The strong  $q$ -dependent increase is entirely due to the elongated shape of the protein. Triangles and red line correspond values obtained from exponential fits to the NSE spectra and to theoretical curves (**Methods 5**, **eq. 21**) without internal dynamics for  $t > 25 \text{ ns}$ . It is evident that rigid body diffusion includes a fast component that is visible at short times below 25 ns.



**Supplementary Figure 6 | Analysis of molecular dynamics simulations, identification of flexible regions, and structure generation and discrimination.** (A) Root mean squared deviation (RMSD) vs. the average structure of three repeats of 2  $\mu$ s MD simulations in the presence and absence of GTP bound to the binding pocket of the LG domain. (B) Autocorrelation analysis of the RMSDs. The autocorrelation function of the RMSD vs. the average structure of the MD simulations in the presence (red) and absence (blue) of GTP are shown as light-colored thick lines.  $t_c$  is the correlation time. The darker colored red and blue lines correspond to a multiexponential model ( $\sum_{i=1}^4 a_i \exp(-\frac{t_c}{\tau_i}) + b$ ). The amplitudes  $a_i$  and the characteristic times  $\tau_i$  are given in the table shown as an inset. (C) To the top the crystallographic B-factors of the C $\alpha$  atoms (PDB-ID: 1DG3) and the NH S<sup>2</sup> order parameters calculated from the MD simulations are shown. The bottom graph illustrated the product of the B-factor normalized to the range of (0,1] and the NH S<sup>2</sup> order parameter. (D) Cumulative probability  $\alpha$  that for a given F-value a proposed structural model is significantly worse than the best-found structural model. The experimental degrees of freedom (dof<sub>d,SAXS</sub>) for SAXS was varied from 11 to 24 taking the values 11, 12, 13, 14, 15, 16, 17, 18, 20, 22, 24 with colors varying from blue to yellow. The cumulative probabilities were calculated using the best model as a reference ( $x = \chi^2 / \min(\chi^2)$ ) and an estimate of dof<sub>m</sub> ~ 10 for the degrees of freedom of the model (eq. 24). The dof<sub>d,SAXS</sub> was varied to assess the influence of the relative weights of DEER, FRET and SAXS in eq. 25. (E) Fraction of discriminated structures vs. p-value of discriminating a pair of structure from the best structure.





**Supplementary Figure 7 | Assessment of the conformers within the conformational space covered by MD simulations using FRET- and EPR-data (Supplementary Table 3A).** We evaluated the conformers obtained by multi-resolution MD simulations (all-atom MD and coarse-grained MD with the Martini force field of Barz et al (39) using our FRET positioning and screening (FPS) toolkit (32) to compute the quality parameter  $\chi_{DEER, FRET}^2$  (eq. 23). The structural features of the conformers are described by the measure,  $RMSD_{C\alpha}$  versus the hGBP1 crystal structure (PDB-ID: 1DG3). For comparison, we added the parameters of the best representative conformers for  $M_1$  and  $M_2$  obtained by our integrative structural modeling (Fig. 5).

## Supplementary Tables

**Supplementary Table 1A** | Inter-label distance analysis of DEER measurements, ensemble fluorescence decays (eTCSPC), and residual donor fluorescence anisotropies. Average distances between the spin-labels are referred to as  $\langle R_{LL,exp} \rangle$ . The width of the inter-spin distance distribution is  $w$ . The center values of the donor-acceptor distance distribution correspond to  $\bar{R}_{DA,exp}(M_1)$  and  $\bar{R}_{DA,exp}(M_2)$  for the states,  $M_1$  and  $M_2$ , respectively. The average donor-acceptor distance and the inter-spin distance simulated for the full-length crystal structure of hGBP1 (PDB-ID: 1DG3) are  $\bar{R}_{DA,sim}$  and  $\langle R_{LL,sim} \rangle$ , respectively, with corresponding distribution widths  $w$ . The uncertainty estimates of central distance of a state determined by FRET is  $\Delta(M_{\{1,2\}})$ .

Category/ Type	DEER <sup>(a)</sup>				ensemble FRET <sup>(b)</sup>				Fluorescence Anisotropy <sup>(c)</sup>
	Experiment		Simulation <sup>(c)</sup>		Experiment		Simulation <sup>(d)</sup>		Experiment
State	Average over all states		Crystal (PDB-ID: 1DG3)		$M_1$	$M_2$	Crystal (PDB-ID: 1DG3)		Donor Alexa488
Joint species fractions $x_1, x_2$					0.61	0.39			
Variant	$\langle R_{LL,exp} \rangle$ / Å	$w$ / Å	$\langle R_{LL,sim} \rangle$ / Å	$w$ / Å	$\bar{R}_{DA,exp}(M_1)$ $\pm \Delta(M_1)$ / Å	$\bar{R}_{DA,exp}(M_2)$ $\pm \Delta(M_2)$ / Å	$\bar{R}_{DA,sim}$ / Å	$w$ / Å	$r_\infty$
N18C/Q344C	64.6	12.2	66.5	9.5	73.6±8.6	67.0±5.5	72.4	12.1	0.15
N18C/V540C					57.8±3.6	36.6±2.7	63.6	8.8	0.11
N18C/Q577C	53.2	7.6	50.5	7.5	64.2±4.7	47.4±2.8	60.1	10.5	0.15
C225/K567C	12.0	5.5	13.0	6.5					
C225/Q577C	22.9	6.0	19.5	10.0					
Q254C/Q344C					81.3±16.5	72.3±7.8	73.9	12.2	0.13
Q254C/V540C					63.6±4.6	36.8±2.7	60.9	12.4	0.30
Q254C/V577C					70.8±9.1	52.9±7.4	73.1	8.9	0.17
Q344C/T481C					37.9±2.6	54.5±3.3	57.6	11.2	0.11
Q344C/A496C	40.0	9.6	42.5	10.0	48.0±2.9	23.5±8.2	48.4	10.6	0.19
Q344C/Q525C	32.0	5.4	29.5	10.2	46.7±2.8	20.7±13.3	41.5	10.7	0.30
Q344C/V540C	46.6	6.8	43.0	14.5	59.3±3.8	45.5±2.8	48.7	11.9	0.10
T481C/Q525C					69.6±6.4	69.5±6.4	71.2	11.0	0.30
A496C/V540C					63.6±4.6	63.6±4.6	66.8	11.6	0.23
A551C/Q577C	20.5	7.7	22.5	5.0					

<sup>(a)</sup>DEER distance distributions for calculation of average inter-spin distances and width were determined by Tikhonov regularization of the experimental DEER-traces (eq. 7). <sup>(b)</sup>The ensemble fluorescence decays were jointly analyzed by a quasi-static homogeneous model (29) with two FRET species with the species fractions  $x_1$  and  $x_2$  as well as a D-only species (eqs. 10, 13) using the donor properties in Tab. S1B and a Förster Radius  $R_0 = 52$  Å. Moreover, the model accounted for the distance distribution with a typical width of 12 Å caused by the flexible dye-linkers (eq. 11). The reported uncertainty estimates, indicated by  $\pm$ , include statistical uncertainties, potential systematic errors of the references, uncertainties of the orientation factor determined by the anisotropy of donor samples, and uncertainties of the AVs due to the differences of the donor and acceptor linker length (Note S1 section 5). The individual components are listed in Tab. S1D. Reference measurements of single D and A labeled variants are summarized in Tab. S1B, respectively. <sup>(c)</sup>For EPR-DEER the inter-spin distance distribution was calculated by a rotamer library analysis (see Methods 7). <sup>(d)</sup>The inter-fluorophores distance distribution and the corresponding average distance and width were calculated by accessible volume simulations.<sup>(32)</sup> <sup>(e)</sup>Residual anisotropies of Alexa488 in FRET labeled (Alexa488, Alexa647) variants of the human guanylate binding protein 1 determined by an analysis of the MFD histograms using a Perrin equation for a bio-exponential anisotropy decay (Fig. S3)

**Supplementary Table 1B** | Fluorescence lifetimes,  $\tau$ , with corresponding species fractions,  $x$ , of Alexa647 and Alexa488 maleimide coupled to different single cysteine variants of the hGBP1 determined by an analysis of the fluorescence intensity decays measured by ensemble TCSPC.

Variant	Alexa647 <sup>(a)</sup>								Alexa488 <sup>(a)</sup>					
	$x_1$	$\tau_1 /$ ns	$x_2$	$\tau_2 /$ ns	$x_3$	$\tau_3 /$ ns	$\langle \tau \rangle_x$ / ns (b)	$\Phi_{F,A}$ (c)	$x_1$ (a)	$\tau_1 /$ ns	$x_2$	$\tau_2 /$ ns	$\langle \tau \rangle_x /$ ns (b)	$\Phi_{F,D}$ (c)
N18C	0.39	1.85	0.49	1.22	0.12	0.10	1.33	0.40	0.82	4.15	0.18	1.35	3.65	0.82
Q254C	0.58	2.23	0.42	1.42			1.89	0.57	0.69	3.60	0.31	0.53	2.65	0.59
Q344C	0.58	2.06	0.42	1.09			1.75	0.52	0.94	3.80	0.06	1.00	3.63	0.81
T481C	0.43	1.89	0.57	1.32			1.57	0.43	0.93	3.78	0.07	1.07	3.59	0.81
A496C	0.43	1.21	0.57	1.88			1.59	0.48	0.84	3.89	0.16	1.14	3.44	0.77
Q525C	0.65	1.93	0.35	1.08			1.63	0.49	0.80	3.51	0.20	0.66	2.94	0.66
V540C	0.65	2.33	0.35	1.43			2.02	0.60	0.85	4.00	0.15	1.86	3.67	0.82
Q577C	0.49	2.06	0.51	1.42			1.73	0.52	0.91	4.15	0.09	1.49	3.91	0.88

<sup>(a)</sup> The number of fluorescence lifetime components corresponds to the minimum number required to sufficiently describe the experimental data, as judged by a  $\chi_r^2$  criterion. <sup>(b)</sup>  $\langle \tau \rangle_x$  is the species weighted average fluorescence lifetime  $\langle \tau \rangle_x = \sum_i x_i \tau_i$ . <sup>(c)</sup>  $\Phi_F$  is the fluorescence quantum yield of the fluorescent dye species estimated by the species averaged fluorescence lifetime  $\langle \tau \rangle_x$ , using  $\langle \tau \rangle_x$ , and  $\Phi_F$  of the free dyes as a reference; (Alexa647,  $\langle \tau \rangle_x = 1.0$  ns,  $\Phi_F = 0.32$ ) (Alexa488,  $\langle \tau \rangle_x = 4.1$  ns,  $\Phi_F = 0.92$ ).

**Supplementary Table 1C** | Complementary inter-dye distance analysis of donor and sensitized acceptor fluorescence decays of sub-ensemble (seTCSPC) obtained from of single-molecule FRET experiments (**Supplementary Figure 3B**) for different FRET labeled (Alexa488, Alexa647) hGBP1 variants. The donor and acceptor fluorescence decays were described by a combination of two normal distributed distances with the central distances of  $\bar{R}_{DA}$  of a state. The fractions  $x_1$  and  $x_2$  correspond to the fraction of the distance  $\bar{R}_{DA}(M_1)$  and  $\bar{R}_{DA}(M_2)$ , respectively.  $x_{DOnly}$  is the fraction of molecules with no energy transfer to an acceptor. The distances recovered by eTCSPC (Tab. 1A) and seTCSPC, respectively, agree nicely within the distinct precision of each data set.

hGBP1 variant	$\bar{R}_{DA}(M_1) / \text{\AA}$	$x_1$	$\bar{R}_{DA}(M_2) / \text{\AA}$ (a)	$x_2$ (a)	$x_{DOnly}$
N18C/Q344C	69.3	1.00	-	-	0.18
N18C/V540C	60.0	0.50	34.1	0.50	0.37
N18C/Q577C	63.3	0.65	45.1	0.35	0.17
Q254C/Q344C	76.1	1.00	-	-	0.21
Q254C/V540C	63.4	0.74	39.3	0.26	0.31
Q344C/T481C	45.0	0.44	59.3	0.56	0.17
Q344C/A496C	47.0	0.77	36.0	0.23	0.45
Q344C/Q525C	51.5	0.63	36.1	0.37	0.40
Q344C/V540C	57.8	0.65	43.8	0.35	0.24
T481C/Q525C	70.6	1.00	-	-	0.20
A496C/V540C	63.9	1.00	-	-	0.37
Q254C/Q577C	70.8	0.84	52.9	0.16	0.34

<sup>(a)</sup> For cases where a single normal distribution was enough to describe the data no second distance and fraction is reported.

**Supplementary Table 1D** | Combined and individual uncertainty contributions of the average inter-dye distances determined by eTCSPC measurements.

Variant	State	Combined uncertainty <sup>(a)</sup>		Statistical uncertainty <sup>(b)</sup>	Reference uncertainty <sup>(c)</sup>		Dye simulation <sup>(d)</sup>	Orientation factor <sup>(e)</sup>
		$\delta_+$	$\delta_-$	$\delta_{stat}$	$\delta_{+,ref}$	$\delta_{-,ref}$	$\delta_{AV}$	$\delta_{\kappa 2}$
N18C/Q344C	(1)	12.1%	11.3%	9.1%	6.0%	4.2%	1.1%	4.9%
N18C/V540C	(1)	6.3%	6.3%	3.1%	1.2%	1.1%	1.4%	4.5%
N18C/Q577C	(1)	7.4%	7.3%	4.6%	2.3%	2.0%	1.2%	4.9%
Q254C/Q344C	(1)	22.0%	18.6%	16.5%	13.5%	6.9%	1.0%	4.7%
Q254C/V540C	(1)	7.2%	7.1%	4.4%	2.2%	1.9%	1.3%	5.8%
Q344C/T481C	(1)	6.9%	6.9%	4.1%	0.1%	0.1%	2.1%	4.5%
Q344C/A496C	(1)	6.0%	6.0%	2.5%	0.4%	0.4%	1.7%	5.4%
Q344C/Q525C	(1)	6.0%	6.0%	2.5%	0.3%	0.3%	1.7%	6.1%
Q344C/V540C	(1)	6.5%	6.4%	3.4%	1.4%	1.3%	1.3%	4.3%
T481C/Q525C	(1)	9.4%	9.1%	6.7%	4.0%	3.1%	1.2%	6.1%
A496C/V540C	(1)	7.2%	7.2%	4.4%	2.2%	1.9%	1.3%	5.7%
Q254C/Q577C	(1)	13.0%	12.7%	11.0%	4.5%	3.4%	1.1%	5.1%
N18C/Q344C	(2)	8.1%	7.9%	5.6%	3.1%	2.5%	1.2%	4.9%
N18C/V540C	(2)	7.3%	7.3%	4.6%	0.1%	0.1%	2.2%	4.5%
N18C/Q577C	(2)	5.8%	5.8%	2.5%	0.4%	0.3%	1.7%	4.9%
Q254C/Q344C	(2)	10.9%	10.3%	8.3%	5.3%	3.8%	1.1%	4.7%
Q254C/V540C	(2)	7.7%	7.7%	4.5%	0.1%	0.1%	2.2%	5.8%
Q344C/T481C	(2)	5.5%	5.5%	2.7%	0.8%	0.8%	1.5%	4.5%
Q344C/A496C	(2)	34.8%	34.8%	34.2%	0.0%	0.0%	3.4%	5.4%
Q344C/Q525C	(2)	64.6%	64.6%	64.2%	0.0%	0.0%	3.9%	6.1%
Q344C/V540C	(2)	5.4%	5.4%	2.6%	0.3%	0.3%	1.8%	4.3%
T481C/Q525C	(2)	10.0%	9.7%	6.7%	4.0%	3.1%	1.2%	6.1%
A496C/V540C	(2)	7.6%	7.5%	4.4%	2.2%	1.9%	1.3%	5.7%
Q254C/Q577C	(2)	14.0%	14.0%	12.9%	0.7%	0.7%	1.5%	5.1%

<sup>(a)</sup> The combined uncertainty used to calculate the relative ( $\delta_{\pm}$ ) and the absolute ( $\delta_{\pm}$ ) uncertainties of the inter-dye distances considers the uncertainty of the dye simulations,  $\delta_{AV}$ , the uncertainty of the orientation factor,  $\delta_{\kappa 2}$ , the uncertainty of the reference sample,  $\delta_{\pm,ref}$ , and the statistical uncertainty determined by the noise of the measurements,  $\delta_{stat}$  (see Note S1, section 5). <sup>(b)</sup> The statistical uncertainties were estimated by sampling the distances that agree with the experimental ensemble TCSPC data (see Tab. S1A). <sup>(c)</sup> The reference uncertainties were calculated assuming an uncertainty of the reference donor fluorescence lifetime of  $\Delta\tau_{D(0)} = 0.15$  ns. <sup>(d)</sup> The dye simulation error considers the labeling uncertainty of the dye. In accessible volume simulations (AV) for the dye pair Alexa488/Alexa647 this labeling uncertainty results in an expected error of  $\Delta AV = 0.8$  Å (24). <sup>(e)</sup> The uncertainty of the distance due to the orientation factor was estimated using a wobbling in a cone model of the dyes using the experimental anisotropies (see Tab. S1A).

**Supplementary Table 2** | Filtered fluorescence correlation spectroscopy (fFCS) of all FRET-labeled variants of the human guanylate binding protein 1 analyzed by a global model with joint relaxation times and individual amplitudes  $A_i$ . Selection criteria for the definition of the filters for the high FRET (HF) and low FRET (LF) species.

hGBP1 variant	Amplitude <sup>(a)</sup>			Burst selection criteria for fFCS filter generation <sup>(b)</sup>			
	$A_1$	$A_2$	$A_3$	HF range, $S_g/S_r$		LF range, $S_g/S_r$	
N18C/Q344C	0.38±0.09	0.50±0.18	0.12±0.20	0.09	2.03	5.82	13.19
N18C/V540C	0.18±0.03	0.37±0.04	0.45±0.06	0.10	1.00	4.00	10.80
N18C/Q577C	0.24±0.06	0.41±0.09	0.36±0.11	0.40	1.50	3.00	26.00
Q254C/Q344C	0.35±0.09	0.00±0.00	0.65±0.09	0.70	1.70	2.80	5.90
Q254C/V540C	0.34±0.03	0.21±0.05	0.45±0.06	0.18	0.56	3.50	8.90
Q344C/T481C	0.24±0.11	0.34±0.14	0.41±0.18	0.10	0.60	1.60	6.30
Q344C/A496C	0.08±0.03	0.30±0.06	0.62±0.07	0.03	0.58	1.70	22.36
Q344C/Q525C	0.00±0.05	0.45±0.09	0.55±0.10	0.07	0.28	2.94	8.07
Q344C/V540C	0.08±0.02	0.33±0.07	0.59±0.07	0.08	0.70	1.92	8.74
T481C/Q525C	0.58±0.13	0.09±0.05	0.32±0.14	0.60	1.52	16.27	25.40
A496C/V540C	0.21±0.07	0.32±0.17	0.47±0.18	0.07	1.77	4.61	11.40
Q254C/Q577C	0.34±0.07	0.45±0.11	0.21±0.13	0.51	1.39	5.18	11.07
<b>Correlation time / <math>\mu</math>s</b>	297.6	22.6	2.0				

<sup>(a)</sup>The correlation times were determined by a joint/global analysis of fFCS curves (Methods 4, eq. 19, Fig. S3C). The amplitudes  $A_1$ ,  $A_2$ , and  $A_3$  are variant specific. The uncertainties were determined by a support plane analysis, which considers the mean and the standard deviation of the individual correlation channels determined by splitting the measurements into smaller sets. <sup>(b)</sup> Filters defining the high FRET (HF) and the low FRET (LF) species were generated by selecting bursts that are within the given ranges. To select high FRET and low FRET bursts the ratio of the green and red signal intensity ratio,  $S_g/S_r$ , was used. Sub-ensemble fluorescence decay histograms of the molecules in these ranges were generated and used to calculate filters for fFCS as previously described (5).

**Supplementary Table 3A | Experimental restraints for rigid body docking.** Analysis results of DEER-EPR and FRET eTCSPC. The labels Alexa488, Alexa647, and MTSSL are referred to by D, A, and R1, respectively. The names of the labeling sites report on the location of the dyes and the introduced mutation. The measurements recovered average inter-label distances  $\langle R_{LL,exp} \rangle$ . For FRET mean distances  $\bar{R}_{DA,exp}$  and uncertainties of the mean are reported ( $\Delta_+$  and  $\Delta_-$ ). The widths of the inter-spin distance distribution  $w_+$  and  $w_-$  are reported for DEER. The measurements are grouped into three classes. Class informs on  $M_1$  and  $M_2$  by two distinct distances. Class (b) informed on  $M_1$ . In class (c) measurements  $M_1$  and  $M_2$  were not resolved into separate states. The simulated average label-to-label distances correspond to the distances of the pair of structures ( $M_1, M_2$ ) best agreeing with SAXS, DEER, and FRET combined.

Labelling site [a]				Experiment						Simulation		Group
#	Technique	1	2	$M_1$			$M_2$			$M_1$	$M_2$	
				$\bar{R}_{DA,exp} / \text{\AA}$	$\Delta_+ / \text{\AA}$	$\Delta_- / \text{\AA}$	$\bar{R}_{DA,exp} / \text{\AA}$	$\Delta_+ / \text{\AA}$	$\Delta_- / \text{\AA}$	$\bar{R}_{DA,sim} / \text{\AA}$		
1	FRET	Q344C <sup>D</sup>	N18C <sup>A</sup>	73.6	8.9	8.3	67.0	5.6	5.4	73.9	62.3	(a)
2		V540C <sup>D</sup>	N18C <sup>A</sup>	57.8	3.6	3.6	36.6	2.7	2.7	63.9	40.3	
3		N18C <sup>D</sup>	Q577C <sup>A</sup>	64.2	4.7	4.7	47.4	2.8	2.8	62.3	54.8	
4		Q344C <sup>D</sup>	Q254C <sup>A</sup>	81.3	17.9	15.1	72.3	8.0	7.6	78.0	79.8	
5		V540C <sup>D</sup>	Q254C <sup>A</sup>	63.6	4.6	4.5	36.8	2.7	2.7	63.2	41.3	
6		Q344C <sup>D</sup>	T481C <sup>A</sup>	37.9	2.6	2.6	54.4	3.3	3.3	49.2	57.3	
7		A496C <sup>D</sup>	Q344C <sup>A</sup>	48.0	2.9	2.9	23.5	8.2	8.2	43.4	38.3	
8		Q344C <sup>D</sup>	Q525C <sup>A</sup>	46.7	2.8	2.8	20.7	13.3	13.3	43.6	28.0	
9		Q344C <sup>D</sup>	V540C <sup>A</sup>	59.3	3.8	3.8	45.5	2.8	2.8	53.1	45.5	
10		Q577C <sup>D</sup>	Q254C <sup>A</sup>	70.8	9.2	9.0	52.9	7.4	7.4	75.2	35.4	
#	Technique	1	2	$\langle R_{SS,exp} \rangle / \text{\AA}$						$\langle R_{SS,sim} \rangle / \text{\AA}$		(b)
				$w_+ / \text{\AA}$	$w_- / \text{\AA}$							
11	DEER	C225C <sup>R1</sup>	K567C <sup>R1</sup>	12.0	5.5	5.5	-[b]	-	-	16.4	58.1	
12		C225C <sup>R1</sup>	Q577C <sup>R1</sup>	22.9	6.0	6.0	-[b]	-	-	29.6	50.1	
				$M_1 \& M_2$			$M_1$	$M_2$				
				$\bar{R}_{DA,exp} / \text{\AA}$	$\Delta_+ / \text{\AA}$	$\Delta_- / \text{\AA}$	$\bar{R}_{DA,sim} / \text{\AA}$					
13	FRET	T481C <sup>D</sup>	Q525C <sup>A</sup>	69.6	6.6	6.3	68.6	72.7				(c)
14		A496C <sup>D</sup>	V540C <sup>A</sup>	63.6	4.6	4.6	71.7	70.7				
#	Technique	1	2	$\langle R_{SS,exp} \rangle / \text{\AA}$	$w_+ / \text{\AA}$	$w_- / \text{\AA}$	$\langle R_{SS,sim} \rangle / \text{\AA}$					
15	DEER	N18C <sup>R1</sup>	Q344C <sup>R1</sup>	64.6	12.2	12.2	73.3	60.9				
16		N18C <sup>R1</sup>	Q577C <sup>R1</sup>	53.2	7.6	7.6	63.9	51.6				
17		A551C <sup>R1</sup>	Q577C <sup>R1</sup>	20.5	7.7	7.7	33.0	20.5				
18		Q344C <sup>R1</sup>	A496C <sup>R1</sup>	40.0	9.6	9.6	38.8	35.8				
19		Q344C <sup>R1</sup>	Q525C <sup>R1</sup>	32.0	2.7	2.7	36.7	25.0				
20		Q344C <sup>R1</sup>	V540C <sup>R1</sup>	46.6	6.8	6.8	51.4	47.9				
								$\chi^2_r$	2.07	1.89		

[a] The names of the labelling sites report on the most likely position of the donor and the acceptor dyes. The distribution among the labelling sites was determined by an analysis of the time-resolved anisotropy decay, anisotropy PDA, and limited proteolysis of the labelled protein. [b] A consistency analysis identifies that  $M_2$  must have long distances ( $\langle R_{SS,exp} \rangle > 5$  nm) beyond the DEER detection limit for this measurement setting (see **Supplementary Note 1** (section 6) and **Fig. S4E**).

**Supplementary Table 3B | Additional restraints for rigid body docking.**

Atom 1		Atom 2		$R_{eq} / \text{\AA}$	$k_{ij+} / \text{\AA}$	$k_{ij-} / \text{\AA}$	Restrain origin
Residue	Atom name	Residue	Atom name				
309	C	310	N	1.5	0.5	0.5	Primary sequence
373	C	374	N	1.5	0.5	0.5	
481	C	482	N	1.5	0.5	0.5	
563	C	564	N	1.5	0.5	0.5	
445	C $\alpha$	348	C $\alpha$	5.1	2	2	X-ray 1DG3
391	C $\alpha$	336	C $\alpha$	8	4	4	
381	C $\alpha$	527	C $\alpha$	8.2	4	4	
323	C $\alpha$	292	C $\alpha$	9.3	4	4	

## Supplementary Notes

### Supplementary Note 1. Quality assessment of labeled samples for fluorescence spectroscopy, uncertainty estimation, and consistency analysis

Mutations and labels introduced to different sites of a protein may influence the conformations the protein adopts. Thus, any kind of modification is a putative cause of alterations in protein structure, function, and activity and may, in the worst-case, invalidate conclusions of following experiments. Moreover, for labels which specifically interact with the studied biomolecule, modelling the positional distribution of a labels by their sterically allowed accessible volume (AV) and/or accessible contact volume (ACV) may lead to inaccurate structural models. The ACV explicitly the fraction of fluorescent dyes bound to the molecular surface. The fraction of bound dyes was estimated by the residual anisotropy.

To address these general concerns we: (1) select potential labeling sites based on biochemical pre-knowledge, e.g., we avoid active/catalytic sites, (2) characterize the effect of the mutations on hGBP1's activity, (3) measure the rotational mobility of the fluorescence dyes by their anisotropy, (4) use the fluorescence quenching of the donor dyes by their environment in combination with coarse-grained simulations as an indicator for their translational mobility. By (2) and (3) we probe the effect of the mutations and the labels on the protein. By (4) we assure correct references for accurate analysis results of the fluorescence decay. By (3) and (4) we test the applicability of the coarse-grained AV and ACV model to describe the spatial distribution by which we recover for a given structural model the theoretical spectroscopic properties.

#### (1) Selection of labeling sites

To avoid alteration of protein function (nucleotide binding and hydrolysis, oligomerization), neither amino acid positions in direct proximity to the nucleotide binding pocket nor inside the G domain dimerization interface nor charged amino acids on the protein surface were taken into consideration for labeling.(76) All chosen positions had an accessible surface area (ASA) value higher than 60 Å<sup>2</sup>. In the end, eight amino acids distributed over the entire protein were chosen.

#### (2) hGBP1's function: Effect of (i) mutations, (ii) labeling, and (iii) temperature

(i) **Mutations.** The used cysteine mutants are based on a cysteine-free hGBP1 construct where all nine native cysteines were mutated to alanine or serine namely: C12A, C82A, C225S, C235A, C270A, C311A, C396A, C407S and C589S. Previously, these mutations were shown to only weakly affect hGBP1's function (24,55). Before introduction of new cysteines for site-specific labelling the *GTPase activity* and *nucleotide binding behavior* were characterized. The GTPase activity of the labeled and unlabeled hGBP1 variants was quantified by an assay as



previously described.<sup>(77)</sup> Briefly, hGBP1's hydrolytic activity was controlled by high performance liquid chromatography using a Chromolith Performance RP-18 end-capped column (Merck, Darmstadt) as described earlier.<sup>(77)</sup> 1  $\mu$ M of protein were incubated with 350  $\mu$ M GTP at 25°C. The samples were analyzed at different time points. The time dependence of the substrate concentration was used to calculate the specific activities of the different protein mutants (**Fig. S4A**). The assay for measuring the protein activity has an error smaller than 10%. However, besides the relative activity the absolute uncertainty in determining the (active) protein concentration needs to be considered. Hence, the overall uncertainty in determining the absolute protein activities is ~30%. Except of A496C and Q344C/A496C, all mutants produced more GMP than GDP, as known for the wildtype hGBP1.<sup>(78)</sup>

**(ii) Labelling.** To check if the fluorophores bound to cysteines in hGBP1 have an impact on the oligomerization behavior an unlabeled and a labeled construct were analyzed by analytical gel filtration in the presence and the absence of a nucleotide, which induces oligomerization (**Fig. S4A**). For this analysis, the variant N18C/Q577C was chosen, because N18C and Q577C are localized in proximity to dimerization interfaces of the LG and helix  $\alpha$ 13, respectively. The fluorophores are attached to the sulfhydryl group of the cysteines via a linker of ~20 Å in length. Thus, they potentially interfere with the self-oligomerization of hGBP1. However, the elugrams of the labeled and unlabeled N18C/Q577C did not show any differences (**Fig. S4A**). This indicates that, at least for this mutant, the labels do not influence for hGBP1 assembly. As shown for hGBP1 Cys9, no dimer formation was observed in the presence of 200  $\mu$ M GppNHp independent of being labelled or not.

In addition to the biochemical activity assays that report on the hydrolytic activity of the GTPase domain, we performed single-molecule FRET measurements of the labeled protein (LP) in the presence of excess unlabeled protein (UP) and GDP-AlFx as a substrate. Under these conditions, hGBP1 forms a dimer and undergoes significant conformational changes as seen by the significant changes of the FRET indicator  $F_D/F_A$  in **Fig. S4C**. We found minor differences among three comparable hGBP1 variants, which are affected in the hydrolysis activity to a different degree by the presence of a fluorescent dye. Hence, we conclude that a fluorescent dye, which affects the hydrolysis activity due to its proximity to hGBP1's GTP binding site has only minor influence on the global domain arrangement that is of interest in this study (**Fig. S4C**).

**(iii) Temperature.** Using a steady-state fluorometer, we measured the variants T481C/Q525C, N18C/V540C, and N18C/Q577C. As anticipated, we found a larger change in the FRET

efficiency in dependency of the temperature for the variants N18C/V540C and N18C/Q577C as compared to the variant T481C/Q525C (**Fig. S4D (i)**). For T481C/Q525C M1 and M2 are merely indistinguishable (see distances). For these measurements, we found that the largest relative change of the populations happens between 10 °C and 25 °C. From these measurements, no absolute populations can be determined. Hence, we performed after we acquired a temperature-controlled time-resolved fluorescence spectrometer a temperature series. One measurement out of this set of measurements is shown below in **Fig. S4D (ii)**. For this variant, we only found minor changes of the relative population of the states M<sub>1</sub> and M<sub>2</sub> (**Fig. S4D (iii)**). We compared the different measured variants by normalizing the observed changes (**Fig. S4D (iv)**). We found an average midpoint for all the variant of ~15°C. Hence, the relative population of the states at higher temperatures as found in a living cell resembles the measurements at room temperature.

### (3) Rotational mobility of the fluorescence dyes

The rotational mobility of the dyes was probed by measuring their time-resolved anisotropy,  $r(t)$ , using multiparameter fluorescence detection in single-molecule experiments. A formal analysis of  $r(t)$  by a multiexponential relaxation model reveals typically “fast” and slow rotational correlation times  $\rho_{fast} < 1$  ns and  $\rho_{slow} > 20$  ns (**Fig. S4B, upper panel**). The fast component we attribute to the rotation of the dye tethered to the protein. The slow component we attribute to the dye which sticks to the protein surface and thus senses the global rotation of the protein. Hence, the anisotropy decay  $r(t)$  reflects local motions of the dye and global rotations of the macromolecule

$$r(t) = \left[ (r_0 - r_\infty) e^{-\frac{t}{\rho_{local}}} + r_\infty \right] e^{-\frac{t}{\rho_{global}}} \cong (r_0 - r_\infty) e^{-\frac{t}{\rho_{local}}} + r_\infty e^{-\frac{t}{\rho_{global}}}. \quad (1)$$

Above  $r_0$  is the fundamental anisotropy (fixed to  $r_0 = 0.38$ ),  $\rho_{global}$  is the global rotation time,  $\rho_{local}$  is the local rotation time, and  $r_\infty$  is the residual anisotropy. The anisotropy difference  $(r_0 - r_\infty)$  relates to the fraction of freely rotating dyes.

To determine  $(r_0 - r_\infty)$  for the donor dyes, the two-dimensional single-molecule histograms of the steady-state anisotropy,  $r_s$ , and the fluorescence lifetime,  $\tau$ , were analyzed with a Perrin equation derived for dyes with a bi-exponential anisotropy decay (**Fig. S4B**). In this analysis,  $r_\infty$  was treated as an unknown parameter, which was determined by optimizing the Perrin equation to the experimental histogram (**Fig. S3A**, blue lines). The Perrin equation for two components is:

$$r_S(\tau) = \frac{r_0 - r_\infty}{1 + \frac{\tau}{\rho_{\text{local}}}} + \frac{r_\infty}{1 + \frac{\tau}{\rho_{\text{global}}}}. \quad (2)$$

Using the formalism described in(79), we obtain  $\kappa^2$  uncertainties ( $\Delta R_{\text{DA}}(\kappa^2)$ ) corresponding to each FRET distance for  $r_\infty$ . Moreover,  $r_\infty$  was used as estimate for the fraction of the dyes bound to the surface of the protein, to calibrate the dye's accessible surface volume (ACV) as previously described.(33) The labeling-site specific  $r_\infty$  are compiled in **Tab. S1A**.

#### (4) Translational mobility of the fluorescence dyes

For all possible labeling sites, we simulated expected fluorescence quantum yields of dynamically quenched donor dyes Alexa488 diffusing within its accessible volume (AV) and accessible surface volume (ACV) using Brownian dynamics simulations with previously published parameters.(29) Finding no significant differences to other reference sample, we corroborate that within the model errors AV/ACVs describe the dye behavior (**Fig. S4B, lower panel**).

To conclude, the introduced mutations and the labeling of the dyes has no major influences on the protein function, i.e., the GTP hydrolysis and the GTP induced self-oligomerization. The time-resolved anisotropy measurements and the dynamic quenching simulations agree with a donor dye freely rotating and diffusing within its AV/ACV.

#### (5) Uncertainty estimation

For comparison of an experimentally derived distance to the distances of a structural model different sources of uncertainties of an inter-dye distances need to be combined. Here, the reported estimates of the distance uncertainties consider relative uncertainties,  $\delta$ , of the accessible volume model (AV),  $\delta_{AV}$ , the orientation factor,  $\delta_{\kappa^2}$ , the reference,  $\delta_{\text{Reference},\pm}$ , and the statistical noise of the data,  $\delta_{\text{stat},\pm}$ . These uncertainties were combined to  $\delta_{R_{DA},\pm}$ , a relative uncertainty of the distance:

$$\delta_{R_{DA},\pm} = \sqrt{\delta_{AV}^2 + \delta_{\kappa^2}^2 + \delta_{\text{Reference},\pm}^2 + \delta_{\text{stat},\pm}^2} \quad (1)$$

$\delta_{AV}$  considers the fact that both dyes were conjugated to the protein by cysteines. Therefore, two FRET species, where the donor is either attached to the first amino acid (DA) or the second (AD), are present in the measured samples. As the donor and acceptor dyes have different geometries, the DA and AD species have distinct distributions of FRET rate constants. We previously demonstrated for the used dyes Alexa488 and Alexa647 well described by AVs, that differences in the FRET rate constant distribution between DA and AD species results in an

uncertainty in the distance of  $\Delta R_{DA,AV} \sim 1 \text{ \AA}$ . This uncertainty was considered by  $\delta_{AV}^2 = R_{DA}/\Delta R_{DA,AV}$ .(29) The uncertainty  $\delta_{\kappa^2}^2$  for the orientation factor  $\kappa^2$  was determined as previously described using a wobbling in a cone model considering the residual anisotropies of the dyes.(32) The asymmetric uncertainty  $\delta_{Reference,\pm}$  considered potential reference errors, propagating to systematic errors of an experimentally determined distance  $R_{DA,exp}$ .

The fluorescence rate constant of the donor in the absence of FRET,  $k_D$ , serves as reference to recover experimental distances,  $R_{DA,exp}$ , in the analysis of fluorescence decays. An inaccurate reference for  $k_D$  propagates to systematic errors of  $R_{DA,exp}$ . We estimate the contribution of an inaccurate reference to  $\delta_{R_{DA,\pm}}$  by  $\delta_{Reference,\pm}$

$$\delta_{Reference,\pm} = \left| 1 - \left( 1 \pm \left( \frac{R_{DA,exp}}{R_0} \right)^6 \cdot \delta_{k_D} \right)^{\frac{1}{6}} \right| \quad (2)$$

Here,  $R_0$  is the Förster radius and  $\delta_{k_D}$  is the relative deviation of the experimentally determined  $k_D$  from the correct (true)  $k_D$ . To estimate  $\delta_{k_D}$  we use the sample-to-sample variation of the donor fluorescence lifetimes (**Tab. S1B**). The contribution of the statistical error  $\delta_{stat,\pm}$  was estimated by support plane analysis and a Monte-Carlo sampling algorithm determining distributions of parameters in agreement with the experimental data.(63) Using the relative uncertainty estimates the absolute uncertainties of the distances were calculated.

#### (6) Consistency analysis identifies mis-assigned distances

The fluorescence decays were analyzed by a model function, which assigns distances to the states by their amplitude. The model free analysis of the DEER data (**eq. 7**) recovered inter-spin distance distributions,  $p(R_{LL})$ , which reflect all conformational heterogeneities with unclear assignment to the corroborated states. The DEER analysis assigns no states to the recovered distributions. Therefore, initially all DEER constraints were assigned to  $M_1$  and  $M_2$  using the width of the distributions as uncertainty. This assignment resulted in structural models inconsistent with the data (**Fig. S4E**). The DEER measurements on C225C/K567C and C225C/Q577C revealed short distances, highlighted by the fast-initial drop of the form factors (**Fig. S2A**, gray traces). Models consistent with  $M_2$  predicted long distances ( $> 5 \text{ nm}$ ) beyond the DEER detection limit at this measurement settings for these variants, **Fig. S2A**, green traces (for  $\sim 6\text{-}7 \text{ nm}$ ). Hence, C225C/K567C and C225C/Q577C were considered only to model  $M_1$  for highly valuable information on the position of the short helix  $\alpha_{13}$  relative to helix  $\alpha_{12}$ . This assignment resulted in a consistent combined set of distances for FRET and DEER used for

RBD (**Tab. S3A**). Concluding, by analysis of the self-consistency of the data with the models, we unambiguously assigned recovered distances or average distances to biomolecular states.

## Supplementary Note 2. MD simulations and PC Analysis

### MD simulations

We performed molecular dynamics (MD) and accelerated MD (aMD)(80) simulations to identify collective degrees of freedom, essential movements, and correlated domain motions of hGBP1 by Principal Component Analysis (PCA).(80) The simulations were started from a known crystal structure of the full-length protein (PDB code: 1DG3) protonated with PROPKA(81) at a pH of 7.4, neutralized by adding counter ions and solvated in an octahedral box of TIP3P water(82) with a water shell of 12 Å around the solute. The obtained system was used to perform unbiased MD simulations and aMD simulations. The Amber14 package of molecular simulation software(69) and the ff14SB(83) force field were used to perform five unrestrained all-atom MD simulations. Three of the five simulations were conventional MD (2 μs each) and two aMD simulations (200 ns each). The “Particle Mesh Ewald”(84) method was utilized to treat long-range electrostatic interactions; the SHAKE algorithm(85) was applied to bonds involving hydrogen atoms. For all MD simulations, the mass of solute hydrogen atoms was increased to 3.024 Da and the mass of heavy atoms was decreased respectively according to the hydrogen mass repartitioning method.(70) The time step in all MD simulations was 4 fs with a direct-space, non-bonded cutoff of 8 Å. For initial minimization, 17500 steps of steepest descent and conjugate gradient minimization were performed; harmonic restraints with force constants of 25 kcal·mol<sup>-1</sup> Å<sup>-2</sup>, 5 kcal·mol<sup>-1</sup>·Å<sup>-2</sup>, and zero during 2500, 10000, and 5000 steps, respectively, were applied to the solute atoms. Afterwards, 50 ps of NVT simulations (MD simulations with a constant number of particles, volume, and temperature) were conducted to heat up the system to 100 K, followed by 300 ps of NPT simulations (MD simulations with a constant number of particles, barostat and temperature) to adjust the density of the simulation box to a pressure of 1 atm and to heat the system to 300 K. A harmonic potential with a force constant of 10 kcal·mol<sup>-1</sup> Å<sup>-2</sup> was applied to the solute atoms at this initial stage. In the following 100 ps NVT simulations the restraints on the solute atoms were gradually reduced from 10 kcal·mol<sup>-1</sup> Å<sup>-2</sup> to zero. As final equilibration step 200 ps of unrestrained NVT simulations were performed. Boost parameters for aMD were chosen by the method as previously suggested.(38)

### PC Analysis

In the MD simulations we found fluctuations of RMSD around the average structure of at most 8 Å RMSD for GTP bound and GTP free hGBP1 (**Fig. S6A**). A correlation analysis of these RMSD trajectories reveals that the dynamics is complex (non-exponential) and predominantly in the 10-100 ns regime (**Fig. 6B**). Structures deviating the most from the X-ray structure kink

at the connector of the LG and the middle domain (**Fig. 3G**). A PCA reveals that the first five principal components describe overall more than 60% of the variance of the MD and aMD simulations (**Fig. 3A**). For PCA the GTPase domain (the least mobile domain) was superposed. The mode vectors of the principal components mapped to a crystal structure of hGBP1 (PDB-ID: 1DG3) illustrate the amplitude and the directionality of the principal components (**Fig. 3F**). The first component (1) describes a motion of the middle domain towards the LG domain. In the second component (2) the middle domain and  $\alpha 13$  move in opposite directions. The third component (3) is like the first component with a two times smaller eigenvalue. Component (4) is like the second component, except that the middle domain and  $\alpha 12/13$  move in the same direction. Component (5) captures a similar directionality of motion for the middle domain and  $\alpha 12/13$  as the second component. In component (5) however, the movement of  $\alpha 12/13$  describes a breathing motion of the catalytic LG domain. The major motions of the PCA can be described by a rotation of the middle domain relative to the GTPase domain (**Fig. 3F**, cyan sphere).

### Supplementary Note 3. Identification of rigid domain and rigid body decomposition

The first step for RBD is the segmentation of hGBP1 into rigid domains that can represent the essential motions of the protein (**Fig. 3F**). Moreover, the segmentation should introduce sufficient degrees of freedom to fulfil the experimental constraints. The substrate free (PDB-ID: 2B92) and a substrate bound form of the LG domain (PDB-ID: 2B92) differ by only 1.1 Å RMSD, and the distance network (**Fig. 1A**) for the label based measurements were designed to probe distance changes between the LG, the middle domain, and  $\alpha_{12/13}$ . Hence, the LG domain (residue 1 to 309) was modeled as a single RB. In the MD simulations  $\alpha_{12/13}$  moved relative to the middle and the LG domain while the middle domain changes its orientation relative to the LG domain. The DEER measurement on the variant A551C/Q577 informs on the position of  $\alpha_{13}$  relative to helix  $\alpha_{12}$ . Consequently,  $\alpha_{12}$  (residue 482 to 563) and  $\alpha_{13}$  (residue 564 to 584) were treated as separate RBs. We note that we treated helix  $\alpha_{12}$  in this work as rigid, because we had no experimental evidence for unfolding or kinking of this helix. Without a rearrangement of the middle domain the motion of  $\alpha_{12/13}$  is highly restricted in a RBD framework. To allow for more flexibility the middle domain was represented by two bodies (residue 310 to 373 and residue 374 to 481). Overall, hGBP1 was decomposed into the LG domain, two RBs for the middle domain, helix  $\alpha_{12}$ , and helix  $\alpha_{13}$ . Therefore, to capture hGBP1's motions and fulfil the experimentally probed degrees of freedom hGBP1 was described by five RBs. Experimental evidence for such a decomposition are the FRET measurements on the variants A496C/V540C, T481C/Q525C, and Q344C/T481C which probe the conformation of  $\alpha_{12}$  and the middle domain. An analysis of the protein mechanics by the  $S^2$  order parameters of the NH bond determined by analysis of the MD simulations and the B-factors of the full-length protein revealed sets of characteristic spikes (**Fig. S6C**). These spikes rationalize the rigid body decomposition and identify flexible regions of the protein, which mainly correspond to flexible loops connecting individual helices. They indicate, that the middle domain, helix  $\alpha_{12}$ , and helix  $\alpha_{13}$  are flexibly linked.



### Supplementary Note 4. Rigid body docking

#### Definition of constraints

As next step of RBD, a set of constraints needs to be defined. The RBD procedure uses for model generation experimental constraints, a repulsion potential as a penalty function for atomic overlaps, and bonds between the RBs. The experimental constraints, bonds connecting the bodies, and the repulsive clash are considered by the terms  $\chi_{DEER,FRET}^2$  (**Methods 7**, eq. 23),  $\chi_{bonds}^2$ , and,  $\chi_{clash}^2$ , respectively. The overall RBD potential  $\chi_{RBD}^2$  is

$$\chi_{RBD}^2 = \chi_{DEER/FRET}^2 + \chi_{bonds}^2 + \chi_{clash}^2. \quad (1)$$

The bond term was a combination of quadratic potentials

$$\chi_{bonds}^2 = \sum_{i,j} \left( \frac{R_{ij} - R_{eq,ij}}{k_{ij,\pm}} \right)^2, \quad (2)$$

where  $R_{ij} = |\vec{r}_j - \vec{r}_i|$  is the distance between the vectors  $\vec{r}_j$  and  $\vec{r}_i$ , defined by the arrangement of the RBs,  $R_{eq,ij}$  is the equilibrium distance of the distance pair, and  $k_{ij,\pm}$  is a constant which depends on the sign of  $R_{ij} - R_{eq,ij}$ .

Overlaps of rigid bodies we penalized by the atomic overlaps in the repulsion potential  $\chi_{clash}^2$ :

$$\chi_{clash}^2 = \sum_{i,j} \begin{cases} 0 & , R_{ij} \geq R_{wi} + R_{wj} \\ \left( \frac{R_{wi} + R_{wj} - R_{ij}}{R_{ctol}} \right)^2 & , R_{ij} < R_{wi} + R_{wj} \end{cases}. \quad (3)$$

Here  $R_{ij}$  is the distance between the atoms with the index  $i$  and  $j$  belonging to different subunits,  $R_{wi}$  and  $R_{wj}$  are their van der Waals radii, and  $R_{ctol}$  is a constant defining the ‘‘clash tolerance’’.

The restraints defining  $\chi_{DEER,FRET}^2$  for  $M_1$  and  $M_2$  are listed in the **Tab. S3A**. Parameters defining contributions to  $\chi_{bonds}^2$ , namely the connection of the N- and C-term.ni and a set of weak bonds based on a crystal structure (PDB-ID: 1DG3) to stabilize the middle domain, are listed in **Tab. S3B**. The rigid body model does not allow for bending. Therefore, a very weak repulsion potential was used for  $\chi_{clash}^2$  ( $R_{ctol} = 6 \text{ \AA}$ ).

#### Rigid body docking

The final docking step generates structural models fulfilling the constraints summarized by the energy function eq. 1 (above). Starting from a random initial arrangement of the RBs, forces drive the RB assembly towards a configuration with a minimum energy.(32) For fast calculations, the forces are applied between the average label position and optimizes the distance between the average label positions  $R_{mp}$ .

$$R_{mp} = \left| \langle \vec{r}_{L1}^{(i)} \rangle - \langle \vec{r}_{L2}^{(j)} \rangle \right| = \left| \frac{1}{n} \sum_{i=1}^n \vec{r}_{L1}^{(i)} - \frac{1}{m} \sum_{j=1}^m \vec{r}_{L2}^{(j)} \right|. \quad (4)$$

Here  $\vec{r}_{L1}^{(i)}$  and  $\vec{r}_{L2}^{(j)}$  are the coordinates of the two labels in the conformation ( $i$ ) and ( $j$ ). Using the mean position of the dyes instead of the full spatial distribution of the dyes reduces the complexity of the RBD and increases its speed (32). DEER and fluorescence decays measurements recover inter-label distance distributions,  $p(R_{LL})$ , and not the distance between the label positions. For a uniformly populated AV

$$\langle R_{LL} \rangle = \left| \langle \vec{r}_{L1}^{(i)} - \vec{r}_{L2}^{(i)} \rangle \right| = \frac{1}{nm} \sum_{j=1}^n \sum_{j=1}^m \left| \vec{r}_{L1}^{(i)} - \vec{r}_{L2}^{(i)} \right| \quad (5)$$

To use average distances  $\langle R_{LL} \rangle$  during RBD a transfer function converted the experimental average inter label distance  $\langle R_{LL} \rangle$  to  $R_{mp}$ .(32) After docking, the spatial distribution of the labels were simulated for the generated structural models to calculate average distances  $\langle R_{LL} \rangle$  as a set of model distances,  $\{R_{\text{model}}\}$ .




Supplement D. Single-molecule FRET reveals  
multiscale chromatin dynamics modulated by HP1  $\alpha$

## ARTICLE

DOI: 10.1038/s41467-017-02619-5

OPEN

# Single-molecule FRET reveals multiscale chromatin dynamics modulated by HP1 $\alpha$

Sinan Kilic <sup>1,4</sup>, Suren Felekyan<sup>2</sup>, Olga Doroshenko<sup>2</sup>, Iuliia Boichenko<sup>1</sup>, Mykola Dimura<sup>2</sup>, Hayk Vardanyan<sup>2</sup>, Louise C. Bryan<sup>1</sup>, Gaurav Arya<sup>3</sup>, Claus A.M. Seidel <sup>2</sup> & Beat Fierz <sup>1</sup>

The dynamic architecture of chromatin fibers, a key determinant of genome regulation, is poorly understood. Here, we employ multimodal single-molecule Förster resonance energy transfer studies to reveal structural states and their interconversion kinetics in chromatin fibers. We show that nucleosomes engage in short-lived (micro- to milliseconds) stacking interactions with one of their neighbors. This results in discrete tetranucleosome units with distinct interaction registers that interconvert within hundreds of milliseconds. Additionally, we find that dynamic chromatin architecture is modulated by the multivalent architectural protein heterochromatin protein 1 $\alpha$  (HP1 $\alpha$ ), which engages methylated histone tails and thereby transiently stabilizes stacked nucleosomes. This compacted state nevertheless remains dynamic, exhibiting fluctuations on the timescale of HP1 $\alpha$  residence times. Overall, this study reveals that exposure of internal DNA sites and nucleosome surfaces in chromatin fibers is governed by an intrinsic dynamic hierarchy from micro- to milliseconds, allowing the gene regulation machinery to access compact chromatin.

<sup>1</sup>Laboratory of Biophysical Chemistry of Macromolecules, Institute of Chemical Sciences and Engineering (ISIC), Ecole Polytechnique Fédérale de Lausanne (EPFL), 1015 Lausanne, Switzerland. <sup>2</sup>Institut für Physikalische Chemie, Lehrstuhl für Molekulare Physikalische Chemie, Heinrich-Heine-Universität, Universitätsstraße 1, 40225 Düsseldorf, Germany. <sup>3</sup>Pratt School of Engineering, Duke University, 144 Hudson Hall, Box 90300, Durham, NC 27708, USA. <sup>4</sup>Present address: Department of Molecular Mechanisms of Disease, University of Zurich, 8057 Zurich, Switzerland. Correspondence and requests for materials should be addressed to C.A.M.S. (email: [cseidel@hhu.de](mailto:cseidel@hhu.de)) or to B.F. (email: [beat.fierz@epfl.ch](mailto:beat.fierz@epfl.ch))

Chromatin is critical to gene regulatory processes, as it dictates the accessibility of DNA to proteins such as transcription factors (TFs) and gene expression machinery<sup>1</sup>. The elucidation of the structure and dynamics of chromatin is a challenge spanning orders of magnitude in spatial (Å to micrometers) and temporal (sub-microseconds to hours) scales<sup>2</sup>. Genomic approaches have enabled researchers to probe the structure of chromatin *in vivo*<sup>3–5</sup>, albeit as static snapshots and averaged over cellular populations. High-resolution structural studies on reconstituted chromatin provided models of chromatin as a two-start helix with two intertwined stacks of nucleosomes and compact tetranucleosomes as basic units (Fig. 1a)<sup>6,7</sup>. Within such a two-start fiber context, inter-nucleosome interactions are mediated by the H4 tail contacting the H2A acidic patch<sup>1</sup>, and by a contact between the C-terminal helices of H2A and H2B<sup>6,7</sup>. Other experiments have supported solenoid chromatin structural models<sup>8</sup> or mixed, heterogeneous populations<sup>9</sup>, depending on

linker DNA length and the presence of linker histones. As observed in the cryo-EM structure of a chromatin fiber (Fig. 1a), tetranucleosomes arrange in a defined interaction register (i.e., defining which nucleosomes interact with each other).

Irrespective of the local architecture, chromatin structure is highly dynamic: Mononucleosomes exhibit partial unwrapping of nucleosome-wound DNA<sup>10–13</sup>, which modulates binding site accessibility for TFs<sup>14,15</sup> and controls the rate of transcription by RNA polymerase<sup>16</sup>. Dynamic rearrangements beyond the nucleosome were observed using fluorescence approaches in tri-nucleosomes<sup>17</sup> and using force spectroscopy on chromatin fibers under tension<sup>18–21</sup>. However, structural rearrangements in unperturbed chromatin fibers, and the timescales thereof, remain unresolved.

Heterochromatin protein 1 $\alpha$  (HP1 $\alpha$ , CBX5), a defining component of transcriptionally silent heterochromatin, has been shown to interact with H3 tri-methylated at lysine 9 (H3K9me3)

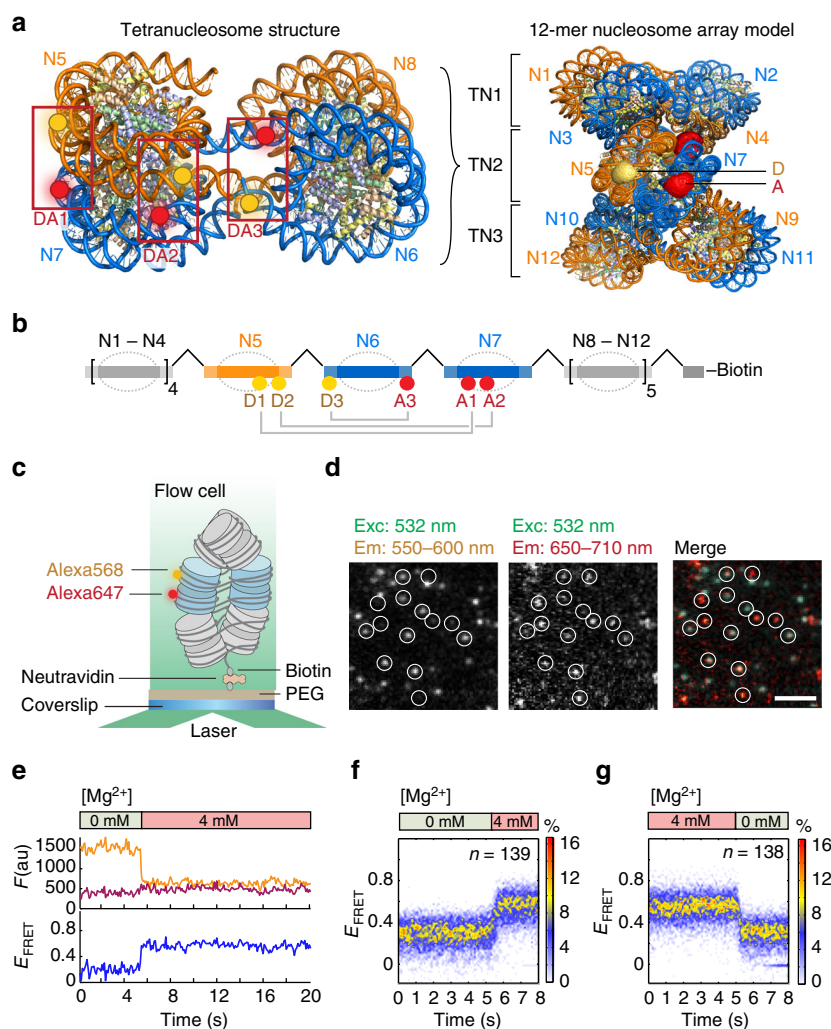


**Fig. 1** smFRET system to detect real-time chromatin conformational dynamics. **a** Left: Tetranucleosome structure based on ref. <sup>6</sup> showing the three dye pairs DA1, DA2, and DA3. Right: 12-mer chromatin fiber as a stack of three tetranucleosome (TN) units, modeled using the cryo-EM structure of a chromatin fiber<sup>7</sup>. For exact dye positions, see Supplementary Fig. 1. The middle tetranucleosome carries the fluorescent labels, whose accessible volume is displayed. D donor, A acceptor labels, N nucleosomes. **b** Schematic view of the preparative DNA ligation used to introduce fluorescent labels. **c** Scheme of the TIRF experiment to measure intra-array smFRET. **d** Microscopic images showing FRET data of single chromatin arrays at 4 mM Mg<sup>2+</sup>, scale bar: 5 μm. **e** Trace from dynamic compaction of chromatin fibers by influx of 4 mM Mg<sup>2+</sup>. **f** DA1 chromatin fibers compact dynamically by influx of 4 mM Mg<sup>2+</sup> at 5 s as reported by a rapid increase in FRET. Displayed: Overlay of indicated number of traces from single fibers. Only traces exhibiting a FRET change were included in the analysis (65%). **g** DA1 chromatin decompacts rapidly upon removal of Mg<sup>2+</sup> by injection of low-salt buffer/EDTA. Only traces exhibiting a FRET change were included in the analysis (74%).

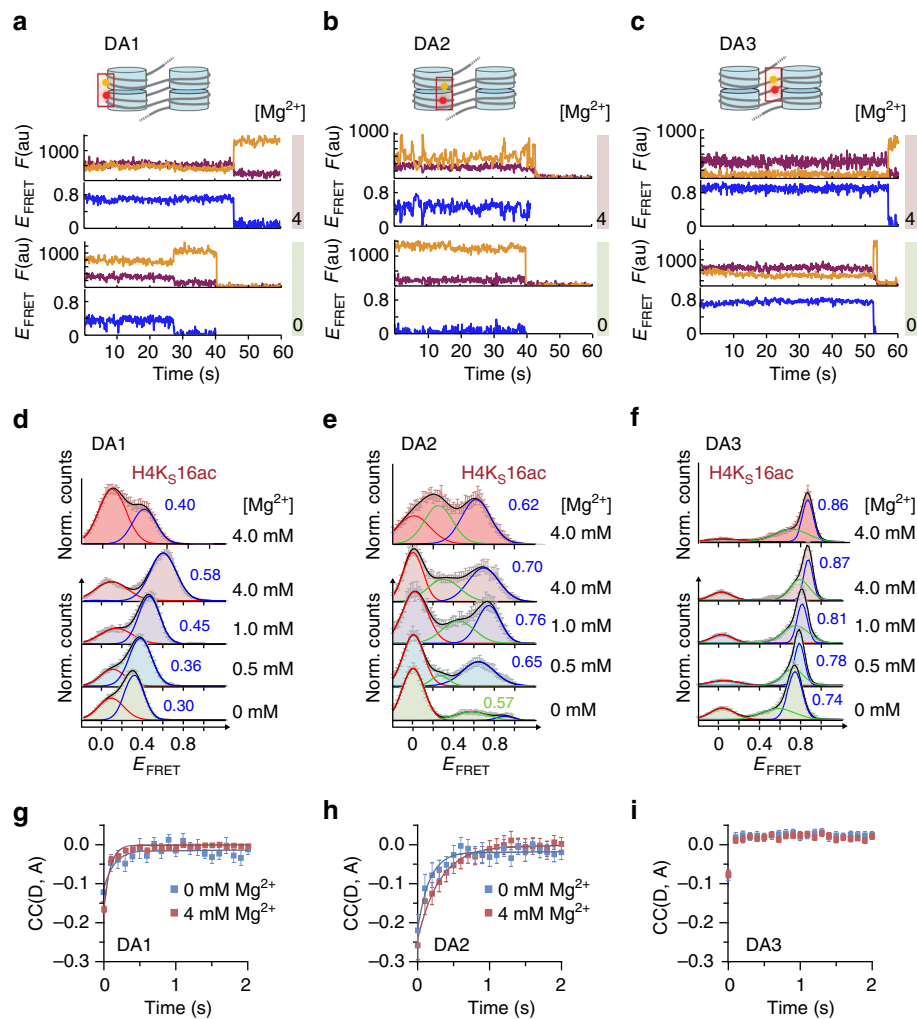


**Fig. 2** Multi-perspective smTIRF-FRET reveals dynamic chromatin compaction. **a** Single-molecule traces (donor: orange, acceptor: red, FRET: blue) for DA1 at 0 mM  $Mg^{2+}$  (bottom), 4 mM  $Mg^{2+}$  (top) until either donor or acceptor dye photobleaching. For analysis methods, see Supplementary Note, step 1 **b** FRET traces for DA2, same conditions as in **a**. **c** FRET traces for DA3, same conditions as in **a**. **d** FRET populations observed for DA1 at the indicated  $Mg^{2+}$  concentrations, as well as in the presence of H4K<sub>S</sub>16ac. **e** FRET populations for DA2, same conditions as in **d**. **f** FRET populations for DA3, same conditions as in **d**. **d-f** Error bars: s.e.m. For the number of traces, parameters of the Gaussian fits, see Supplementary Table 5. **g** Donor-acceptor channel cross-correlation analysis of DA1. Fits, 0 mM  $Mg^{2+}$ : cross-correlation relaxation time  $t_R = 140 \pm 101$  ms ( $n = 76$ ); 4 mM  $Mg^{2+}$ :  $t_R = 73 \pm 13$  ms ( $n = 229$ ). **h** Donor-acceptor channel cross-correlation analysis of DA2. Fits, 0 mM  $Mg^{2+}$ :  $t_R = 169 \pm 79$  ms ( $n = 61$ ); 4 mM  $Mg^{2+}$ :  $t_R = 312 \pm 108$  ms ( $n = 52$ ). **i** Donor-acceptor channel cross-correlation analysis of DA3. **g-i** Error bars: s.e.m. For the number of traces, see Supplementary Table 5. Fit uncertainties correspond to 95% confidence intervals of a global fit of the indicated number of traces. For the percentage of dynamic traces, see Supplementary Table 6

in a multivalent fashion. HP1 $\alpha$  is a key architectural protein and is involved in establishing a compact chromatin state, thereby contributing to gene silencing<sup>22–28</sup>. Importantly, it has been revealed that HP1 $\alpha$  is highly dynamic, with residence times on chromatin from milliseconds to seconds<sup>23,27,29,30</sup>. Thus, it is not clear how HP1 proteins induce chromatin compaction. Moreover, no detailed information is available about the internal structure of such compact states. The lack of precise information on chromatin dynamics in general, and of chromatin-effector complexes in particular, is mainly due to experimental constraints arising from the megadalton scale, molecular complexity, and structural heterogeneity of chromatin. Knowledge of the timescale of chromatin structural rearrangements, modulated by histone PTMs or by chromatin effectors<sup>21,25,31,32</sup>, is however central for understanding the role of chromatin in gene regulation.

In this study, we combine two single-molecule Förster resonance energy transfer (smFRET)<sup>33</sup> methods, covering detection timescales from microseconds up to seconds, to directly map local

chromatin structural states and measure their interconversion dynamics. We fluorescently label chromatin fibers at three distinct sets of internal positions yielding structural information from several vantage points. Using two fluorescent dye pairs with different distance sensitivities (i.e., Förster Radii,  $R_0$ ) allows us to measure a wide range of inter-dye distances ( $R_{DA}$ ) with sub-nm precision. Employing this multipronged approach combined with dynamic structural biology methods (building on our FRET positioning and screening toolkit, FPS)<sup>34</sup>, we identify distinct structural states in chromatin fibers and determine their exchange kinetics. We reveal that nucleosomes engage in stacking interactions, which rapidly interchange on the micro- to millisecond timescale. HP1 $\alpha$  binding to modified chromatin fibers results in a compact but dynamic chromatin state, as HP1 $\alpha$  transiently stabilizes stacked nucleosomes. Together, our study establishes a dynamic-register model of local chromatin fiber motions regulated by effector proteins.

## Results

**Reconstitution of site-specifically labeled chromatin fibers.** A key prerequisite for our smFRET studies is the introduction of a single dye pair with base-pair precision into chromatin fibers. We thus developed a method to assemble chromatin DNA constructs containing 12 copies of the “601” nucleosome positioning sequence<sup>35</sup> separated by 30 bp linker DNA. We used preparative ligations of two recombinant and three synthetic fragments, the latter of which carried the fluorescent labels (Fig. 1b, Supplementary Figs. 1–3, and Supplementary Tables 1–4). A convergent DNA assembly procedure with intermediate purification steps ensured the efficient and accurate incorporation of exactly one donor and one acceptor dye into chromatin DNA at defined positions. Guided by structural modeling<sup>6,7,17</sup>, we decided on three dye configurations (Donor–Acceptor position 1, DA1), DA2 and DA3 (Fig. 1b), employing Alexa Fluor 568 (Alexa568) as FRET donor and Alexa Fluor 647 (Alexa647) as FRET acceptor. This pair has the advantage of a large Förster radius  $R_0 = 82 \text{ \AA}$ , enabling measurement of large inter-dye distances (up to 150  $\text{\AA}$ ). Each dye pair was positioned in the center of the 12-mer nucleosome array (N1–N12) to probe distinct contacts and motions (Fig. 1a, b). DA1 senses stacking between nucleosomes N5 and N7 at a position close to the H2A–H2B four-helix bundle contacts<sup>17</sup>. DA2 measures inter-nucleosome interactions closer to the dyad (N5–N7). DA3 reports on dynamic modes within the linker DNA flanking the central nucleosome (N6). Chromatin fibers were reconstituted on double-labeled DNA templates (either DA1, DA2, or DA3) using recombinant human histone octamers (Supplementary Fig. 4). Ensemble measurements confirmed that all three dye configurations in chromatin resulted in increasing FRET as a function of magnesium-induced compaction, compatible with a two-start fiber model<sup>6,7</sup> (Supplementary Fig. 5a–l). Chromatin fibers labeled on nucleosome positions N5 and N6 (nearest-neighbor in sequence), which only make contact in a one-start fiber configuration, did not demonstrate measurable FRET. This finding, together with structural modeling, ruled out that solenoid or one-start fiber structures contribute to the measured FRET signal (Supplementary Fig. 5m–o).

### smFRET reveals structural heterogeneity in chromatin fibers.

We proceeded to investigate the conformational and dynamic properties of the assembled chromatin fibers using single-molecule imaging. In a first set of experiments, we applied single-molecule total internal reflection fluorescence (smTIRF) microscopy with a time resolution of 100 ms, to investigate chromatin structure and dynamics on the millisecond to seconds timescale (Fig. 1c). We immobilized DA1-labeled chromatin fibers in flow channels and measured their donor and acceptor fluorescence emission (Fig. 1d). Traces were selected according to a predefined set of selection criteria, e.g., the presence of a donor and an acceptor dye, and a minimal trace length in time (Supplementary Fig. 6g). We then generated time traces of FRET efficiency ( $E_{\text{FRET}}$ ) (Supplementary Note, step 1). Chromatin compaction induced by rapid injection of bivalent cations (4 mM  $\text{Mg}^{2+}$ ) resulted in a fast (<0.5 s) increase in  $E_{\text{FRET}}$  (Fig. 1e, f). Conversely, rapid removal of  $\text{Mg}^{2+}$  ions induced chromatin decompaction on a similarly rapid timescale (Fig. 1g). We can thus directly observe real-time conformational changes in single chromatin fibers. Moreover, these experiments reveal that the formation of chromatin higher-order structure occurs on the millisecond timescale.

Next, we systematically explored chromatin conformational changes as a function of bivalent cation concentration (0, 0.5, 1.0, and 4.0 mM  $\text{Mg}^{2+}$ ) from our three structural vantage points (Fig. 2). We recorded time traces of FRET efficiency for DA1

(Fig. 2a), DA2 (Fig. 2b), and DA3 (Fig. 2c), which demonstrated an increase in  $E_{\text{FRET}}$  with  $\text{Mg}^{2+}$  for all positions, albeit to different extents. For DA1,  $E_{\text{FRET}}$  histograms revealed a broad FRET distribution, which could be described with two Gaussians centered at low (<0.1) and intermediate (0.3–0.6) FRET efficiency values (Fig. 2d). In contrast, DA3 and DA2 showed a more complex pattern with one population at low  $E_{\text{FRET}}$  and at least two populations associated with intermediate-to-high FRET efficiency (Fig. 2e, f). With increasing  $\text{Mg}^{2+}$  concentration, for all arrays (DA1–3) the populations with  $E_{\text{FRET}} > 0.1$  gradually shifted to higher FRET efficiency values, indicating an induction of nucleosome stacking.

As a confirmation that we indeed measured nucleosome stacking, we investigated the effect of acetylation of H4 at K16, which has been shown to abolish a key contact between the H4 tail and the H2A acidic patch of the neighboring nucleosome<sup>31</sup>. We thus synthesized a close chemical analog of this modification, H4K<sub>5</sub>16ac (Supplementary Fig. 7). Inclusion of H4K<sub>5</sub>16ac resulted in a significant reduction in internucleosomal stacking contacts observed by DA1 (Fig. 2d). A reduction in nucleosomal contacts was also registered by DA2 (Fig. 2e), whereas DA3 did not demonstrate a measurable change compared to the unmodified fiber (Fig. 2f). Thus, H4K16 acetylation results in a loss of defined and stable nucleosome stacking by disrupting a key internucleosomal interaction, while keeping the overall fiber geometry intact.

Considering unmodified chromatin fibers, we further resolved anti-correlated fluctuations in the time traces of donor and acceptor fluorescence emission (Fig. 2a–c), in particular for DA2, indicating structural dynamics. Cross-correlation analysis of donor and acceptor fluorescence fluctuations [CC(D,A)] revealed structural motions for DA2 positions (relaxation time  $t_R = 0.2\text{--}0.3 \text{ s}$ , Fig. 2h), fast dynamics at the detection limit for DA1 ( $t_R \sim 0.1 \text{ s}$ , Fig. 2g) and quasistatic behavior for DA3 (Fig. 2i). Together, the data from DA1–3 point toward complex multiscale dynamics featuring multiple FRET species in rapid exchange, which are not clearly resolvable with smTIRF.

### Chromatin fibers exist in two structural registers.

We thus employed a second approach, smFRET with confocal multiparameter fluorescence detection (MFD)<sup>36</sup>, to study freely diffusing single chromatin fibers (Fig. 3a). This method extends the accessible dynamic timescale to the sub-microsecond range and resolves structural states with sub-nm accuracy<sup>34</sup>. For a set of excitation lasers (485 and 635 nm), our experimental setup allowed the application of pulsed interleaved excitation (PIE)<sup>37</sup> to filter out detections arising from donor-only molecules. To analyze MFD data, each photon burst (i.e., a single-molecule detection) is plotted in a 2D histogram as a function of two FRET indicators: the intensity-derived  $E_{\text{FRET}}$  and the average (fluorescence-weighted) donor lifetime  $\langle \tau_{\text{D(A)}} \rangle_{\text{F}}$  (Fig. 3b, c). As an example, molecules with two conformational states A and D, which remain static during their passage through the confocal volume are located as two populations on a static FRET line (dark red line, Fig. 3b). In contrast, molecules undergoing structural exchange dynamics with a characteristic relaxation time  $t_R$  between the limiting structural states A and D are detected by a broadened intermediate peak, reminiscent of NMR signals in the intermediate exchange regime (Fig. 3c). Moreover, these dynamically broadened populations are located on a dynamic FRET line (blue line, Fig. 3c), which connects the limiting FRET species involved in the fast exchange (intersection of blue and red line in Fig. 3c)<sup>38</sup>.

We performed MFD measurements for chromatin fibers carrying FRET dye pairs in configurations DA1–3 (exciting at



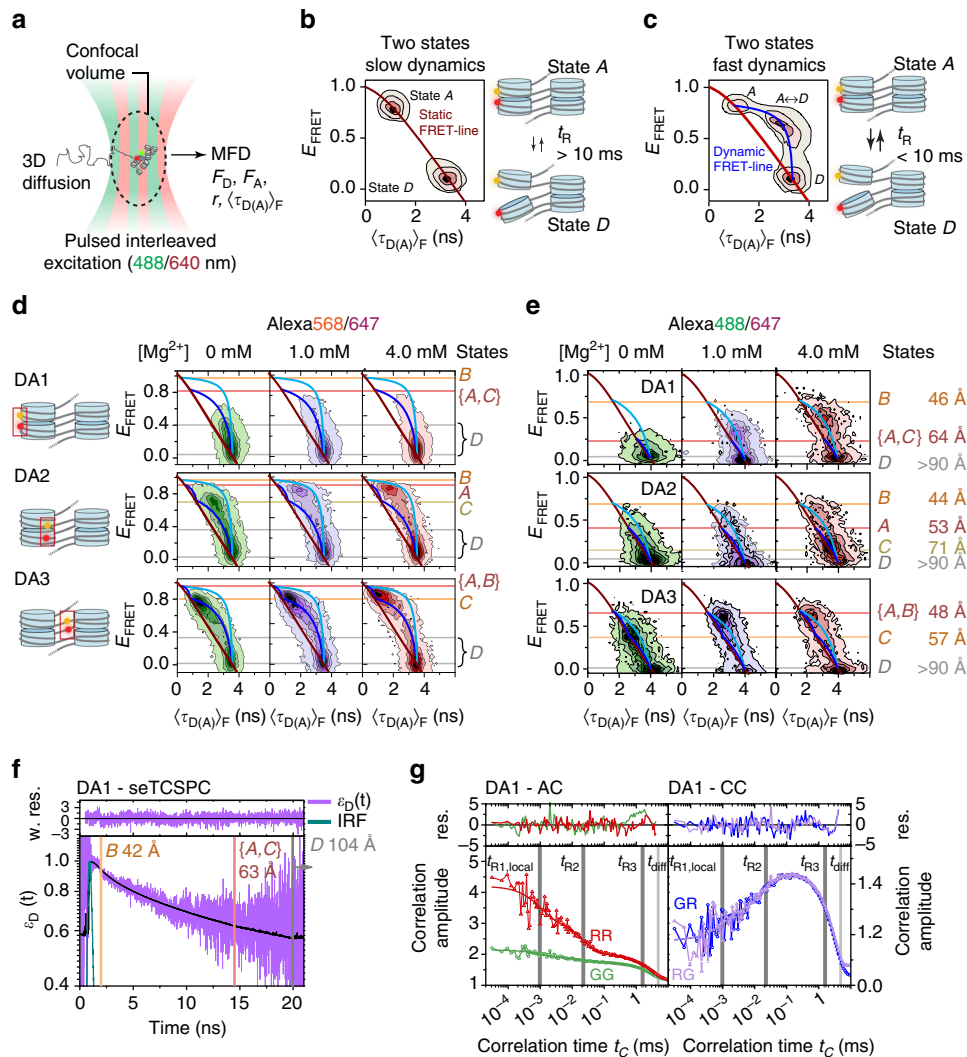


**Fig. 3** Multiscale chromatin dynamics in two registers revealed by MFD. **a** Scheme of PIE-MFD: Species-averaged donor and acceptor emission intensities ( $F_D$ ,  $F_A$ ), intensity-averaged donor lifetime ( $\langle\tau_{D(A)}\rangle_F$ ) and anisotropy ( $r$ ) are simultaneously measured for each molecule diffusing through the confocal volume. **b** Principle of MFD analysis: If dynamics between two states A and D are slow (relaxation time  $t_r \gg 10$  ms), distinct structural states are resolved by  $E_{\text{FRET}}$  and  $\langle\tau_{D(A)}\rangle_F$ , falling on the static FRET line (red). **c** Fast dynamics ( $t_r < 10$  ms) result in an intermediate peak (labeled A  $\leftrightarrow$  D) on a dynamic FRET line (blue). Peak shape analysis reveals  $t_r$  (Fig. 5). **d** 2D-MFD histograms for chromatin fibers DA1-3 (Alexa568/647) at indicated  $\text{Mg}^{2+}$  concentrations. These histograms contain contributions from donor-only labeled chromatin fibers. Red line: static FRET line. Dark and bright blue lines: Two dynamic FRET lines for the two tetranucleosome registers 1 and 2, indicating dynamic exchange with  $t_r < 10$  ms (for parameters of all FRET lines, see Supplementary Note, step 2). Red, orange, yellow, and gray lines: FRET species A–D (see also Fig. 4a). **e** 2D-MFD histograms for chromatin fibers DA1-3 labeled with Alexa488/647 at indicated  $\text{Mg}^{2+}$  concentrations. Red line: static FRET line; dark and bright blue lines: dynamic FRET lines. **f** Subensemble fluorescence lifetime analysis for DA1-labeled fibers (Alexa488/647) at 1 mM  $\text{MgCl}_2$  and  $E_{\text{FRET}} > 0.065$ . The FRET-induced donor decay  $\varepsilon_D(t)$  was fitted with contributions from FRET species {A, C}, B and D (for details and fit parameters of eqs. 3.1–6, see Supplementary Note, step 3), corresponding to the indicated inter-dye distances. IRF: instrument response function. **g** Auto- (left panel) and cross (right panel)-correlation functions of the donor (G) and acceptor (R) emission channels for the same subensemble as in **f**. Global analysis of FCS curves reveals FRET dynamics with two global structural relaxation times ( $t_{R2} = 27 \mu\text{s}$  (27%);  $t_{R3} = 3.1$  ms (56 %)), a term describing local fluctuations ( $t_{R1,\text{local}} = 2.6 \mu\text{s}$  (17%)) and an apparent diffusion time for all curves ( $t_{\text{diff}} = 4.96$  ms) (for details and fit parameters of Eq. 4.1, see Supplementary Note, step 4)

530 nm, which precluded PIE), which revealed a complex population distribution involved in dynamic exchange (Fig. 3d) not observed in free DNA or donor-only labeled chromatin fibers (Supplementary Fig. 8c, d). Due to the absence of PIE in those measurements, donor-only labeled chromatin fibers ( $E_{\text{FRET}} = 0$ ) contributed also to the total observed signal. An iterative 11-step workflow (Supplementary Fig. 9) allowed us to resolve distinct structural states by their characteristic FRET efficiencies and dynamics. Based on this analysis, the data could only consistently be described by two dynamic FRET lines (dark and bright blue

lines, Fig. 3d), indicating two coexisting subpopulations of dynamic chromatin fibers, which are distinct within the observation time of  $\sim 10$  ms.

From the intersections of the dynamic with the static FRET lines, we identified four limiting FRET species involved in the exchange: A, B, C, and D, indicated by the horizontal lines in Fig. 3d. Braces (e.g., {A, C}) indicate conformational states sharing indistinguishable FRET efficiencies. Importantly, a complementary analysis procedure within our workflow (Supplementary Fig. 9), subensemble fluorescence lifetime analysis,



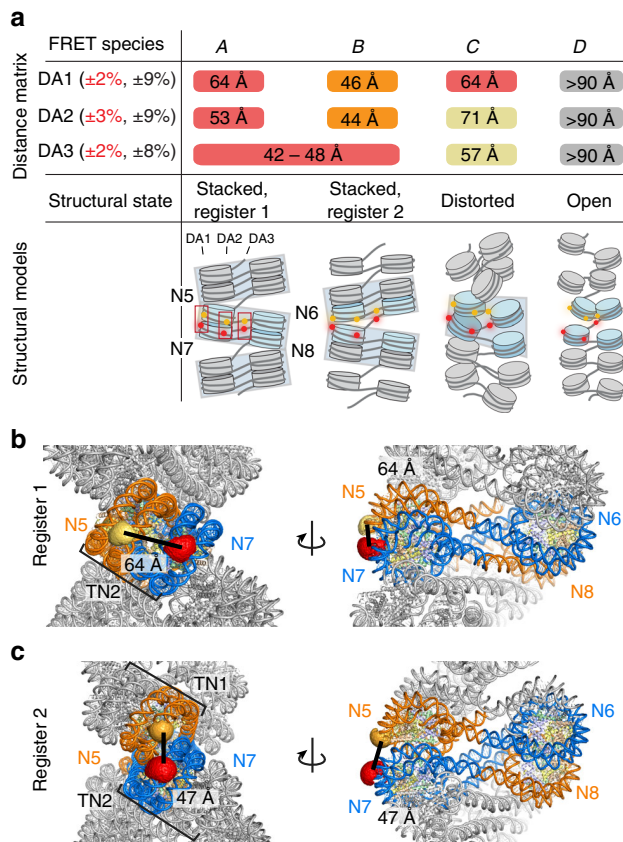


**Fig. 4** Chromatin fibers exist in two rapidly interchanging tetranucleosome stacking registers. **a** Matrix of the inter-dye distances  $R_{DA}$  for DA1, DA2, and DA3 obtained from dynPDA. Species that cannot be discriminated with a given FRET pair are labeled with the same color and/or a continuous box. Percentages given in brackets: uncertainties in the observed distances. Red: precision ( $\Delta R_{DA}(R_{DA})$ ), relevant for relative  $R_{DA}$ , calculated as s.d. between three PDA analyses of data sets comprising a fraction (70%) of all measured data (subsampling). Black: Absolute uncertainty, mainly determined by the uncertainty in  $R_0$  (Supplementary Note, step 9 and Supplementary Table 7). The combined average inter-dye distances  $R_{DA}$  over DA1–3 allow us to map each FRET species to a class of corresponding structural states of chromatin (Supplementary Figs. 12 and 13, Supplementary Table 8, and Supplementary Note, steps 9 and 10). The registers of tetranucleosome units are indicated by light gray boxes. **b** Structural model of a chromatin array, consisting of a stack of three tetranucleosomes (register 1) with DA1-positioned dyes in the central tetranucleosome, based on ref. 7. The inter-dye distance was evaluated using simulated dye accessible contact volumes (ACV)<sup>34</sup>. **c** Molecular structure of a chromatin array, consisting of a stack of two tetranucleosomes, flanked by two unstacked nucleosomes at each side (register 2) with DA1-positioned dyes on the two central tetranucleosomes and inter-dye distance from ACV calculations. Molecular models for DA2 and DA3 are reported in Supplementary Figs. 12 and 13

corroborated the FRET species for each labeling pair DA1–3. Similarly, model-free fluorescence correlation analysis from DA1–3 revealed conformational dynamics with at least three relaxation times, thus involving at least four kinetic species (A–D). Finally, the FRET line parameters were determined in independent experiments<sup>38</sup> (see Supplementary Note, step 2).

In summary, for all vantage points DA1–3 our analysis revealed compact chromatin fibers ( $E_{FRET} > 0.8$ ) in rapid exchange with extended structures (Fig. 3d). At least two independent dynamic transitions were consistently resolved, as indicated by

the two dynamic FRET lines, revealing distinct limiting FRET species with high  $E_{FRET}$  (compact species, A–C) and with very low  $E_{FRET}$  (open species, D), respectively. The existence of two dynamic transitions, as indicated by the two FRET lines, directly revealed two populations of chromatin fibers. Each population shows unique internal exchange dynamics but no interchange between the populations is observed during the ~10 ms observation time. Chromatin fibers are thus structurally and dynamically heterogeneous at the local level.

**Revealing structural states in dynamic chromatin fibers.** To delineate the fiber architectures corresponding to these populations, we performed MFD experiments using Alexa Fluor 488 as a FRET donor ( $R_0 = 52$  Å). This FRET donor substantially improved the spatial resolution at shorter distances (Supplementary Fig. 8b). Importantly, excitation at 485 nm enabled us to employ PIE. We thus could exclude donor-only labeled chromatin fibers. In agreement with the previous MFD measurements (Fig. 3d), FRET distributions were also located on two dynamic FRET lines (Fig. 3e). Due to the altered distance sensitivity of the Alexa488/647 FRET pair, compact states (A, B, and C) were now better resolved. As a result, in these experiments the dynamic FRET lines fell closer to the static FRET lines (while remaining well defined), as compared to measurements with Alexa568/647. Together, these measurements with two different labeling schemes confirm the existence of four structural states in two distinct fiber populations interchanging with fast internal dynamics.

Subensemble fluorescence lifetime analysis provides an alternative method to directly resolve the individual FRET efficiencies (and thus  $R_{DA}$  values) within a dynamic ensemble. In effect, it provides a nanosecond snapshot of the coexisting FRET species, independent of their exchange dynamics. We thus averaged photon bursts from DA1 (selecting only bursts with  $E_{FRET} > 0.065$ ) and computed a FRET-induced fluorescence decay of the donor  $\epsilon_D(t)$  (Fig. 3f and Supplementary Note, step 3)<sup>39</sup>. The nonlinear decay of  $\epsilon_D(t)$  on a log scale directly demonstrated the existence of at least three FRET species. We employed a global analysis to resolve the inter-dye distances characteristic for the three corresponding FRET species {A, C}, B and D (Fig. 3f and Supplementary Fig. 10), closely matching the limiting FRET states observed in 2D-MFD histograms (Fig. 3d, e).

Fluorescence correlation analysis enables a direct and model-free assessment of molecular dynamics. We thus analyzed the autocorrelation functions for the donor and acceptor channels, as well as the cross-correlation between donor and acceptor fluorescence channels (Fig. 3g, and Supplementary Fig. 11, and Supplementary Note, step 4). For DA1, this analysis directly confirmed the existence of structural dynamics between the FRET species {A, C}, B and D, revealing two slow kinetic exchange processes with relaxation time constants  $t_R$  of 27  $\mu$ s and 3.1 ms. However, solely based on this analysis, the relaxation times could not be attributed to individual conformational dynamics.

**Resolving conformational dynamics in chromatin fibers.** An integrated approach is required to characterize the two dynamic populations in chromatin fibers, and to resolve their underlying structural states. We thus proceeded along our workflow for dynamic structural biology (Supplementary Fig. 9 and Supplementary Note): Using the combined information from TIRF measurements, MFD histograms, subensemble lifetime analysis, and fluorescence correlation analysis for DA1–3, we were able to analyze the experimental data with dynamic photon distribution analysis (dynPDA)<sup>38</sup> (Supplementary Note, steps 6–8). This is an approach comparable to the analysis of NMR relaxation

dispersion experiments, resolving subpopulations and their exchange dynamics. While dynPDA is an inherently iterative method, for clarity we first address structural considerations followed by a discussion of the observed dynamics.

Our dynamic–structural biology approach revealed high-precision inter-dye distances (displayed as a distance matrix in Fig. 4a) for species (A–D) with respect to the three vantage points of the samples DA1–3 (Fig. 4a). Using the recovered inter-dye distance sets as constraints, we assigned molecular structures to species (A–D), based on available high-resolution structural data<sup>6,7</sup> and coarse-grained simulations<sup>40</sup> (Fig. 4b, c, Supplementary Figs. 12 and 13, and Supplementary Note, steps 9 and 10). Distance constraints from DA1 and DA2 showed that FRET species A and B correspond to conformational states with defined tetranucleosome units in two different interaction registers relative to the FRET labels. Register 1 (A) positions the label pairs in the same tetranucleosome unit (Fig. 4a, b). This chromatin fiber conformation is consistent with the reported cryo-EM structure of a 12-mer chromatin fiber<sup>7</sup>. Register 2 (B) positions the FRET labels across two neighboring tetranucleosome units, indicating a fiber structure that exhibits altered nucleosome interactions (Fig. 4a, c). Species (C) corresponds to a distorted (twisted) tetranucleosome state within register 1. Finally, species (D) corresponds to an ensemble of open chromatin fiber conformations.

From the DA1 vantage point, the two compact species (A) and (C) shared a single inter-dye distance, resulting in the apparent FRET species {A, C}. This can be rationalized as the DA1 dye pair is close to a key internucleosomal interaction, mediated via the H2A–H2B four-helix bundle<sup>6,7</sup>. This interaction restricts local internucleosomal motions. DA2, in contrast, detected the distorted tetranucleosome state (C), which for this vantage point exhibits an increased inter-dye distance. Hence, stacked nucleosomes exhibit more structural flexibility close to the dyad. Finally, all three dye pairs DA1–3 reported on the species (D), accounting for open chromatin devoid of local internucleosomal interactions.

**A dynamic register model for chromatin dynamics.** To uncover fundamental motions within chromatin fibers, the kinetic connectivity of the chromatin structural states must be elucidated. We thus employed all the previously discussed information to formulate kinetic models, which were employed to fit the experimental FRET efficiency histograms by dynPDA (Fig. 5a–c, Supplementary Fig. 14, and Supplementary Note, steps 5–8). To find an appropriate kinetic model, we performed global fits over the  $Mg^{2+}$  dependence for each data set DA1–3. We tested a set of 3- and 4-state kinetic models describing distinct kinetic connectivities between species (A–D) (Fig. 5d–f and Supplementary Fig. 15). In agreement with two dynamic populations detected in MFD plots, a successful and consistent fit for all label pairs was achieved with a kinetic model containing two branches: one branch connecting species (A, C) to (D), the second branch connecting species (B) to (D) (Fig. 5d–f and Supplementary Figs. 16–18). The revealed kinetic information provided insights into the dynamics of chromatin fibers: an analysis of DA1 (Fig. 5d) indicated that stacked nucleosome (A, register 1) exchange with open conformations (D) with a relaxation time  $\tau_R = 3.7 \pm 0.3$  ms (uncertainties of relaxation times: s.d. between three PDA analyses of data sets comprising a fraction (70%) of all measured data (subsampling)). These motions are two orders of magnitude slower compared to fluctuations between tetranucleosomes (B–D, register 2,  $\tau_R = 60 \pm 10$   $\mu$ s). This is consistent with the significant free energy (around 13 kT) associated with nucleosome stacking<sup>20</sup>. DA2 provided further insight into intra-tetranucleosome dynamics (Fig. 5e), where structural distortions

(i.e., torsional fluctuations and partial nucleosome disengagement, species C) occur on a  $0.5 \pm 0.06$  ms timescale, followed by a transition to D within  $2.6 \pm 0.5$  ms. DA3, finally, reported on linker DNA fluctuations (Fig. 5f). Here, we detected increased (C–D) transition rates, indicating a contribution from transient DNA unwrapping dynamics<sup>12,13,41</sup>. Analyzing the populations of species A–D for DA1–3 over the range of  $Mg^{2+}$  concentrations revealed a coherent picture of the dynamic chromatin structure (Fig. 5g–i): Compact conformers in register 1 (A, C) were about twice as highly populated as register 2 contacts (B). Thus, register 1 with maximally three formed tetranucleosomes is energetically more favorable than register 2 that can only encompass two stacked tetranucleosome units. Compact conformers were increasingly more populated at higher bivalent ion concentrations, but remained in rapid exchange with open and compact chromatin. Finally, between 20 and 40% of all observed chromatin fibers did not show any measurable dynamics on the MFD timescale (observed for all species (A–D), see Supplementary Figs. 16–18). This indicates the presence of chromatin structures separated by significant barriers from the rapidly exchanging structural ensemble (locked states), consistent with the observation of slow dynamics in TIRF-FRET measurements.

Together, our smFRET measurements revealed intriguing multiscale chromatin dynamics across five orders of magnitude in time. We propose a unified model (the dynamic-register model) to describe higher-order chromatin structure and its local dynamics (Fig. 6 and Supplementary Note, step 11). In a chromatin fiber a nucleosome can, at any time, engage in tetranucleosome contacts with only one of its two neighbors within the two-start helix. On a short range, this results in at least two interchanging interaction registers. The exchange pathway between registers 1 and 2 always leads through local fiber unfolding and subsequent reformation of the (altered) tetranucleosome contacts.

A chromatin fiber has more conformational degrees of freedom than those directly probed by FRET in this study. Thus, we use structural and dynamic features to subdivide the observable FRET species A–D further into an ensemble of conformational states (indicated by the numerical index in Fig. 6). Fluctuations observable in smTIRF-FRET (and quasistatic molecules in MFD) indicate the existence of nucleosome interactions stable for a few hundreds of milliseconds (locked states  $A_1, B_1$ ) as well as dynamic species (unlocked states  $A_2, B_2$ ). In register 1, we observed rearrangements of the nucleosome interface allowing tetranucleosomes to open on a millisecond timescale (to  $A_3, C$ , and the ensemble of open states  $D_n$ ). In contrast, neighboring tetranucleosomes in register 2 are only loosely associated, resulting in sub-millisecond interaction dynamics governed by shallow energy barriers ( $B_2$  to  $D_1$  and  $D_n$ ). Importantly, this dynamic ensemble of higher-order structures (or supertertiary structure<sup>42</sup>) with multiple conformational states and dynamic transitions is a fundamental property of chromatin fibers. Elementary states are observed both in extended and compact fibers, but are populated to different extents. Our analysis thus suggests that these elementary states and their transitions govern the biochemical accessibility, regulation, and biological function of chromatin.

**HP1 $\alpha$  induces a dynamically compacted chromatin structure.** Having established this dynamic model of chromatin, we asked how HP1 $\alpha$  affects the internal structure and dynamics of chromatin fibers. Previous studies indicated that HP1 $\alpha$  can compact chromatin<sup>25,43</sup> and that it can cross-bridge H3K9me3-modified nucleosomes<sup>28</sup>. However, no information was available about the internal structure of HP1 $\alpha$ -complexed chromatin. Single-

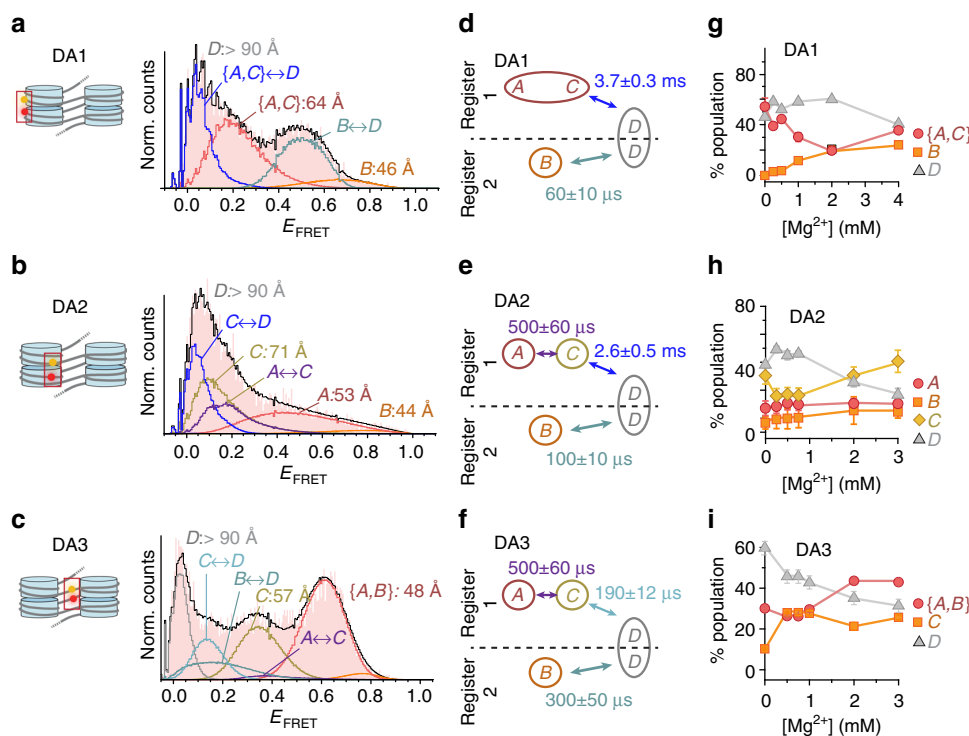


**Fig. 5** Chromatin exhibits multiscale dynamics. **a–c** dynPDA analysis of MFD data (for a detailed description, see Supplementary Note, steps 6–8). Red histogram: Experimental data, black line: PDA fit to the kinetic models corresponding to the indicated state connectivities (Fig. 5d–f). Gaussian distributions in orange hues or gray: Distributions corresponding to FRET states indicated in Fig. 4a: A (red), B (orange), C (yellow), and D (gray). Blue hues: Distributions originating from dynamic exchange between FRET species:  $A \leftrightarrow C$  (violet),  $C \leftrightarrow D$  (dark blue),  $B \leftrightarrow D$  (gray blue). **a** dynPDA analysis of MFD data for DA1 (at 4 mM  $Mg^{2+}$ ) using the kinetic connectivity outlined in Fig. 5d. **b** dynPDA analysis of MFD data for DA2 (at 3 mM  $Mg^{2+}$ ) using the kinetic connectivity outlined in Fig. 5e. **c** dynPDA analysis of MFD data for DA3 (at 3 mM  $Mg^{2+}$ ) using the kinetic connectivity outlined in Fig. 5f. **d–f** Kinetic connectivity maps for DA1–3 used for dynPDA, which describe the experimental data. Two dynamic equilibria (registers) are observed: Register 1 comprises species A, C, and D (as characterized by their inter-dye distance,  $R_{DA}$ ), exchanging with the indicated relaxation times. Register 2 comprises species B and D in equilibrium. Register exchange within D is not permitted in the model on the investigated timescales, as indicated by the dashed line. The indicated time constants are given for 2 mM  $Mg^{2+}$ . For the individual rate constants, see Supplementary Figs. 16–18). Uncertainties: s.d. between three PDA analyses of data sets comprising a fraction (70%) of all measured data (subsampling). **g** Relative combined populations of observed species A–D for DA1 as a function of  $[Mg^{2+}]$  (for the individual contributions of static and dynamic molecules, see Supplementary Figs. 16–18). **h** Relative combined populations for species A–D for DA2. **i** Relative combined populations for species A–D for DA3. For the full PDA fits, see Supplementary Figs. 16–18. Error bars: s.d. between three dynPDA analyses of data sets comprising a fraction (70%) of all measured data (subsampling). In some cases, the error bars are smaller than the symbol size

molecule-binding studies revealed that HP1 $\alpha$  interacts with chromatin on the 250 ms timescale<sup>27</sup>, matching the time resolution of our FRET-TIRF approach. We thus reconstituted DA1 and DA2 chromatin fibers containing either unmethylated (H3K9me0) or chemically produced H3K9me3 (Supplementary Fig. 19a, b) and measured smFRET in the presence of 1  $\mu$ M HP1 $\alpha$  using TIRF microscopy (Fig. 7a, b). The presence of HP1 $\alpha$  resulted in H3K9me3-dependent chromatin compaction as observed by an increase in  $E_{FRET}$  from the vantage points DA1 and, in particular, from DA2 (Fig. 7c, d). The larger effect on DA2 indicates that HP1 $\alpha$  stabilizes nucleosome stacking primarily toward the center of the chromatin fiber, where the FRET efficiency reaches the value ( $E_{FRET} > 0.8$ ) of the limiting species A, B resolved by MFD measurements (Fig. 3d). This comparison directly shows that the HP1 $\alpha$ -compacted state involves the same inter-nucleosome contacts as observed in the absence of HP1 $\alpha$ .

HP1 $\alpha$  is post-translationally modified in particular by phosphorylation of its N-terminal extension (NTE)<sup>44</sup>. Intriguingly, this modification not only stabilizes H3K9me3 binding<sup>45–47</sup> leads to HP1 $\alpha$  oligomerization and phase separation behavior important for heterochromatin establishment<sup>48,49</sup>. We thus produced phosphorylated HP1 $\alpha$  (pHP1 $\alpha$ , Supplementary Fig. 19f–i). Phosphorylation indeed increased the compacting

effect by stabilization of nucleosome binding and by strengthening HP1 $\alpha$  interactions beyond the dimer (Fig. 7c, d). Intriguingly, the analysis of FRET traces by cross-correlation analysis of donor and acceptor fluorescence revealed high-amplitude dynamic fluctuations with a sub-second relaxation time in the presence of HP1 $\alpha$  (Fig. 7e, f). Thus, chromatin fibers compacted by HP1 $\alpha$  do not adopt a stably closed conformation, but in contrary remain highly dynamic and exhibit structural fluctuations on the sub-second timescale.

Finally, we wondered how fast HP1 $\alpha$  could compact chromatin fibers. We thus injected 1  $\mu$ M HP1 $\alpha$  into flow cells containing H3K9me3-modified chromatin fibers and monitoring FRET via the DA2 FRET pairs. The accumulated traces revealed an increase of compaction with a time constant of  $1.1 \pm 0.4$  s (Fig. 7g, h, fit uncertainties correspond to 95% confidence intervals, global fit of  $n = 86$  traces). Thus, HP1 $\alpha$  needs to accumulate on chromatin to reach a critical density before compaction can take effect.

In summary, we find that HP1 $\alpha$  transiently stabilizes interacting nucleosomes in chromatin fibers. This is most likely achieved by cross-bridging nucleosomes through H3K9me3 interactions<sup>24,25,28</sup> (Fig. 7i), a process which occurs on the hundreds of milliseconds timescale consistent with measured residence times for HP1 $\alpha$ <sup>27</sup>.



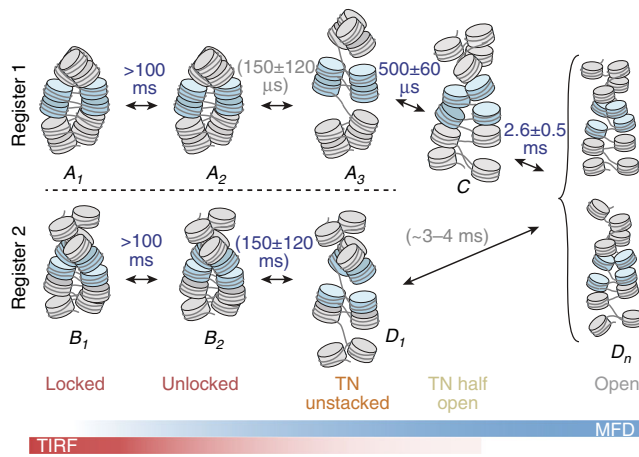


**Fig. 6** The dynamic register model of chromatin fiber dynamics (for details see text). The colored bars indicate the sensitivities of the two applied smFRET methods. The letters A, B, C, and D correspond to observed FRET species (Fig. 4a). Nucleosomes highlighted in blue are labeled and thus observed in the experiment. Numbered states correspond to different chromatin conformations, which exhibit the same FRET efficiency for DA1-3 but which can be kinetically differentiated. FRET species A includes conformational states  $\{A_1, A_2, A_3\}$  for which stacked nucleosomes are observed. FRET species B includes all states  $\{B_1, B_2\}$  corresponding to observation across two neighboring tetranucleosome units. FRET species D (low-FRET states) includes locally unstacked nucleosomes ( $D_1$ ) and the ensemble of open fibers ( $D_n$ ). Gray relaxation time constants are indirectly inferred; blue relaxation times are directly observed. The error ranges represent s.d. between observations of the same dynamic process with different FRET label pairs (for  $B_2 \leftrightarrow D_1$ ), or directly from PDA subsampling (Fig. 5)

## Discussion

The structural dynamics of chromatin dictate biochemical access to the DNA and thus directly impinge on dynamic regulatory processes, such as TF binding, transcription, or DNA repair. A detailed knowledge of the structural states and exchange timescales within chromatin is therefore of critical importance. Previous experiments indicated that chromatin is highly dynamic<sup>17–21</sup>, but stopped short of a detailed structural and kinetic exploration of unconstrained chromatin fibers.

Here, we employed two distinct smFRET approaches with access to complementary experimental timescales to reveal the structural and dynamic landscape of chromatin fibers. Based on our results, we formulated a dynamic-register model (Fig. 6) describing the fundamental dynamic modes governing biochemical access to compact chromatin. Our data are in agreement with the tetranucleosome as a fundamental unit of chromatin fibers<sup>21</sup>. We however discover a distinct set of motions within and between tetranucleosome units that introduce dynamic heterogeneity into chromatin structure. Individual tetranucleosomes can spontaneously open on the millisecond timescale. In contrast, interactions between neighboring tetranucleosomes fluctuate in the microsecond time regime. Neighboring tetranucleosomes can exchange their interaction register on the hundred millisecond timescale, by concerted unfolding, followed by refolding in the alternative register.

The existence of such a fundamental dynamic landscape of chromatin is analogous to the situation in proteins, where intrinsic motions govern function<sup>50,51</sup>. In chromatin, fiber dynamics are coupled to processes such as the target search of TFs, e.g., through sliding and hopping<sup>52</sup>. As these interaction modes require direct access to the DNA, local chromatin dynamics control the fundamental timescale of DNA sampling

and thereby set a speed limit for TF-binding kinetics. Intriguingly, direct observations of TF chromatin sampling *in vivo* reveal that these interactions occur on similar timescales as the local chromatin dynamics revealed in this work<sup>53,54</sup>. Finally, dynamic coupling mechanisms are not limited to TFs, but extend to other processes such as chromatin remodeling<sup>55</sup> or gene transcription itself<sup>56</sup>.

Our measurements revealed that individual nucleosomes engage in short-lived (milliseconds to hundreds of milliseconds) stacking interactions with their neighbors, forming tetranucleosome units. Tetranucleosome contacts hinder access to linker DNA<sup>6</sup> and occlude the nucleosome acidic patch, the major interaction site for many chromatin effectors<sup>57–59</sup>. In agreement, structural<sup>6,7</sup> and force spectroscopy studies reported tetranucleosomes as basic organizational units of chromatin<sup>21</sup>. The observation of both a population of short-lived (milliseconds) as well as long-lived tetranucleosome states (locked states with lifetimes of hundreds of milliseconds) demonstrates that several inter-nucleosome interactions have to be released to allow rapid local fiber dynamics. One intriguing possibility is that long-lived (locked) states arise due to stabilizing long-range inter-nucleosomal interactions outside the tetranucleosome unit, which provide additional stability to chromatin fiber structure.

Importantly, we found that tetranucleosome contacts alternate between different registers on the 100-ms timescale. The interchange between registers requires cooperative motions between neighboring tetranucleosome units, at least over the range of four to eight nucleosomes. It is thus conceivable that structural disturbances in the fiber, e.g., by a bound TF, have long range effects on neighboring genomic loci by a modulation of DNA site exposure dynamics. Indeed, cooperative and collaborative effects between TF-binding sites have been observed over distances significantly exceeding a single nucleosome<sup>60</sup>, pointing toward a role of long-range chromatin organization.

Several genome-wide studies have determined the existence and prevalence of tetranucleosome contacts *in vivo*, employing analysis of nucleosome contacts by electron microscopy<sup>61</sup>, Micro-C<sup>4</sup> or *in situ* radical fragmentation of chromatin<sup>5</sup>. Long stretches of ordered chromatin structure are however not readily observed in interphase nuclei<sup>62</sup>. Our findings regarding the rapid dynamics and heterogeneity provide a rationale of this absence of order over large spatial and temporal scales. Rather, internucleosomal contacts are in constant exchange, forming local transient structures that are permissive for chromatin effectors.

The inherent flexibility and structural adaptability gives chromatin an inhomogeneous dynamic secondary structure with conformational fluctuations ranging over several orders of magnitude in time and space. This makes chromatin an ideal hub for interactions with diverse partners, including architectural such as H1, as well as a large range of chromatin effectors. Our developed methods for dynamic structural biology of chromatin enabled us to systematically determine local effects on such dynamic interactions.

Here we explored how HP1 $\alpha$ , a key heterochromatin component, affects chromatin fibers depending on the presence of H3K9me3. We found that HP1 $\alpha$  transiently stabilizes internucleosome contacts, most probably through multivalent engagement of two PTMs on different nucleosomes<sup>27</sup>. This results in an increased population of compact states, reducing local chromatin accessibility. In agreement, the presence of HP1 $\alpha$  *in vivo* is correlated with increased tetranucleosome contacts<sup>5</sup>.

Strikingly, HP1 $\alpha$ -compacted chromatin fibers remained highly dynamic (Fig. 7i). First, HP1 $\alpha$  interacts with DNA in addition to H3K9me3<sup>28,46</sup>, which might directly modulate local chromatin motions. Second, HP1 $\alpha$  has a stronger compacting effect around the nucleosome dyad. This suggests that the protein has a

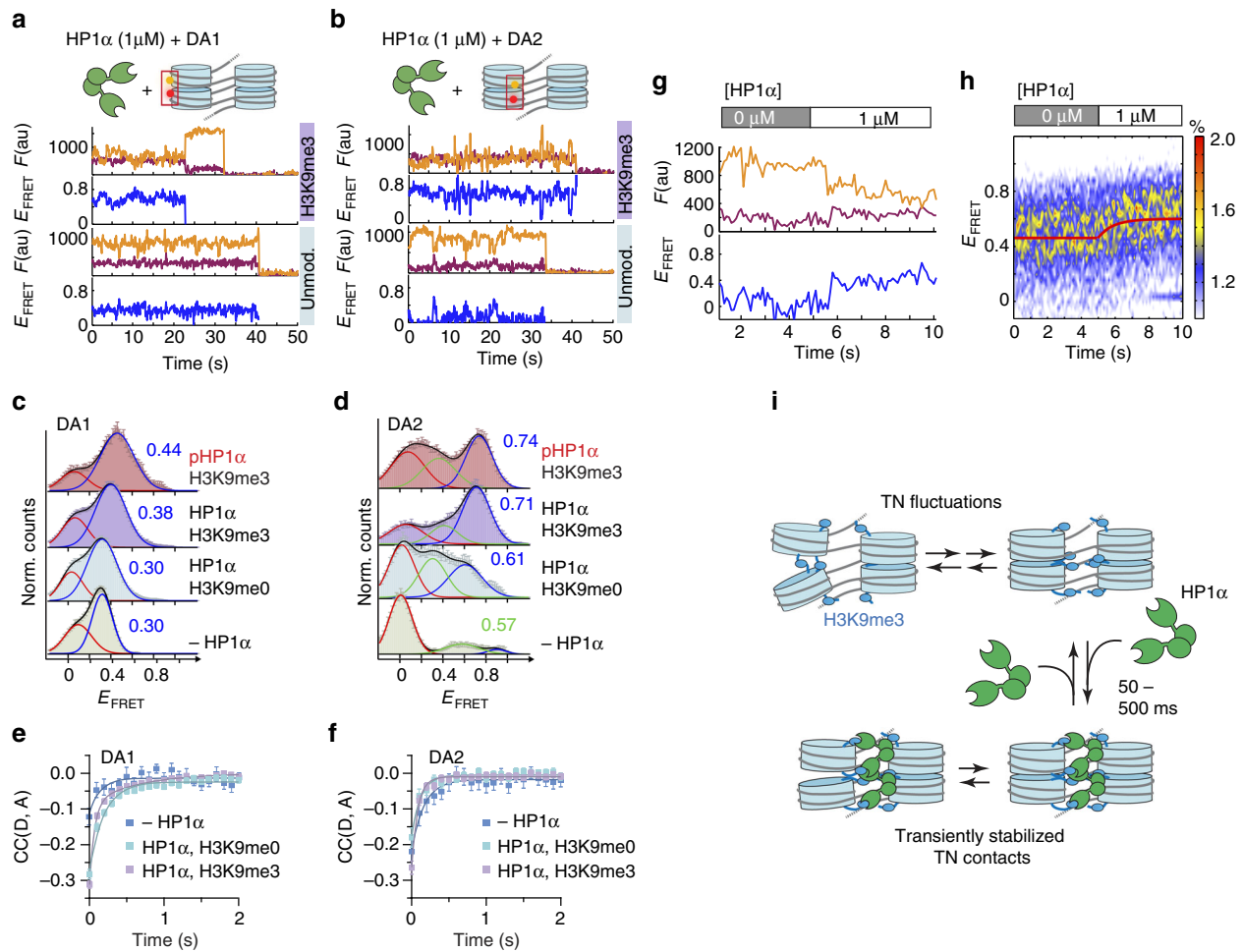


**Fig. 7** HP1 $\alpha$  binding results in dynamically compacted chromatin. **a** FRET traces for DA1, containing no modification or H3K9me3 in the presence of 1  $\mu$ M HP1 $\alpha$  and the absence of Mg $^{2+}$ . **b** FRET trace for DA2, containing no modification or H3K9me3 in the presence of 1  $\mu$ M HP1 $\alpha$ . **c** FRET populations for DA1, showing H3K9me3-dependent compaction by HP1 $\alpha$  and phosphorylated HP1 $\alpha$  (pHP1 $\alpha$ ). **d** FRET populations for DA2, demonstrating close contacts induced by HP1 $\alpha$ /pHP1 $\alpha$ . **e**, **d** Error bars: s.e.m. For the number of traces, parameters of the Gaussian fits, see Supplementary Table 5. **e** Donor-acceptor channel cross-correlation analysis of DA1 in the presence of 1  $\mu$ M HP1 $\alpha$ . Fits, H3K9me0:  $t_{R,1} = 200 \pm 25$  ms ( $n = 530$ ), H3K9me3:  $t_{R,1} = 64 \pm 13$  ms (72%),  $t_{R,2} = 640 \pm 126$  ms (28%) ( $n = 430$ ). **f** Donor-acceptor channel cross-correlation analysis of DA2 in the presence of 1  $\mu$ M HP1 $\alpha$ . Fits, H3K9me0:  $t_R = 123 \pm 38$  ms ( $n = 99$ ); H3K9me3:  $t_{R,1} = 66 \pm 16$  ms (88%),  $t_{R,2} = 930 \pm 543$  ms (12%) ( $n = 106$ ). Fit uncertainties correspond to 95% confidence intervals of a global fit of the indicated number of traces. For the percentage of dynamic traces, see Supplementary Table 6. **e**, **f** Error bars: s.e.m. For the number of traces, see Supplementary Table 5. **g** Stochastic compaction of chromatin induced by injection of HP1 $\alpha$  at 5 s. **h** 2D histogram of multiple injections. Only traces exhibiting a FRET change were included in the analysis (42%). The fit yields a time constant of  $1.1 \pm 0.4$  s (fit uncertainties correspond to 95% confidence intervals, global fit of  $n = 86$  traces). **i** Model of transient stabilization of tetranucleosomes, which still retain some internal flexibility, by HP1 $\alpha$

tendency to bind at central as opposed to peripheral sites within a chromatin fiber. Third, individual HP1 $\alpha$  molecules do not remain stably bound to fibers, but exhibit rapid exchange dynamics *in vitro*<sup>27</sup> and *in vivo*<sup>23,29,30</sup> on the hundreds of millisecond to seconds timescale. Rapid HP1 $\alpha$  turnover will thus stochastically release the stabilization of local nucleosome stacking interactions allowing local exposure of internal sites.

Functionally, the dynamic HP1 $\alpha$ -compacted state remains permissive for biochemical access to the fiber, albeit to a reduced degree. Moreover, we expect bound HP1 $\alpha$  to impair tetranucleosome register exchange, as this requires transient opening of two neighboring tetranucleosomes. Together, these effects therefore contribute to repression of transcription in heterochromatin. Nevertheless, as all DNA sites and nucleosome surfaces are eventually exposed, effectors such as pioneer TFs<sup>63</sup> or even the transcription machinery can still invade the heterochromatin state. In agreement, heterochromatin regions generally are transcribed at low levels<sup>64</sup>. Moreover, local accessibility makes

rapid chromatin regulation possible as a function of cellular stimuli<sup>65</sup>.

In summary, our single-molecule studies reveal dynamic heterogeneity within chromatin fibers, where the intrinsic dynamics are determined by a complex energy landscape. Dynamic higher order or supertertiary structure is governed by interactions of tetranucleosomes that form the fundamental structural units and provide local cooperativity through register exchange dynamics. Chromatin effectors, such as HP1 $\alpha$ , selectively modulate this energy landscape by stabilizing specific conformations from the rapidly exchanging ensemble, thereby enacting a biological output. Thus, the mutual interplay between chromatin dynamics and effector proteins controls downstream biological processes.

## Methods

**Plasmid generation, purification, and DNA fragment isolation.** Plasmids for chromatin DNA production (recP1, recP5) were generated in DH5 $\alpha$  cells grown in 6 L 2xTY medium and isolated by alkaline lysis followed by preparative gel

filtration as follows: After 18–20 h culture, cells were harvested by centrifugation, resuspended and homogenized in 80 mL alkaline lysis solution I (50 mM glucose, 25 mM Tris, 10 mM EDTA, pH 8.0). Homogenate was diluted to 120 mL with the same solution. An aliquot of 240 mL alkaline lysis solution II (0.2 M NaOH, 1% SDS) was added and mixed. An aliquot of 240 mL alkaline lysis solution III (4 M KAc, 2 M Acetic acid) was added to neutralize the solution followed by mixing and subsequent incubation for 15 min at 4 °C. The supernatant was recovered by centrifugation and filtered through miracloth. In total, 0.52 volumes of isopropanol were added and the mixture was allowed to stand for 20 min at room temperature, followed by centrifugation at 11,000 × *g* for 20 min at room temperature. The pellet was redissolved in 30 mL TE 10/50, 100 units of RNase A were added and allowed to digest 2 h at 37 °C. Solid KCl was added to a final concentration of 2.0 M and the volume was adjusted to 35–40 mL. The sample was centrifuged and the supernatant loaded onto a 50 mL superloop. This was injected into a 550 mL sepharose 6 XK 50/30 column and the pure plasmid was collected in the dead volume. The plasmid was precipitated with 0.5 volumes of isopropanol and redissolved in TE 10/0.1.

An aliquot of 75–85 pmol of plasmid DNA was buffer exchanged to H<sub>2</sub>O and mixed with CutSmart buffer (NEB) and water to a final volume of 200 μL. Fifty units of BsaI-HF and 50 units of DraIII-HF were added to digest for 8–10 h, then another 20 units of each enzyme was added to get the digestion to completion (additional 20 units were added if not complete). Sixty units of EcoRV-HF were added and digestion was continued for 6–10 h (Supplementary Fig. 1f–i). Two rounds of stepwise PEG precipitation were performed to separate the excised fragment of interest from the plasmid backbone fragments using concentrations of PEG from 7.0 to 8.5% (Supplementary Fig. 1j, k). After two rounds, a final cleanup step was done using a Zymo Clean and Concentrator 100 column.

**Preparation of fluorescently labeled DNA fragments.** An aliquot of 5–10 nmol of oligonucleotide at a concentration of ~1 mM, washed by ethanol precipitation, was diluted with 25 μL oligo labeling buffer (0.1 M sodium tetraborate, pH 8.5 (9.25 for TFP ester labeling). A 0.6 μL sample was taken and diluted with 50 μL oligonucleotide RP-HPLC solvent A (95% 0.1 M TEAA, 5% ACN). An aliquot of 40 μL of this was injected for analysis by RP-HPLC on an InertSustain 3 μm, 4.6 × 150 mm GL sciences C18 analytical column using a gradient of 0–100% oligonucleotide RP-HPLC solvent B (70% 0.1 M TEAA, 30% ACN) in 20 min. An aliquot of 5 μL of 5 mM NHS-ester dye in DMSO was added and the reaction allowed to proceed 4–8 h at room temperature. The progression of the reaction was monitored by RP-HPLC. Further, dye was added if required, until >50% oligonucleotide was labeled. The oligonucleotide was precipitated twice with ethanol to remove residual dye. It was redissolved in 30 μL MQ H<sub>2</sub>O and diluted with 70 μL oligo RP-HPLC solvent A. Labeled oligonucleotides were purified by RP-HPLC using the same gradient and column as above and collected manually followed by ethanol precipitation. The purified labeled oligonucleotide was redissolved in MQ H<sub>2</sub>O to give a concentration of 2.5 μM (Supplementary Fig. 2a–i).

Labeled PCR segments were generated by mixing Thermopol (1x), template (0.02 ng μL<sup>-1</sup>), forward primer (0.250 μM), reverse primer (0.250 μM), and dNTPs (0.2 mM each) with water in *N* × 50 μL to the final concentrations given in the parentheses. *N* × 1.25 units Taq DNA polymerase was added, the solution was gently mixed followed by aliquoting 50 μL into each of *N* PCR tubes. Thermocycling was done with 12 s initial denaturation at 94 °C followed by 30 cycles of 12 s denaturation at 94 °C, 12 s annealing at 60–65 °C, and 12 s extension at 72 °C. Final extension was done for 12 s at 72 °C. PCR product from the *N* tubes were pooled and stored in the freezer.

An aliquot of 450–500 μL of PCR product was purified with 3x QIAquick PCR purification columns according to the manufacturer's protocol. Following elution, the DNA was ethanol precipitated and redissolved in ~100 μL MQ H<sub>2</sub>O. PCR-generated pieces were digested by mixing 75–85 pmol of each piece in 200 μL with 10x CutSmart to a final concentration of 1x and a sample taken. The pieces were digested as done for the recombinant pieces. Samples were taken and analyzed on a 2% agarose gel alongside the undigested samples (Supplementary Fig. 2j). The digestion reactions were purified with QIAquick PCR purification columns and the concentration was determined by UV spectroscopy.

**Convergent DNA ligations for 12 × 601 arrays.** An aliquot of 30–60 pmol of each DNA piece was used for large-scale ligation to generate the intermediates in combined volumes of 200–400 μL (Supplementary Fig. 3a). P2 was ligated to P1 in 20% excess for 2 h, then P3 was added in 20% excess relative to P2 and ligation allowed to proceed overnight. P4 was ligated to P5 in 20% excess for 2 h, then the biotinylated anchor was added in twofold excess relative to P5 and the ligation allowed to proceed 12–16 h (Supplementary Fig. 3b–d). The pieces were purified by PEG precipitation using a stepwise (0.5% steps) increase in PEG from 7.0 to 8.0% (Supplementary Fig. 3e, f). Pellets were redissolved in 60 μL TE buffer (10 mM Tris, 0.1 mM EDTA, pH 8.0) and redissolved pellets and the final supernatant were analyzed by agarose gel to verify that the pellets at 7.0 and 7.5% typically contained the intermediates separated from the starting pieces. These were pooled and stored for later ligations. An aliquot of 15–35 pmol of the 6 × 601 intermediates were mixed using 5–10% excess P4–P5-anchor in 1x T4 DNA ligase buffer with 600 U of ligase and left to ligate for 10–16 h. The formation of the product was confirmed by agarose gel electrophoresis and purified by stepwise PEG precipitation in the range

5.0–6.0% (Supplementary Fig. 3g, h). The pellets were redissolved in TE(10/0.1) and analyzed by gel electrophoresis to pool the purified double-labeled array DNA.

**Chemically modified histones.** Preparation of H4K<sub>16</sub>ac was performed by radical-mediated thiol-ene addition<sup>66</sup>. H4 carrying a K16 to cysteine point mutation (K16C) was expressed and purified from inclusion bodies<sup>27</sup>. For the installation of the acetyl-lysine analog, H4K16C was dissolved in 0.2 M acetate buffer, pH 4 to a final concentration of 1 mM. Subsequently, 50 mM *N*-vinylacetamide, 5 mM VA-044 and 15 mM glutathione were added, and the reaction was incubated at 45 °C for 2 h. The reaction was monitored by HPLC and MS until complete, followed by semi-preparative RP-HPLC purification of the product (Supplementary Fig. 7a, b).

For the synthesis of H3K9me3<sup>27</sup>, a peptide corresponding to H3(1–14)K9me3-NHNH<sub>2</sub> (carrying a C-terminal hydrazide) was produced by solid phase peptide synthesis. Truncated H3 [H3(Δ1–14)A15C] was expressed as an N-terminal fusion to small ubiquitin like modifier (SUMO) carrying a His6-tag. After a denaturing Ni:NTA affinity purification, the protein was refolded and SUMO was cleaved by SUMO protease, followed by purification of H3(Δ1–14)A15C by RP-HPLC. In a typical ligation reaction, 3 μmol H3(1–14)K9me3-NHNH<sub>2</sub> was dissolved in ligation buffer (200 mM phosphate pH 3, 6 M GdmCl) at –10 °C. NaNO<sub>2</sub> was added dropwise to a final concentration of 15 mM. The reaction was subsequently incubated at –20 °C for 20 min. H3(Δ1–14)A15C was dissolved in ligation buffer (200 mM phosphate pH 8, 6 M GdmCl, 300 mM mercaptophenyl acetic acid (MPAA)) and added to the peptide. The pH was adjusted to 7.5 and after completion of the reaction (as observed by RP-HPLC), the product (H3K9me3A15C) was purified by semi-preparative RP-HPLC. H3K9me3A15C was finally dissolved in desulfurization buffer (200 M phosphate pH 6.5, 6 M GdmCl, 250 mM tris(2-carboxyethyl)phosphine (TCEP)). Glutathione (40 mM) and a radical initiator, VA-044 (20 mM), were added, and the pH was readjusted to 6.5. The reaction mixture was incubated at 42 °C until the protein was completely desulfurized, followed by semi-preparative HPLC purification (Supplementary Fig. 19a, b).

**Chromatin assembly.** Chromatin arrays were reconstituted on a scale of 6.5–30 pmol (based on 601 DNA). 12 × 601 array DNA was mixed with 1.5 molar excess of MMTV buffer DNA, NaCl to a final concentration of 2 M and water, followed by mixing and addition of 2–2.4 molar equivalents of histone octamers, containing either recombinant or chemically prepared modified histones (Supplementary Figs. 7 and 19). The mixture was transferred to a micro-dialysis tube and dialyzed with a linear gradient from TEK2000 (10 mM Tris, 0.1 mM EDTA, 2000 mM KCl) to TEK10 over 16–18 h. The dialysis tube was transferred to 200–600 mL TEK10 for another 1 h of dialysis. The chromatin assembly mixture was taken out of the dialysis tube and centrifuged at 21,000 × *g* for 10 min followed by transfer of the supernatant to a fresh tube. The concentration and volume of the mixture was determined. Gel analysis was done with 0.25–0.50 pmol of chromatin assembly sample (calculated based on the total 260 nm absorption and the extinction coefficient for each nucleosome repeat) mixed to 10 μL with TEK10 and 5–7% sucrose added from a 25% stock. Samples were run in 0.7% agarose gels made with 0.25x TB, using the same as running buffer at 90 V for 90–100 min.

For ensemble FRET analysis, which requires removal of MMTV DNA and nucleosomes, 5–10% of the volume was taken aside for analysis and the remainder was mixed with an equal volume of 6 mM Mg<sup>2+</sup> for precipitation on ice for 10 min followed by 10 min centrifugation at 21,000 × *g*. The supernatant was transferred to another tube and the chromatin pellet redissolved in a similar volume of TEK10 as present prior to precipitation. Similar volumes as taken for chromatin assembly analysis were used for subsequent analysis of the recovered chromatin. For Scal digestion, a similar volume of sample in 1x CutSmart buffer was mixed with 10 units of Scal-HF followed by digestion for 5–7 h. Samples of chromatin before and after precipitation and after Scal digestion were analyzed as described above. Gels were visualized in fluorescence channels and then stained with GelRed for visualization of DNA and nucleosome/chromatin bands (Supplementary Fig. 4a–o).

**Ensemble FRET measurements on chromatin.** Chromatin samples isolated after magnesium precipitation were diluted to a final volume of typically 220–250 μL, resulting in a concentration that yields a spectral count of around 90,000–130,000 cps for maximum donor fluorescence emission, prior to chromatin compaction. The sample was then split in 4 × 50 μL volumes. TEK10 and Mg<sup>2+</sup> from stocks of 10 or 50 mM was added along with TEK10 to a final volume of 55 μL, 5 min prior to measuring. After standing 5 min, the sample was transferred to the fluorescence micro-cuvette for measurement of the spectra (two repeats), followed by measurement of the donor anisotropy (two repeats). This was done for all the samples in the range 0–4 mM Mg<sup>2+</sup> (Supplementary Fig. 5a–l, o). For all measurements, the following settings were used on the fluorescence spectrometer: excitation at 575 nm with 4 nm slit width, and detection over the range of 585–700 nm with 5 nm slit width. For anisotropy measurements, the emission slit width was opened to 10 nm and measurements were performed at 592 nm.



**Preparing of flow chambers.** Borosilicate glass slides with two rows of four holes and borosilicate coverslips were sonicated standing upright in glass containers for 20 min in MQ H<sub>2</sub>O, then in acetone and then in ethanol. They were cleaned in piranha solution (25% v/v H<sub>2</sub>O<sub>2</sub> and 75% v/v H<sub>2</sub>SO<sub>4</sub>) in the same glass containers for 1 h, followed by washing with MQ H<sub>2</sub>O until reaching neutral pH. A 500 mL Erlenmeyer flask was cleaned in the same way. The Erlenmeyer flask, coverslips and slides were all sonicated in acetone for 10 min. A solution of 3% v/v amino-propyltriethylsilane in acetone was prepared in the Erlenmeyer flask and used to immerse the microscopy glass and incubated for 20 min. The aminosilane was disposed, the slides were washed in water and dried with N<sub>2</sub>. Flow chambers were assembled from one glass slide and one coverslip separated by double sided 0.12 mm tape positioned between each hole in the glass slide. The ends were sealed with epoxy glue and the silanized slides stored under vacuum in the freezer until use.

Silanized glass flow chambers stored in the freezer were allowed to warm for 20–30 min. Then a pipette tip as inlet reservoir and outlet sources were neatly fitted in each of the 2 × 4 holes on each side of the flow chamber and glued in place with epoxy glue. The glue was allowed to solidify for 30–40 min. Subsequently, 350 µL of 0.1 M tetraborate buffer at pH 8.5 was used to dissolve ~1 mg of biotin-mPEG (5000 kDa)-SVA, and 175 µL from this was transferred to 20 mg mPEG(5000 kDa)-SVA to generate a transparent clouding-point solution after 10 s of centrifugation. This was mixed to homogeneity with a pipette and centrifuged again for 10 s before 40–45 µL aliquots were loaded into each of the four channels in the flow chamber. The PEGylation reaction was allowed to continue for the next 2½–4 h, after which the solution was washed out with degassed ultra-pure water.

**smTIRF measurements.** Measurements were carried out with a micro-mirror TIRF system<sup>67</sup> (MadCityLabs) using Coherent Obis Laser lines at 405, 488, 532 and 640 nm, a 100x NA 1.49 Nikon CFI Apochromat TIRF objective (Nikon) as well as an iXon Ultra EMCCD camera (Andor), operated by custom-made Labview (National Instruments) software. For imaging, buffers with/without biomolecules were deposited in the inlet reservoir of microfluidic flow cells and drawn into the chamber with tubing connected from the outlet to a 1 mL syringe operated manually or with a motor-driven syringe pump. For each experiment, the imaging chambers were washed with 200–300 µL T50 (10 mM TrisHCl, pH 8.5, 50 mM NaCl), followed by incubation with 50 µL 0.2 mg mL<sup>-1</sup> neutravidin for 5 min. This was washed out with another 400–500 µL T50. Then, 0.5–2 µL of chromatin assembly reaction at a concentration of 5–40 ng µL<sup>-1</sup> was loaded into the chamber while monitoring acceptor emission, to assess chromatin coverage. Chromatin was loaded until reaching 150–400 chromatin arrays in a 25 × 50 µm field of view. Excess chromatin was washed out with T50 followed by exchange to imaging buffer (40 mM KCl, 50 mM Tris, 2 mM Trolox, 2 mM nitrobenzyl alcohol (NBA), 2 mM cyclooctatetraene (COT), 10% glycerol and 3.2% glucose) supplemented with GODCAT (100x stock solution: 165 U mL<sup>-1</sup> glucose oxidase, 2170 U mL<sup>-1</sup> catalase). For imaging, a programmed sequence was employed to switch the field of view to a new area followed by adjusting the focus. Then the camera was triggered to acquire 1300–2000 frames with 532 nm excitation and 100 ms time resolution followed by a final change to 640 nm excitation. For sequences requiring timed programmed injection, after 5000 ms the pump was triggered (Fig. 1). For experiments with magnesium and HP1α, the mixture with the desired concentration was prepared and loaded into the inlet reservoir followed by injection into the channel and imaging as described above.

From acquired movies, the background was extracted in ImageJ using a rolling ball algorithm. Trace extraction and analysis was performed in custom-written MATLAB software. The donor and the acceptor images were non-isotropically aligned using a transformation matrix generated from 8 to 10 sets of peaks appearing in both the donor and the acceptor channels. Peaks were automatically detected in the initial acceptor image prior to donor excitation and the same peaks were selected in the donor channel. Peaks that were tightly clustered, close to the edges or above a set intensity threshold in either the donor or the acceptor channels indicating aggregation were removed from analysis. The analysis was then limited to the peaks appearing in both the donor and the acceptor channel and these traces were extracted for further analysis.

Traces were selected based on the following criteria: (1) Initial total fluorescence of the donor and the β-corrected acceptor of >600 counts over baseline (at 900 EM gain). (2) At least 5 s prior to bleaching of acceptor or donor. Note that for injection experiments (Fig. 1f, g or Fig. 7h), the required trace length was raised to 10 s. (3) Single bleaching event for donor or acceptor. (3.a) If acceptor bleaches first; leads to anti-correlated increase in donor to same total fluorescence level as prior to bleaching. (3.b) If donor bleaches first, the acceptor dye must still be fluorescent when directly probed at the end of the experiment. (4) Bleaching of the donor dye during the 120 s of acquisition to allow an unambiguous determination of background levels. See Supplementary Fig. 6 for a graphical representation.

**MFD sample cell preparation.** 24 × 40 × 1.5 mm coverslips were silanized as described above for the cleaning and passivation to generate the microfluidic channels. Two silicon gaskets were cut out with a scalpel and placed on top of a coverslip. An aliquot of 20 mg mPEG(5000 kDa)-SVA was suspended in 175 µL 0.1 M tetraborate buffer at pH 8.5. The mPEG-SVA suspension was centrifuged at 13,300 × g for 10 s and pipetted up and down before distributing approximately 40 µL in each silicon gasket on a coverslip to PEGylate. The PEGylation reaction

was allowed to proceed for the next 1–2 h before the solution was washed away by first removing the mPEG(5000 kDa)-SVA solution and then washing three times with MQ H<sub>2</sub>O. For one of the washes, the water was allowed to stay in the gasket for 5 min before removing it. The gaskets were then filled with measurement buffer, and stayed like this until usage.

**MFD measurement procedures.** Chromatin fibers with the FRET pair Alexa488/647: MFD measurements with pulsed interleaved excitation (PIE) were essentially performed as shown in ref.<sup>68</sup> employing a confocal epi-illuminated setup based on an Olympus IX70 inverted microscope. In PIE measurements, donor and acceptor are sequentially excited by rapidly alternating laser pulses. MFD can be performed on both dyes, allowing computation of the donor–acceptor ratio (stoichiometry, S) for each particle. Excitation is achieved using 485 nm and 635 nm pulsed diode lasers (LDH-D-C 485 and LDH-P-C-635B, respectively; both PicoQuant (Berlin, Germany)) operated at 32 MHz and shifted by 15.625 ns (total frequency of both Lasers 64 MHz) focused into the sample solution by a 60×/1.2 NA water immersion objective (UPLAPO 60x, Olympus, Germany). Laser power in the sample was  $L_G = 36 \mu\text{W}$  and  $L_R = 7.5 \mu\text{W}$ , respectively. We used the excitation beamsplitter FF550/646 (AHF, Germany) to split laser light and fluorescence. For confocal detection, a 100 µm pinhole was applied for spatial filtering. The fluorescence photon train was divided into its parallel and perpendicular components by a polarizing beamsplitter cube (VISHT11, Gsänger) and then into spectral ranges below and above 595 nm by dichroic detection beamsplitters (595 LPXR, AHF). After separating, the fluorescence signal according to color and polarization, each of the four channels was split again using 50/50 beamsplitters in order to get dead time free filtered FCS curves, resulting in a total of eight detection channels. Photons were detected by eight avalanche photodiodes (green channels: τ-SPAD-100, PicoQuant; red channels: SPCM-AQR-14, Perkin Elmer). Additionally, green (HQ 520/35 nm for Alexa488) and red (HQ 720/150 nm for Alexa647) bandpass filters (AHF, Germany) in front of the detectors ensured that only fluorescence from the acceptor and donor molecules were registered, while residual laser light and Raman scattering from the solvent were blocked. The detector outputs were recorded by a TCSPC module (HydraHarp 400, PicoQuant) and stored on a PC. Data were taken for at least 90 min per sample. Bursts of fluorescence photons are distinguished from the background of 0.5–1 kHz by applying certain threshold intensity criteria<sup>68</sup>. For analysis, several parameters, including fluorescence lifetime, anisotropy, and FRET efficiency, were computed per burst to classify the molecules according to multidimensional relations between these parameters. For MFD measurements at SMD conditions, assembled chromatin was diluted to a concentration of approximately 50 pM (1–100 µL from assembly stock solution) in measurement buffer (40 mM KCl, 50 mM Tris and 10% v/v glycerol, pH ~7.2) containing the desired amount of magnesium. This was then deposited into the silicon gaskets on a passivated coverslip that had been washed with the same measurement buffer prior to deposition of the sample.

Chromatin fibers with the FRET pair Alexa568/647: MFD measurements were performed with one color excitation using a 530 nm amplified pulsed diode laser (LDH-FA 530B, PicoQuant (Berlin, Germany)) with a repetition rate of 64 MHz. The rest of the setup was identical except the customized dichroic beamsplitters (excitation beamsplitter F68-532m zt532/640/NIR rpc (AHF, Germany), dichroic detection beamsplitters F48-642, T640LPXR (AHF) and bandpass filters (HQ 595/50 (AHF)) for the new donor Alexa568 and adapted bandpass filters (HQ 730/140, (AHF)) for the acceptor Alexa647.

**Dynamic structural biology analysis.** All procedures (11 steps) are outlined in Supplementary Fig. 9 and described in detail in the Supplementary Note. Long timescale dynamics were analyzed by smTIRF (Figs. 1–2 and step 1). Short timescale dynamics were detected in MFD plots (Fig. 3 and step 2). The FRET efficiency levels corresponding to the chromatin structural states were determined by sub-ensemble fluorescence lifetime measurements (step 3 and Supplementary Fig. 10) and dynamic PDA of signal intensities (step 7 and Supplementary Figs. 16–18). Dynamics were analyzed by burst-ID FCS analysis (step 4 and Supplementary Fig. 11). Contributions from photobleaching and blinking were analyzed (step 5 and Supplementary Fig. 14). Kinetic models consistent with the analysis from steps 1–5 were formulated (step 6, Fig. 5 and Supplementary Fig. 15), and used for fitting using dynamic PDA (step 7 and Supplementary Figs. 16–18). Obtained kinetic and structural models were validated (step 8). Uncertainties in the measured distances were evaluated (step 9) and structural models of compact (step 9, Supplementary Fig. 12) and open chromatin fibers (step 10, Supplementary Fig. 13) were produced. Finally, models were validated to produce a global structural and kinetic model (step 11).

**Code availability.** All custom-made computer code is available upon request from the corresponding authors.

**Data availability.** The smTIRF data sets have been deposited at [www.zenodo.org](http://www.zenodo.org) under the accession codes 1040772, 1069675, and 1069677. All other data supporting these findings are available from the corresponding authors on reasonable request.

Received: 10 July 2017 Accepted: 11 December 2017

Published online: 16 January 2018

## References

- Luger, K., Dechassa, M. L. & Tremethick, D. J. New insights into nucleosome and chromatin structure: an ordered state or a disordered affair? *Nat. Rev. Mol. Cell Biol.* **13**, 436–447 (2012).
- Cuvier, O. & Fierz, B. Dynamic chromatin technologies: from individual molecules to epigenomic regulation in cells. *Nat. Rev. Genet.* **18**, 457–472 (2017).
- Bonev, B. & Cavalli, G. Organization and function of the 3D genome. *Nat. Rev. Genet.* **17**, 661–678 (2016).
- Hsieh, T. H. et al. Mapping nucleosome resolution chromosome folding in yeast by micro-C. *Cell* **162**, 108–119 (2015).
- Risca, V. I., Denny, S. K., Straight, A. F. & Greenleaf, W. J. Variable chromatin structure revealed by in situ spatially correlated DNA cleavage mapping. *Nature* **541**, 237–241 (2017).
- Schalch, T., Duda, S., Sargent, D. F. & Richmond, T. J. X-ray structure of a tetranucleosome and its implications for the chromatin fibre. *Nature* **436**, 138–141 (2005).
- Song, F. et al. Cryo-EM study of the chromatin fiber reveals a double helix twisted by tetranucleosomal units. *Science* **344**, 376–380 (2014).
- Robinson, P. J., Fairall, L., Huynh, V. A. & Rhodes, D. EM measurements define the dimensions of the “30-nm” chromatin fiber: evidence for a compact, interdigitated structure. *Proc. Natl Acad. Sci. USA* **103**, 6506–6511 (2006).
- Grigoryev, S. A., Arya, G., Correll, S., Woodcock, C. L. & Schlick, T. Evidence for heteromorphic chromatin fibers from analysis of nucleosome interactions. *Proc. Natl Acad. Sci. USA* **106**, 13317–13322 (2009).
- Li, G. & Widom, J. Nucleosomes facilitate their own invasion. *Nat. Struct. Mol. Biol.* **11**, 763–769 (2004).
- Koopmans, W. J., Brehm, A., Logie, C., Schmidt, T. & van Noort, J. Single-pair FRET microscopy reveals mononucleosome dynamics. *J. Fluoresc.* **17**, 785–795 (2007).
- Wei, S., Falk, S. J., Black, B. E. & Lee, T. H. A novel hybrid single molecule approach reveals spontaneous DNA motion in the nucleosome. *Nucleic Acids Res.* **43**, e111 (2015).
- Gansen, A. et al. Nucleosome disassembly intermediates characterized by single-molecule FRET. *Proc. Natl Acad. Sci. USA* **106**, 15308–15313 (2009).
- Luo, Y., North, J. A., Rose, S. D. & Poirier, M. G. Nucleosomes accelerate transcription factor dissociation. *Nucleic Acids Res.* **42**, 3017–3027 (2014).
- Poirier, M. G., Bussiek, M., Langowski, J. & Widom, J. Spontaneous access to DNA target sites in folded chromatin fibers. *J. Mol. Biol.* **379**, 772–786 (2008).
- Hodges, C., Bintu, L., Lubkowska, L., Kashlev, M. & Bustamante, C. Nucleosomal fluctuations govern the transcription dynamics of RNA polymerase II. *Science* **325**, 626–628 (2009).
- Poirier, M. G., Oh, E., Tims, H. S. & Widom, J. Dynamics and function of compact nucleosome arrays. *Nat. Struct. Mol. Biol.* **16**, 938–944 (2009).
- Cui, Y. & Bustamante, C. Pulling a single chromatin fiber reveals the forces that maintain its higher-order structure. *Proc. Natl Acad. Sci. USA* **97**, 127–132 (2000).
- Pope, L. H. et al. Single chromatin fiber stretching reveals physically distinct populations of disassembly events. *Biophys. J.* **88**, 3572–3583 (2005).
- Kruihof, M. et al. Single-molecule force spectroscopy reveals a highly compliant helical folding for the 30-nm chromatin fiber. *Nat. Struct. Mol. Biol.* **16**, 534–540 (2009).
- Li, W. et al. FACT remodels the tetranucleosomal unit of chromatin fibers for gene transcription. *Mol. Cell* **64**, 120–133 (2016).
- Bannister, A. J. et al. Selective recognition of methylated lysine 9 on histone H3 by the HP1 chromo domain. *Nature* **410**, 120–124 (2001).
- Cheutin, T. et al. Maintenance of stable heterochromatin domains by dynamic HP1 binding. *Science* **299**, 721–725 (2003).
- Canzio, D. et al. Chromodomain-mediated oligomerization of HP1 suggests a nucleosome-bridging mechanism for heterochromatin assembly. *Mol. Cell* **41**, 67–81 (2011).
- Azzaz, A. M. et al. Human heterochromatin protein 1alpha promotes nucleosome associations that drive chromatin condensation. *J. Biol. Chem.* **289**, 6850–6861 (2014).
- Muller-Ott, K. et al. Specificity, propagation, and memory of pericentric heterochromatin. *Mol. Syst. Biol.* **10**, 746 (2014).
- Kilic, S., Bachmann, A. L., Bryan, L. C. & Fierz, B. Multivalency governs HP1alpha association dynamics with the silent chromatin state. *Nat. Commun.* **6**, 7313 (2015).
- Hiragami-Hamada, K. et al. Dynamic and flexible H3K9me3 bridging via HP1beta dimerization establishes a plastic state of condensed chromatin. *Nat. Commun.* **7**, 11310 (2016).
- Festenstein, R. et al. Modulation of heterochromatin protein 1 dynamics in primary Mammalian cells. *Science* **299**, 719–721 (2003).
- Muller, K. P. et al. Multiscale analysis of dynamics and interactions of heterochromatin protein 1 by fluorescence fluctuation microscopy. *Biophys. J.* **97**, 2876–2885 (2009).
- Shogren-Knaak, M. et al. Histone H4-K16 acetylation controls chromatin structure and protein interactions. *Science* **311**, 844–847 (2006).
- Fierz, B. et al. Histone H2B ubiquitylation disrupts local and higher-order chromatin compaction. *Nat. Chem. Biol.* **7**, 113–119 (2011).
- Ha, T. et al. Probing the interaction between two single molecules: fluorescence resonance energy transfer between a single donor and a single acceptor. *Proc. Natl Acad. Sci. USA* **93**, 6264–6268 (1996).
- Kalinin, S. et al. A toolkit and benchmark study for FRET-restrained high-precision structural modeling. *Nat. Methods* **9**, 1218–1225 (2012).
- Lowary, P. T. & Widom, J. New DNA sequence rules for high affinity binding to histone octamer and sequence-directed nucleosome positioning. *J. Mol. Biol.* **276**, 19–42 (1998).
- Sisamakos, E., Valeri, A., Kalinin, S., Rothwell, P. J. & Seidel, C. A. M. Accurate single-molecule FRET studies using multiparameter fluorescence detection. *Methods Enzymol.* **475**, 455–514 (2010).
- Laurence, T. A., Kong, X., Jager, M. & Weiss, S. Probing structural heterogeneities and fluctuations of nucleic acids and denatured proteins. *Proc. Natl Acad. Sci. USA* **102**, 17348–17353 (2005).
- Kalinin, S., Valeri, A., Antonik, M., Felekyan, S. & Seidel, C. A. M. Detection of structural dynamics by FRET: a photon distribution and fluorescence lifetime analysis of systems with multiple states. *J. Phys. Chem. B* **114**, 7983–7995 (2010).
- Peulen, T. O., Opanasyuk, O. & Seidel, C. A. M. Combining graphical and analytical methods with molecular simulations to analyze time-resolved FRET measurements of labeled macromolecules accurately. *J. Phys. Chem. B* **121**, 8211–8241 (2017).
- Arya, G., Zhang, Q. & Schlick, T. Flexible histone tails in a new mesoscopic oligonucleosome model. *Biophys. J.* **91**, 133–150 (2006).
- Ngo, T. T., Zhang, Q., Zhou, R., Yodh, J. G. & Ha, T. Asymmetric unwrapping of nucleosomes under tension directed by DNA local flexibility. *Cell* **160**, 1135–1144 (2015).
- Tompa, P. On the supertertiary structure of proteins. *Nat. Chem. Biol.* **8**, 597–600 (2012).
- Fan, J. Y., Rangasamy, D., Luger, K. & Tremethick, D. J. H2A.Z alters the nucleosome surface to promote HP1alpha-mediated chromatin fiber folding. *Mol. Cell* **16**, 655–661 (2004).
- LeRoy, G. et al. Heterochromatin protein 1 is extensively decorated with histone code-like post-translational modifications. *Mol. Cell. Proteomics* **8**, 2432–2442 (2009).
- Nishibuchi, G. et al. N-terminal phosphorylation of HP1alpha increases its nucleosome-binding specificity. *Nucleic Acids Res.* **42**, 12498–12511 (2014).
- Hiragami-Hamada, K. et al. N-terminal phosphorylation of HP1alpha promotes its chromatin binding. *Mol. Cell. Biol.* **31**, 1186–1200 (2011).
- Bryan, L. C. et al. Single-molecule kinetic analysis of HP1-chromatin binding reveals a dynamic network of histone modification and DNA interactions. *Nucleic Acids Res.* **45**, 10504–10517 (2017).
- Larson, A. G. et al. Liquid droplet formation by HP1alpha suggests a role for phase separation in heterochromatin. *Nature* **547**, 236–240 (2017).
- Strom, A. R. et al. Phase separation drives heterochromatin domain formation. *Nature* **547**, 241–245 (2017).
- Henzler-Wildman, K. & Kern, D. Dynamic personalities of proteins. *Nature* **450**, 964–972 (2007).
- Eisenmesser, E. Z. et al. Intrinsic dynamics of an enzyme underlies catalysis. *Nature* **438**, 117–121 (2005).
- Halford, S. E. & Marko, J. F. How do site-specific DNA-binding proteins find their targets? *Nucleic Acids Res.* **32**, 3040–3052 (2004).
- Morisaki, T., Muller, W. G., Golob, N., Mazza, D. & McNally, J. G. Single-molecule analysis of transcription factor binding at transcription sites in live cells. *Nat. Commun.* **5**, 4456 (2014).
- Chen, J. et al. Single-molecule dynamics of enhanceosome assembly in embryonic stem cells. *Cell* **156**, 1274–1285 (2014).
- Blosser, T. R., Yang, J. G., Stone, M. D., Narlikar, G. J. & Zhuang, X. Dynamics of nucleosome remodelling by individual ACF complexes. *Nature* **462**, 1022–1027 (2009).
- Fitz, V. et al. Nucleosomal arrangement affects single-molecule transcription dynamics. *Proc. Natl Acad. Sci. USA* **113**, 12733–12738 (2016).
- Mattiroli, F., Uckelmann, M., Sahtoe, D. D., van Dijk, W. J. & Sixma, T. K. The nucleosome acidic patch plays a critical role in RNF168-dependent ubiquitination of histone H2A. *Nat. Commun.* **5**, 3291 (2014).
- Leung, J. W. et al. Nucleosome acidic patch promotes RNF168- and RING1B/BMI1-dependent H2AX and H2A ubiquitination and DNA damage signaling. *PLoS Genet.* **10**, e1004178 (2014).



59. McGinty, R. K., Henrici, R. C. & Tan, S. Crystal structure of the PRC1 ubiquitylation module bound to the nucleosome. *Nature* **514**, 591–596 (2014).
60. Karczewski, K. J. et al. Cooperative transcription factor associations discovered using regulatory variation. *Proc. Natl Acad. Sci. USA* **108**, 13353–13358 (2011).
61. Grigoryev, S. A. et al. Hierarchical looping of zigzag nucleosome chains in metaphase chromosomes. *Proc. Natl Acad. Sci. USA* **113**, 1238–1243 (2016).
62. Ricci, M. A., Manzo, C., Garcia-Parajo, M. F., Lakadamyali, M. & Cosma, M. P. Chromatin fibers are formed by heterogeneous groups of nucleosomes in vivo. *Cell* **160**, 1145–1158 (2015).
63. Zaret, K. S. & Carroll, J. S. Pioneer transcription factors: establishing competence for gene expression. *Genes Dev.* **25**, 2227–2241 (2011).
64. Keller, C. et al. HP1(Swi6) mediates the recognition and destruction of heterochromatic RNA transcripts. *Mol. Cell* **47**, 215–227 (2012).
65. Ayoub, N., Jeyasekharan, A. D., Bernal, J. A. & Venkitaraman, A. R. HP1-beta mobilization promotes chromatin changes that initiate the DNA damage response. *Nature* **453**, 682–686 (2008).
66. Li, F. et al. A direct method for site-specific protein acetylation. *Angew. Chem. Int. Ed. Engl.* **50**, 9611–9614 (2011).
67. Larson, J. et al. Design and construction of a multiwavelength, micromirror total internal reflectance fluorescence microscope. *Nat. Protoc.* **9**, 2317–2328 (2014).
68. Kudryavtsev, V. et al. Combining MFD and PIE for accurate single-pair Forster resonance energy transfer measurements. *Chemphyschem* **13**, 1060–1078 (2012).

### Acknowledgements

We thank Jun-ichi Nakayama for the CK2 expression plasmid, Nicolas Sambiagio for assistance with sample preparations. We thank Manuel M. Müller, Jeffrey C. Hansen, Wilma K. Olson, and Nicolas Clauvelin for stimulating discussions during the initial phase of this research. This work was supported by the Sandoz Family Foundation, the Swiss National Science Foundation (Grant 31003A\_173169), the European Research Council through the Consolidator Grant 2017 chromo-SUMMIT (724022) and EPFL (B. F.), the Boehringer Ingelheim Foundation (S.K.), and the European Research Council through the Advanced Grant 2014 hybridFRET (671208) to C.A.M.S.

### Author contributions

B.F. coordinated the project. B.F., S.K. and C.A.M.S. conceived and designed the studies. B.F. supervised chromatin synthesis and reconstitution, and smTIRF studies. C.A.M.S.

supervised the confocal smFRET studies and quantitative FRET analysis. S.K. synthesized labeled chromatin fibers, modified histones, and performed smTIRF experiments. I.B. produced phosphorylated HP1 $\alpha$  and performed TIRF experiments. L.C.B. produced synthetic histones. S.F., O.D., S.K. and H.V. performed and analyzed confocal FRET experiments. Kinetic modeling was performed by S.F., C.A.M.S. and B.F. PDA was performed by S.F. G.A. performed coarse-grained simulations. G.A. and B.F. generated chromatin models. O.D. and M.D. performed FPS analysis with chromatin models. All authors were involved in data analysis and interpretation. All coauthors wrote the manuscript.

### Additional information

**Supplementary Information** accompanies this paper at <https://doi.org/10.1038/s41467-017-02619-5>.

**Competing interests:** The authors declare no competing financial interests.

**Reprints and permission** information is available online at <http://npg.nature.com/reprintsandpermissions/>

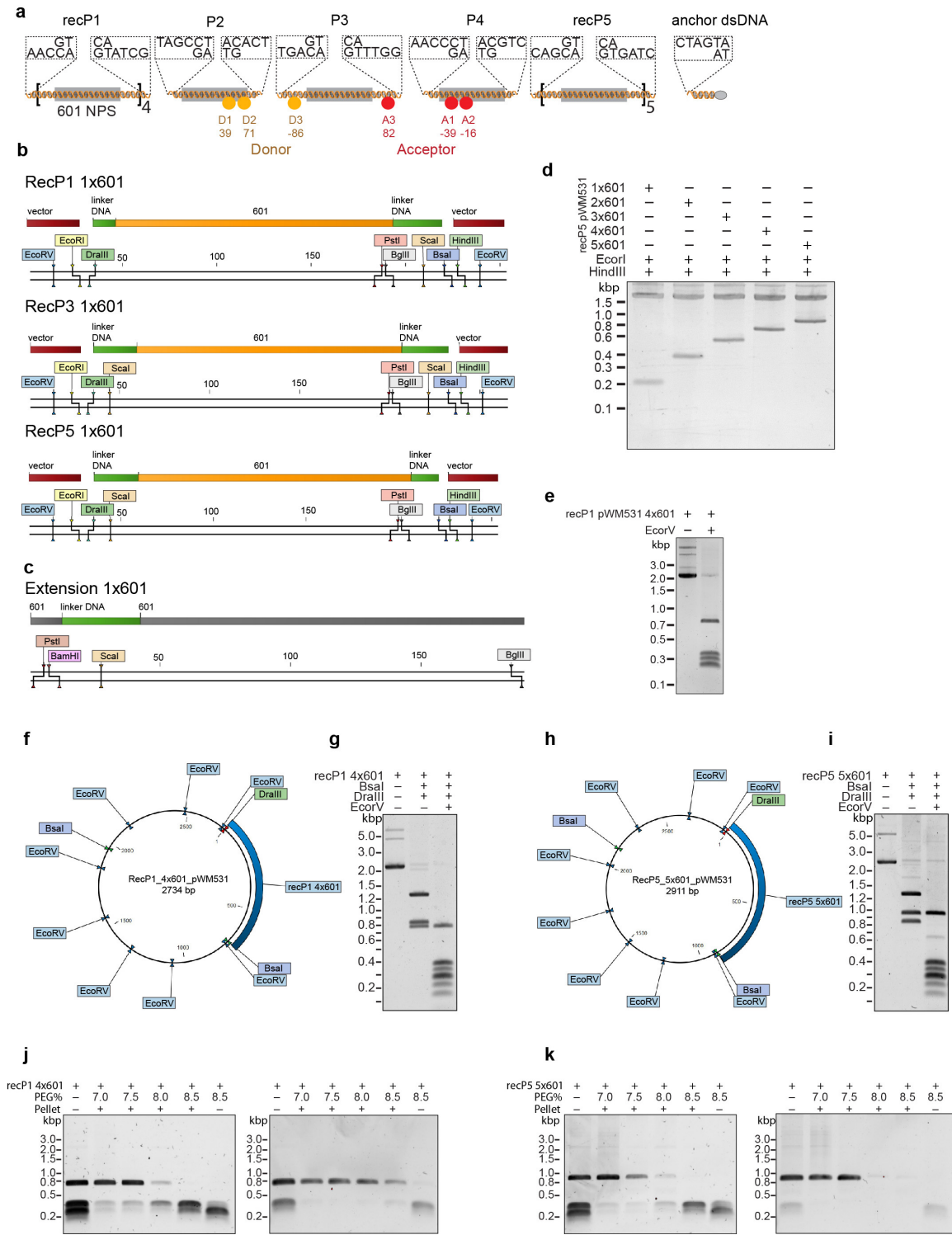
**Publisher's note:** Springer Nature remains neutral with regard to jurisdictional claims in published maps and institutional affiliations.



**Open Access** This article is licensed under a Creative Commons Attribution 4.0 International License, which permits use, sharing, adaptation, distribution and reproduction in any medium or format, as long as you give appropriate credit to the original author(s) and the source, provide a link to the Creative Commons license, and indicate if changes were made. The images or other third party material in this article are included in the article's Creative Commons license, unless indicated otherwise in a credit line to the material. If material is not included in the article's Creative Commons license and your intended use is not permitted by statutory regulation or exceeds the permitted use, you will need to obtain permission directly from the copyright holder. To view a copy of this license, visit <http://creativecommons.org/licenses/by/4.0/>.

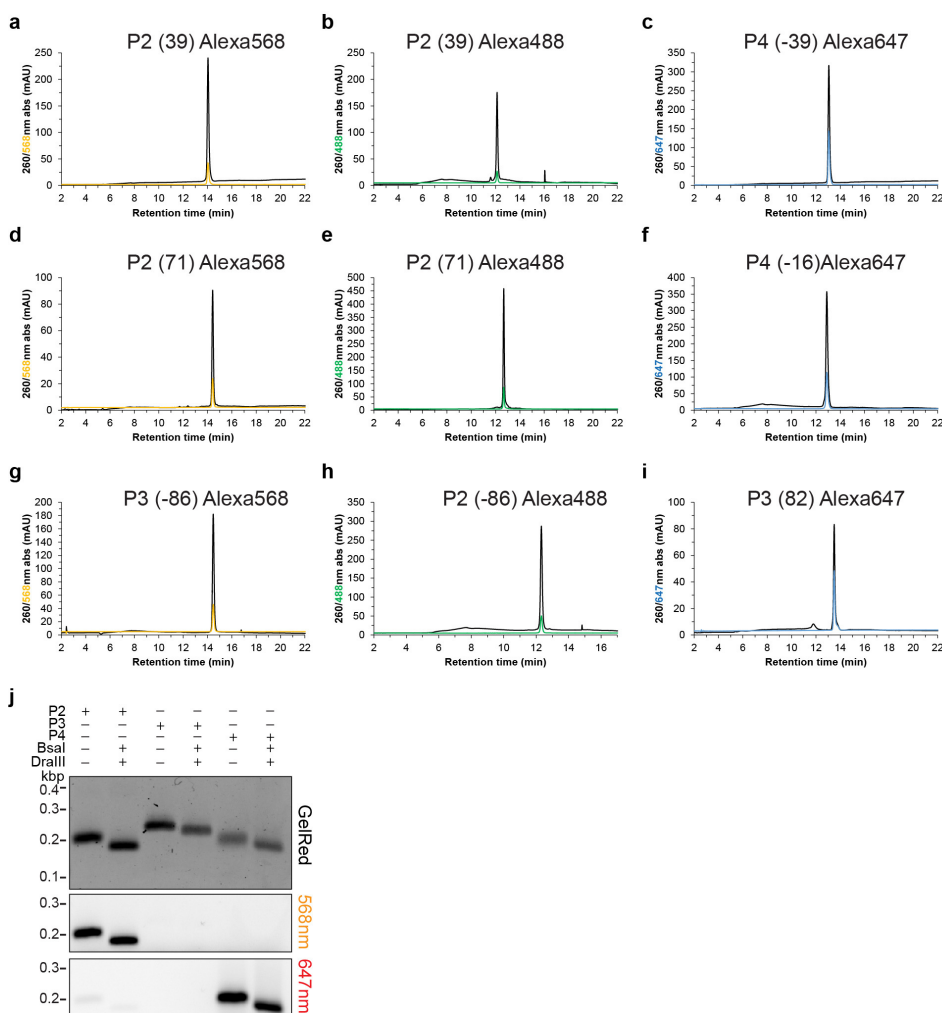
© The Author(s) 2018

Supplementary Figures

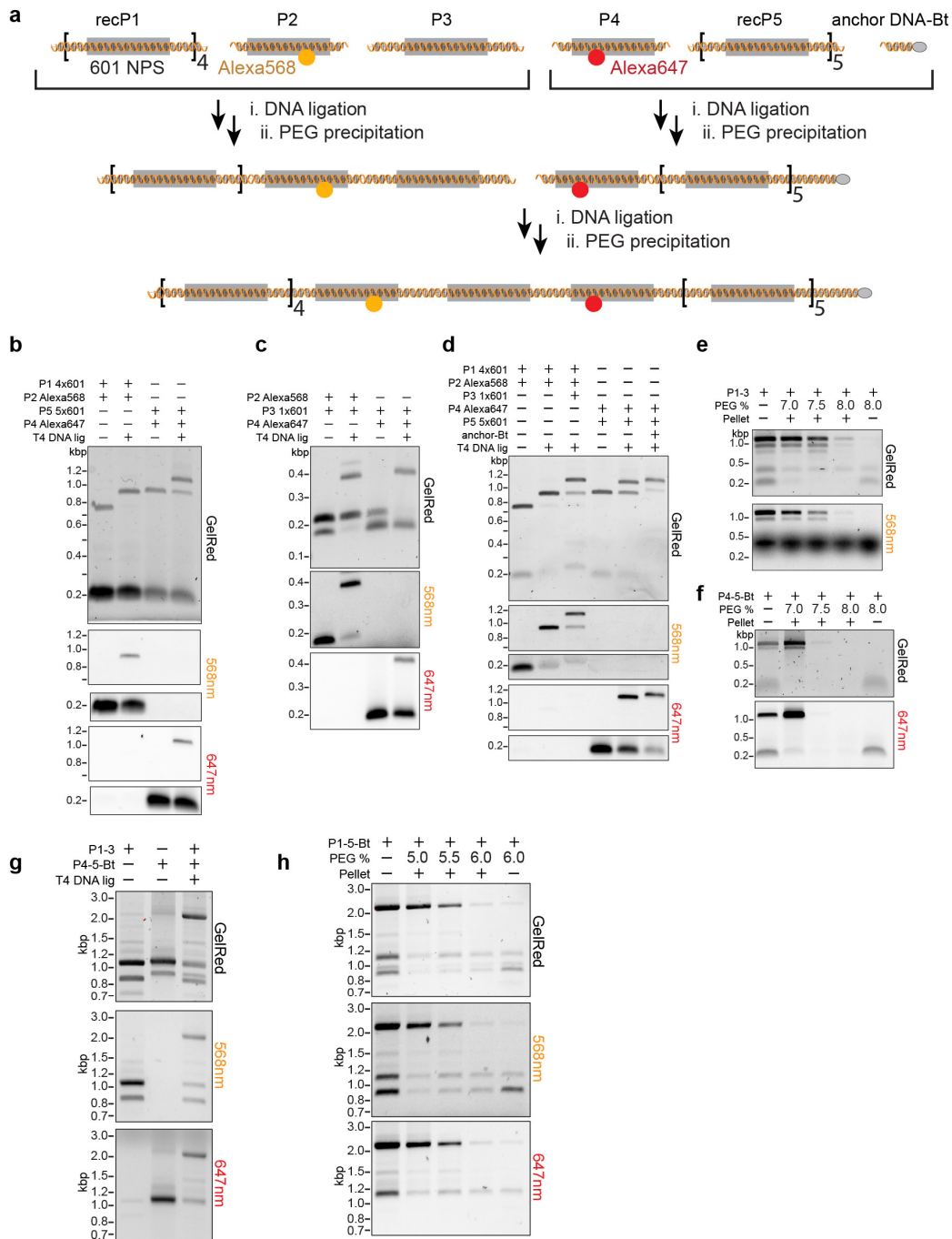


**Supplementary Figure 1 | Design, cloning and isolation of recombinant chromatin DNA fragments P1 and P5.**

**(a)** General design of the library allowing the introduction of FRET pairs into 12-mer chromatin array DNA by a preparative 6-piece ligation of two recombinant (recP1, recP5) and 4 synthetic (P2, P3, P4, anchor) DNA fragments. The anchor contains a biotin for immobilization (grey sphere). Donor (Alexa Fluor 568 (Alexa568) or Alexa Fluor 488, (Alexa488)), Acceptor (Alexa Fluor 647, (Alexa647)). The exact label positions (D1, D2, D3 and A1, A2, and A3; to form DA1, DA2 and DA3) are indicated relative to the 601 sequence, and are compiled in **Supplementary Table 3 & 4**. **(b)** Design of the three recombinant constructs for cloning of chromatin DNA fragments. EcoRV, BsaI and DraIII sites are for DNA fragment excision and plasmid fragmentation. Scal sites are for quality control of chromatin assemblies to result in individual nucleosomes. PstI and BglII sites are for extension of the array. **(c)** Design of 1x601 nucleosome positioning sequence extension piece. PstI, BamHI and BglII sites are for extension of the array. **(d)** Cloned array DNA pieces of increasing lengths from 1-5x601 excised from the plasmid backbone in recP5. **(e)** Excision of 4x601 DNA from recP1 by EcoRV after modular transfer from other piece. **(f)** Scheme of recP1 4x601 in pWM531 outlining restriction sites for EcoRV, BsaI and DraIII. **(g)** Excision of piece of recP1 4x601 with non-palindromic overhangs by complete digestion first with BsaI and DraIII followed by plasmid backbone fragmentation by EcoRV. **(h)** Scheme of recP5 4x601 in pWM531 outlining restriction sites for EcoRV, BsaI and DraIII. **(i)** Excision of piece of recP1 4x601 with non-palindromic overhangs by complete digestion first with BsaI and DraIII followed by plasmid backbone degradation with EcoRV. **(j-k)** Purification of excised recP1 4x601 **(i)** and recP5 5x601 **(j)** from plasmid backbone fragments by iterative PEG precipitation. For uncropped gels, see **Supplementary Figure 20**.

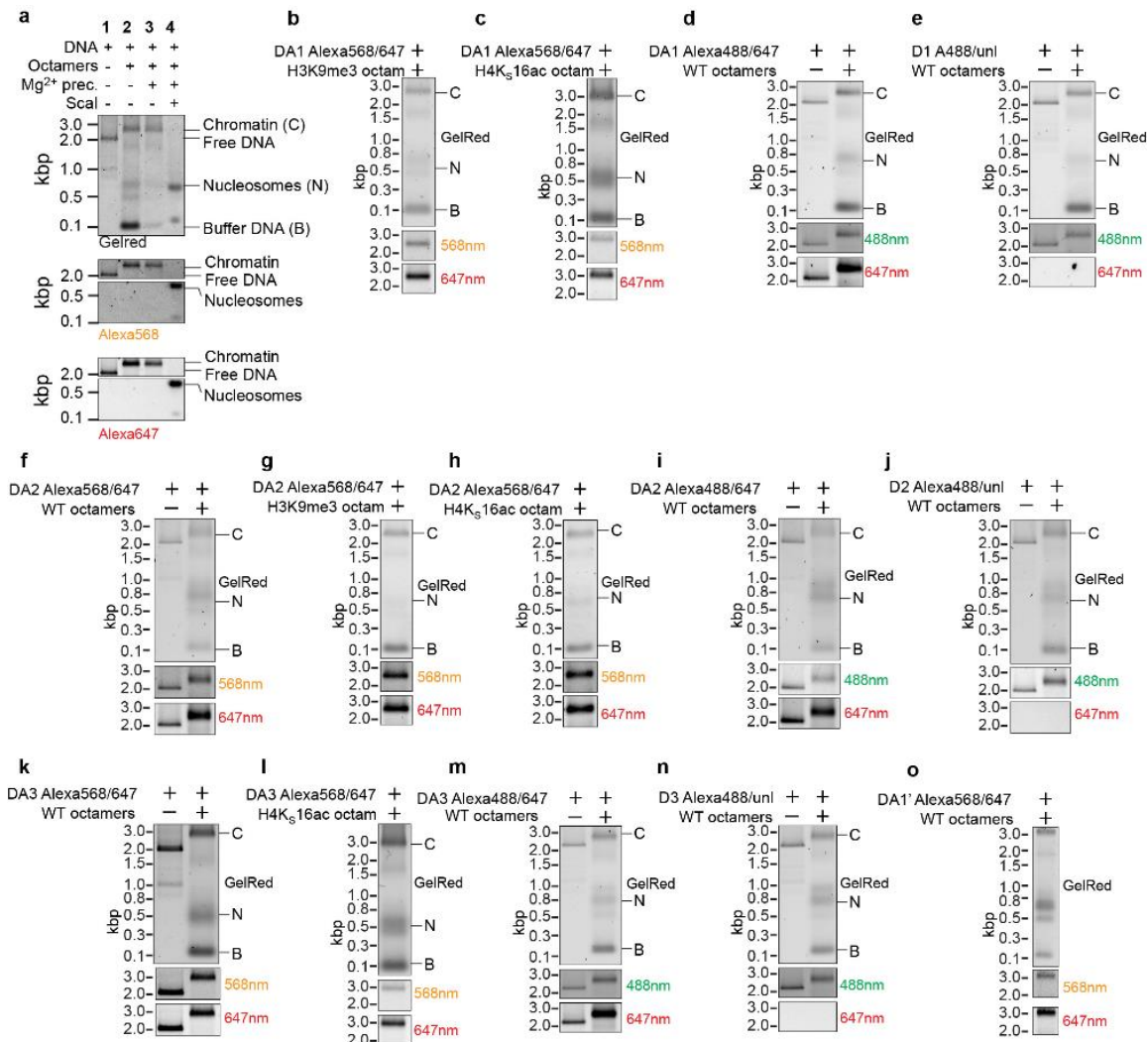


**Supplementary Figure 2 | Synthetic oligonucleotide labeling and production of synthetic/PCR-amplified fragments P2-P4.** (a-i) RP-HPLC analysis of final labeled oligonucleotides for introduction of site-specific labels into PCR pieces. The number in brackets is the final labeling position relative to the nucleosome dyad (see also **Supplementary Tables 1-4**). (j) Agarose gel analysis of example PCR-generated pieces P2 (Alexa568 labeled), P3 (unlabeled) and P4 (Alexa647 labeled) before and after digestion with Bsal and DraIII to produce unique non-palindromic cohesive ends. For uncropped gels, see **Supplementary Figure 20**.



**Supplementary Figure 3 | Production of 12x 601 array DNA containing FRET labels.** (a) Scheme for convergent assembly and purification of 12x array DNA shown for DA1. Pieces recP1 4x601, P2 1x601 and P3 1x601 are ligated and the intermediate 6x601 purified by PEG precipitation from the individual pieces. A similar procedure was used to generate P4 1x601, recP5 5x601 and the dsDNA anchor to produce another 6x601 intermediate and biotinylated (Bt) anchor for TIRF immobilization. The two intermediate 6x601 pieces are

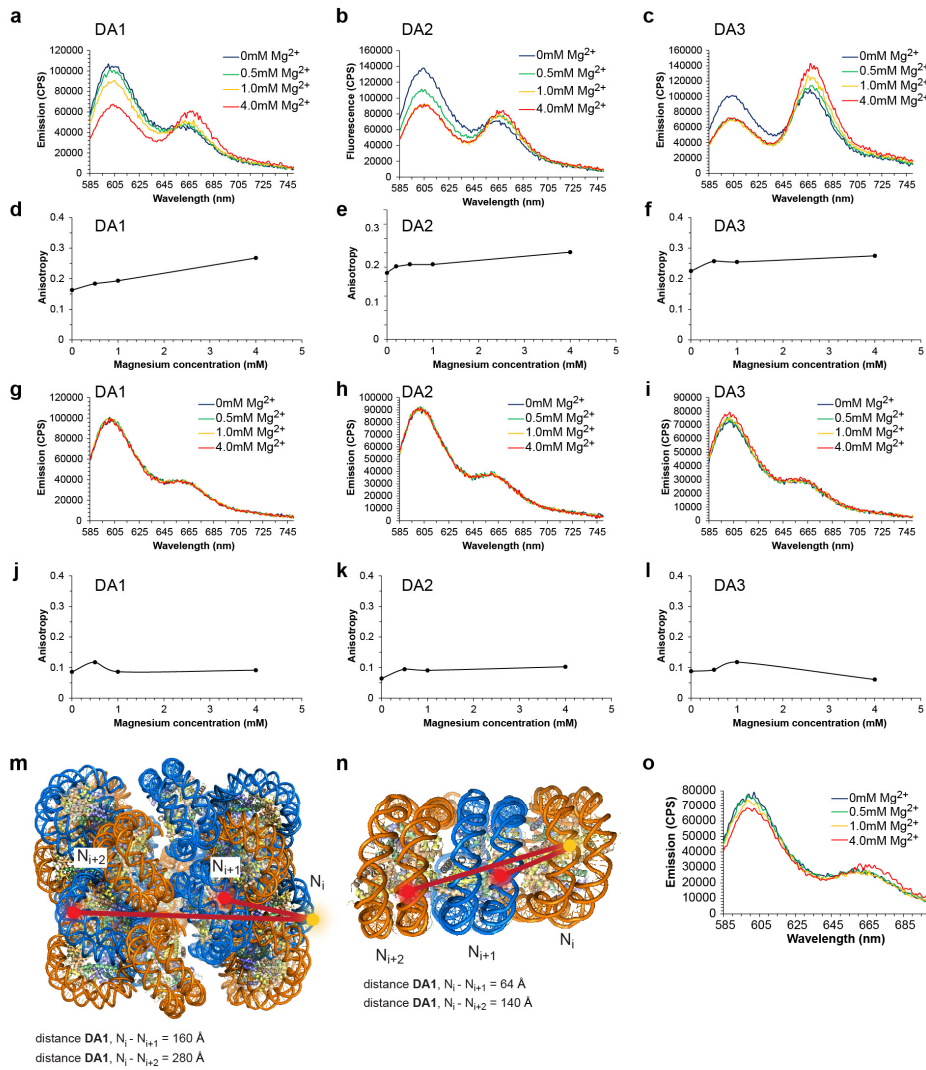
ligated to produce the 12x601 array DNA with internal fluorophores and the Bt-anchor followed by PEG precipitation to separate from the intermediates. **(b-c)** Test ligations to ensure complete digestion of recP1 4x601 and recP5 5x601, P2 1x601, P3 1x601 at key junctions. Complete displacement of the starting pieces upon ligation with excess cognate pieces shows full digestion. **(d)** Samples from large-scale ligations to produce intermediates analyzed to show near-completion of every ligation step. **(e-f)** PEG purification of the 6x601 intermediates to separate from 1x601 pieces that might interfere with final ligation between intermediates. **(g)** Ligation to produce final 12x601 piece displaying the intermediates before and after ligation. **(h)** PEG purification of final 12x601 arrays with <5% remaining of singly labeled and/or DNA lacking the Bt-anchor. For uncropped gels, see **Supplementary Figure 20**.



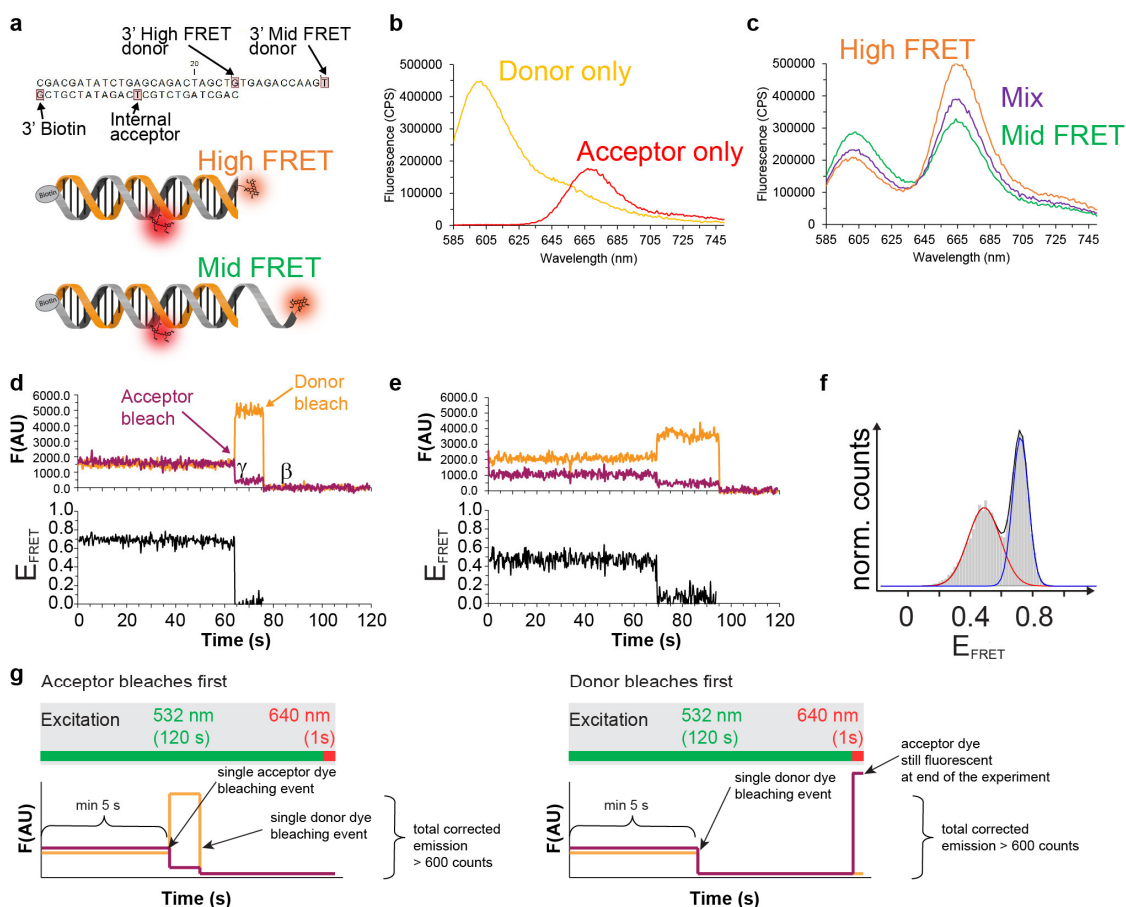
**Supplementary Figure 4 | Chromatin formation on DA1-3 fluorescently labeled DNA.** (a) Analysis of chromatin formation on fluorescently labeled array DNA by agarose gel electrophoresis. Lane 1: Free DA1-labeled array DNA. Lane 2: Assembled chromatin arrays. To avoid overloading array DNA with histone octamers, low-affinity buffer DNA (B) is added, resulting in the formation of a small amount of buffer nucleosomes (N). Lane 3: Chromatin arrays are purified by Mg<sup>2+</sup> precipitation. Lane 4: Digestion with the restriction enzyme Scal liberates mononucleosomes. The absence of higher-order aggregates or significant amounts of free DNA demonstrates the saturation of chromatin arrays. (b), Formation of DA1 chromatin arrays with Alexa568/647 labels and H3K9me3 containing histone octamers, (c), DA1 chromatin arrays with Alexa568/647 labels and H4K<sub>s</sub>16ac octamers. (d) DA1 chromatin arrays with Alexa Fluor 488 (Alexa488) and Alexa647 labels. e, D1 chromatin arrays with an Alexa488 label (Donor-only). (f) DA2 chromatin arrays with Alexa568/647 labels

and unmodified histone octamers. **(g)** DA2 chromatin arrays with Alexa568/647 labels and H3K9me3 containing octamers. **(h)** DA2 chromatin arrays with Alexa568/647 labels and H4K<sub>5</sub>16ac containing histone octamers. **(i)** DA2 chromatin arrays with Alexa488/647 labels and unmodified histone octamers. **(j)** D2 chromatin arrays with an Alexa488 label (Donor only). **(k)** DA3 chromatin arrays with Alexa568/647 labels and unmodified histone octamers. **(l)** DA3 chromatin arrays with Alexa568/647 labels and H4K<sub>5</sub>16ac histone octamers. **(m)** DA3 chromatin arrays with Alexa488/647 labels and unmodified histone octamers. **(n)** D3 chromatin arrays with an Alexa488 label (Donor only). **(o)** DA1' chromatin arrays with Alexa568/647 with an n, n+1 dye spacing to test FRET in solenoid structures. For uncropped gels, see **Supplementary Figure 20**.

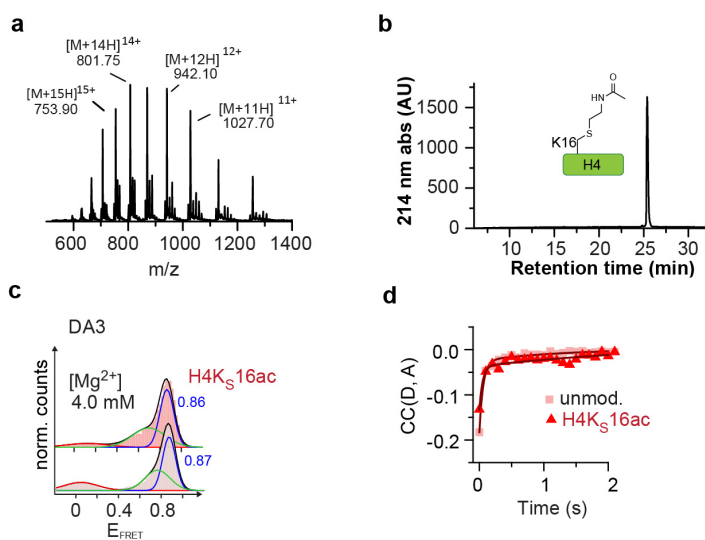




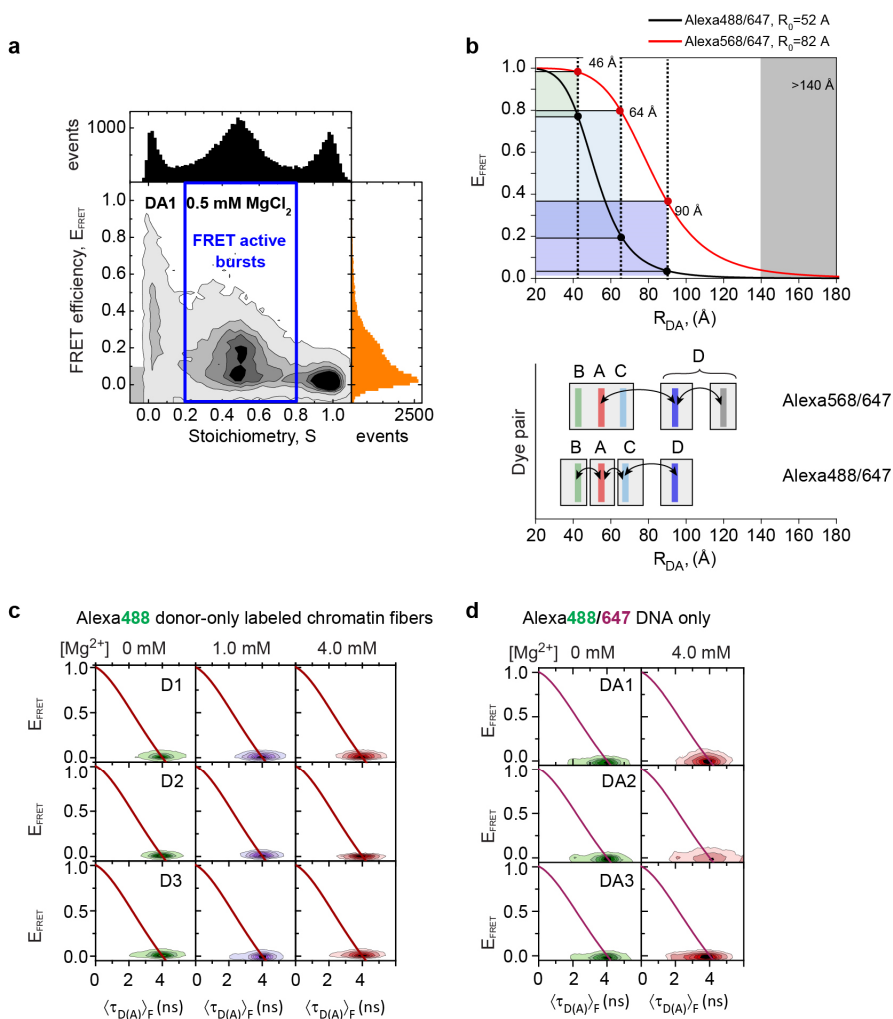
**Supplementary Figure 5 | Fluorescence spectra and donor anisotropies in chromatinized and non-chromatinized double-labeled array DNA (Alexa568/647).** (a-c) Ensemble spectra of chromatin samples upon compaction with magnesium, showing distinct responses dependent on the positions of the FRET pairs. (d-f) Anisotropy of the donor in the chromatin arrays at increasing magnesium concentrations. (g-i) Spectra of the double-labeled DNA samples in absence of nucleosomes. (j-l) Anisotropy of the donor in absence of nucleosomes. (m) Alternative chromatin structure (interdigitated solenoid) based on a model from ref. <sup>1</sup>, exhibiting inter-dye distances (DA1) outside the FRET detection radius (see also **Supplementary Fig. 8b**). (n) Alternative chromatin structure (solenoid) with continuous stacking of nucleosomes, exhibiting inter-dye distances within FRET detection radius only for N<sub>i</sub>, N<sub>i+1</sub> labeling distance. (o) Fluorescence data on **DA1'** chromatin array with a N<sub>i</sub>, N<sub>i+1</sub> label configuration, exhibiting minor FRET increase and thus indicating that solenoid structures do not contribute to the measured FRET signal.



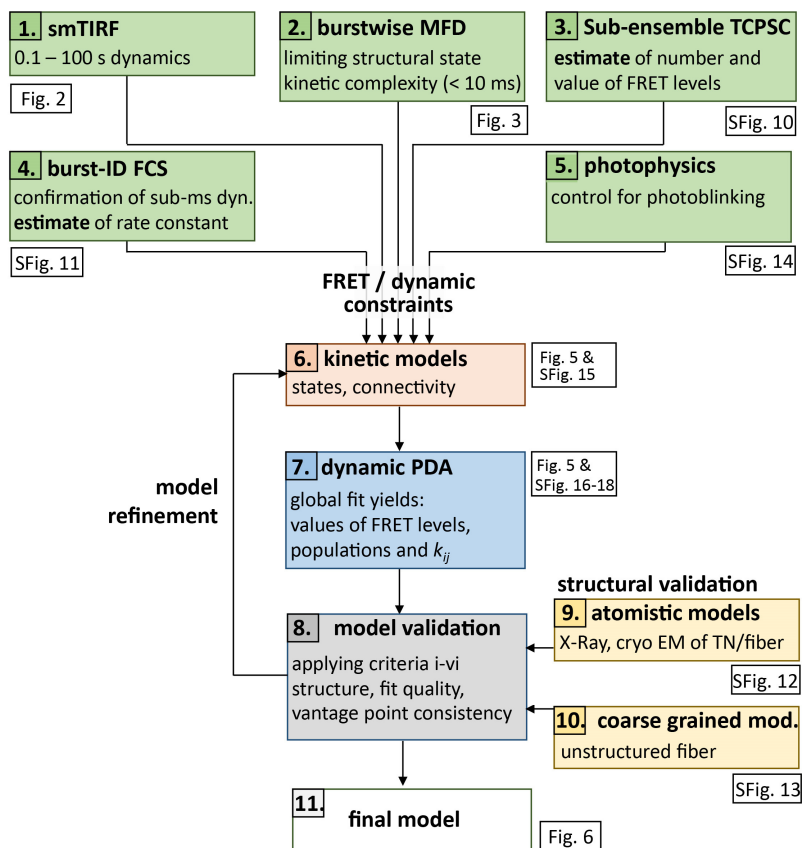
**Supplementary Figure 6 | Characterization of FRET pair at the single-molecule level.** (See **Supplementary Note, step 1: smTIRF**). **(a)** Sequences and locations of fluorophores and biotin on constructs used to calibrate ensemble and smFRET with Alexa Fluor 568 and Alexa Fluor 647. **(b)** Spectra acquired from ensemble FRET by excitation at 575nm from single-stranded oligonucleotides labeled with each of the two respective dyes. **(c)** Spectra from the individual dsDNA constructs showing distance-dependent FRET. **(d)** Schematic of the two annealed dsDNA constructs. **(e)** Trace from high FRET DNA piece at the single-molecule level with TIRF with indications of bleaching events, the relative detection efficiencies  $\gamma$ , between donor and acceptor and the donor bleedthrough to the acceptor  $\beta$ , for calculations of the corresponding FRET efficiencies. **(e)** Trace from mid FRET DNA piece with sm FRET. **(f)** Histograms from mixture between two DNA pieces showing the ability to distinguish between different populations using the FRET pair. **(g)** Trace selection criteria: Shown are the two types of acceptable traces that were used for all smTIRF analyses, as judged by trace length, emission and dye bleaching behavior. For details see **Materials and Methods** or **Supplementary Note**, paragraph **smTIRF measurements**.



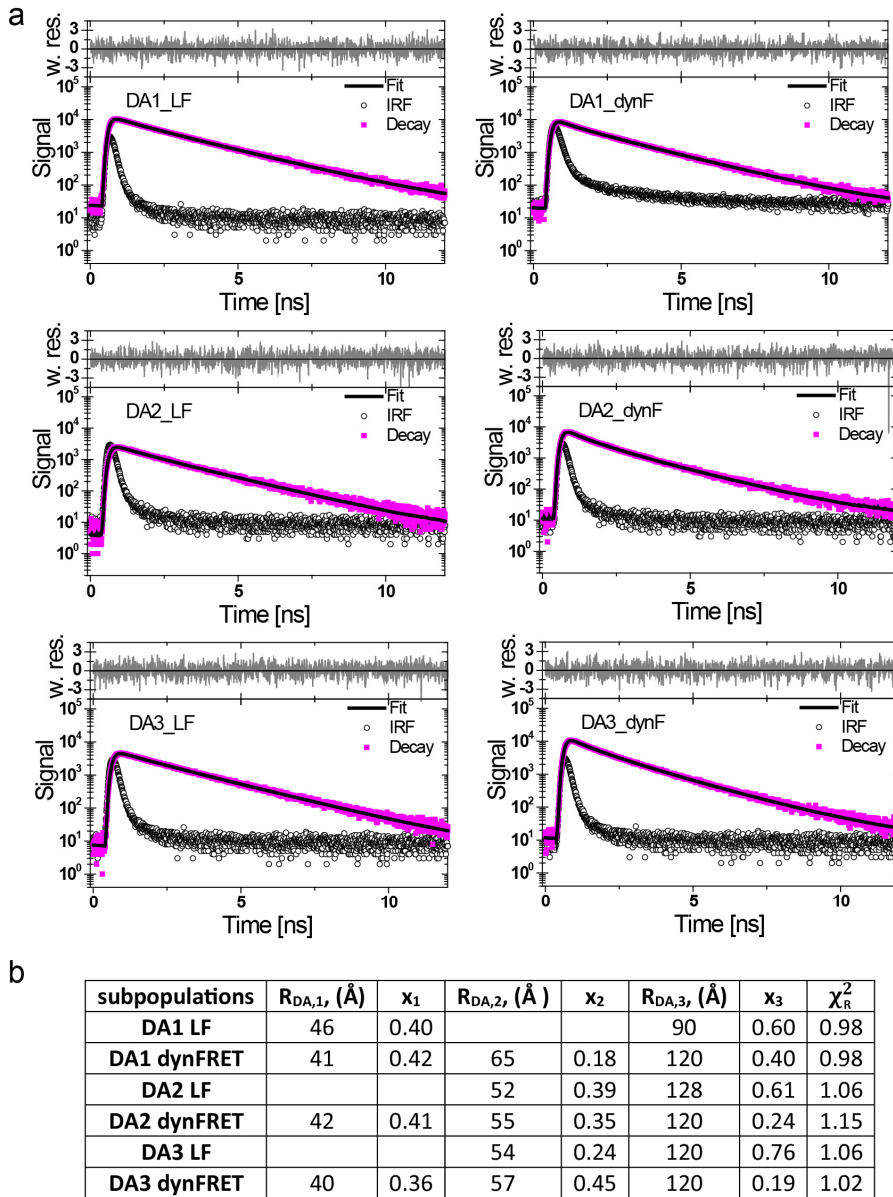
**Supplementary Figure 7 | H4K<sub>5</sub>16ac analytical data and impact in DA3.** H4K<sub>5</sub>16ac is produced by reacting the mutant H4, H4K16C, with N-vinylacetamide in the presence of radical promoter (VA-044) and glutathione<sup>2</sup>. **(a)** MS spectrum of semisynthetic H4K<sub>5</sub>16ac. (Expected mass: 11211Da, observed mass 11211Da) **(b)** RP-HPLC analysis of H4K<sub>5</sub>16ac. **(c)** FRET histogram for DA3 at 4mM Mg<sup>2+</sup> with or without acetylation on H4 K16. **(d)** Donor-acceptor channel cross-correlation analysis of DA1, overlay of data for 4 mM Mg<sup>2+</sup> for unmodified chromatin, as well as H4K<sub>5</sub>16ac at 4 mM Mg<sup>2+</sup>. The fit for H4K<sub>5</sub>16ac results in a relaxation time  $t_R = 50$  ms. For the percentage of dynamic traces, see **Supplementary Table 6**.



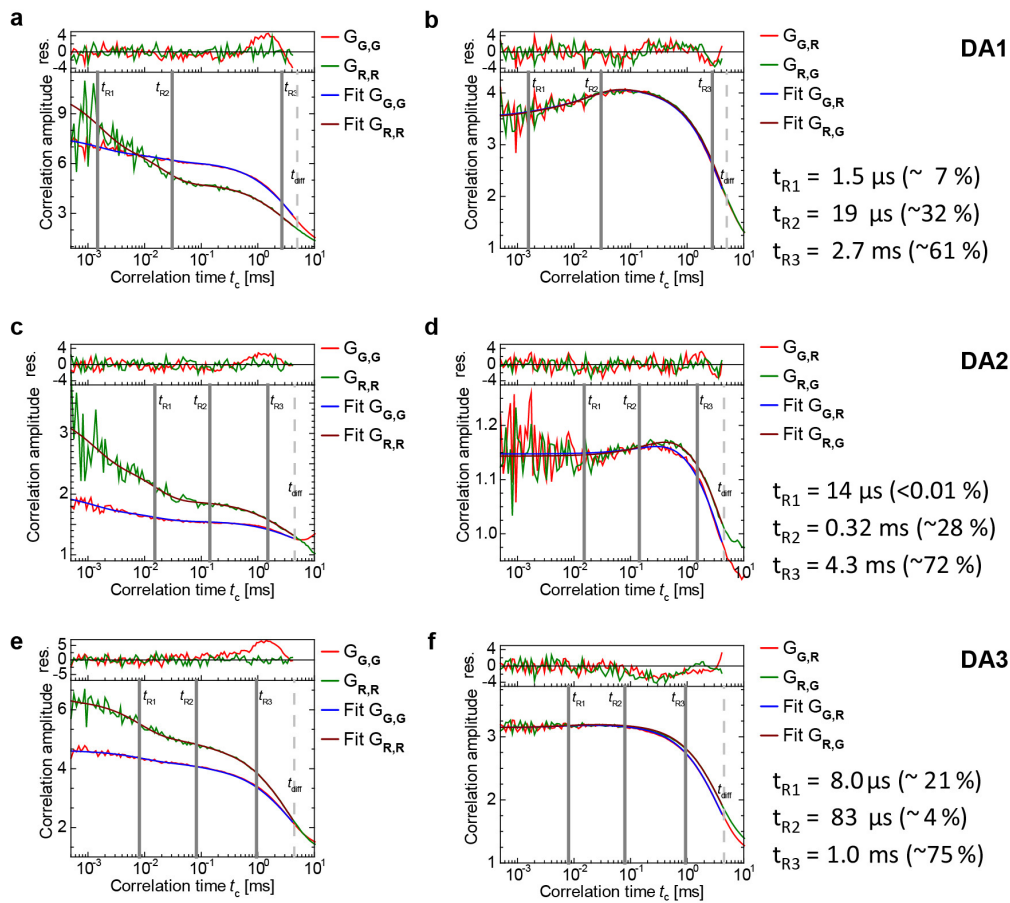
**Supplementary Figure 8 | MFD measurements of chromatin arrays DA1-3 with Alexa568/647 and Alexa488/647 labeling schemes.** (See **Supplementary Note, step 2: 2D MFD plots with FRET lines**). **(a)** MFD histogram of  $E_{FRET}$  vs Stoichiometry for DA1 (Alexa488/647) in 0.5 mM Mg<sup>2+</sup>. Blue box: Selection of bursts of double-labeled chromatin arrays capable of FRET (FRET active population). **(b)**  $E_{FRET}$  as a function of inter-dye distance for the two employed dye-pairs, Alexa568/647 and Alexa488/647. For illustration, representative inter-dye distances and their associated  $E_{FRET}$  values observed in DA1 are indicated. Alexa568/647 and Alexa488/647 have different sensitivities: Alexa568/647 allows the detection of long-range dynamics beyond 120 Å, whereas Alexa488/647 enables the investigation of sub-states and their exchange dynamics below 70 Å. **(c)** MFD plots of donor-only, Alexa488-labeled chromatin fibers (D1, D2 and D3). Dark red line: static FRET line. See **Supplementary Methods, step 2, Static and dynamic FRET-lines**. **(d)** MFD plots of Alexa488/647 labeled DNA (DA1, DA2 and DA3), demonstrating the absence of FRET or dynamics without the presence of chromatin.

**Dynamic single - molecule structural biology workflow:**

**Supplementary Figure 9 | Dynamic single-molecule structural biology workflow.** (See **Supplementary Note**, Dynamic structural biology analysis). The workflow is comprised of 11 steps: 5 experimental methods (shaded in green), design of the kinetic model (orange), data analysis with dynamic PDA methods (in blue), validation of the model (gray), structural validation (in yellow) and confirmation of the final model (white). Small boxes: Indicating Figures containing the relevant data, “SFig” refers to Supplementary Figures.

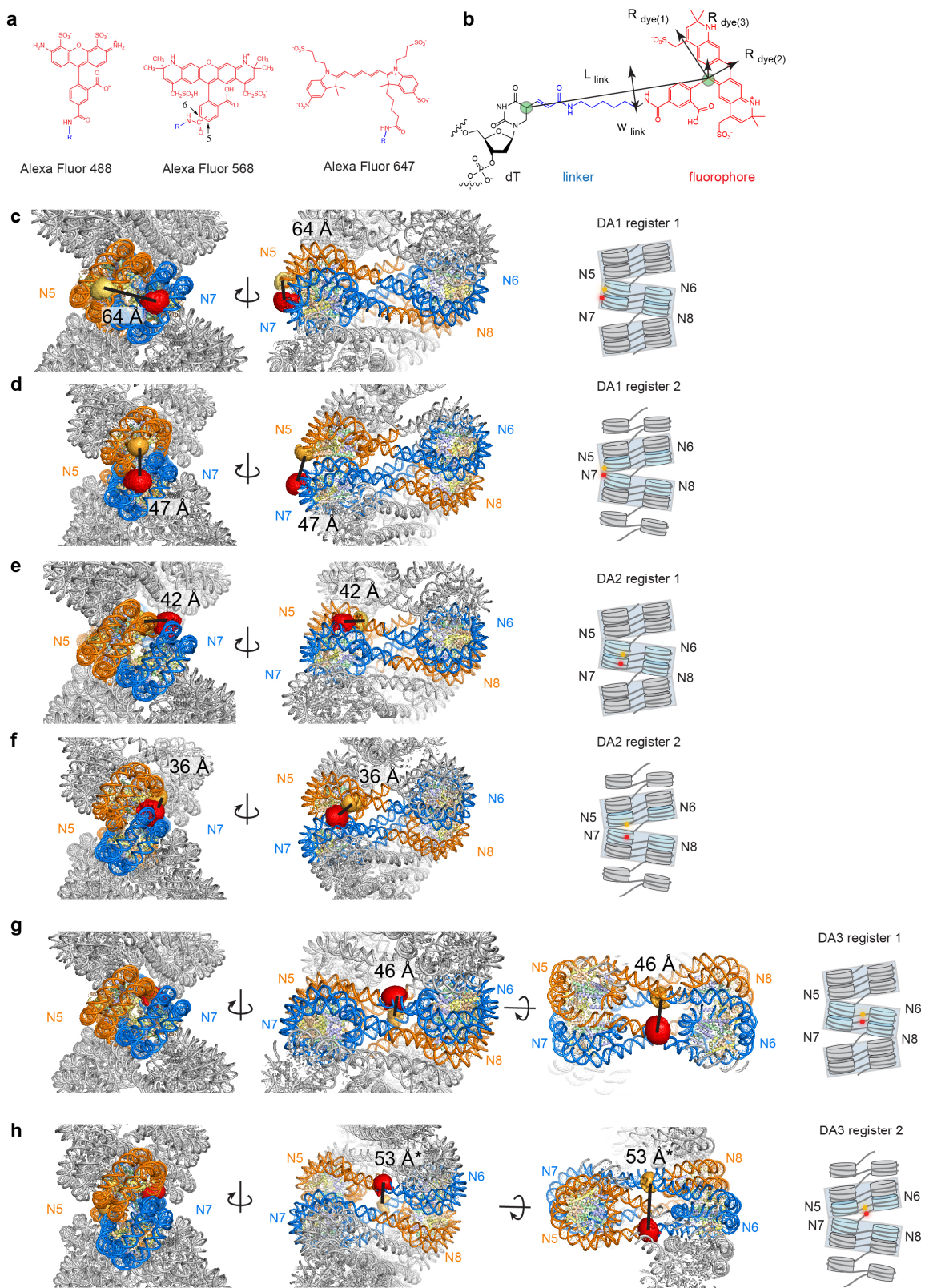


**Supplementary Figure 10 | seTCSPC of DA1-3 (Alexa488/647) in 0.5 mM  $Mg^{2+}$ .** (See **Supplementary Note, step 3: Sub-ensemble TCSPC**). **(a)** Fluorescence decays (magenta) with corresponding fit (black line). Left panel: fits for accumulated LF bursts; right panel: fits for accumulated dynF bursts. In the global fit (see **Supplementary Note, step 3**) the DOnly decay  $f_{D(0)}$  was approximated by a single donor fluorescence lifetime ( $\tau_{D(0)} = 4.1$  ns) and the decay of the FRET-population  $f_{D(A)}$  with 3 Gaussian distributed distances and the same fixed half-width  $\sigma_{DA} = 6$  Å. The fit quality is illustrated by weighted residuals (in the upper panel) by  $\chi_R^2$ . **(b)** Fit results for the LF and dynF populations by eq.(3.3) - (3.4). IRF: Instrument response function.



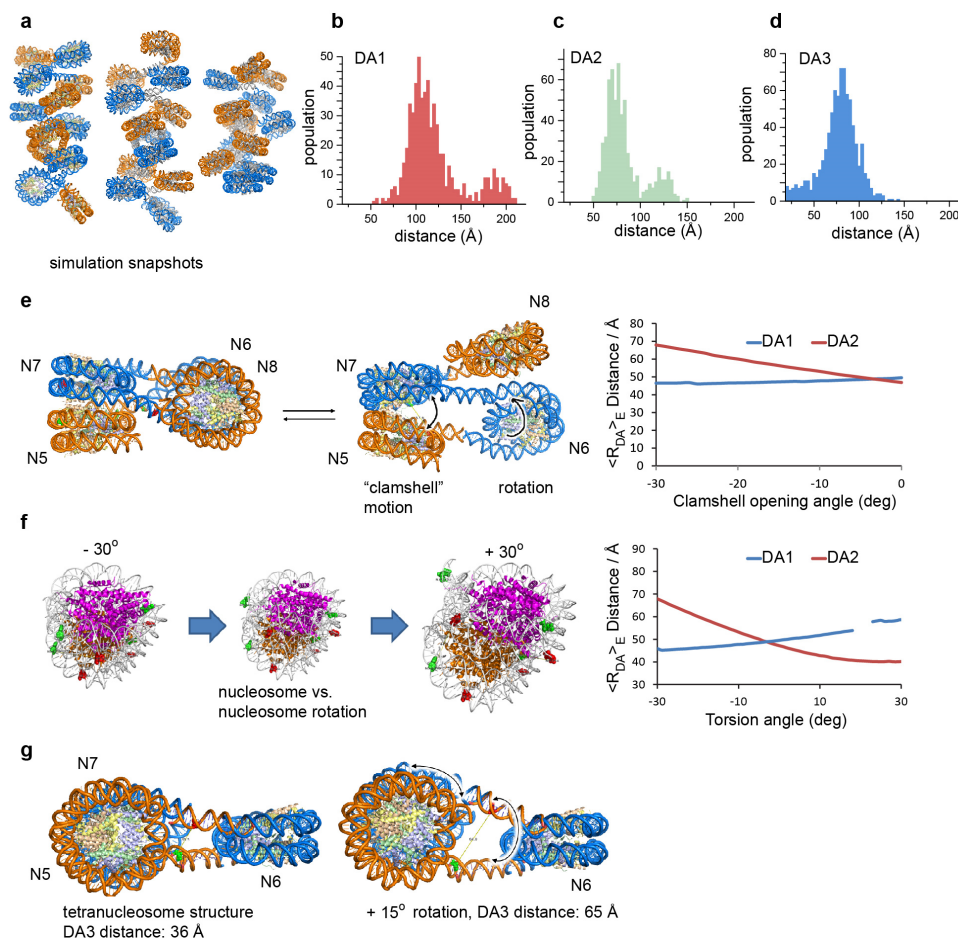
**Supplementary Figure 11 | Model-free dynamic analysis by fluorescence correlation functions of arrays DA1-3 (Alex488/647) at 0.75 mM  $\text{Mg}^{2+}$ .** (See **Supplementary Note, step 4: Burst-ID FCS**). The analysis by auto- and cross-correlation functions<sup>3</sup> shows FRET related anti-correlated dynamics with three relaxation time  $t_{R1}$ ,  $t_{R2}$ , and  $t_{R3}$  in the ms- and sub-ms time range. **(a)** Burst-ID donor-donor ( $G_{G,G}$ ) and acceptor-acceptor ( $G_{R,R}$ ) auto-correlation functions for DA1 chromatin fibers with an additional bunching term in the auto-correlation functions to consider also dye blinking with the corresponding amplitudes  $B^{(G)} = 0.09$  and  $B^{(R)} = 0.27$ , respectively, and the relaxation time  $t_B = 44 \text{ ns}$ . **(b)** Burst-ID cross-correlation functions  $G_{G,R}$  and  $G_{R,G}$  of donor-acceptor (G-R) and acceptor-donor (R-G) signal, respectively. The timescales of observed processes are obtained by a global fit of all correlation functions for one FRET pair and are shown on the right. **(c-d)** Auto- and cross-correlation functions for DA2 with the additional bunching amplitudes  $B^{(G)} = 0.25$  and  $B^{(R)} = 0.33$ , respectively, and the relaxation time  $t_B = 1.2 \mu\text{s}$ . **(e-f)** Auto- and cross-correlation functions for DA3 at with the additional bunching amplitudes  $B^{(G)} = 0.12$  and  $B^{(R)} = 0.25$ , respectively, and the relaxation time  $t_B = 0.13 \mu\text{s}$ .



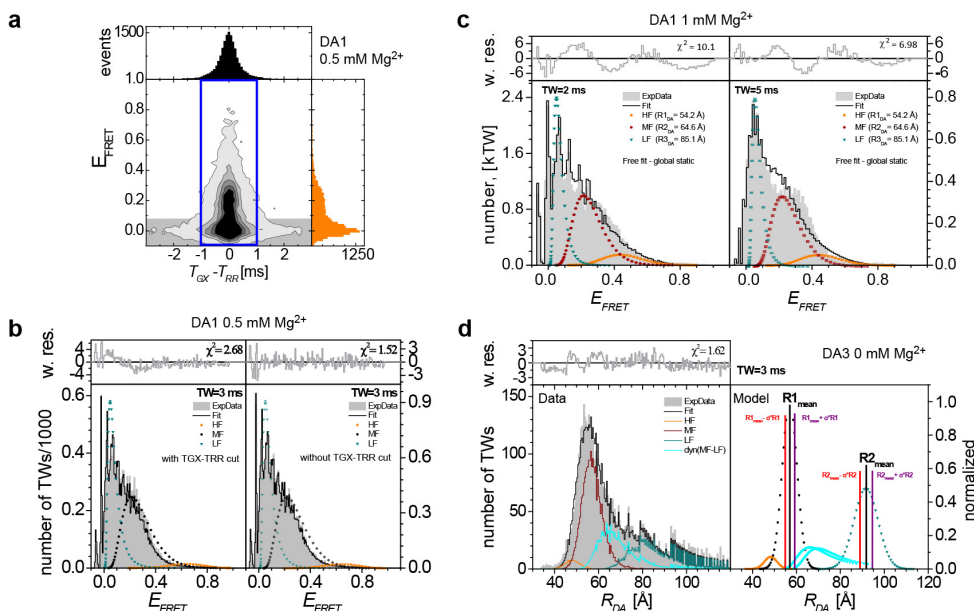




**Supplementary Figure 12 | Structural models for the compact chromatin state.** (See **Supplementary Note, step 9:** Structural models of compact chromatin states). For a comparison between measured and calculated distances, see **Supplementary Table 8.** **(a)** Chemical structures of the fluorescent labels Alexa488, Alexa568 and Alexa647. **(b)** Chemical structure of the dye linked to a dT nucleotide. To calculate the dye accessible contact volumes for these dyes, the structure was approximated by an ellipsoid ( $R_{dye(1)}$ ,  $R_{dye(2)}$  and  $R_{dye(3)}$ ) connected by a linker of length ( $L_{link}$ ) and width ( $w_{link}$ ). Accessible contact volume dye model was used where part of AV which is closer than 3 Å from the macromolecular surface is defined to have higher dye density  $\rho_{dye}$ <sup>4</sup>. For the parameters used for the different dyes, see **step 9: FRET positioning and screening calculations.** **(c)** Molecular structure of a compact chromatin array, consisting of a stack of 3 tetranucleosomes (4-4-4, register 1) with DA1-positioned dyes in the central tetranucleosome. The model was produced by fitting nucleosomes into the electron density of the cryoEM structure of a 177-bp nucleosome array, ref. <sup>5</sup>. The inter-dye distance was evaluated using simulated dye accessible contact volumes (ACV)<sup>6</sup>. **(d)** Molecular structure of a chromatin array, consisting of a stack of 2 tetranucleosomes, flanked by two unstacked nucleosomes at each side (2-4-4-2, register 2) with DA1-positioned dyes on the two central tetranucleosomes and inter-dye distance from ACV-calculations. **(e)** Inter-dye distance for DA2 dyes in register 1 compacted arrays. **(f)** Inter-dye distance for DA2 dyes in register 2 compacted arrays. **(g)** Inter-dye distance for DA3 dyes in register 1 compacted arrays. Linker DNA was introduced extending the nucleosomal DNA connecting neighboring nucleosomes. The distance is calculated between the phosphate groups of the modified bases (P-P distance). **(h)** Inter-dye distance for DA3 dyes in register 2 compacted arrays. Linker DNA was introduced extending the nucleosomal DNA connecting neighboring nucleosomes. Shown are calculated P-P distances.



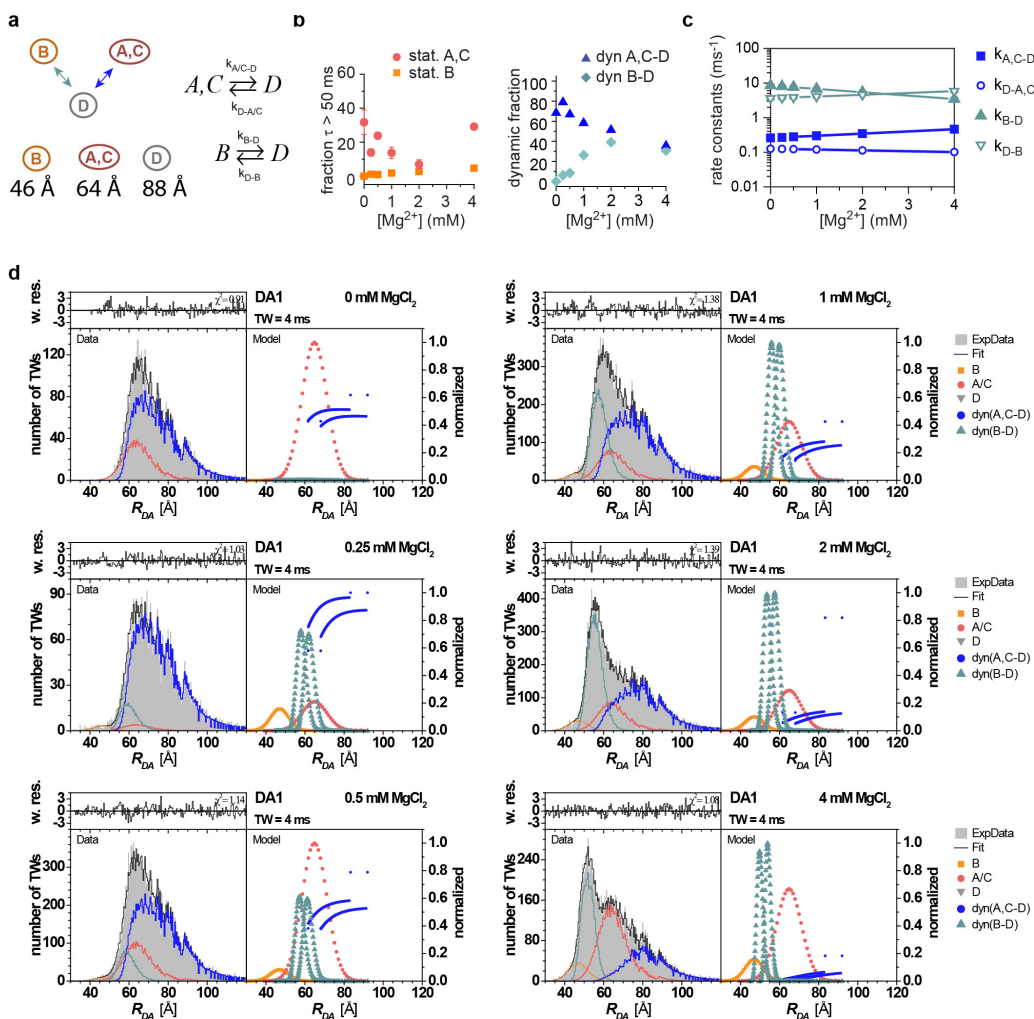
**Supplementary Figure 13 | Structural models open and dynamic chromatin states.** (See **Supplementary Note, step 10**: Structural models of open and dynamic states). **(a)** Representative snapshots from coarse grained simulations of chromatin fibers following ref. <sup>7</sup>. **(b)** Calculated distance distributions between DA1 dye pairs (between phosphate groups of the modified bases, P-P distances) in the open chromatin ensembles for 100 structures with 12 nucleosomes each. **(c)** Calculated P-P distance distributions between DA2 dye pairs in open chromatin ensembles from the same structure set as in **b**. **(d)** Calculated P-P distance distributions between DA3 dye pairs in open chromatin ensembles for the same structure set as in **b**. **(b-d)** Distances are calculated between P atoms of the labeled nucleotide. **(e)** Dependence of DA1 and DA2 FRET averaged inter-dye distance on "clamshell"-type opening of the tetranucleosome interface. DA1 is not sensitive to this mode of motion, in contrast to DA2. **(f)** Dependence of DA1 and DA2 inter-dye distance on rotational motions between two nucleosomes. DA2 shows stronger angular dependency compared to DA1. **(g)** Effect of rotational motion on DA3 FRET averaged inter-dye distance showing that this dye pair is sensitive to the distorted tetranucleosome state (State C in **Fig. 4a**).



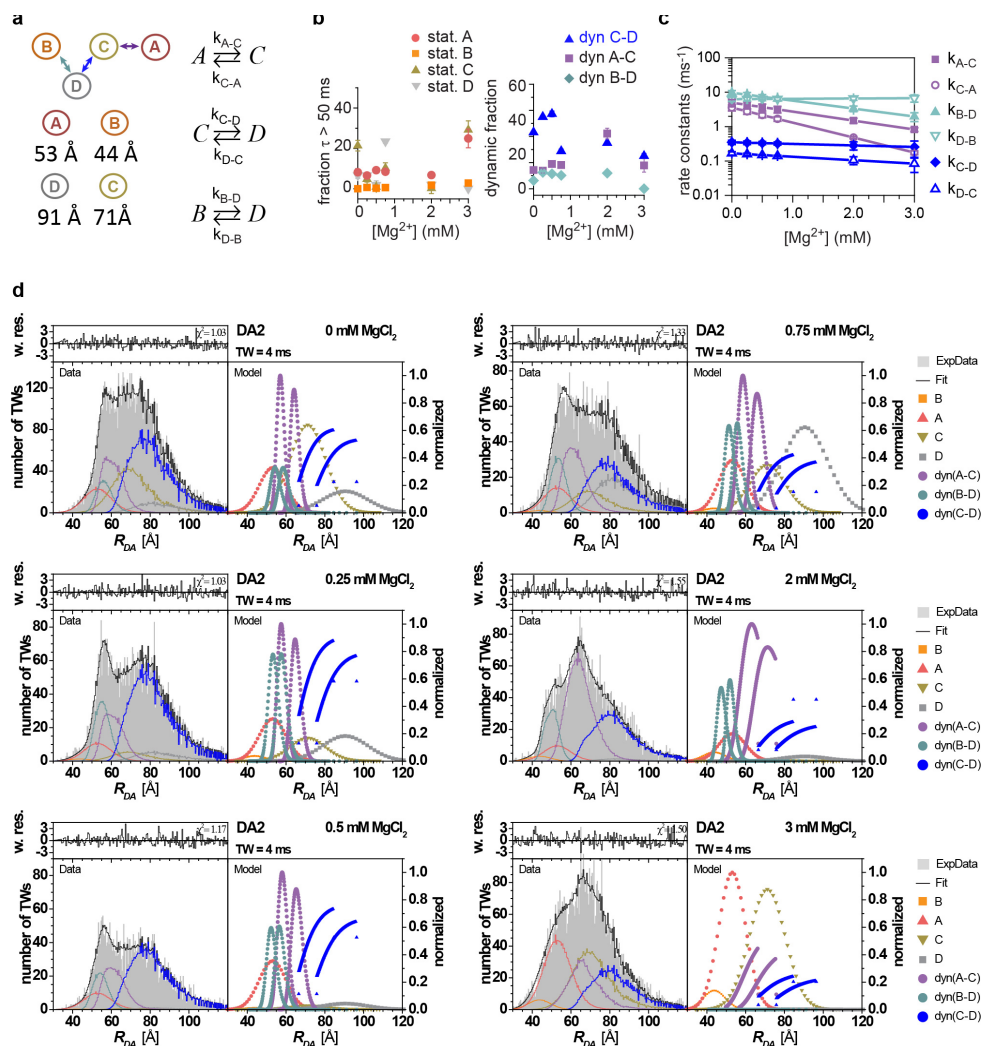
**Supplementary Figure 14 | Photobleaching and photoblinking analysis & principles of PDA analysis.** (See **Supplementary Note, step 5:** Photobleaching and photoblinking analysis, and **step 7:** General description of PDA analysis). **(a)** Example of the photobleaching and photoblinking analysis for DA1 (Alex488/647) in 0.5 mM Mg<sup>2+</sup>. FRET efficiency vs  $T_{GX}-T_{RR}$  is arranged in a 2D histogram, demonstrating the procedure of the macrotime filter ( $|T_{GX}-T_{RR}| < 1$  ms). Bursts selected for the macrotime cut are in the blue box. For a definition of the parameter see **Dynamic Analysis, step 5.** **(b)** PDA analysis of the FRET efficiency histograms of the selected bursts (right panel) and un-filtered bursts (left panel). The difference between the two analyses is very small. **Principles of PDA analysis:** **(c)** DA1 (Alexa488/647) in 1 mM Mg<sup>2+</sup>. A global fit for two TWs (2 ms (left panel) and 5 ms (right panel) using a joint fit model (3 static Gaussian distributed distances) demonstrates that a static model inappropriate. Experimental data histogram is shown in gray, fit in black line and resulting static FRET states in orange, dark cyan and wine. **(d)** Dynamic PDA analysis overview using DA3 (Alexa488/647) at 0 mM Mg<sup>2+</sup> as an example. Left panel: experimental data histogram is shown in gray and resulting shot-noise limited model distribution as a black line. It is described by the contribution of a High FRET species (HF, orange), medium FRET species (MF, wine), low FRET species (LF, dark cyan) and a dynamic species in a two-state dynamic distribution between MF and LF (cyan line). Right panel: The model distance distribution is given by a sum of static Gaussian-distributed distances (R1, MF: (wine symbols), R2, LF: (dark cyan symbols)) and dynamic mixing between  $(R1_{mean}-\sigma_1$  and  $R2_{mean}-\sigma_2)$  and  $(R1_{mean}+\sigma_1$  and  $R2_{mean}+\sigma_2)$  distributions (cyan symbols), where  $\sigma_i=\sigma \cdot R_i$  and  $\sigma=0.06$ .

Connectivity plot	Equations	Selection criteria:					
		i. connectivity	ii. state #	iii. parameter boundaries	iv. fit stability	v. goodness of fit	vi. consistency
<b>DA1</b>							
1.	$A, C \rightleftharpoons D$ $A, C \rightleftharpoons B$ $B \rightleftharpoons D$	+	+	-	-	+	-
2.	$A, C \rightleftharpoons D$ $B \rightleftharpoons D$	+	+	+	+	+	+
<b>DA2</b>							
1.	$A, C \rightleftharpoons D$ $A, C \rightleftharpoons B$	-	+	-	-	+	-
2.	$B \rightleftharpoons D$ $A, C \rightleftharpoons D$	+	+	-	-	-	+
3.		-	+	+	+	+	-
4.	$A \rightleftharpoons C$ $C \rightleftharpoons D$ $A \rightleftharpoons D$ $B \rightleftharpoons D$	+	+	-	-	-	+
5.	$A \rightleftharpoons C$ $A \rightleftharpoons D$ $B \rightleftharpoons D$	-	+	+	+	+	+
6.	$A \rightleftharpoons C$ $C \rightleftharpoons D$ $B \rightleftharpoons D$	+	+	+	+	+	+
<b>DA3</b>							
1.	$A \rightleftharpoons C$ $C \rightleftharpoons D$ $B \rightleftharpoons D$	-	-	-	+	+	+
2.	$A, B \rightleftharpoons C$ $C \rightleftharpoons D$ $A, B \rightleftharpoons D$	+	+	+	-	+	-
3.	$A, B \rightleftharpoons D$ $C \rightleftharpoons D$	-	+	+	+	+	-
4.	$A, B \rightleftharpoons C$ $C \rightleftharpoons D$	+	+	+	+	-	-
5.	$A \rightleftharpoons C$ $C \rightleftharpoons D$ $B \rightleftharpoons D$	+	+	+	+	+	+

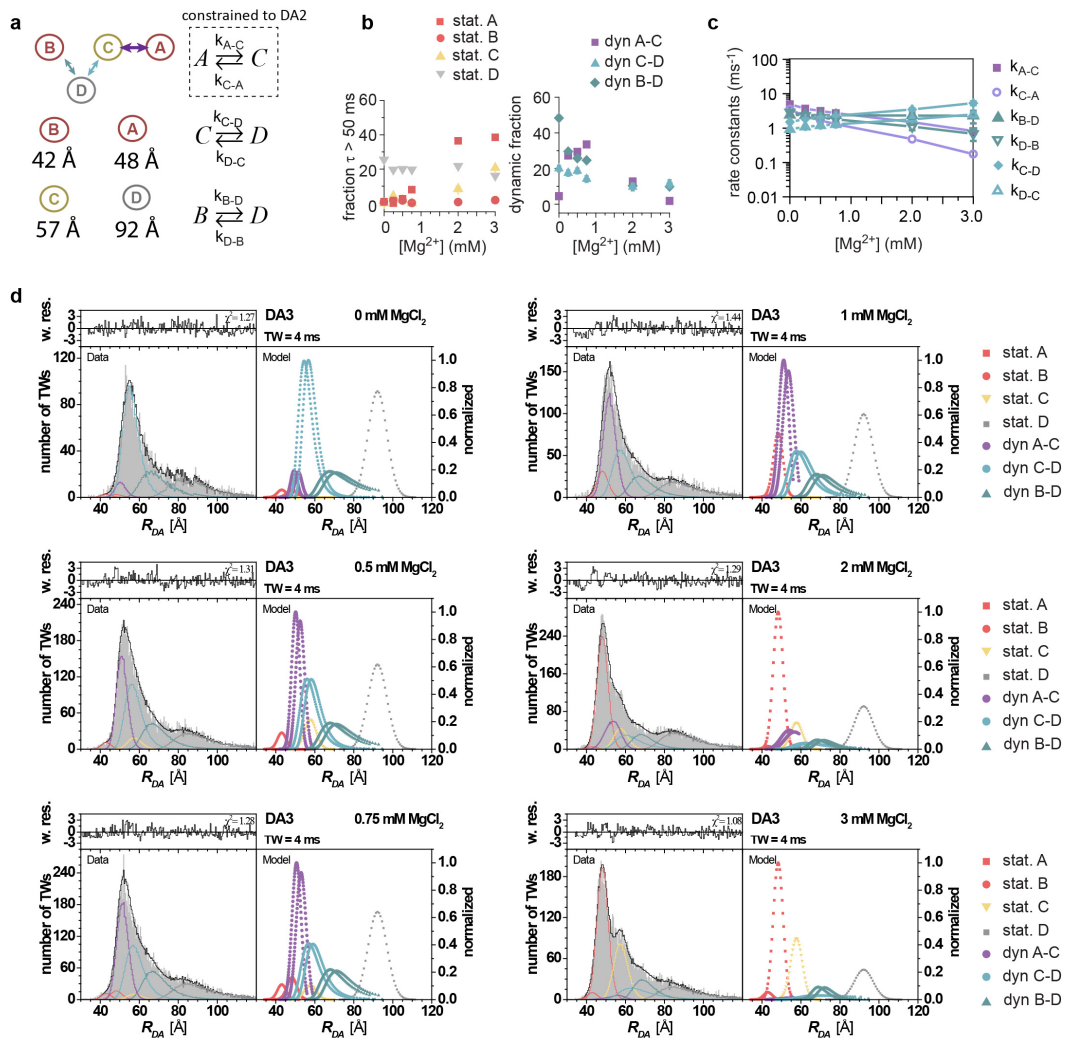
**Supplementary Figure 15 | List of the trial models in PDA analysis for DA1-3.** (See **Supplementary Note, step 8: Validation of kinetic models**). The first column represents sketches of applied models for particular FRET dye configuration. The model was evaluated with several selection criteria, see **step 8, Validation of kinetic models**. Cases when criteria meets the model are marked in green, the discrepancy are in red. The model was chosen if all criteria are satisfied.



**Supplementary Figure 16 | PDA fit of MFD data for DA1 (Alexa488/647).** (See **Supplementary Note, step 7:** General description of PDA analysis & **step 8:** Validation of kinetic models). **(a)** Minimal dynamic model used to globally fit the experimental data. Distances in Å are given for the states {A,C} (are not differentiated by DA1), B, and D. **(b)** Left panel: Fractions of molecules which appear static on the MFD timescale (10 ms). Right panel: Dynamic fractions – molecule exchanging between the indicated states with rate constants given in c. **(c)** Rate constants obtained from the global PDA fit. **(b-c)** Error bars: s.d. between three PDA analyses of datasets comprising a fraction (70%) of all measured data (subsampling). Note that in some cases the error bars are smaller than the symbol size. **(d)** Individual PDA fits of the model given in c to the experimental data at the indicated conditions, showing the fit, residuals as well as the underlying static (symbols in red hues and grey) and dynamic (symbols in blue hues) molecular distributions.



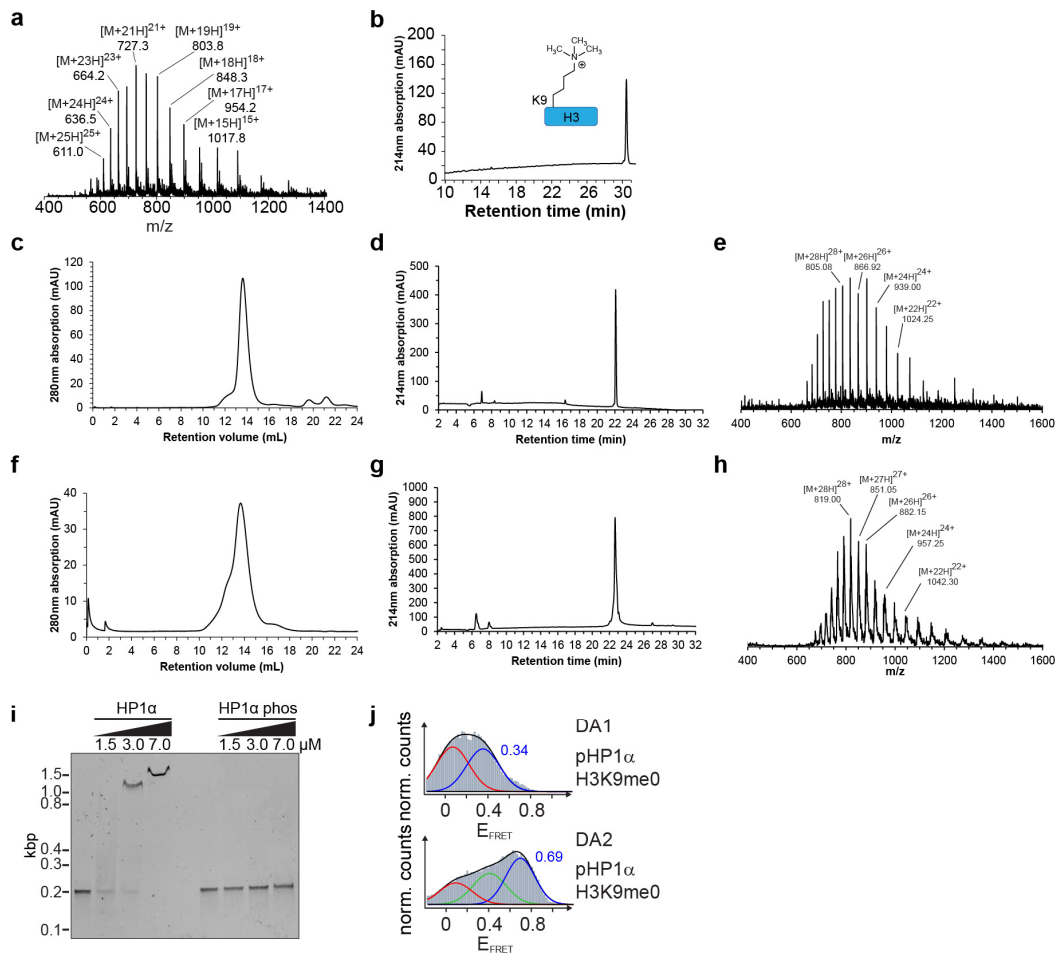
**Supplementary Figure 17 | PDA fit of MFD data for DA2 (Alexa488/647).** (See **Supplementary Note, step 7:** General description of PDA analysis & **step 8:** Validation of kinetic models). **(a)** Minimal dynamic model used to globally fit the experimental data. Distances in Å are given for the states A, B, C and D. **(b)** Left panel: Fractions of molecules which appear static on the MFD timescale (10 ms). Right panel: Dynamic fractions – molecule exchanging between the indicated states with rate constants given in **c**. **(c)** Rate constants obtained from the global PDA fit. **(b-c)** Error bars: s.d. between three PDA analyses of datasets comprising a fraction (70%) of all measured data (subsampling). Note that in some cases the error bars are smaller than the symbol size. **(d)** Individual PDA fits of the model given in **a** to the experimental data at the indicated conditions, showing the fit, residuals as well as the underlying static (symbols in red hues and grey) and dynamic (symbols in blue hues) molecular distributions.



**Supplementary Figure 18 | PDA fit of MFD data for DA3 (Alexa488/647).** (See **Supplementary Note, step 7:**

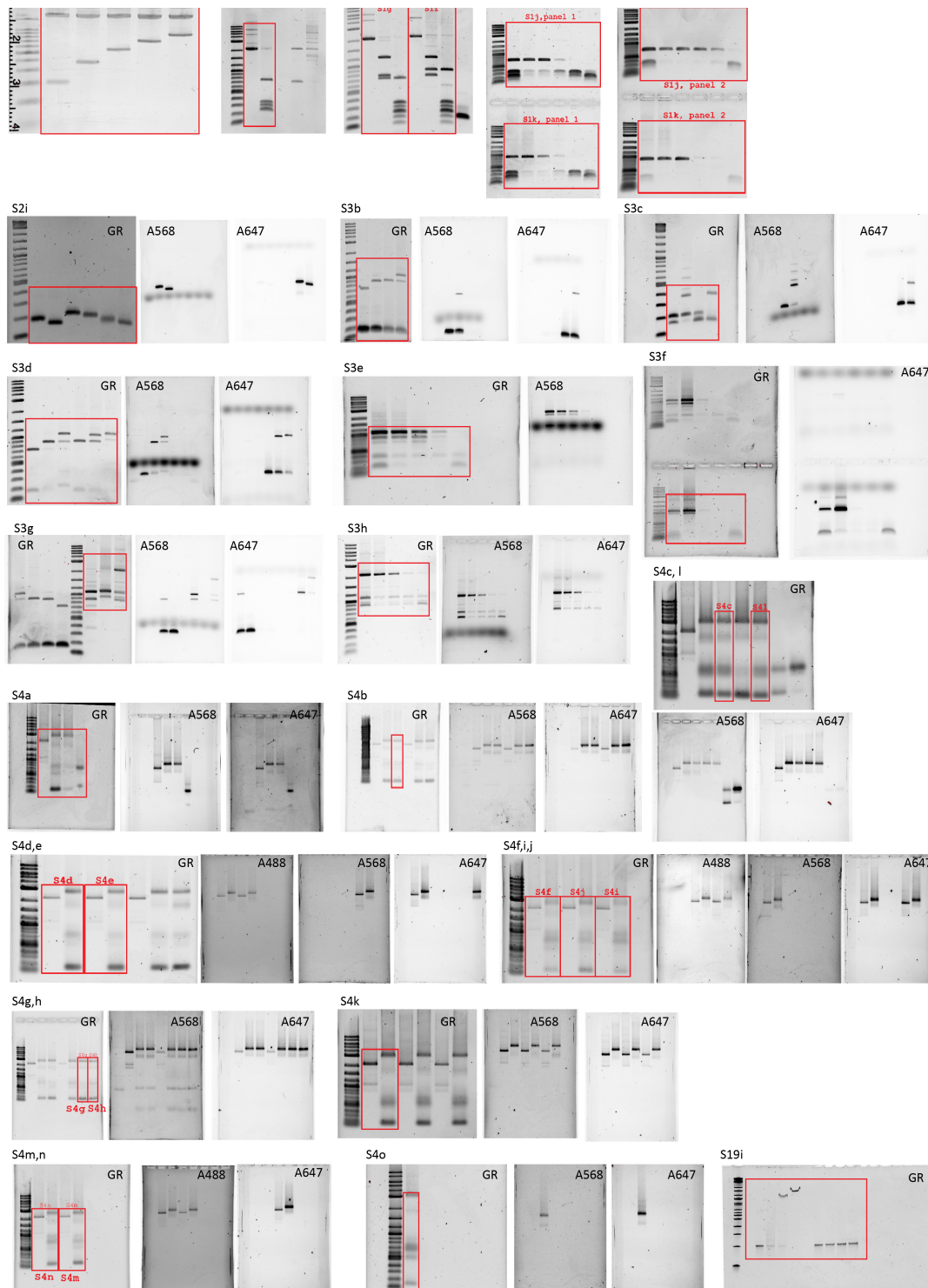
General description of PDA analysis & **step 8:** Validation of kinetic models). **(a)** Minimal dynamic model used to globally fit the experimental data. Distances are given in Å. **(b)** Left panel: Fractions of molecules which appear static on the MFD timescale (10 ms). Right panel: Dynamic fractions – molecule exchanging between the indicated states with rate constants given in **c**. **(c)** Rate constants obtained from the global PDA fit. **(b-c)** Error bars: s.d. between three PDA analyses of datasets comprising a fraction (70%) of all measured data (subsampling). Note that in some cases the error bars are smaller than the symbol size. **(d)** Individual PDA fits of the model given in **a** to the experimental data at the indicated conditions, showing the fit, residuals as well as the underlying static (symbols in red hues and grey) and dynamic (symbols in blue hues) molecular distributions.





**Supplementary Figure 19 | Expression and purification of wt and phosphorylated HP1 $\alpha$ .** H3K9me3 is produced by expressed protein ligation. The modified histone peptide H3(1-14)K9me3-NH<sub>2</sub> is converted to a C-terminal thioester and ligated to the N-terminally truncated histone protein H3( $\Delta$ 1-14)A15C, followed by desulfurization<sup>8</sup>. **(a)** MS spectrum of semisynthetic H3K9me3. (Expected mass: 15251.8Da, observed mass 15252.0 Da) **(b)** RP-HPLC analysis of H3K9me3. **(c)** Gel-filtration analysis of HP1 $\alpha$ , which elutes at the expected volume for the dimeric protein. **(d)** HPLC analysis of HP1 $\alpha$  with a 0-70%B gradient. **(e)** ESI-MS analysis of HP1 $\alpha$  (Expected mass 22506.2Da, observed mass 22513.0Da) **(f)** Gel-filtration analysis of phosphorylated HP1 $\alpha$  (phosHP1 $\alpha$ ), which elutes at the expected volume for the dimeric protein with a shoulder potentially accounting for a tetrameric population. **(g)** HPLC analysis of phosHP1 $\alpha$  with a 0-70%B gradient. **(h)** ESI-MS phosHP1 $\alpha$  (Expected mass 22906.2Da, observed mass 22905.0), demonstrating the presence of 5 P<sub>i</sub> groups. **(i)** Gel-shift with HP1 $\alpha$  and phosHP1 $\alpha$  demonstrating a loss in nonspecific DNA binding affinity for the phosphorylated protein in accordance with ref.<sup>9</sup>. **(j)** Histograms of pHP1 $\alpha$  incubated with DA1 or DA2 containing unmethylated H3.





**Supplementary Figure 20 | Images of all uncropped gels.** All uncropped gels from Supplementary Figures S1, S2, S3, S4 and S19, stained with GelRed (GR) or imaged using fluorescence from the indicated dyes.

## Supplementary Tables

Fragment	Sequence
P1	<p>-100 -95 -90 -85 -80 -75 -70 -65 -60 -55 -50 -45 -40 -35 -30 -25            CACTTGGTGGCGCCGCTGGAGAATCCCGGTGCCGAGGCCGCTCAATTGGTCGTAGACAGCTCTA            -20 -15 -10 -5 0 5 10 15 20 25 30 35 40 45 50 55  <b>GCACCGCTTAAACGCACGTACGCGCTGTCCCCCGGTTTAAACCGCCAAGGGGATTACTCCCTAGTCTCCAGGCACGTGT</b>            60 65 70 75 80 85 90 95 100 105  <b>CAGATACTGCAGAGATCTCTAGATCCATGGAGTACTTGGTCTCATAGC</b></p>
P2	<p>-100 -95 -90 -85 -80 -75 -70 -65 -60 -55 -50 -45 -40 -35 -30 -25            GATCGGTCTCATAGCCTGGAGAATCCCGGTGCCGAGGCCGCTCAATTGGTCGTAGACAGCTCTA            -20 -15 -10 -5 0 5 10 15 20 25 30 35 40 45 50 55  <b>GCACCGCTTAAACGCACGTACGCGCTGTCCCCCGGTTTAAACCGCCAAGGGGATTACTCCCTAGTCTCCAGGCACGTGT</b>            60 65 70 75 80 85 90 95 100 105  <b>CAGATATATACATCTGTCACTGTGGATC</b></p>
P3	<p>-100 -95 -90 -85 -80 -75 -70 -65 -60 -55 -50 -45 -40 -35 -30 -25            CACACTGTGCCAAGTACTTACGCGCCGCTGGAGAATCCCGGTGCCGAGGCCGCTCAATTGGTCGTAGACAGCTCTA            -20 -15 -10 -5 0 5 10 15 20 25 30 35 40 45 50 55  <b>GCACCGCTTAAACGCACGTACGCGCTGTCCCCCGGTTTAAACCGCCAAGGGGATTACTCCCTAGTCTCCAGGCACGTGT</b>            60 65 70 75 80 85 90 95 100 105  <b>CAGATACTGCAGAGATCTCTAGATCCATGGAGTACTTGGTCTCAAACC</b></p>
P4	<p>-100 -95 -90 -85 -80 -75 -70 -65 -60 -55 -50 -45 -40 -35 -30 -25            GATCGGTCTCAAACCTGGAGAATCCCGGTGCCGAGGCCGCTCAATTGGTCGTAGACAGCTCTA            -20 -15 -10 -5 0 5 10 15 20 25 30 35 40 45 50 55  <b>GCACCGCTTAAACGCACGTACGCGCTGTCCCCCGGTTTAAACCGCCAAGGGGATTACTCCCTAGTCTCCAGGCACGTGT</b>            60 65 70 75 80 85 90 95 100 105  <b>CAGATATATACATCTGTCACTGTGGATC</b></p>
P5	<p>-100 -95 -90 -85 -80 -75 -70 -65 -60 -55 -50 -45 -40 -35 -30 -25            CACGTCTGCCAAGTACTTACGCGCCGCTGGAGAATCCCGGTGCCGAGGCCGCTCAATTGGTCGTAGACAGCTCTA            -20 -15 -10 -5 0 5 10 15 20 25 30 35 40 45 50 55  <b>GCACCGCTTAAACGCACGTACGCGCTGTCCCCCGGTTTAAACCGCCAAGGGGATTACTCCCTAGTCTCCAGGCACGTGT</b>            60 65 70 75 80 85 90 95 100 105  <b>TCAGATACTGCAGAGATCTCTAGATCCGGTCTCACTAA</b></p>

**Supplementary Table 1 | Sequences of 1x601 pieces for recombinant and PCR-generated pieces.** 601 sequences (for recombinant pieces with slight end modifications) indicated in bold. The labeled base pairs are indicated in red. The numbering is given as number of base-pairs relative to the dyad in the 601 sequence.

Name	Sequence
P2_pos39_rev	5'-GATCCACAGTGTGACAGGATGTATATATCTGACACGTGCCTGGAGACTAGGGAG-3'
P2_pos71_rev	5'-GATCCACAGTGTGACTGGATGTATATATCTGACACGTGC-3'
P3_pos-86_fwd	5'-GATCGCACACTGTGCCAAGTACTTACGCGCCGCCCTGGAGAATCC-3'
P3_pos82_rev	5'-GATCGCGTTTGGAGACCAAGTACTCCATGGATCTAGAGATCTCTGC-3'
P4_pos-39_fwd	5'-GATCGGTCTCAAACCTGGAGAATCCCGGTGCCGAGGCCGCTCAATTGGTCGTAGACAGC3'
P4_pos-16_fwd	5'-GATCGGTCTCAAACCTGGAGAATCCCGGTGCCGAGGCCGCTCAATTGGTCGTAGACAGC- CAGCTCTAGCACCGCTTAAACGCACGTACGC-3'
recP5_Anchor_fwd	5'-ph-CTAATAGTCTGCTAGTACTCGTCTAGATCCATGGTCCGATTACGCGG-3'
recP5_Anchor_rev	5'-biotin-CCGCGTAATCGGACCATGGATCTAGCGACGAGTACTGAGCAGACTA-3'

**Supplementary Table 2 | Oligonucleotide sequences used for labeling and anchoring.** The numbering for the label positions is given relative to the nucleosome dyad.

Piece	Donor fluorophore	Labeling position(s)	Acceptor fluorophore	Labeling position(s)
P2	Alexa Fluor 488	39	-	-
P2	Alexa Fluor 568	39	-	-
P2	Alexa Fluor 488	71	-	-
P2	Alexa Fluor 568	71	-	-
P2	-	-	-	-
P3	Alexa Fluor 488	-86	Alexa Fluor 647	82
P3	Alexa Fluor 568	-86	Alexa Fluor 647	82
P3	-	-	-	-
P4	-	-	Alexa Fluor 647	-39
P4	-	-	Alexa Fluor 647	-16
P4	-	-	-	-

**Supplementary Table 3 | Overview of 1x601 PCR pieces generated from labeled and unlabeled primers.**

Position of label and the donor/acceptor fluorophore used are indicated. The positions are indicated as base-pairs relative to the dyad in the 601 sequence (see also **Supplementary Tables 1 and 2**).

Construct	Donor	Donor Position	Acceptor	Acceptor position
DA1	Alexa488	N5 (39)	Alexa647	N7 (-39)
DA1	Alexa568	N5 (39)	Alexa647	N7 (-39)
D1	Alexa488	N5 (39)	unlabeled	N/A
DA1'	Alexa488	N5 (39)	Alexa647	N6 (-39)
DA2	Alexa488	N5 (71)	Alexa647	N7 (-16)
DA2	Alexa568	N5 (71)	Alexa647	N7 (-16)
D2	Alexa488	N5 (71)	unlabeled	N/A
DA3	Alexa488	N6 (-86)	Alexa647	N6 (82)
DA3	Alexa568	N6 (-86)	Alexa647	N6 (82)
D3	Alexa488	N6 (-86)	unlabeled	N/A

**Supplementary Table 4 | Overview of constructed 12x601 DNA pieces with different combinations of labels.** The nucleosome position is indicated as  $N_i$ , with  $i = 1-12$ . The number in brackets is the label position relative to the dyad in the 601 sequence (see also **Supplementary Tables 1-3**).

Data	n	Peak 1			Peak 2			Peak 3				
		$A_1$	$C_1$	$\sigma_1$	$A_2$	$C_2$	$\sigma_2$	$A_1$	$C_1$	$\sigma_1$		
<b>D</b>	0mM Mg <sup>2+</sup>	448	2.45	0.07	0.17	5.02	0.30	0.14	-	-	-	
	0.5mM Mg <sup>2+</sup>	205	1.81	0.09	0.17	5.18	0.36	0.14	-	-	-	
	1.0mM Mg <sup>2+</sup>	156	1.68	0.12	0.22	5.13	0.45	0.14	-	-	-	
	4.0mM Mg <sup>2+</sup>	789	1.65	0.07	0.22	4.17	0.58	0.17	-	-	-	
<b>A</b>	4.0mM Mg <sup>2+</sup> Ac	146	3.76	0.08	0.20	2.38	0.40	0.17	-	-	-	
	<b>1</b>	HP1a K9me0	964	1.88	0.01	0.14	4.02	0.30	0.20	-	-	-
		HP1a K9me3	797	1.79	0.04	0.17	3.82	0.38	0.20	-	-	-
		HP1a_p K9me0	179	3.32	0.04	0.14	3.19	0.33	0.17	-	-	-
HP1a_p K9me3		262	1.28	0.03	0.17	3.88	0.44	0.22	-	-	-	
<b>D</b>	0mM Mg <sup>2+</sup>	174	5.37	0.00	0.14	0.44	0.90	0.10	0.92	0.57	0.22	
	0.5mM Mg <sup>2+</sup>	132	3.98	0.01	0.14	1.88	0.65	0.22	0.81	0.27	0.10	
	1.0mM Mg <sup>2+</sup>	103	2.83	0.02	0.17	2.07	0.75	0.17	1.23	0.45	0.22	
	4.0mM Mg <sup>2+</sup>	138	2.86	0.00	0.14	1.96	0.70	0.22	1.31	0.30	0.22	
<b>A</b>	4.0mM Mg <sup>2+</sup> Ac	113	1.35	0.01	0.22	2.13	0.62	0.20	1.84	0.25	0.20	
	<b>2</b>	HP1a K9me0	260	2.45	0.01	0.17	1.52	0.61	0.22	1.81	0.30	0.17
		HP1a K9me3	252	1.20	0.05	0.22	3.49	0.71	0.17	1.12	0.41	0.17
		HP1a_p K9me0	901	0.63	0.04	0.17	3.01	0.66	0.17	2.21	0.33	0.22
HP1a_p K9me3		275	1.67	0.07	0.22	2.40	0.74	0.17	1.37	0.36	0.22	
<b>D</b>	0mM Mg <sup>2+</sup>	216	1.40	0.03	0.17	5.90	0.74	0.10	1.34	0.58	0.22	
	0.5mM Mg <sup>2+</sup>	165	0.85	0.05	0.20	7.57	0.78	0.00	2.94	0.72	0.14	
	1.0mM Mg <sup>2+</sup>	155	1.29	0.03	0.14	6.08	0.81	0.10	2.66	0.75	0.17	
	4.0mM Mg <sup>2+</sup>	145	1.34	0.02	0.14	6.75	0.87	0.00	3.39	0.79	0.14	
<b>A</b>	4.0mM Mg <sup>2+</sup> Ac	130	0.45	0.04	0.22	7.13	0.86	0.10	2.14	0.70	0.22	

**Supplementary Table 5 | Gaussian fits of FRET distributions from Fig. 2 and 4.** Histograms of the  $E_{FRET}$  values of combined traces (number of traces:  $n$ ) were fitted using the indicated number of Gaussians with amplitude  $A_i$ , center  $C_i$  and width  $\sigma_i$ . Ac: Chromatin fiber contains H4K<sub>5</sub>16Ac

	0mM Mg <sup>2+</sup>	4.0mM Mg <sup>2+</sup>	4.0mM Mg <sup>2+</sup> Ac	HP1	
				H3K9me0	H3K9me3
<b>DA1</b>	17 %	29 %	22 %	55 %	54 %
<b>DA2</b>	35 %	38 %	26 %	38 %	42 %
<b>DA3</b>	20 %	20 %	19 %	X	X

**Supplementary Table 6 | Percentage of dynamic traces observed in smTIRF.** Traces are identified as dynamic by cross-correlation (CC) analysis of donor versus acceptor fluorescence emission. Dynamic traces exhibit a CC amplitude of  $< -0.1$  and a CC relaxation time  $> 100$  ms.

<b>Contributions to <math>\Delta R_{DA}</math></b>	<b>DA1</b>	<b>DA2</b>	<b>DA3</b>
<b>Calibration contributions to the uncertainty, <math>\Delta R_{DA,cal}</math> in step 2 [a]</b>			
Uncertainty of the correction factor, $\gamma$ , $\Delta R_{DA}(\Delta\gamma)$ , mainly due to $\Delta\Phi_{FA}$ (Summary 9.3: $\langle\Phi_{FA}\rangle = 0.368$ with $\Delta\Phi_{FA} = 0.017$ )	0.008	0.008	0.008
Uncertainty of correction factors, $\alpha$ , $\beta$ and $\delta$ , $\Delta R_{DA}(\Delta\alpha, \Delta\beta, \Delta\delta)$	< 0.005	< 0.005	< 0.005
Uncertainty of signal correction by background, $B_{x_{em} x_{ex}}$ , $\Delta B_{x_{em} x_{ex}}$	< 0.005	< 0.005	< 0.005
<b>Contributions to the uncertainty <math>\Delta R_0</math> [b]</b>			
Uncertainty of refractive index, $\Delta R_0(n)$ [c]	0.040	0.040	0.040
Uncertainty of donor fluorescence quantum yield $\Phi_{FD}$ , $\Delta R_0(\Phi_{FD})$ [c]	0.020	0.020	0.020
Uncertainty of spectral overlap integral $J$ , $\Delta R_0(J)$ [c]	0.025	0.025	0.025
Uncertainty of FRET orientations factor, $\kappa^2$ , $\Delta R_0(\kappa^2)$ [d]	0.071	0.070	0.060
<b>Total accuracy <math>\Delta R_0</math></b>	<b>0.088</b>	<b>0.087</b>	<b>0.079</b>
<b>Noise contributions to the uncertainty <math>\Delta R_{DA,noise}(R_{DA})</math></b>			
Precision to fit $R_{DA}$ by dynPDA, $\Delta R_{DA}(R_{DA})$ [e]	0.020	0.030	0.020
Uncertainty by A heterogeneity, $\Delta R_{DA}(A_{het})$ [f]	0.0001	0.0038	0.0051
<b>Total uncertainty to compute <math>R_{DA}</math>, <math>\Delta R_{DA}(\Delta R_{DA,cal}, \Delta R_0, \Delta R_{DA,noise}(R_{DA}), \Delta A_{het})</math> [g]</b>	<b>0.090</b>	<b>0.092</b>	<b>0.081</b>

[a] Adapted from ref. <sup>10</sup>.

[b] Adapted from ref. <sup>11</sup>.

[c] Values from ref. <sup>11</sup>.

[d] We computed the densities of  $\kappa^2$  (see section 3.5 of ref. <sup>12</sup>) using the residual anisotropies of the donor,  $r_{inf,D}$  (Summary 9.2), and of the acceptor,  $r_{inf,A}$  (Summary 9.4), to determine the uncertainty  $\Delta\kappa^2$  and the corresponding  $\Delta R_0(\kappa^2)$ .

[e] See Step 9, section **Determination of uncertainties in measured  $R_{DA}$  distances** and **Supplementary Figures 16-18**.

[f] See step 9, Summary 9.3.

[g] Calculated according to eq. (9.7).

**Supplementary Table 7 | Accuracy and precision of the inter-dye distance calculation  $R_{DA}$ .** Relative uncertainties are reported for individual contributions (see **Supplementary Note, Step 9**) followed by the calculated total accuracy  $\Delta R_0$ , and the total uncertainty  $\Delta R_{DA}$ . For values in % multiply by 100. Error propagation was performed according to refs. <sup>10,11</sup> using eq. (9.7).

	Model	Experiment	Model	Experiment
	$\langle R_{DA,m} \rangle_E$ , register 1, (Å)	$\langle R_{DA,exp} \rangle_E$ , register 1, (Å)	$\langle R_{DA,m} \rangle_E$ , register 2, (Å)	$\langle R_{DA,exp} \rangle_E$ , register 2, (Å)
<b>DA1</b>	64	64	47	46
<b>DA2</b>	41	53	36	44
<b>DA3</b>	48 [a]	42-48	53 [a]	42-48

[a] linear linker DNA to connect the two nucleosomes in a register was assumed.

**Supplementary Table 8 | Correlation between FRET-averaged inter-dye distances of the structural models,  $\langle R_{DA,m} \rangle_E$ , and of the experiments,  $\langle R_{DA,exp} \rangle_E$ , for the Alexa488/647 FRET pair.** Experimental distances  $\langle R_{DA,exp} \rangle_E$  of DA 1-3 were obtained from PDA analysis (**Supplementary Figures 16 - 18**). The model distances were calculated for the tetranucleosome model (register 1 and 2) considering the total experimental uncertainty  $\Delta R_{DA}(\Delta E_{FRET}, \Delta R_0, \Delta R_{DA,noise}(R_{DA}, \Delta A_{het}))$  (**Supplementary Table 7**) using ACV analysis (**Supplementary Note, step 9**, sections Determination of the uncertainties for structural modeling (ACV parameters), and FRET positioning and screening calculations (**Supplementary Figures 12 and 13**). Considering DA2, there are two possible explanations for the deviations between  $\langle R_{DA,m} \rangle_E$  and  $\langle R_{DA,exp} \rangle_E$ : (1) Local dynamics could be present (clamshell and torsion by 10 degrees, see **Supplementary Fig. 13**). (2) In addition, in view of the low  $Mg^{2+}$  concentrations and the absence of H1, the stacking of the nucleosome arrays could differ in solution from that in the X-ray<sup>13</sup> or cryoEM<sup>5</sup> structure.

## Supplementary Note

Dynamic structural biology analysis: .....	30
Step 1. smTIRF .....	32
Step 2: 2D MFD plots with FRET lines and calibration of the FRET measurements .....	33
Calculation of FRET efficiencies EFRET from fluorescence signals .....	34
Expanding the dynamic range of smFRET studies. ....	35
Static and dynamic FRET lines. ....	35
Step 3: Sub-ensemble TCSPC.....	36
Step 4: Burst-ID FCS .....	38
Step 5: Photobleaching and photoblinking analysis.....	39
Step 6. Evaluation of kinetic networks between FRET species compatible with experimental data.....	40
Step 7. General description of PDA analysis.....	40
Calculation of donor acceptor distances from fluorescence signals .....	41
Dynamic PDA. ....	41
Step 8: Validation of kinetic models.....	43
Step 9: Relating measured $R_{DA}$ distances to structural models of compact chromatin states .....	43
Determination of the uncertainties for structural modeling. ....	44
Summary of dye properties of the donor Alexa488.....	44
Summary of acceptor dye properties.....	45
Determination of uncertainties in measured $R_{DA}$ distances.....	47
Model building.....	48
FRET positioning and screening calculations.....	48
Step 10: Structural models of open and dynamic states.....	49
Coarse grained simulations .....	50
Step 11: Final model and its validation - A unified model of chromatin dynamics.....	51

### Dynamic structural biology analysis:

We used a combination of experimental observables (described in detail below) for structural and kinetic analyses to establish a model for chromatin dynamics, as shown in **Fig. 6**. We established an 11-step workflow for dynamic structural biology (**Supplementary Fig. 9**), involving a sequence of steps:

**Step 1:** Measuring FRET efficiencies over time in **smTIRF** we explored chromatin dynamics in the 100 ms – seconds regime. Employing cross-correlation analysis we observed that between 20-55% of fibers showed dynamics on the 50-500 ms timescale (**Fig. 2** and **Supplementary Table 6**).

**Step 2: 2D MFD plots.** We measured smFRET with confocal multi-parameter fluorescence detection (MFD).  $E_{FRET}$  vs fluorescence-weighted average fluorescence lifetime of the donor dye in presence of the acceptor  $\langle \tau_{D(A)} \rangle_F$  enabled us to identify rapid dynamics and allowed us to detect the coexisting dynamic chromatin populations in two different tetranucleosome interaction registers (register 1 and 2). In the presence of dynamic exchange between conformations with different  $E_{FRET}$  and exchange kinetics faster than the molecular dwell time in the confocal detection volume ( $< 10$  ms), deviations from the ideal relationship between  $\langle \tau_{D(A)} \rangle_F$  and  $E_{FRET}$  (the static FRET line) can be detected in burst-wise analysis<sup>14</sup>. This is because  $E_{FRET}$  values derived from fluorescence intensities are averaged per molecular species fractions, whereas average fluorescence lifetimes are computed per brightness by the applied maximum-likelihood analysis<sup>15</sup>. This disagreement is captured by a dynamic FRET line. For the chromatin arrays DA1-3 MFD plots indeed directly indicated a dynamic process as a large fraction of the detected molecules fell on dynamic FRET-lines (**Fig. 3d,e**). Importantly, measurements with DA1, DA2 or DA3 labeled DNA (absence of histones) as well as measurements with chromatin samples bearing only donor dyes (D1, D2 and D3; **Supplementary Table 4**) did not show comparable FRET states or dynamics (**Supplementary Fig. 8c,d**).

**Step 3: Sub-ensemble Time Correlated Single Photon Counting (seTCSPC)** resolved the FRET efficiency levels corresponding to chromatin structural states (**Supplementary Fig. 10**).

**Step 4: Burst-ID fluorescence correlation spectroscopy (FCS)** of donor-donor, donor-acceptor or cross-correlation confirmed complex sub-millisecond dynamics in a model-free approach and yielded estimates of the involved timescales (DA1-3, 0.75 mM  $Mg^{2+}$ , **Supplementary Fig. 11**).

**Step 5: Photobleaching and photoblinking analysis** was employed to confirm that the observed dynamic processes originate from structural transitions and did not contain contributions from photophysics of the dyes (**Supplementary Fig. 14a**).

**Steps 6-11:** The combined obtained data was used to **formulate kinetic models and assign states and connectivity between the states (step 6)**. Subsequently a unified kinetic model was used in dynamic PDA analysis (**step 7, Fig. 5 and Supplementary Fig. 16-18**). A global fit to the experimental data yields improved FRET efficiency levels values with corresponding population fractions and exchange rate constants. Afterwards the model was judged by applying a selection of criteria (**Supplementary Fig. 15**) including an evaluation of goodness of fit, the stability of the fit results (**step 8**) as well as by determination of the parameter uncertainties (**step 9**) and structural validation such as atomistic models (**step 9**) and coarse grained simulations (**step 10**). The procedure finally results in a complete model of chromatin dynamics (**step 11**).



**Step 1. smTIRF**

From donor- ( $F_D$ ) and acceptor fluorescence emission intensity ( $F_A$ ) traces FRET efficiency ( $E_{FRET}$ ) traces were calculated, using

$$E_{FRET} = \frac{F_A - \beta F_D}{F_A - \beta F_D + \gamma F_D} \text{ and } \gamma = \frac{\Delta F_{A,bleach}}{\Delta F_{D,bleach}} \quad (0.1)$$

The values of  $\beta = 0.141$  and  $\gamma = 0.468$  were experimentally determined for the dye pair Alexa568/647 in our experimental setup. The bin size for all histograms was set to 0.02.  $E_{FRET}$  histograms of each trace of length  $> 5$  s were normalized to total counts. Final histograms were calculated averaging the FRET histograms of all traces ( $> 100$  traces) and fitted using 2 or 3 Gaussian functions  $\sum_i A_i e^{-(x-c_i)^2/\sigma_i}$  (**Supplementary Table 5**).

Cross-correlation analysis was performed using

$$C_{cross}(t) = \langle \Delta F_D(0) \cdot \Delta F_A(t) \rangle / \langle \Delta F_D(0) \cdot \Delta F_A(0) \rangle \quad (0.2)$$

where  $\Delta F_D$  and  $\Delta F_A$  are the variances of donor and acceptor fluorescence at time 0 or  $t$ , was calculated in Matlab using a maximum lag of 10 s. Traces shorter than 10 s, as well as traces which spent less than 20% of the time at  $E_{FRET} < 0.2$  were excluded from the analysis. The cross-correlation data was fitted with a bi-exponential function in OriginPro (OriginLab Corporation). To determine the fraction of dynamic traces (**Supplementary Table 6**) the individual cross-correlation decays from each trace was analyzed. Traces considered dynamic showed an amplitude  $< -0.1$  and a decay time constant  $> 0.1$  s.

This analysis revealed that chromatin fibers exhibit dynamics on the 50-500 ms timescale, but that such fluctuations were only observed in a subset of individual arrays. This argues for the existence of 'locked' states where tetranucleosome interactions are stable over time (**Figure 6**).

## Step 2: 2D MFD plots with FRET lines and calibration of the FRET measurements

**Burst selection.** The bursts of all samples were identified and selected from the MFD data trace as described in ref. <sup>16</sup>. Double-labeled chromatin arrays with the DA pair Alexa488/647 capable for FRET (FRET-active) were selected by Pulsed Interleaved Excitation (PIE) using  $E_{FRET}$  vs  $S$  (stoichiometry) 2D histograms. For subsequent analysis we selected bursts with  $0.2 < S < 0.8$  to separate double-labeled species from single dye labeled molecules and  $|T_{GX} - T_{RR}| < 1$  ms to remove contributions from photophysical processes <sup>17</sup> (**Supplementary Fig. 8a**). For PIE<sup>18</sup>, the corrected stoichiometry  $S$  is defined as

$$S = \frac{F_{D|D} + F_{A|D}}{F_{D|D} + F_{A|D} + F_{A|A}} \quad (2.1)$$

$F_{X_{em}|X_{ex}}$  corresponds to a fully corrected fluorescence intensity computed from observed signal  $^{obs}S$  considering background intensities and other experimental correction factors  $\alpha$ ,  $\beta$ ,  $\gamma$ ,  $\delta$  defined in eq. (2.3). The meaning of the indices is as follows: ( $D/D$ ) is the donor intensity if the donor was excited, ( $A/D$ ) is the acceptor intensity if the donor was excited and ( $A/A$ ) is the acceptor intensity if the acceptor was excited.

The stoichiometry  $S$  is computed from the observed signals  $^{obs}S$  in two steps:

(i) The registered primary signal  $^{obs}S$  was corrected for the mean background  $\langle B \rangle$  signal contribution in the green and red channels, respectively:

$$I_{X_{em}|X_{ex}} = ^{obs}S_{X_{em}|X_{ex}} - \langle B_{X_{em}|X_{ex}} \rangle \quad (2.2)$$

$I_{X_{em}|X_{ex}}$  corresponds to a background corrected signal:  $I_{G|G}$  is the background corrected signal in the donor channel ( $G$ ) after donor excitation ( $G$ ),  $I_{R|G}$  is the background corrected signal in the acceptor channel ( $R$ ) at wavelength  $G$  for donor excitation and  $I_{R|R}$  is the background corrected signal in the acceptor channel after acceptor excitation, respectively.

(ii) The background corrected signals  $I$  were used together with four correction factors  $\alpha$ ,  $\beta$ ,  $\gamma$ ,  $\delta$  to compute  $S$  according to:

$$S = \frac{\gamma \cdot I_{G|G} + (I_{R|G} - (\alpha \cdot I_{G|G} + \beta \cdot I_{R|R}))}{\gamma \cdot I_{G|G} + (I_{R|G} - (\alpha \cdot I_{G|G} + \beta \cdot I_{R|R})) + \frac{1}{\delta} \cdot I_{R|R}} \quad (2.3)$$

$$\text{with } \alpha = \frac{g_{R|D}}{g_{G|D}}; \beta = \frac{\sigma_{A|G} L_G}{\sigma_{A|R} L_R}; \gamma = \frac{g_{R|A} a \Phi_{F,A}}{g_{G|D} \Phi_{F,D(0)}}; \delta = \frac{\sigma_{A|R} L_R}{\sigma_{D|G} L_G}$$

The parameter  $\alpha$  is a correction factor for the spectral donor fluorescence crosstalk (leakage) into the red “acceptor” detection channel.  $\beta$  normalizes the direct acceptor excitation rates in the FRET experiment to that in the PIE experiment defined by the acceptor excitation cross-sections  $\sigma_{A|G}$  at donor excitation and

$\sigma_{A|R}$ , and the direct excitation irradiances [Photons/cm<sup>2</sup>]  $L_G$  and  $L_R$  for the donor and acceptor at the wavelengths G and R.  $\gamma$  is a correction factor for the fluorescence quantum yields  $\Phi_{F,D(0)}$ ,  $\Phi_{F,A}$ , the fraction of the fluorescent trans state of Alexa647  $a$ , and the detection efficiencies of the green donor  $g_{G|D}$  and the red acceptor channel  $g_{R|A}$ , respectively.  $\delta$  normalizes the donor excitation rate for the FRET studies to the direct acceptor excitation rate of the PIE experiment defined by the excitation cross-sections for D  $\sigma_{D|G}$  and A  $\sigma_{A|R}$  respectively, and the direct excitation irradiances [photons/cm<sup>2</sup>]  $L_G$  and  $L_R$  for the donor and acceptor at the wavelengths G and R.

For chromatin samples with the FRET pair Alexa568/647 we did not employ PIE (i.e.  $\delta$  is n.a.). The direct acceptor excitation rate at the donor excitation wavelength ( $\delta \gg 0$ ) could however be used to identify double-labeled DA species. Thus, double-labeled chromatin arrays with the DA pair Alexa568/647 capable for FRET (FRET-active) were selected by a minimal number of acceptor photons (red cut) due to direct acceptor excitation by  $L_G$ . In this way contributions from DOnly molecules were reduced. The following parameters were used for the two studied FRET pairs for given experimental setup (see **MFD measurement procedures**):

parameter	FRET pair D/A	
	Alexa488/647	Alexa568/647
$\alpha$	0.016	0.146
$\beta$	0	0.131
$g_{G D}/g_{R A}$	0.95	1.45
$\Phi_{F,D(0)}$ [a]	0.8	0.69
$a \Phi_{F,A}$ [a]	0.368	0.368
$\gamma$	0.5	0.38
$\delta$	0.83	n.a.

[a] average values for the FRET pairs DA1-3. The determined values are compiled in the summary tables reported in step 9.

### Calculation of FRET efficiencies EFRET from fluorescence signals

The corrected FRET efficiency  $E_{FRET}$  is defined via fully corrected fluorescence intensities  $F$ :

$$E_{FRET} = \frac{F_{A|D}}{F_{D|D} + F_{A|D}} \quad (2.4)$$

In analogy to  $S$ ,  $E_{FRET}$  can be computed by the observed intensities and corresponding correction parameters  $\alpha$ ,  $\beta$ ,  $\gamma$  defined in eq. (2.3):

$$E_{FRET} = \frac{(I_{R|G} - (\alpha \cdot I_{G|G} + \beta \cdot I_{R|R}))}{\gamma \cdot I_{G|G} + (I_{R|G} - (\alpha \cdot I_{G|G} + \beta \cdot I_{R|R}))} \quad (2.5)$$

**Expanding the dynamic range of smFRET studies.** We used the FRET pairs Alexa568/647 (Förster Radius  $R_0 = 82 \text{ \AA}$ ) and Alexa488/647 ( $R_0 = 52 \text{ \AA}$ ) to exploit different distance sensitivities (**Fig. 3d,e**): Alexa568/647 allows for the detection of long-range dynamics beyond  $120 \text{ \AA}$ , whereas Alexa488/647 enables the investigation of sub-states and their exchange dynamics below  $60 \text{ \AA}$ .

**Static and dynamic FRET lines.** All MFD plots (**Fig. 3d,e**) for DA1-3 (Alexa488/647 and Alexa568/647) are presented with static and dynamic FRET lines, to demonstrate the presence of two distinct chromatin populations (register 1 and 2). Each population exhibits kinetic exchange faster than the molecular dwell time ( $< 10 \text{ ms}$ ) within the bursts. The theoretical dependence between FRET efficiency and species weighted average donor fluorescence lifetime in presence of acceptor dye is described as

$$E_{static} = 1 - \frac{\langle \tau \rangle_x}{\tau_{D(0)}}. \quad (2.6)$$

Here we use an empirical dependence of species weighted average donor lifetime  $\langle \tau \rangle_x$  on fluorescence weighted average donor lifetime  $\langle \tau \rangle_F$  as a polynomial with  $c_i$  coefficients obtained by numerical simulations<sup>12</sup>

$$\langle \tau \rangle_x = \sum_{i=0}^n c_i (\langle \tau \rangle_F)^i. \quad (2.7)$$

Here we used the following joint parameters for DA1-3 constructs, which are common for the two FRET pairs Alexa568/647 and Alexa568/647, respectively:

Alexa568/647 labeling (**Fig. 3d**):  $c_0 = -0.0083$ ,  $c_1 = 0.0848$ ,  $c_2 = 0.2926$ ,  $c_3 = -0.6606$ ,  $c_4 = 0.0085$  with  $\tau_{D(0)} = 3.5 \text{ ns}$ .  
and

Alexa488/647 labelling (**Fig. 3e**)  $c_0 = -0.0056$ ,  $c_1 = 0.0838$ ,  $c_2 = 0.4007$ ,  $c_3 = -0.3806$ ,  $c_4 = 0.00225$  with  $\tau_{D(0)} = 4.0 \text{ ns}$ .

The dynamic FRET line are described as

$$E_{dyn} = 1 - \frac{\tau_{F1} \cdot \tau_{F2}}{\tau_{D(0)} \cdot (\tau_{F1} + \tau_{F2} - \langle \tau \rangle_x)} \quad (2.8)$$

where  $\tau_{F1}$  and  $\tau_{F2}$  are the donor fluorescence lifetimes defining the limiting FRET states of the respective line. We have assumed that the limiting states of each DA sample remain the same for all  $\text{Mg}^{2+}$  concentrations.

Alexa568/647, dynamic FRET line for register 1 between A and D states with  $\tau_{D(0)} = 3.5 \text{ ns}$  (**Fig. 3d**, dark blue):

DA1 between A/C and D states:  $\tau_{F1} = 0.8 \text{ ns}$ ,  $\tau_{F2} = 3.45 \text{ ns}$ ,  $c_1 = 1.2458$ ,  $c_2 = 0.84821$ .

DA2 between A and C:  $\tau_{F1} = 0.56 \text{ ns}$ ,  $\tau_{F2} = 1.2 \text{ ns}$ ,  $c_1 = 1.4285$ ,  $c_2 = -0.5695$ ; and between C and D:  $\tau_{F1} = 1.15 \text{ ns}$ ,  $\tau_{F2} = 3.5 \text{ ns}$ ,  $c_1 = 1.1778$ ,  $c_2 = 0.6221$ .

DA3 between A/B and C:  $\tau_{F1}=0.25$  ns,  $\tau_{F2}=0.8$  ns,  $c_1=1.626$ ,  $c_2=0.5523$ ; and between C and D:  $\tau_{F1}=0.8$  ns,  $\tau_{F2}=3.5$  ns,  $c_1=1.2473$ ,  $c_2=0.8655$ .

Alexa568/647, dynamic FRET line for register 2 between B and D states with  $\tau_{D(0)}=3.5$  ns (**Fig. 3d**, light blue):

DA1-3:  $\tau_{F1}=0.25$  ns,  $\tau_{F2}=3.5$  ns,  $c_1=1.5198$ ,  $c_2=1.819$ .

Alexa488/647, dynamic FRET line for register 1 between A and D states with  $\tau_{D(0)}=4.0$  ns (**Fig. 3e**, dark blue):

DA1:  $\tau_{F1}=3.12$  ns,  $\tau_{F2}=3.92$  ns,  $c_1=1.0895$ ,  $c_2=0.317$ ;

DA2:  $\tau_{F1}=2.53$  ns,  $\tau_{F2}=3.96$  ns,  $c_1=1.1605$ ,  $c_2=0.6339$ ;

DA3:  $\tau_{F1}=2.57$  ns,  $\tau_{F2}=3.96$  ns,  $c_1=1.154$ ,  $c_2=0.6082$ .

Alexa488/647, dynamic FRET line for register 2 between B and D states with  $\tau_{D(0)}=4.0$  ns (**Fig. 3e**, light blue):

DA1 and DA2:  $\tau_{F1}=1.55$  ns,  $\tau_{F2}=3.92$  ns,  $c_1=1.376$ ,  $c_2=-1.4852$ ;

DA3:  $\tau_{F1}=1.6$  ns,  $\tau_{F2}=3.95$  ns,  $c_1=1.3607$ ,  $c_2=-1.4248$ .

Importantly, measurements with DA1, DA2 or DA3 double labeled DNA (absence of histones) as well as measurements with chromatin samples bearing only donor dyes (D1, D2 and D3; **Supplementary Table 4**) did not show comparable FRET states or dynamics (**Supplementary Fig. 8c,d**).

### Step 3: Sub-ensemble TCSPC

For defining the limiting states for dynamic FRET lines indicated by FRET efficiency levels (**Fig. 3e** orange, wine and gray lines), we performed sub-ensemble Time Correlated Photon Counting (seTCSPC) analysis of DA1-3 (Alexa488/647), which were selected from the sample as double-labeled species by PIE (**Supplementary Fig. 8a**). Characteristic populations for each respective limiting state are analyzed for bursts with a low FRET efficiencies ( $0 < E_{FRET} < 0.199$ ) of the low FRET population (LF) and for bursts with higher FRET efficiencies ( $0.2 < E_{FRET} < 1.0$ ) of the dynamic FRET population (dynF). To retrieve the required information about the limiting states, we analyzed bursts of each population separately. The specific fluorescence decays were analyzed by a fit model described previously<sup>19</sup>. The fluorescence decay of the donor reference (DOnly, in the absence of FRET) was approximated by a single fluorescence lifetime,  $\tau_{D(0)}$ :

$$f_{D(0)}(t) = f_{D(0)}(0) \exp(-t / \tau_{D(0)}) \quad (3.1)$$

Hence, the FRET-rate ( $k_{FRET}$ ) is only determined by the donor-acceptor distance and their relative orientation. In the presence of FRET, the donor fluorescence decay can be expressed using the donor-acceptor distance distribution  $p(R_{DA})$ :

$$f_{D(A)}(t) = f_{D(A)}(0) \int_{R_{DA}} p(R_{DA}) \exp\left(-\frac{t}{\tau_{D(0)}} \left[1 + (R_0 / R_{DA})^6\right]\right) dR_{DA} \quad (3.2)$$

Here we assumed Gaussian distribution of donor-acceptor distances ( $p(R_{DA})$ ) with a mean of  $\langle R_{DA} \rangle$  and a half-width of  $\sigma_{DA}$  which is expressed as:

$$p(R_{DA}) = \frac{1}{\sqrt{2\pi}\sigma_{DA}} \exp\left(-\frac{(R_{DA} - \langle R_{DA} \rangle_{\text{exp}})^2}{2\sigma_{DA,\text{exp}}^2}\right) \quad (3.3)$$

In addition, a fraction of Donor-only molecules ( $x_{D\text{only}}$ ) and a constant offset  $c$  was considered to describe the experimentally observed fluorescence decay  $f(t)$ :

$$f(t) = (1 - x_{D\text{only}}) \cdot f_{D(A)}(t) + x_{D\text{only}} \cdot f_{D(0)}(t) + c \quad (3.4)$$

Combining the donor fluorescence decay in the presence,  $f_{D(A)}(t)$ , and in the absence,  $f_{D(0)}(t)$ , of FRET by a time-dependent ratio a measure of FRET,  $\varepsilon_D(t)$ , is obtained:

$$\varepsilon_D(t) = \frac{f_{D(A)}(t)}{f_{D(0)}(t)} \quad (3.5)$$

We refer to this ratio as the FRET-induced donor decay,  $\varepsilon_D(t)$ , as it quantifies the quenching of the donor by FRET (see **Main Text, Fig. 3f**) with rate constant  $k_{FRET}$ .  $\varepsilon_D(t)$  allows us to directly display the underlying inter-dye distances that correspond to a characteristic time for the FRET species  $j$  (where  $j$  can be the species A, B, C and D, respectively) (eq. (3.6)).

$$t_{FRET,j} = \frac{1}{k_{FRET}} = \tau_{D(0),ref} \left( \frac{R_{DA,j}}{R_0 (\tau_{D(0),ref})} \right)^6 \quad (3.6)$$

Note that each Förster Radius  $R_0$  has been computed with a specific fluorescence quantum yield of the donor  $\Phi_{F,D(0),ref}$  as reference which must be converted to a radiative rate constant by multiplying with the corresponding fluorescence lifetime  $\tau_{D(0),ref}$ . In this work  $\tau_{D(0),ref}$  was 4.0 ns.

The fluorescence decays of the specific donor-only reference and the corresponding FRET samples (DA1, DA2 and DA3, respectively) were analyzed in joint fit as described in detail in ref. <sup>10</sup> to determine the FRET species specific inter-dye distances  $R_{DA,j}$ . The DA1 Alexa488/647 subpopulation ( $E_{FRET} > 0.065$ , dynF, see also **Figure 3f**) and subpopulation with  $E_{FRET} < 0.065$ , LF) at 1 mM  $Mg^{2+}$  was fitted by eq. (3.1)-(3.4) with a global DOnly decay approximated by a single donor fluorescence lifetime ( $\tau_{D(0)}=4.1$  ns) by a model with 3 Gaussian distributed distances and the same half-width  $\sigma_{DA}=6$  Å. The fit quality is judged by  $\chi^2_r$ . The fit results for the subpopulations LF and dynF are collected in the following table:

subpopulations of DA1	$R_{DA,1}$ (Å)	$x_1$	$R_{DA,2}$ (Å)	$x_2$	$R_{DA,3}$ (Å)	$x_3$	$\chi^2_r$
LF	42	0.28	63	0.49	104	0.23	1.11
dynF		0.40		0.47		0.13	1.07

Further seTCSPC analysis of the fluorescence intensity decay curves for all Alexa488/647 FRET pairs, DA1-3 in 0.5 mM  $Mg^{2+}$  with corresponding fits by eq. (3.4) are shown in **Supplementary Fig. 10**. This analysis yielded a good estimate of the FRET parameters of the structural states underlying the dynamic populations (register 1 and 2). Note, that it is difficult to resolve distances of this FRET pair above 90 Å by seTCSPC.

#### Step 4: Burst-ID FCS

To perform an unbiased check for the presence of exchange kinetics detected by FRET<sup>3</sup>, we computed the color correlation functions (auto- (green-green ( $G,G$ ) and red-red ( $R,R$ ))- and cross- (green-red ( $G,R$ ) and red-green ( $R,G$ )) functions, respectively) for the signal of those bursts, which were selected from the sample as double-labeled species by PIE (**Supplementary Fig. 8a**). These burst-ID cross-correlation functions  $G_{G,R}$  and  $G_{R,G}$  together with auto-correlation functions  $G_{G,G}$  and  $G_{R,R}$  were globally fitted by eq. 4.1 with three relaxation times  $t_{Rj}$ . To fit the color auto( $i=m$ )- and cross( $i\neq m$ )- correlation functions in a global approach, we have used a set of equations previously presented<sup>5,20</sup>

$$G_{i=m}(t_c) = 1 + \frac{1}{N_{Br}} \cdot G_{diff}^{(i)}(t_c) \cdot \left[ 1 - B^{(i)} + B^{(i)} \cdot \exp(-t_c/t_B) + \sum_{j=1}^n AC_{Rj}^{(i)} \cdot \left( \exp\left(-\frac{t_c}{t_{Rj}}\right) - 1 \right) \right] \quad (4.1)$$

$$G_{i\neq m}(t_c) = 1 + \frac{1}{N_{CC}} \cdot G_{diff}^{(i,m)}(t_c) \cdot \left[ 1 - CC^{(i,m)} \cdot \sum_{j=1}^n X_{Rj}^{(i,m)} \cdot \exp\left(-\frac{t_c}{t_{Rj}}\right) \right]$$

where  $t_{Rj}$  are the relaxation times that correspond to the exchange times between selected color signals ( $i=G,R$  and  $m=G,R$ ) with corresponding absolute amplitudes of the auto-correlation function  $AC_R^{(i)}$  and the relative normalized amplitudes of the cross-correlation function  $CC^{(i,m)}$  with the fractions  $X_R^{(i,m)}$ .  $B^{(i)}$  is the amplitude of an additional bunching term associated to photophysics with the relaxation time  $t_B$  in the

measured samples which was globally fitted for the auto-correlation functions.  $N_{br}$  is the average number of bright molecules from the color auto-correlation functions in the focus and  $N_{CC}$  of the color cross-correlations corresponds to the inverse of the initial amplitude  $G_{i,m}(0)$ .  $G_{diff}^{(x)}(t_c)$  is the apparent diffusion term in the correlation function:

$$G_{diff}^{(x)}(t_c) = \left(1 + \frac{t_c}{t_{diff}^{(x)}}\right)^{-1} \cdot \left(1 + \left(\frac{\omega_0}{z_0}\right)^2 \cdot \frac{t_c}{t_{diff}^{(x)}}\right)^{-\frac{1}{2}} \quad (4.2)$$

A 3-dimensional Gaussian shaped volume element with parameters  $\omega_0$  and  $z_0$  is considered. We assume that  $G_{diff}(t_c) = G_{diff}^{(i)}(t_c) = G_{diff}^{(m)}(t_c)$  take the form of eq. (4.2). The selective correlation spectroscopy for the dynF population ( $E_{FRET} > 0.065$ ) of DA1-labeled fibers (Alexa488/647) at 1 mM  $Mg^{2+}$  (see **Figure 3g**) by eq. (4.1) are compiled in the following table:

$i, m$	$N_{Br}$	$z_0/w_0$	$t_{diff}$ , [ms]	$B^{(G)}$	$t_B$ , [ $\mu$ s]	$AC_{R1}^{(i)}$ or $X_{R1}^{(i,m)}$	$t_{R1}$ , [ $\mu$ s]	$AC_{R2}^{(i)}$ or $X_{R2}^{(i,m)}$	$t_{R2}$ , [ $\mu$ s]	$AC_{R3}^{(i)}$ or $X_{R3}^{(i,m)}$	$t_{R3}$ , [ms]	$CC^{(i,m)}$
$G, G$	0.69	70	5.26	0.039	0.192	0.142	2.6	0.089	27.3	0.005	3.14	-
$R, R$	0.26			0.256		0.183		0.259		0.080		-
$G, R$	0.72			0		0.168		0.271		0.561		0.42
$R, G$	0.74			0								0.42

Additional model-free correlation analysis from all FRET vantage points DA1-3 (488/647) at 0.75 mM  $Mg^{2+}$  revealed conformational dynamics with at least three relaxation times, thus involving at least four kinetic states (**Supplementary Fig. 11**).

### Step 5: Photobleaching and photoblinking analysis

To detect possible photobleaching and photoblinking, we calculated the difference of the burst length in two PIE-channels  $T_{GX}$  and  $T_{RR}$ , where  $T_{GX}$  corresponds to the mean observation time of the photons detected in the donor or acceptor channels after donor excitation ( $G$ ) and  $T_{RR}$  corresponds to mean observation time of the red photons after direct excitation of acceptor ( $R$ ) (for details see ref<sup>17</sup>). In case of acceptor photobleaching and/or photoblinking the mean burst time of the acceptor fluorescence emissions is decreased and the mean burst time of donor fluorescence emission is increased simultaneously. This would lead to an increasing  $T_{GX}$  and to a decreasing  $T_{RR}$ , so that  $|T_{GX}-T_{RR}|$  of the analyzed bursts would deviate significantly from zero, if photobleaching and/or photoblinking were present. However, as shown in **Supplementary Fig. 14a**, significant photobleaching and photoblinking was not present under our measurement conditions, because the  $|T_{GX}-T_{RR}|$  distribution is symmetric and narrow. Additionally, we checked for the presence of potentially weak



photobleaching and photoblinking processes by applying the macro time filter  $|T_{GX}-T_{RR}| < 1$  ms threshold criterion for burst selection (**Supplementary Fig. 14b, left panel**). The influence of the presence and absence of this selection criterion on the shape of the FRET efficiency distribution is demonstrated for double labeled bursts of DA1 (Alexa488/647) in 0.5 mM  $Mg^{2+}$ . We fitted two FRET efficiency  $E_{FRET}$  histograms with and without applied macro time filter (**Supplementary Fig. 14b**) by Photon Distribution Analysis (PDA, see **step 7**) for a 3 ms time window. The obtained FRET distributions and means with (left panel) and without (right panel) burst selection did not significantly differ from each other which proves the absence of marked acceptor photobleaching and photoblinking processes.

### **Steps 6-11. Establishing a dynamic model for chromatin dynamics**

#### **Step 6. Evaluation of kinetic networks between FRET species compatible with experimental data**

The detected FRET species, which correspond to structurally meaningful chromatin conformers, form a kinetic network. Using the above presented observations from the various experiments (TIRF, seTCSPC, burst-ID FCS, MFD) kinetic and structural models for chromatin dynamics were formulated (**Supplementary Fig. 15**). The models to be evaluated involved four kinetic states (A-D) in two exchanging dynamic populations (register 1 and 2), corresponding to different tetranucleosome interactions.

In an iterative process, we used dynamic PDA (**step 7**) to refine the parameters and fit the experimental data using the developed kinetic models, followed by model validation (**step 8**). From the obtained, refined parameters, combined with structural molecular modeling (**steps 9-10**), a global model for chromatin conformational change was formulated (**step 11, Fig. 5**). The model encompasses a locally dynamic fiber which fluctuates between different tetranucleosome stacking registers on the millisecond timescale. Associations between tetranucleosomes are loose and exchange in the microsecond region. Finally, tetranucleosome open on the millisecond timescale and couple to static locked states, which persist structured over 50-500 ms. The individual **steps 7-11** for this analysis are described below.

#### **Step 7. General description of PDA analysis**

Each sample with a specific FRET dye configuration (DA1, DA2 or DA3) was measured at various  $Mg^{2+}$  concentrations under single-molecule conditions. The signals of the selected FRET bursts (**Supplementary Fig. 8a**) were split into equal time windows (TW). The FRET efficiency is calculated from the number of photons of donor and acceptor dyes in the prompt time-to-amplitude converter (TAC) channels defined by the donor excitation pulse with a repetition frequency of 32 MHz. In PIE experiments the acceptor excitation laser pulse is delayed by 15.625 ns, which defines the delayed TAC window for computation of the stoichiometry  $S$  (see

**step 2, Calculation of donor acceptor distances from fluorescence signal).** For each TW (only full length time windows were used and incomplete pieces at the end of bursts were excluded) the values for the FRET parameters ( $R_{DA}$ ,  $E_{FRET}$ ) were calculated as described in **step 2, Calculation of donor acceptor distances from fluorescence signal**, and plotted in a 1D frequency histogram with 201 bins (**Supplementary Fig. 16-18**). The fundamental idea in PDA is computing the distribution of the chosen FRET indicator for a given FRET efficiency (or FRET-averaged donor-acceptor distance,  $\langle R_{DA} \rangle_E$ )<sup>4,14</sup> taking into account photon shot-noise. Due to the flexibility of the dye linker, FRET pairs exhibit a distribution of FRET efficiencies or apparent distances even on rigid molecules, which is caused by distinct acceptor brightnesses<sup>21</sup>. This distance distribution is well approximated by a Gaussian distribution with a half width  $\sigma \sim 6$  Å.

### Calculation of donor acceptor distances from fluorescence signals

The FRET-averaged distance  $\langle R_{DA} \rangle_E$  between the dyes could be calculated from the mean FRET efficiency defined in eq. (2.4)

$$\langle R_{DA} \rangle_E = R_0 \left( \langle E_{FRET} \rangle - 1 \right)^{1/6} \quad (7.1)$$

In this work we calculated  $\langle R_{DA} \rangle_E$  directly from the observed intensities and corresponding correction parameters  $\alpha$ ,  $\beta$ ,  $\gamma$ ,  $\delta$  defined in **Step 2**:

$$\langle R_{DA} \rangle_E = R_0 \left( \frac{\gamma \cdot I_{GG}}{I_{RG} - (\alpha \cdot I_{GG} + \beta \cdot I_{RR})} \right)^{1/6} \quad (7.2)$$

using the following FRET pair specific Förster Radii  $R_0$ :

parameter	FRET pair D/A	
	Alexa488/647	Alexa568/647
$R_0$ [Å]	52	82

**Dynamic PDA.** Considering the sample DA1 (Alexa488/647) in 1mM  $Mg^{2+}$ , we demonstrate the effect of dynamics on the  $E_{FRET}$  histograms for two time windows of different length (TW=2ms and TW=5ms, **Supplementary Fig. 14c**). A global fit of both TWs using a joint models with static Gaussian distributions indicates that a model without dynamic exchange terms cannot describe both data sets appropriately, because the exchange dynamics influences the width of the distributions in each TW differently. Therefore we used dynamic PDA<sup>14</sup> in the subsequent analysis, which can describe exchange dynamics comparable to NMR dispersion experiments. For each data set histograms were created for 4 different TWs (2, 3, 4 and 5 ms). All histograms created for  $Mg^{2+}$  concentrations (number of  $[Mg^{2+}] \times 4$ ) were globally fitted by the kinetic

models described below. Each FRET species of assembled chromatin was modelled by a Gaussian distribution of distances and was approximated by 51 bins. To describe the histograms of dynamic mixing between two Gaussian distributed FRET species (e.g. species A, species B, ...), this results in  $\binom{2}{51} = 50 \cdot 51 / 2 = 1275$  (all possible pairs of distances) dynamic mixing distributions. In contrast, the distributions of two FRET species undergoing dynamic mixing are approximated by 201 bins. Then, for each pair of interconverting Gaussian distributed species (e.g. dyn A-B, dyn B-C, ...), the shot-noise limited total histogram could be calculated as a sum of all  $1275 \cdot 201 = 256275$  shot-noise limited FRET parameter distributions. We have shown that shot-noise limited FRET parameter histograms from Gaussian distributed distances ( $R_{\text{mean}}, \sigma$ ) and the sum of shot-noise limited FRET parameter histograms of two fixed distances  $R_{\text{mean}} - \sigma$  and  $R_{\text{mean}} + \sigma$  are very similar<sup>14</sup>. Thus, in order to simulate dynamics between two Gaussian distributed species and to reduce computational cost, the model distribution can be approximated with the sum of two dynamic distributions between ( $R1_{\text{mean}} - \sigma1$  and  $R2_{\text{mean}} - \sigma2$ ) and ( $R1_{\text{mean}} + \sigma1$  and  $R2_{\text{mean}} + \sigma2$ ) (**Supplementary Fig. 14d**).

MFD data were then globally fitted using dynamic PDA and assuming a kinetic model<sup>14</sup>. To satisfy the observations of coexisting dynamic and quasi-static molecules in smTIRF experiments, each dynamic PDA model assumed the co-existence of molecules existing in a number of individual FRET species showing no dynamics on the MFD timescale ( $t_R > 50$  ms, static fraction, stat A, stat B, ...), with populations of molecules which exchange between FRET species (dynamic fractions, dyn A-B, dyn B-C, ...). Secondly, we assumed the inter-dye distances in the basic FRET species (A, B, C, D) to be invariant to  $Mg^{2+}$ . Thus, a sum of Gaussian distributed FRET species (static fractions,  $R_{DAi}$ ) and dynamically mixing Gaussian distributed FRET species pairs (dyn i-j) corresponding to the selected kinetic model (see list of trial models in **Supplementary Fig. 15**) was used to globally fit the group of histograms for each FRET dye configuration over all  $Mg^{2+}$  concentrations (**Fig. 5a-c** and final models in **Supplementary Fig. 16-18**). Thirdly, the dynamics of exchanging molecules was described by models with a series of two-state kinetic exchange terms connecting the quasi-static populations. Final models are shown in **Fig. 5d-f** and **Supplementary Fig. 16-18**. Importantly, global fits were employed to evaluate the  $Mg^{2+}$  dependencies, assuming a linear relationship between the logarithms of the rate constants and the ionic strength:

$$\log(k_{ij}) = m \cdot [Mg^{2+}] + k_{ij,0}, \quad (7.3)$$

similar to observations in protein folding<sup>22</sup>.

**Step 8: Validation of kinetic models.**

Based on the model-free FCS analysis (**Supplementary Fig. 11**), yielding 3 relaxation times, at least four kinetically relevant species are expected. As our dye configurations (DA1-3) are not equally sensitive to all structural exchanges processes and states (**Fig. 4a**) we tested models containing 3 or 4 states for each dye configuration in the dynamic PDA analysis, employing various connectivities. For each configuration DA1-3 different kinetic models were evaluated based on a number of criteria:

- i.* Physical meaningful connectivity of species,
- ii.* Minimal number of species,
- iii.* Cutoff for rate constants ( $10^6 \text{ s}^{-1} > k_{ij} > 10^2 \text{ s}^{-1}$ ) and m-values ( $-25 < m < 25$  (see equation (7.3)); assuming a change of less than  $\pm 100$ -fold in each rate constant within the tested  $\text{Mg}^{2+}$  concentrations),
- iv.* Stable fit results over the different  $\text{Mg}^{2+}$  concentration,
- v.* Acceptable goodness of fit ( $\chi^2_r < 1.4$ ),
- vi.* Consistency with models from other FRET vantage points (DA1, DA2 and DA3),
- vii.* Transitions between FRET species which are structurally meaningful.

A number of different models were tested and based on criteria *i-vi* (**Supplementary Fig. 15**). The models shown in Fig. 3d were deemed to be the most probable to describe the experimental data. Finally, from the static and dynamic fractions, weighted by the associated rate constants, the relative populations of each state were calculated (**Fig. 5g-i**) according to  $P_i = P_i^s + P_{ij}^d \cdot k_{ij} / (k_{ij} + k_{ji})$ , where  $P_i$  denotes the population of state  $i$ ,  $P_i^s$  is the static fraction,  $P_{ij}^d$  is the dynamic fraction between states  $i$  and  $j$  and  $k_{ij}$ ,  $k_{ji}$  are the associated rate constants.

**Steps 9-11. Assignment of the states**

For a structural interpretation of the detected inter-dye distances from MFD and PDA, we determined the uncertainties in our analysis and subsequently applied structural modeling, using both available structures and coarse grained modeling, in combination with modeling of the conformational distributions of the dyes.

**Step 9: Relating measured  $R_{DA}$  distances to structural models of compact chromatin states**

Here, first we define the uncertainties in the measured parameters, followed by the construction of molecular models for the compact states.

**Determination of the uncertainties for structural modeling.** As a first test for the suitability of the dyes Alexa488 and Alexa647 for an accurate structural analysis based on FRET data, we checked the fluorescence lifetimes of the donor-only and acceptor samples and time-resolved anisotropies  $r(t)$  using the FRET samples identified by PIE. The results (see **summaries 9.1-2** of donor dye properties, **summaries 9.3-4** of acceptor dye properties below) indicate that there is no strong quenching as compared to the free dyes in solution and that all dyes are sufficiently mobile at these positions. Anisotropy decays were analyzed by eq. (9.1).

$$r(t) = \sum_i r_i \exp(-t / \rho_i) \text{ and } \sum_i r_i = r_0 \quad (9.1)$$

Here  $r_i$  denotes the depolarization fractions related to order parameters, and  $\rho_i$  the corresponding depolarization times mainly by dye rotation. In the  $r(t)$  analysis we applied the fundamental anisotropies  $r_0 = 0.38$  for Alexa488 and Alexa647, respectively. We used the amplitude of the longest depolarization time  $r_i$  to approximate the residual anisotropy  $r_{inf}$  for computing the dye and position specific fraction of trapped dyes using eq. (9.2).

$$x_{trapped} = r_{inf} / r_0 \quad (9.2)$$

The fraction of trapped dyes is needed to parametrize the contact volume for improving the accuracy of the estimated spatial dye density in ACV simulations described in **step 9**, section **FRET positioning and screening calculations** below.

**Summary of dye properties of the donor Alexa488.** In the tables below the fluorescence lifetimes and anisotropy contributions of this donor dye are compiled.

Summary 9.1. Fluorescence lifetimes of the donor dye Alexa488

Species	$\tau$ (ns)
<b>DA1</b>	
Average	4.2
Std, $\Delta$	< 0.1
<b>DA2</b>	
Average	4.1
Std, $\Delta$	< 0.1
<b>DA3</b>	
Average	4.1
Std, $\Delta$	< 0.1
<b>Average of DA1-3</b>	
Average	4.1
Std, $\Delta$	< 0.1

**Summary 9.2.** Fluorescence anisotropy and rotational correlation times of the donor dye Alexa488

Species	$\rho_1$ (ns)	$\rho_2$ (ns)	$\rho_3$ (ns)	$\rho_4$ (ns)	$r_1$	$r_2$	$r_3$	$r_{04}=r_{inf,D}$
<b>DA1</b>								
Average [a]	< 0.3	1.1	4.8	> 40	0.162	0.052	0.087	0.080
Std, $\Delta$		0.2	0.9		0.014	0.011	0.014	0.012
$X_{trapped}$								<b>0.210</b>
<b>DA2</b>								
Average [a]	< 0.3	0.6	5.0	> 40	< 0,01	0.196	0.102	0.083
Std, $\Delta$		0.1	1.1			0.069	0.030	0.009
$X_{trapped}$								<b>0.218</b>
<b>DA3</b>								
Average [a]	< 0.3	0.6	3.3	> 40	0.032	0.199	0.092	0.057
Std, $\Delta$		0.03	0.5		0.007	0.012	0.009	0.003
$X_{trapped}$								<b>0.149</b>

[a] The fit values with using eq. (9.1) are averages for measurements at 0.0, 0.5, 1.0 and 4 mM Mg<sup>2+</sup>.

**Summary of acceptor dye properties.** In the tables below the fluorescence lifetimes and anisotropy contributions of the acceptor dye Alexa647 is summarized. In practice, as all cyanine based dyes, Alexa647 can have several dye populations in distinct environments with specific brightnesses when coupled to biomolecules referred to as acceptor heterogeneity,  $A_{het}$ . This typical behavior is also seen in nucleosome arrays (see Summary 9.3). In this case a fixed DA distance is usually not sufficient to describe FRET species, and a Gaussian distance distribution with a mean apparent distance  $\langle \tilde{R} \rangle$  and an apparent distribution half width ( $hw_{app}$ ) has to be used instead. As shown by Kalinin and colleagues<sup>21</sup>  $\langle \tilde{R} \rangle$  is slightly biased towards longer distances as compared to  $\langle R_{DA} \rangle_E$  (eq. (9.3)).

$$\langle \tilde{R} \rangle = \langle R_{DA} \rangle_E \langle \Phi_{FA} \rangle^{1/6} \langle (\Phi_{FA})^{-1/6} \rangle \quad (9.3)$$

where  $\Phi_{FA}$  is the acceptor fluorescence quantum yield. Note that the fraction of fluorescent trans states  $\alpha$  (usually  $\alpha = 0.8$ ) cancels out in eq. (9.3)-(9.4). In this work, the correction factors  $\langle \Phi_{FA} \rangle^{1/6} \langle \Phi_{FA}^{-1/6} \rangle$  are very close to unity (Summary 9.3) and thus can be disregarded for the calculation of interdye distances (i.e. in this work  $\langle \tilde{R} \rangle \cong \langle R_{DA} \rangle_E$ ). Applying the rules for error propagation for the function  $\tilde{R}(\Phi_{FA})$ , one obtains also an relation for the variance and half width ( $\sigma$ ) of the apparent DA distance (eq. 9.4).

$$\sigma(\tilde{R}) / R_{DA} = \langle \Phi_{FA} \rangle^{1/6} [\text{var}(\Phi_{FA}^{-1/6})]^{1/2} \quad (9.5)$$

The fact that relative experimental half widths ( $\sigma/R_{DA}$ ) (**Supplementary Figures 16-18**,  $\sigma/R_{DA}(\text{DA1}) = 0.1$ ,  $\sigma/R_{DA}(\text{DA2}) = 0.13$ ,  $\sigma/R_{DA}(\text{DA3}) = 0.06$ ) are much broader than the values caused by acceptor heterogeneity

(Summary 9.4) may indicate significant heterogeneity of the nucleosome arrays which would be actually not surprising. Note that the difference is the smallest (less than factor 2) for DA3.

Summary 9.3. Fluorescence lifetimes and other dye parameters of the acceptor dye Alexa647 with  $a=0.8$ .

Species	$\tau_1$ (ns)	$\tau_2$ (ns)	$x_1$	$x_2$	$\langle \tau_A \rangle_x$ (ns)	$\alpha \Phi_{FA}$ [a,b]	A heterogeneity, $A_{het}$ $\langle \Phi_{FA} \rangle^{1/6} / \langle (\Phi_{FA})^{-1/6} \rangle$	$\sigma/R_{DA}$
<b>DA1</b>								
Average [b]	1.38	1.68	0.55	0.45	1.43	0.390	1.0001	0.005
Std, $\Delta$	0.04	0.31	0.37	0.37	0.01	0.002	< 0.0001	0.001
<b>DA2</b>								
Average	0.92	1.49	0.32	0.68	1.32	0.362	1.0038	0.035
Std, $\Delta$	0.10	0.005	0.18	0.18	0.06	0.015	0.0007	0.005
<b>DA3</b>								
Average	0.90	1.49	0.36	0.64	1.28	0.350	1.0051	0.040
Std, $\Delta$	0.09	0.06	0.12	0.12	0.01	0.002	0.0003	0.002
<b>Average of DA1-3</b>								
Average					1.34	0.368		
Std, $\Delta$					0.06	0.017		

[a] We used the reference value of Cy5 labeled dsDNA with  $\langle \tau_A \rangle_x = 1.17$  ns and  $\Phi_{FA} = 0.4$  which was measured with low irradiances at a steady state fluorescence spectrometer, i.e.  $a=0$ .

[b] The fit values are averages for measurements at 0.0, 0.5, 1.0 and 4 mM  $Mg^{2+}$  using a fit with a series of exponentials  $f_A(t) = \sum_i x_i \exp(-t/\tau_i)$  and  $\sum_i x_i = 1$ .

Summary 9.4. Fluorescence anisotropy and rotational correlation times of the acceptor dye (Alexa647)

Species	$\rho_1$ (ns)	$\rho_2$ (ns)	$\rho_3$ (ns)	$r_1$	$r_2$	$r_3=r_{inf,A}$
<b>DA1</b>						
Average [a]	< 0.3	1.6	10.2	0.063	0.054	0.263
Std, $\Delta$		0.7	0.4	0.007	0.026	0.020
$X_{trapped}$						<b>0.692</b>
<b>DA2</b>						
Average [a]	< 0.3	0.9	13.7	0.072	0.056	0.252
Std, $\Delta$		0.6	4.1	0.003	0.019	0.018
$X_{trapped}$						<b>0.663</b>
<b>DA3</b>						
Average [a]	< 0.3	1.0	9.9	0.081	0.090	0.209
Std, $\Delta$		0.3	0.03	0.007	0.013	0.016
$X_{trapped}$						<b>0.549</b>

[a] The fit values with using eq. (9.1) are averages for measurements at 0.0, 0.5, 1.0 and 4 mM  $Mg^{2+}$ .

### Determination of uncertainties in measured $R_{DA}$ distances

The uncertainty in the measured  $R_{DA}$  distances, used for structural modeling, is obtained by determining the individual uncertainties of all quantities separately, and then propagating them towards an uncertainty in the distance. Considering the DA distance,  $R_{DA}$ , two main factors determine the uncertainty,  $\Delta R_{DA}$  in this study: (1) the precision (noise) of the measurement,  $\Delta_{\text{noise}}$  and (2) the uncertainty of the calibration,  $\Delta_{\text{cal}}$ . The total uncertainty of the distance,  $\Delta R_{DA}$ , is estimated by combining these error sources. With the assumption that the contributions follow a normal distribution,  $\Delta R_{DA}$  is given by:

$$\Delta R_{DA} = \left[ \Delta_{\text{noise}}^2 + \Delta_{\text{cal}}^2 \right]^{1/2} \quad (9.6)$$

The distance,  $R_{DA}$ , can be expressed as a function of experimental observable fluorescence intensities and correction and conversion parameters (see eq. 7.2). Thus  $\Delta_{\text{cal}}^2$  can be expanded as<sup>10</sup>

$$\Delta R_{DA} = \left[ \Delta_{\text{noise}}^2 + \left( \Delta_{B_{GG}}^2 + \Delta_{B_{RG}}^2 + \Delta_{\alpha}^2 + \Delta_{\beta}^2 + \Delta_{\gamma}^2 + \Delta R_0^2 \right) \right]^{1/2} \quad (9.7)$$

*Calibration contributions to the uncertainty,  $\Delta R_{DA,cal}$ .* All equations used to compute the contributions  $\Delta R_{DA,cal}$  were described in detail by Peulen et al. (eqs. 39-46 in ref. <sup>10</sup>).

*Contributions to the uncertainty  $\Delta R_0$ .* The overall uncertainty for the Förster radius,  $\Delta R_0$ , is estimated by the uncertainties of the local refractive index,  $n$ , the exact donor fluorescence quantum yield,  $\Phi_{F,D}$ , spectral overlap integral,  $J$ , and the FRET orientations factor,  $\kappa^2$ , ref. <sup>11</sup> (eq. (9.8)).

$$\Delta R_0(n^{-4}, \Phi_{F,D}, J, \kappa^2) = \sqrt{\Delta R_0(n)^2 + \Delta R_0(\Phi_{F,D})^2 + \Delta R_0(J)^2 + \Delta R_0(\kappa^2)^2} \sim 0.08 - 0.09 \cdot R_0 \quad (9.8)$$

*Contributions to the uncertainty  $\Delta R_{DA}(R_{DA})$  by noise.* We have to determine the precision of the dynamic PDA fits,  $\Delta R_{DA}(R_{DA})$  caused by statistical noise. Here, we performed a subsampling analysis, where the dynamic PDA fit procedure was repeated three times using a 70% subsample of the total dataset. The standard deviations from these three fits are reported in **Supplementary Figures 16-18**, and determine the precision of our fitting procedure. The overall precision in  $R_{DA}$ ,  $\Delta R_{DA}(R_{DA})$ , from dynamic PDA is reported in **Supplementary Table 7**: 2% (DA1 and DA3) and 3% (DA2).

*Contributions to the total uncertainty  $\Delta R_{DA}(R_{DA})$ .* The individual errors are listed in **Supplementary Table 7**. They are then propagated using eq. (9.7), to estimate the total uncertainty of the determined distances. Together, these analyses result in a total uncertainty for  $R_{DA}$  for DA1 of 9%, for  $R_{DA}$  for DA2 of 9% and  $R_{DA}$  for DA3 of 8% (**Supplementary Table 7**).



**Model building.** We built models using the cryo-EM structure of a 12-mer nucleosomal array with 177 bp nucleosome repeat length<sup>5</sup>. We then modeled the accessible contact volume (ACV) for dyes in the DA1, DA2 or DA3 configuration and employed these distance distributions to calculate an average, conformation-weighted inter-dye distance (see below, **FRET positioning and screening calculations**). Importantly, we considered two possible fiber structures: The 12-mer array could exist as a stack of three tetranucleosome (TN) units (TN1(N1-N4); TN2(N5-N8); TN3(N9-N12), 4-4-4, register 1) as observed in the cryoEM structure (see Fig. 1a). Alternatively, tetranucleosomes could stack in a different register (TN1(N3-N6); TN2(N7-N10), with four unstacked nucleosomes at both ends, 2-4-4-2, register 2). This would put the DA1-3 dye pairs into neighboring tetranucleosomes. Finally, if the nucleosome-nucleosome interactions are local and fiber compaction is not fully cooperative, both registers are expected to be populated. We thus produced models for both registers and calculated the expected inter-dye distances for DA1-3 in register 1 and 2 (**Supplementary Fig. 12 and Supplementary Table 8**). The observed deviations for DA2 can be rationalized by rotational motions between two nucleosomes (see **Supplementary Fig. 13 e,f**). A "clamshell" motion by  $\sim 10^\circ$  would be sufficient to explain the experimental data of DA2 (488/647). Note that DA1 is relatively insensitive to these motions.

**FRET positioning and screening calculations.** The dye distribution was modeled by the accessible contact volume approach (ACV)<sup>4</sup> which is similar to the accessible volume (AV)<sup>6</sup>, but additionally defines an area close to the surface as contact volume. Here donor and acceptor fluorophores are approximated by an ellipsoid with an empirical radius  $R_{dye(i)}$  and where central atom of the dye is connected via flexible linkage with effective length  $L_{link}$  and width  $w_{link}$  to the C<sub>5</sub> atom in the dT nucleotide. All geometric parameters for the dyes were: Alexa488:  $L_{link} = 20 \text{ \AA}$ ,  $w_{link} = 4.5 \text{ \AA}$ ,  $R_{dye(1)} = 5 \text{ \AA}$ ,  $R_{dye(2)} = 4.5 \text{ \AA}$ ,  $R_{dye(3)} = 1.5 \text{ \AA}$ , Alexa568:  $L_{link} = 22 \text{ \AA}$ ,  $w_{link} = 4.5 \text{ \AA}$ ,  $R_{dye(1)} = 7.8 \text{ \AA}$ ,  $R_{dye(2)} = 1.9 \text{ \AA}$ ,  $R_{dye(3)} = 1.5 \text{ \AA}$ , Alexa647:  $L_{link} = 22 \text{ \AA}$ ,  $w_{link} = 4.5 \text{ \AA}$ ,  $R_{dye(1)} = 11 \text{ \AA}$ ,  $R_{dye(2)} = 3 \text{ \AA}$ ,  $R_{dye(3)} = 1.5 \text{ \AA}$  (**Supplementary Fig. 12**). In the ACV model the part of AV which is closer than  $3 \text{ \AA}$  from the macromolecular surface (referred to as contact volume) is defined to have a distinct spatial dye density  $\rho_{dye}$ . In this model, where a dye freely diffuses within the AV and its diffusion is hindered close to the surface, the spatial density  $\rho_{dye}$  along  $R$  is approximated by a step function:  $\rho_{dye}(R < 3 \text{ \AA}) = \vartheta_{CV,dye} \cdot \rho_{dye}(R \geq 3 \text{ \AA})$ . Here  $\vartheta_{CV,dye}$  corresponds to the relative dye density in the contact volume relative to outer volume.  $\vartheta_{CV,dye}$  is adjusted such that fraction of trapped dyes, determined by the residual anisotropy (see table above) is met. Note that  $\vartheta_{CV,dye}$  is specific for each ACV because the shape, size, and surface area to the nucleosome varies slightly for each dye position. In the following table, we indicate the fraction of trapped dye and the dye density in the contact volume relative to the outer volume  $\vartheta_{CV,dye}$  for DA1-3:

**Summary 9.5.** Parameters for modeling the contact volume in the ACV simulations

	Donor register 1	Donor register 2	Acceptor register 1	Acceptor register 2
<b>DA1</b>				
$X_{trapped}$ [a]	0.210		0.692	
$\vartheta_{CV,dye}$	0.1	0.3	1.6	3.1
<b>DA2</b>				
$X_{trapped}$	0.218		0.663	
$\vartheta_{CV,dye}$	0.3	0.1	2.1	2.3
<b>DA3</b>				
$X_{trapped}$	0.149		0.549	
$\vartheta_{CV,dye}$	0.2	0.2	1.6	1.6

[a] computed by eq. 9.2 with values from the Summary 9.2 (donor) and Summary 9.4 (acceptor).

### Step 10: Structural models of open and dynamic states

To model the unfolded and open chromatin state, we further resorted to computational modeling. Specifically, we performed Monte Carlo simulations of an established coarse-grained model of the chromatin fiber<sup>7,23</sup> (see below **Coarse grained simulations**) to generate an ensemble of open chromatin conformations in the same temperature and salt conditions as the experiments, but in the absence of inter-nucleosome stacking interactions between the H4 histone tail and the acidic patch. From this larger ensemble of conformations, a hundred relatively uncorrelated structures were picked and used to build all-atom models of the chromatin configurations (**Supplementary Fig. 13a**). We then measured inter-dye distances for all nucleosomes in these structures for DA1-3 and produced distance distribution histograms (**Supplementary Fig. 13b,c,d**). These histograms showed that expected peak inter-dye distances were 110 Å (and a smaller fraction of structures with 190 Å) for DA1, 80 Å and 120 Å for DA2 and 90 Å for DA3. These distances match distances expected for states D in the PDA (**Fig. 4a**).

Finally, to understand the intra-tetranucleosome dynamics observed for DA2 (**Fig. 4a,b**) we employed the tetranucleosome X-ray structure<sup>13</sup> to test how structural distortions affect inter-dye distances for DA1 and DA2 (**Supplementary Fig. 13e,f**) and DA3 (**Supplementary Fig. 13g**). DA2 was found to be more sensitive to tetranucleosome distortions, and distances observed for state C could be modeled by a 30° change in the tetranucleosome interaction angle (**Supplementary Fig. 13e**) or by a 30° rotation of one nucleosome relative to its neighbor (**Supplementary Fig. 13f**). Importantly, these conformations still allow interactions at the H2B and H2A four-helix bundle<sup>5</sup> to persist. To illustrate the effect of nucleosome structural motions on each of FRET dye configurations (DA1, DA2, DA3), we plot FRET-average inter-dye distance as a function of the motion coordinate (**Supplementary Fig. 13e,f**). We used tetranucleosome structural models<sup>13</sup> as a starting point for our illustrations. First we tested, how the DA1 and DA2 inter-dye distances change with respect to the

clamshell-like opening angle between the two nucleosome units (N5, N7, **Supplementary Fig. 13e**). To define the clamshell rotation coordinate, we chose an axis going through the phosphorous atom of the unit N7, chain B, residue 55 and the phosphorous atom of the unit N7, chain A, residue -30. Thus, clamshell motion is the rotation of the unit N7 around the specified axis with the origin at the phosphorous atom of N7, chain B, residue 55. Second, we tested the DA1 and DA2 distance change with respect to the in-plane nucleosome rotation. To define this second rotational motion coordinate we chose the rotation axis between the centers of mass of the nucleosome units N5 and N7. Thus N7 is rotated around the specified axis with the origin at the center of mass of N7.

As the result we have observed that DA2 distance senses nucleosome clamshell motion while DA1 does not (**Supplementary Fig. 13e**).  $\langle R_{DA} \rangle_E$  for DA2 changes from 69 Å to 48 Å in the angular range of  $-30^\circ$  to  $0^\circ$ . DA1 is not sensitive to this motion and varies only from 47 to 50 Å. In the case of in-plane rotation,  $\langle R_{DA} \rangle_E$  for DA2 drops from 70 Å to 50 Å, when angle ranges from  $-30^\circ$  to  $30^\circ$ .  $\langle R_{DA} \rangle_E$  for DA1 is also sensitive to this motion and shows an increase of  $\langle R_{DA} \rangle_E$  from 45 Å to 58 Å.

### Coarse grained simulations

The 12-nucleosomes chromatin fibers with 177bp repeats ( $\sim 30$ bp linker DNAs) were treated at a coarse-grained resolution using a mesoscopic model developed and validated by Arya and Schlick<sup>23,24</sup>. According to this model, each nucleosome core (histone octamer plus wound DNA) is treated as a rigid body with an irregular surface described by 300 charged beads; the linker DNAs are treated as charged bead-chains with each bead representing a 3 nm-long segment of double-stranded DNA; and the histone tails (N termini of H2A, H2B, H3, and H4 and C termini of H2A) are also treated as charged bead-chains, where each bead represents five amino acid residues. The core, linker, and tail beads are assigned excluded volume potentials, to prevent them from overlapping with each other, and charges, to reproduce the electrostatic field of their corresponding atomistic counterpart at the specified salt concentration. The linker DNAs are assigned an intramolecular force field to reproduce experimentally obtained bending and torsional rigidity of DNA, and the histone tails are assigned an intramolecular force field to reproduce the configurational properties of atomistic histone tails. In this study, the nucleosome entry/exit angle was set to  $130^\circ$ , compatible with the trajectory of linker DNA in the tetranucleosome structure of Song et al.<sup>5</sup>, and the monovalent salt concentration was set to 50 mM. The effects of  $Mg^{2+}$  were treated phenomenologically, with suitably modified Debye length and persistence length of the linker DNA, as described elsewhere<sup>23</sup>.

To generate an equilibrium ensemble of fiber conformations at 293 K, we used a tailored Monte Carlo simulation approach as described elsewhere<sup>24</sup>. Briefly, the simulations employed four Monte Carlo “moves”: global pivot rotation of the end portions of the fiber about a randomly picked nucleosome core or linker DNA

bead, local translation and rotation of a randomly picked linker DNA bead or nucleosome core, and configurational bias regrowth of a randomly picked histone tail. The simulations were performed for 40 million steps, with the above four Monte Carlo moves implemented at a relative frequency of 0.2: 0.1: 0.1: 0.6, respectively. We picked a total of 100 uncorrelated fiber conformations from the simulated ensemble, which were then used to generate the corresponding atomistic models of the fiber (**Supplementary Fig. 13a-d**).

### **Step 11: Final model and its validation - A unified model of chromatin dynamics**

Based on the analyses presented above (**steps 1-10**) we formulated a unified model for chromatin dynamics (**Fig. 6**). The model encompasses two dynamic populations, corresponding to two tetranucleosome registers (register 1 and 2). From dynPDA of DA1 – 3, ranges for the exchange rate constants were determined and are given in Fig. 4i. The presented model is well supported by the whole of the experimental data and is corroborated by matching results from different analyses yielding FRET efficiency states, dynamics rate constants and populations (**Steps 2 - 4**) and dynamic PDA (**Step 6**).

### **Supplementary References**

1. Robinson, P.J., Fairall, L., Huynh, V.A. & Rhodes, D. EM measurements define the dimensions of the "30-nm" chromatin fiber: evidence for a compact, interdigitated structure. *Proc. Natl. Acad. Sci. U.S.A.* **103**, 6506-11 (2006).
2. Li, F., Allahverdi, A., Yang, R., Lua, G.B.J., Zhang, X., Cao, Y., Korolev, N., Nordenskiöld, L. & Liu, C.-F. A direct method for site-specific protein acetylation. *Angew. Chem. Int. Ed. Engl.* **50**, 9611-14 (2011).
3. Felekyan, S., Sanabria, H., Kalinin, S., Kühnemuth, R. & Seidel, C.A.M. Analyzing Förster resonance energy transfer with fluctuation algorithms. *Methods Enzymol.* **519**, 39-85 (2013).
4. Dimura, M., Peulen, T.O., Hanke, C.A., Prakash, A., Gohlke, H. & Seidel, C.A.M. Quantitative FRET studies and integrative modeling unravel the structure and dynamics of biomolecular systems. *Curr. Opin. Struct. Biol.* **40**, 163-185 (2016).
5. Song, F., Chen, P., Sun, D., Wang, M., Dong, L., Liang, D., Xu, R.M., Zhu, P. & Li, G. Cryo-EM study of the chromatin fiber reveals a double helix twisted by tetranucleosomal units. *Science* **344**, 376-80 (2014).
6. Kalinin, S., Peulen, T., Sindbert, S., Rothwell, P.J., Berger, S., Restle, T., Goody, R.S., Gohlke, H. & Seidel, C.A.M. A toolkit and benchmark study for FRET-restrained high-precision structural modeling. *Nat. Methods* **9**, 1218-25 (2012).
7. Arya, G., Zhang, Q. & Schlick, T. Flexible histone tails in a new mesoscopic oligonucleosome model. *Biophys. J.* **91**, 133-50 (2006).
8. Kilic, S., Bachmann, A.L., Bryan, L.C. & Fierz, B. Multivalency governs HP1alpha association dynamics with the silent chromatin state. *Nat. Commun.* **6**, 7313 (2015).
9. Nishibuchi, G., Machida, S., Osakabe, A., Murakoshi, H., Hiragami-Hamada, K., Nakagawa, R., Fischle, W., Nishimura, Y., Kurumizaka, H., Tagami, H. & Nakayama, J. N-terminal phosphorylation of HP1alpha increases its nucleosome-binding specificity. *Nucleic Acids Res.* **42**, 12498-511 (2014).
10. Peulen, T.O., Opanasyuk, O. & Seidel, C.A.M. Combining Graphical and Analytical Methods with Molecular Simulations To Analyze Time-Resolved FRET Measurements of Labeled Macromolecules Accurately. *J. Phys. Chem. B* **121**, 8211-8241 (2017).

11. Hellenkamp, B. et al. Precision and accuracy of single-molecule FRET measurements - a worldwide benchmark study. *arXiv:1710.03807 [q-bio.QM]* (2017).
12. Sindbert, S., Kalinin, S., Nguyen, H., Kienzler, A., Clima, L., Bannwarth, W., Appel, B., Muller, S. & Seidel, C.A.M. Accurate distance determination of nucleic acids via Forster resonance energy transfer: implications of dye linker length and rigidity. *J. Am. Chem. Soc.* **133**, 2463-80 (2011).
13. Schalch, T., Duda, S., Sargent, D.F. & Richmond, T.J. X-ray structure of a tetranucleosome and its implications for the chromatin fibre. *Nature* **436**, 138-41 (2005).
14. Kalinin, S., Valeri, A., Antonik, M., Felekyan, S. & Seidel, C.A.M. Detection of structural dynamics by FRET: a photon distribution and fluorescence lifetime analysis of systems with multiple states. *J. Phys. Chem. B* **114**, 7983-95 (2010).
15. Sisamakias, E., Valeri, A., Kalinin, S., Rothwell, P.J. & Seidel, C.A.M. Accurate single-molecule FRET studies using multiparameter fluorescence detection. *Methods Enzymol.* **475**, 455-514 (2010).
16. Fries, J.R., Brand, L., Eggeling, C., Kollner, M. & Seidel, C.A.M. Quantitative identification of different single molecules by selective time-resolved confocal fluorescence spectroscopy. *J. Phys. Chem. B* **102**, 6601-6613 (1998).
17. Kudryavtsev, V., Sikor, M., Kalinin, S., Mokranjac, D., Seidel, C.A.M. & Lamb, D.C. Combining MFD and PIE for accurate single-pair Forster resonance energy transfer measurements. *ChemPhysChem* **13**, 1060-78 (2012).
18. Lee, N.K., Kapanidis, A.N., Wang, Y., Michalet, X., Mukhopadhyay, J., Ebright, R.H. & Weiss, S. Accurate FRET measurements within single diffusing biomolecules using alternating-laser excitation. *Biophys. J.* **88**, 2939-53 (2005).
19. Vopel, T., Hengstenberg, C.S., Peulen, T.O., Ajaj, Y., Seidel, C.A.M., Herrmann, C. & Klare, J.P. Triphosphate induced dimerization of human guanylate binding protein 1 involves association of the C-terminal helices: a joint double electron-electron resonance and FRET study. *Biochemistry* **53**, 4590-600 (2014).
20. Felekyan, S., Kalinin, S., Sanabria, H., Valeri, A. & Seidel, C.A.M. Filtered FCS: species auto- and cross-correlation functions highlight binding and dynamics in biomolecules. *ChemPhysChem* **13**, 1036-53 (2012).
21. Kalinin, S., Sisamakias, E., Magennis, S.W., Felekyan, S. & Seidel, C.A.M. On the origin of broadening of single-molecule FRET efficiency distributions beyond shot noise limits. *J. Phys. Chem. B* **114**, 6197-206 (2010).
22. Song, B., Cho, J.H. & Raleigh, D.P. Ionic-strength-dependent effects in protein folding: analysis of rate equilibrium free-energy relationships and their interpretation. *Biochemistry* **46**, 14206-14 (2007).
23. Arya, G. & Schlick, T. A tale of tails: how histone tails mediate chromatin compaction in different salt and linker histone environments. *J. Phys. Chem. A* **113**, 4045-59 (2009).
24. Grigoryev, S.A., Arya, G., Correll, S., Woodcock, C.L. & Schlick, T. Evidence for heteromorphic chromatin fibers from analysis of nucleosome interactions. *Proc. Natl. Acad. Sci. U.S.A.* **106**, 13317-22 (2009).

Supplement E. Structural assemblies of the di- and oligomeric G-protein coupled receptor TGR5 in live cells: an MFIS-FRET and integrative modelling study

---

# SCIENTIFIC REPORTS



OPEN

## Structural assemblies of the di- and oligomeric G-protein coupled receptor TGR5 in live cells: an MFIS-FRET and integrative modelling study

Annemarie Greife<sup>1</sup>, Suren Felekyan<sup>1</sup>, Qijun Ma<sup>1</sup>, Christoph G. W. Gertzen<sup>2</sup>, Lina Spomer<sup>3</sup>, Mykola Dimura<sup>1</sup>, Thomas O. Peulen<sup>1</sup>, Christina Wöhler<sup>3</sup>, Dieter Häussinger<sup>3</sup>, Holger Gohlke<sup>2</sup>, Verena Keitel<sup>3</sup> & Claus A. M. Seidel<sup>1</sup>

Received: 14 July 2016

Accepted: 21 October 2016

Published: 11 November 2016

TGR5 is the first identified bile acid-sensing G-protein coupled receptor, which has emerged as a potential therapeutic target for metabolic disorders. So far, structural and multimerization properties are largely unknown for TGR5. We used a combined strategy applying cellular biology, Multiparameter Image Fluorescence Spectroscopy (MFIS) for quantitative FRET analysis, and integrative modelling to obtain structural information about dimerization and higher-order oligomerization assemblies of TGR5 wildtype (wt) and Y111 variants fused to fluorescent proteins. Residue 111 is located in transmembrane helix 3 within the highly conserved ERY motif. Co-immunoprecipitation and MFIS-FRET measurements with gradually increasing acceptor to donor concentrations showed that TGR5 wt forms higher-order oligomers, a process disrupted in TGR5 Y111A variants. From the concentration dependence of the MFIS-FRET data we conclude that higher-order oligomers – likely with a tetramer organization – are formed from dimers, the smallest unit suggested for TGR5 Y111A variants. Higher-order oligomers likely have a linear arrangement with interaction sites involving transmembrane helix 1 and helix 8 as well as transmembrane helix 5. The latter interaction is suggested to be disrupted by the Y111A mutation. The proposed model of TGR5 oligomer assembly broadens our view of possible oligomer patterns and affinities of class A GPCRs.

TGR5 (GPBAR-1, M-BAR) is the first identified G-protein coupled bile acid receptor<sup>1</sup> and is widely expressed in tissues, including liver, intestine, and the central and enteric nervous system<sup>2,3</sup>. Animal studies suggest that TGR5 activation leads to anti-inflammatory effects and influences energy homeostasis and glucose metabolism, thereby playing a role in the pathogenesis of obesity and diabetes<sup>4</sup>. Therefore, TGR5 has emerged as a potential therapeutic target to treat metabolic disorders. The most potent TGR5 bile acid agonist is tauro lithocholic acid (TLCA/TLC)<sup>1</sup>. In model cell lines it was shown that TGR5 couples to  $G\alpha_s$ , leading to stimulation of adenylate cyclase (AC) and formation of cyclic AMP (cAMP)<sup>1</sup>.

To date, no high-resolution crystal structure of TGR5 is available, and knowledge on TGR5 regulation and oligomerization is scarce. Homology models of TGR5 have been presented based on template structures of other seven transmembrane (7TM) domain receptors<sup>5–8</sup>. We previously reported that the amino acids 285–294 at the TGR5 C-terminus form an alpha-helical stretch important for plasma membrane localization and thus responsiveness to extracellular ligands<sup>9</sup>.

It is now well established that class C GPCRs form homo- and hetero-oligomers<sup>10</sup>. Oligomer formation of GPCRs affects a broad range of biological functions ranging from intracellular trafficking, protein turnover,

<sup>1</sup>Chair for Molecular Physical Chemistry, Heinrich Heine University Düsseldorf, 40225 Düsseldorf, Germany. <sup>2</sup>Institute for Pharmaceutical and Medicinal Chemistry, Heinrich Heine University Düsseldorf, 40225 Düsseldorf, Germany.

<sup>3</sup>Clinic for Gastroenterology, Hepatology and Infectious Diseases, Heinrich Heine University Düsseldorf, 40225 Düsseldorf, Germany. Correspondence and requests for materials should be addressed to H.G. (email: gohlke@hhu.de) or V.K. (email: verena.keitel@med.uni-duesseldorf.de) or C.A.M.S. (email: cseidel@hhu.de)

receptor function, signal enhancement or blockage upon ligand binding, G-protein independent signaling to internalization and receptor desensitization (for an overview see refs 11 and 12). However, for class A GPCRs such as TGR5, there are controversial data about the functional significance of homo- and hetero-oligomer formation<sup>10</sup>. Studies with rhodopsin<sup>13,14</sup>,  $\mu$ -opioid<sup>15</sup> and  $\beta_2$ -adrenergic receptors trapped as either monomers or dimers in nanodiscs demonstrated that monomers are functional and activate G-proteins; sometimes monomers are even more efficient than homo-dimers<sup>10</sup>. The same GPCRs were also shown to be stable as dimers or tetramers in living cells<sup>13–15</sup>. Many researchers proved at least dimerization by using biophysical approaches such as bioluminescence and Förster Resonance Energy Transfer techniques (BRET and FRET), as well as single molecule analysis<sup>16</sup> and atomic force microscopy in native disc membranes<sup>17</sup>. FRET describes the distance dependent energy transfer from an excited donor (D) to an acceptor (A) fluorophore and is used to study biomolecules in living cells which are fused to genetically encoded fluorescent proteins (FP) for convenience, although other molecular tags are also being used.

Several oligomer models exist for GPCRs, based on predictions of relative stabilities of dimer interfaces by molecular simulations and bioinformatics studies as well as wet-lab techniques. Extended biased molecular dynamics simulations suggested a model in which homo-dimers characterized by stable interactions involving transmembrane helix 1 (TM1) transiently interact with the other protomer via other helices such as TM4<sup>18</sup>. Bioinformatics studies predicted a role for transmembrane helices TM1 and TM4 to TM6 in dimerization; mutation of residues in this region disrupted dimerization<sup>19,20</sup>. AFM, crystallography and FRET studies of the  $\beta_1$ - and  $\beta_2$ -adrenergic receptors<sup>21</sup>, muscarinic receptor M<sub>3</sub><sup>22</sup>, rhodopsin<sup>17,23</sup> and the  $\mu$ -opioid receptor<sup>24</sup> suggested that oligomerization interfaces are most probably formed by TM1-TM2-helix(H)8 and TM4-TM5 or TM5-TM6. So far, several spatial arrangements of tetrameric GPCRs are discussed. For muscarinic receptor M<sub>3</sub> a rhombic arrangement of tetramers seems to be preferred rather than linear or squared ones<sup>22</sup>, whereas for rhodopsin either a more linear or squared arrangement are discussed<sup>10,17,22</sup>. We will discuss our data in respect to these findings to suggest TGR5 oligomerization models.

To perform protein-protein interaction studies in living cells without disturbance and with high spatial resolution, we applied Multiparameter Image Fluorescence Spectroscopy (MFIS). It combines fluorescence lifetime imaging and fluorescence anisotropy microscopy allowing a comprehensive analysis of the biophysical properties of homo- and heteromeric molecular complexes by FRET. MFIS is based on Multiparameter Fluorescence Detection (MFD), which has been established as a standard tool to investigate biomolecules in *in vitro* experiments<sup>25–27</sup>. Similar to MFD, MFIS-FRET records photons one by one, which allows for parallel recording of all fluorescence parameters (fundamental anisotropy, fluorescence lifetime, fluorescence intensity, time, excitation spectrum, fluorescence spectrum, fluorescence quantum yield, and distance between fluorophores) and additionally pixel/image information over time periods of hours with picosecond accuracy. The multidimensional analysis of correlated changes of several parameters measured by FRET, fluorescence fluctuation, fluorescence lifetime and anisotropy increases the robustness of the analysis significantly. The economic use of photon information even allows detection of fluorescent fusion proteins that are expressed at very low levels. We already showed the reliability of this technique for molecular interaction studies in different environments in human and plant cells<sup>28,29</sup>.

The main focus of this study is to use a combined strategy applying cellular biology, co-immunoprecipitation experiments, MFIS-FRET, molecular modelling and simulations to obtain information about oligomerization of TGR5 and the influence of a mutation in the TGR5 ERY domain on oligomerization.

## Results

**TGR5 forms homo-complexes but the complex affinity differs between TGR5 variants.** To characterize the complex formation of TGR5, we used three TGR5 variants, TGR5 wt, TGR5 Y111A, and TGR5 Y111F. The tyrosine residue at position 111 is part of the highly conserved ERY motif, which is important for GPCR function<sup>30</sup> and also predicted to be phosphorylated by EGFR using NetPhos<sup>31</sup>.

Immunofluorescence staining in MDCK and HEK293 cells as well as FACS analysis of transfected HEK293 cells demonstrated that all TGR5 variants were correctly localized at the plasma membrane in about 92% of the transfected cells (Fig. 1a,b). Furthermore, TGR5 responsiveness towards TLC was investigated using a cAMP-responsive luciferase assay<sup>9</sup>, where luciferase activity served as a measure for the second messenger cAMP following TGR5 activation. Forskolin (F) elevates cAMP independent of TGR5 and was used as positive control. Stimulation of TGR5 wt, TGR5 Y111A, or TGR5 Y111F with TLC led to a significant dose-dependent increase in luciferase activity in all three cases (Fig. 1c).

To analyze the interaction between TGR5 wt proteins or TGR5 wt with TGR5 Y111A, we performed Co-immunoprecipitation experiments (Co-IP). His-tagged TGR5 wt and either TGR5 wt-YFP or TGR5 Y111A-YFP proteins were expressed in HEK293 cells. Immunoprecipitation of His-tagged TGR5 wt was carried out with an anti-His antibody. The interaction of TGR5 proteins was visualized using an anti-GFP antibody, which recognized the TGR5 C-terminal YFP (Fig. 2a lane 3). Co-IP clearly showed that TGR5 forms homo-complexes. Compared to the interaction between TGR5 wt proteins, the interaction between TGR5 wt and TGR5 Y111A is significantly reduced by about 40% as measured by densitometry (Fig. 2b).

**Pixel-wise MFIS-FRET analysis demonstrates remarkable differences in FRET properties between TGR5 variants.** To further analyze differences in the complex formation found by Co-IP we used the genetically encoded fluorescent proteins GFP and mCherry attached to the C-terminus of TGR5 to measure FRET by MFIS-FRET in live cells. GFP and mCherry are commonly used as a FRET pair with a Förster radius  $R_0 = 52 \text{ \AA}$ <sup>32</sup>. As shown in Fig. 3a and SI Fig. 1a, all TGR5-GFP and TGR5-mCherry variants (wt, Y111A and Y111F) are strongly co-localized at the cell membrane of HEK293 cells. To visualize the heterogeneity within and between cells, the MFIS-FRET images were accurately analyzed in a pixel-wise manner to compute all relevant fluorescence parameters. During this procedure, photons are pixel-wise selected, grouped according to



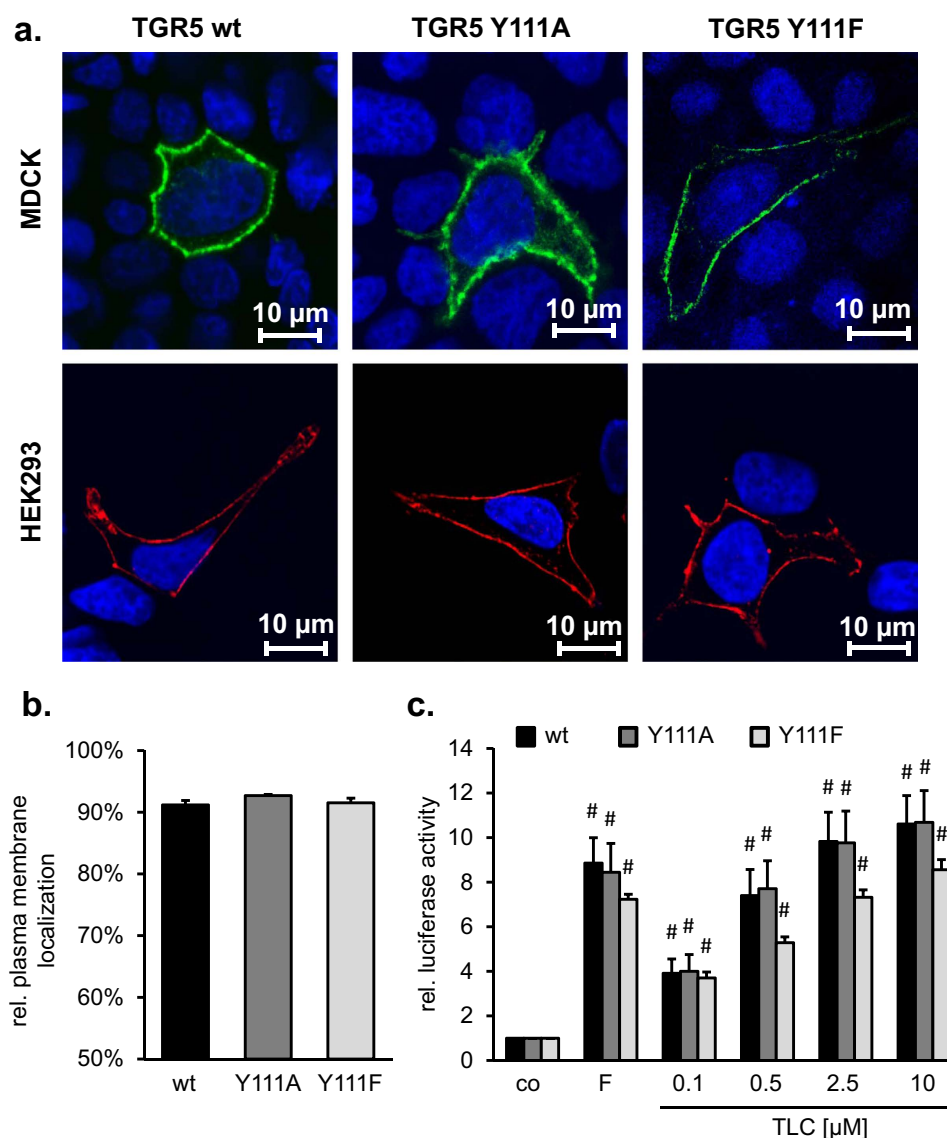


**Figure 1. Localization and functional analysis of TGR5 wt and Y111 variants.** (a) Localization of TGR5 by confocal laser scanning microscopy. MDCK cells (upper panels) were transiently transfected with FLAG-TGR5-YFP constructs. The YFP-fluorescence was detected in the plasma membrane for TGR5 wt as well as for the TGR5 Y111A and TGR5 Y111F variants. HEK293 cells (lower panels) were transiently transfected with TGR5-pcDNA constructs. TGR5 was stained using the RVL2 antibody (in red). TGR5 as well as the TGR5 Y111A and TGR5 Y111F variants were present in the plasma membrane. Nuclei were stained with Hoechst (blue). Bars = 10  $\mu\text{m}$ . (b) Relative quantification of TGR5 plasma membrane localization using flow cytometry. The amount of FLAG-TGR5-YFP within the plasma membrane corresponds to the amount of positive FLAG-tag labelling (=extracellular labelling) divided by the total amount of YFP-fluorescence. TGR5 Y111A and TGR5 Y111F were detected on the cell surface in 92.7% and 91.5% of the transfected cells, which was similar to the TGR5 wt with 91.2% ( $n = 3$  independent transfection experiments). (c) TGR5 receptor activity was determined using a cAMP responsive luciferase assay. HEK293 cells were co-transfected with TGR5 (pcDNA3.1+), a cAMP responsive luciferase reporter construct, and a Renilla expression vector. Luciferase activity served as a measure of the rise in intracellular cAMP following activation of TGR5. Forskolin (F, 10  $\mu\text{M}$ ) was used as TGR5-independent positive control. TGR5 Y111A and TGR5 Y111F did not affect receptor responsiveness to the bile acid taurothiocholate (TLC). Results (wt  $n = 8$ ; TGR5 Y111A  $n = 9$ ; TGR5 Y111F  $n = 6$ ) are expressed as mean + SEM. #Significantly different ( $p \leq 0.01$ ) from DMSO (co = control).

their properties, and selectively integrated to reduce noise (see SI methods). For a direct proof of FRET, it is necessary to show that the observed signal changes are due to differences in FRET efficiency  $E$  and not due to local

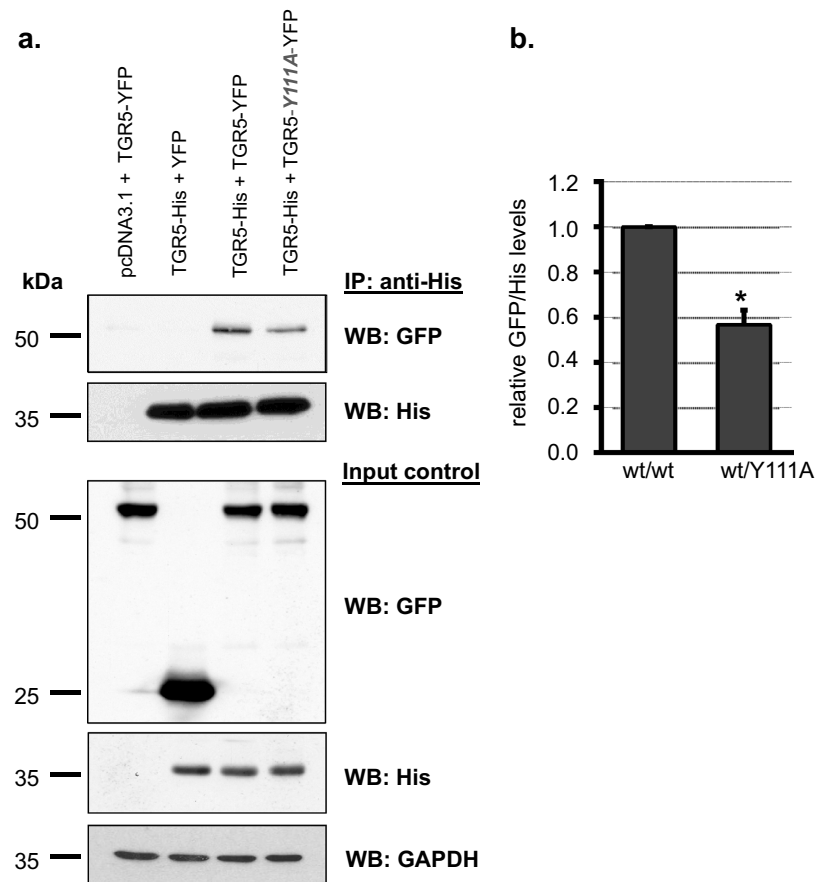


**Figure 2. Detection of TGR5 multimerization by co-immunoprecipitation.** (a) HEK293 cells were transiently transfected with pcDNA3.1 and TGR5-YFP, TGR5-His and pEYFP, TGR5-His and TGR5-YFP, or TGR5-His and TGR5 Y111A-YFP. Immunoprecipitation (IP) was carried out using an anti-His antibody. Equal volumes of the precipitate were deglycosylated with N-glycosidase-F, separated by SDS-PAGE, and blotted onto PVDF membranes. For Western blotting (WB) horseradish-peroxidase-coupled primary antibodies against His and GFP were used. TGR5-YFP was co-precipitated with TGR5-His. Mutation of tyrosine 111 to alanine in TGR5-YFP reduced the amount of co-precipitated variant receptor. Cell lysates (50  $\mu$ g total protein lysates) served as input controls and were separated by SDS-PAGE and proteins were blotted onto PVDF membranes. WB was carried out with horseradish-peroxidase-coupled primary antibodies against His and GFP or an antibody against glyceraldehyde-3-phosphate dehydrogenase (GAPDH). (b) Densitometric analysis of the anti-GFP and anti-His Western blots. Relative TGR5-TGR5 interaction was determined as relative GFP to His levels. Results are expressed as mean  $\pm$  SEM (n = 4), \*Significantly different from wt-His/wt-YFP interaction,  $p < 0.05$ .

changes of fluorophore properties or transfection artifacts. Thus, it is mandatory to analyze both FRET indicators: (i) FRET-induced donor quenching due to the presence of acceptor and (ii) the occurrence of FRET-sensitized acceptor fluorescence<sup>33</sup>.

A selection of these relevant FRET indicators is displayed in images of the TGR5 wt donor-only reference sample (Fig. 3b) and the FRET sample (Fig. 3c, first row): signal intensity  $S$  of the donor GFP in the green detection channel by donor excitation ( $S_{em,ex} = S_{G,G}$ ;  $\lambda_{ex} = 488$  nm), signal intensity of the directly excited acceptor mCherry in the yellow detection channel  $S_{Y,Y}$  ( $\lambda_{ex} = 559$  nm), and as a result of FRET the FRET-sensitized mCherry signal  $S_{Y,G}$ . Moreover, the quenching of the donor by FRET is judged by comparing the fluorescence-weighted average lifetimes of the donor in absence  $\langle \tau_{D(0)} \rangle_f$  and presence of acceptor  $\langle \tau_{D(A)} \rangle_f$ , respectively. If no FRET occurs, we only expect signals in the green channel. This is indeed observed for the reference measurement TGR5-GFP (Fig. 3b). Furthermore,  $\langle \tau_{D(0)} \rangle_f$  does not change, as expected.

Compared to cells transfected with the donor-only reference TGR5-GFP (Fig. 3b), the MFIS-FRET measurements of the FRET sample suggest the presence of FRET, as the FRET-sensitized acceptor signal was detectable (Fig. 3c,  $S_{Y,G}$  image), and  $\langle \tau_{D(A)} \rangle_f$  (Fig. 3c, lifetime image) is clearly reduced compared to  $\langle \tau_{D(0)} \rangle_f$ . The same observations were made also for TGR5 variants Y111A and Y111F (Fig. 3c and SI Fig. 1b).

The correlated FRET-specific change of both FRET-indicators is best visualized in a 2D-histogram plotting the ratio of the corrected fluorescence intensities of donor and acceptor ( $F_D/F_A$ ) (SI Table S1) versus donor

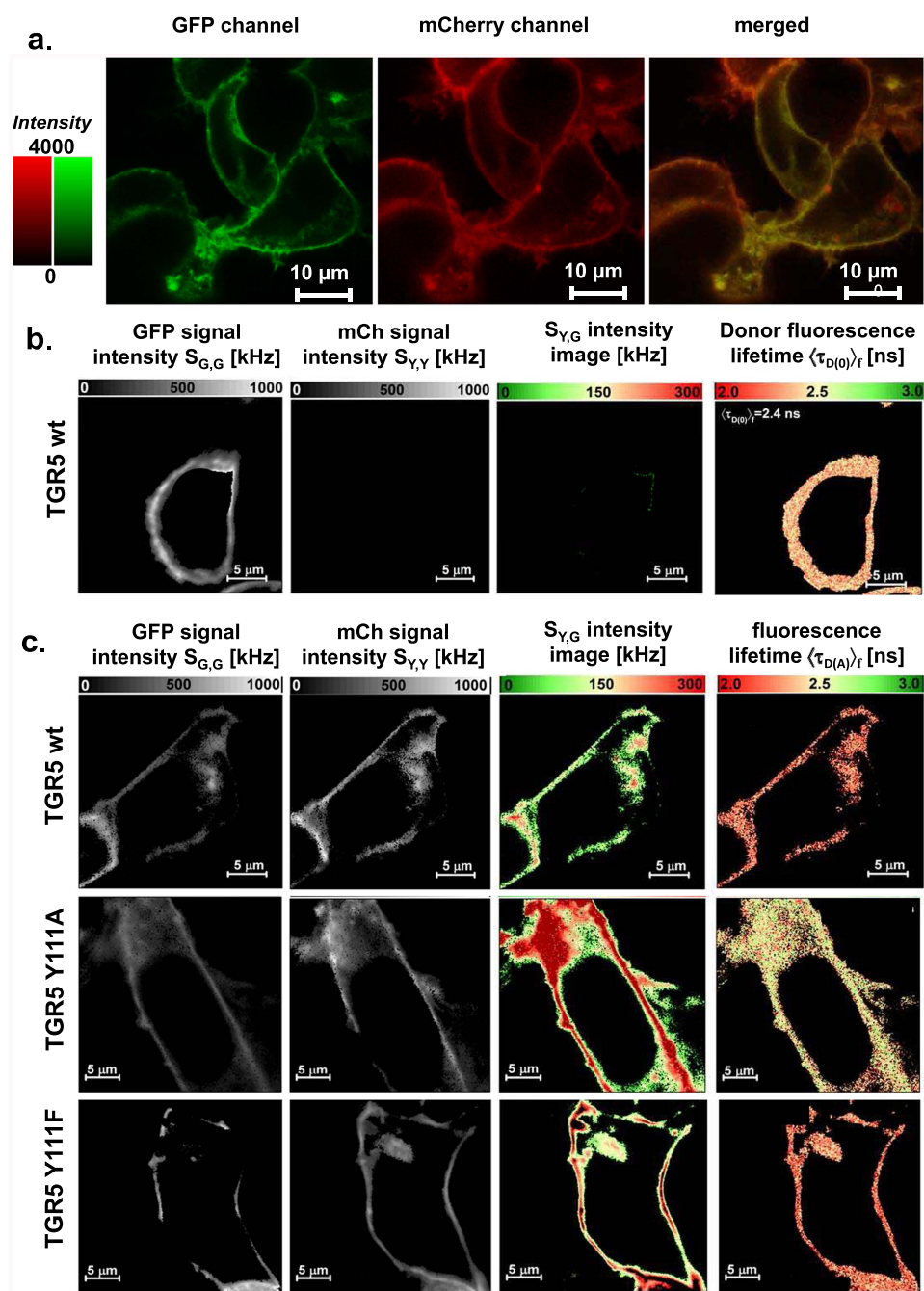


**Figure 3. Detection of TGR5 multimerization by pixel-wise MFIS-FRET analysis.** (a) HEK293 cells, transiently transfected with TGR5-GFP and TGR5-mCherry (transfection ratio 1:10), were imaged for co-localization of GFP and mCherry using sequential scanning and a scanning resolution of  $1024 \times 1024$  pixels. Each TGR5-GFP and TGR5-mCherry picture is shown in a false color saturation mode and then overlaid by using green and yellow intensity colors. TGR5 wt-GFP and TGR5 wt-mCherry are clearly co-localized at the cell membrane. Scale bar 10  $\mu\text{m}$ . The TGR5 Y111 variants are shown in SI Fig. 1. (b) MFIS analysis of TGR5 wt-GFP transfected HEK293 cells by comparing (from left to right) the signal intensity of the donor GFP ( $S_{G,G}$ ), signal intensity of the acceptor mCherry ( $S_{Y,Y}$ ), the detection of yellow mCherry photons after excitation of GFP ( $S_{Y,G}$ ; S: signal, Y: yellow emission, G: green excitation) as a result of FRET, and changes in the donor fluorescence lifetime  $\langle\tau_{D(0)}\rangle_f$ . For TGR5 wt-GFP only the donor signal but no acceptor signal is detected. The MFIS analysis of TGR5 Y111 variants is shown in SI Fig. 1. (c) The same parameters were used for TGR5 GFP/mCherry samples. The MFIS measurements show FRET ( $S_{Y,G}$  and changes in  $\langle\tau_{D(A)}\rangle_f$ ) in all TGR5 variants, which indicates at least homo-dimerization.

fluorescence lifetime ( $\langle\tau_D\rangle_f$ ), where the color scale corresponds to the pixel frequency with black being highest (Fig. 4a). The correlated shift of both indicators proves the molecular proximity of TGR5 wt and TGR5 Y111A/F monomers suggesting the presence of at least homo-dimers. To study whether also higher order oligomers form, we performed acceptor titration experiments with varying donor to acceptor transfection levels resulting in an anticipated 40-fold higher acceptor concentration in the last titration step. Here, the FRET-indicators ( $F_D/F_A$ ) and  $\langle\tau_{D(A)}\rangle_f$  allow for a qualitative interpretation of the measurements without applying a specific model. FRET senses the local proximity of binding partners within  $\sim 80$  Å. Hence, if small oligomers exist  $\langle\tau_{D(A)}\rangle_f$  the fluorescence intensity ratio ( $F_D/F_A$ ) will decrease with increasing acceptor concentration, whereas they do not change if only dimers exist. For TGR5 wt and TGR5 Y111F,  $\langle\tau_{D(A)}\rangle_f$  reduced significantly by 17% and 14%, respectively, whereas for TGR5 Y111A  $\langle\tau_{D(A)}\rangle_f$  reduced only by 7%. This behavior is also found in the fluorescence intensity ratios  $F_D/F_A$ . Here, significant transfection-level dependent FRET-changes are found for TGR5 wt and TGR5 Y111F, while only minor changes are found for TGR5 Y111A (Fig. 4a). The correlated shift of both FRET-indicators confirms that changes in FRET are indeed due to different concentrations. This suggests a significant formation of TGR5 wt and TGR5 Y111F oligomers but no or only few oligomers for TGR5 Y111A. We observed the distinct properties of TGR5 Y111A also via the fluorescence properties of the fused GFP, which was measured always as donor-only reference sample in the FRET experiments. While GFP fused to TGR5 wt and TGR5 Y111F had a fluorescence lifetime  $\langle\tau_{D(0)}\rangle_f = 2.4$  ns,  $\langle\tau_{D(0)}\rangle_f$  increased to 2.8 ns in the Y111A variant (SI Fig. 1b). In addition to the lifetime shift, we found a spectral red shift of 13 nm in the emission spectrum of TGR5 Y111A excited at 488 nm as compared to TGR5 wt (SI Fig. 1c).

### TGR5 wt and TGR5 Y111F form higher-order oligomers, whereas TGR5 Y111A forms primarily dimers.

The pixel-wise analysis of the fluorescence data by the fluorescence-averaged lifetime  $\langle\tau_D\rangle_f$  and the fluorescence intensity ratios ( $F_D/F_A$ ) does not allow us to resolve multiple species because the information contained in the recorded fluorescence decays is reduced to two numbers. Hence, sample heterogeneities that naturally arise in imaging cannot be resolved. To overcome this limitation, the fluorescence decays are analyzed directly by pixel-integrated analysis with high precision. Here, two fluorescence decay curves  $f(t)$  are compared: the decay of a FRET sample  $f_{D(A)}(t)$  and that of the donor-only reference  $f_{D(0)}(t)$  (Fig. 4b). This comparison is conveniently done by computing the time-resolved FRET-induced donor decay  $\varepsilon(t)$ , which is defined by the ratio of the two decays  $f_{D(A)}(t)/f_{D(0)}(t)$  as described in eq. (1). The supporting Figure 2 shows how  $\varepsilon(t)$  plots can be interpreted. The FRET-induced donor decay  $\varepsilon(t)$  allows visually identifying the population of all donor species. For instance, species with no-FRET give rise to a constant offset, while FRET-species cause decay. The slope of this decay in a semi-logarithmic plot as shown in Fig. 4b provides a measure of the rate constant of FRET, which increases with decreasing donor acceptor distance. A non-exponential decay indicates a mixture of distinct FRET species in which the donor and the acceptor are separated by different distances. The donor is quenched by all acceptors in its vicinity.

In Fig. 4b, the experimental fluorescence decays of all variants are displayed as  $\varepsilon(t)$  curves. Differences in the constant offset and the slope of the decays are clearly visible. For a better comparison of the slopes only the fraction of the FRET species was determined in a fit (equation (1), results see SI Table S2 and SI Figure 2) and displayed in Fig. 4b ( $\varepsilon_{FRET}(t)$  curves). At a low donor to acceptor transfection level (DA 1:40), the decay has two distinct regions: a steep slope and a shallow slope region. The steep slope corresponds to a high rate constant of FRET, while the shallow slope corresponds to a low rate constant of FRET. For TGR5 wt and TGR5 Y111F, the slope depends on the transfection ratio, while no such dependency is observed for TGR5 Y111A.

To quantify these changes we formally describe the fluorescence decays by two FRET-rate constants, which are for convenience given in units of apparent distances  $R_{DA,app}$  (equation (5) and SI Table S2, SI Fig. 3). For all TGR5 variants, this  $k_{FRET}$  fit resulted in a short apparent distance  $R_{DA,app-1}$  with a small fraction and a long apparent distance  $R_{DA,app-2}$  with a large fraction. As shown in Fig. 4c, in TGR5 wt and TGR5 Y111F both apparent distances  $R_{DA,app-1}$  and  $R_{DA,app-2}$  became shorter ( $R_{DA,app-1} = 40\text{--}20$  Å;  $R_{DA,app-2} = 75\text{--}50$  Å) with increasing acceptor concentration. Furthermore, the species fractions also changed: the short distance-fraction increased from 7% to 30% in an acceptor-dependent manner, leading at the same time to a strong reduction of the long distance-fraction from 39% to 12%. We quantified this change by computing the mean energy transfer efficiency  $E_{mean}$  (equation (7)) of the FRET active species, which markedly increased for TGR5 wt and TGR5 Y111F in contrast to TGR5 Y111A. Considering TGR5 wt and TGR5 Y111F, the FRET efficiency changes significantly with the acceptor concentration (Fig. 4c), while this is not the case for TGR5 Y111A. Hence, the concentration of oligomers is very low for TGR5 Y111A, so that these data are best suited to study the structural features of the dimer.

Of note, to rule out any overexpression artifacts, we additionally considered proximity FRET using the titration experiments. Due to the single-molecule sensitivity of our confocal microscope, we could perform FRET experiments with acceptor concentrations of  $\sim 1$   $\mu\text{M}$ , which corresponds to a molecule density of  $< 0.002$  acceptor molecules/ $\text{nm}^2$  (see SI Notes). At these concentrations proximity FRET is negligible ( $E < 0.1$ )<sup>34</sup>.

**The TGR5 ligand TC has no influence on the oligomerization state of TGR5.** It has been shown that activation by ligands can influence GPCR oligomerization<sup>10</sup>. To determine the ligand effect on TGR5, we tested whether taurocholate (TC) stimulation, a bile acid less cytotoxic than TLC in live cells, affects oligomerization of TGR5 wt, TGR5 Y111A, and TGR5 Y111F. A time series analysis was designed, where MFIS-FRET was measured in three cells before, directly after as well as 10 and 20 min after addition of 10  $\mu\text{M}$  water soluble TC. We monitored FRET via the species-averaged donor fluorescence lifetime  $\langle\tau_{D(A)}\rangle_x$ . As shown in Fig. 5,  $\langle\tau_{D(A)}\rangle_x$  was neither changed in donor samples (TGR5 GFP) nor in FRET samples (TGR5 GFP/mCherry). A more detailed FRET analysis of the time series experiments showed that neither the distances nor the species fractions changed markedly due to addition of TC (SI Fig. 4). These results indicate that TC does not influence the oligomerization state of TGR5 variants.

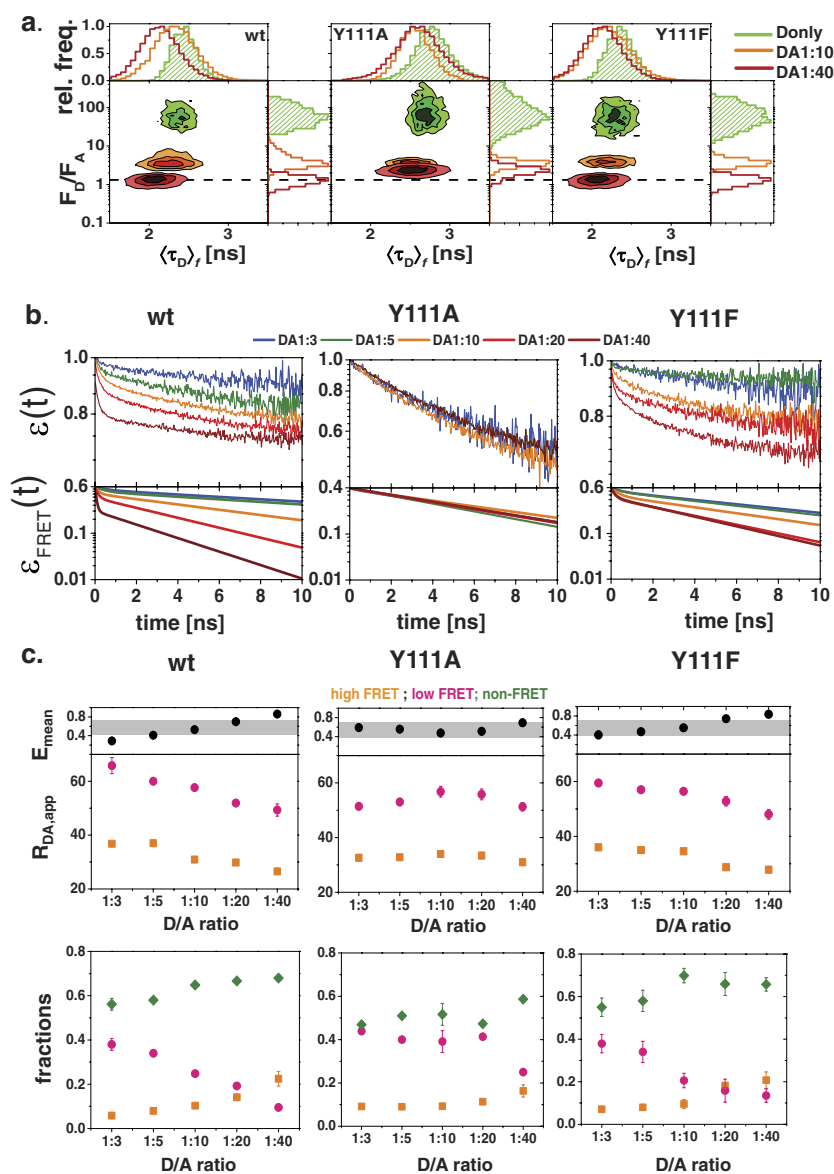


**Figure 4. Pixel-integrated analyses of TGR5 FRET properties.** (a) The MFIS-FRET 2D plots are generated with Origin 8.6 and show an overlay of two histograms of the (background, crosstalk and spectral shift) corrected fluorescence intensity ratio ( $F_D/F_A$ ) vs.  $\langle \tau_{D(A)} \rangle_f$ ; TGR5 wt and TGR5 Y111F donors (in green) showed a  $\langle \tau_{D(0)} \rangle_f = 2.4$  ns and a high green to yellow signal. With increasing amounts of the acceptor mCherry (orange and red islands) both parameters were strongly reduced in TGR5 wt and TGR5 Y111F, but not in TGR5 Y111A. All samples were corrected for relative brightness, relative direct mCherry excitation in the green detection channel, spectral shift of the Y111A variant, and background in the green and yellow channels (see methods 5.10 eqs 2 and 3). (b) FRET-induced donor quenching  $\varepsilon(t)$  derived from sub-ensemble fluorescence measurements on TGR5 variants at different donor-to-acceptor ratios. The time-axis measures the time between excitation and detection of donor photons. The upper row shows the experimental data. In the bottom row the offset (Non-FRET fraction) is subtracted and the result is termed  $\varepsilon_{FRET}(t)$ . In TGR5 wt and TGR5 Y111F, FRET clearly increased in a mCherry-dependent manner, whereas in TGR5 Y111A all  $\varepsilon_{FRET}(t)$  curves behaved similar. (c) FRET-decays from sub-ensemble analysis at different donor-to-acceptor (D/A) ratios were fitted with a two- $k_{FRET}$  fit to obtain two apparent distances  $R_{DA,1}$  and  $R_{DA,2}$  (upper row) with their corresponding FRET fractions (lower row) and to calculate the mean efficiency  $E_{mean}$ .  $E_{mean}$  increased in an acceptor-dependent manner in TGR5 wt and TGR5 Y111F, whereas  $E_{mean}$  changed only slightly in TGR5 Y111A. These changes in  $E_{mean}$  correlate with a reduction of both apparent distances  $R_{DA,1}$  and  $R_{DA,2}$  in TGR5 wt and TGR5 Y111F: In the lower row, the  $R_{DA,1}$  fractions increase, whereas the  $R_{DA,2}$  fractions decrease in an acceptor-dependent manner. Orange:  $R_{DA,1}$  and  $R_{DA,1}$  fraction, pink:  $R_{DA,2}$  and  $R_{DA,2}$  fraction, green: non-FRET fraction, the grey bar in  $E_{mean}$  represents average  $E_{mean}$  for TGR5 Y111A.



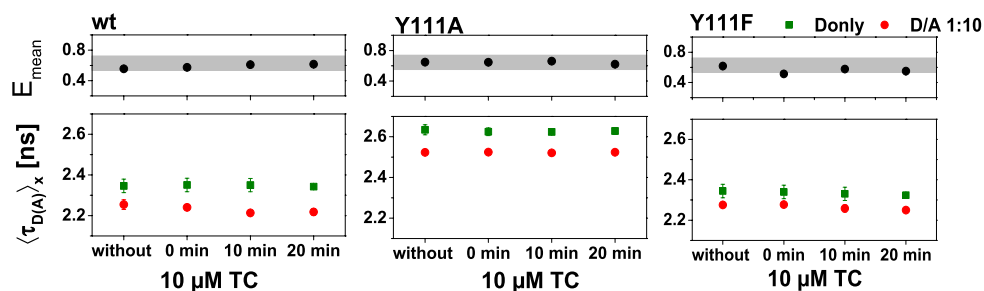


**Figure 5. Influence on FRET after treatment with TGR5 ligand TC.** HEK293 cells were transiently transfected with TGR5-GFP alone (Only, green) or with TGR5-GFP and TGR5-mCherry at a ratio D/A 1:10 (DA, red). For time-series analysis three cells were selected using the Olympus time laps function, and MFIS-FRET measurements were taken before addition of  $10 \mu\text{M}$  TC (without), immediately after addition of TC ( $t=0$ ), and after 10 min and 20 min, respectively. The species-averaged donor fluorescence lifetime  $\langle \tau_{D(A)} \rangle_x$  was determined and plotted against time, as well as the mean efficiency  $E_{\text{mean}}$  which was calculated from data shown in SI Fig. 4. Each point represents the average of nine cells. No lifetime changes were observed for Only samples and DA samples in the presence of the agonist TC.

**Structural arrangement of homo-di- and oligomeric TGR5.** Next, we analysed which structural features of the TGR5 complexes can be extracted from the observed FRET parameters. Previous studies by Sindbert *et al.*<sup>35</sup> and Kalinin *et al.*<sup>36</sup> have shown that the extent of FRET between two flexibly linked fluorescent probes can be accurately predicted by calculating the distance distribution between all fluorophore positions that are sterically accessible (accessible volume, AV) for a given structural model. As both fused fluorescent proteins have flexible connecting amino acid residues (SI Table 3) creating a large, widely distributed structural ensemble<sup>37</sup>, computer simulations generating probe distributions can be readily applied to study TGR5 assemblies by FRET.

**Simulation of the expected FRET properties.** The structural model of the TGR5 monomer required for FRET modelling was generated by performing multi-template homology modelling based on seven template structures of related class A GPCRs (see SI methods “structural models of TGR5 dimers and tetramers” and ref. 38). As shown in Fig. 6a, we generated three possible homo-dimerization models with interfaces involving TM1-TM2-H8 (for convenience abbreviated as 1/8 dimer), TM4-TM5 (4/5 dimer), or TM5-TM6 (5/6 dimer). To assure accuracy, we compared two procedures for calculating the distance distributions between fluorophore positions for the TGR5 models: (i) Explicit linker simulations based on explicit peptide linker/GFP-MD-simulations followed by calculations of conformational free energies to weight each linker-GFP configuration in the presence of a TGR5 dimer and an implicit membrane bilayer (SI Fig. 5, see also SI methods). This thermodynamic ensemble (TE)-approach is expected to be more accurate than the following procedure but the computations are time consuming. (ii) Implicit linker simulations by AV-calculations weighted by a Gaussian chain distribution, so that entropic effects and geometric factors in terms of steric exclusion effects by the TGR5 oligomer and the membrane are taken into account (SI methods). The AV approach has to be calibrated to be accurate but it has the advantage that the computation is very fast.

The TE-approach results in a hemispherical arrangement of GFP on the cytoplasmic side, which is centred on the attachment point at helix 8 of TGR5 (SI Fig. 5) and each linker/GFP configuration is Boltzmann weighted according to the conformational free energy (SI Fig. 5). Configurations of lower probability are found when GFP approaches TGR5 due to energetically unfavourable contacts. The Boltzmann-weighted distribution of distances between the linker N-terminus and the GFP fluorophore shows a peak distance of about 45 Å, while the minimal distance is about 35 Å. This is due to the fact that the fluorophore is located 20 Å away from the linker C-terminus inside the  $\beta$ -barrel structure of GFP and thus is inaccessible to the linker’s N-terminus. The peak linker length (without considering GFP) is about 25 Å. This is about 5 Å longer than the average radius of gyration of a Gaussian chain polypeptide of the same number of residues (33 amino acids yielding  $3.5 \text{ \AA} * 33^{0.5} = 20 \text{ \AA}^{39}$ ). The deviation shows that the linker with GFP does not exactly behave like a ‘perfect’ Gaussian chain. The Boltzmann-weighted fluorophore position map (Fig. 6c, SI Fig. 5) was used for inter-dye distance distribution calculations.

The implicit model (Fig. 6c) was tested as an alternative to account for dye-linker diffusion. The accessible volume (AV) approach was used to estimate all possible dye positions within the linker length from the attachment point without steric clashes with the macromolecular surfaces. The fluorophores are approximated by a sphere with a defined radius, which is estimated from the physical dimensions of the molecules (left panel). The connecting linker is modelled as a flexible cylinder. To take entropic effects into account, the linker was assumed to obey Gaussian chain behaviour. Thus, the fluorophore distribution density gradually drops as the distance from the attachment point increases. For the implicit model, the 55 amino acid residues (SI methods and SI Table S3) between the structured parts of the TGR5 C-terminus and GFP were considered as a flexible sequence with unknown structure with a length of  $\sim 203.5 \text{ \AA}$  at maximal extension.

Both methods for linker simulations gave very similar results. The (1/8) dimerization model shows a distance distribution between fluorophore positions between 25–150 Å with the highest probability at 55 Å and 60 Å for the explicit and implicit linker models, respectively. The distances between fluorophores in models (4/5) and (5/6)

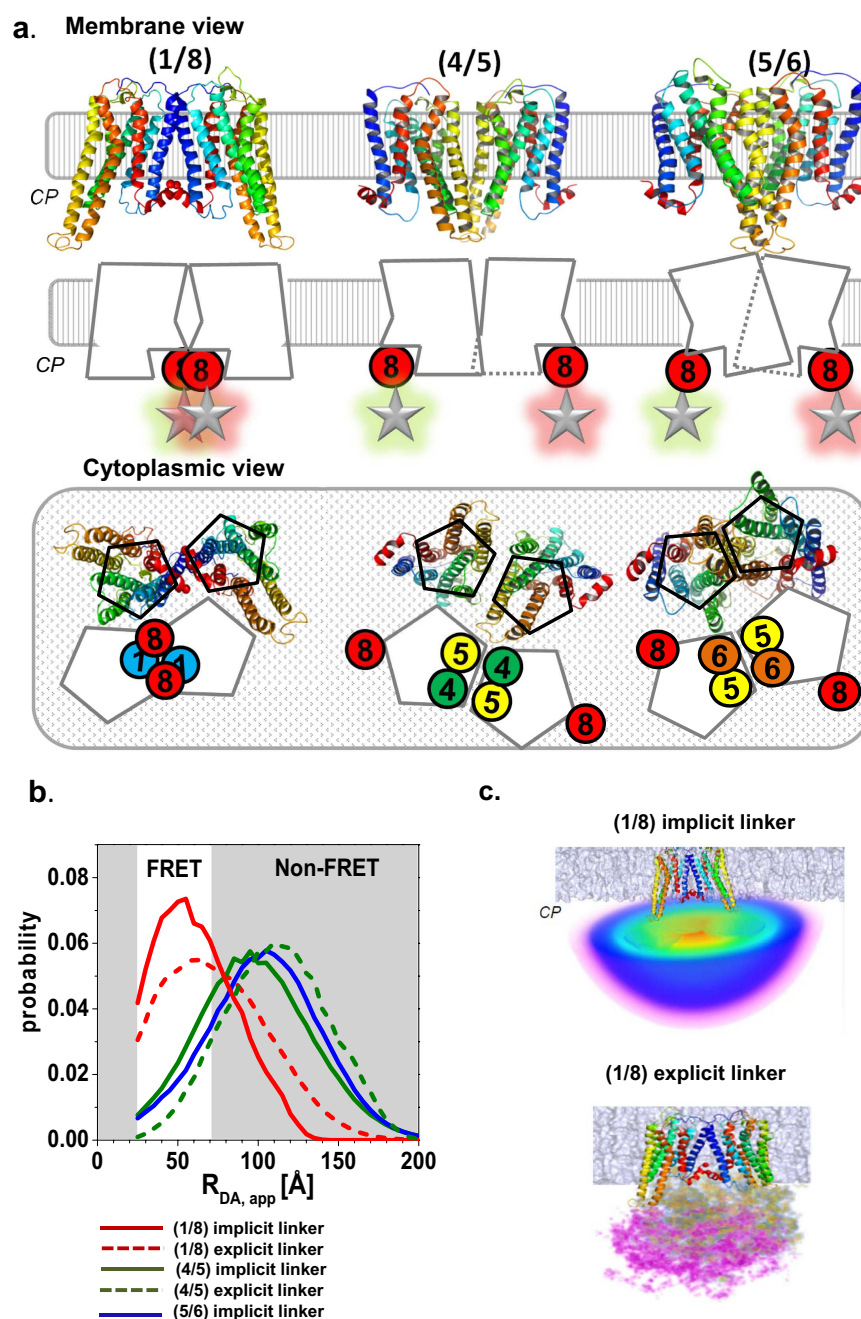


**Figure 6. Homo-dimerization models and their distance distributions.** (a) Homo-dimerization models with the following interfaces from left to right: (1/8), (4/5) and (5/6). TGR5 monomer helices are rainbow-coloured starting with TM1 in blue to H8 in red. Top row: membrane view of the interface models in cartoon and schematic representation (circles representing TMs). Bottom row: cytoplasmic view of the interface models. The fluorescent proteins, which are attached to the cytoplasmic H8, are presented as stars glowing in green for donor (eGFP) and red for acceptor (mCherry). Abbreviation: CP = cytoplasm. (b) Distance probability distributions calculated with an explicit (dotted line) and implicit linker (solid line) for the homo-dimerization models (1/8) (red), (4/5) (green), and (5/6) (blue). The non-FRET area is shaded in grey. (c) Positional distributions of the fluorescent probes for the TGR5 (1/8) interface. The implicit linker simulations yield weighted AVs for both fluorophores which overlap and create one huge sphere (top panel). The probability of the allowed fluorophore positions decrease from red, yellow over green, blue to pink. The explicit linker simulations yield a thermodynamic ensemble (bottom panel) depicted as an orange-blue and purple volume map, respectively. The ensembles also overlap to a high degree. Higher saturation represents higher fluorophore position occupancy. Both methods gave very similar results.

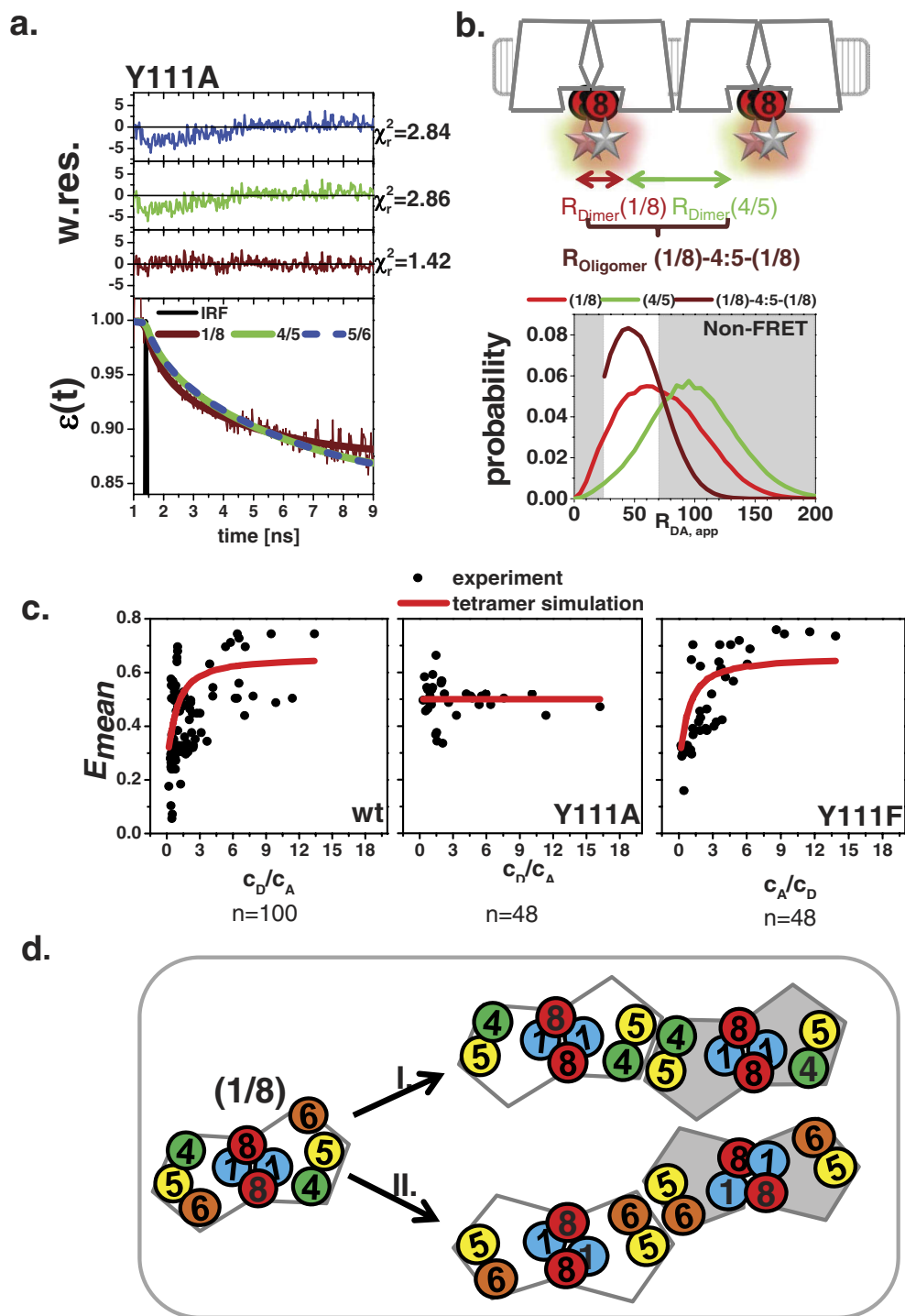


**Figure 7. TGR5 oligomerization models.** (a) Fit of the FRET-induced donor quenching curve  $\varepsilon(t)$  on TGR5 Y111A with two species normalized to unity: (i) Dimer (fraction  $x_{\text{Dimer}}$ ) with the complete distance distribution (FRET and Non-FRET) of the corresponding dimer models (Fig. 6b) and (ii) donor only/ FRET inactive molecules. Only the distance distribution of the 1/8 dimer model gives a satisfactory fit as judged by the weighted residuals and the reduced chi squared  $\chi_r^2$ . Fit results of TGR5 Y111A for  $x_{\text{Dimer}}$ : 1/8 dimer: 0.27; 4/5 dimer: 0.59; 5/6 dimer: 0.73. (b) The schematic presentation shows the two individual apparent distances from the interfaces (1/8) and (4/5). Both  $R_{\text{Dimer}}$  can be converted into FRET rates. In an oligomer the two FRET rates add up and have to be convolved to calculate the new apparent distance  $R_{\text{oligomer}}$ . The resulting distance distribution is similar to the dimer (1/8). (c) Dependence of the TGR5 oligomerization monitored by the FRET efficiency (experiment (black) and modeled (red)) on the donor acceptor ratio  $c_A/c_D$ . In the cells the donor,



acceptor and total TGR5 concentration (including inactive mCherry (30%)) varied between 0.25–6.3  $\mu\text{M}$ , 0.1–5.0  $\mu\text{M}$  and 0.5–13  $\mu\text{M}$ , respectively. The dimer is composed of a donor acceptor distance of 45 Å, and the tetramer is composed out of two dimers separated by 100 Å. The modeled dissociation constant of the dimer  $K_{D1}$  was fixed to 10 nM for all TGR5 variants. The values for the modeled dissociation constants of the oligomer (Tetramer) were:  $K_{D2}(\text{TGR5 wt}) = 70 \text{ nM}$ ,  $K_{D2}(\text{TGR5 Y111F}) = 200 \text{ nM}$ ,  $K_{D2}(\text{TGR5 Y111A}) = 2000 \text{ nM}$ . (d) Two possible oligomers are reasonable I. ((1/8)-4:5-(1/8)) and II. (1/8)-5:6-(1/8): TGR5 monomers form a dimer with the contact sites in TM1 (blue circle) and H8 (red circle). H8 is attached to fluorescent fusion proteins (GFP and mCherry). In a tetramer contact sites in TM4 (green circle) and TM5 (yellow) (I) or TM5 (yellow) and TM6 (orange) (II) create a second interface promoting a linear oligomer organization.

are similarly distributed with the highest probability at around 95–110 Å; i.e. the distance of most conformers is too large for significant FRET. Implicit and explicit linker models thus show very similar inter-dye distance distributions for all dimer models: The implicit model shows a 5 Å shift towards the higher length for the (1/8) dimer and a 15 Å shift towards the shorter length for the (4/5) dimer model.

Finally we can conclude that both linker simulation techniques predicted FRET and should distinguish a 1/8 dimer from 4/5 dimer and 5/6 dimer, respectively, because the FRET probe distance distributions have a characteristic peak at short distances (Fig. 6b). However, the FRET probe distance distributions of the two dimers involving TM5 are expected to be not distinguishable in our FRET experiments (Fig. 6b).

**In the first step of oligomerization contact sites in TM1 and helix 8 are involved.** The shape of the distance distribution (determined by our linker simulation) and the concentration-dependent change in  $E_{mean}$  (using MFIS-FRET titration experiments) should allow us to distinguish (i) oligomerization interfaces and (ii) oligomerization pattern.

The concentration-independent FRET efficiency (Fig. 4) of the TGR5 Y111A variant suggests the preferential presence of homo-dimers. Therefore, it is a perfect variant to test which of our distance probe distributions describes the FRET-induced donor quenching curve  $\varepsilon(t)$  best. Figure 7a shows the fits using a model with the complete distance distribution (FRET and Non-FRET) of the corresponding dimer models (Fig. 6b, SI Table 4). Only the distance distribution of the 1/8 dimer model gives a statistically satisfactory fit as judged by the weighted residuals (*w. res.*) and the smallest  $\chi_r^2$ . Hence, TM1 and helix 8 most likely form the primary oligomerization interface.

From the same titration experiments, we conclude that TGR5 wt and TGR5 Y111F are able to form higher-order oligomers because of the concentration-dependent increase in FRET efficiency (Fig. 4c). This finding implies that at least a second interface should exist for TGR5 homo-oligomer formation. As shown in Fig. 6b, the average apparent distances between fluorescent proteins attached to TGR5 helix 8 (without a coupled G-protein) were 120 Å for the (4/5) dimer model and 103 Å for (5/6) model, respectively, and the effective apparent oligomer distance for both patterns is approximately 49 Å (brown curve in Fig. 7b) due to the presence of multiple acceptors. We applied a dimer/tetramer simulation to our MFIS data to estimate the two corresponding association constants (Fig. 7c, SI Fig. 6) by analysing the dependence of the mean FRET efficiency  $E_{mean}$  on the ratio of donor to acceptor concentration ( $c_D/c_A$ ). Moreover, the spread in the FRET efficiencies observed in Fig. 7c is also caused by the distinct protein concentrations in the cell and is taken into account in the simulations (SI Fig. 6a–c). For TGR5 wt and Y111F ( $K_D$  in 100 nM range), the simulations indicate that almost all dimers form tetramers, whereas TGR5 Y111A forms predominantly dimers ( $K_D$  in  $\mu\text{M}$  range).

## Discussion

We pursued a combined strategy applying cellular biology, MFIS-FRET, molecular modelling and simulations with a focus on dimerization and higher-order oligomerization of TGR5. We studied the influence of a mutation in the TGR5 ERY motif (TGR5 Y111A and Y111F) located in the transmembrane helix 3 (TM3) on oligomerization.

For our oligomerization studies we replaced the tyrosine residue in the highly conserved “D/ERY” motif in TM 3 and belongs to one of two clusters important for structural stability in GPCRs<sup>40</sup>. Mutation studies in Rhodopsin showed that the tyrosine (Y) mutation alone did not or only marginally affect receptor function<sup>41</sup> regarding receptor expression, G-protein binding and ligand affinity in contrast to the residues D/ER. Consistent with literature results<sup>41</sup>, the TGR5 Y111 variants, Y111A and Y111F, were normally localized at the plasma membrane and activated by both bile acid agonists TLC and TC to a level comparable to TGR5 wt. These findings implicated no obvious impaired ligand binding affinities or G-protein coupling. However, we observed significant differences in oligomer formation between Y111A and Y111F as assessed by Co-IP experiments and FRET measurements in live cells.

As the overall protein concentrations are very low (1–7  $\mu\text{M}$ ), we can rule out any overexpression artifacts due to proximity FRET (see SI notes). Therefore our MFIS-FRET titration data are best described with models assuming formation of the 1/8 dimer as the first step in oligomerization (Fig. 7a). In the second step, we suggest that TM5 (Fig. 7d) is involved as known from other oligomerization models of class A GPCRs<sup>15,19,20</sup>. According structural models were as templates for predicting the distance distributions in Fig. 7b. As shown in Fig. 7d and SI Fig. 7, oligomer array configurations<sup>15,19,20</sup> either could have a row or a rhomboid tetramer organization. One might assume that TGR5 oligomers most likely resemble in a one-dimensional row-like array mediated by a single oligomerization interface, because a single mutation in the ERY motif, Y111A in TM3, affects the association significantly (factor 10).

As shown in Fig. 8, the Y111 residue can interact with TM4-TM5 or TM5-TM6 dependent on the oligomerization. In both cases, the potential interaction sites involving TM5 can be affected during oligomerization. This

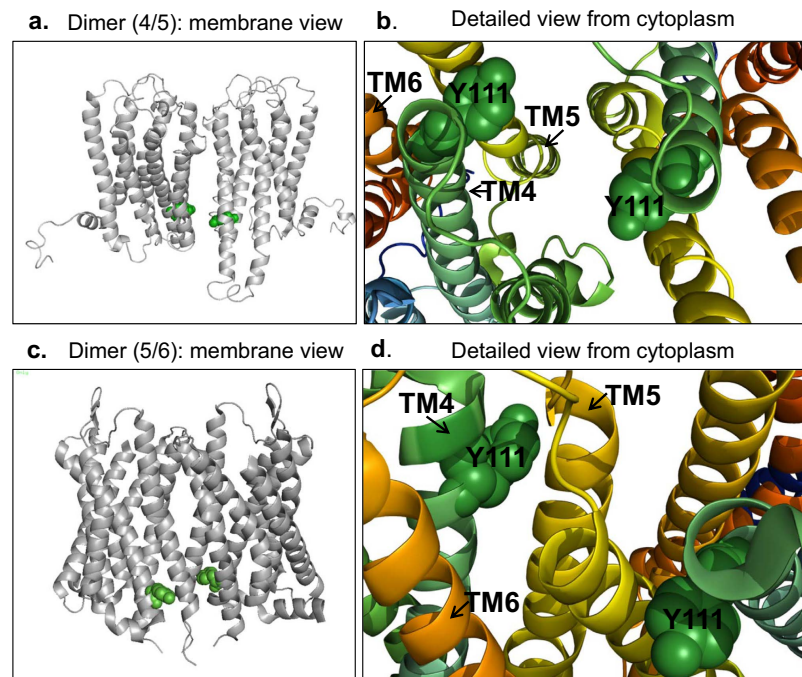


**Figure 8. Influence of the Y111 residue on oligomerization.** (a,c) The dimerization models of the (4/5) and (5/6) interface are displayed as a grey colored cartoon viewed from the membrane. Residue Y111 located in TM3 is depicted as a green sphere in each TGR5 monomer. (b,d) Blow-up of the region around residue Y111 to show possible interactions between Y111 from one TGR5 molecule with residues in TM4 (green), TM5 (yellow) and TM6 (orange) in a second TGR5 molecule.

observation is supported by two crystal structures: In the (4/5) model, as shown in CXCR4 (PDB ID: 3ODU), a charge-assisted interaction between Y111 and R146 (TM4) is possible; likewise an interaction is possible in the (5/6) model between Y111 and R280 (helix 8), as shown in the  $\mu$ -opioid receptor (PDB ID: 4DK2).

It was reported that GPCR oligomerization could be affected by ligand binding<sup>10</sup>, therefore we addressed this question in a time-series FRET analysis by ligand stimulation with TC. From simulation experiments, we expect that after G-protein binding the average apparent distances between TGR5-GFP and TGR5-mCherry get longer. Effective oligomers distributions with and without G-protein are indistinguishable, because a distance distribution difference of less than 8 Å is smaller than the anticipated accuracy of the models (see SI Table 5). In fact, the MFIS-FRET measurements showed no change in FRET properties after TC treatment, an observation that is also supported by literature<sup>22</sup>. As an indicator of G-protein binding, we successfully proved cAMP increase after ligand treatment in all TGR5 variants, which has also been shown recently<sup>9,42,43</sup>. We have no evidence that TGR5 oligomerization is affected by ligand treatment and subsequent G-protein coupling.

It is not too surprising that G protein activation does not change when reducing TGR5 higher oligomer formation, because rhodopsin and  $\beta$ -AR receptors in a monomeric, dimeric and oligomeric state, respectively, are capable to activate the respective G-protein<sup>11,14,44,45</sup>. Moreover, as described by Scarselli *et al.*<sup>46</sup>, PALM experiments using a class A GPCR suggested that oligomerization remains unchanged by the addition of the agonist. This is in line with our findings for our class A receptor TGR5 and the bile acid ligands. While the function of higher-order oligomers for most GPCRs is still unknown, identification of dimer/oligomer interfaces will allow for targeted disruption of dimer/oligomer formation and thus elucidation of the biological relevance of these complexes. This has just been demonstrated for rhodopsin where disruption of dimerization with small peptides decreased receptor stability<sup>44</sup>. We recently showed that the loss of  $\alpha$ -helicity in the TGR5 C-terminus, which constitutes the major interaction surface in the 1/8 interface, severely impairs TGR5 membrane localization and activity<sup>9</sup>. One can thus speculate that this influence on membrane localization and activity results from a distorted TGR5 dimerization in the ER. Additionally, the design of bivalent ligands targeting a homodimer can reduce off-target effects caused by the transactivation or inhibition of GPCRs in heterodimers<sup>47</sup>. Knowledge of the primary dimerization interface of a GPCR can guide the development of such bivalent ligands. The discovery that TGR5 forms higher order oligomers and that Y111 is important for this process thus is the first step for deciphering and modulating the functional relevance of TGR5 oligomerization.

To conclude, TGR5 wt forms homo-oligomers. Dimerization involves interaction contact sites in TM1 and helix 8, while its oligomerisation additionally involves TM5. Both modelled patterns, (1/8)-5:6-(1/8) and (1/8)-4:5-(1/8), are currently possible with Y111 forming charge-assisted and/or polar interactions with residues within the mentioned interfaces.

## Methods

**Multiparameter Fluorescence imaging spectroscopy (MFIS).** All measurements in live cells were performed on an inverted confocal laser scanning microscope (FV1000 Olympus, Hamburg, Germany) additionally equipped with a single photon counting device with picosecond time-resolution (Hydra Harp 400, PicoQuant, Berlin, Germany) with home built extensions for MFD as described in<sup>28</sup>. Using a 60x water immersion objective (Olympus UPlanSApo NA 1.2) the sample was excited with selected wavelengths (GFP at 488 nm with 400 nW, mCherry at 559 nm with 650 nW) of a NCH white light laser with a pulse-repetition rate of 40 MHz. The emitted light was collected and separated into its parallel and perpendicular polarization and into its green and red component (beam splitter 595DCLX, AHF, Germany). GFP fluorescence was then detected by single photon avalanche detectors (PDM50-CTC, Micro Photon Devices, Bolzano, Italy) in a narrow range of its emission spectrum (bandpass filter: BS 520/35, AHF, Tübingen, Germany). mCherry fluorescence was detected by cooled hybrid detectors (HPMC-100-40, Becker&Hickl, Berlin, Germany, with custom designed cooling), of which the detection wavelength range was set by the bandpass filters HC 607/70 (AHF). MFIS images were generated via raster-scanning the sample in a continuously moving beam manner. Images were taken with 20 μs pixel dwell time and a resolution of 103 nm per pixel. With 488 nm excitation, series of 40 frames were merged into one image; with 559 nm excitation, series of 20 frames were merged together. Images were further analyzed using custom-designed software available from our homepage (<http://www.mpc.hhu.de/software.html>). Description of sample preparation and microscope calibration can be found in the SI methods 1 and 2.

**Pixel-integrated, time-resolved  $\varepsilon(t)$  illustration.** To identify appropriate pixel in the cells for further pixel-integrated analysis, we computed all fluorescence parameters for each pixel and selected the pixels in 2D-histograms of several FRET indicators (see SI methods 2 pixel-wise analysis). A pixel population with homogeneous properties was selected and then integrated for subsequent pixel-integrated sub-ensemble analysis. The time-dependent FRET parameter  $\varepsilon(t)$  contains information on the underlying FRET-rate distribution and is proportional to the probability that FRET occurs at a certain time. After pixel selection,  $\varepsilon(t)$  was plotted for direct visualization of molecular species with different FRET efficiencies in sub-ensemble data.  $\varepsilon(t)$  is calculated as the ratio of normalized fluorescence decays of the FRET sample  $f_{D(A)}(t)$  and donor-only sample,  $f_{D(0)}(t)$  (see eqs 3–4).

$$\varepsilon(t) = \frac{f_{D(A)}(t)}{f_{D(0)}(t)} \quad (1)$$

$$\text{With } f_{D(A)}(t) = \varepsilon(t) \cdot f_{D(0)}(t) \quad (2)$$

$\varepsilon(t)$  is the probability density function of the occurring FRET governed by FRET rate constant(s),  $k_{FRET}$ . The decaying part of  $\varepsilon(t)$  represents the features of FRET: high- or low-FRET can be directly read out from the decay slope. The amplitude of the decaying part indicates the FRET-active species fraction,  $x_{FRET}$ . Accordingly, the offset of  $\varepsilon(t)$  is the FRET-inactive fraction,  $(1 - x_{FRET})$ .

**Pixel-integrated MFIS-FRET analysis using  $k_{FRET}$  models.** To determine FRET parameters from pixel-integrated, sub-ensemble data the reference samples were fitted by a multi-exponential relaxation model accounting for a multi-exponential fluorescence decay of the donor in the absence of FRET:

$$f_{D(0)}(t) = \sum_m x_D^{(m)} \cdot \exp(-t \cdot k_D^{(m)}) \quad (3)$$

in which  $m=3$  considers that FPs in living cells usually show at least a bi-exponential characteristic<sup>32</sup>. Fit parameters in donor decay include three normalized pre-exponential factors  $x_D^{(m)}$  ( $\sum x_D^{(m)} = 1$ ) and three decay rate constants  $k_D^{(m)}$ , which are the reciprocals of fluorescence lifetimes. The quenched donor decay  $f_{D(A)}(t)$  is given by:

$$f_{D(A)}(t) = \sum_m x_D^{(m)} \cdot \exp(-t \cdot (k_D^{(m)} + k_{FRET})) \quad (4)$$

and  $k_{FRET}$  is the FRET rate constant. The fitted parameters in the  $1 - k_{FRET}$  model are  $x_{FRET}$  and  $k_{FRET}$ .

From the  $\varepsilon(t)$  diagrams it's clear that our data have to be fitted with  $m=2$ , then we say it's a two-state model, from which we obtain two FRET rate constants and therefore two apparent distances. The quenched donor decay  $f_{D(A)}(t)$  in eq. 4 is now extended:

$$f_{D(A)}(t) = \sum_m x_D^{(m)} \cdot (x_{FRET}^{(1)} \cdot \exp(-t \cdot (k_D^{(m)} + k_{FRET}^{(1)})) + x_{FRET}^{(2)} \cdot \exp(-t \cdot (k_D^{(m)} + k_{FRET}^{(2)}))) \quad (5)$$

$k_{FRET}^{(1)}, k_{FRET}^{(2)}$  are the FRET rate constants and FRET species fractions,  $x_{FRET}^{(1)}, x_{FRET}^{(2)}$ . In the FRET-samples molecules not performing FRET are considered as No-FRET fraction. Each FRET rate constant is converted to an apparent distance  $R_{DA,app}^{(1)}$

$$R_{DA,app}^{(1)} = R_0 \cdot (k_{FRET}^{(1)} \cdot \tau_0)^{-\frac{1}{6}} \quad (6)$$

in which the unquenched GFP fluorescence lifetime is  $\tau_0 = 2.4$  ns and the Förster radius between GFP and mCherry is  $R_0 = 52$  Å (including static  $\kappa^2 = 0.476$ ).

**Mean energy transfer efficiency.** The mean (steady-state) transfer efficiency  $E_{mean}$  is obtained using the FRET fractions and the apparent distances ( $R_{DA,app}$ ) obtained from eq. 6.

$$E_{mean} = \frac{x_1}{1 + (R_{DA,app-1}/R_0)^6} + \frac{x_2}{1 + (R_{DA,app-2}/R_0)^6} \quad (7)$$

**Effective energies of linker/GFP conformations in the presence of TGR5 dimers and an implicit membrane.**

Molecular dynamics simulations of GFP bound to a linker have been performed as detailed in the SI methods. Snapshots of the MD simulations of the linker/GFP construct extracted in intervals of 50 ps were stripped of water molecules and ions, and the principle axis with the lowest moment of inertia of the first residue of the linker was aligned along the z-axis. The snapshots were then rotated in steps of 90° around the z-axis to increase the sampling density and subsequently placed in proximity to residue 295 of either TGR5 monomer for any of the TGR5 dimers (1/8 interface; 4/5 interface) (SI Fig. 4). For each snapshot, the effective conformational energy  $E_{effective, conf}$  (i.e., the sum of gas phase energy and solvation free energy) was computed using the FEW<sup>mem</sup> program<sup>48,49</sup>, with the TGR5 dimers embedded in an implicit membrane of 34 Å width and using dielectric constants of 34, 4, and 1 for the outer to inner membrane slabs with a width of 5, 6, and 6 Å, respectively (SI Fig. 4)<sup>50,51</sup>; for water and protein, dielectric constants of 80 and 1 were used, respectively. The counter ion concentration for the APBS calculation<sup>52</sup> was set to 0.15 mM. For all other parameters, default values as set in FEW<sup>mem</sup> were used. All snapshots in which GFP penetrated the membrane, or in which GFP or the linker clashed with the TGR5 dimer, were omitted, leaving ~10,000 snapshots for the analysis. The distribution of the C-alpha atom of the central residue of the fluorophore from these snapshots shows that GFP essentially moves within a hemisphere on the cytosolic side of the membrane beneath the dimer (SI Fig. 4).

**Thermodynamic Ensemble (TE) using explicit linker/GFP configurations.** From the explicit linker/GFP configurations, the thermodynamic ensemble (TE)-distribution is computed as a weighted average of the linker distance. The weights were determined according to a Boltzmann distribution

$$P_{Boltzman} = e^{\frac{-\Delta G}{RT}} \quad (8)$$

$R$  is the gas constant,  $T$  is 300 K, and  $\Delta G$  is the difference between the Gibbs energy of the current snapshot and the energetically most favorable one.  $G$  is determined as the difference between  $E_{effective, conf}$  (see section above) and the contribution from the configurational entropy  $S$

$$G = E_{effective, conf} - TS \quad (9)$$

We assumed that  $S$  is dominated by the configurations of the linker, whereas configurations of GFP are assumed to provide no contribution. This seems justified given that GFP is structurally much more stable than the linker: the linker largely consists of the TGR5 C-terminus, a part of GPCRs that has either been not fully resolved in any GPCR structure due to its high flexibility<sup>53–55</sup> or, when resolved in small parts, shows random coil formation<sup>56</sup>. Thus, we considered the linker a random hetero-polymer for which low energy conformations can structurally vary largely. Therefore, a random energy model<sup>57</sup> was used to describe its energy landscape. According to the random energy model, the entropy of a configuration with a given  $E_{effective, conf}$  is<sup>57</sup>

$$S = R \ln \Omega P \quad (10)$$

with  $\Omega$  being the overall number of conformational states. The probability of occurrence  $P$  for each energy state is obtained from

$$P = \frac{1}{\sqrt{2\pi\sigma^2}} \exp\left(\frac{-(E_{effective, conf} - \mu)^2}{2\sigma^2}\right) \quad (11)$$

with  $\mu$  being the mean and  $\sigma$  the standard deviation of the frequency distribution of  $E_{effective, conf}$ . The assumption underlying eq. 11 is that the energy is Gaussian distributed<sup>57</sup>, which is approximately fulfilled in our case (data not shown).

MM-PBSA calculations show a range of  $E_{effective, conf}$  of several hundred  $kcal\ mol^{-1}$  for proteins of sizes similar to that used in the present study<sup>58,59</sup>. In agreement with this,  $E_{effective, conf}$  computed for the linker/GFP configurations attached to the TGR5 dimer spans a range of ~1,000  $kcal\ mol^{-1}$ . However, such an energy range would lead to unrealistically low probabilities for the higher energy configurations. We thus linearly scaled  $E_{effective, conf}$  such that the linker/GFP configuration with the highest energy has a probability of occurrence in a Boltzmann distribution of  $1/\Omega$  (SI Fig. 4). Finally with the scaled energies,  $P$  (eq. 11),  $S$  (eq. 10), and  $G$  (eq. 9) were calculated, and from these the weights according to eq. 8 for the weighted average of distances between 35 and 90 Å (SI Fig. 4).

To conclude, the TEs were constructed by explicit peptide linker/GFP MD simulations followed by calculations of conformational free energies (eqs 8–11) to weight each linker-GFP configuration. In the TE approach, the weights of the points obtained from the explicit linker model were used to assign the weights of the inter-probe distances.



## References

1. Kawamata, Y. *et al.* A G protein-coupled receptor responsive to bile acids. *J Biol Chem* **278**, 9435–9440, doi: 10.1074/jbc.M209706200 (2003).
2. Keitel, V. & Haeussinger, D. Perspective: TGR5 (Gpbar-1) in liver physiology and disease. *Clinics and Research in Hepatology and Gastroenterology* **36**, 412–419, doi: 10.1016/j.clinre.2012.03.008 (2012).
3. Keitel, V., Reich, M. & Haussinger, D. TGR5: Pathogenetic Role and/or Therapeutic Target in Fibrosing Cholangitis? *Clin Rev Allerg Immun* **48**, 218–225, doi: 10.1007/s12016-014-8443-x (2015).
4. Pols, T. W., Noriega, L. G., Nomura, M., Auwerx, J. & Schoonjans, K. The bile acid membrane receptor TGR5 as an emerging target in metabolism and inflammation. *J Hepatol* **54**, 1263–1272, doi: 10.1016/j.jhep.2010.12.004 (2011).
5. Macchiarulo, A. *et al.* Probing the Binding Site of Bile Acids in TGR5. *ACS Med Chem Lett* **4**, 1158–1162, doi: 10.1021/ml400247k (2013).
6. Sindhu, T. & Srinivasan, P. Exploring the binding properties of agonists interacting with human TGR5 using structural modeling, molecular docking and dynamics simulations. *RSC advances* **5**, 14202–14213, doi: 10.1039/c4ra16617e (2015).
7. Yu, D. D. *et al.* Stereoselective synthesis, biological evaluation, and modeling of novel bile acid-derived G-protein coupled Bile acid receptor 1 (GP-BAR1, TGR5) agonists. *Bioorg Med Chem* **23**, 1613–1628, doi: 10.1016/j.bmc.2015.01.048 (2015).
8. Gertzen, C. G. W. *et al.* Mutational mapping of the transmembrane binding site of the G-protein coupled receptor TGR5 and binding mode prediction of TGR5 agonists. *Eur J Med Chem* **104**, 57–72, doi: 10.1016/j.ejmech.2015.09.024 (2015).
9. Spomer, L. *et al.* A Membrane-proximal, C-terminal alpha-Helix Is Required for Plasma Membrane Localization and Function of the G Protein-coupled Receptor (GPCR) TGR5. *J Biol Chem* **289**, 3689–3702, doi: 10.1074/jbc.M113.502344 (2014).
10. Ferre, S. *et al.* G Protein-Coupled Receptor Oligomerization Revisited: Functional and Pharmacological Perspectives. *Pharmacol Rev* **66**, 413–434, doi: 10.1124/pr.113.008052 (2014).
11. Lohse, M. J. Dimerization in GPCR mobility and signaling. *Curr Opin Pharmacol* **10**, 53–58, doi: 10.1016/j.coph.2009.10.007 (2010).
12. Rivero-Muller, A., Jonas, K. C., Hanyaloglu, A. C. & Huhtaniemi, I. In Oligomerization in Health and Disease Vol. 117 *Progress in Molecular Biology and Translational Science* (eds Giraldo, J. & Ciruela, F.) 163–185 (2013).
13. Bayburt, T. H., Leitz, A. J., Xie, G., Oprian, D. D. & Sligar, S. G. Transducin activation by nanoscale lipid bilayers containing one and two rhodopsins. *J Biol Chem* **282**, 14875–14881, doi: 10.1074/jbc.M701433200 (2007).
14. Whorton, M. R. *et al.* Efficient coupling of transducin to monomeric rhodopsin in a phospholipid bilayer. *J Biol Chem* **283**, 4387–4394, doi: 10.1074/jbc.M703346200 (2008).
15. Kuzsak, A. J. *et al.* Purification and Functional Reconstitution of Monomeric mu-Opioid Receptors allosteric modulation of agonist binding by g(i2). *J Biol Chem* **284**, 26732–26741, doi: 10.1074/jbc.M109.026922 (2009).
16. Calebiro, D. *et al.* Single-molecule analysis of fluorescently labeled G-protein-coupled receptors reveals complexes with distinct dynamics and organization. *Proc Natl Acad Sci USA* **110**, 743–748, doi: 10.1073/pnas.1205798110 (2013).
17. Fotiadis, D. *et al.* Atomic-force microscopy: Rhodopsin dimers in native disc membranes. *Nature* **421**, 127–128, doi: 10.1038/421127a (2003).
18. Johnston, J. M., Wang, H., Provasi, D. & Filizola, M. Assessing the Relative Stability of Dimer Interfaces in G Protein-Coupled Receptors. *PLoS Comput Biol* **8**, doi: e1002649 10.1371/journal.pcbi.1002649 (2012).
19. Filizola, M. & Weinstein, H. The study of G-protein coupled receptor oligomerization with computational modeling and bioinformatics. *FEBS J* **272**, 2926–2938, doi: 10.1111/j.1742-4658.2005.04730.x (2005).
20. Simpson, L. M., Taddese, B., Wall, I. D. & Reynolds, C. A. Bioinformatics and molecular modelling approaches to GPCR oligomerization. *Curr Opin Pharmacol* **10**, 30–37, doi: 10.1016/j.coph.2009.11.001 (2010).
21. Huang, J., Chen, S., Zhang, J. J. & Huang, X.-Y. Crystal structure of oligomeric beta(1)-adrenergic G protein-coupled receptors in ligand-free basal state. *Nat Struct Mol Biol* **20**, 419–+, doi: 10.1038/nsmb.2504 (2013).
22. Patowary, S. *et al.* The muscarinic M-3 acetylcholine receptor exists as two differently Sized complexes at the plasma membrane. *Biochem J* **452**, 303–312, doi: 10.1042/bj20121902 (2013).
23. Salom, D. *et al.* Crystal structure of a photoactivated deprotonated intermediate of rhodopsin. *Proc Natl Acad Sci USA* **103**, 16123–16128, doi: 10.1073/pnas.0608022103 (2006).
24. Manglik, A. *et al.* Crystal structure of the mu-opioid receptor bound to a morphinan antagonist. *Nature* **485**, 321–U170, doi: 10.1038/nature10954 (2012).
25. Kudryavtsev, V. *et al.* Monitoring dynamic systems with multiparameter fluorescence imaging. *Anal Bioanal Chem* **387**, 71–82, doi: 10.1007/s00216-006-0917-0 (2007).
26. Kudryavtsev, V. *et al.* Combining MFD and PIE for Accurate Single-Pair Forster Resonance Energy Transfer Measurements. *ChemPhysChem* **13**, 1060–1078, doi: 10.1002/cphc.201100822 (2012).
27. Sisamakís, E., Valeri, A., Kalinin, S., Rothwell, P. J. & Seidel, C. A. M. In *Methods in Enzymology, Vol 475: Single Molecule Tools, Pt B: Super-Resolution, Particle Tracking, Multiparameter, and Force Based Methods Vol. 475 Methods in Enzymology* (ed Walter, N. G.) 455–514 (2010).
28. Weidtkamp-Peters, S. *et al.* Multiparameter fluorescence image spectroscopy to study molecular interactions. *Photochem Photobiol Sci* **8**, 470–480, doi: 10.1039/b903245m (2009).
29. Stahl, Y. *et al.* Moderation of Arabidopsis Root Sterness by CLAVATA1 and ARABIDOPSIS CRINKLY4 Receptor Kinase Complexes. *Curr Biol* **23**, 362–371, doi: 10.1016/j.cub.2013.01.045 (2013).
30. Rovati, G. E., Capra, V. & Neubig, R. R. The highly conserved DRY motif of class A G protein-coupled receptors: Beyond the ground state. *Mol Pharmacol* **71**, 959–964, doi: 10.1124/mol.106.029470 (2007).
31. Blom, N., Sicheritz-Ponten, T., Gupta, R., Gammeltoft, S. & Brunak, S. Prediction of post-translational glycosylation and phosphorylation of proteins from the amino acid sequence. *Proteomics* **4**, 1633–1649, doi: 10.1002/pmic.200300771 (2004).
32. Akrap, N., Seidel, T. & Barisas, B. G. Forster distances for fluorescence resonant energy transfer between mCherry and other visible fluorescent proteins. *Anal Biochem* **402**, 105–106, doi: 10.1016/j.ab.2010.03.026 (2010).
33. Sisamakís, E., Valeri, A., Kalinin, S., Rothwell, P. J. & Seidel, C. A. M. Accurate single-molecule FRET studies using multiparameter fluorescence detection. *Methods in Enzymology* **475**, 455–514, doi: 10.1016/s0076-6879(10)75018-7 (2010).
34. King, C., Sarabipour, S., Byrne, P., Leahy, D. J. & Hristova, K. The FRET Signatures of Noninteracting Proteins in Membranes: Simulations and Experiments. *Biophys J* **106**, 1309–1317, doi: 10.1016/j.bpj.2014.01.039 (2014).
35. Sindbert, S. *et al.* Accurate distance determination of nucleic acids via Forster resonance energy transfer: implications of dye linker length and rigidity. *J Am Chem Soc* **133**, 2463–2480, doi: 10.1021/ja105725e (2011).
36. Kalinin, S. *et al.* A toolkit and benchmark study for FRET-restrained high-precision structural modeling. *Nat Methods* **9**, 1218–1225, doi: 10.1038/nmeth.2222 (2012).
37. Evers, T. H., van Dongen, E. M., Faesen, A. C., Meijer, E. W. & Merckx, M. Quantitative understanding of the energy transfer between fluorescent proteins connected via flexible peptide linkers. *Biochemistry* **45**, doi: 10.1021/bi061288t (2006).
38. Gertzen, C. G. W. *et al.* Mutational mapping of the transmembrane binding site of the G-Protein coupled receptor TGR5 and binding mode prediction of TGR5 agonists. *Eur J Med Chem* doi: 10.1016/j.ejmech.2015.09.024 (2015).
39. Grosberg, A. Y. & Khokhlov, A. R. *Statistical physics of macromolecules*. (AIP Press, 1994).
40. Unal, H. & Karnik, S. S. Domain coupling in GPCRs: the engine for induced conformational changes. *Trends Pharmacol Sci* **33**, 79–88, doi: 10.1016/j.tips.2011.09.007 (2012).

41. Auger, G. A., Pease, J. E., Shen, X. Y., Xanthou, G. & Barker, M. D. Alanine scanning mutagenesis of CCR3 reveals that the three intracellular loops are essential for functional receptor expression. *Eur J Immunol* **32**, 1052–1058, doi: 10.1002/1521-4141(200204)32:4<1052::aid-immu1052>3.0.co;2-1 (2002).
42. Duboc, H., Tache, Y. & Hofmann, A. F. The bile acid TGR5 membrane receptor: From basic research to clinical application. *Dig Liver Dis* **46**, 302–312, doi: 10.1016/j.dld.2013.10.021 (2014).
43. Jensen, D. D. *et al.* The Bile Acid Receptor TGR5 Does Not Interact with beta-Arrestins or Traffic to Endosomes but Transmits Sustained Signals from Plasma Membrane Rafts. *J Biol Chem* **288**, 22942–22960, doi: 10.1074/jbc.M113.455774 (2013).
44. Jastrzebska, B. *et al.* Disruption of Rhodopsin Dimerization with Synthetic Peptides Targeting an Interaction Interface. *J Biol Chem* **290**, 25728–25744, doi: 10.1074/jbc.M115.662684 (2015).
45. Whorton, M. R. *et al.* A monomeric G protein-coupled receptor isolated in a high-density lipoprotein particle efficiently activates its G protein. *Proc Natl Acad Sci USA* **104**, 7682–7687, doi: 10.1073/pnas.0611448104 (2007).
46. Scarselli, M. *et al.* Revealing G-protein-coupled receptor oligomerization at the single-molecule level through a nanoscopic lens: methods, dynamics and biological function. *FEBS J* **283**, 1197–1217, doi: 10.1111/febs.13577 (2016).
47. Hiller, C., Kuhhorn, J. & Gmeiner, P. Class A G-Protein-Coupled Receptor (GPCR) Dimers and Bivalent Ligands. *J Med Chem* **56**, 6542–6559, doi: 10.1021/jm4004335 (2013).
48. Homeyer, N. & Gohlke, H. FEW: A workflow tool for free energy calculations of ligand binding. *J Comput Chem* **34**, 965–973, doi: 10.1002/jcc.23218 (2013).
49. Homeyer, N. & Gohlke, H. Extension of the free energy workflow FEW towards implicit solvent/implicit membrane MM-PBSA calculations. *Biochim Biophys Acta, Gen Subj* **1850**, 972–982, doi: 10.1016/j.bbagen.2014.10.013 (2015).
50. Stern, H. A. & Feller, S. E. Calculation of the dielectric permittivity profile for a nonuniform system: application to a lipid bilayer simulation. *J Chem Phys* **118**, 3401–3412 (2003).
51. Nymeyer, H. & Zhou, H. X. A method to determine dielectric constants in nonhomogeneous systems: application to biological membranes. *Biophys J* **94**, 1185–1193, doi: 10.1529/biophysj.107.117770 (2008).
52. Baker, N. A., Sept, D., Joseph, S., Holst, M. J. & McCammon, J. A. Electrostatics of nanosystems: Application to microtubules and the ribosome. *Proc Natl Acad Sci USA* **98**, 10037–10041, doi: 10.1073/pnas.181342398 (2001).
53. Jaakola, V. P. *et al.* The 2.6 angstrom crystal structure of a human A2A adenosine receptor bound to an antagonist. *Science* **322**, 1211–1217, doi: 10.1126/science.1164772 (2008).
54. Palczewski, K. *et al.* Crystal structure of rhodopsin: A G protein-coupled receptor. *Science* **289**, 739–745 (2000).
55. Hanson, M. A. *et al.* Crystal structure of a lipid G protein-coupled receptor. *Science* **335**, 851–855, doi: 10.1126/science.1215904 (2012).
56. Wu, B. *et al.* Structures of the CXCR4 Chemokine GPCR with Small-Molecule and Cyclic Peptide Antagonists. *Science* **330**, 1066–1071, doi: 10.1126/science.1194396 (2010).
57. Wales, D. J. *Energy landscapes*. (Cambridge Molecular Science, 2003).
58. Fogolari, F. & Tosatto, S. C. Application of MM/PBSA colony free energy to loop decoy discrimination: toward correlation between energy and root mean square deviation. *Protein Sci* **14**, 889–901, doi: 10.1110/ps.041004105 (2005).
59. Gohlke, H. & Case, D. A. Converging free energy estimates: MM-PB(GB)SA studies on the protein-protein complex Ras-Raf. *J Comput Chem* **25**, 238–250, doi: 10.1002/jcc.10379 (2004).

### Acknowledgements

We are grateful to Dr. Nadine Homeyer and Daniel Mulnaes, Heinrich-Heine-University, Düsseldorf, for technical help with FEW<sup>mem</sup> and TopModel, respectively. We are also grateful to Manuel Frohnapfel and Lucas Wäschenbach for assistance during the TGR5 MFIS measurements and to Oleg Opanasyuk for scientific discussions. This work was supported by the Deutsche Forschungsgemeinschaft through the Collaborative Research Center SFB 974 (“Communication and Systems Relevance during Liver Damage and Regeneration”, Düsseldorf) and INST 208/704-1 FUGG (to H.G.) to purchase the hybrid compute cluster used in this study. We are grateful for the computing time provided by the John von Neumann Institute for Computing (NIC) to H.G. on the supercomputer JURECA at Jülich Supercomputing Centre (JSC) (project ID: 10766; user ID: HDD15).

### Author Contributions

V.K., H.G. and C.A.M.S. conceived the study and supervised the project. A.G. and Q.M. performed the MFIS-FRET measurements. S.F. and A.G. analyzed the MFIS-FRET data. L.S. and C.W. performed molecular biology experiments and provided biological material. T.O.P. performed oligomer and tetramer simulations. C.G. and M.D. performed structural modeling of TGR5 dimers and tetramers and explicit and implicit linker simulations. H.G. analyzed molecular modeling and simulation data. A.G., C.G., V.K., H.G. and C.A.M.S. wrote the paper. All authors reviewed the manuscript. D.H. approved the manuscript.

### Additional Information

**Supplementary information** accompanies this paper at <http://www.nature.com/srep>

**Competing financial interests:** The authors declare no competing financial interests.

**How to cite this article:** Greife, A. *et al.* Structural assemblies of the di- and oligomeric G-protein coupled receptor TGR5 in live cells: an MFIS-FRET and integrative modelling study. *Sci. Rep.* **6**, 36792; doi: 10.1038/srep36792 (2016).

**Publisher's note:** Springer Nature remains neutral with regard to jurisdictional claims in published maps and institutional affiliations.



This work is licensed under a Creative Commons Attribution 4.0 International License. The images or other third party material in this article are included in the article's Creative Commons license, unless indicated otherwise in the credit line; if the material is not included under the Creative Commons license, users will need to obtain permission from the license holder to reproduce the material. To view a copy of this license, visit <http://creativecommons.org/licenses/by/4.0/>

© The Author(s) 2016

**Supporting Information****Structural assemblies of the di- and oligomeric G-protein coupled receptor TGR5 in live cells: an MFIS-FRET and integrative modelling study**

<sup>1</sup>Annemarie Greife, <sup>1</sup>Suren Felekyan, <sup>1</sup>Qijun Ma, <sup>2</sup>Christoph G.W. Gertzen, <sup>3</sup>Lina Spomer, <sup>1</sup>Mykola Dimura, <sup>1</sup>Thomas O. Peulen, <sup>3</sup>Christina Wöhler, <sup>3</sup>Dieter Häussinger, <sup>2\*</sup>Holger Gohlke, <sup>3\*</sup>Verena Keitel, <sup>1\*</sup>Claus A.M. Seidel

<sup>1</sup> Chair for Molecular Physical Chemistry, Heinrich Heine University Düsseldorf, 40225 Düsseldorf, Germany;

<sup>2</sup> Institute for Pharmaceutical and Medicinal Chemistry, Heinrich Heine University Düsseldorf, 40225 Düsseldorf, Germany;

<sup>3</sup> Clinic for Gastroenterology, Hepatology and Infectious Diseases, Heinrich Heine University Düsseldorf, 40225 Düsseldorf, Germany

\*Corresponding authors: C.A.M. Seidel, H. Gohlke, V. Keitel

**Content**

<b>Supporting Tables</b>	<b>p.3-7</b>
<b>Supporting Figures</b>	<b>p.8-17</b>
<b>Supporting Notes</b>	<b>p.18</b>
<b>Supporting Methods</b>	<b>p.19-33</b>
<b>Glossary</b>	<b>p.34-35</b>
<b>Supporting References</b>	<b>p.36-37</b>



### Supporting Tables

**Supporting Table 1:** Parameters for determination of the corrected green to yellow fluorescence intensity ratio  $F_D/F_A$  necessary for the 2D histograms. The background  $B$  was determined from untransfected cells. The green to yellow fluorescence intensity ratio ( $F_D/F_A$ ) was corrected for crosstalk (characterized by the crosstalk factor  $\alpha$ ), background  $\langle B \rangle$ , detection efficiencies of D ( $g_G$ ) and A ( $g_Y$ ). The acceptor fluorescence used for 2D-FRET must also be corrected for additional direct acceptor excitation  $DE$  and relative concentration dependent brightness  $DE_{rel}$ . All samples were corrected for distinct fluorescence quantum yields  $\Phi$  and a spectral shift factor  $\gamma$  (especially for TGR5 Y111A) which is considered in the corrected green detection efficiency ( $g_G^*$ ).

	$\alpha$	$\langle B_G \rangle$ [kHz]	$\langle B_Y \rangle$ [kHz]	$\gamma$	$\Phi$	$DE_{rel}$ [kHz]
<b>wt</b>	0.09	0.3	1	1	1	DA1:10= +0.76 DA1:40= +3.78
<b>Y111A</b>	0.28	0.3	2	0.61	1.125	DA1:10= +4.28 DA1:40= +0
<b>Y111F</b>	0.1	0.3	1	1	1	DA1:10= +1.76 DA1:40= +3.02

**Supporting Table 2:** Parameters for  $\varepsilon(t)$  diagram in **Fig. 4** for each TGR5 variant. The parameters  $b_0$ - $b_4$  are obtained from the fit equation  $f = b_0 + b_1 \cdot e^{-\frac{x}{b_2}} + b_3 \cdot e^{-\frac{x}{b_4}}$ .  $b_0$  determines the Non-FRET fraction (Donly fraction),  $b_1$  and  $b_3$  are the two FRET fractions and  $b_2$  and  $b_4$  are the corresponding decay times. **Supporting Figure 2** shows how to generate and interpret  $\varepsilon(t)$  diagrams.

TGR5	Fit	DA1:3	DA1:5	DA1:10	DA1:20	DA1:40
<b>wt</b>	$b_0$ :	0.90	0.84	0.89	0.81	0.82
	$b_1$ :	0.01	0.04	0.03	0.04	0.04
	$b_2$ :	0.30	0.18	0.23	0.33	0.46
	$b_3$ :	0.09	0.13	0.08	0.16	0.15
	$b_4$ :	5.70	8.04	1.89	3.80	5.12
<b>Y111A</b>	$b_0$ :	0.42	0.42	0.45	0.43	0.43
	$b_1$ :	0.02	0.01	0.19	0.03	0.03
	$b_2$ :	0.73	0.63	5.28	0.56	0.72
	$b_3$ :	0.55	0.56	0.36	0.55	0.55
	$b_4$ :	6.09	5.02	5.26	4.48	4.90
<b>Y111F</b>	$b_0$ :	0.73	0.74	0.69	0.68	0.77
	$b_1$ :	0.11	0.06	0.18	0.09	0.02
	$b_2$ :	5.73	2.7	3.88	2.30	0.43
	$b_3$ :	0.15	0.19	0.13	0.23	0.21
	$b_4$ :	771.45	90.75	765.84	24.83	2.80

**Supporting Table 3: Sequence Information for AV-simulation.** Untranslated region, TGR5 coding sequence, linker and GFP (4EUL) or mCherry (2H5Q) sequence of the analyzed TGR5 variants are summarized and used for TGR5 dimer and oligomer simulations. The position of the Y111 residue in the ERY motif for mutagenesis is highlighted. Sequences with unknown secondary or tertiary structures are underlined and are kept flexible in AV simulations.

	<b>TGR5 wt-FP</b>
5'UTR	none
TGR5	MTPNSTGEVPSPIPKGALGLSLALASLIITANLLLALGIAWDRRLRSPPAGCFFL SLLLAGLLTGLALPTLPGLWNQSRRGYWSCLLVYLAPNFSFLSLLANLLL VH GER <b>Y</b> MAVLRPLQPPGSIRLALLLTWAGPLLFASLPALGWNHWTPGANCSQA IFPAPYLYLEVYGLLLPAVGAAAFLSVRVLATAHRQLQDICRLERA VCRDEPS ALARALTWRQARAQAGAMetLLFGLCWGPYVATLLLSVLAYEQRPPPLGPGTL LSLLSLGSASAAAVPVAMetGLGDQRYTAPWRAAA <u>QRCLOGLWGRASRDSP</u> <u>GPSIAYHPSSQSSVDLNLNY</u>
Cloning Linker	<u>GSTGRH</u>
GFP (4EUL) = donor (D)	<u>MVSKGEELFTGVVPILEVELDGDVNGHKFSVSGEGEGDATYGKLTCLKFICTTG</u> KLPVPWPTLVTTFGYGLQCFARYPDHMKQHDFFKSAMPEGYVQERTIFFKDD GNYKTRAEVKFEGDTLVNRIELKGIDFKEDGNILGHKLEYNYNSHNVYIMAD KQKNGIKVNFKIRHNIEDGSVQLADHYQQNTPIGDGPVLLPDNHYSYQSALS KDPNEKRDHMVLLLEFVTAAGITLGMDELYK*
mCherry (2H5Q) = acceptor (A)	<u>MVSKGEEDNMAIIEKFMRFKVHMEGSVNGHEFEIEGEGEGRPYEGTQTAKLK</u> VTKGGPLPFAWDILSPQFMYGSKAYVKHPADIPDYKLSFPEGFKWERVMNF EDGGVVTVTQDSSLQDGEFIYKVKLRGTNFPDGPVMQKKTMGWEASSERM YPEDGALKGEIKQRLKLDGGHYDAEVKTTYKAKKPVQLPGAYNVNIKLDIT SHNEDYTIVEQYERAEGRHSTGGMDELY*

**Supporting Table 4: Comparison of results from different fit models.** Donor fluorescence lifetime decay histograms in presence of acceptor in TGR5 variants are fitted based on  $2k$ -FRET and AV simulated distance distributions for different dimer (1/8), (4/5) and oligomer (1/8)-4:5-(1/8) interfaces with only one fit parameter – Donly fraction. Interface dimer (4/5) yields very low Donly fractions compared to all other models: it is known that ~30 % of mCherry acceptor dyes are not active in cells; hence at least ~30 % Donly fractions are expected. Based on this we concluded that interface dimer (4/5) as the primary dimer interface in TGR5 variants are less likely.  $wt^1$  is DA1:3, all other DA ratios are 1:20.

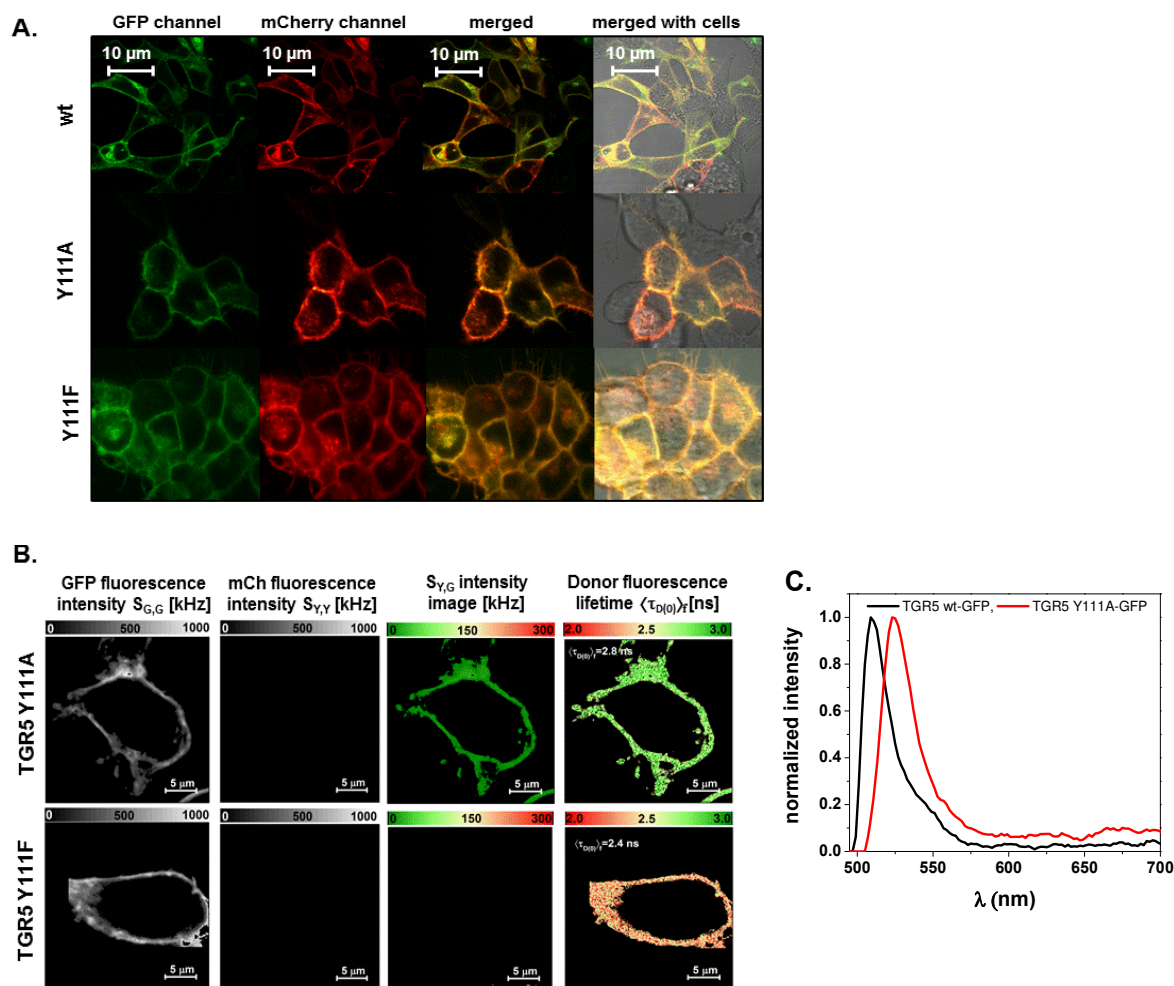
	$wt^1$		wt		Y111A		Y111F	
	Donly fraction	$\chi^2$	Donly fraction	$\chi^2$	Donly fraction	$\chi^2$	Donly fraction	$\chi^2$
Two $k_{FRET}$	0.74	1.61	0.64	1.59	0.69	1.39	0.62	1.61
dimer (4/5)	0.43	1.65	0.00	1.83	0.00	4.94	0.14	1.54
dimer (1/8)	0.82	1.91	0.67	2.68	0.58	2.61	0.74	1.83
oligomer	n.d	n.d	0.74	2.82	0.65	2.86	0.78	1.88

**Supporting Table 5: Overview of the mean distances  $\langle R_{DA} \rangle$  calculated for the possible tetramer models with or without G-Protein.** The primary interfaces for dimerization are in brackets (x/x) and secondary interfaces for oligomerization are abbreviated -x:x-. The numbers are the corresponding (transmembrane) helices involved in binding interactions. The apparent mean distances  $\langle R_{DA} \rangle_{app}$  of each label pair involved in dimerization are bold. A schematic presentation of the tetramer models is shown in **Supporting Figure 4**. For example in the model (1/8)-4:5-(1/8) (with G-Protein always determined as label C, even when it is absent) label pairs A-E and B-D with the primary interfaces (1/8) show a distance 59-66 Å measured between the fluorescent proteins attached to helix 8, and the label pair A-B with the secondary interface -4:5- shows a mean distance of 133 Å. Further calculated distances in this oligomer are measured from label pairs A-D, B-E, B-D and are comparable to the distances obtained from A-B.

Label pair	$\langle R_{DA} \rangle, [\text{Å}]$					
	with G-Protein			without G-Protein		
	(1/8)-4:5-(1/8)	(1/8)-5:6-(1/8)	(5/6)-4:5-(5/6)	(1/8)-4:5-(1/8)	(1/8)-5:6-(1/8)	(5/6)-4:5-(5/6)
<b>A-B</b>	133	119	<b>128</b>	98	94	<b>103</b>
<b>A-D</b>	134	<b>63</b>	128	97	<b>64</b>	120
<b>A-E</b>	<b>66</b>	129	65	<b>58</b>	93	72
<b>B-D</b>	<b>59</b>	108	64	<b>57</b>	91	69
<b>B-E</b>	131	<b>80</b>	116	99	<b>71</b>	106
<b>D-E</b>	136	123	<b>104</b>	101	94	<b>103</b>

## Supporting Figures

### Supporting Figure 1

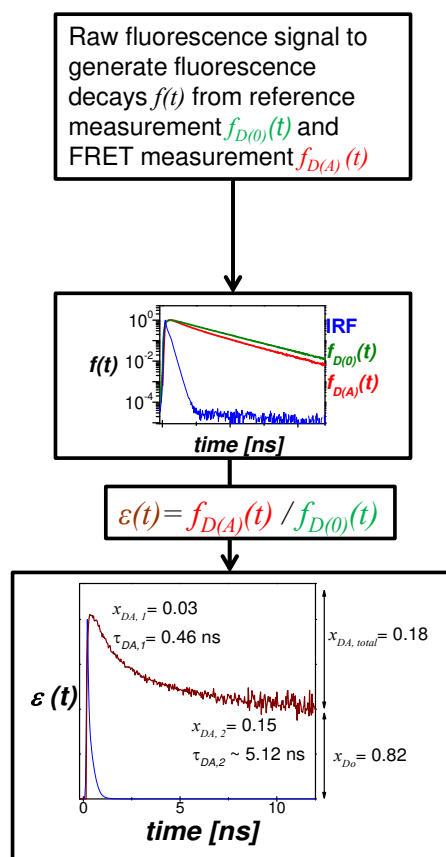


### Supporting Figure 1: Live cell imaging and MFIS analysis of TGR5 donors

(a) HEK293 cells, transiently transfected with TGR5-GFP and TGR5-mCherry (transfection ratio 1:10), were imaged for co-localization of GFP and mCherry using sequential scanning and a scanning resolution of 1024 x 1024 pixels. Each TGR5-GFP and TGR5-mCherry picture is shown in a false color saturation mode and then overlaid by using green and yellow intensity colours. TGR5-GFP and TGR5-mCherry wt, Y111A and Y111F (from top to bottom) are clearly co-localized at the cell membrane. Scale bar 10  $\mu$ m. (b) MFIS analysis of TGR5 transfected

HEK293 cells by comparing (from left to right and top to bottom row) the GFP fluorescence intensity, mCherry fluorescence intensity, the donor fluorescence lifetime  $\langle\tau_{D(0)}\rangle_f$ , and mCherry photons after excitation of GFP ( $S_{Y,G}$ ). The fluorescence-averaged donor lifetime in the absence of an acceptor  $\langle\tau_{D(0)}\rangle_f$  in the Y111A variant is 2.8 ns compared to 2.4 ns for Y111F. The presence of green photons in the yellow channel is due to a higher crosstalk, background and red shift in the Y111A variant. **(c)** GFP was excited at 488 nm and emission spectrum was measured from 495 nm to 700 nm in a 2 nm step size and a 2 nm spectral band width at Olympus FluoView1000 microscope. TGR5 wt-GFP shows the typical emission maximum at 510 nm, whereas TGR5 Y111A-GFP shows a 13 nm red shift towards 523 nm. Three cells for each curve were measured, the background was subtracted and the average intensity normalized to the maximum. The Y111A MFIS data were corrected for the spectral shift.

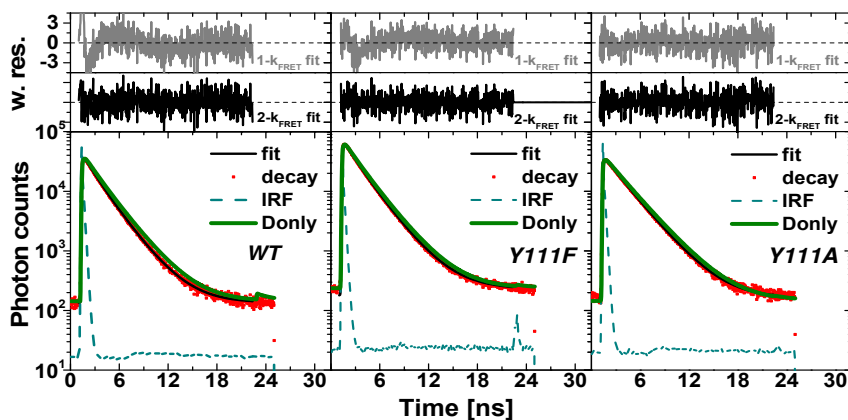
## Supporting Figure 2



**Supporting Figure 2. Guideline for presentation and interpretation of  $\varepsilon(t)$  diagrams:** In the first step, the raw fluorescence signal decays  $f(t)$  from the reference measurement  $f_{D(0)}(t)$  (green) and from the FRET measurement  $f_{D(A)}(t)$  (red) are selected and corrected with the instrument response function curve (IRF, blue) for a time shift. In the second step, the  $f_{D(A)}(t)$  decay is divided through  $f_{D(0)}(t)$  decay (**equation (1) in main text**). The resulting decay  $\varepsilon(t)$  is normalized to 1 and plotted versus time in ns. As example the TGR5 wt DA1:40 experiment is used. In this case the non-FRET fraction  $x_D$  (b0 in Table S2) is 0.82. The corresponding total FRET fraction  $x_{DA,total}$  is 0.18. As the decay is clearly bi-exponential, two FRET fractions  $x_{DA,1}$ ,  $x_{DA,2}$  (b1, b3) and the corresponding fluorescence lifetimes  $\tau_{DA,1}$ ,  $\tau_{DA,2}$  (b2, b4) are resolvable by the equation used in Table S2.



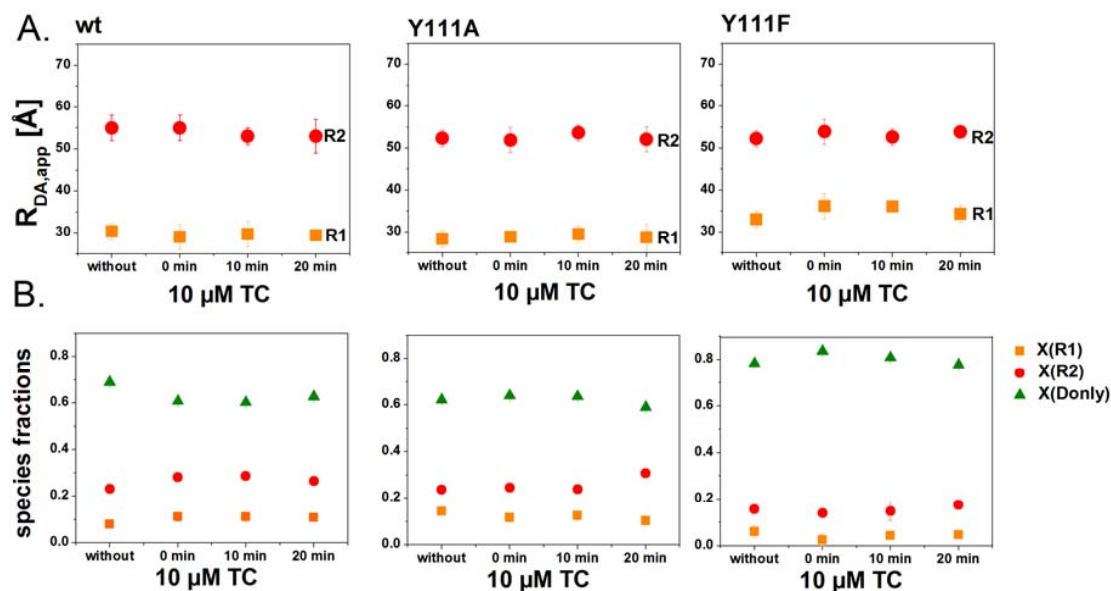
## Supporting Figure 3



## Supporting Figure 3: Fit fluorescence decays with different models for TGR5 variants.

Fitting the sub-ensemble fluorescence decays of the FRET samples (DA1:10) with  $k_{FRET}$  models showed that two FRET rates are necessary to fit these data accurately. The decays of Donly (TGR5-GFP) and FRET samples are in olive and red, respectively. The fitted decay with the 2- $k_{FRET}$  model and the fitting residuals are plotted in black. The fitting residuals with 1- $k_{FRET}$  model are plotted in grey.

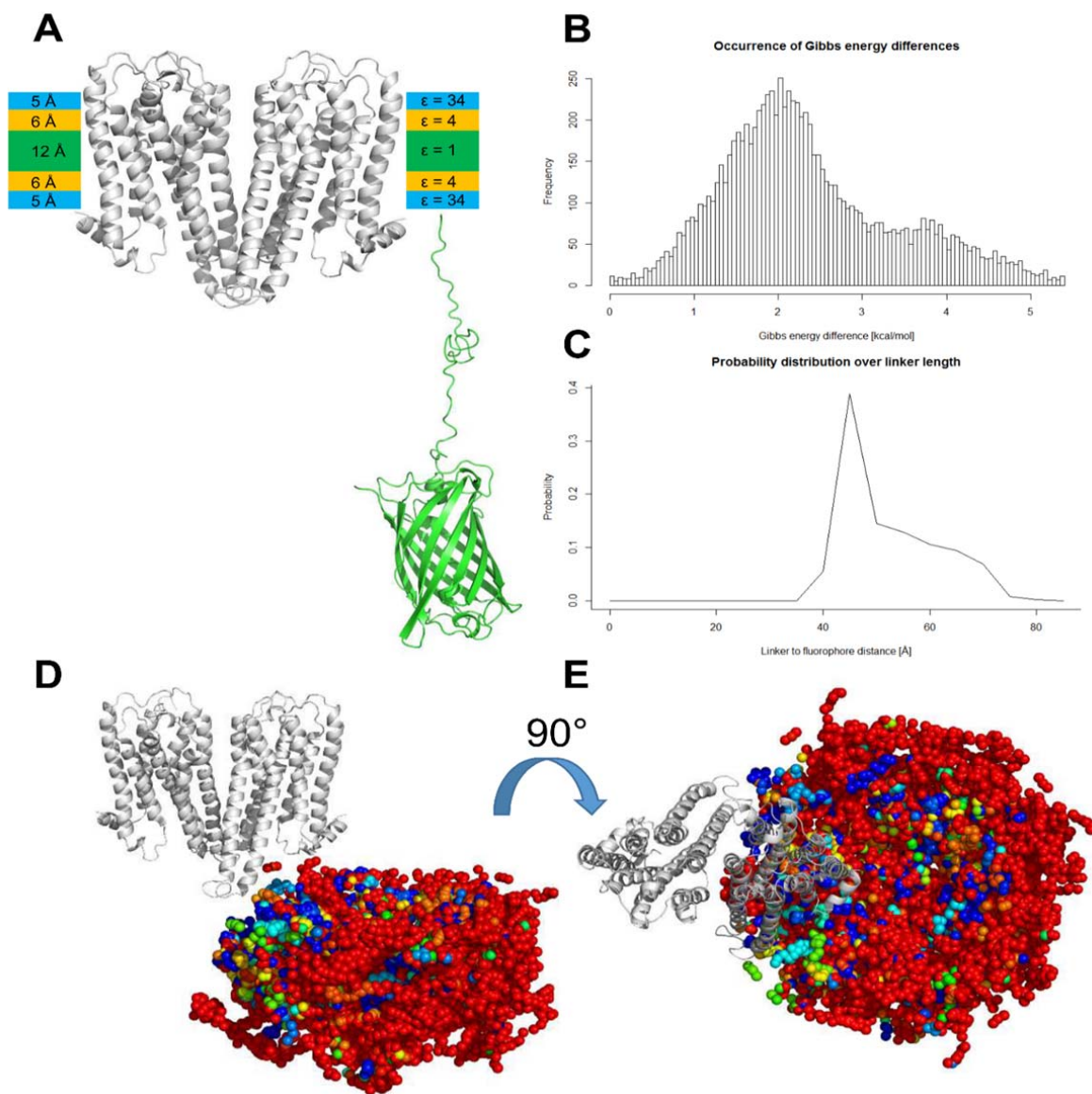
## Supporting Figure 4



## Supporting Figure 4: Time-series analysis after TC ligand stimulation.

HEK293 cells were transiently transfected with TGR5-GFP alone (Only) or with TGR5-GFP and TGR5-mCherry with the D/A ratio of 1:10. To study changes in FRET after ligand addition, three cells were selected using the Olympus Time laps function and measured at different time points, including before adding 10  $\mu$ M TC (without), immediately after TC addition ( $t=0$ ), 10 min after and 20 min after. The apparent distances  $R_{DA}$  species fractions were fitted using self-made software. **(a)** The apparent distances are plotted versus time. Each point represents the average of nine cells (three measurements with three cells). **(b)** The species fractions X(R1), X(R2) and the Non-FRET fraction X(Only) at four time points (representing without TC,  $t=0$ ,  $t=10$  min and  $t=20$  min) are plotted, but no substantial change due to ligand addition could be detected. Orange=R1=high FRET distance, red=R2= low FRET distance, green=Only fraction.

## Supporting Figure 5

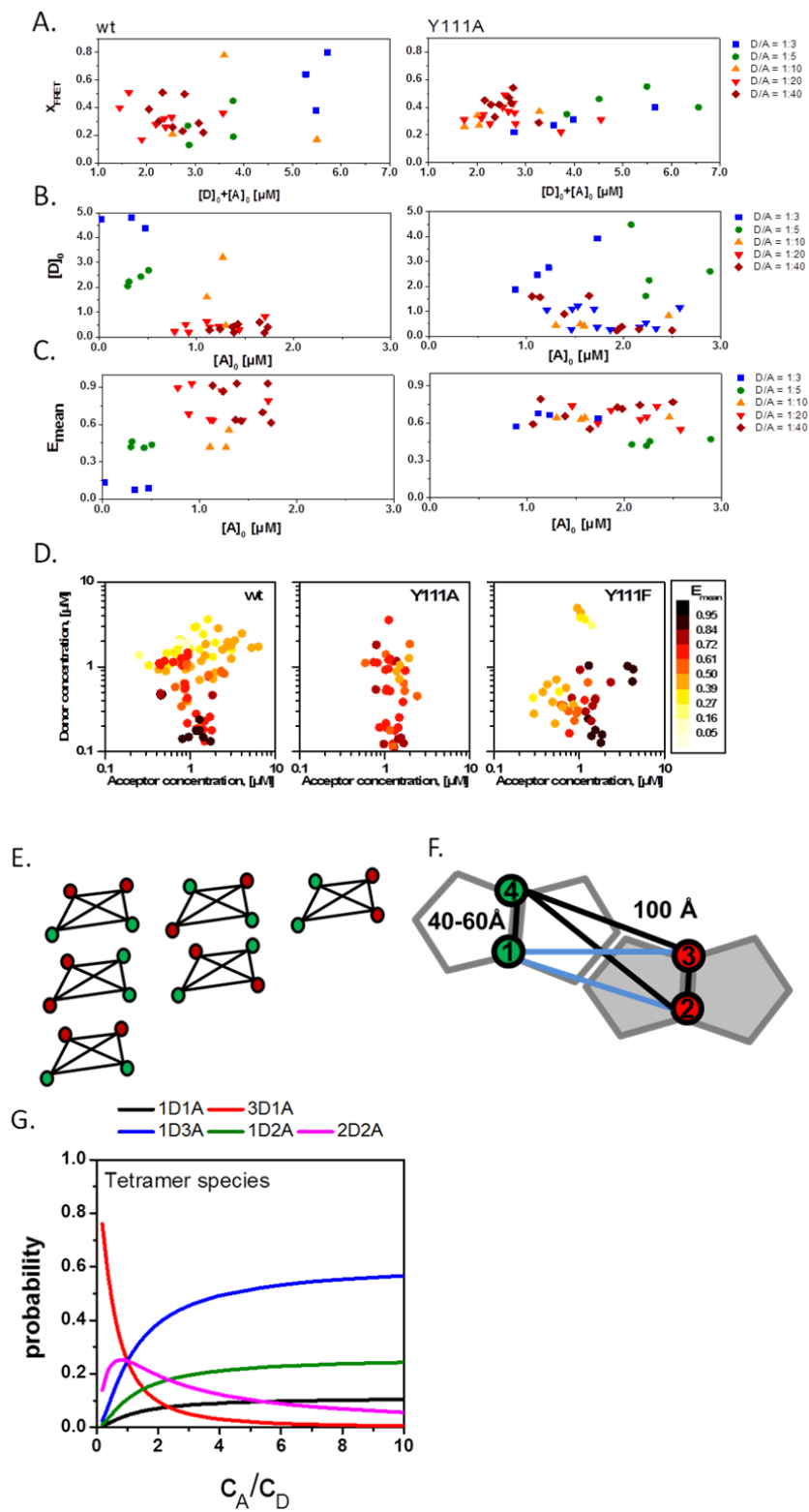


**Supporting Figure 5: Explicit linker/GFP simulation and probability distribution of linker/GFP configurations.**

**(a)** Starting structure of the TGR5 4/5 dimer (grey) and of the linker and GFP after the initial minimization (green). The linker and GFP were simulated separately from the TGR5 dimer; the structure shown here illustrates one of the composite models used for the MM-PBSA

calculations. At the 'wad' in the middle of the linker, several proline residues are present. The positioning of the implicit membrane slabs is shown in colored bars next to the TGR5 dimer. The bars on the left show the thickness of each membrane layer used in the FEW<sup>mem</sup> calculations, while the bars on the right show the respective electric permittivity. **(b)** Frequency distribution of Gibbs energies (**equation (9)** in the main text) relative to the energetically most favorable snapshot after linear scaling (see main text). **(c)** Probability distribution of the Boltzmann-weighted distance between the fluorophore and the N-terminus of the linker. **(d) + (e)**. Ensemble of linker/GFP configurations represented in terms of the C-alpha atom of the central residue of the fluorophore generated by MD simulations with added rotations in relation to the TGR5 4/5 dimer (grey) in side **(d)** and exoplasmic view **(e)**. The coloring of the C-alpha atoms corresponds to their probability ranging from lowest (blue) to highest (red). Conformations with a low probability are more frequently found in close contact to the dimer.

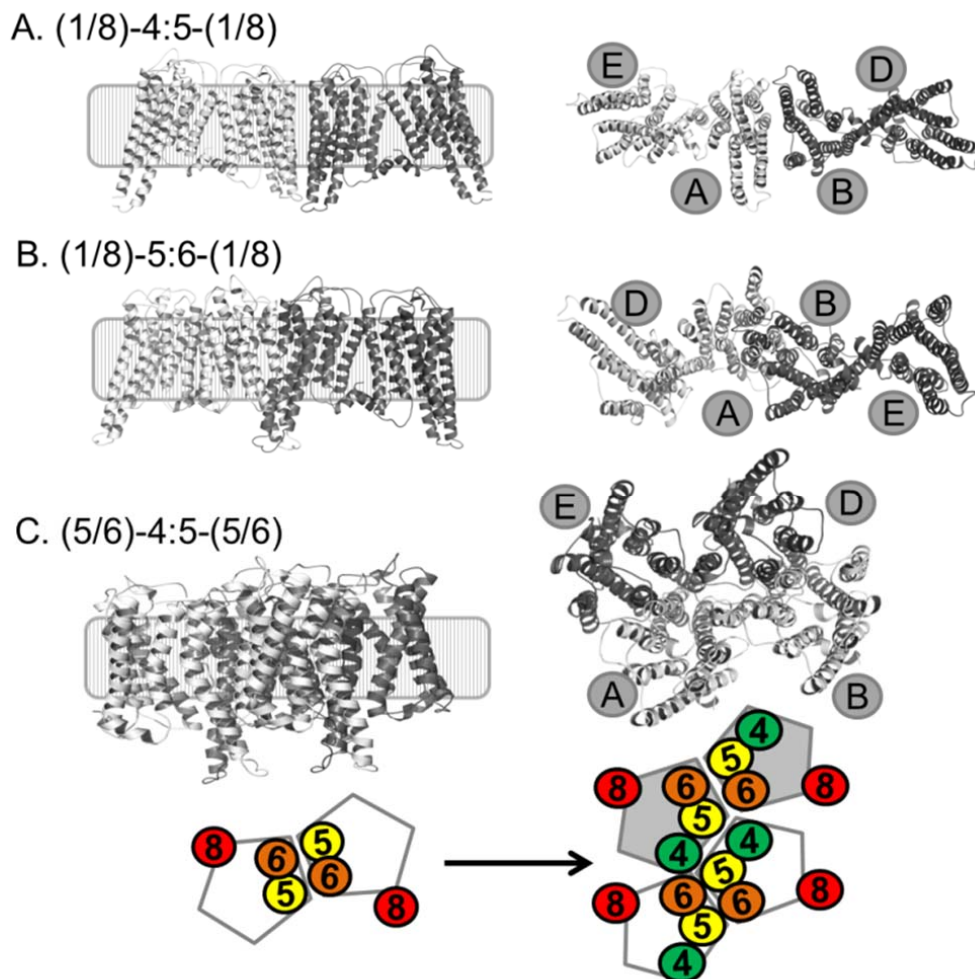
Supporting Figure 6



**Supporting Figure 6: Characterization and estimation of the association constants with a dimer/tetramer fit model.**

HEK293 cells were transiently transfected with TGR5 wt (left plots) or Y111A (right plot) donor to acceptor ratios varying from 1:3 to 1:40. **(a)** The total protein concentration  $[D]_0 + [A]_0$  (eq.(4-6)) and the FRET species fractions  $x_{\text{FRET}}$  were obtained from MFIS measurements and plotted to calculate the dissociation constant  $K_D$ . The FRET species fractions calculated from different D/A ratios were distributed equally in a concentration range of 1-7  $\mu\text{M}$ . From these data  $K_D$  cannot be directly determined. The upper limit for  $K_D$  should be less than 1  $\mu\text{M}$ . **(b)** The real donor  $[D]_0$  and acceptor  $[A]_0$  concentrations from the D/A transfection experiments were plotted for wt and Y111A to estimate differences in experimental and real concentration ratios between donor and acceptor. **(c)**  $E_{\text{mean}}$  increases in an  $[A]_0$  dependent manner in wt but not in Y111A transfected cells. **(d)** Overview on the concentration ranges of donor and acceptor and its influence on  $E_{\text{mean}}$ , whose size is depicted in color. Variant specific interaction patterns are readily visible. **(e)** Description of our data by a minimal dimer/tetramer model to. In this model we assume that a tetramer is constituted of a dimer of dimers. In a tetramer the sum of donor, acceptor and unlabeled molecules is constant (eqs. (7-9)). Six tetramer configurations for a case of two acceptor (red) and two donor molecules (green) are possible. **(f)** Composition of a simplified rectangular tetramer molecule with random arrangement of two donors and two acceptors according to a linear organization of the GPCR. The positions of the green and red circles in the pentagram represent the fluorescent proteins attached to helix 8. **(g)** Probabilities of all tetramer species composed of a certain number of donor and acceptors (1D1A, 3D1A, 1D3A, 1D2A, 2D2A) in dependence of the acceptor to donor ratio. In our case the most probable scenario is the 2D2A case which describes our data best.

## Supporting Figure 7



## Supporting Figure 7: GPCR tetramer organization and AV simulations.

(a)-(c) Cartoon presentation made with the free software PyMol<sup>1,2</sup> from the membrane view (right) and cytoplasmic view (left) for three possible tetramer organizations. The labels A, B, D and E refer to the TGR5 monomers and are used for distance distribution calculations (Supporting Table 5). The corresponding dimers are colored in light grey or dark grey.

## **Supporting Notes**

### **Proximity FRET**

Pixel-wise analysis of the fluorescence data in TGR5 Y111A compared to wt and Y111F showed strong differences in the FRET properties, which were only detectable in an acceptor concentration-dependent manner (**Figure 4**, main text). Thus, we tested whether the observed FRET could simply be caused by a very high local concentration of acceptor proteins in the membrane, so that donor and acceptor are in proximity even though they do not interact. This phenomenon is called “*proximity FRET*”.

Due to the single-molecule sensitivity of our confocal microscope, we could perform FRET experiments with acceptor concentrations of  $\sim 1\text{-}6\ \mu\text{M}$  in 1.23 fl, which corresponds to a molecule density of less than  $\sim 0.02$  acceptor molecules/nm<sup>2</sup>. According to King *et al.*<sup>3</sup>, proximity FRET is negligible ( $E < 0.1$ ) at these concentrations.

The pixel-integrated, time-resolved FRET analysis  $\varepsilon(t)$  supported the pixel-wise analysis and clearly demonstrated the presence of different FRET species in TGR5 wt and Y111F and therefore the formation of higher-order oligomers as compared to Y111A.



## **Supporting Methods**

### **1. Molecular biology**

#### **Cell culture reagents**

Cell culture media were from PAA (Coelbe, Germany). Foetal calf serum (FCS) was from Biochrom (Berlin, Germany). Tauroolithocholic acid (TLC), Taurocholic acid (TC) and Forskolin (F) were purchased from Sigma-Aldrich (Taufkirchen, Germany) and Calbiochem (San Diego, CA, USA), respectively.

#### **Cloning of TGR5**

Human TGR5 was cloned as previously described<sup>4</sup>. Constructs were cloned into the pcDNA3.1+ (TGR5-pcDNA: complete CDS; TGR5-His: stop codon in complete CDS replaced by C-terminal 8xHis-tag), pGFP-N1, and pmcherry-N1 (stop codon in the complete CDS replaced by a restriction site) vectors. The FLAG-TGR5-YFP construct with an N-terminal FLAG-tag and a C-terminal YFP-tag was cloned into the pEYFP-N1 vector. All vectors were from Clontech, Palo Alto, CA. The Y111A and Y111F mutations were introduced into different TGR5 cDNA constructs using the QuikChange Site-Directed Mutagenesis Kit (Agilent Technologies, Santa Clara, USA)<sup>4</sup>. All cloning strategies and mutagenesis primer sequences can be obtained upon request. Successful cloning and mutagenesis was verified by sequencing (GenBank accession numbers: TGR5:NM\_001077191.1).

#### **Immunofluorescence and confocal laser scanning microscopy**

Human embryonic kidney 293 (HEK293) cells and Madin Darbin canine kidney cells (MDCK), grown on glass coverslips or transparent filter wells, were transiently transfected with TGR5 wt, Y111A or Y111F in pcDNA3.1+ and pEYFP-N1 vectors using Lipofectamine2000 (Invitrogen)

for 48 h according to the manufacturer's recommendations. After fixation with  $-20^{\circ}\text{C}$  cold methanol for 30 sec, cells were incubated with RVL2<sup>5</sup> antibody against TGR5 and Cyanine-3 (1:500) conjugated secondary antibodies, which were purchased from Dianova (Hamburg, Germany). Nuclei were stained with Hoechst 34580 (1:20000; Invitrogen). Images were analysed on a Zeiss LSM510META confocal microscope using a multi-tracking modus. A 63 x objective and a scanning resolution of 1024 x 1024 pixels was used for all samples.

### **Flow cytometry**

TGR5 plasma membrane protein amount was quantified by flow cytometry (FACS) using a FACS-CANTO-II (BD Biosciences; Heidelberg, Germany) as previously described<sup>4,6</sup>. HEK293 cells were transiently transfected with the FLAG-TGR5-YFP constructs using Lipofectamine2000. The N-terminal FLAG-tag was detected with the anti-FLAG M2-antibody (Sigma-Aldrich) using the Zenon PacificBlue Label-Kit (Invitrogen) according to manufacturer's instructions. TGR5 plasma membrane expression was calculated by the amount of FLAG-tag positive cells divided by the total amount of TGR5 positive cells as determined by YFP-fluorescence.

### **Reporter gene assay**

HEK293 cells were transiently transfected with TGR5 wt and TGR5 Y111A and TGR5 Y111F variants in the pcDNA3.1+ construct (0.5 ug), pEYFP-N1-empty vector (1.1 ug), reporter PlasmLuc (1.6 ug; Bayer AG; Leverkusen, Germany), and Renilla expression vector (0.1  $\mu\text{g}$ ; Promega; Madison, WI, USA) using Lipofectamine2000. The PlasmLuc-reporter gene construct contains 5 cAMP-responsive elements (CREs) upstream of the luciferase gene. Luciferase activity was normalized to transfection efficacy, which was monitored by cotransfection with the Renilla expression vector, and served as measure for the rise in intracellular cAMP. Luciferase

activity was determined 16 hours after stimulation with DMSO, TLC or Forskolin<sup>4,6</sup>. The increase in TLC- and Forskolin-dependent luciferase activity is relative to the DMSO stimulation, which was set equal to 1.0.

### **Co-immunoprecipitation**

HEK293 cells were cotransfected with TGR5-YFP and TGR5-His. Cells transfected with the empty vector (pcDNA or pEYFP-N1) and only one of the TGR5 cDNAs (TGR5-His or TGR5-YFP) served as controls. Cells were lysed with a buffer containing 50 mM Tris-HCl pH 8.0, 1% Nonidet® P40 (AppliChem) and complete protease inhibitor cocktail tablets (Roche). Protein concentration was determined by Bradford assay, and 0.05 mg protein from each sample was set aside as input control. 1.6 mg protein from each sample was used for immunoprecipitation with the  $\mu$ MACS His-tagged protein isolation kit (Miltenyi Biotec, Bergisch-Gladbach, Germany). His-tagged TGR5 was labelled with the anti-His microbeads and loaded onto the MACS columns. His-tagged proteins were eluted from the columns with 60  $\mu$ l elution buffer and divided into two equal samples of 25  $\mu$ l each. These as well as the input control samples were subjected to deglycosylation using the N-glycosidase-F Kit (Roche Diagnostics, Mannheim, Germany) for 10 min at 37°C. The deglycosylation reaction was stopped with 10% Laemmli buffer, heated to 95°C for 3 min. IP samples and input controls were separated by SDS page and proteins were transferred to PVDF membranes. His-tagged proteins were detected with the HRP-coupled anti-His antibody (dilution 1:5000, Miltenyi Biotec). YFP-coupled proteins were detected using the HRP-coupled anti-GFP antibody (dilution 1:5000, Miltenyi Biotec). Glyceraldehyde-3-phosphate dehydrogenase (GAPDH) was detected with an antibody from GeneTex (dilution 1:10000) and a secondary HRP-coupled anti-mouse antibody (dilution 1:10000, Dako). Densitometry was performed using the Totallab-100 software (Nonlinear Dynamics, Durham,

NC). The relative amount of TGR5 oligomerization was calculated by dividing the amount of TGR5-YFP protein through the amount of TGR5-His protein. Wildtype TGR5-YFP/TGR5-His was set to 1.0.

## **2. MFIS-FRET: microscopy and analysis**

### **Sample preparation for MFIS-FRET experiments**

For live cell experiments HEK293 were seeded on 8 well chambered glass slides (Labtek, Nunc, USA) one day before transfection. Cells were transiently transfected with 0.5  $\mu\text{g}$  DNA at a density of about 80% using FuGene6 (Promega) according to the manufacturer's protocol 24 to 48 h before analysis. Cell vitality and successful transfection was visually inspected before MFIS measurements.

### **Microscope calibration**

Calibration measurements with Rhodamine 110 delivered the G-factor  $G = Sg_{\perp}/Sg_{\parallel}$  for the GFP emission wavelength range (green channels). The G-factor accounts for the detection efficiency difference between detectors of both polarizations ( $g_{\perp}$  and  $g_{\parallel}$ ). The instrument response function (IRF) was measured with the back-reflection of the laser beam using a mirror and was used for iterative re-convolution in the fitting process. Furthermore, untransfected cells and water were measured at 488 nm and 559 nm for background determination.

### **Time series experiments of TGR5 stimulation by Taurocholic acid (TC)**

To study the effect of bile acid agonists on the FRET parameters we used the water-soluble ligand TC, because addition of DMSO (necessary to dissolve TLC) affects the fluorescence signal significantly. For the time series experiments the time laps viewer function supplied by Olympus LSM was used. The motorized table was calibrated, and three cells were selected and

monitored over a 40 minutes time period. FRET measurements were taken every 10 minutes: before the addition of TC immediately after addition ( $t = 0$  min), and after ten and twenty minutes ( $t = 10$  min;  $t = 20$  min). Cells were excited with 488 nm and 559 nm laser light as described above. Where necessary, changes in focus and system drift were corrected.

### Pixel-wise analysis

To determine fluorescence-weighted lifetimes in a pixel-wise analysis, the histograms presenting the decay of fluorescence intensity after the excitation pulse were built for each pixel with 128 ps per bin. We used a maximum likelihood estimator (MLE) to determine the fluorescence-weighted averaged lifetime of donor molecules  $\langle \tau_{D(A)} \rangle_f$  in a single pixel using a model function containing only two variables,  $\langle \tau_{D(A)} \rangle_f$  and the scatter contribution fraction.

### MFIS-FRET 2D histograms

For oligomerization analysis, we plotted the 2D histograms of donor lifetime  $\langle \tau_{D(A)} \rangle_f$  vs the green to yellow fluorescence intensity ratio ( $F_D/F_A$ ) (see equations (2) and (3)) corrected for crosstalk (characterized by the crosstalk factor  $\alpha$ ), background  $\langle B \rangle$ , detection efficiencies of D ( $g_G$ ) and A ( $g_Y$ ). The acceptor fluorescence used for 2D-FRET must also be corrected for additional direct acceptor excitation  $DE$  and relative concentration dependent brightness  $DE_{rel}$ . Furthermore all samples were corrected for distinct fluorescence quantum yields  $\Phi$  and a spectral shift factor  $\gamma$  (especially for TGR5 Y111A) which is considered in the corrected green detection efficiency ( $g_G^*$ ).

$$F_D = \frac{S_G - \langle B_G \rangle}{g_G^*} \quad (1)$$

$$F_A = \frac{S_Y - (\langle B_Y \rangle + DE_{rel}) - \alpha(S_G - \langle B_G \rangle)}{g_Y} \quad (2)$$

The crosstalk factor  $\alpha$  is determined as the ratio between donor photons detected in the yellow channels and those detected in the green channels for the Donor only (Only) labeled sample. The corrected detection efficiency  $g_G^*$  is determined as the ratio of the spectral shift influenced by green detection (0.69) and expected green detection (1.12) multiplied with the quantum yield  $\Phi_{Y111A}$  obtained from a self-made detection efficiency software. The  $F_D/F_A$  parameters for each variant are provided in **Supporting Table 1**

The simultaneous reduction in both FRET indicators  $\langle \tau_{D(A)} \rangle_f$  and  $(F_D/F_A)$  indicate FRET due to proteins interaction. For a given sub-population selection of the donor fluorescence decay histogram with 32 ps time resolution was constructed for further pixel-integrated sub-ensemble analysis, and the species-averaged fluorescence lifetime of the donor  $\langle \tau_{D(A)} \rangle_x$  was calculated based on fit results (species fractions  $x_i$  and lifetimes  $\tau_{D(A)}$ )

$$\langle \tau_{D(A)} \rangle_x = \sum_{i=1}^n x_i \cdot \tau_{D(A),i} \quad (3)$$

$n$  is the number of exponents used in donor fluorescence lifetime fitting.

### Determination of acceptor and donor concentration from MFIS experiments

TGR5 monomers were either labelled with donor or acceptor fluorescent proteins and transiently transfected into cells with different donor-to-acceptor concentration ratios. The fractions of active donor (denoted as  $D$ ) and active acceptor (denoted as  $A$ ) is  $f_D$  and  $f_A$  respectively. The rest are inactive FPs, which we considered as dark (i.e. no fluorescence emission) and dysfunctional (i.e. FRET-negative). To calculate the protein concentrations from fluorescence intensity, the detection volume of our microscope and GFP and mCherry brightness are required. The

detection volume was determined as  $1.23 \cdot 10^{-15}$  l from FCS measurements of Cyanine 3B (Cy3B). The fitting model applied to the obtained FCS curve assumes a 3-dimensional Gaussian-shaped volume, and a single diffusing species including transitions to a triplet state as described in <sup>7</sup>. The brightness of enhanced GFP and mCherry *in vivo* were individually characterized from FCS measurements of freely diffusing FPs in cytoplasm. We found that with 0.6  $\mu$ W of 559 nm laser excitation at the objective, mCherry brightness is 0.68 kcpm in cytoplasm. With 0.4  $\mu$ W of 485 nm laser excitation at the objective, GFP brightness is 0.56 kcpm in cytoplasm.

The average mCherry fluorescence intensity of an image with mCherry excitation ( $S_{Y,Y}^m$ ) was first corrected for detector dead time, and then used to calculate the total concentration of mCherry,  $[A]_0$ , with the determined detection volume and the mCherry brightness:

$$\begin{aligned} [A]_0 &= \frac{S_{Y,Y}^m}{\text{brightness [kcpm]} * \text{confocal volume [fl]}} \\ &= \frac{S_{Y,Y}^m}{0.68 \text{ kcpm} * 0.8 \text{ fl}} \end{aligned} \quad (4)$$

The average GFP fluorescence intensity of an image with GFP excitation was also corrected for detector dead time, and then the obtained intensity ( $S_{G,G}^m$ ) was further corrected for the quenching effect due to FRET:

$$S_{G,G} = \frac{S_{G,G}^m}{(1 - x_{FRET}) + x_{FRET} \cdot (1 - E)} \quad (5)$$

$S_{G,G}$  is the unquenched GFP fluorescence intensity in the absence of FRET, the energy transfer efficiency E and fraction of FRET-active population,  $x_{FRET}$ , were calculated as described in the main method sections.  $S_{G,G}$  was then used to calculate the total concentration of GFP,  $[D]_0$ . The wavelength dependent confocal volume is 0.5 fl.

Assuming the concentration of the FPs reflects the concentration of their host proteins, the TGR5 concentration (without non-fluorescent molecules) in  $\mu\text{M}$  was determined as:

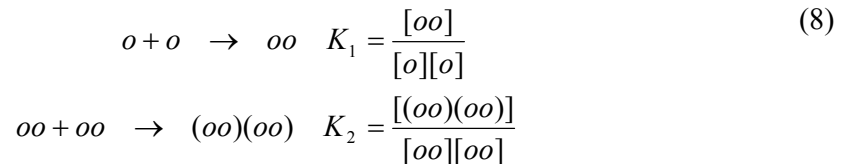
$$\text{protein concentration} = [A]_0 + [D]_0 = c_A + c_D \quad (6)$$

### Estimation of the association constants for oligomerization

The total protein concentration and the protein association constants have to be considered to determine the oligomerization state or the chemical speciation. To calculate the transfer-efficiency for a given oligomerization the spatial organization of the molecules within the oligomers and the concentration of donor, acceptor and non-fluorescent molecules has to be considered. The total protein concentration (**equation (6)**) is given by the sum of the acceptor, the donor and the unlabeled protein concentration:

$$c_T = c_A + c_D + c_U \quad (7)$$

Here the unlabeled protein concentration  $c_u$  equals the concentration of immature mCherry. The protein concentrations were calculated using the brightness of free GFP and free mCherry as reference. Even though higher-order oligomerization is anticipated we used a simple dimer/tetramer model to describe our data as this allows for a quantitative description. In this model we assume that a tetramer is constituted of a dimer of dimers (**Supporting Fig. 6**). Hence, starting from a monomer two equilibriums have to be treated:





Here  $o$  is a monomer,  $oo$  a dimer and  $(oo)(oo)$  is a tetramer. We use the monomer  $o$  as a master species. Then the total protein concentration is given by:

$$c_T = [o] + 2 \cdot [oo] + 4 \cdot [(oo)(oo)] \quad (9)$$

Now, the concentrations of the three species  $o$ ,  $oo$  and  $(oo)(oo)$  for any given the total protein concentration is obtained by solving the three equations above.

To calculate the transfer efficiency we assume that donor, acceptor and unlabeled molecules behave biochemically identical. Hence, the probability of an oligomer composition is given by the probability of finding a donor, acceptor or unlabeled molecule and the counting statistics. The probabilities of finding a donor, acceptor or unlabeled molecule depend on their respective concentrations. For instance the probability of an acceptor molecule is given by the respective species and total protein concentration:

$$p_A = \frac{c_A}{c_T} \quad (10)$$

In a tetramer the sum of donor, acceptor and unlabeled molecules is constant. The probability of a certain tetramer composition is obtained by the multinomial distribution:

$$\begin{aligned} p(n_D, n_A, n_U) &= N \cdot p_D^{n_D} p_A^{n_A} p_U^{n_U} \\ &= \frac{(n_D + n_A + n_U)!}{n_D! n_A! n_U!} \cdot p_D^{n_D} p_A^{n_A} p_U^{n_U} \end{aligned} \quad (11)$$

$N$  is the number of combinations for a given composition. Each combination might have a different FRET-rate distribution. Hence, in case of two donors and two acceptors 6 combinations as shown in **Supporting Fig. 6** contribute to the signal. If only species with at least one donor and one acceptor are considered the FRET-rate constants of overall 38 distinct species and their respective probabilities and FRET-rate constant distributions have to be calculated. The species

probabilities summarized by their donor and acceptor composition in dependence of the acceptor to donor ratio  $c_A/c_D$  are illustrated in **Supporting Fig. 6**.

FRET-rate constants are additive. Therefore in case of multiple acceptors the total FRET-rate constant experienced by a donor (i) is given by the sum of all FRET-rate constants of all acceptors (j):

$$k_{RET}^{(i)} = \frac{1}{\tau_0} \cdot \sum_j \left( \frac{R_{DA}^{(ij)}}{R_0} \right)^6 \quad (12)$$

Here  $R_{DA}^{(ij)}$  is the donor acceptor distance between the donor (i) and the acceptor (j) which is determined by the spatial arrangement of the oligomer. For instance, in the case as illustrated in **Supporting Fig. 6** the two FRET-rates experienced by the donor at position 1 and the donor at position 4 are given by:

$$k_{RET}^{(1)} = \frac{1}{\tau_0} \cdot \left( \left( \frac{R_{DA}^{(13)}}{R_0} \right)^6 + \left( \frac{R_{DA}^{(12)}}{R_0} \right)^6 \right) \quad (13)$$

$$k_{RET}^{(4)} = \frac{1}{\tau_0} \cdot \left( \left( \frac{R_{DA}^{(42)}}{R_0} \right)^6 + \left( \frac{R_{DA}^{(43)}}{R_0} \right)^6 \right)$$

These FRET-rates result in first approximation in bi-exponential fluorescence decay, if the coupling between the two donors is not considered.

For a given structural arrangement all FRET-rate constants for all possible compositions (one donor one acceptor, two donors one acceptor, etc.) were calculated (**Supporting Fig. 6**). Later the average transfer-efficiencies of the tetramer compositions containing at least one donor and one acceptor were calculated.

It has to be considered that the contribution to the fluorescence signal depends on the number of donor molecules. For instance a tetramer constituted out of three donors and one acceptor molecule contributes three times more to the total signal as compared to a tetramer only constituted out of one donor, one acceptor and two unlabeled molecules.

The predicted transfer efficiency for each data point depends now only on the equilibrium association constants  $K_1$ ,  $K_2$  and the spatial arrangement of the fluorophores in the dimer and the tetramer. To reduce the number of free parameters we assumed that the tetramer can be described by a rectangular geometry where one edge is approximately 100 Å long while the second edge is between 40-50 Å long (**Supporting Fig. 6**). This assumption is in line with the homology models (**Supporting Table 5** and **Supporting Fig. 7**). Furthermore, only FRET molecules have been selected. Therefore, the first equilibrium from monomer to dimer is not monitored and only the equilibrium constant of the tetramer formation is probed. Thus, only  $K_2$  and the dimer distance in the range of 40-60 Å is reflected in the data. For the measurements we find that a short distance of approximately 45 Å describes the data best. For the TGR5 wt and Y111F variant we find predominately a tetrameric or higher-order oligomer configuration while in case of the Y111A mutant the molecules are predominately in a dimeric configuration.

### **Statistical analysis**

Experiments were performed independently at least three times. For MFIS-FRET at least nine cells per series in three independent experiments were measured. Results are expressed as mean  $\pm$  standard error of the mean (SEM) and analysed using the two-sided student t-test. A  $p \leq 0.01$  was considered statistically significant.

### 3. Molecular modelling and simulation

#### Structural models of TGR5 dimers and tetramers

**Dimer models** with the interface TM1 and H8 (1/8) were generated by structurally aligning two homology models of TGR5<sup>8</sup> onto the dimeric crystal structure of the human  $\kappa$ -opioid receptor (PDB ID: 4DJH<sup>9</sup>) via the ‘cealign’ command in Pymol<sup>2</sup>. For dimer models with the 4/5 interface and the 5/6 interface the same procedure was applied using the human CXCR4 receptor (PDB ID: 3ODU<sup>10</sup>) and the murine  $\mu$ -opioid receptor (PDB ID: 4DKL<sup>11</sup>) as alignment templates, respectively.

**Tetramer models** were built in a similar fashion. Here, two TGR5 dimers with the same dimer interface, e.g. (1/8), were aligned on another TGR5 dimer with a different interface, e.g. (4/5). With this procedure six tetramers were generated: (1/8) and (5/6) dimers with an oligomeric interface of (4/5); (1/8) and (4/5) dimers with an oligomeric interface of (5/6); (4/5) and (5/6) dimers with an oligomeric interface of (1/8). Subsequently, the interface residues of the respective dimer and tetramer models were energy minimized in Maestro<sup>12,13</sup> using the VSGB 2.0 solvation model<sup>14</sup>. Finally, either dimer and tetramer model were submitted to the OPM server<sup>15</sup> to compute its orientation in a membrane.

#### Explicit linker simulations: Molecular dynamics simulations of GFP bound to a linker

For computing a thermodynamic ensemble (TE) of GFP positions with an explicit linker/GFP construct, initially, the structure of the TGR5 C-terminal residues 296-330, for which no experimental structural information is available, and the nine residues that connect the C-terminus to GFP (total sequence: QRCLQGLWGRASRDS PGPSIAYHPSSQSSVDLIDLN YGSTGRHVS) was generated with the ‘Protein building’ approach in Maestro. Phi and psi angles of zero were chosen, resulting in a straight peptide conformation and, hence, a structurally

unbiased starting structure for the molecular dynamics (MD) simulations. This linker was subsequently fused to enhanced GFP (PDB ID: 4EUL<sup>16</sup>), and the resulting structure was capped with acetyl and *N*-methyl amide groups at the N- and C-termini, respectively, and protonated with PROPKA<sup>17</sup> according to pH 7.4. We assumed the thermodynamic ensemble (TE) of mCherry to be identical to that of GFP.

Then, the linker/GFP construct was neutralized by adding counter ions and solvated in an octahedral box of TIP3P water<sup>18</sup> with a minimal water shell of 12 Å around the solute. The Amber14 package of molecular simulation software<sup>19,20</sup> and the ff14SB and GAFF<sup>21</sup> force fields were used to perform an all-atom MD simulations. To cope with long-range interactions, the “Particle Mesh Ewald” method<sup>22</sup> was used, and the SHAKE algorithm<sup>23</sup> was applied to bonds involving hydrogen atoms. The time step for all MD simulations was 2 fs with a direct-space, non-bonded cut-off of 8 Å. The first linker residue was fixed with positional harmonic restraints with a force constant of 100 kcal mol<sup>-1</sup> Å<sup>-2</sup> throughout the simulations to emulate that this residue would be bound to TGR5 embedded in a membrane. At the beginning, 17500 steps of steepest decent and conjugate gradient minimization were performed; during 2500, 10000, and 5000 steps positional harmonic restraints with force constants of 25 kcal mol<sup>-1</sup> Å<sup>-2</sup>, 5 kcal mol<sup>-1</sup> Å<sup>-2</sup>, and zero, respectively, were applied to the solute atoms. Thereafter, 50 ps of NVT-MD (MD simulations with a constant number of particles, volume, and temperature) were conducted to heat up the system to 100 K, followed by 300 ps of NPT-MD (MD simulations with a constant number of particles, pressure, and temperature) to adjust the density of the simulation box to a pressure of 1 atm and to heat the system to 300 K. During these steps, a harmonic potential with a force constant of 10 kcal mol<sup>-1</sup> Å<sup>-2</sup> was applied to the solute atoms. As the final step in thermalization, 300 ps of NVT-MD simulations were performed while gradually reducing the restraint forces on the solute atoms to zero within the first 100 ps of this step. Afterwards, six

independent production runs of NVT-MD simulations with 150 ns length each were performed. For this, the starting temperatures of the simulations at the beginning of the thermalization were varied by a fraction of a Kelvin. The conformations obtained in these simulations were pooled for further analyses.

### **Implicit linker simulations**

Inter-dye distance distributions for all TGR5 dimer and tetramer models were calculated using an modified Accessible Volume (AV) approach<sup>24</sup>. Firstly, the different protein models (see 5.14) were embedded in an explicit membrane via the CHARMM-GUI membrane builder<sup>25</sup>. Here, a membrane with 5500 lipids of 1,2-dioleoyl-*sn*-glycero-3-phosphocholine (DOPC) per layer was created employing default settings of the CHARMM-GUI. This resulted in a membrane bilayer of about 1.5 million atoms and a side length of about 620 Å to prevent the linker/GFP construct (which has an extended length of about ~229 Å) from wrapping around the edge of the membrane. As neither ions nor water were needed for AV calculations, the steps of ion and water addition were omitted during the creation of the membrane.

For the AV simulations the fluorescent probe was attached to the C-terminal amino acid of the TGR5 via a flexible linker of 203.5 Å corresponding to 55 amino acids (36 amino acids of the TGR5 C-terminus, a 6 amino acid cloning linker, and the first 13 amino acids of the GFP's (PDB ID: 4EUL) N-terminus, **see Supporting Table 2**) with a length of 3.7 Å each<sup>26</sup>. A dye radius of 25 Å was used as an approximation for the GFP size, resulting in a total length of ~229 Å for the linker/GFP construct. The distance between linker attachment points in most of the screened oligomer models was shorter than the effective size of the AVs resulting in AV overlap. The AVs were constructed considering geometric factors in terms of steric exclusion effects caused by the TGR5 oligomer and the membrane. To account for clashes between the dyes, which are

not addressed in the AV simulations, the inter-dye distance probability was set to zero for all distances below 25 Å. To account also for entropic effects, we introduced position weights for the implicitly modelled linker according to the Gaussian chain model, so that the non-uniform dye position probability distribution in the AV was scaled (**Supporting Fig. 7**)<sup>27</sup>. In the Gaussian chain model a segment length of 7.4 Å was used, as obtained from the calibration aimed to reproduce the accurate end-to-end distance probability distribution from coarse-grained Monte-Carlo simulations of the peptide linker, similar to previously published results for the flexibly linked GFP dimer<sup>28</sup>. The obtained AV positional distributions were used to determine the inter-probe distance distribution by measuring all distances from positions in one AV distribution with respect to all positions in the second AV distribution. Considering oligomerization (tetramer) where two acceptors may be present in the vicinity of one donor, we computed the apparent distance distribution shifts towards shorter distances by convolution of the two inter-probe distance distributions ((1/8) and (4/5)) (**Supporting Fig. 5**).

## Glossary

$F_D/F_A$	fluorescence intensity ratio
$B$	background
$\alpha$	crosstalk factor
$g$	detection efficiencies
$DE$	direct acceptor excitation
$DE_{rel}$	relative concentration dependent brightness
$\Phi$	distinct fluorescence quantum yields
$\gamma$	spectral shift factor
$g_G^*$	corrected green detection efficiency
$\varepsilon(t)$	pixel-integrated, time-resolved FRET analysis
DA	donor acceptor FRET pair
$f(t)$	fluorescence signal decay
D(0)	unquenched donor
D(A)	Donor quenched by acceptor
IRF	instrument response function
$x$	species fraction
$x_D$	donor (Donly) or Non-FRET fraction
$x_A$	acceptor fraction
AV	Accessible Volume
$\langle R_{DA} \rangle_{app}$	Apparent mean distance between Donor and Acceptor
$\langle \tau_{D(0)} \rangle_f$	Fluorescence-averaged unquenched donor fluorescence lifetime
$S_{em,ex}$	Signal <sub>emission, excitation</sub>
$S_{G,G}$	Signal of green photons emitted after excitation of GFP
$S_{Y,G}$	Signal of mCherry photons emitted after excitation of GFP
$c$	Concentration
$[D]_0, [A]_0$	Real donor and acceptor concentration



$E_{mean}$	Mean Transfer efficiency
wt	wildtype
MFIS-FRET	Multiparameter Fluorescence Imaging Spectroscopy-Förster Resonance Energy Transfer

## Supporting References

- 1 DeLano, W. L. & Lam, J. W. PyMOL: A communications tool for computational models. *Abstr Pap Am Chem S* **230**, U1371-U1372 (2005).
- 2 Schrödinger, L. The PyMOL molecular graphics system, version 1.3 r1. Py-MOL, The PyMOL Molecular Graphics System, Version 2010,. (2010).
- 3 King, C., Sarabipour, S., Byrne, P., Leahy, D. J. & Hristova, K. The FRET Signatures of Noninteracting Proteins in Membranes: Simulations and Experiments. *Biophys J* **106**, 1309-1317, doi:10.1016/j.bpj.2014.01.039 (2014).
- 4 Spomer, L. *et al.* A Membrane-proximal, C-terminal alpha-Helix Is Required for Plasma Membrane Localization and Function of the G Protein-coupled Receptor (GPCR) TGR5. *J Biol Chem* **289**, 3689-3702, doi:10.1074/jbc.M113.502344 (2014).
- 5 Keitel, V. *et al.* The Membrane-Bound Bile Acid Receptor TGR5 Is Localized in the Epithelium of Human Gallbladders. *Hepatology* **50**, 861-870, doi:10.1002/hep.23032 (2009).
- 6 Hov, J. R. *et al.* Mutational Characterization of the Bile Acid Receptor TGR5 in Primary Sclerosing Cholangitis. *Plos One* **5**, doi:e1240310.1371/journal.pone.0012403 (2010).
- 7 Weidtkamp-Peters, S. *et al.* Multiparameter fluorescence image spectroscopy to study molecular interactions. *Photochem Photobiol Sci* **8**, 470-480, doi:10.1039/b903245m (2009).
- 8 Gertzen, C. G. W. *et al.* Mutational mapping of the transmembrane binding site of the G-Protein coupled receptor TGR5 and binding mode prediction of TGR5 agonists. *Eur J Med Chem* doi:10.1016/j.ejmech.2015.09.024 (2015).
- 9 Wu, H. *et al.* Structure of the human kappa-opioid receptor in complex with JD1c. *Nature* **485**, 327-U369, doi:10.1038/nature10939 (2012).
- 10 Wu, B. *et al.* Structures of the CXCR4 Chemokine GPCR with Small-Molecule and Cyclic Peptide Antagonists. *Science* **330**, 1066-1071, doi:10.1126/science.1194396 (2010).
- 11 Manglik, A. *et al.* Crystal structure of the mu-opioid receptor bound to a morphinan antagonist. *Nature* **485**, 321-U170, doi:10.1038/nature10954 (2012).
- 12 Maestro (Schrödinger, LLC., New York, NY, 2014).
- 13 Version 9.9.013 (Schrödinger LLC, New York, NY, 2014).
- 14 Li, J. *et al.* The VSGB 2.0 model: A next generation energy model for high resolution protein structure modeling. *Proteins-Structure Function and Bioinformatics* **79**, 2794-2812, doi:10.1002/prot.23106 (2011).
- 15 Lomize, M. A., Lomize, A. L., Pogozheva, I. D. & Mosberg, H. I. OPM: Orientations of proteins in membranes database. *Bioinformatics* **22**, 623-625, doi:10.1093/bioinformatics/btk023 (2006).
- 16 Arpino, J. A. J., Rizkallah, P. J. & Jones, D. D. Crystal Structure of Enhanced Green Fluorescent Protein to 1.35 angstrom Resolution Reveals Alternative Conformations for Glu222. *Plos One* **7**, doi:e4713210.1371/journal.pone.0047132 (2012).
- 17 Bas, D. C., Rogers, D. M. & Jensen, J. H. Very fast prediction and rationalization of pK(a) values for protein-ligand complexes. *Proteins-Structure Function and Bioinformatics* **73**, 765-783, doi:10.1002/prot.22102 (2008).
- 18 Jorgensen W, C. J., Madura JD, Impey R and Klein ML. Comparison of simple potential functions for simulating liquid water. *The Journal of Chemical Physics* **79**, doi:10.1063/1.445869 (1983).
- 19 Case, D. A. *et al.* The Amber biomolecular simulation programs. *J Comput Chem* **26**, 1668-1688, doi:10.1002/jcc.20290 (2005).
- 20 D.A. Case, V. B., J.T. Berryman, R.M. Betz, Q. Cai, D.S. Cerutti, T.E. Cheatham, III, T.A. Darden, R.E. Duke, H. Gohlke, A.W. Goetz, S. Gusarov, N. Homeyer, P. Janowski, J. Kaus, I. Kolossváry, A. Kovalenko, T.S. Lee, S. LeGrand, T. Luchko, R. Luo, B. Madej, K.M. Merz, F.

- Paesani, D.R. Roe, A. Roitberg, C. Sagui, R. Salomon-Ferrer, G. Seabra, C.L. Simmerling, W. Smith, J. Swails, R.C. Walker, J. Wang, R.M. Wolf, X. Wu and P.A. Kollman AMBER 14. (2014).
- 21 Wang, J. M., Wolf, R. M., Caldwell, J. W., Kollman, P. A. & Case, D. A. Development and testing of a general amber force field. *J Comput Chem* **25**, 1157-1174, doi:10.1002/jcc.20035 (2004).
- 22 Darden, T., York, D. & Pedersen, L. PARTICLE MESH EWALD - AN N.LOG(N) METHOD FOR EWALD SUMS IN LARGE SYSTEMS. *J Chem Phys* **98**, 10089-10092, doi:10.1063/1.464397 (1993).
- 23 Ryckaert, J. P., Ciccotti, G. & Berendsen, H. J. C. NUMERICAL-INTEGRATION OF CARTESIAN EQUATIONS OF MOTION OF A SYSTEM WITH CONSTRAINTS - MOLECULAR-DYNAMICS OF N-ALKANES. *J Comput Phys* **23**, 327-341, doi:10.1016/0021-9991(77)90098-5 (1977).
- 24 Kalinin, S. *et al.* A toolkit and benchmark study for FRET-restrained high-precision structural modeling. *Nat Methods* **9**, 1218-1225, doi:10.1038/nmeth.2222 (2012).
- 25 Jo, S., Lim, J. B., Klauda, J. B. & Im, W. CHARMM-GUI Membrane Builder for mixed bilayers and its application to yeast membranes. *Biophys J* **97**, 50-58, doi:10.1016/j.bpj.2009.04.013 (2009).
- 26 Evers, T. H., van Dongen, E. M., Faesen, A. C., Meijer, E. W. & Merks, M. Quantitative understanding of the energy transfer between fluorescent proteins connected via flexible peptide linkers. *Biochemistry* **45**, 13183-13192, doi:10.1021/bi061288t (2006).
- 27 Chiang, J., Li, I., Pham, E. & Truong, K. FPMOD: a modeling tool for sampling the conformational space of fusion proteins. *Conference proceedings : ... Annual International Conference of the IEEE Engineering in Medicine and Biology Society. IEEE Engineering in Medicine and Biology Society. Conference* **1**, 4111-4114, doi:10.1109/IEMBS.2006.259224 (2006).
- 28 Evers, T. H., van Dongen, E. M., Faesen, A. C., Meijer, E. W. & Merks, M. Quantitative understanding of the energy transfer between fluorescent proteins connected via flexible peptide linkers. *Biochemistry* **45**, doi:10.1021/bi061288t (2006).